Journal of Experimental and Theoretical Physics, Vol. 91, No. 2, 2000, pp. 227–238.
Translated from Zhurnal Éksperimental'noĭ i Teoreticheskoĭ Fiziki, Vol. 118, No. 2, 2000, pp. 259–272.

GRAVITATION, ASTROPHYSICS

Cosmological Inflation Models Admitting Natural Emergence to the Radiation-Dominated Stage and the Matter Domination Era

V. M. Zhuravlev* and S. V. Chervon**

Ul'yanovsk State University, Institute of Theoretical Physics, Ul'yanovsk, 432700 Russia
**e-mail: zhuravl@sv.uven.ru*
***e-mail: chervon@sv.uven.ru*

Received December 30, 1999

Abstract—A model of the evolution of the uniform and isotropic spatially-flat universe, where the inflation stage emerges naturally into the radiation-dominated stage and the matter-dominated era, is proposed on the basis of exact solutions of the self-consistent equations of a gravitating self-acting scalar field. It is shown that the model contains two basic physical mechanisms, one of which is related with the decay of Higgs bosons and provides for the inflation stage, while the second mechanism is associated with the adiabatic expansion of the universe filled with matter with a definite equation of state and gives a Friedmann expansion regime. © *2000 MAIK "Nauka/Interperiodica".*

1. INTRODUCTION

The theory of cosmological inflation is an integral part of the general theory of the evolution of the universe, which solves the problems of the horizon (uniformity), flatness, and relic monopoles and at the same time describes quite accurately the large-scale structure, based on the quantum effects of the microphysics of the early universe. Thus, a general picture emerges of the evolution of the universe from Planck times to present via the stage of inflationary expansion to the radiation-dominated stage followed by a transition to the matter-dominated era. However, the theory of inflation contains definite difficulties concerning the choice of the appropriate model for the completion of the inflationary stage and the emergence of evolution into the radiation-dominated stage: there arises the so-called problem of "emergence" from inflation, which is classified in the original work of Guth [1] as the central problem of the inflationary scenario. To solve this problem it is necessary to have a model that contains a phase-transition type mechanism for substantial conversion of matter. Models of this type have been known since the first works on inflation [2, 3]. Investigations in this direction continue today (see, for example, [4]). However, existing models are constructed, as a rule, on the basis of very complicated assumptions about the character of the physical processes leading to the inflationary scenario and the emergence out of this scenario. This concerns first and foremost the theories which treat the inflationary stage on the basis of the quantum behavior of matter and the universe as a whole. The Lagrangians or energy-momentum tensors of these models are very complicated and often contain phenomenological parameters which are not known accurately, which makes it impossible to understand in detail the essence of the processes occurring in the universe during inflation as well as before and after inflation (see, for example, [2]). The mathematical complexity of these models makes it necessary to use approximate methods for investigating them, adapted to each of the time intervals of the evolution of the universe, which are separated by short time intervals where phase transformations of matter occur. Analysis of the status of the problem shows that thus far a simple model, which describes equally successfully the evolution of the universe over the entire time interval from the onset of the inflationary epoch to the modern Freidman stage, has not been proposed.

In the present paper we propose a cosmological model of inflation (based on exact solutions of the self-consistent equations of a spatially-flat universe) generated by a self-acting scalar field. In this model the problem of the general evolution of the universe is solved qualitatively on the basis of quite simple and clearly identified mechanisms for the appearance of inflation and completion of inflation with natural emergence into the radiation-dominated stage (RD stage) and the matter-dominated era. This approach is largely based on the results of investigations concerned with the search for exact solutions in models of cosmological inflation, which are reflected in the monograph [5] and in [6–9], and it rests strongly on the results of [10, 11].

In this paper attention is focused precisely on the solution of the problem of emergence from inflation, since the transition from radiation domination in the universe to matter domination has been studied quite well [12, 13]. We recall that the existence of the inflationary stage in the evolution of the universe, when the

scaling factor increased extremely rapidly, is one of the main requirements which modern observational data impose on the theory of the early universe [3]. The completion of the inflation stage should be accompanied by the emergence of inflation into a sequence of Freidmann-expansion epochs, where the scaling factor evolves according to a power law, $R(t) \propto t^s$, where $s < 1$. Here $s = 1/2$ for the RD stage and $s = 2/3$ for the matter-dominated regime. We note that each value of s corresponds to a definite equation of state of matter in the standard big-bang theory [12].

In models of the evolution of the early universe, which are constructed on the basis of the theory of a self-acting scalar field (SSF), the inflationary regime is not specific and is due to a large number of self-action potentials for the inflation field [8, 10]. However, the condition for completion of the inflationary stage with emergence into a prescribed Freidmann-expansion stage is specific, and it is realized only if special requirements are met. Specifically, a model of inflation which admits an analytical emergence into the RD stage and dust-like matter is proposed in [4]. In contrast to our approach, in [4] the dependence of the Hubble "constant" $H \equiv \dot{R}/R$ on $\ln R$ was used, and the number of e increases in the radius of the universe is taken as a dynamical variable.

The slow slide approximation [3] plays a special role in the construction of the inflation scenario. This approximation is based on an analysis of the simplified equations of cosmological evolution. Since substantial progress in understanding the mechanism leading to the formation of the large-scale structure has been made precisely in this direction, it is important to establish the relation between our approach and the solutions obtained with the slow-slide regime.

Until recently, virtually all inflationary scenarios were based on approximate solutions of the models of a gravitating SSF. Searches for exact solutions for inflation models became somewhat active only in the last five years (see [10] and the literature cited there). Specifically, we call attention to the models constructed by adjusting the self-action potential (for example, [8, 14, 15]) on the basis of definite considerations about the general character of the evolution of either the scaling factor or the inflationary field. This approach presumes that the exactly constructed potential and its specific form will suggest a corresponding model of elementary-particle physics and hence also the physical reasons for the appearance and completion of inflation. We note that in the present paper our goal is not to study in detail the behavior of all matters considered from the standpoint of the evolution of density disturbances in them. This work requires additional investigations. Our problem is to develop a quite general method for constructing inflation models with appropriate asymptotic properties of emergence into a particular stage of the Friedmann expansion. Moreover, the Λ term is not present explicitly in the models studied in the present paper. However, we note that the self-action potential of the scalar field can be interpreted in terms of a variable cosmological Λ term. This question has been examined in [16] and in detail in the review [17]. From the standpoint of these works the inflation models constructed in the present paper likewise can be viewed as models with a variable cosmological Λ-term, which describe the accelerated expansion of the universe which is observed in the current matter-dominated epoch.

The present paper is organized as follows. The first auxiliary model is studied in Section 2. An asymptotic condition for cosmological models of the general evolution of the universe, which actually means that the total energy of the inflanton field approaches zero in the modern epoch, is formulated on the basis of an analysis of the massive scalar field model. A model with a Higgs-type self-action potential is investigated in detail, as a simple model satisfying the indicated condition. Exact solutions admitting an inflation regime, whose appearance is due to the decay of Higgs bosons, are found. Certain drawbacks of the model are noted: breakdown of the principle of energy dominance and emergence into an asymptotically static universe.

A second auxiliary model, admitting emergence into a Friedmann regime of evolution, is studied in Section 3. This model is based on one of the solutions obtained in [10]. An exact solution which is the product of a power-law function of the cosmic time by an exponential function, is found.

A model of the general evolution of the universe, which admits an inflationary regime and emergence from this regime into a Friedmann evolution, is constructed in Section 4 on the basis of two auxiliary models. The change in the scaling factor, the scalar field, and the potential is analyzed using plots.

Certain features of the proposed model and the ways for further investigations of new models of this type are examined in Section 5. It is noted, specifically, that a situation is possible where a power-law regime (possibly power-law inflation), which converts into an exponential regime, dominates at the pre-inflation stage.

In the Conclusions (Section 7) it is noted that our model qualitatively describes all basic aspects of the general evolution of the universe and that there arises the problem of performing quantitative calculations in matching the model with the observational data on large-scale structure.

2. ON THE AGREEMENT BETWEEN THE EXACT AND APPROXIMATE SOLUTIONS OF THE MODEL

The standard cosmological model of SSF, which includes an inflation stage, for a spatially-flat, uniform, and isotropic universe is described by the system of equations [3]

$$H^2 = \frac{\kappa}{3}\left(\frac{1}{2}\dot{\phi}^2 + V(\phi)\right), \qquad (1)$$

$$\ddot{\phi} + 3H\dot{\phi} = -\frac{d}{d\phi}V(\phi), \quad (2)$$

where ϕ is a scalar field, $V(\phi)$ is the self-action potential of the scalar field,

$$H(t) = \frac{d}{dt}\ln R(t),$$

$R(t)$ is a scaling factor and κ is the gravitational constant. The standard procedure for constructing approximate solutions of this system of equations for the inflation regime consists in neglecting in this equation the terms $\ddot{\phi}$ and $\dot{\phi}^2$ as compared with $H\dot{\phi}$ and H^2; this is the basis for the "slow slide" approximation. As a result of this procedure, the initial equations assume the following simple form:

$$H^2 = \frac{\kappa}{3}V(\phi), \quad (3)$$

$$3H\dot{\phi} = -\frac{d}{d\phi}V(\phi), \quad (4)$$

which are much easier to integrate. For example, following the review [18], we obtain

$$R_s(\phi) = R_0\exp\left\{-\kappa\int\frac{V}{V'}d\phi\right\}. \quad (5)$$

We shall show that the exact equations (1) and (2) can be represented in the form of Eqs. (3) and (4) by introducing an effective self-action potential. The relation

$$\dot{\phi} = U(\phi), \quad (6)$$

where $U(\phi)$ is a function of ϕ, which holds for any function $\phi = \phi(t)$, is satisfied formally. We now introduce the effective self-action potential $W(\phi)$ according to the rule

$$W(\phi) = V(\phi) + \frac{1}{2}U^2(\phi). \quad (7)$$

The function $W(\phi)$ is the total energy of the field as a function of the values of the field. Using Eq. (7), Eqs. (1) and (2) can be put into the form

$$H^2 = \frac{\kappa}{3}W(\phi), \quad (8)$$

$$3H\dot{\phi} = -\frac{d}{d\phi}W(\phi). \quad (9)$$

As one can see, Eqs. (8) and (9) are identical to the truncated Eqs. (3) and (4) to within a substitution of $W(\phi)$ for $V(\phi)$. The scaling factor (5) in the exact model is

$$R(\phi) = R_0\exp\left\{-\kappa\int\frac{W}{W'}d\phi\right\}. \quad (10)$$

The equations (8) and (9) lead to the relation

$$\sqrt{3\kappa}UW^{1/2} = -W', \quad (11)$$

which, together with Eq. (7), describes the relation between the functions $W(\phi)$ and $U(\phi)$, so that only one of these functions is arbitrary. Using the relation (11) we obtain

$$R(t) = R_0\exp\left\{\int_{t_0}^{t}\sqrt{\frac{\kappa}{3}W(t)}dt\right\}. \quad (12)$$

The equations of the SSF model in the form (8) and (9) are the starting point for the inflation model, being considered here, with emergence into a Friedmann regime of evolution.

Solving Eq. (11) for W, we obtain

$$W(\phi) = \frac{3\kappa}{4}\left(-\int U(\phi)d\phi + \sqrt{W_0}\right)^2 \geq 0, \quad (13)$$

where $\sqrt{W_0}$ is a real integration constant. Hence it follows that in the present model the total energy of the field and therefore the effective potential W are nonnegative quantities.

In what follows we shall employ the following terminology for the potentials $V(\phi)$ and $W(\phi)$. We shall call the SSF potential $V(\phi)$ in the representation of the exact equations (1) and (2) the true or physical potential. We shall call the effective potential $W(\phi)$ the effective potential of the total energy (the total energy potential for brevity) in order to distinguish it from the effective potentials employed in quantum field theories. We also call attention to the fact that $V(\phi)$ or $W(\phi)$ can be regarded, depending on the interpretation of the model, as time-variable quantities, equivalent to the cosmological Λ term. This interpretation, as already noted above, has been analyzed in [16, 17].

3. ASYMPTOTIC CONDITIONS FOR EMERGENCE INTO A FRIEDMANN REGIME OF EVOLUTION

In order to use the obtained representation to construct models describing in a natural manner the emergence of the evolution of the universe into a Friedmann regime as $t \longrightarrow \infty$, it is necessary to formulate correctly the asymptotic conditions for such a transition. It turns out that the following requirement, which follows from an obvious analysis of the observational data, is a sufficient condition for this. Since in the present epoch the inflanton field is not observed in the observational data, this energy should be vanishingly small in the limit $t \longrightarrow \infty$. Therefore a natural requirement for models which should describe the cosmological evolution on

time intervals including the early universe and the modern epoch should be the asymptotic condition

$$\frac{1}{2}(\dot{\phi}(t))^2 + V(\phi) \longrightarrow 0 \text{ as } t \longrightarrow \infty. \quad (14)$$

This requirement can be decomposed into two other requirements:

$$\dot{\phi}(t) = U(\phi(t)) \longrightarrow 0 \text{ as } t \longrightarrow \infty, \quad (15)$$

$$V(\phi(t)) \longrightarrow 0 \text{ as } t \longrightarrow \infty. \quad (16)$$

Recently, there appeared experimental results attesting to the existence of a variable Λ term in the present-day universe [16, 17]. From the standpoint of these works, the asymptotic conditions correspond to $\Lambda \longrightarrow 0$ as $t \longrightarrow \infty$.

We note that Eq. (11), written in the form

$$\frac{d}{d\phi}\sqrt{W} = -\frac{\sqrt{3\kappa}}{2}U$$

or

$$W = \left(\sqrt{W_0} - \frac{\sqrt{3\kappa}}{2}\int U d\phi\right)^2,$$

where $\sqrt{W_0}$ is a constant of integration, gives a simple proof of the assertion that when the condition (15) is satisfied the system evolves into a state with a value of the field ϕ_∞ such that the potentials W and V simultaneously possess local extrema. It is also easy to calculate that the minimum of the potentials is attained if

$$\frac{d}{d\phi}U = \frac{\ddot{\phi}}{\dot{\phi}} = \frac{d}{dt}\ln\dot{\phi} > 0, \quad (17)$$

and the maximum is attained if

$$\frac{d}{d\phi}U = \frac{\ddot{\phi}}{\dot{\phi}} = \frac{d}{dt}\ln\dot{\phi} < 0. \quad (18)$$

Thus, the condition (17) corresponds to stable states being reached in the limit $t \longrightarrow \infty$, and unstable states in the case (18).

We also call attention to the fact that the condition (14) [correspondingly, Eqs. (15) and (16)] does not limit the growth of the field itself. Indeed, if $\phi \sim \ln t$ and $V(\phi) \longrightarrow 0$ as $t \longrightarrow \infty$, then the energy of the field approaches zero, while the field grows logarithmically. This fact is important for the Friedmann stage (see [10] and Section 5 below). Ordinarily, the scenarios of evolution of the universe are determined on a finite interval of evolution of the field, and it is assumed that the universe completes the transition from an unstable state for $\phi = 0$ to a stable state for $\phi = \phi_c < \infty$, which corresponds to a minimum of the self-action potential of the field [2, 3]. This example shows that this approach is not unique; moreover, it is shown in Section (5) that an asymptotic logarithmic growth of the field ϕ as energy approaches zero should exist in order to reach the Friedmann regime. Consequently, a stable state corresponding to a minimum of the potential at the point $\phi \longrightarrow \infty$ is attained only asymptotically as $t \longrightarrow \infty$. The fact that this was neglected seems to have created definite difficulties for constructing models with emergence into the Friedmann stage.

4. MODEL WITH AN EFFECTIVE HIGGS POTENTIAL

One of the simplest models satisfying the requirement (15) is the model where

$$\dot{\phi} = U(\phi(t)) = u_0 e^{-\mu t}, \quad \mu > 0. \quad (19)$$

For Eq. (19) we have

$$\phi(t) = \phi_\infty - \frac{u_0}{\mu}e^{-\mu t}, \quad (20)$$

so that

$$U(\phi) = \mu(\phi_\infty - \phi(t)).$$

Substituting this relation into Eq. (11), we find

$$W(\phi) = \left(\frac{\lambda}{4}(\phi - \phi_\infty)^2 - \sqrt{V_\infty}\right)^2, \quad (21)$$

$$R(\phi) = R_0 \exp\left\{-\kappa\int_{\phi_0}^{\phi}\frac{\lambda(\phi-\phi_\infty)^2 - 4\sqrt{V_\infty}}{4\lambda(\phi-\phi_\infty)}d\phi\right\}$$

$$= R_0 \exp\left\{\frac{\kappa}{8}(\phi_0 - \phi_\infty)^2\right\}\left|\frac{\phi-\phi_\infty}{\phi_0-\phi_\infty}\right|^\alpha \quad (22)$$

$$\times \exp\left\{-\frac{\kappa}{8}(\phi-\phi_\infty)^2\right\}.$$

Here

$$\lambda = \mu\sqrt{3k}, \quad \alpha = \frac{\kappa}{\lambda}\sqrt{V_\infty},$$

V_∞ is the potential in the limit as $t \longrightarrow \infty$, and ϕ_0 is the value of the field at an initial moment t_0. It is easy to see that for the potential (22) the condition (16) also holds if $V_\infty = 0$.

From the relation (7) we find the physical potential

$$V(\phi) = \left(\frac{\lambda}{4}(\phi-\phi_\infty)^2 - \sqrt{V_\infty}\right)^2 - \frac{1}{2}\mu^2(\phi_\infty - \phi)^2. \quad (23)$$

In this case this physical potential is the well-kwoun potential of the ϕ^4 theory with the Higgs mechanism for

spontaneous symmetry breaking. According to this theory the effective mass of a Higgs boson here will be

$$M_h = \sqrt{\lambda\sqrt{V_\infty} + \mu^2}.$$

The minima of the potential $V(\phi)$ occur at the points

$$\phi^\pm = \phi_\infty \pm 2\sqrt{\lambda\sqrt{V_\infty} + \frac{\mu^2}{\lambda^2}}$$

$$= \phi_\infty \pm 2\sqrt{\mu\sqrt{3\kappa V_\infty} + \frac{1}{3\kappa}},$$

and the maximum occurs at the point ϕ_∞ (see Figs. 1 and 2). If $V_\infty = 0$, we have, correspondingly,

$$M_h = \mu, \quad \phi^\pm = \phi_\infty + 2\sqrt{\frac{1}{3\kappa}}. \tag{24}$$

The relations (21), (22), (23), and (20) together give the exact solution of the problem of the evolution of the scale factor for this model. Substituting the function $\phi = \phi(t)$ into the expression for $R(\phi)$ we obtain

$$R(t) = R_0 \exp\left\{\frac{\kappa}{8}(\phi_0 - \phi_\infty)^2\right\}\left(-\frac{u_0}{\mu}\right)^\alpha$$

$$\times \left|\frac{1}{\phi_0 - \phi_\infty}\right|^\alpha e^{-\mu\alpha t}\exp\left\{-\frac{\kappa u_0^2}{8\mu^2}e^{-2\mu t}\right\}.$$

The condition (16), as already mentioned above, leads to the requirement $V_\infty = \alpha = 0$, which gives a simpler formula for the evolution of the scaling factor:

$$R(t) = R_\infty \exp\left\{-\frac{\kappa u_0^2}{8\mu^2}e^{-2\mu t}\right\}, \tag{25}$$

where

$$R_\infty = R_0 \exp\left\{\frac{\kappa}{8}(\phi_0 - \phi_\infty)^2\right\}.$$

Hence

$$H(t) = \frac{\dot R}{R} = \frac{\kappa u_0^2}{4\mu}e^{-2\mu t}. \tag{26}$$

We also call attention to the fact that although the solution (25) is a particular solution for the potential $V(t)$ considered as a function of time, all admissible solutions $R(t)$ corresponding to a fixed function $V(t)$ can nonetheless be constructed. This procedure is possible, since, as shown in [10], the function $R^3(t)$ satisfies a linear ordinary Schrödinger-type differential equation, in which the function $3\kappa V(t)$ plays the role of the potential energy.

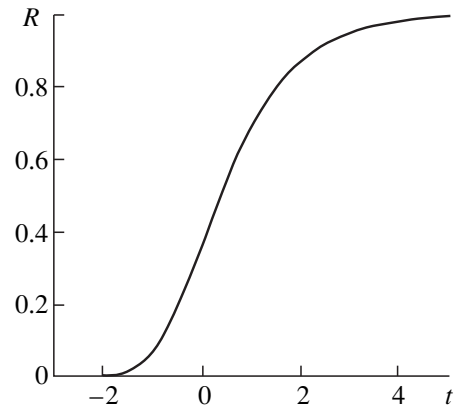

Fig. 1. Characteristic time dependence of the scale factor in a model with a Higgs potential.

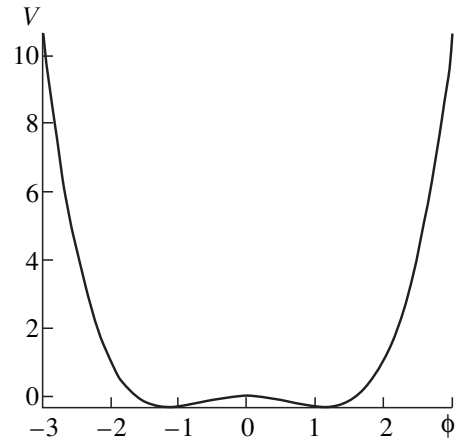

Fig. 2. Characteristic form of the Higgs self-action potential.

This evolution regime corresponds to the model of a chaotic inflation with the self-action potential of the ϕ^4 theory [3]. The initial conditions make it possible to give the following estimates:

$$U(\phi) \approx M_P^2, \quad u_0 \approx M_P^2,$$

where $M_P = \sqrt{\hbar c/G}$ is the Planck mass.

We shall show that an inflationary regime exists on some time interval preceding the moment

$$t_* = \frac{1}{2\mu}\ln\frac{\kappa u_0^2}{8\mu^2},$$

when the rate of change of the scaling factor assumes its maximum value. The Hubble constant and the scaling factor at this moment in time are, respectively,

$$H(t_*) = 2\mu, \quad R(t_*) = \frac{R_\infty}{e}.$$

An important point for the inflationary scenario is that the inflation occurs before the moment t_* over a comparatively short time. Indeed, setting

$$k = \frac{R(t_*)}{R(t_1)}, \quad t_* > t_1,$$

we obtain for $\Delta t = t_* - t_1$ the formula

$$\Delta t = \frac{1}{2\mu}\ln(1 + \ln k).$$

For example, the scaling factor increases by a factor of $k = e^{100}$ in a time of the order of

$$\Delta t \sim \frac{\ln 10}{\mu}.$$

After the time t_* the scaling factor grows slowly, increasing from $R(t_*)$ by a factor of e as $t \longrightarrow +\infty$; in the process, the field decreases and asymptotically approaches the value ϕ_∞, which corresponds to a local maximum of the potential energy. The scaling factor approaches asymptotically the constant value R_∞, so that asymptotically the expansion of the universe stops. Figure 1 demonstrates these properties of the solution obtained.

It follows from the relations (24) that the conditions (19) and (20) can be regarded as the classical equivalent of the decay of the field of Higgs bosons with mass $M_h = \mu$ and characteristic decay time $\tau_h \approx 1/\mu$. Thus, in the present model it is this mechanism that gives the inflationary expansion regime. The most important property of the model is that it contains, in itself, an emergence from the inflationary regime, but into an asymptotically static universe. It is this property that distinguishes it from other inflationary models. However, in accordance with the modern ideas the universe should asymptotically pass into the Friedmann expansion regime. Consequently, this model can be regarded only as a prototype of a more correct theory, describing the emergence into a Friedmann regime. To construct such a theory we shall examine some drawbacks of this model.

In the model considered here with an effective Higgs potential, the principle of energy dominance breaks down in the period of time when the field passes near the minimum of the self-action potential. Phenomena of this kind are well known to be possible at phase transitions [3]. For $V_\infty = 0$ the physical potential $V(\phi)$ possesses a region of negative values near its minima (see Fig. 2). For values of the field where $V(\phi) < 0$ we have

$$\varepsilon = T_{00} = \frac{1}{2}\dot{\phi}^2 + V(\phi) < p$$

$$= T_{11} = T_{22} = T_{33} = \frac{1}{2}\dot{\phi}^2 - V(\phi),$$

which corresponds to breakdown of the energy-dominance condition [19]. It is this circumstance that seems to determine the asymptotic emergence of the system into an unstable state, corresponding to a maximum of the potential energy. To prevent breakdown of the energy-dominance condition V_∞ can be chosen to be a quite large positive quantity. Then, however, the model possesses a nonzero cosmological constant in the limit $t \longrightarrow \infty$ and inflation is not completed after the moment t_*. Consequently, this modification of the model is not entirely satisfactory.

We note that matter in a model with an effective Higgs potential possesses the "exotic" equation of state

$$p = \frac{4\mu}{\sqrt{3\kappa}}\varepsilon^{1/2} - \varepsilon, \tag{27}$$

which as $t \longrightarrow \infty$ becomes

$$p \sim \frac{4\mu}{\sqrt{3\kappa}}\varepsilon^{1/2}. \tag{28}$$

A similar equation of state for matter was obtained in [10] for a different model of inflation, constructed on the basis of a variational principle of the minimum of the variation of the field in a fixed time interval; this corresponds to the formulation of the slow-slide regime. Matter with such an equation of state is not "normal" matter or radiation. Consequently, to obtain the correct asymptotic behavior in the limit $t \longrightarrow \infty$ the model obtained must be modified taking account of the fact that the transition into the Friedmann stage is possible if matter in a state close to thermodynamic equilibrium with the equation of state of the type $p = \gamma\varepsilon$ remains in the universe by the time the boson field decays. Then the adiabatic expansion of the universe will be precisely a Friedmann expansion. On the basis of this assumption, we shall now consider the following auxiliary model.

5. MODELS WITH EMERGENCE INTO A FRIEDMANN EVOLUTION REGIME

Evolution regimes corresponding to the condition

$$V(\phi(t)) = \frac{n}{3\kappa t^2}, \tag{29}$$

where n is a constant number satisfying the inequality $n \geq -1/4$, were examined and analyzed in [10]. As shown in [10], different power-law evolutions of the scaling factor correspond to such a history of the potential with various values of n:

$$R(t) = Ct^{\beta/3}, \tag{30}$$

where

$$\beta = \frac{1}{2} + \sqrt{\frac{1}{4} + n} > 0$$

correspond to different equations of state of matter:

$$p = \gamma\varepsilon, \quad \gamma = \frac{\beta - n}{\beta + n} = \frac{1 - 2n + \sqrt{1 + 4n}}{1 + 2n + \sqrt{1 + 4n}}.$$

Generally speaking, the solution (30) can be studied for arbitrary values $\beta > 0$, including regimes with power-law inflation with $\beta > 3$. However, such a model requires special substantiation of the abrupt or smooth variation of the constant m, which is necessary in order to emerge from inflation (see [10] for a more detailed discussion). Consequently in our case we shall confine our attention only to Friedmann regimes, i.e., $0 < \beta < 3$. Power-law inflation was studied [8–10].

The limiting value $n = -1/4$ corresponds to the equation of state with $\gamma = 3$; $n = 0$ corresponds to the most stringent equation of state with $\gamma = 1$; $n = 2$ corresponds to dust with $\gamma = 0$; and, $n = 3/4$ corresponds to pure radiation with $\gamma = 1/3$. In general, all Friedmann regimes with $\beta \le 1$ correspond to the condition $-1/4 \le n \le 6$. As follows from the character of the model, the model corresponds to a description of adiabatic expansion of a universe filled with matter with an equation of state close to the equilibrium equation. The field ϕ can be regarded as a potential of the 4-velocity of the flow of an ideal liquid with one or another equation of state of matter. Evidently, the radiation-domination regime (RD stage), $p = \varepsilon/3$, and the matter-domination era, $p \approx 0$ [12] are of special interest.

On the basis of the approach being considered, the choice of the function $V(t)$ in the form (29) corresponds to the choice

$$U(t) = \frac{m}{t}. \tag{31}$$

For this functional dependence of U on t the conditions (15) and (16), evidently, are also satisfied. Following, Eqs. (6)–(8) we obtain the relations

$$\phi(t) = \phi_1 + m\ln t,$$

$$U(\phi) = m\exp\left\{-\frac{1}{m}(\phi - \phi_1)\right\}, \quad \phi_1 = \text{const},$$

$$W(\phi) = \left(\sqrt{V_1} + \frac{\sqrt{3\kappa}}{2}m^2\exp\left\{-\frac{1}{m}(\phi - \phi_1)\right\}\right)^2,$$

$$V(\phi) = \left(\sqrt{V_1} + \frac{\sqrt{3\kappa}}{2}m^2\exp\left\{-\frac{1}{m}(\phi - \phi_1)\right\}\right)^2$$

$$-\frac{1}{2}m^2\exp\left\{-\frac{2}{m}(\phi - \phi_1)\right\}.$$

Substituting in the expression for $V(\phi)$ the function $\phi = \phi(t)$, we obtain

$$V(t) = \left(\sqrt{V_1} + \frac{\sqrt{3\kappa}}{2}\frac{m^2}{t}\right)^2 - \frac{1}{2}\frac{m^2}{t^2}.$$

The function $R = R(t)$ is determined from Eq. (12). In the present case it has the form

$$R(t) = R_0 t^{\kappa m^2/2}\exp\left\{\sqrt{\frac{\kappa}{3}V_1}\,t\right\}. \tag{32}$$

All possible power laws for the evolution of the scaling factor, which correspond to time dependences of the potential energy (29), are obtained for $V_1 = 0$. It is in this case that an emergence into the Friedmann regime (30) is obtained; in addition,

$$\beta = \frac{3}{2}\kappa m^2.$$

It should be noted that in the model considered, based on Eqs. (29) and (31), there is no inflation, and the Friedmann regime will arise asymptotically as $t \longrightarrow \infty$ for any other evolution regime differing from Eqs. (29) and (31) by the presence of rapidly decreasing terms. It is only necessary that the rate of decrease be greater than t^{-2} in Eq. (29) and t^{-1} in Eq. (31), for example, exponential. This observation is the basis of the new model, which unites the results obtained in Sections 4 and 5.

We now present an example concerning the possibility of an oscillatory emergence into a Friedmann regime, similar to the approximate solution obtained in [2]. Instead of Eq. (31) we shall consider the next variant of the evolution of the function $U(t)$:

$$\dot{\phi} = U(t) = \frac{m + a\sin(\Omega t)}{t}, \tag{33}$$

where a and Ω are constants, where $|a| < m$. In this case the evolution of the field is as follows:

$$\phi(t) = \phi_0 + m\ln t + a\int\frac{\sin(\Omega t)}{t}dt$$

$$= \phi_0 + m\ln t + a\,\mathrm{Si}(\Omega t).$$

Here and below $\mathrm{Si}(t)$ and $\mathrm{Ci}(t)$ are the sine and cosine integrals. Hence

$$W(t) = \frac{3\kappa}{4}\left(\int U^2(t)dt + \sqrt{W_0}\right)^2$$

$$= \frac{3\kappa}{4}\left(-\frac{2m^2 + a^2}{2t} + \frac{4am\sin(\Omega t) + a^2\cos(2\Omega t)}{2t}\right.$$

$$\left. - 2am\Omega\,\mathrm{Ci}(\Omega t) + a^2\Omega\,\mathrm{Si}(2\Omega t) + \sqrt{W_0}\right)^2.$$

As one can see, for a definite choice of the constants the energy $W(t)$ of the field satisfies the asymptotic condition (14). Hence we obtain

$$V(t) = W(t) - \frac{1}{2}U^2(t)$$

$$= \frac{3\kappa}{4}\left(-\frac{2m^2 + a^2}{2t} + \frac{4am\sin(\Omega t) + a^2\cos(2\Omega t)}{2t}\right.$$

$$\left. - 2am\Omega\mathrm{Ci}(\Omega t) + a^2\Omega\mathrm{Si}(2\Omega t) + \sqrt{W_0}\right)^2$$

$$-\frac{1}{2t^2}(2m^2 + a^2 + 4am\sin(\Omega t) - a^2\cos(2\Omega t)).$$

In accordance with Eq. (12) we obtain

$$R(t) = R_0 t^{\kappa m^2/2}$$

$$\times \exp\left\{\sqrt{\frac{\kappa}{3}}(\sqrt{W_0} + a^2\Omega)t\right\}e^{\Theta(t)},$$

where

$$\Theta(t) = 2am\mathrm{Si}(\Omega t) + \frac{a^2}{2}\mathrm{Ci}(2\Omega t)$$

$$-2am\Omega\int_{t_0}^{t}\mathrm{Ci}(\Omega t)dt + a^2\Omega\int_{t_0}^{t}(\mathrm{Si}(2\Omega t) - 1)dt.$$

Since the function $\Theta(t)$ oscillates as $t \longrightarrow \infty$, near some constant value, now, in contrast to Eq. (32), the condition for inflation to be completed as $t \longrightarrow \infty$ is

$$\sqrt{W_0} + a^2\Omega = 0.$$

When this condition is satisfied, $R(t)$ asymptotically emerges into a Friedmann expansion regime of the type (30) but with damped oscillations. For small values of the parameter a we have

$$R(t) = R_0 t^{\kappa m^2/2}$$

$$\times\left(1 + 2am\mathrm{Si}(\Omega t) - 2am\Omega\int_{t_0}^{t}\mathrm{Ci}(\Omega t)dt + O(a^2)\right),$$

which is similar to the approximate solution obtained in [2].

It is also easy to calculate the asymptotic form of the potential as a function of the field. In the limit $t \longrightarrow \infty$, we have

$$\phi(t) \longrightarrow \phi_0 + m\ln t,$$

$$V(t) \longrightarrow \frac{3\kappa}{4}(-2am\Omega\mathrm{Ci}(\Omega t)$$

$$+ a^2\Omega(\mathrm{Si}(2\Omega t) - 1) + \sqrt{W_0} + a^2\Omega)^2.$$

Thus, when inflation is completed

$$V(\phi) \sim \frac{3\kappa}{4}(-2am\Omega\mathrm{Ci}(\Omega e^{(\phi-\phi_0)/m})$$

$$+ a^2\Omega[\mathrm{Si}(2\Omega e^{(\phi-\phi_0)/m}) - 1])^2.$$

This potential is an oscillatory function as $\phi \longrightarrow \infty$ with the amplitude of the oscillations decreasing as $\phi \longrightarrow \infty$. Since $\phi \longrightarrow \infty$ as $t \longrightarrow \infty$, oscillations in the evolution regime are due to the passage of the system through an infinite number of potential wells and not by a periodic motion of the system inside an individual well.

We also note that if instead of Eq. (33) the evolution of the field is determined by the relation

$$\dot{\phi} = U(t) = \frac{m}{t} + a\sin(\Omega t),$$

then the energy of the field with such evolution grows as

$$W \propto t^4,$$

which does not agree with the requirement (14), and evolution ends with collapse of the universe as $t \longrightarrow \infty$. In general, these examples show that in order for the requirements (15) and (14) to be satisfied, it is necessary that $\dot{\phi} \longrightarrow \infty$ as $t \longrightarrow \infty$. However, the asymptotic condition

$$V(\phi(t)) \longrightarrow \frac{m}{t^2} \text{ at } t \longrightarrow \infty$$

give the Friedmann laws of evolution, for which $\phi \propto \ln t$ in the same limit $t \longrightarrow \infty$.

6. INFLATION MODEL WITH NATURAL EMERGENCE INTO FRIEDMANN EXPANSION

To construct a model of the evolution of the universe which admits an inflation regime with natural emergence into a RD stage and a matter-dominated era, we shall consider a linear superposition of the auxiliary models studied in Sections 4 and 5. Specifically, we shall consider a model corresponding to the relations

$$\dot{\phi} = U(t) = ue^{-\mu t} + \frac{m}{t}, \tag{34}$$

$$\phi(t) = \phi_c - \frac{u}{\mu}e^{-\mu t} + m\ln t. \tag{35}$$

In this model, though the field grows logarithmically as $t \longrightarrow \infty$, the kinetic energy of the field decreases, which makes possible for the condition (15) to be satisfied. This model contains three parameters, whose meaning is clear from the preceding analysis of the models (19)

and (31). On the basis of this analysis it becomes clear that this model for definite values of these three parameters will admit an inflationary stage and completion of this stage with emergence into Friedmann expansion. The emergence into the Friedmann regime will always occur as $t \longrightarrow \infty$, since the exponentially decaying component in the expression for the energy of the field decays more rapidly than the component which decays as t^{-1}. An inflationary regime of the type examined in Section 4 is possible if a period when

$$ue^{-\mu t} \gg \frac{m}{t}, \tag{36}$$

exists in the history of the evolution of the universe in this model. Evidently, the parameters μ, m, and u can be chosen so that the condition (36) will be satisfied. We shall show this by direct calculations.

The relations (34) and (35) cannot be represented explicitly as a function of $U = U(\phi)$. However, it can be represented in the form of the function $U = U(\phi, t)$. For example,

$$U(\phi, t) = \frac{m}{t} + m\mu \ln t - \mu(\phi - \phi_c).$$

A deviation of the model (34) from the model (31) can be seen in this form.

We shall now calculate the effective potential W using the relations (11), (34), and (35). In this case we obtain

$$W(t) = \left(\sqrt{V_0} + \int_{t_0}^{t} U^2(t)dt\right)^2 = \left(\sqrt{V_0} - \frac{u^2}{2\mu}e^{-2\mu t} - \frac{m}{t} + 2um\int_{t_0}^{t}\frac{e^{-\mu t}}{t}dt\right)^2, \tag{37}$$

$$V(t) = \frac{3\kappa}{4}\left(\sqrt{V_0} - \frac{u^2}{2\mu}e^{-2\mu t} - \frac{m}{t} + 2um\int_{t_0}^{t}\frac{e^{-\mu t}}{t}dt\right)^2 - \left(ue^{-\mu t} + \frac{m}{t}\right)^2. \tag{38}$$

Since it is impossible to obtain an explicit expression for the potentials $W(\phi)$ and $V(\phi)$ as functions of the field ϕ, we shall investigate them as a function of time. For this it is convenient to employ the expression (12). Figures 3 and 4 show the variations of the scale factor $R(t)$ with time for the model (34), (35) for several values of the parameter m (Fig. 3) and u (Fig. 4). The figures were constructed in the units $c = 1$ and $\kappa = 1$. According to the figures, as u, which characterizes the initial energy of the field in the pre-inflation epoch, increases, the rate of inflation increases. At the same time, as the parameter m, characterizing the energy density of matter at the moment of emergence into the Friedmann regime, increases, the rate of inflation decreases. Thus the rate of inflation matched with the observational data and admitting an emergence into a Friedmann expansion regime with the required equation of state of matter can be obtained by varying the parameters u and m.

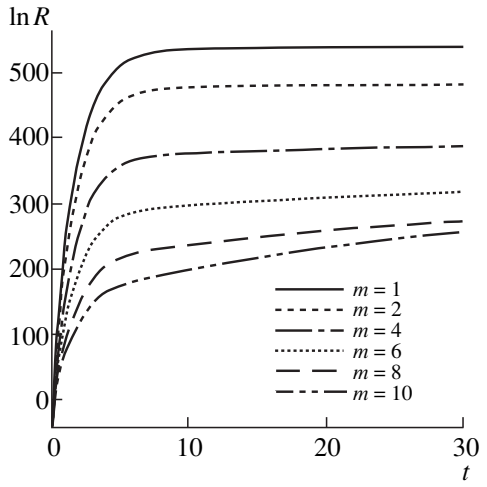

Fig. 3. Time dependence of the scale factor R in a model with emergence from inflation for various values of the parameter m.

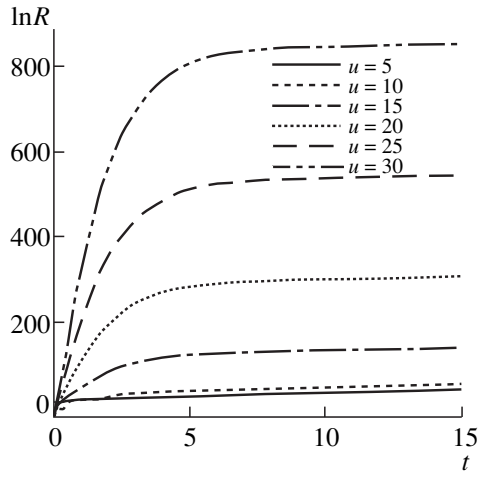

Fig. 4. Time dependence of the scale factor R in a model with emergence from inflation for various values of the parameter u.

Plots of the variations of $\phi = \phi(t)$ and $V = V(t)$ with time for the same values of the model parameters are presented in Figs. 5–8. Plots of the function $V = V(\phi)$, calculated from the plots of the functions $\phi = \phi(t)$ and $V = V(t)$, are presented in Figs. 9 and 10. It is evident that in the course of the entire evolution for all values of the model parameters m and u the potential remains

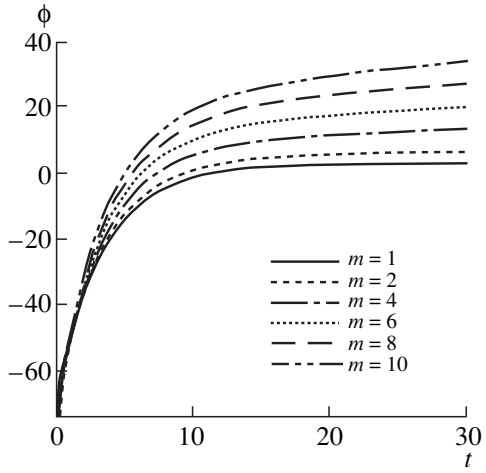

Fig. 5. Time dependence of the field ϕ in a model with emergence from inflation for various values of the parameter m.

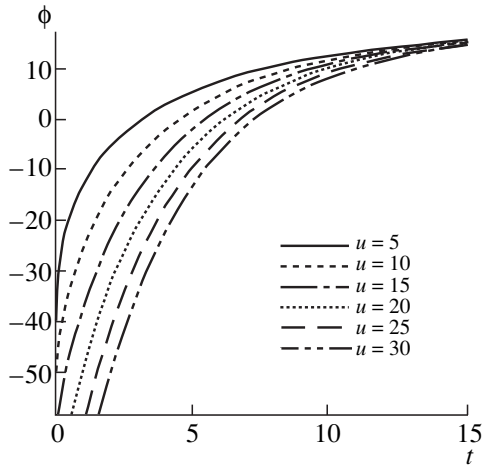

Fig. 6. Time dependence of the field ϕ in a model with emergence from inflation for various values of the parameter u.

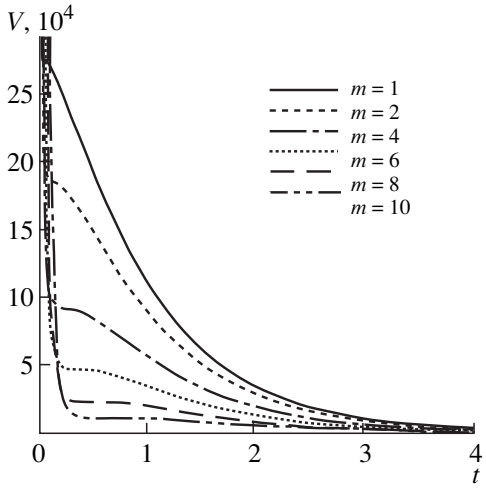

Fig. 7. Time dependence of the self-action potential V in a model with emergence from inflation for various values of the parameter m.

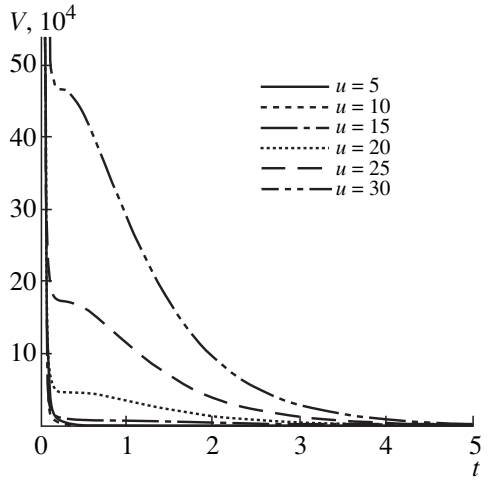

Fig. 8. Time dependence of the self-action potential V in a model with emergence from inflation for various values of the parameter u.

a positive function and therefore the condition of energy dominance of the model does not break down. Thus, from this standpoint the new model (34), (35) is more acceptable than the model with an effective Higgs potential.

Comparing the plots in Figs. 4–10 shows that the inflation stage is associated with the system passing a region of values of the field where the potential energy at first has a local minimum and then a maximum or a region with an almost constant value of the potential energy. At this same time a phase transition occurs and matter transforms from the "field" state into a state with an equation of state of an ideal liquid, which distinguishes this model from the ϕ^4 model. Likewise, in contrast to the ϕ^4 model, associated with the relations (19), after inflation is completed the system approaches a minimum of the potential energy and not a maximum. From this point of view the model (34), (35) is preferable to the model (19), since the system passes into a stable state, though over an infinitely long time.

Thus, the model constructed for cosmological inflation with natural emergence gives a satisfactory qualitative description of the dynamics of the expansion of the universe in the entire time interval, starting with the preinflationary epoch and ending with the universe emerging into the Friedmann regime of the present-day matter-dominated epoch. The model contains only three basic parameters μ, m, and u. The interpretation of this model and the meaning of its basic parameters can be based on a preliminary analysis performed in the

preceding sections of this paper. As one can judge according to a model with an effective Higgs potential (Section 4), the parameter μ can be interpreted as the mass of the Higgs boson and u can be interpreted as a parameter characterizing the initial energy of the field and determining the moment of the onset of the inflationary stage with respect to the start of the big bang, which corresponds in the present model to the moment $t = 0$. The parameter m should be interpreted from the standpoint of the model with emergence into a Friedmann expansion, described in Section 5, i.e., as a quantity characterizing the matter density at the moment the universe emerges into the Friedmann regime. This parameter determines the type of equation of state of matter at the Friedmann stage.

An important detail of the proposed models with emergence into a Friedmann stage should be noted. In all of these models the emergence into a Friedmann regime is accompanied by a mandatory increase in the field ϕ according to a logarithmic law. Taking account of the fact that from the standpoint of the theory of elementary particles the value of a uniform scalar field determines the instantaneous value of the mass of the particles, in the models considered the particle masses M should grow according to the law

$$M \propto \ln^2 t$$

at the post-inflation stage. The growth of the particle masses which is determined by the time elapsed from the moment the inflationary stage ends apparently is not seen in the experimental data. Consequently, a new interpretation of the growth of the field must be sought. The simplest explanation is that a part of the field growing logarithmically describes ordinary matter and the part decreasing exponentially is due to the boson field, i.e., it is a proper field. If it is assumed that the particle masses depend exclusively on the "field" component of the general field, then we arrive at the standard concept according to which the field approaches a constant value corresponding to the present-day particle masses. In addition, the present-day values of the field and mass are reached immediately after inflation is completed. Hence it follows that to explain this effect it is natural to assume at the outset the existence of two interacting scalar fields or two types of matter—a scalar field and matter.

We note that in the model considered here there arises a situation where the power-law expansion regime dominates at the preinflationary stage, i.e., where the exponentially decreasing term in Eq. (34) is still small compared with the term decreasing as $1/t$. If we wish to eliminate in this case dominance of the power-law regime, which could contradict certain general ideas about the character of the preinflationary epoch, then the model can be modified somewhat so that the term in Eq. (34) which decreases as $1/t$ would be zero initially, at $t = 0$ (start of the big bang). An example of such a

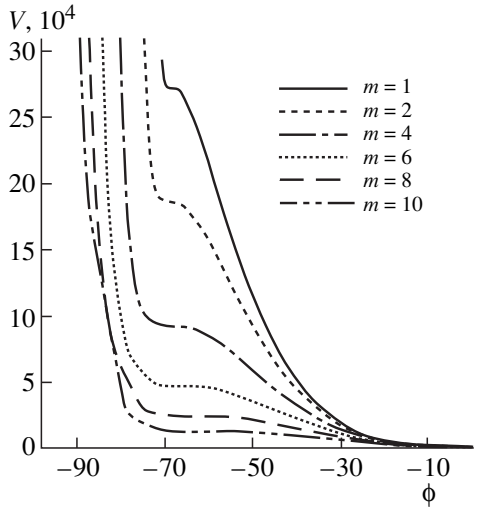

Fig. 9. Self-action potential V as a function of the field ϕ, calculated in accordance with the plots in Figs. 5 and 7.

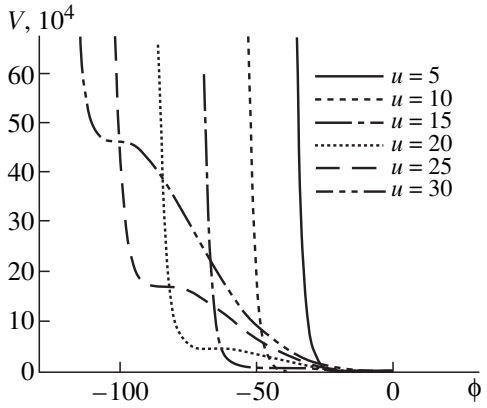

Fig. 10. Self-action potential V as a function of the field ϕ in a model with emergence from inflation for various values of the parameter u, calculated from the plots in Figs. 6 and 8.

model is a model based on the following laws of evolution of the functions $\dot{\phi} = U$ and ϕ:

$$\dot{\phi} = U(t) = ue^{-\mu t} + \frac{mt}{t^2 + q^2}, \tag{39}$$

$$\phi(t) = \phi_c - \frac{u}{\mu}e^{-\mu t} + \frac{m}{2}\ln(t^2 + q^2). \tag{40}$$

This model has the same Friedmann asymptotic behavior as the preceding model, but it does not contain the singularity at the initial moment in time, and the "real" component of the field dynamics near $t = 0$ is small. Many such modifications of the model (34), (35) can be proposed. Consequently, the final choice should be made on the basis of additional physical considerations associated with clarification of the quantum properties of matter at the preinflationary stage of evolution and with an increase in the density disturbances in such models.

In summary, in the model considered here there are two physical mechanisms which are basic and which determine almost the entire history of the development of the universe. The first mechanism is, in all probability, decay of the Higgs-boson field, which corresponds to a characteristic exponentially decaying term in the expression (35) with exponent equal to the mass μ of the Higgs boson. According to the preceding analysis, this mechanism is responsible for the appearance of the inflationary stage.

The second mechanism, associated with the term in Eq. (35) that decreases as the reciprocal of the time, is adiabatic thermodynamic expansion of the universe after decay of the Higgs bosons with a definite type of equation of state of matter. It can be inferred that the parameter n and the related parameter m changed very little at the preinflationary stage as a result of phase transitions from the values

$$n = \frac{3}{4}, \quad m = \sqrt{\frac{1}{\kappa}}, \quad \gamma = \frac{1}{3}$$

to the radiation-dominated stage to

$$n = 2, \quad m = 2\sqrt{\frac{1}{3\kappa}}, \quad \gamma = 0$$

at the present dust-dominated stage. It should be noted that the asymptotic Friedmann law of the expansion of the universe is uniquely related with the asymptotic logarithmic growth of the inflanton field (although the total energy of the field decreases). Thus, in SSF models this regime corresponds to an asymptotic transition of the system into a state with a minimum potential energy and is not necessarily accompanied by an oscillatory regime of the field, with which the secondary heating of matter, filling the universe, at the post-inflation stage of the evolution of the universe [3] is usually associated.

7. CONCLUSIONS

In the present paper we have constructed a model of the evolution of a uniform and isotropic universe, admitting an inflationary stage with natural emergence into a radiation-dominated stage and a matter-dominated era. This model was constructed as a superposition of two auxiliary models, the first of which is responsible for the inflation stage (a model with a Higgs effective potential) and the second is responsible for the Friedmann stage, including the matter-dominated stage.

Our model qualitatively describes all basic aspects of the evolution of the universe over an infinitely long time interval, it determines the basic mechanisms responsible for the dynamics of the universe, and it can serve as a starting point for constructing a more accurate theory of cosmological evolution which would contain the quantitative calculations matching the microphysics of the inflationary stage with the observed large-scale structure.

ACKNOWLEDGMENTS

We thank the participants of V.N. Mel'nikov's gravitation seminar for constructive criticism and helpful discussions of certain aspects of this work. We are also grateful to A.A. Starobinsky and B.E. Spokoiny for a helpful discussion of the prospects of these models at the 10th All-Russia Gravitation Conference in Vladimir (1999).

This work was supported in part by the Russian Foundation for Basic Research (project no. 98-02-18040) and the program "Universities of Russia" (project no. 9900777), as well as the project "Cosmomicrophysics" of the State Science and Technology Program "Astronomy. Fundamental Investigations of the Cosmos."

REFERENCES

1. A. H. Guth, Phys. Rev. D **23**, 347 (1981).
2. A. A. Starobinsky, Phys. Lett. B **91**, 99 (1980).
3. A. D. Linde, *Physics of Elementary Particles and Inflation Cosmology* (Nauka, Moscow, 1990).
4. R. Maartens, D. R. Taylor, and N. Roussos, Phys. Rev. D **52**, 3358 (1995).
5. S. V. Chervon, in *Nonlinear Fields in Theory of Gravitation and Cosmology* (Srednevolzhsk. Nauchnyĭ Tsentr, Ul'yanovsk, 1997), p. 191.
6. S. V. Chervon and V. M. Zhuravlev, Izv. Vyssh. Uchebn. Zaved., Fiz., No. 8, 83 (1996).
7. S. V. Chervon, V. K. Shchigolev, and V. M. Zhuravlev, Izv. Vyssh. Uchebn. Zaved., Fiz., No. 2, 41 (1996).
8. S. V. Chervon, V. M. Zhuravlev, and V. K. Shchigolev, Phys. Lett. B **398**, 269 (1997).
9. S. V. Chervon, Gravitation Cosmology **3**, 145 (1997).
10. V. M. Zhuravlev, S. V. Chervon, and V. K. Shchigolev, Zh. Éksp. Teor. Fiz. **114**, 223 (1998) [JETP **87**, 223 (1998)].
11. S. V. Chervon and V. M. Zhuravlev, Izv. Vyssh. Uchebn. Zaved., Fiz. (2000) (in press); S. V. Chervon and V. V. Zhuravl, gr-qc/9907051 (1999).
12. Ya. B. Zel'dovich and I. D. Novikov, in *Structure and Evolution of the Universe* (Nauka, Moscow, 1975), p. 736.
13. S. Weinberg, *Gravitation and Cosmology: Principles and Applications of the General Theory of Relativity* (Wiley, New York, 1972; Mir, Moscow, 1975).
14. A. B. Burd and J. D. Barrow, Nucl. Phys. **308**, 929 (1988).
15. B. E. Spokoiny, Phys. Lett. B **315**, 40 (1993).
16. A. A. Starobinsky, Pis'ma Zh. Éksp. Teor. Fiz. **68**, 721 (1998) [JETP Lett. **68**, 757 (1998)].
17. V. Sahni and A. A. Starobinskiy, astro-ph-9904398 (1999); submitted to Int. J. Mod. Phys. D (2000).
18. S. Gottlöber, V. Müller, H.-J. Schmidt, and A. A. Starobinsky, Int. J. Mod. Phys. D **1**, 257 (1992).
19. S. W. Hawking and G. F. R. Ellis, *The Large-Scale Structure of Space-Time* (Cambridge Univ. Press, Cambridge, 1973; Mir, Moscow, 1977).

Translation was provided by AIP

Journal of Experimental and Theoretical Physics, Vol. 91, No. 2, 2000, pp. 239–244.
Translated from Zhurnal Éksperimental'noĭ i Teoreticheskoĭ Fiziki, Vol. 118, No. 2, 2000, pp. 273–278.

NUCLEI, PARTICLES, AND THEIR INTERACTION

Superradiation of a System of Nuclear Spins

D. S. Bulyanitsa, A. V. Druzhin, and E. D. Trifonov*
St. Petersburg State Pedagogical University, St. Petersburg, 191186 Russia
**e-mail: trifonov@ET1023.spb.edu*
Received November 24, 1999

Abstract—The superradiation of a system of nuclear spins is investigated taking into account the broadening of the NMR spectrum due to the stochasticity of the local magnetic field. The effect of the local field generated by nuclear spins randomly distributed in space is investigated. In this case it is possible to achieve better agreement with the experimentally observed characteristics of this phenomenon. Specifically, the possibility of a monopulse regime with a high initial inversion of the spin polarization is explained. © *2000 MAIK "Nauka/Interperiodica".*

1. INTRODUCTION

The fundamental idea of the possibility of observing superradiation [1] in a system of nuclear spins in a magnetic field was advanced by Bloembergen and Pound in 1954 [2]. The effect was observed experimentally much later [3, 4]. The theoretical interpretation of this experiment on the basis of a solution of a system of Maxwell–Bloch equations (see also the monograph [7]) was proposed in [5, 6]. Further elaboration of the theory of superradiation of nuclear spins is contained in [8–14]. Our semiclassical approach [5, 6], which reproduces the basic features of the observed effect, contained a number of artificial assumptions. Specifically, the observed regime of powerful monopulses with high initial spin polarization could not be explained with the Larmor frequency scanning used in the experiment. It was necessary to assume that the generation of superradiation does not develop if the detuning of the frequency is greater than the line width of the radio frequency resonator. To obtain the experimental value of the generation threshold and the polarization reversal threshold the value of the transverse relaxation time was set artificially.

In the present paper we do not make these assumptions and we show that the broadening due to the random value of the local magnetic field generated by magnetic dipoles distributed stochastically throughout the volume of the sample can play the role of an additional relaxation mechanism. We do not pretend to give an exact description of the experiment mentioned above; we only indicate the quite general laws of the phenomenon under study.

2. BLOCH EQUATIONS TAKING ACCOUNT OF THE LOCAL NONUNIFORMITY OF THE MAGNETIC FIELD

Our system consists of a sample with randomly distributed point nuclear spins. The sample is placed in a radio frequency resonator (induction coil) with characteristic frequency Ω, quality factor Q, and filling factor η.

The initial equations for describing the dynamics of such a system are an equation for the oscillatory circuit and the Bloch equations for the magnetization of the sample [6]

$$\frac{d^2H_x(t)}{dt^2} + \frac{\Omega}{Q}\frac{dH_x(t)}{dt} + \Omega^2 H_x(t) = -4\pi\eta\frac{d^2M_x(t)}{dt^2}, \quad (1)$$

$$\frac{dM_x(t, \omega')}{dt} = \gamma(M_y(t, \omega')B_z - M_z(t, \omega')B_y(t)) - \frac{M_x(t, \omega')}{T_2}, \quad (2)$$

$$\frac{dM_y(t, \omega')}{dt} = \gamma(M_z(t, \omega')B_x(t) - M_x(t, \omega')B_z) - \frac{M_y(t, \omega')}{T_2}, \quad (3)$$

$$\frac{dM_z(t, \omega')}{dt} = \gamma(M_x(t, \omega')B_y(t) - M_y(t, \omega')B_x(t)). \quad (4)$$

Here γ is the gyromagnetic ratio for a nuclear spin; the x-axis is aligned along the axis of the coil, and the z-axis is oriented in the direction of the external field $\mathbf{H}_0$; $\mathbf{M}(t)$ is the magnetization vector;

$$B_x = H_x + 4\pi M_x, \quad B_y = H_y + 4\pi M_y,$$

$$B_z = H_0 + H_z'$$

are the components of the magnetic field, where H_z' is the z component of the local magnetic field produced by the magnetic moments of the nuclei; and, $H_x(t)$ is the ac magnetic field of the coil. The vector $\mathbf{M}(t, \omega')$ with components $M_x(t, \omega')$, $M_y(t, \omega')$, and $M_z(t, \omega')$ deter-

mines the partial magnetization of the sample. The total magnetization can be expressed in terms of the partial magnetization as follows:

$$\mathbf{M}(t) = \int \mathbf{M}(t, \omega') w(\omega') d\omega', \tag{5}$$

where $w(\omega')$ is the distribution function of the shift of the Larmor frequencies and is due to the local nonuniformity of the magnetic field. We note that the second derivative of the x component of the total magnetization appears on the right-hand side of Eq. (1). The system of equations (1)–(4) is semiphenomenological: we explicitly take account of the inhomogeneous broadening due to the stochastic nature of the local field, and the homogeneous broadening is taken into account through the transverse relaxation constant T_2. For simplicity, we assume that the nuclear spins have only two possible orientations—parallel or antiparallel to the external field.

We shall now determine the distribution function $w(\omega')$. It is obviously related with the distribution function $W(H_z')$ of the local magnetic field H_z'. Of course, the local magnetic field possesses not only a z component, but it is more important to take account of this component than the other components because it makes the largest contribution to the change in the Larmor frequency.

We have for the z component of the magnetic field generated at the origin of coordinates by the ith magnetic moment μ, located at a point with the coordinates r, θ, and ϕ,

$$H^{(i)} = \mu \frac{3\cos^2\theta - 1}{r^3}. \tag{6}$$

Then

$$H_z' = \sum_i H^{(i)}. \tag{7}$$

We denote by $n_1 = N_1/V$ and $n_2 = N_2/V$ the average densities of the magnetic moments oriented parallel and antiparallel, respectively, to the magnetic field. Here N_1 and N_2 are the numbers of such magnetic moments in the sample, and V is the volume of the sample. Then the z component of the magnetization of the sample is

$$M_z = \mu(n_1 - n_2). \tag{8}$$

We express the distribution function $W(H_z')$ in the standard manner in terms of the δ function using the formula

$$W(H_z') = \left\langle \delta\left(H_z' - \sum_{i=1}^{N_1} H^{(i)} - \sum_{k=1}^{N_2} H^{(k)} \right) \right\rangle, \tag{9}$$

where the first summation extends over the magnetic moments oriented parallel to the field and the second summation extends over the magnetic moments oriented antiparallel to the field, and the brackets denote averaging over the arrangement of the magnetic moments. A derivation of this distribution for the particular case $n_1 = n_2$ is presented in [15].

Representing the δ function as the integral

$$\delta(f) = \frac{1}{2\pi} \int_{-\infty}^{\infty} \exp(ixf) ds \tag{10}$$

and neglecting the correlations in the arrangement of the spins, we obtain

$$W(H_z') = \frac{1}{2\pi} \times \int_{-\infty}^{\infty} \exp(ixH_z') \exp[-nA(x) - \Delta n i B(x)] ds. \tag{11}$$

Here $n = n_1 + n_2$, and $\Delta n = n_1 - n_2$,

$$A(x) = \mu \int (1 - \cos(xH(r, \theta))) d^3 r, \qquad B(x) = \mu \int \sin(xH(r, \theta)) d^3 r. \tag{12}$$

It is easy to see that $A(x)$ and $B(x)$ are linear functions of x. Performing the integration over the volume we obtain

$$nA(x) = ax, \quad \Delta n B(x) = bx, \tag{13}$$

where

$$a = \frac{8\pi^2}{9\sqrt{3}} n\mu = 5.065 n\mu, \tag{14}$$

$$b = \frac{4\pi}{3} \Delta n \mu \int_0^{\infty} \frac{dy}{y^2} \int_0^1 \sin[y(3t^2 - 1)] dt = -0.669 \Delta n \mu. \tag{15}$$

Substituting the expression (13) into Eq. (11) we obtain finally

$$W(H_z') = \frac{1}{\pi} \int_0^{\infty} e^{-ax} \cos[(H_z' - b)x] dx = \frac{a}{\pi} \frac{1}{a^2 + (H_z' - b)^2}. \tag{16}$$

Therefore the distribution is Lorentzian, and the constants b and a determine, respectively, the average value of the local field and the half-width of the distribution. For the experimental data of [4] ($n = 4.5 \times 10^{22}$ cm^{-3}, $\mu = 1.4 \times 10^{-23}$ G cm^3) $a = 5.065 \times 6.3 \times 10^{-1}$ G $= 3.2 \times 10^{-4}$ T, and $b = -4.3 \times 10^{-5}$ G. At the same time, the field corresponding to the resonance frequency of the circuit is 1.25 T.

In deriving the distribution (16) we assumed the sample to be spherical. However, an investigation of the convergence of the integrals in Eq. (12) with large values of r shows that the region of integration can be limited to several average interspin distances. Consequently, it can be assumed that the real shape of a macroscopic sample will not greatly influence the form of the distribution of the local field.

In accordance with such a distribution of the magnetic field, we obtain a spin ensemble for which the Larmor frequencies

$$\omega = \omega_0 + \omega' = \gamma H_0 + \gamma H_z'$$

satisfy the distribution $w(\omega') = \gamma^{-1} W(\omega'/\gamma)$:

$$w(\omega') = \frac{a\gamma}{\pi}\frac{1}{(a\gamma)^2 + (\omega' - b\gamma)^2}. \tag{17}$$

We know make in the main system of equations the substitution

$$\begin{aligned} H_x &= h(t)e^{-i\omega_0 t} + h^*(t)e^{i\omega_0 t}, \\ M_x(\omega', t) + iM_y(\omega', t) &= m(\omega', t)e^{-i\omega_0 t}. \end{aligned} \tag{18}$$

Assuming the characteristic duration of the superradiation pulse to be much greater than the period of the radio frequency oscillations (in the experiment of [4] these quantities were 100 μs and 10^{-2} μs, respectively), we shall use the approximation of slowly varying amplitudes, taking

$$\left|\frac{dh}{dt}, \frac{dm}{dt}\right| \ll \omega_0 |h, m|. \tag{19}$$

In addition, we shall assume that the frequency ω_0 is close to the characteristic frequency Ω of the oscillatory circuit. Then Eq. (1) for the oscillatory circuit becomes

$$\begin{aligned} &\frac{dh(t)}{dt} + \left(\frac{\Omega}{2Q} - i\Delta\right)h(t) \\ &= i\pi\eta\omega_0 \int_{-\infty}^{\infty} m(\omega', t)w(\omega')d\omega', \end{aligned} \tag{20}$$

where $\Delta = \omega_0 - \Omega$.

We shall also neglect the derivative in Eq. (20) for the field compared with the linear term which is larger, i.e., we shall assume that the field follows the magnetization adiabatically

$$h(t) = i\alpha M(t), \tag{21}$$

where

$$M(t) = \int_{-\infty}^{\infty} m(\omega', t)w(\omega')d\omega', \tag{22}$$

$$\alpha = \frac{\pi\eta\omega_0}{\Omega/2Q - i\Delta}. \tag{23}$$

Assuming $\Delta \ll \Omega/2Q$ and $\eta Q \gg 1$, we set $B_{x,y} \simeq H_{x,y}$ on the basis of Eq. (21). Then, with the substitution (18) the system of equations becomes

$$h(t) = i\alpha M(t), \tag{24}$$

$$\begin{aligned} \frac{dm(\omega', t)}{dt} &= -i\omega' m(\omega', t) \\ &+ i\gamma M_z(\omega', t)h(t) - \frac{m(\omega', t)}{T_2}, \end{aligned} \tag{25}$$

$$\frac{M_z(\omega', t)}{dt} = i\frac{\gamma}{2}(m(\omega', t)h^*(t) - m^*(\omega', t)h(t)). \tag{26}$$

Eliminating h, using (21), from Eqs. (25) and (26) we obtain

$$\begin{aligned} \frac{dm(\omega', t)}{dt} &= -i\omega' m(\omega', t) \\ &- \gamma\alpha M(t)M_z(\omega', t) - \frac{m(\omega', t)}{T_2}, \end{aligned} \tag{27}$$

$$\begin{aligned} &\frac{dM_z(\omega', t)}{dt} \\ &= \frac{\gamma}{2}(m(\omega', t)\alpha^* M^*(t) + m^*(\omega', t)\alpha M(t)). \end{aligned} \tag{28}$$

Now, it is convenient to introduce $M_0 = n\mu$ as the unit of magnetization and $(\gamma M_0)^{-1}$ as the unit of time. We obtain finally

$$\begin{aligned} \frac{dm(\omega', t)}{dt} &= -i\omega' m(\omega', t) \\ &- \tilde{\alpha} M(t)M_z(\omega', t) - \frac{m(\omega', t)}{T_2}, \end{aligned} \tag{29}$$

$$\begin{aligned} \frac{dM_z(\omega', t)}{dt} &= \frac{1}{2}(m(\omega', t)\tilde{\alpha}^* M^*(t) \\ &+ m^*(\omega', t)\tilde{\alpha} M(t)), \end{aligned} \tag{30}$$

where

$$\tilde{\alpha} = \frac{\omega_0}{\Omega}\frac{2\pi Q\eta}{1 - i\tilde{\Delta}}, \quad \tilde{\Delta} = \frac{2Q}{\Omega}\Delta, \tag{31}$$

and the distribution (17) in the new units will have the form

$$w(\omega') = \frac{A}{\pi}\frac{1}{A^2 + (\omega' - B)^2}, \tag{32}$$

where in accordance with Eqs. (14) and (15)

$$A = 5.065, \tag{33}$$

$$B = -0.669. \tag{34}$$

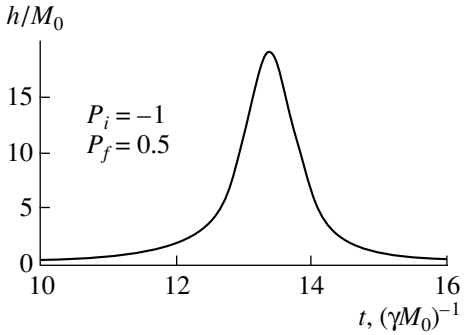

Fig. 1. Shape of the superradiation pulse: $\eta Q = 12$, $\Delta \approx \Delta_c$.

The transverse relaxation time T_2 can be estimated according to the magnitude of the dipole-dipole interaction at an average distance $\mu^2 n$. In the time units chosen we have

$$T_2^{-1} \sim \frac{\mu}{\gamma\hbar}. \tag{35}$$

For the proton $\mu/\gamma\hbar = 0.5$, and therefore $T_2^{-1} \sim 1/2$.

Using such estimates, Eqs. (29) and (30) assume a quite universal form.

3. SOLUTION OF THE BLOCH EQUATIONS AND ANALYSIS OF THE RESULTS

We investigated first the threshold condition for superradiation. If the influence of the local field is neglected, then according to (27) the threshold condition can be represented in the form [6]

$$|P_i| \mathrm{Re}\tilde{\alpha} > T_2^{-1}, \tag{36}$$

where $P_i = M_z(0)/M_0$ is the initial value of the spin polarization. Hence we obtain the threshold value for the detuning:

$$|\tilde{\Delta}_0| = \sqrt{2\pi\eta Q|P_i|T_2 - 1}.$$

To estimate the influence of the stochasticity of the local field and to describe the various regimes of superradiation, we solved the Bloch equations (29) and (30) numerically. We neglected the parameter B, which determines the shift of the distribution of the Larmor frequencies, because it is small compared to the width of this distribution, determined by the quantity $2A$. We chose the following values for the parameters characterizing the system: $\eta Q = 3, 6, 12$; $T_2^{-1} = 0.1A$, $0.2A$, and $0.5A$.

The range of the frequencies ω_k' from $-5A$ to $5A$ was divided into N equal intervals, with each of which Eq. (29) was put into correspondence. The initial values of m_k were chosen to be random:

$$m_k = m_0 e^{-i\varphi}.$$

Here $m_0 = 10^{-6}\mu_p$ (μ_p is the proton magnetic moment), $k = 1, \ldots, N$, and φ is the random phase in the range $0, 2\pi$.

The numerical experiment was performed without scanning the Larmor frequencies ($\Delta = \mathrm{const}$). The delay in the appearance of a pulse, the pulse amplitude and duration, the final polarization of the sample, and the shape and number of pulses were determined (Fig. 1). Since the scan rate in the experiment was low (50 Oe/s [4]) compared with the deexcitation rate, the appearance of a pulse corresponds to a condition close to the threshold condition ($\Delta \approx \Delta_c$).

Three basic results obtained by solving the system of equations (29) and (30) should be noted.

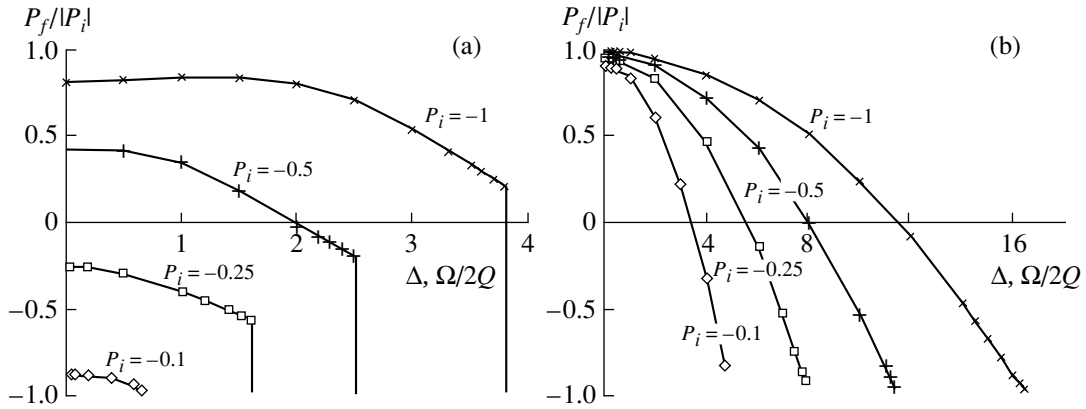

Fig. 2. Final polarizations $P_f/|P_i|$ as a function of the detuning Δ, expressed in units of $\Omega/2Q$ for various initial polarizations P_i: $\eta Q = 6$, $T_2^{-1} = 0.5$, (a) taking account of the distribution of the local fields, (b) neglecting the distribution of the local fields. The detunings for which the final polarizations P_f drop sharply to the initial value correspond to the threshold values Δ_c.

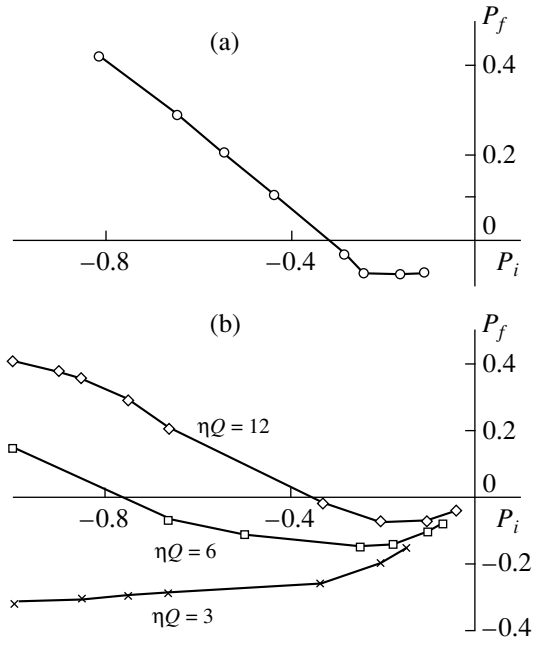

Fig. 3. Final polarizations P_f obtained for detunings Δ close to the threshold values as a function of the initial polarization P_i: (a) experimental data, (b) numerical results. Each curve corresponds to a different value of the product ηQ.

(1) The dependence of the threshold detuning Δ_c on the initial polarization P_i, T_2, and product ηQ was determined (Fig. 2). It is evident that the nonuniformity of the local magnetic field greatly decreases the threshold value of the detuning. Moreover, if the local field is neglected, the final polarizations $P_f(\Delta)$ vary smoothly up to the initial values, and if the local field is taken into account, then a sharp jump is observed.

(2) The dependence on the generation threshold P_{i1} on T_2 and ηQ was determined. For $\eta Q = 6$ and $T_2 = 1/2$ the generation threshold was 7%, which corresponds to the experimental value obtained in [4].

(3) The dependence of the P_{ir} reversal threshold on T_2 and ηQ was determined (Fig. 3b). If $P_i > P_{ir}$, then superradiation occurs with polarization reversal (by a change in the sign of P_f); this explains the possibility of a multipulse generation regime (Fig. 3b). However, for $\eta Q = 6$ and $T_2 = 1/2$ the reversal threshold was 74% (33% in the experiment). It is evident that qualitative agreement with experiment obtains for $\eta Q = 12$ and $T_2^{-1} = 1/2$ (Figs. 3a and 3b).

The value of $P_f(\Delta_c)$ (Fig. 3b) was determined by extrapolating the curve $P_f(\Delta)$ to Δ_c, and value of Δ_c was determined from the minimum of the curve $|h(t)|$ with slow scanning of Δ in the decreasing direction.

4. CONCLUSIONS

In summary, we have shown that local magnetic-field nonuniformities, which are caused by the random distribution of the spins over the volume and the random orientation of the spins, strongly influence the nuclear superradiation process.

A qualitatively new result obtained with this approach, as compared with [5] and [6], was an explanation of the possibility of a monopulse regime with large initial polarization P_i, in agreement with the experiment of [4]. It is not necessary to use detunings less than the threshold value, as assumed in [5].

In our model of superradiation the constant local field, generated by the random uniform distribution of magnetic moments over the sample, is taken into account. It is well-known that in this case the distribution is Lorentzian, if there are no correlations in the arrangement of the magnetic moments [15]. For example, if the fact that the magnetic moments cannot approach one another closer than a certain minimum distance is taken into account, then the wings of the distribution are suppressed and, of course, the contour becomes deformed [16, 17]. In this sense one talks about the approach to a Gaussian distribution. In the present paper we employ a truncated Lorentzian distribution neglecting be deformation of the contour (see Section 3). Similar arguments are also valid for the local field generated by paramagnetic impurities. For a sufficiently high impurity density, the magnetic field which they produce can predominate over the local field of the nuclear spins. This does not change our model in any essential way. A detailed analysis and calculations for a specific system (propandiole) [4] is a subject for a separate publication.

ACKNOWLEDGMENTS

We thank A. I. Kovalev and A. I. Zaitsev for a discussion of the results of this work.

This work was supported by the Ministry of Education of the Russian Federation.

REFERENCES

1. K. R. Dicke, Phys. Rev. **93**, 99 (1954).
2. N. Blombergen and R. Pound, Phys. Rev. **95**, 8 (1954).
3. Yu. F. Kiselev, A. F. Prudkoglyad, A. S. Shumovskiĭ, and V. I. Yukalov, Zh. Éksp. Teor. Fiz. **94** (2), 344 (1988) [Sov. Phys. JETP **67**, 413 (1988)].
4. N. A. Bazhanov, A. I. Kovalev, *et al.*, Preprint No. 1358 LIYaF (Inst. of Nuclear Physics, Leningrad, 1988).
5. N. A. Bazhanov, D. S. Bulyanitsa, A. I. Kovalev, *et al.*, Fiz. Tverd. Tela (Leningrad) **31**, 206 (1989) [Sov. Phys. Solid State **31**, 291 (1989)].
6. N. I. Bazhanov, D. S. Bulyanitsa, A. I. Kovalev, *et al.*, Zh. Éksp. Teor. Fiz. **97**, 1995 (1990) [Sov. Phys. JETP **70**, 1128 (1990)].

7. M. G. Benedict, A. M. Ermolaev, V. A. Malyshev, *et al.*, *Super-Radiance: Multiatomic Coherent Emission* (IOP Publ., Bristol, 1996).
8. A. V. Andreev and A. É. Tsyganov, Kvantovaya Élektron. (Moscow) **18**, 1379 (1991).
9. T. S. Belozerova, V. K. Henner, and V. I. Yukalov, Phys. Rev. B **46**, 682 (1992).
10. V. I. Yukalov, Phys. Rev. Lett. **75**, 3000 (1995).
11. V. I. Yukalov, Phys. Rev. B **53**, 9232 (1996).
12. N. P. Fokina, K. O. Khutsishvili, and S. G. Chkhaidze, Zh. Éksp. Teor. Fiz. **102**, 1013 (1992) [Sov. Phys. JETP **75**, 552 (1992)].
13. N. P. Fokina, K. O. Khutsishvili, S. G. Chkhaidze, and A. M. Lomidze, Fiz. Tverd. Tela (St. Petersburg) **37**, 1910 (1995) [Phys. Solid State **37**, 1040 (1995)].
14. D. A. Kostarov, N. P. Fokina, and K. O. Khutsishvili, Zh. Éksp. Teor. Fiz. **112**, 551 (1997) [JETP **85**, 300 (1997)].
15. A. Abragam, *The Principles of Nuclear Magnetism* (Clarendon Press, Oxford, 1961; Inostrannaya Literatura, Moscow, 1963).
16. S. A. Al'tshuler and B. M. Kozyrev, *Electron Paramagnetic Resonance* (Nauka, Moscow, 1972; Academic, New York, 1964).
17. F. S. Dzheparov and E. K. Henner, Zh. Éksp. Teor. Fiz. **104**, 3667 (1993) [JETP **77**, 753 (1993)].

Translation was provided by AIP

Journal of Experimental and Theoretical Physics, Vol. 91, No. 2, 2000, pp. 245–254.
Translated from Zhurnal Éksperimental'noĭ i Teoreticheskoĭ Fiziki, Vol. 118, No. 2, 2000, pp. 279–290.

ATOMS, SPECTRA, RADIATION

On the Collisional Transfer of Nonequilibrium in the Velocity Distribution of Resonant Particles in a Laser Radiation Field

A. I. Parkhomenko and A. M. Shalagin*

Institute of Automatics and Electrometry,
Siberian Division, Russian Academy of Sciences, Novosibirsk, 630090 Russia
**e-mail: shalagin@iae.nsk.su*

Received December 28, 1999

Abstract—The collisional transfer of nonequilibrium in the velocity distribution of resonant particles in a laser radiation field is investigated theoretically. It is shown numerically that the transfer effect is weak. This makes it possible to use simpler approximate one-dimensional quantum kinetic equations instead of three-dimensional equations to solve spectroscopy and light-induced gas kinetics problems, where it is important to take account of the velocity dependence of the collision frequency. It is shown for anomalous light-induced drift, calculations of which are most sensitive to neglecting the transfer effect, that in a wide range of spectroscopy and light-induced gas kinetics problems the transfer of nonequilibrium can be neglected without risking the loss of important fine details of the phenomena being described. © *2000 MAIK "Nauka/Interperiodica".*

1. INTRODUCTION

It is well known that the action of laser radiation on a gas of resonant particles gives rise to, on account of the Doppler effect, nonequilibrium of the velocity distributions of particles in the combining (affected by the radiation) levels. An important circumstance is that the radiation directly creates nonequilibrium only for the projection v_z of the particle velocity $\mathbf{v}$ on the wave vector $\mathbf{k}$ ($v_z = \mathbf{k} \cdot \mathbf{v}/k$). The radiation does not directly perturb the distribution of the particles over the projection $\mathbf{v}_\perp$, orthogonal to the wave vector $\mathbf{k}$, of the velocity $\mathbf{v}$. Consequently, in the absence of collisions the elements $\rho_{ij}(\mathbf{v})$ of the density matrix of the resonant particles can be represented in the factorized form

$$\rho_{ij}(\mathbf{v}) = W(\mathbf{v}_\perp)\rho_{ij}(v_z), \tag{1}$$

where

$$W(\mathbf{v}_\perp) = \frac{1}{(\sqrt{\pi}\bar{v})^2}\exp\left[-\left(\frac{\mathbf{v}_\perp}{\bar{v}}\right)^2\right], \qquad \bar{v} = \sqrt{\frac{2k_BT}{M}}, \tag{2}$$

$W(\mathbf{v}_\perp)$ is the Maxwell distribution over the projection $\mathbf{v}_\perp$ of the velocity $\mathbf{v}$, M is the mass of the resonant particles, k_B is Boltzmann constant, and T is temperature. The factorization (1) makes it possible to reduce the three-dimensional quantum kinetic equations for the density matrix $\rho_{ij}(\mathbf{v})$ to the one-dimensional equations for $\rho_{ij}(v_z)$ by substituting the expression (1) into the initial three-dimensional equations and then integrating the equations over $\mathbf{v}_\perp$.

When collisions are taken into account the factorization (1) becomes approximate, since the collisions, generally speaking, "transfer" nonequilibrium in the v_z distribution to the distribution over the orthogonal projections $\mathbf{v}_\perp$ of the velocity $\mathbf{v}$. On the basis of intuitive qualitative considerations, however, it is often assumed that the transfer effect is weak [1, 2] and in many cases it can be neglected. Thus, the absence of transfer to the orthogonal projections $\mathbf{v}_\perp$ is incorporated in the most widely used collision models (the strong-collision model, the weak-collision model, the Keilson–Storer model for the kernel of the collision integral), which are ordinarily used to solve spectroscopy and light-induced gas kinetics problems [1–3]. In these collision models the factorization (1) does not break down, and consequently, just as in the absence of collisions, the three-dimensional equations for $\rho_{ij}(\mathbf{v})$ reduce to one-dimensional equations for $\rho_{ij}(v_z)$, which greatly simplifies the solution of the problems.

In the models enumerated above the collision frequencies do not depend on the velocity. This is a necessary condition for absence of collisional transfer of nonequilibrium to the velocity projections orthogonal to the wave vector $\mathbf{k}$ [4].

At present the velocity dependence of the collision frequency must be taken into account in order to solve many spectroscopy problems (see, for example, [5–9]) and light-induced gas kinetics problems (see, for example, [10–14]). This is especially clearly seen in the example of the experimentally observed anomalous

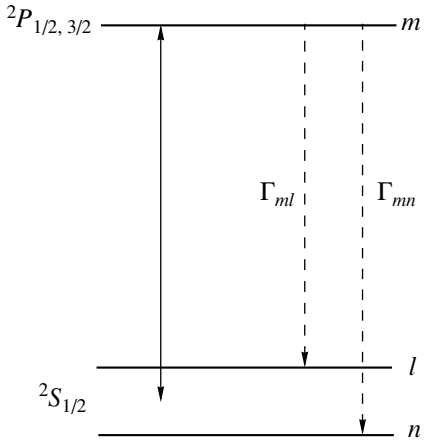

Fig. 1. Scheme of energy levels. The solid arrow denotes a transition under the action of radiation; the dashed arrows show spontaneous radiative transitions.

light-induced drift (LID) of gases [15–19], which is entirely due to the velocity dependence of the transport collision frequencies [10–14]. Transfer of nonequilibrium to the orthogonal projections $\mathbf{v}_\perp$ of the velocity will always be incorporated in the collision models, used for solving such problems, with velocity-dependent collision frequencies. Consequently, the factorization (1) in these models breaks down and the equations to be solved must necessarily be three-dimensional. It is obvious that it is much more difficult in many cases to find and to analyze the solution of three-dimensional equations than in the one-dimensional situation. Consequently, the question of the possibility of using simpler approximate one-dimensional equations for solving spectroscopy and light-induced gas-kinetics problems, where it is important to take account of the velocity dependence of the collision frequency, becomes urgent. In other words, it is important to know the error due to switching from three- to one-dimensional equations. The magnitude of this error is completely due to the effectiveness of the collision transfer of nonequilibrium in the v_z distribution of resonant particles to the orthogonal projections $\mathbf{v}_\perp$ of their velocity. The scheme of the transition to one-dimensional equations is well known [1, 2, 20]: the relation (1) is substituted into the initial three-dimensional quantum kinetic equations for the density matrix $\rho_{ij}(\mathbf{v})$ and the resulting equations are integrated over $\mathbf{v}_\perp$, which results in one-dimensional quantum kinetic equations for $\rho_{ij}(v_z)$ with one-dimensional collision integrals

$$S_{ij}(v_z) = \int S_{ij}(\mathbf{v})d\mathbf{v}_\perp, \qquad (3)$$

where $S_{ij}(\mathbf{v})$ are the three-dimensional collision integrals.

A quantitative analysis of the accuracy of the solution, given by the one-dimensional quantum kinetic equations for velocity-dependent collision frequencies, was first made in the recent work [4]. In [4] the interaction of a laser radiation with two-level particles, undergoing collisions with buffer-gas particles, was studied. The form of the spectral absorption line, the work of the probe field, and the shape of the LID line (velocity of light-induced drift as a function of the radiation frequency) were calculated. The so-called "kangaroo" model [21], which is an extension of the strong-collision model to velocity-dependent transport collision frequencies, was used for the collision integral. In [4] the collision frequencies were calculated for power-law interaction potentials. It was shown that collisional transfer of nonequilibrium in the velocity distribution of resonant particles is strongest for the anomalous LID. Nonetheless, the error introduced by using the one-dimensional collision integrals is small even in this case.

In the present paper we propose to investigate the collisional transfer of nonequilibrium for the anomalous LID in a real system—for lithium atoms in an atmosphere of inert buffer gases. The error introduced by using the one-dimensional collision integrals is investigated in detail. Lithium atoms are described by a three-level Λ scheme, and the model of velocity-isotropic "arrival" [14] with velocity-dependent transport collision frequencies, which were calculated on the basis of realistic Pascale–Vandeplanque interaction potentials [22], is used for the collision integrals. A more complicated shape of the anomalous LID line than for two-level particles, which were studied in [4], is characteristic for lithium atoms modeled by a three-level scheme. Moreover, for lithium atoms in an atmosphere of inert buffer gases, optical pumping of the hyperfine components of the ground state is important because there is no collisional exchange between the hyperfine components [23]. Nonetheless, it was found that even in this case, which is more complicated than the one studied in [4] and which uses a more general collisional model than in [4], the one-dimensional quantum kinetic equations are applicable in a wide range with a relatively small error due to the transfer from three- to one-dimensional collision integrals.

2. GENERAL RELATIONS

Let us consider the interaction of a traveling monochromatic wave with a gas of three-level absorbing particles in a mixture with a buffer gas. The level scheme of the absorbing particles is shown in Fig. 1. Here the levels n and l are the components of the hyperfine structure of the ground state. The level m corresponds to an excited electronic state. Particles undergo radiative relaxation from the level m to the levels n and l with constants Γ_{mn} and Γ_{ml}, respectively. We neglect collisions between the absorbing particles, making the assumption that the density N_b of the buffer gas is much higher than the density N of the absorbing gas.

This level scheme reflects well the real structure of the ground and first excited states of lithium atoms (^{7}Li or ^{6}Li). Indeed, the ground level $^2S_{1/2}$ of these atoms is split into two hyperfine components. For ^{7}Li atoms the hyperfine splitting of the ground state $\omega_{ln} = 5.049 \times 10^9$ s^{-1} [24] is comparable to the Doppler width of the resonance line, and consequently the ground state is modeled by two levels n and l. For ^{6}Li atoms the hyperfine splitting $\omega_{ln} = 1.434 \times 10^9$ s^{-1} [24] is several times less than the Doppler width of the resonance line, but we shall also model the ground state by two levels. For ^{7}Li atoms (the spin of the nucleus is 3/2) the level n is characterized by the statistical weight $g_n = 3$ (the total angular momentum of the atom $F = 1$), and the level l is characterized by the statistical weight $g_l = 5$ ($F = 2$). For ^{6}Li atoms (spin-1 nucleus) $g_n = 2$ ($F = 1/2$) and $g_l = 4$ ($F = 3/2$).

The level m (with statistical weight g_m) models a group of levels consisting of the hyperfine structure components of the excited states $^2P_{1/2}$ or $^2P_{3/2}$. This modeling of the group of levels by a single level is possible because for ^{7}Li and ^{6}Li atoms the hyperfine splitting in these excited states is quite small compared with the Doppler width of the resonance line. The radiation affects only one of the hyperfine components of the excited state: $^2P_{1/2}$ or $^2P_{3/2}$.

The limiting case of strong collisional coupling between the hyperfine components $^2P_{1/2}$ and $^2P_{3/2}$ (the Massey parameter is much less than 1) holds for lithium atoms. For excitation of atoms into the state $^2P_{1/2}$ and into the state $^2P_{3/2}$ the scattering cross sections are virtually identical [25]. Consequently, from the standpoint of collisions a pair of hyperfine components can be interpreted as a single level and the velocity of light-induced drift as a function of the offset of the radiation frequency will be the same for excitation of the D_1 or D_2 lines of lithium atoms. This result (the existence of single transfer characteristics for an atom in the ^2P state) is also confirmed in LID experiments with sodium atoms [26], for which, just as for lithium atoms, the limiting case of strong collisional coupling between the hyperfine components $^2P_{1/2}$ and $^2P_{3/2}$ holds.

The interaction of particles with radiation under stationary and spatially uniform conditions can be described by the following equations for the density matrix [1, 2]:

$$\begin{aligned}
\Gamma_m \rho_m(\mathbf{v}) &= S_m(\mathbf{v}) + N[P_n(\mathbf{v}) + P_l(\mathbf{v})], \\
\Gamma_{mi}\rho_m(\mathbf{v}) + S_i(\mathbf{v}) &= NP_i(\mathbf{v}), \\
\left[\frac{\Gamma_m}{2} - i(\Omega_{0i} - \mathbf{k}\cdot\mathbf{v})\right]\rho_{mi}(\mathbf{v}) &= S_{mi}(\mathbf{v}) + iG\left[\rho_i(\mathbf{v}) - \frac{g_i}{g_m}\rho_m(\mathbf{v})\right],
\end{aligned} \tag{4}$$

where

$$\begin{aligned}
NP_i(\mathbf{v}) &= -2\mathrm{Re}[iG^*\rho_{mi}(\mathbf{v})], \quad |G|^2 = \frac{BI}{2\pi}, \\
B &= \frac{\lambda^2\Gamma_m}{4\hbar\omega}\frac{g_m}{g_n + g_l}, \quad \Gamma_m = \Gamma_{mn} + \Gamma_{ml}, \\
\Omega_{0i} &= \omega - \omega_{mi}, \quad i = n, l.
\end{aligned} \tag{5}$$

Here $\rho_i(\mathbf{v})$ is the velocity distribution of the particles in level i; $N = N_n + N_l + N_m$ is the density of absorbing particles $\left(N_i = \int \rho_i(\mathbf{v})d\mathbf{v}\right)$; $S_m(\mathbf{v})$, $S_i(\mathbf{v})$, and $S_{mi}(\mathbf{v})$ are collision integrals; ω, λ and $\mathbf{k}$ are the frequency, wavelength, and wave vector of the radiation; Γ_{mi} is the spontaneous relaxation rate of the level m in the channel $m \longrightarrow i$; ω_{mi} is the m–i collision frequency; and, I is the radiation intensity. The formula for the second Einstein coefficient B in Eq. (5) takes account of the fact that in the three-level model chosen the ratio of the radiative transition rates from level m into the hyperfine components n and l is determined by the ratio of the statistical weights [27]: $\Gamma_{mn}/\Gamma_{ml} = g_n/g_l$. The probability $P_i(\mathbf{v})$ of radiation absorption per unit time on a transition m–i of a particle with a fixed velocity $\mathbf{v}$ is determined by the off-diagonal element of the density matrix (or coherence) $\rho_{mi}(\mathbf{v})$. We note that the last equation in Eqs. (4) for the off-diagonal element $\rho_{mi}(\mathbf{v})$ is valid when the coherence $\rho_{ln}(\mathbf{v})$ between the hyperfine components n and l is neglected. For lithium atoms this approximation is valid for not too high radiation intensities: $I \ll 10$ W/cm^2 [28].

We shall integrate over the velocity $\mathbf{v}$ the second equation in Eq. (4) and take a count of the fact that in the presence of elastic collisions $\int S_i(\mathbf{v})d\mathbf{v} = 0$. Ultimately, it follows from the equations obtained that

$$\frac{P_n}{P_l} = \frac{\Gamma_{mn}}{\Gamma_{ml}} = \frac{g_n}{g_l}, \tag{6}$$

where $P_i = \int P_i(\mathbf{v})d\mathbf{v}$. This relation shows that the ratio of the integral radiation absorption probabilities on the transitions m–n and m–l is independent of intensity and radiation frequency. It characterizes the optical pumping of hyperfine components of the ground state and is a consequence of the absence of collisional exchange between the hyperfine components n and l.

In the absence of phase memory in collisions on optical transitions (a common assumption for atomic spectroscopy) the off-diagonal collision integral has the form

$$S_{mi}(\mathbf{v}) = -[\gamma_{mi}(v) + i\Delta_{mi}(v)]\rho_{mi}(\mathbf{v}), \quad i = n, l, \tag{7}$$

where $\gamma_{mi}(v)$ and $\Delta_{mi}(v)$ are the collisional broadening and the collisional shift of the levels, respectively.

Since the interaction potentials of the atoms in the states $i = n, l$ with buffer particles are essentially identical, the transitions m–n and m–l can be assigned the same collisional characteristics:

$$\begin{aligned}\gamma_{mn}(v) &= \gamma_{ml}(v) \equiv \gamma(v),\\ \Delta_{mn}(v) &= \Delta_{ml}(v) \equiv \Delta(v).\end{aligned} \tag{8}$$

We find for the absorption probability $P_i(\mathbf{v})$ (5), taking account of Eq. (7),

$$NP_i(\mathbf{v}) = \frac{BI}{\pi} Y_i(\mathbf{v}) \left[\rho_i(\mathbf{v}) - \frac{g_i}{g_m} \rho_m(\mathbf{v}) \right], \tag{9}$$

where

$$\begin{aligned} Y_i(\mathbf{v}) &= \frac{\Gamma(v)}{\Gamma^2(v) + [\Omega_i(v) - \mathbf{k}\cdot\mathbf{v}]^2},\\ \Gamma(v) &= \frac{\Gamma_m}{2} + \gamma(v),\\ \Omega_i(v) &= \Omega_{0i} - \Delta(v), \quad i = n, l. \end{aligned} \tag{10}$$

Here $\Gamma(v)$ is the homogeneous half-width of an absorption line on the transitions m–n and m–l.

We shall use the model of velocity-isotropic "arrival" for the diagonal collisional integrals:

$$\begin{aligned} S_i(v) &= -\nu_i(v)\rho_i(\mathbf{v}) + S_i^{(2)}(v),\\ i &= n, l, m, \end{aligned} \tag{11}$$

where the arrival term $S_i^{(2)}(v)$ is a function of the modulus of the velocity $v = |\mathbf{v}|$. The quantity $\nu_i(v)$ in Eq. (11) is the transport collision frequency [29]. The collision model (11) takes account of the velocity dependence of the collision frequency and, at the same time, makes it possible to obtain an analytical solution for the problem under study.

The relation between the transport collision frequency $\nu_i(v)$ in Eq. (11) and the characteristics of an elementary scattering event is given by the formula (see [2])

$$\nu_i(v) = \frac{q}{v^3} \int_0^\infty u^2 \exp\left(-\frac{u^2 + v^2}{\bar{v}_b^2} \right) F(uv)\sigma_i(u)du, \tag{12}$$

where

$$\begin{aligned} F(uv) &= \frac{2uv}{\bar{v}_b^2}\cosh\left(\frac{2uv}{\bar{v}_b^2}\right) - \sinh\left(\frac{2uv}{\bar{v}_b^2}\right),\\ q &= \frac{\mu}{M}\frac{N_b \bar{v}_b}{\sqrt{\pi}}, \quad \mu = \frac{MM_b}{M + M_b}, \quad \bar{v}_b = \sqrt{\frac{2k_B T}{M_b}}, \end{aligned} \tag{13}$$

N_b and M_b are, respectively, the density and mass of the buffer particles, u is the magnitude of the relative velocity of the resonance and buffer particles before a collision, and $\sigma_i(u)$ is the transfer cross section for the scattering of an absorbing particle in the state i by a buffer particle. It can be assumed, to a high degree of accuracy, that the transport collision frequencies on hyperfine components n and l are equal [13]:

$$\nu_l(v) = \nu_n(v). \tag{14}$$

The light-induced drift velocity of the absorbing particles is determined by the relation

$$\mathbf{u}_L \equiv \frac{\mathbf{j}_n + \mathbf{j}_l + \mathbf{j}_m}{N}, \quad \mathbf{j}_i = \int \mathbf{v}\rho_i(\mathbf{v})d\mathbf{v}, \tag{15}$$

where $\mathbf{j}_i$ is the partial flux of particles in the state i. For Eqs. (4), (11), and (15) we obtain, taking account of the relation (14), for the drift velocity the formula

$$\begin{aligned} \mathbf{u}_L &= \int \mathbf{v}\tau(v)[P_n(\mathbf{v}) + P_l(\mathbf{v})]d\mathbf{v},\\ \tau(v) &= \frac{\nu_n(v) - \nu_m(v)}{\nu_n(v)[\Gamma_m + \nu_m(v)]}. \end{aligned} \tag{16}$$

3. DRIFT VELOCITY FOR WEAK RADIATION INTENSITY

In what follows we shall confine our attention to low radiation intensity for calculating the drift velocity:

$$I \ll \frac{\Gamma(\Gamma_m + \nu_m)}{B}, \tag{17}$$

where ν_m and Γ are the characteristic (average) values of $\nu_m(v)$ and $\Gamma(v)$. Under the condition (17) the population of the excited level can be neglected in Eq. (9) [$\rho_m(v) = 0$], and the velocity distribution of the populations in the hyperfine components $i = n, l$ in the ground state can be assumed to be close to the Maxwell distribution [$\rho_i(\mathbf{v}) = N_i W(\mathbf{v})$, where $W(\mathbf{v})$ is Maxwell distribution]. Then we obtain from Eq. (9)

$$P_i(\mathbf{v}) = \frac{BI}{\pi}\frac{N_i}{N} Y_i(\mathbf{v}) W(\mathbf{v}). \tag{18}$$

Combining Eqs. (6) and (18) and applying the normalization condition $N_n + N_l \simeq N$ [here the fact that $N_m \ll N$ in the conditions (17) is taken into account], we find

$$\begin{aligned} \frac{N_n}{N} &= \frac{w_n \langle Y_l \rangle}{w_n \langle Y_l \rangle + w_l \langle Y_n \rangle}, \quad \frac{N_l}{N} = 1 - \frac{N_n}{N},\\ \langle Y_i \rangle &= \int Y_i(\mathbf{v}) W(\mathbf{v}) d\mathbf{v}, \quad w_i = \frac{g_i}{g_n + g_l}, \quad i = n, l. \end{aligned} \tag{19}$$

Substituting the expressions (18) and (19) into Eq. (16) and integrating over the directions of the velocity $\mathbf{v}$ we obtain the final expression for the velocity $\mathbf{u}_L$ of light-induced drift, which we represent in the form

$$\mathbf{u}_L \equiv \frac{\mathbf{k}}{k} u_L, \quad u_L = u_0 u(x), \tag{20}$$

where the parameter u_0 with the dimensions of velocity is given by

$$u_0 = \frac{2BI}{\pi^{3/2}k\Gamma_m}, \tag{21}$$

and the dimensionless velocity $u(x)$ is a function of the dimensionless detuning x of the radiation frequency is given by

$$u(x) = \frac{1}{w_n\langle Y_l\rangle + w_l\langle Y_n\rangle} \times \int_0^\infty t\tau_0(t)\exp(-t^2)[w_n\langle Y_l\rangle f_n(t) + w_l\langle Y_n\rangle f_l(t)]dt. \tag{22}$$

Here the functions of the dimensionless velocity $t = v/\bar{v}$ were used:

$$f_i(t) = x_i(t)\psi_i(t) + \frac{y(t)}{2}\ln\left[\frac{y^2(t) + [t - x_i(t)]^2}{y^2(t) + [t + x_i(t)]^2}\right],$$

$$\psi_i(t) = \arctan\frac{t + x_i(t)}{y(t)} + \arctan\frac{t - x_i(t)}{y(t)},$$

$$\tau_0(t) = \frac{\nu_n(\bar{v}t) - \nu_m(\bar{v}t)}{\nu_n(\bar{v}t)\left[1 + \frac{\nu_m(\bar{v}t)}{\Gamma_m}\right]}, \tag{23}$$

$$y(t) = \frac{\Gamma(\bar{v}t)}{k\bar{v}}, \quad x_i(t) = \frac{\Omega_i(\bar{v}t)}{k\bar{v}},$$

$$\bar{v} = \sqrt{\frac{2k_BT}{M}}, \quad i = n, l.$$

In Eq. (22) the quantities $\langle Y_i\rangle$, defined in Eqs. (19), assume the form

$$\langle Y_i\rangle = \frac{2}{\sqrt{\pi}k\bar{v}}\int_0^\infty t\exp(-t^2)\psi_i(t)dt, \quad i = n, l. \tag{24}$$

It is convenient to introduce for the dimensionless detuning x of the radiation frequency in Eq. (20) the quantity

$$x = \frac{\Omega}{k\bar{v}}, \tag{25}$$

where

$$\Omega = \omega - \omega_0, \quad \omega_0 = w_n\omega_{mn} + w_l\omega_{ml}. \tag{26}$$

The frequency ω_0 corresponds to the "center of gravity" of the transition frequencies ω_{mn} and ω_{ml}, taking account of the statistical weights of the levels n and l.

In the region of "normal" LID [where we can set $\tau_0(t) = \text{const}$ in Eq. (22)] the shape of the LID line has a very simple dispersion-like form and the drift velocity $\mathbf{u}_L$ vanishes only at the point $x = 0$ [30] (see Fig. 4 below), just as for two-level particles. Even though lithium atoms are described by a three-level Λ scheme, the shape of the "normal" LID line for them has the simple "two-level" form because of optical pumping of the hyperfine components of the ground state as a result of the absence of collisional exchange between the hyperfine components in the case of inert buffer gases. The great simplicity of the shape of the "normal" LID line of lithium atoms makes it possible to observe easily the very small deviations from this shape in an experiment.

In calculating the drift velocity of atoms in a mixture of two different buffer gases, the relation

$$\nu_i(\bar{v}t) = \nu_{1i}(\bar{v}t) + \nu_{2i}(\bar{v}t), \quad i = n, m, \tag{27}$$

where the indices 1 and 2 denote the types of buffer particles, should be substituted in Eq. (23) for $\tau_0(t)$.

4. DRIFT VELOCITY USING ONE-DIMENSIONAL COLLISION INTEGRALS IN THE CALCULATIONS

The switch from three- to one-dimensional kinetic equations (4) is made, as already mentioned in the introduction, by substituting the approximate factorization $\rho_i(\mathbf{v}) = W(\mathbf{v}_\perp)\rho_i(v_z)$, $i = n, l, m$ into the initial equations (4) and then integrating these equations over $\mathbf{v}_\perp$. We find from the equations obtained in this manner that the LID velocity is given by a relation formally analogous to Eq. (16):

$$\mathbf{u}_L^{(1)} = \frac{\mathbf{k}}{k}\int_{-\infty}^\infty v_z\tau^{(1)}(v_z)[P_n^{(1)}(v_z) + P_l^{(1)}(v_z)]dv_z,$$
$$\tau^{(1)}(v_z) = \frac{\nu_n^{(1)}(v_z) - \nu_m^{(1)}(v_z)}{[\nu_n^{(1)}(v_z)\Gamma_m + \nu_m^{(1)}(v_z)]}, \tag{28}$$

where $\nu_i^{(1)}(v_z) \equiv \nu_i^{(1)}(|v_z|)$ is the one-dimensional collision frequency, related with the three-dimensional frequency $\nu_i(v)$ by the formula

$$\nu_i^{(1)}(v_z) \equiv \int \nu_i(v)W(\mathbf{v}_\perp)d\mathbf{v}_\perp. \tag{29}$$

Using the relation $\mathbf{v}^2 = \mathbf{v}_\perp^2 + v_z^2$ Eq. (29) becomes

$$\nu_i^{(1)}(v_z) = \frac{2}{\bar{v}^2}\exp\left(\frac{v_z^2}{\bar{v}^2}\right)\int_{|v_z|}^\infty v\nu_i(v)\exp\left(-\frac{v^2}{\bar{v}^2}\right)dv. \tag{30}$$

The radiation absorption probabilities $P_i^{(1)}(v_z)$ in Eq. (28) under the condition (17) of low radiation intensity are given by a formula which is formally similar to Eq. (18):

$$P_i^{(1)}(v_z) = \frac{BI}{\pi}\frac{N_i^{(1)}}{N}Y_i^{(1)}(v_z)W(v_z), \quad i = n, l, \tag{31}$$

where

$$Y_i^{(1)}(v_z) = \frac{\Gamma^{(1)}(v_z)}{[\Gamma^{(1)}(v_z)]^2 + [\Omega_i^{(1)}(v_z) - kv_z]^2},$$

$$\Gamma^{(1)}(v_z) = \frac{\Gamma_m}{2} + \gamma^{(1)}(v_z), \qquad (32)$$

$$\Omega_i^{(1)}(v_z) = \Omega_{0i} - \Delta^{(1)}(v_z),$$

$$W(v_z) = \frac{1}{\sqrt{\pi}\bar{v}}\exp\left(-\frac{v_z^2}{\bar{v}^2}\right), \quad i = n, l.$$

In Eq. (32) the one-dimensional analogs $\gamma^{(1)}(v_z) \equiv \gamma^{(1)}(|v_z|)$ and $\Delta^{(1)}(v_z) \equiv \Delta^{(1)}(|v_z|)$ of the three-dimensional quantities $\gamma(v)$ and $\Delta(v)$ are given by formulas similar to Eqs. (29) and (30), and the relative population $N_i^{(1)}/N$ of the level i is given by a formula similar to Eq. (19) for N_i/N with $\langle Y_i\rangle$ replaced by $\langle Y_i^{(1)}\rangle$ in it, where

$$\langle Y_i^{(1)}\rangle = \int_{-\infty}^{\infty} Y_i^{(1)}(v_z)W(v_z)dv_z. \qquad (33)$$

The formula (28) for the drift velocity $\mathbf{u}_L^{(1)}$ assumes the form, after $P_i^{(1)}(v_z)$ from Eq. (31) is substituted into it,

$$\mathbf{u}_L^{(1)} = \frac{\mathbf{k}}{k}\frac{BI}{\pi}\int_{-\infty}^{\infty} v_z\tau^{(1)}(v_z) \times\left[\frac{N_n^{(1)}}{N}Y_n^{(1)}(v_z) + \frac{N_l^{(1)}}{N}Y_l^{(1)}(v_z)\right]W(v_z)dv_z. \qquad (34)$$

It can be shown that if the transport collision frequencies $\nu_i(v)$, the collisional broadening $\gamma(v)$, and the collisional shift $\Delta(v)$ of the levels do not depend on the velocity, then the formulas (20) and (22) for $\mathbf{u}_L$ and (34) for $\mathbf{u}_L^{(1)}$ are identical, as should be.

In the limit of large Doppler broadening ($\Gamma \ll k\bar{v}$) and for $\Delta(v)$ = const the formula (34) for the drift velocity assumes its simplest form

$$\mathbf{u}_L^{(1)} = \frac{\mathbf{k}}{k}\bar{v}\frac{BI}{\sqrt{\pi}(k\bar{v})^2} \times\frac{w_n\Omega_n\tau^{(1)}\left(\frac{\Omega_n}{k\bar{v}}\right) + w_l\Omega_l\tau^{(1)}\left(\frac{\Omega_l}{k\bar{v}}\right)}{w_n\exp\left[\left(\frac{\Omega_n}{k\bar{v}}\right)^2\right] + w_l\exp\left[\left(\frac{\Omega_l}{k\bar{v}}\right)^2\right]}. \qquad (35)$$

An expression for the drift velocity which is so simple to analyze and does not contain integrals cannot be obtained using three-dimensional equations.

5. COMPARATIVE ANALYSIS

We have investigated the collisional transfer of nonequilibrium in the velocity distribution of resonant particles in a laser radiation field by directly comparing the results of numerical calculations of the LID velocity of lithium atoms in an atmosphere of inert buffer gases using the formulas (20) and (22) (three-dimensional approach) and (34) (one-dimensional approach). The transport collision frequencies $\nu_i(t) \equiv \nu_i(t\bar{v}) \equiv \nu_i(v)$ for the systems Li–X, where X is an inert gas atom, was calculated numerically using Eq. (12) and the transfer cross sections $\sigma_i(u)$, calculated in [11] on the basis of semiempirical Pascale–Vandeplanque interaction potentials [22].

Under Doppler broadening conditions for the absorption line ($\Gamma \ll k\bar{v}$) the effect of the $\Gamma(v)$-dependence of the homogeneous half-width of the absorption line $\Omega_i(v)$ and the detunings v of the radiation frequency on the drift velocity $\mathbf{u}_L$ is negligible and can be neglected [14]. For homogeneous broadening ($\Gamma > k\bar{v}$) this dependence can also be neglected in our problem (see the discussion of Fig. 6a below in this connection). Consequently, we set $\Gamma(v) = \Gamma$ = const and $\Omega_i(v) = \Omega_i$ = const in the numerical calculations. The specific values of the quantities $\Gamma = \Gamma_m/2 + \gamma$ for different systems Li–X were determined from the data of [31] for collisional broadening γ of the absorption line (γ = 3.86 MHz/torr for Li–Ne, γ = 5.31 MHz/torr for Li–Ar, γ = 7.00 MHz/torr for Li–Kr, and γ = 7.96 MHz/torr for Li–Xe).

For $\Omega_i(v)$ = const the dimensionless detuning x (25) of the radiation frequency is related with the detunings $x_i(t) = x_i$ by the relations

$$x_n = x - \delta w_l, \quad x_l = x + \delta w_n, \quad \delta = \frac{\omega_{ln}}{k\bar{v}}, \qquad (36)$$

where δ is the dimensionless distance between the components of the hyperfine structure of the ground state.

Figures 2 and 3 show the dependences, calculated using the formulas (12) and (30) on the dimensionless velocities $t = v/\bar{v}$ and $t_z = v_z/\bar{v}$ of three-dimensional, $\nu_i(t)$, and one-dimensional, $\nu_i^{(1)}(t_z) \equiv \nu_i^{(1)}(\bar{v}t_z)$, transport collision frequencies and the relative differences of the transport collision frequencies

$$\frac{\Delta\nu}{\nu} \equiv \frac{\nu_m(t) - \nu_n(t)}{\nu_n(t)}, \qquad \frac{\Delta\nu^{(1)}}{\nu^{(1)}} \equiv \frac{\nu_m^{(1)}(t_z) - \nu_n^{(1)}(t_z)}{\nu_n^{(1)}(t_z)} \qquad (37)$$

for lithium atoms in various buffer gases. The characteristic feature for the one-dimensional quantities $\nu_i^{(1)}(t_z)$ and $\Delta\nu^{(1)}/\nu^{(1)}$ is the smoother velocity dependence compared with the three-dimensional quantities

$\nu_i(t)$ and $\Delta\nu/\nu$. The sign-alternating velocity dependence of the relative difference of the transport collision frequencies gives rise to the anomalous LID and the strong sensitivity of the shape of the anomalous LID line to the character of the dependence of $\Delta\nu/\nu$ on v [10–14]. This is why the shape of the anomalous LID line is most sensitive to collisional transfer of nonequilibrium in the velocity distribution of resonant particles.

Figures 4–6 show the results of numerical calculations of the dimensionless drift velocities $u(x)$ and $u^{(1)}(x)$ obtained using the three-dimensional and one-dimensional descriptions of the LID, respectively. The dimensionless drift velocity $u^{(1)}(x)$ is determined by the expression $u^{(1)}(x) = \mathbf{k} \cdot \mathbf{u}_L^{(1)}/ku_0$, similar to the expression (20) for $u(x)$ with $\mathbf{u}_L$ in it replaced by $\mathbf{u}_L^{(1)}$ from Eq. (34) and $u(x)$ replaced by $u^{(1)}(x)$.

Figure 4 shows the dependence of the drift velocities $u(x)$ and $u^{(1)}(x)$ of ^{7}Li atoms on the detuning of the radiation frequency in Ne buffer gas at temperature T = 300 K. In this case the shape of the drift velocity line corresponds to "normal" LID ($\Delta\nu/\nu$ as a function of v does not change sign) and is described well by the LID theory with transport collision frequencies which do not depend on the velocity v [14]. The difference of the velocities $u(x)$ and $u^{(1)}(x)$ was found to be so small that, as one can see from Fig. 4, the plots of $u(x)$ and $u^{(1)}(x)$ merge and are seen as one curve. Analysis shows that such a weak difference between $u(x)$ and $u^{(1)}(x)$ occurs for any character of the broadening of the absorption line (Doppler, $y = \Gamma/k\bar{v} \ll 1$, or homogeneous, $y > 1$). This result [merging of the plots of $u(x)$ and $u^{(1)}(x)$] is even unexpected to some extent: under conditions where the collision frequency depends on the velocity for the "normal" LID, though the values of $u(x)$ and $u^{(1)}(x)$ are expected to be close, they are not expected to coincide to such a high degree. Thus, the influence of the collisional transfer of nonequilibrium on the shape of the "normal" LID line is so small that it can always be neglected.

For the anomalous LID (with sign-alternating dependence of $\Delta\nu/\nu$ on v, as shown in Fig. 3) the difference between the plots of $u(x)$ and $u^{(1)}(x)$ is now clearly seen, though it is small (Figs. 5 and 6). For homogeneous broadening of the absorption line ($y > 1$) the difference between $u(x)$ and $u^{(1)}(x)$ does not exceed 20% (Fig. 5c and 6c) and does not lead to loss of any important details in the dependence of the drift velocity on the radiation frequency. For Doppler broadening ($y \ll 1$) neglecting the collisional transfer of nonequilibrium in the velocity distribution of resonant particles can result, as one can see in Fig. 5b, in a loss of some subtle details in the shape of the LID line (in Fig. 5b the function $u^{(1)}(x)$ possesses one zero, while the function $u(x)$ possesses three zeros. However, in most cases neglecting the collisional transfer of nonequilibrium does not

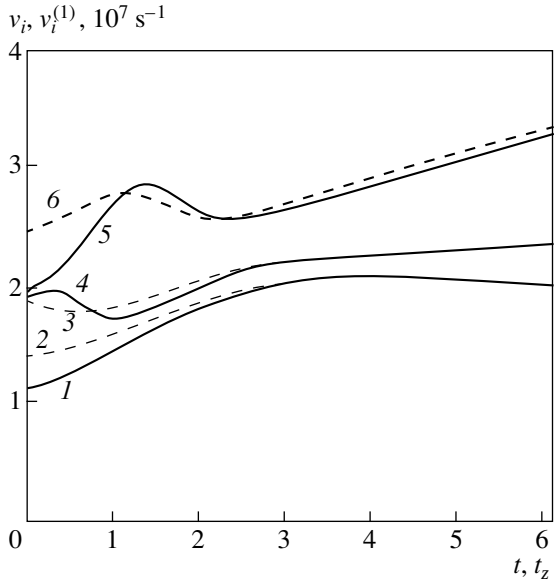

Fig. 2. Three-dimensional, ν_i, and one-dimensional, $\nu_i^{(1)}$, transport collision frequencies as a function of the dimensionless velocities $t = v/\bar{v}$ and $t_z = v_z/\bar{v}$ of lithium atoms at temperature T = 300 K and buffer-gas pressure P = 1 torr: (*1*) $\nu_n(t)$ for the system ^{7}Li–Ne; (*2*) $\nu_n^{(1)}(t_z)$ for ^{7}Li–Ne; (*3*) $\nu_n^{(1)}(t_z)$ for ^{7}Li–Kr; (*4*) $\nu_n(t)$ for ^{7}Li–Kr; (*5*) $\nu_m(t)$ for ^{7}Li–Kr; (*6*) $\nu_m^{(1)}(t_z)$ for ^{7}Li–Kr.

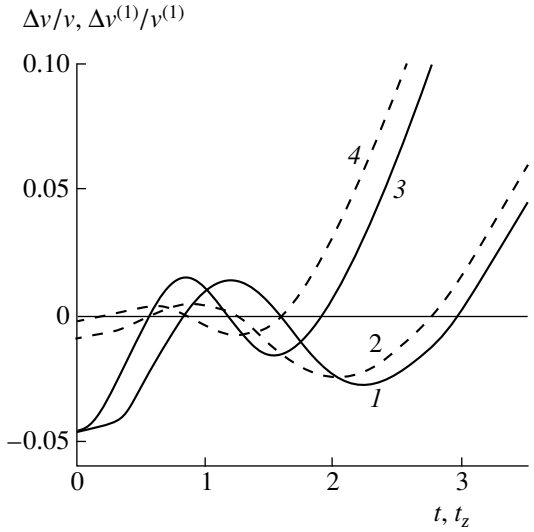

Fig. 3. Relative difference of the three-dimensional $\Delta\nu/\nu$ and one-dimensional $\Delta\nu^{(1)}/\nu^{(1)}$ transport collision frequencies as a function of the velocity for various systems: (*1*, *2*) ^{7}Li–(Ne + Kr) at T = 300 K and neon fractions in the buffer mixture ξ = 0.875 ($\xi = N_{Ne}/N_b$, where N_{Ne} is the neon density, N_b is the total density of buffer particles); (*3*, *4*) ^{6}Li–(Ne + Kr) at T = 600 K and ξ = 0.865. The solid curves (*1* and *3*) $\Delta\nu/\nu$; dashed curves (*2* and *4*) $\Delta\nu^{(1)}/\nu^{(1)}$.

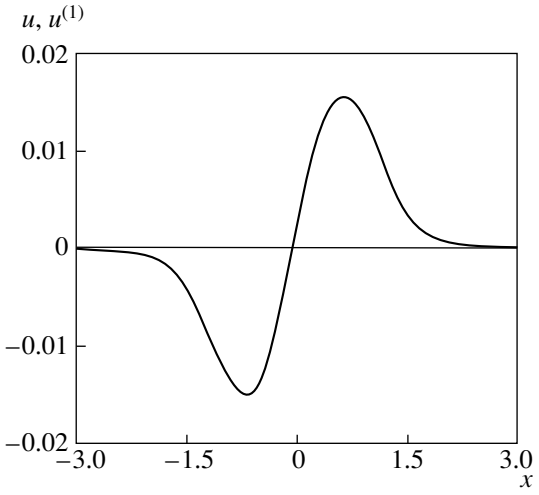

Fig. 4. Drift velocities u and $u^{(1)}$ versus the dimensionless detuning of the radiation frequency $x = \Omega/k\bar{v}$ for ^{7}Li atoms in Ne buffer gas for the "normal" LID at temperature T = 300 K and buffer gas pressure P = 5 torr ($y = \Gamma/k\bar{v} = 0.33$). The plots of $u(x)$ and $u^{(1)}(x)$ merge and are seen as a single curve.

result in a loss of important fine details in the dependence of the drift velocity on the radiation frequency, as one can see in Figs. 5a, 6a, and 6b [quite complicated oscillating functions $u(x)$].

We investigated the dependences of the drift velocities u and $u^{(1)}$ on the detuning of the radiation frequency for the anomalous LID of lithium atoms in other buffer mixtures also (Ne + Ar, Ne + Xe) and obtained the same conclusions from the computational results [weak difference between the functions $u(x)$ and $u^{(1)}(x)$], as in the case of the computational results, shown in Figs. 5 and 6, for the drift of lithium atoms in the buffer mixture Ne + Kr. Thus, even for the anomalous LID the influence of the collisional transfer of nonequilibrium on the shape of the LID line is small, and in many cases it can be neglected even when investigating quite fine important details in the radiation frequency dependence of the drift velocity.

Since the anomalous manifestation of the LID is entirely due to the sign-alternating velocity dependence of the difference of the transport collision frequencies $\Delta\nu \equiv \nu_n(v) - \nu_m(v)$, it should be expected that all subtle details of the shape of the LID line also remain when the velocity dependence of the collision frequency is neglected in the denominators of the factors $\tau(v)$ in Eq. (16) or $\tau^{(1)}(v_z)$ in Eq. (34). The calculations whose results are shown in Fig. 6a confirm this. The curve *2* in this figure illustrates the dependence, calculated using Eq. (34), $u^{(1)}(x)$ for the system ^{6}Li–(Ne + Kr). The curve *3* corresponds to the dependence $u^{(1)}(x)$ calculated using Eq. (34) with the frequency $\nu_i^{(1)}(v_z)$ ($i = m, n$) in the denominator of the factor $\tau^{(1)}(v_z)$ is replaced by the average transfer frequency

$$\langle\nu_i\rangle = \frac{2}{\bar{v}^2}\int(\mathbf{n}\cdot\mathbf{v})^2 W(\mathbf{v})\nu_i(v)d\mathbf{v} = \frac{8}{3\sqrt{\pi}\bar{v}^5}\int_0^\infty v^4\exp\left(-\frac{v^2}{\bar{v}^2}\right)\nu_i(v)dv, \quad (38)$$

where $\mathbf{n}$ is a unit vector in an arbitrarily chosen direction. The average transfer frequency $\langle\nu_i\rangle$ is related by a simple formula with the diffusion coefficient D_i of particles in the state i: $D_i = \bar{v}^2/2\langle\nu_i\rangle$.

It is evident in Fig. 6a that the error introduced by the substitution $\nu_i^{(1)}(v_z) \longrightarrow \langle\nu_i\rangle$ in the denominator of the factor $\tau^{(1)}(v_z)$ is indeed negligible. This result indirectly confirms the correctness of the approximation $\Gamma(v) = \Gamma \equiv$ const and $\Omega_i(v) = \Omega_i$ = const used in the numerical calculations [these quantities appear in the

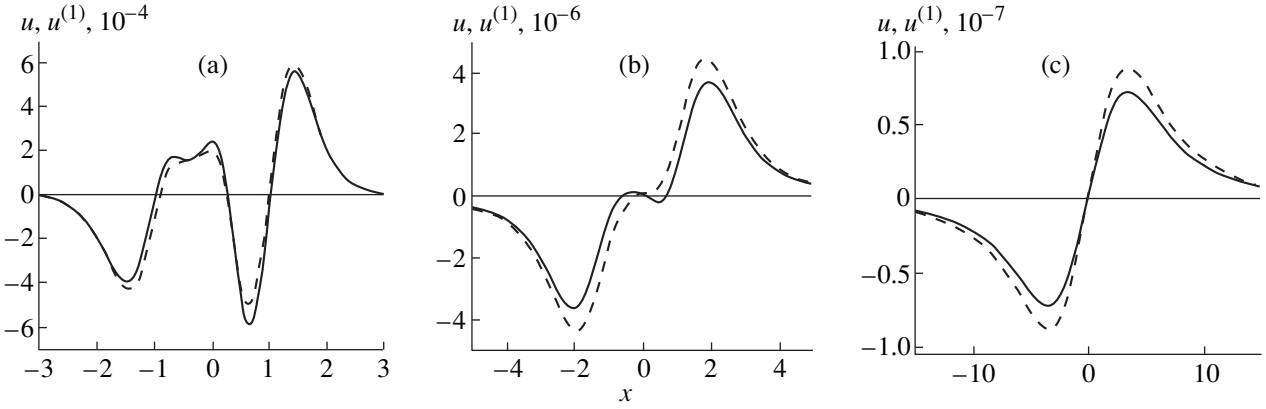

Fig. 5. Drift velocities u (solid curves) and $u^{(1)}$ (dashed curves) versus the detuning of the radiation frequency x for ^{7}Li atoms in the buffer mixture Ne + Kr for the anomalous LID at temperature T = 300 K, neon fraction ξ = 0.875 and various pressures: (a) P = 5 torr (y = 0.036); (b) P = 150 torr (y = 1.02); (c) P = 750 torr (y = 5.08).

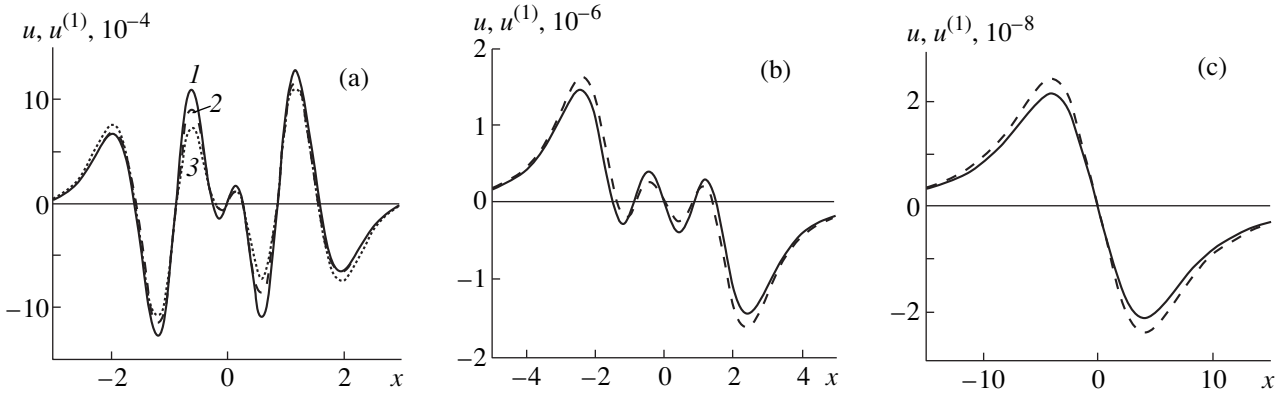

Fig. 6. Same as in Fig. 5 for the system ^{6}Li–(Ne + Kr) at T = 600 K, ξ = 0.865; (a) P = 5 torr (y = 0.013), (*1*) $u(x)$, (*2*) calculation of $u^{(1)}(x)$ using Eq. (34); (*3*) calculation of $u^{(1)}(x)$ using Eq. (34) with the frequencies $\nu_i^{(1)}(v_z)$ in the denominator of the factor $\tau^{(1)}(v_z)$ replaced by $\langle\nu_i\rangle$ (38); (b) P = 500 torr (y = 1.12); (c) P = 2500 torr (y = 5.59).

denominator of the expression for $Y_i(\mathbf{v})$ and $Y_i^{(1)}(v_z)$ in the formulas for the drift velocity]. In addition, this result makes it possible to find, from the experimental data on LID, the velocity dependence of the difference of the one-dimensional transport collision frequencies of atoms in the ground and excited states for collisions of the atoms with buffer gases: $\Delta\nu^{(1)} \equiv \nu_n^{(1)}(v_z) - \nu_m^{(1)}(v_z)$. We shall explain this for the example of LID of ^{6}Li atoms under conditions of Doppler broadening of the absorption line, when Eq. (35) is valid (Fig. 6a).

For ^{6}Li atoms the hyperfine splitting of the ground state ω_{ln} is small compared with the Doppler width $k\bar{v}$ of the line (at T = 600 K, $\delta = \omega_{ln}/k\bar{v} = 0.12$) and consequently we can set in Eq. (35) $\Omega_l \approx \Omega_n \approx \Omega$, i.e., a two-level model gives a good description of LID of ^{6}Li atoms. We obtain from Eq. (35)

$$\tau^{(1)}\left(\frac{\Omega}{k\bar{v}}\right) = \mathbf{k}\cdot\mathbf{u}_L^{(1)}\frac{k\bar{v}\sqrt{\pi}}{BI\Omega}\left[\left(\frac{\Omega}{k\bar{v}}\right)^2\right]. \qquad (39)$$

The drift velocity $\mathbf{u}_L^{(1)}$ appearing in this formula can be measured experimentally according to the LID; all other quantities are known. Thus, the dependence of $\tau^{(1)}$ on $v_z = \Omega/k\bar{v}$ can be found directly from the experimental data on LID. Since the drift velocity $\mathbf{u}_L^{(1)}$ is insensitive to the substitution $\nu_i^{(1)}(v_z) \longrightarrow \langle\nu_i\rangle$ in the denominator of the expression for $\tau^{(1)}(v_z)$ (see Fig. 6a), the plots $\tau(\Omega/k\bar{v})$ and $\Delta\nu^{(1)}(\Omega/k\bar{v})$ will have the same form.

It follows from Eq. (35) with $\Omega_l \approx \Omega_n \approx \Omega$ that, specifically, the drift velocity $\mathbf{u}_L^{(1)}$ and the difference of the one-dimensional transport collision frequencies $\Delta\nu^{(1)}$ vanish for the same values of $\Omega/k\bar{v}$, except the point $\Omega = 0$, where $\mathbf{u}_L^{(1)} = 0$ for any values of $\Delta\nu^{(1)}$ (we recall that $\Delta\nu^{(1)}$ is an even function of $\Omega/k\bar{v}$). This is clearly seen by comparing the positions of the zeros of the function $u^{(1)}$ on the $x = \Omega/k\bar{v}$ axis (Fig. 6a) and the positions of the zeros of the function $\Delta\nu^{(1)}/\nu^{(1}$ on the $t_z = \Omega/k\bar{v}$ axis (curve *4* in Fig. 3).

The examples of the application of Eq. (35) which were presented above clearly demonstrate the advantage of the one-dimensional approach for describing the LID from the standpoint of the analysis of the experimental data on LID for the purpose of extracting important information about the physics of interatomic collisions.

6. CONCLUSIONS

In the present work the question of collisional transfer of nonequilibrium in the velocity distribution of resonant particles, which is important for the physics of the interaction of laser radiation with gases, was investigated quantitatively. The radiation directly produces a nonequilibrium only for the projection v_z of the velocity $\mathbf{v}$ of the particles on the wave vector $\mathbf{k}$. The collisions "transfer" nonequilibrium in the v_z distribution to the distribution over the projections $\mathbf{v}_\perp$ of the velocity $\mathbf{v}$ orthogonal to $\mathbf{k}$. The collisional transfer is weak. In a number of well-known effects due to the interaction of laser radiation with gases, the role of collisional transfer of nonequilibrium is greatest in the anomalous LID.

The shape of the anomalous LID line (drift velocity as a function of the radiation frequency) is strongly sensitive to the sign-alternating velocity v dependence of the difference of the transport collision frequencies $\Delta\nu \equiv \nu_n(v) - \nu_m(v)$ for atoms in the ground and excited states in collisions with buffer particles. It is this circumstance that is responsible for the great sensitivity of the shape of the anomalous LID line to collisional transfer of nonequilibrium.

Collisional transfer of nonequilibrium has been investigated in this work by direct comparison of the drift velocities $\mathbf{u}_L$ and $\mathbf{u}_L^{(1)}$ of lithium atoms in an atmosphere of inert buffer gases. The drift velocity $\mathbf{u}_L$ was calculated taking into account the collisional transfer of nonequilibrium on the basis of three-dimensional quantum kinetic equations, and the drift velocity $\mathbf{u}_L^{(1)}$ was calculated from approximate one-dimensional equations obtained neglecting the transfer of nonequilibrium.

The computational results showed that in the case of the "normal" LID (when the difference $\Delta\nu$ of the transport collision frequencies as a function of the velocity v does not change sign) the collisional transfer of nonequilibrium has no appreciable effect on the shape of the LID line. This means that one-dimensional collision integrals can always be used instead of three-dimensional integrals to describe the "normal" LID without risking a loss of any important fine details in the radiation frequency dependence of the drift velocity.

When the transfer effect is neglected, the largest error arises in the description of the anomalous LID. However, it was found that to describe the anomalous LID the one-dimensional collision integrals can be used in most cases instead of the three-dimensional integrals without risking a loss of fine details in the radiation frequency dependence of the drift velocity.

The advantages of the one-dimensional over the three-dimensional approach to describing the LID is manifested in the analysis of the experimental data on LID for the purpose of using the data for scientific applications. This was demonstrated in the present paper for the anomalous LID of ^{6}Li atoms. Analysis of the experimental data on LID, using the formulas obtained with the one-dimensional approach, makes it possible to find the velocity v_z dependent difference of the one-dimensional transport collision frequencies $\Delta\nu^{(1)} \equiv \nu_n^{(1)}(v_z) - \nu_m^{(1)}(v_z)$ of the atoms in the ground and excited states in collisions of the atoms with buffer gases.

ACKNOWLEDGMENTS

We are grateful to J. Pascale for kindly providing detailed tabulated data on the interaction potentials of alkali-metal atoms with inert-gas atoms.

The investigations presented in this work were supported by the Russian Foundation for Basic Research (project no. 98-02-17924).

REFERENCES

1. S. G. Rautian, G. I. Smirnov, and A. M. Shalagin, *Nonlinear Resonances in Atomic and Molecular Spectra* (Nauka, Novosibirsk, 1979).
2. S. G. Rautian and A. M. Shalagin, *Kinetic Problems of Nonlinear Spectroscopy* (North-Holland, Amsterdam, 1991).
3. S. G. Rautian and I. I. Sobel'man, Usp. Fiz. Nauk **90**, 209 (1966) [Sov. Phys. Usp. **9**, 701 (1967)].
4. T. Privalov and A. Shalagin, Phys. Rev. A **59**, 4331 (1999).
5. A. S. Pine, J. Quant. Spectrosc. Radiat. Transf. **62**, 397 (1999).
6. P. Duggan, P. M. Sinclair, A. D. May, and J. R. Drummond, Phys. Rev. A **51**, 218 (1995).
7. I. Shannon, M. Harris, D. R. McHugh, and E. L. Lewis, J. Phys. B **19**, 1409 (1986).
8. E. V. Podivilov, A. I. Chernykh, and D. A. Shapiro, Zh. Éksp. Teor. Fiz. **105**, 1214 (1994) [JETP **78**, 653 (1994)].
9. A. I. Parkhomenko, Opt. Spektrosk. **82**, 235 (1997) [Opt. Spectrosc. **82**, 212 (1997)].
10. I. Kuščer, L. J. F. Hermans, P. L. Chapovsky, *et al.*, J. Phys. B **26**, 2837 (1993).
11. F. Kh. Gel'mukhanov and A. I. Parkhomenko, J. Phys. B **28**, 33 (1995).
12. B. Nagels, P. L. Chapovsky, L. J. F. Hermans, *et al.*, Phys. Rev. A **53**, 4305 (1996).
13. F. Kh. Gel'mukhanov, A. I. Parkhomenko, T. I. Privalov, and A. M. Shalagin, J. Phys. B **30**, 1819 (1997).
14. A. I. Parkhomenko, Zh. Éksp. Teor. Fiz. **116**, 1587 (1999) [JETP **89**, 856 (1999)].
15. G. J. van der Meer, J. Smeets, S. P. Pod'yachev, and L. J. F. Hermans, Phys. Rev. A **45**, R1303 (1992).
16. P. L. Chapovsky, G. J. van der Meer, J. Smeets, and L. J. F. Hermans, Phys. Rev. A **45**, 8011 (1992).
17. E. J. van Duijn, H. I. Bloemink, E. R. Eliel, and L. J. F. Hermans, Phys. Lett. A **184**, 93 (1993).
18. E. J. van Duijn, R. Nokhai, and L. J. F. Hermans, J. Chem. Phys. **105**, 6375 (1996).
19. F. Yahyaei-Moayyed and A. D. Streater, Phys. Rev. A **53**, 4331 (1996).
20. P. R. Berman, T. W. Mossberg, and S. R. Hartmann, Phys. Rev. A **25**, 2550 (1982).
21. A. Brissaud and U. Frish, J. Math. Phys. **15**, 524 (1974).
22. J. Pascale and J. Vandeplanque, J. Chem. Phys. **60**, 2278 (1974).
23. W. Happer, Rev. Mod. Phys. **44**, 169 (1972).
24. A. A. Radtsig and B. M. Smirnov, *Reference Data on Atoms, Molecules, and Ions* (Énergoatomizdat, Moscow, 1986; Springer-Verlag, Berlin, 1985).
25. R. H. G. Reid, J. Phys. B **8**, L493 (1975).
26. S. N. Atutov, I. M. Ermolaev, and A. M. Shalagin, Zh. Éksp. Teor. Fiz. **92**, 1215 (1987) [Sov. Phys. JETP **65**, 679 (1987)].
27. I. I. Sobelman (Sobel'man), *Atomic Spectra and Radiative Transitions* (Nauka, Moscow, 1977; Springer-Verlag, Berlin, 1979).
28. A. D. Streater and J. P. Woerdman, J. Phys. B **22**, 677 (1989).
29. L. V. Il'ichev and A. I. Parkhomenko, Zh. Éksp. Teor. Fiz. **112**, 856 (1997) [JETP **85**, 462 (1997)].
30. S. N. Atutov, A. I. Parkhomenko, S. P. Pod'yachev, and A. M. Shalagin, J. Phys. B **25**, 2943 (1992).
31. N. Allard and J. Kielkopf, Rev. Mod. Phys. **54**, 1103 (1982).

Translation was provided by AIP

Journal of Experimental and Theoretical Physics, Vol. 91, No. 2, 2000, pp. 255–264.
Translated from Zhurnal Éksperimental'noĭ i Teoreticheskoĭ Fiziki, Vol. 118, No. 2, 2000, pp. 291–301.

ATOMS, SPECTRA, RADIATION

Contribution to the Theory of Parametric Generation of Cyclotron Radiation

M. A. Erukhimova and M. D. Tokman*

Institute of Applied Physics, Russian Academy of Sciences, Nizhnii Novgorod, 603600 Russia
**e-mail: tokman@appl.sci.nnov.ru*

Received November 23, 1999

Abstract—A linear theory of the cyclotron parametric instability in systems which are classical analogues of quantum lasers without inversion is developed. The cyclotron interaction of different types of modulated electron beams with a bichromatic field, produced by waves propagating at an angle with respect to a constant magnetic field, is investigated. It is shown that simultaneous amplification of two parametrically coupled modes with different frequencies and positive energy is possible in this system with modulation of the active and reactive components of the susceptibility of an electronic ensemble. The results obtained are important from the standpoint of the general theory of radiation processes in electron beams and plasma and for the advancement of microwave electronics. *© 2000 MAIK "Nauka/Interperiodica".*

1. INTRODUCTION

In the last few years there has been a definite trend toward increased understanding of classes of charged-particle ensembles that are capable of stimulated emission. Attention is being focussed on the parametric interaction of coherent high-frequency (HF) modes in a modulated medium of electrons-oscillators (quantum and classical). It has turned out that parametric interaction under certain conditions leads not to the transfer of energy from one mode to another (scattering) but rather to the amplification of both modes, under conditions where the electron ensemble is "inversionless," i.e., stable with respect to the generation of each HF mode separately. This effect is very popular in quantum electronics, where for the last ten years special attention has been devoted to the investigation of an object which at first glance seems to be paradoxical—a laser without inversion.

In [1–3] attempts were made to construct classical analogues of a laser without inversion. Equations describing the excitation of waves, identical to the equations for a quantum system, were obtained in [3] for a cyclotron-resonance "inversionless maser," operating according to the principle of the well-known quantum Λ-scheme [4]. In [3] the generation of cyclotron radiation at two harmonics of the gyrofrequency by a modulated ensemble of electrons with an energy variance (modulation was produced at the difference harmonic) was studied. It was shown that from the macroscopic standpoint the amplification mechanism in such a system (just as in the analogous quantum scheme) corresponds to the parametric interaction of the modes in a medium with a modulated conductivity (active susceptibility), where the instability is due to a definite synchronization of the beats of the HF field with the low-frequency (LF) oscillations of the conductivity.

Formally, the parametric interaction of two HF modes in a medium with modulated electrodynamic characteristics (fixed LF pumping approximation) can be described in the simplest case by the following well-known equations [5, 6]:[1]

$$\begin{aligned} \beta_1 \dot{E}_1 + \gamma_1 E_1 &= \delta\varepsilon E_2, \\ \beta_2 \dot{E}_2 + \gamma_2 E_2 &= -\delta\varepsilon^* E_1, \end{aligned} \tag{1}$$

where $E_{1,2}$ are the complex amplitudes of waves with frequencies and waves vectors $\omega_{1,2}$ and $\mathbf{k}_{1,2}$, $\delta\varepsilon$ is the complex amplitude of the perturbation of an electrodynamic parameter of the medium with frequency $\Omega = \omega_1 - \omega_2$ and wave vector $\boldsymbol{\kappa} = \mathbf{k}_1 - \mathbf{k}_2$, the constants β_1 and β_2 are determined by the linear dispersion of the waves, and the quantities $\gamma_{1,2}$ are the linear damping constants. Simultaneous amplification of two HF modes in the system (1) is possible only if the coefficients β_1 and β_2 have different signs. This well-known case corresponds to waves whose energies have different signs; a negative-energy wave in the temporal problem corresponds to $\beta_j < 0$ (here $j = 1$ or 2). It is important to note that the amplification of negative-energy waves is also possible without parametric coupling of the modes: for $\beta_j < 0$, $\gamma_j > 0$ and $\delta\varepsilon = 0$ the solution of the corresponding equation of the system (1) is unstable. (For the amplification of a negative-energy wave dissipation is a feedback mechanism, making it possible to obtain an excess of energy of a nonequilibrium medium [5,7]. In the absence of dissipation parametric

[1] The equations (1) correspond, for example, to the temporal problem for uniform waves.

coupling with a positive-energy wave can play the role of feedback [8].) For positive-energy waves (the case of interest to us) simultaneous amplification of HF modes occurs with a sign change on the right-hand side of one of the equations (1) or with pre-multiplication of the right-hand sides of (1) by i (the substitution $\delta\varepsilon \longrightarrow i\delta\varepsilon$ reduces both variants into one another). The modulation studied in [3] of an active medium results in this form of the equations for parametrically coupled modes.

However, the question of the possibility of the amplification of two positive-energy HF modes parametrically coupled as a result of the modulation of the reactive component of the susceptibility of the medium remained open. It is interesting that from the standpoint of the quantum analogy, which interprets parametric interaction of waves as scattering of photons,[2] such processes seem impossible at first glance on the basis of the law of conservation of the total number of photons (the Manley–Rowe relation [8]). However, the development of the theory of quantum and classical inversionless generators of bichromatic radiation [3, 4, 10] casts doubt on the universality of the corresponding "forbiddenness." Indeed, in these systems a definite phase of the beats of the HF field relative to the LF modulation of the medium is maintained in principle, and for a fixed phase of the waves the change in the number of photons in the modes for an elementary interaction event becomes indefinite [11].

In analyzing the radiation processes in ensembles of electrons it is important to keep in mind that the reactive and active components of their electric susceptibility are formed, generally speaking, by different groups of particles. The reactive response of an electronic ensemble to an external HF field is due to nonresonant particles, and the active response is due to resonant particles, i.e., particles under conditions of Cherenkov or cyclotron synchronization with HF waves [5]. For example, in kinetic calculations of the conductivity of electron ensembles [5, 7, 9] Landau's pole rule relates the reactive component to a principal-value integral in phase space and the active component to a corresponding "resonance" pole. The parametric amplification of two HF modes which is indicated in [3] is due exclusively to the modulation of the distribution function of particles in resonance with both partial HF waves (and not only their beats, as ordinarily happens in the standard induced scattering [8]). The distribution function averaged over one period of LF modulation can be stable, and in this sense it is an inversionless distribution.

In the present paper a linear theory of parametric generation of cyclotron radiation due to modulation of an electron beam is developed. A more realistic (than in [3]), from the standpoint of practical applications, scheme of parametric generation of cyclotron radiation is studied: in first place, generation of the Brillouin components of waveguide modes which have the same "transverse" structure and different frequencies and propagate at an angle with respect to a constant magnetic field is investigated [inversionless variant of a cyclotron antiresonance maser (CARM)]; the frequencies of the modes correspond to (or are close to) the frequency of cyclotron resonance with electrons at the first harmonic; in the second place, the initial momentum distribution function of the particles corresponds to a very common sources used in electronics—a magneto-injector gun [12], where the beam is monoenergetic and has a large pitch-angle variance. The monoenergetic nature of the beams (neglecting the space charge) in such guns is due to the characteristic features of the geometry of the accelerating electrodes and the magnetic system (see [12]). The absence of a large variance of the relativistic electron gyrofrequencies in such guns has led to their extensive use in various cyclotron-resonance masers. At the same time, in such systems it is difficult to overcome the pitch-angle variance of the electrons, which engenders Doppler broadening of the cyclotron resonance for nontransverse propagation of waves relative to the magnetic field.

Investigations of this system showed that it is much more interesting than the scheme studied in [3] from the standpoint of obtaining various parametric generation regimes. Specifically, instability of bichromatic radiation due to modulation of the reactive susceptibility of the electronic ensemble has been achieved in such a system.

A formulation of the problem with an indication of a number of distinguishing features of this system is given in Section 2. Two cases are studied. In the first case, a description of which is contained in Section 3, the modulation of the distribution function is given in a form in which the above-mentioned inversionless parametric generation regime of a bichromatic field due to modulation of the conductivity of the medium is obtained. The most interesting result, which greatly expands our current understanding of parametric radiation processes, is presented in Section 4. It is demonstrated that for a definite form of the modulated distribution function (a specific model of the LF modulation process is considered) parametric generation of bichromatic radiation due to modulation of not the active but rather the reactive component of the susceptibility of the electron beam is possible in this system. The results obtained are discussed in the Conclusions.

2. BASIC INITIAL RELATIONS

Let us consider two linearly polarized plane waves propagating at an angle with respect to a constant magnetic field $\mathbf{B} = \mathbf{z}_0 B$. The waves have the same transverse

[2] The system (1) corresponds to scattering of waves by a prescribed (external) modulation of the medium. For induced scattering the structure of the wave equations is similar, but the quantity $\delta\varepsilon$ is proportional to $E_1 E_2^*$ [5, 8, 9].

(with respect to the magnetic field) wave number but different frequencies:

$$\mathbf{E} = \mathbf{y}_0 \sum_{j=1}^{2} \mathrm{Re} E_j \exp\left(ik_\perp x + ik_{\|j} z - i\omega_j t - i\frac{\pi}{2} \right). \quad (2)$$

Let these waves be in resonance with electrons having the momentum components $p_\|^0 = mc\rho_\|^0$ and $p_\perp^0 = mc\rho_\perp^0$ at the first harmonic of the cyclotron frequency:

$$\omega_j = \omega_B/\gamma_0 + ck_{\|j}\beta_\|^0, \quad (3)$$

where $\omega_B = eB/mc$, m is the electron rest mass, c is the speed of light, and γ_0 and $\beta_\|^0$ are, respectively, the relativistic gamma factor and the longitudinal velocity of resonance particles scaled to the velocity of light. Let us consider the interaction of this field with an ensemble of electrons whose momenta are close to the resonance value. This ensemble can be described by the distribution function over truncated variables $f(r, \chi, \theta, z, X, t)$, where the quantities r and χ characterize the deviations of the longitudinal and transverse momenta of a particle from the resonance values:

$$r = \rho_\| - \rho_\|^0, \quad \chi = \rho_\perp^2/2 - \rho_\perp^{02}/2,$$

θ is the cyclotron rotation phase and X is the transverse coordinate of the center of a "Larmor circle." Describing the particle motion on the basis of the "nonlinear pendulum" approximation [12–14], the following form of the Liouville equation can be used:

$$\left(\frac{\partial}{\partial t} + \omega_H \frac{\partial}{\partial \theta} + c\beta_\| \frac{\partial}{\partial z} \right) f + \sum_{j=1}^{2} F_j \left(\frac{\omega_B}{\omega_j} \frac{\partial}{\partial \chi} + n_{\|j} \frac{\partial}{\partial r} \right) f = 0. \quad (4)$$

Here,

$$\omega_H = \frac{\omega_B}{\gamma_0}\left(1 - \frac{\chi}{\gamma_0^2} - \frac{\beta_\|^0 r}{\gamma_0} \right),$$

$$\beta_\| = \beta_\|^0 + \frac{r}{\gamma_0}(1 - \beta_\|^{02}) - \frac{\beta_\|^0 \chi}{\gamma_0^2},$$

$$F_j = G\mathrm{Re}\alpha_j \exp(i\theta + ik_\perp X + ik_{\|j} z - i\omega_j t),$$

$$G = (\rho_\perp^0/\gamma_0) J_1'(k_\perp r_H),$$

F_j is the effective "force" exerted by the jth wave on the particle (strictly speaking, this is the dimensionless interaction-phase-dependent power of the energy transfer between the particle and the jth wave), $n_{\|j} = ck_{\|j}/\omega_j$ is the longitudinal refractive index of the wave, $r_H = c\rho_\perp^0/\omega_B$ is the gyroradius of resonant particles, J_1' is the derivative of the Bessel function with respect to its argument, and $\alpha_j = eE_j/mc$ is the normalized amplitude of the wave.

We shall also use the truncated equations [15] for the wave amplitudes. Let us consider a "boundary-value" problem, assuming the fields to be functions of the coordinate z and constant in time and also assuming the wave vectors and frequencies to be related by the "vacuum" dispersion relation (naturally, the electron density is assumed to be quite low)

$$\omega_j = c\sqrt{k_\perp^2 + k_{\|j}^2}. \quad (5)$$

We obtain

$$\frac{ck_{\|j}}{\omega_j}\frac{\partial \alpha_j}{\partial z} = -\frac{2\pi e}{mc} I_j, \quad (6)$$

where the amplitudes I_j of the resonant harmonics of the current can be expressed in terms of the distribution function as follows:

$$I_j = ecG\langle \int d\chi dr d\theta f(\chi, r, \theta, z, X, t) \times \exp(-i\theta - ik_\perp X - ik_{\|j} z + i\omega_j t) \rangle_{X,z,t}. \quad (7)$$

Here the brackets denote averaging over the corresponding "fast variables."

The parametric coupling of the waves under study is due to the modulation of the electron distribution function with respect to the longitudinal coordinate z with the difference wave sector

$$\kappa = k_{\|1} - k_{\|2} \quad (8)$$

and with respect to time with frequency

$$\Omega = \omega_1 - \omega_2 \quad (9)$$

(for definiteness we assume that $\omega_1 > \omega_2$). At the boundaries of the generation region $z = 0$ we prescribe an unperturbed distribution function modulated in time:

$$f_{in}|_{z=0} = f_{in}(\chi, r, \Omega t), \quad (10)$$

where f_{in} is assumed to be periodic in t. In the absence of HF fields, for $z > 0$ the distribution function is determined from (10) by making the substitution $t \longrightarrow t - z/c\beta_\|$. Assuming

$$\kappa \frac{\langle \beta_\| - \beta_\|^0 \rangle}{\beta_\|^0} z \ll 1, \quad (11)$$

we neglect the "ballistic" relaxation of the modulated distribution function (here $\langle \beta_\| - \beta_\|^0 \rangle$ is the characteristic variance of the translational velocity of the electrons with respect to $\beta_\|^0$). Under the conditions (11) the unperturbed distribution function can be represented in the form

$$f_{in}|_{z>0} = f_{in}(\chi, r, \Psi), \quad (12)$$

where $\Psi = \kappa z - \Omega t$. The corresponding limit can be obtained more accurately directly in the expression for the HF current (see [3]). However, it can be shown that this has no effect on the final result.

Solving the kinetic equation (4) in the linear approximation in the field (see, for example, [3]), we obtain the following expressions for the resonance harmonics of the current (7):

$$\begin{aligned} I_1(z) &= -ecG^2\alpha_1\left\langle \int d\chi dr \hat{\xi}\left(\Delta_1, \frac{z}{c\beta_\parallel^0}\right)\hat{L}_1 f_{in}(r, \chi, \Psi)\right\rangle_{z,t} \\ &- ecG^2\alpha_2\left\langle \int d\chi dr \exp(-i\Psi)\hat{\xi}\left(\Delta_2, \frac{z}{c\beta_\parallel^0}\right)\hat{L}_2 f_{in}(r, \chi, \Psi)\right\rangle_{z,t}, \\ I_2(z) &= -ecG^2\alpha_2\left\langle \int d\chi dr \hat{\xi}\left(\Delta_2, \frac{z}{c\beta_\parallel^0}\right)\hat{L}_2 f_{in}(r, \chi, \Psi)\right\rangle_{z,t} \\ &- ecG^2\alpha_1\left\langle \int d\chi dr \exp(i\Psi)\hat{\xi}\left(\Delta_1, \frac{z}{c\beta_\parallel^0}\right)\hat{L}_1 f_{in}(r, \chi, \Psi)\right\rangle_{z,t}. \end{aligned} \tag{13}$$

Here

$$\Delta_j = \omega_j - \omega_H - ck_{\parallel j}\beta_\parallel = \frac{\omega_j}{\gamma_0}\left(\frac{\chi}{\gamma_0} + r(\beta_\parallel^0 - n_{\parallel j})\right) \tag{14}$$

is the detuning of the cyclotron synchronization from the jth HF wave; the operator $\hat{\xi}(\Delta, \tau)$ is determined by the expression

$$\begin{aligned} \hat{\xi}(\Delta, \tau) &= \frac{i}{\Delta}(1 - \exp(i\Delta\tau)) \\ &= \frac{i}{\Delta}(1 - \cos(\Delta\tau)) + \frac{\sin(\Delta\tau)}{\Delta}; \end{aligned} \tag{15}$$

the differential operators $\hat{L}_j$ appearing explicitly in the kinetic equation (4) have the form

$$\begin{aligned} \hat{L}_j &= \frac{\omega_B}{\omega_j}\frac{\partial}{\partial\chi} + n_{\parallel j}\frac{\partial}{\partial r} \\ &= \gamma_0(1 - n_{\parallel j}\beta_\parallel^0)\frac{\partial}{\partial\chi} + n_{\parallel j}\frac{\partial}{\partial r}. \end{aligned}$$

The operator $\hat{L}_j$ determines in momentum space a direction in which distribution function of the resonance particles varies under the action of the jth mode.

Only the zeroth and first Fourier harmonic of the modulated distribution function (12) "participate" in the formation of the resonance responses (13). This makes it convenient to represent the distribution function in the form

$$f_{in}(\chi, r, \Psi) = f_0(\chi, r) + f_M(\chi, r)\cos(\Psi + \phi_0). \tag{16}$$

Analyzing the expressions obtained for the resonance harmonics of the current (13), it is convenient to switch to new integration variables, thereby reducing the problem in two-dimensional phase space to one-dimensional phase space (a very similar technique is described in [9]). According to the wave on whose parameters any particular integral in the expressions (13) depends, we make the linear substitution of variables

$$\{r, \chi\} \longrightarrow \{\Delta_j, l_j\},$$

where Δ_j is the detuning of synchronization determined by the equation (14);

$$l_j = -n_{\parallel j}\frac{\chi}{\gamma_0} + r(1 - n_{\parallel j}\beta_\parallel^0) \tag{17}$$

is the coordinate that remains constant in a direction of action of the operator $\hat{L}_j$.[3] The operator $\hat{L}_j$ assumes the form

$$\hat{L}_j = \frac{\omega_j}{\gamma_0}(1 - n_{\parallel j}^2)\frac{\partial}{\partial\Delta_j}.$$

The detuning Δ_j increases in the direction of action of the operator $\hat{L}_j$. It should be kept in mind that the waves under study are fast, i.e., $n_{\parallel j} < 1$. In addition, we shall assume for definiteness that the waves propagate in the positive direction along the z-axis, i.e., $n_{\parallel j} > 0$. In the new variables, using Eq. (16), we obtain for the current harmonics I_1 and I_2

$$\begin{aligned} I_1(z) &= -ecG^2\gamma_0\alpha_1 \\ &\times \int d\Delta_1 \hat{\xi}\left(\Delta_1, \frac{z}{c\beta_\parallel^0}\right)\frac{d}{d\Delta_1}\Phi_0^{(1)}(\Delta_1) \\ &- \frac{1}{2}ecG^2\gamma_0\alpha_2\exp(i\varphi_0) \end{aligned}$$

[3] It is easy to show that this is the well-known integral of motion of a particle in the field of a wave $r - n_\parallel(\gamma - \gamma_0)$ [9].

$$\times \int d\Delta_2 \hat{\xi}\left(\Delta_2, \frac{z}{c\beta_\parallel^0}\right)\frac{d}{d\Delta_2}\Phi_M^{(2)}(\Delta_2),$$

$$I_2(z) = -ecG^2\gamma_0\alpha_2 \times \int d\Delta_2 \hat{\xi}\left(\Delta_2, \frac{z}{c\beta_\parallel^0}\right)\frac{d}{d\Delta_2}\Phi_0^{(2)}(\Delta_2) - \frac{1}{2}ecG^2\gamma_0\alpha_1\exp(-i\varphi_0) \times \int d\Delta_1 \hat{\xi}\left(\Delta_1, \frac{z}{c\beta_\parallel^0}\right)\frac{d}{d\Delta_1}\Phi_M^{(1)}(\Delta_1). \quad (18)$$

Here, $\Phi_0^{(j)}(\Delta_j)$ and $\Phi_M^{(j)}(\Delta_j)$ are, respectively, the constant component and the amplitude of the oscillating component of the function

$$\Phi^{(j)}(\Delta_j, \Psi) = \int f_{in}(r(\Delta_j, l_j), \chi(\Delta_j, l_j), \Psi)dl_j = \Phi_0^{(j)}(\Delta_j) + \Phi_M^{(j)}(\Delta_j)\cos(\Psi + \phi_0). \quad (19)$$

In what follows we shall consider the asymptotic solution corresponding to Landau's "pole rule", making the assumption that the operator $\hat{\xi}(\Delta_j, z/c\beta_\parallel^0)$ (15) corresponds to the well-known asymptotic form (see, for example, [11, 16]):

$$\hat{\xi}(\Delta, \tau)|_{\tau\to\infty} \longrightarrow \frac{iP}{\Delta} + \pi\delta(\Delta). \quad (20)$$

Here the symbol P denotes a principal-value integral. This representation is valid at distances (see [3, 11, 17])

$$\langle\delta\Delta_j\rangle\frac{z}{c\beta_\parallel^0} \gg 1,$$

where $\langle\delta\Delta_j\rangle$ is the smallest characteristic scale of variation of the functions $\Phi_0^{(j)}(\Delta_j)$ and $\Phi_M^{(j)}(\Delta_j)$. Neglecting the "ballistic" relaxation of the distribution function and by virtue of the constraint (11) the following relativistically invariant condition must be satisfied:

$$k_{\parallel j}\frac{\langle\delta\Delta_j\rangle}{n_{\parallel j}\omega_j} \gg \kappa\langle\beta_\parallel - \beta_\parallel^0\rangle,$$

which, generally speaking, can be stronger or weaker than the simple condition of spectral closeness of the components of the HF fields

$$k_{\parallel j} \gg \kappa.$$

Analyzing the expression (18) we can determine the characteristic feature of the system that permits the realization of various parametric generation regimes that correspond to different types of modulation of the electron distribution function. The response to the jth HF field is determined by the character of the integral dependence of the particle number density in phase space on the detuning Δ_j of synchronization with this field, i.e., the form of the effective one-dimensional distribution function $\Phi^{(j)}(\Delta_j,\Psi)$ (19). The average component of this function $\Phi_0^{(j)}(\Delta_j)$ determines the independent—"linear"—behavior of the HF fields; the amplitude of the oscillating component $\Phi_M^{(j)}(\Delta_j)$ determines their parametric coupling. Specifically, we obtain from the formula (18), taking account of Eq. (20), the following obvious negativity condition for the linear increment for the jth HF field (i.e., the stability condition ("noninversion") of the electron distribution function averaged over the modulation phase

$$\left.\frac{d\Phi_0^{(j)}(\Delta_j)}{d\Delta_j}\right|_{\Delta_j=0} < 0. \quad (21)$$

This condition means that the gradient of the function $f_0(\chi, r)$ on the line of exact synchronization $\Delta_j = 0$ in the direction of action of the operator $\hat{L}_j$ is negative on the average.

A characteristic feature of the system under study is that for different components of the bichromatic field the detunings of synchronization $\Delta_1(r, \chi)$ and $\Delta_2(r, \chi)$ (just as the operators $\hat{L}_1$ and $\hat{L}_2$) have a different dependence on the coordinates in phase space. The resonance curves of the two waves with $k_{\parallel j} \neq 0$, determined by the equations

$$\Delta_j(\rho_\parallel, \rho_\perp) = \omega_j - \omega_B/\gamma - ck_{\parallel j}\beta_\parallel = 0,$$

intersect at a single point. Near the common resonance point the detunings are determined by Eq. (14). For the waves under study, which have the same transverse wave numbers, the slopes of the resonance curves in the (r, χ) plane, determined by the parameter $n_{\parallel j} - \beta_\parallel^0$, have different signs, since from the condition of compatibility of Eqs. (3) and (5) follows

$$n_{\parallel 1} > \beta_\parallel^0, \quad n_{\parallel 2} < \beta_\parallel^0. \quad (22)$$

Figure 1 shows the lines of exact resonance $\Delta_j = 0$ and the directions of action of the operators $\hat{L}_j$. The detuning is positive above and negative below the line of exact synchronization. For this arrangement of the resonance curves in phase space there exist directions (close to the vertical) in which the detunings of the synchronization with two HF waves increase or decrease simultaneously, and the directions (close to the horizontal) in which the detuning of synchronization increases with one HF wave and decreases with the other. In the parametric generation system studied in [3] the waves in resonance with the particles at two harmonics of the cyclotron frequency propagate in a direc-

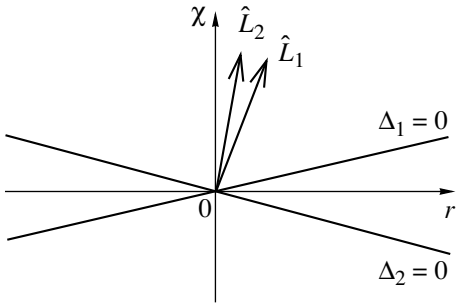

Fig. 1. Lines of exact synchronization ($\Delta_j = 0$) and directions of action of the operators $\hat{L}_j$ for the components of a bichromatic field (2) near a common resonant point.

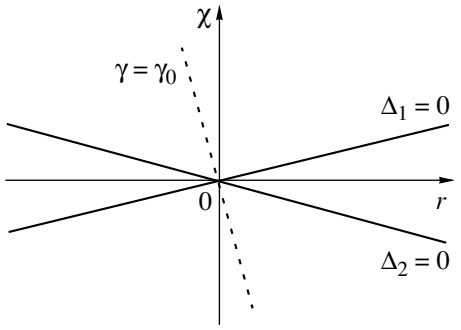

Fig. 2. Relative arrangement of the line of constant energy $\gamma = \gamma_0$ and the curves of exact resonance with HF fields $\Delta_j = 0$ (near a common resonance point).

tion transverse to the magnetic field. For such waves the resonance currents either coincide or they do not intersect at all. A similar situation also occurs for a Cherenkov resonance. In these cases the changes in the detunings of synchronization for both spectral components occur identically along any lines in phase space.

On account of the indicated features of cyclotron resonance, the effective one-dimensional distribution functions $\Phi^{(1)}(\Delta_1, \Psi)$ and $\Phi^{(2)}(\Delta_2, \Psi)$ and, correspondingly, the responses to the first and second HF fields can differ substantially or there may be no fundamental differences, depending on the form of the modulated electron distribution in momentum space. In consequence, the character of the parametric coupling of the fields, the wave excitation equations, and the amplification conditions can assume a substantially different form for different types of modulated distribution functions.

In what follows we shall examine different parametric wave-generation regimes that can occur in this system.

3. PARAMETRIC INSTABILITY ON THE MODULATION OF THE DISTRIBUTION FUNCTION OF RESONANT PARTICLES

Let the modulated electron distribution function have a form such that the difference in the arrangement of resonant particles in momentum space for two waves, which was noted in the preceding section, is not fundamental, i.e., the responses to the first and second HF fields excited in a modulated electronic medium are similar. For this the electron distribution on the line of constant detuning of synchronization should change with the detuning in a similar manner for the first and second HF fields, i.e., the functions $\Phi^{(1)}(\Delta_1, \Psi)$ and $\Phi^{(2)}(\Delta_2, \Psi)$ (19) should be similar in a definite sense. An obvious example of such a distribution is an ensemble of electrons having energy $mc^2\gamma_0$ and a distribution of pitch angles[4] near the point $(\rho_\parallel^0, \rho_\perp^2)$ with a *t*- and *z*-modulated function describing this variance. The investigation of the interaction of fields with a monoenergetic electron distribution in this case is fully justified, since it is characteristic for real electronic magneto-injector guns used in cyclotron-resonance masers (see Introduction). In the variables χ and r such a distribution corresponds to the following form of the function (16):

$$f_{in}(r, \chi, \Psi) = \delta(\chi + \rho_\parallel^0 r)(g_0(r) + g_M(r)\cos(\Psi + \varphi_0)), \quad (23)$$

where

$$\gamma - \gamma_0 = \chi/\gamma_0 + \beta_\parallel^0 r,$$

which is valid near resonance. As one can see from Fig. 2, the line $\gamma = \gamma_0$, on which the electronic ensemble is concentrated, is oriented in phase space in a manner so that the detunings Δ_1 and Δ_2 vary in an identical manner along it. We obtain that the dependences of the particle number density in phase space on the detunings of synchronization with the first and second HF fields, described by the effective one-dimensional distribution functions $\Phi^{(1)}(\Delta_1, \Psi)$ and $\Phi^{(2)}(\Delta_2, \Psi)$ respectively, are similar:

$$\Phi^{(j)}(\Delta_j, \Psi) = \frac{1 - n_{\parallel j}^2}{\gamma_0 n_{\parallel j}}\left(g_0\left(-\Delta_j \frac{\gamma_0}{n_{\parallel j}\omega_j}\right) + g_M\left(-\Delta_j \frac{\gamma_0}{n_{\parallel j}\omega_j}\right)\cos(\Psi + \varphi_0)\right). \quad (24)$$

[The derivation of this formula took account of the relations (14) and (17).] As result the responses to the first and second HF fields excited in such a modulated electronic medium will be simply proportional to one another.

[4] The variance of the pitch angle leads to broadening of the cyclotron resonance as result of the Doppler effect.

Substituting the expressions for the resonance harmonics of the current (18), using Eqs. (24) and (20), into the wave excitation equation (6), we obtain the system

$$\begin{cases} \dfrac{d\alpha_1}{dz} + (\gamma_l + i\delta_l)\alpha_1 \\ \quad = -a\exp(i\varphi_0)(\gamma_n + i\delta_n)\alpha_2, \\ \dfrac{d\alpha_2}{dz} + b(\gamma_l + i\delta_l)\alpha_2 \\ \quad = -\exp(-i\varphi_0)(\gamma_n + i\delta_n)\alpha_1, \end{cases} \tag{25}$$

where the coefficients are determined by the formulas

$$\gamma_l = \frac{2\pi^2 e^2 G^2 \gamma_0 (1 - n_{\|1}^2)}{mc\omega_1 n_{\|1}^3} \frac{dg_0}{dr}\bigg|_{r=0},$$

$$\gamma_n = \frac{\pi^2 e^2 G^2 \gamma_0 (1 - n_{\|1}^2)}{mc\omega_1 n_{\|1}^2 n_{\|2}} \frac{dg_M}{dr}\bigg|_{r=0},$$

$$\delta_l = -\frac{2\pi e^2 G^2 \gamma_0 (1 - n_{\|1}^2)}{mc\omega_1 n_{\|1}^3} \int \frac{P dg_0/dr}{r} dr, \tag{26}$$

$$\delta_n = -\frac{\pi e^2 G^2 \gamma_0 (1 - n_{\|1}^2)}{mc\omega_1 n_{\|1}^2 n_{\|2}} \int \frac{P dg_M/dr}{r} dr,$$

$$a = \frac{(1 - n_{\|2}^2)}{(1 - n_{\|1}^2)} \frac{\omega_1}{\omega_2} \frac{n_{\|1}}{n_{\|2}}, \quad b = a\frac{n_{\|1}}{n_{\|2}}.$$

The system (25) obtained is similar to the system of equations studied in [3] for the problem of parametric inversionless generation of waves in a direction transverse to a magnetic field at two harmonics of the cyclotron frequency and corresponds to the equations describing inversionless amplification in a quantum Λ scheme [3, 4]. The exponential solution [$\alpha_{1,2} \propto \exp(\mu t)$] of the system (25) is determined by the characteristic equation

$$(\mu + \gamma_l + i\delta_l)(\mu + b(\gamma_l + i\delta_l)) = a(\gamma_n + i\delta_n)^2$$

and the ratio

$$\frac{\alpha_1}{\alpha_2} = -\frac{a\exp(i\varphi)(\gamma_n + i\delta_n)}{\mu + \gamma_l + i\delta_l}.$$

Inversionless generation corresponds to a regime where the distribution function averaged over the modulation phase is stable with respect to partial HF fields, i.e., $\gamma_l < 0$, and the corresponding condition (21), which in this case has the form

$$\frac{dg_0}{dr}\bigg|_{r=0} > 0$$

is satisfied. In the simplest case, where $\delta_l = \delta_n = 0$,[5] an unstable solution exists in the system if

$$a\gamma_n^2 > b\gamma_l^2,$$

which reduces to the amplification condition

$$\frac{1}{2}\left|\frac{dg_M}{dr}\right|_{r=0} > \frac{dg_0}{dr}\bigg|_{r=0}. \tag{27}$$

The inequality (27) ensures quite strong modulation of the real part of the conductivity of medium. It is important that in the situation under consideration the responses to the first and second HF fields are modulated in-phase.

In the present system the conditions for inversionless amplification based on the mechanism discussed in [3] are obtained. Parametric generation of a bichromatic field by means of modulation of a distribution function of the resonant particles that is optimally phased with the beats of the HF field or, in other words, modulation of the active susceptibility of the electronic medium occurs.

4. PARAMETRIC GENERATION A BICHROMATIC FIELD IN A REACTIVE MEDIUM

We shall now consider a different regime of parametric generation of bichromatic radiation in our system.

Once again, we shall consider first a monoenergetic beam of electrons with energy $mc^2\gamma_0$ and a pitch-angle distribution near the point $(\rho_\|^0, \rho_\perp^2)$:

$$f_0 = \delta(\chi + \rho_\|^0 r) g(r).$$

Let the beam in the modulating section of length L_M interact with a longitudinal "pump" field [a method for producing the modulated distribution (23) was not stipulated in the preceding section]

$$\mathbf{E} = \mathbf{z}_0 \mathrm{Re}(E_0 \exp(i\kappa z - i\Omega t)),$$

where κ and Ω are determined by the formulas (8) and (9). For a sufficiently short modulating interval, where

$$L_M \ll \sqrt{\frac{c\gamma_0 \beta_\|^{0^2}}{\kappa(1 - \beta_\|^{0^2})|\alpha_0|}}, \quad \kappa L_M \frac{\langle \rho_\| - \rho_\|^0 \rangle}{\rho_\|^0} \ll 1 \tag{28}$$

(here $\alpha_0 = eE_0/mc$, $\langle \rho_\| - \rho_\|^0 \rangle$ is the characteristic variance of the longitudinal momentum relative to $\rho_\|^0$), we

[5] The coefficients δ_l can be made to vanish by modifying the external electrodynamic system. The quantity δ_n is 0, for example, for odd functions $g_M(r)$.

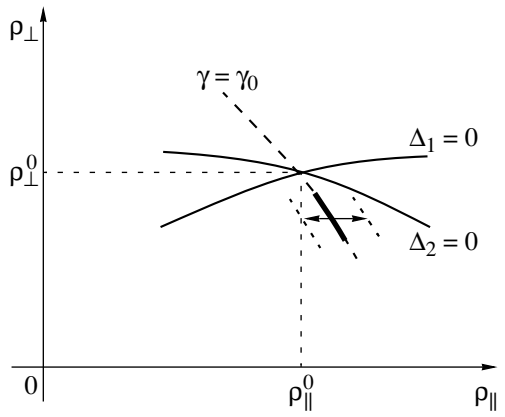

Fig. 3. Oscillations of the electron beam with distribution function (29) in momentum space relative to the lines of exact synchronization with HF fields.

have the following distribution at the exit from the modulating section:

$$f_{in}\big|_{z=0} = \delta\left(\chi + \rho_{\|}^{0}\left(r + \frac{L_M}{c\beta_{\|}^{0}}\mathrm{Re}\alpha_0\exp(-i\Omega t)\right)\right) \times g\left(r + \frac{L_M}{c\beta_{\|}^{0}}\mathrm{Re}\alpha_0\exp(-i\Omega t)\right). \quad (29)$$

The longitudinal field does not change the squared transverse momentum of the particles, and on account of the conditions (28) the change in the longitudinal momentum dependence depends only on the phase of a particle at the entrance into the modulating gap. Thus, we obtain in momentum space oscillations of the electron beam, initially concentrated on the line $\gamma(r, \chi) = \gamma_0$, as a whole along the r-axis with amplitude

$$A_r = \frac{L_M}{c\beta_{\|}^{0}}|\alpha_0|.$$

We shall now analyze, on the basis of the results obtained in Section 2, the character of the interaction of the bichromatic HF radiation with an ensemble of electrons with a distribution function of the form (29).

The effective one-dimensional distribution functions $\Phi^{(j)}(\Delta_j, \Psi)$ (19), determining the value of the linear and parametric components of the resonant current harmonics I_1 and I_2 (18), in this case assume the form

$$\Phi^{(j)}(\Delta_j, \Psi) = \frac{1-n_{\|j}^{2}}{\gamma_0 n_{\|j}} \times g\left(-\Delta_j\frac{\gamma_0}{n_{\|j}\omega_j} + A_r\left(1-\frac{\beta_{\|}^{0}}{n_{\|j}}\right)\cos(\Psi+\varphi_0)\right),$$

where φ_0 is the phase of the complex amplitude of the pump field α_0. The functions $\Phi^{(1)}(\Delta_1, \Psi)$ and $\Phi^{(2)}(\Delta_2, \Psi)$ describe the oscillations along the corresponding coordinates Δ_1 and Δ_2. It is of fundamental importance that these oscillations occur in antiphase, since the parameters $1 - \beta_{\|}^{0}/n_{\|1}$ and $1 - \beta_{\|}^{0}/n_{\|2}$ have different signs [see Eq. (22)]. This is due to, on the one hand, the character of the LF modulation of the electronic ensemble and, on the other hand, the cyclotron resonance conditions for two HF waves with different $k_{\perp}$. In momentum space the particle beam oscillates along the $\rho_{\|}$-axis—in the direction in which the detuning of synchronization with one HF field increases and at the same time the detuning with the other field decreases (see Fig. 3). In consequence we obtain that the amplitudes of the oscillating components of the functions $\Phi^{(j)}(\Delta_j, \Psi)$

$$\Phi_M^{(j)}(\Delta_j) = 2\langle\cos(\Psi+\varphi_0)\Phi^{(j)}(\Delta_j, \Psi)\rangle_{\Psi},$$

which determine the values of the parametric components of the resonant harmonics of the current, have different signs. As a result, the wave excitation equations will assume the form

$$\begin{cases} \dfrac{d\alpha_1}{dz} + (\gamma_1 + i\delta_1)\alpha_1 \\ \quad = -\exp(i\varphi_0)(\gamma_{12} + i\delta_{12})\alpha_2, \\ \dfrac{d\alpha_2}{dz} + (\gamma_2 + i\delta_2)\alpha_2 \\ \quad = \exp(-i\varphi_0)(\gamma_{21} + i\delta_{21})\alpha_1. \end{cases} \quad (30)$$

Assuming the components of the HF fields to be spectrally close ($|k_{\|j}| \gg \kappa$) (the parameters ω_1, ω_2 and $n_{\|1}$, $n_{\|2}$ are assumed to be the same where their differences are not fundamental), we obtain the following expressions for the coefficients in Eqs. (30):

$$\gamma_1 = \gamma_2 = \gamma = \frac{2\pi^2 e^2 G^2}{mc}\frac{1-n_{\|}^{2}}{n_{\|}^{2}} \times \frac{d}{d\Delta}\left\langle g\left(\Delta\frac{\gamma_0}{n_{\|}\omega} + A_r\left(1-\frac{\beta_{\|}^{0}}{n_{\|2}}\right)\cos\Psi\right)\right\rangle_{\Psi}\Bigg|_{\Delta=0},$$

$$\delta_1 = \delta_2 = \delta = -\frac{2\pi^2 e^2 G^2 \gamma_0}{\omega mc}\frac{1-n_{\|}^{2}}{n_{\|}^{2}} \times \int\frac{P}{\Delta}\left\langle g\left(\Delta\frac{\gamma_0}{n_{\|}\omega} + A_r\left(1-\frac{\beta_{\|}^{0}}{n_{\|2}}\right)\cos\Psi\right)\right\rangle_{\Psi} d\Delta, \quad (31)$$

$$\gamma_{12} = \gamma_{21} = \Gamma = \frac{2\pi^2 e^2 G^2}{mc}\frac{1-n_{\|}^{2}}{n_{\|}^{2}} \times \frac{d}{d\Delta}\left\langle \cos\Psi g\left(\Delta\frac{\gamma_0}{n_{\|}\omega} + A_r\left(1-\frac{\beta_{\|}^{0}}{n_{\|2}}\right)\cos\Psi\right)\right\rangle_{\Psi}\Bigg|_{\Delta=0},$$

$$\delta_{12} = \delta_{21} = D = -\frac{2\pi^2 e^2 G^2 \gamma_0}{\omega m c}\frac{1-n_\parallel^2}{n_\parallel^2}$$

$$\times \int \frac{P}{\Delta}\left\langle \cos\Psi g\left(\Delta\frac{\gamma_0}{n_\parallel\omega} + A_r\left(1-\frac{\beta_\parallel^0}{n_{\parallel 2}}\right)\cos\Psi\right)\right\rangle_\Psi d\Delta.$$

Here the fact that for $|k_{\parallel j}| \gg \kappa$ the parameters $1 - \beta_\parallel^0/n_{\parallel 1}$ and $1 - \beta_\parallel^0/n_{\parallel 2}$ are close in absolute magnitude and equal

$$1-\frac{\beta_\parallel^0}{n_{\parallel 2}} \approx -\left(1-\frac{\beta_\parallel^0}{n_{\parallel 1}}\right) = -\frac{1}{2}\frac{\kappa}{k_\parallel}(1-n_\parallel^2).$$

was taken into account.

For exponential modes $\alpha_{1,2} \propto \exp(\mu_\pm z)$, which are solutions of the system (30), we obtain, using Eq. (31), the growth rates

$$\mu_\pm = -\gamma - i\delta \pm i\Gamma \mp D$$

and the amplitude ratio

$$\left(\frac{\alpha_1}{\alpha_2}\right)_\pm = \pm i\exp(i\varphi_0).$$

When $\gamma \geq 0$, which means the system is stable with respect to "partial" generation of HF fields, the condition for amplification of a bichromatic mode becomes

$$|D| > \gamma. \tag{32}$$

In this scheme, in contrast to previous schemes, the amplification of a bichromatic field is due not to oscillations of the active part of the susceptibility of the medium but rather to oscillations of its reactive part, determined by the integral

$$\int \frac{P}{\Delta}\frac{d}{d\Delta}\Phi^{(j)}(\Delta_j, \Psi)d\Delta.$$

Especially interesting is the generation regime in the absence of resonant particles, when an electron beam with a limited pitch-angle variance, initially detuned from resonance with the HF waves, undergoes HF oscillations (in momentum space) without crossing the line of exact resonance (see Section 3). At any given moment there are no particles which are resonant with the HF fields and therefore the linear growth rate γ is zero, while the coefficient D "formed" from nonresonant particles is different from zero. In accordance with the condition (32) we have amplification of a bichromatic field.

Thus amplification of two positive-energy HF fields interacting parametrically in a modulated reactive medium occurs in this scheme. The specific nature of the modulation of the distribution function in phase space, when the detuning of cyclotron synchronization of electrons with different spectral components of the bichromatic field are modulated in antiphase, plays a fundamental rule in this process. In consequence, the oscillations of the corresponding electric susceptibilities of the electron beam are "antiphase" (although the modulation of the distribution function itself has the standard monochromatic form). As result, a sign change occurs on one of the right-hand sides in the standard system of equations of the type (1), resulting in the appearance of instability. The energy comes from the kinetic energy of the beam, but to demonstrate this fact it is necessary to go beyond the linear theory described here. For generation as result of modulation of the conductivity the corresponding nonlinear analysis is performed in [3].

5. CONCLUSIONS

The parametric generation, examined here, of cyclotron radiation with modulation of the reactive susceptibility is due exclusively to the characteristic arrangement of the "curves of cyclotron resonance" in the momentum space of relativistic particles. We shall give an example illustrating the "sensitivity" of this effect to the resonance conditions.

Let us consider a system with a Cherenkov interaction. Let

$$V_{\parallel 1} = \omega_1/k_{\parallel 1} > V_{\parallel 2} = \omega_2/k_{\parallel 2}$$

and let the region of HF modulation in velocity space be concentrated in the interval $V_{\parallel 2} < V_\parallel < V_{\parallel 1}$. As the Cherenkov resonance with the mode $(\omega_1, k_{\parallel 1})$ is approached, the particles move away from resonance with the mode $(\omega_2, k_{\parallel 2})$—the situation seems to be the same as in the cyclotron system studied in Section 4. However, for particles from the velocity interval between the values $V_{\parallel 1,2}$ the sign of the detuning of the Cherenkov resonance relative to the modes $(\omega_1, k_{\parallel 1})$ and $(\omega_2, k_{\parallel 2})$ is different. Thus the oscillations of the detunings of synchronization $\omega_1 - k_{\parallel 1}V_\parallel$ and $\omega_2 - k_{\parallel 2}V_\parallel$ are in-phase. (Accordingly, even a strict calculation demonstrates the impossibility of parametric amplification of a bichromatic field in a Che-renkov system with a purely reactive susceptibility. Amplification as result of modulation of the active susceptibility is possible in this case; see [3].)

An important (and in a certain sense fundamental) question is the question of the realization of parametric instabilities of bichromatic radiation in a "reactive" ensemble of quantum oscillators. Analysis shows that such a regime is impossible on the basis of the standard three-level Λ scheme for systems with homogeneous line broadening, but for systems with a large number of levels and/or inhomogeneous broadening the question remains open. In principle, the system studied in this paper (an ensemble of electrons in a magnetic field) admits a transition from a "classical" distribution function to a population distribution over Landau quantum levels.

Parametric generation by modulation of the distribution of nonresonant particles is very important from the standpoint of experimental realization of an inversionless cyclotron maser effect, since in the presence of LF modulation of electron beams the active and reac-

tive components of the electric susceptibility of an electronic ensemble are inevitably modulated. As far as the general question of the prospects for producing inversionless electronic devices is concerned, parametric generation of bichromatic cyclotron radiation can be used, in principle, in microwave frequency converters (see [3] for a discussion of the possible advantages of such a system). Here we have demonstrated that for the electron momentum distributions typical for ordinary magneto-injector guns a "linear" LF modulation regime, which does not change the average (unmodulated) components of the distribution function and requires minimal power from an LF source, is adequate.[6] Thus the efficiency of such a frequency multiplier can be quite high. However, to determine the possible power of such schemes it is first necessary to develop a corresponding nonlinear theory.

ACKNOWLEDGMENTS

We thank A.V. Gaponov-Grekhov and A.G. Litvak for a number of stimulating discussions and for encouragement.

This work was supported by the Russian Foundation for Basic Research (project no. 99-02-16230).

REFERENCES

1. B. Sherman, G. Kurizki, D. E. Nikonov, and M. O. Scully, Phys. Rev. Lett. **75**, 4602 (1995).
2. D. E. Nikonov, B. Sherman, G. Kurizki, and M. O. Scully, Opt. Commun. **123**, 363 (1996).
3. A. V. Gaponov-Grekhov and M. D. Tokman, Zh. Éksp. Teor. Fiz. **112**, 1176 (1997) [JETP **85**, 640 (1997)].
4. O. Kocharovskaya, Phys. Rep. **219**, 175 (1992).
5. B. B. Kadomtsev, *Collective Phenomena in a Plasma* (Nauka, Moscow, 1988).
6. N. Bloembergen, *Nonlinear Optics* (Benjarnin, New York, 1965; Mir, Moscow, 1966).
7. A. B. Mikhailovskii, *Theory of Plasma Instabilities* (Atomizdat, Moscow, 1975, 2nd ed.; Consultants Bureau, New York, 1974).
8. A. A. Galeev and R. Z. Sagdeev, in *Revieuws of Plasma Physics*, Ed. by M. A. Leontovich (Atomizdat, Moscow, 1973; Consultants Bureau, New York, 1979), Vol. 7.
9. A. I. Akhiezer, I. A. Akhiezer, R. V. Polovin, *et al.*, *Plasma Electrodynamics*, Ed. by A. I. Akhiezer *et al.* (Nauka, Moscow, 1974; Pergamon, Oxford, 1975).
10. O. Kocharovskaya, P. Mandel, and Y. V. Radeonychev, Phys. Rev. A **45**, 1997 (1992).
11. V. M. Faĭn, *Photons and Nonlinear Medium* (Sov. Radio, Moscow, 1972).
12. V. L. Bratman, N. S. Ginzburg, G. S. Nusinovich, *et al.*, in *Relativistic High-Frequency Electronics*, Ed. by A. V. Gaponov-Grekhov (Inst. Prikl. Fiz. Akad. Nauk SSSR, Gorki, 1979), p. 157.
13. A. B. Kitsenko, I. M. Pankratov, and K. N. Stepanov, Zh. Tekh. Fiz. **45**, 912 (1975) [Sov. Phys. Tech. Phys. **20**, 575 (1975)].
14. A. G. Litvak, A. M. Sergeev, E. V. Suvorov, *et al.*, Phys. Fluids B **5**, 4347 (1993).
15. N. S. Ginzburg, Zh. Tekh. Fiz. **56**, 1433 (1986) [Sov. Phys. Tech. Phys. **31**, 851 (1986)].
16. T. O'Neil, Phys. Fluids **8**, 2255 (1965).
17. E. V. Suvorov and M. D. Tokman, Plasma Phys. **25**, 723 (1983).

[6] That is, it requires such power only in second-order in the amplitude of the modulating field. The case of a monotonic electron energy spectrum is a counterexample. Low-frequency modulation in a nonlinear particle "capture" regime (see [3]) is required in order to reach the threshold of inversionless generation; modulation in this case is inevitably accompanied by a larger distortion of the average components of the distribution function: the energy input is proportional to $\sqrt{E_0}$, where E_0 is the amplitude of the field in the modulating section (see also [16]).

Translation was provided by AIP

Journal of Experimental and Theoretical Physics, Vol. 91, No. 2, 2000, pp. 265–272.
Translated from Zhurnal Éksperimental'noĭ i Teoreticheskoĭ Fiziki, Vol. 118, No. 2, 2000, pp. 302–311.

ATOMS, SPECTRA, RADIATION

Contribution to the Theory of Bremsstrahlung in Scattering Media

A. V. Koshelkin

Moscow State Engineering Physics Institute, Moscow, 115409 Russia
e-mail: koshelkn@gpd.mephi.msk.su

Received February 1, 2000

Abstract—Bremsstrahlung of particles in matter is investigated on the basis of a method developed for finding the two-particle Green's functions in nonequilibrium media. A closed system of equations for the exact two-particle Green's functions in a medium, which completely determined the bremsstrahlung spectrum in matter, is obtained by summing a series of irreducible diagrams. The radiation of fast charged particles undergoing multiple elastic collisions in a static medium is investigated in detail. For quite strong scattering in matter, the spectrum found differs substantially from the spectrum found previously by A. B. Migdal [Dokl. Akad. Nauk SSSR **96**, 49 (1954)] (Landau–Pomeranchuk–Migdal effect). *© 2000 MAIK "Nauka/Interperiodica".*

1. INTRODUCTION

The influence of the scattering medium on the radiation of fast charged particles was first studied in [2, 3], where it was indicated that bremsstrahlung is suppressed in the long-wavelength region of the spectrum as a result of multiple elastic scattering of such particles in matter (Landau–Pomeranchuk effect). Migdal [1] constructed a quantitative theory of this effect. The method proposed in [1] for calculating the bremsstrahlung spectrum in matter was further elaborated [4–7] in an investigation of the influence of the dispersion properties of a scattering medium [4, 6], the boundary of the medium [5], and inelastic processes occurring in matter [6, 7] on the frequency distribution of bremsstrahlung. In the last few years the effect of a medium on bremsstrahlung has been investigated in [8–13], where an application of the path integral for calculating bremsstrahlung in matter [8, 9] is developed, the radiation of systems of charged particles is investigated [10, 11], and the manifestation of the Landau–Pomeranchuk–Migdal effect in QCD [12–14] and in the Coulomb interaction of particles in a scattering medium [15] is examined.

However, the works mentioned above do not take account of the effect of the scattering medium in the time before the bremsstrahlung photon is created; this is manifested in the linear dependence of the spectral energy density of the radiation on the time interval during which the particle moves in matter. This limitation can be eliminated by starting the investigation of bremsstrahlung in matter from the exact expression for the photon production probability, proportional to the two-particle Green's function in the medium.

The method for finding the Green's functions in a nonequilibrium medium was first formulated in [16–19], where a diagrammatic technique, which in principle makes it possible to calculate the Green's function in any order of perturbation theory, is developed. The Green's functions method for nonequilibrium media was further developed in [20–22]. However, the theory formulated in [16–22] concerns finding the single-particle Green's functions, while there exists a wide range of problems whose solution, generally speaking, cannot be reduced to calculating such functions. Examples of such problems are, specifically, the problems of scattering of particles and quasiparticles in a medium, questions concerning the study of the creation and annihilation of particles in the presence of multiple scattering in matter, and so on. Actually, the solution of any problem where the interaction Lagrangian is proportional to the particle current in the medium requires, generally speaking, calculation of the two-particle Green's functions. This is due to the fact that any observable quantity is proportional to the probability of the process being studied, which in turn is a bilinear function of the particle current.

In the present paper a method of calculating two-particle Green's functions in a nonequilibrium medium is developed. It is shown that, in contrast to the equilibrium situation [19], in the case at hand the particle states are determined by a set of Green's functions. Closed systems of equations are obtained for the exact vertex functions and for the two-particle Green's functions in a nonequilibrium medium.

The spectral energy density of bremsstrahlung of fast charged particles, multiply scattered elastically in a static medium (transport approximation), is found and investigated in detail on the basis of the method developed for calculating two-particle Green's functions. It is shown that for sufficiently weak scattering of particles in matter the spectrum obtained is identical to the frequency distribution found previously in [1]. In the

1063-7761/00/9102-0265$20.00

opposite limiting case of a strongly scattering medium the bremsstrahlung spectrum in matter is restructured, which is manifested as a dependence of the radiation energy on the parameters of the problem (radiation frequency, particle energy, time period of particle motion in matter) that is substantially different from that obtained in [1–3].

2. BREMSSTRAHLUNG AND TWO-PARTICLE GREEN'S FUNCTIONS IN A MEDIUM

The probability of photon creation is determined by the well-known expression [22, 23]

$$d^4w = \frac{2\pi e_\mu e_\nu^*}{\omega}\int d^4x_1 d^2x_2 \exp(-ik(x_1 - x_2)) \times \langle j^{\mu+}(x_1) j^\nu(x_2)\rangle \frac{d^3k}{(2\pi)^3}, \quad (1)$$

where $k = (\omega, \mathbf{k})$ is the 4-vector of the photon, e_α is the polarization vector of the photon, $j^\mu(x)$ is the current operator, in the Heisenberg representation, for particles creating a photon, and x is the 4-coordinate. The brackets indicate averaging over a state of the particles in the medium, which can also be a nonequilibrium state.

The bilinear combination of currents, which appears in Eq. (1), can be represented in the following form:

$$\langle j^{\mu+}(x_1) j^\nu(x_2)\rangle = \langle i|(\hat{O}^\mu)_{\alpha,\beta}((\hat{O}^\dagger)^\nu)_{\gamma,\delta}|j\rangle \times \langle \Psi^\dagger_\delta(x_1)\Psi_\gamma(x_1)\Psi_\beta(x_2)\Psi^\dagger_\alpha(x_2)\rangle, \quad (2)$$

where $\langle i|(\hat{O}^\mu)_{\alpha,\beta}((\hat{O}^\dagger)^\nu)_{\gamma,\delta}|j\rangle$ is the matrix element of an operator that does not depend on the 4-coordinates, $\Psi(x)$ psi operators in the Heisenberg representation, and α, β, γ, and δ are spin variables.

Thus, the problem of calculating the spectral-angular distribution of bremsstrahlung reduces to finding the two-particle Green's function in a medium.

We shall determine the exact two-particle Green's function in a nonequilibrium medium as follows:

$$K_{\delta,\beta;\gamma,\alpha}(x_4, x_2; x_3, x_1) \equiv K(4, 2; 3, 1) = \langle T\{\hat{\Psi}_3\hat{\Psi}_4\hat{\Psi}_1^+\hat{\Psi}_2^+\}\rangle \equiv$$

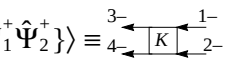

, (3)

where $\hat{\Psi}_i$ are field operators in the Heisenberg representation and T is the standard chronological ordering symbol for the cofactors in a product. The brackets indicate averaging over an arbitrary, including nonstationary, quantum state of particles in a medium.

Switching from the Heisenberg to the interaction representation, we have for $K(4, 2; 3, 1)$

$$K(4, 2; 3, 1) = \langle \hat{S}^{-1} T\{\hat{\Psi}_{03}\hat{\Psi}_{04}\hat{\Psi}^+_{01}\hat{\Psi}^+_{02}\hat{S}\}\rangle. \quad (4)$$

The symbol $\hat{S}$ is the standard S operator, determining the interaction of particles in the interaction representation, and $\hat{\Psi}_{01}$ are field operators in the same representation.

Following the notations used in the Keldysh nonequilibrium diagrammatic technique [18, 24], we introduce the exact single-particle Green's functions:

$$iG^{--}(2, 1) = \langle T\{\hat{\Psi}_1\hat{\Psi}_2\}\rangle = {}^{2-}\!\!\leftarrow\!\!{}^{1-},$$
$$iG^{++}(2, 1) = \langle \tilde{T}\{\hat{\Psi}_1\hat{\Psi}_2\}\rangle = {}^{2+}\!\!\leftarrow\!\!{}^{1+},$$
$$iG^{+-}(2, 1) = \langle \{\hat{\Psi}_1\hat{\Psi}_2\}\rangle = {}^{2-}\!\!\leftarrow\!\!{}^{1+},$$
$$iG^{-+}(2, 1) = \mp\langle \{\hat{\Psi}^+_2\hat{\Psi}_1\}\rangle = {}^{2+}\!\!\leftarrow\!\!{}^{1-}, \quad (5)$$

where T denotes an antichronological product of the cofactors [18, 24].

The one- and two-particle Green's functions are related with one another by the obvious equation

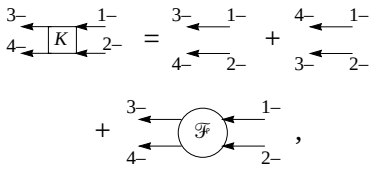

(6)

where $\mathcal{F}$ denotes the sum of all diagrams which cannot be represented as two unconnected continuous lines corresponding to single-particle Green's functions. In Eq. (6), as well as everywhere below, summation is assumed over the variables corresponding to the points of intersection of the lines in the diagrams and integration is assumed over the corresponding variables.

The function $\mathcal{F}$ is a sum of all exact vertex functions $\Gamma(a, b, c, d)$, corresponding to various sets of the parameters a, b, c, d, which can assume the values plus sign or minus sign:

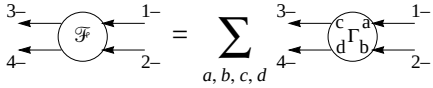

. (7)

It is obvious that the number of terms in the latter sum is $2^4 = 16$. Thus, the problem of calculating the two-particle Green's function reduces to finding all possible different exact vertex functions $\Gamma(d, b; c, a)$.

3. EQUATIONS FOR THE EXACT VERTEX FUNCTIONS

We note that any vertex function $\Gamma(d, b; c, a)$ can be represented as a series of diagrams as follows:

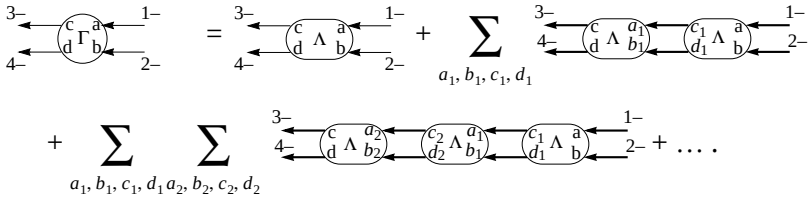

(8)

The symbol Λ denotes an exact irreducible diagram consisting of a sum of all possible diagrams which cannot be sectioned by a vertical line so that the line would intersect only two continuous lines corresponding to single-particle Green's functions.

Summing the diagrams in the expression (8) we obtain

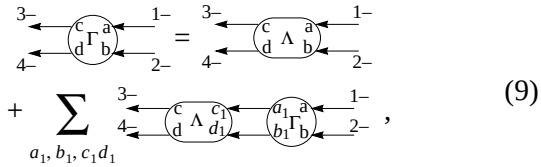

(9)

where the parameters a, b, c, d and a_1, b_1, c_1, d_1 assume the values + or –, and summation and integration are assumed over the variables corresponding to the points of intersection of the lines in the diagrams.

The latter equation can be written analytically as

$$\hat{\Gamma}(4, 2; 3, 1) = \hat{\Lambda}(4, 2; 3, 1) - \int dX_5 dX_6 dX_7 dX_8 \times \hat{\Lambda}(4, 6; 3, 5)\hat{K}^{(0)}(6, 8; 5, 7)\hat{\Gamma}(8, 2; 7, 1), \quad (10)$$

where G^{ab} are the single-particle Green's functions determined by Eqs. (5); X_i denotes the 4-coordinates and a spin variable, and $\hat{\Lambda}$, $\hat{K}^{(0)}$, and $\hat{\Gamma}$ are 4×4 matrices constructed from the corresponding functions, and each matrix element is determined by the set of symbols + and – corresponding to the values of the parameters a, b, c, and d in Eq. (7):

$$\hat{\Gamma} \equiv (\Gamma)_{ij} = \Gamma_{(b,d);\,(a,c)}, \quad \hat{\Lambda} \equiv (\Lambda)_{ij} = \Lambda_{(b,d);\,(a,c)}, \quad \hat{K}^{(0)} \equiv (K^{(0)})_{ij} = K^{(0)}_{(b,d);\,(a,c)} = G^{ac}G^{bd}. \quad (11)$$

Specifically, the matrix $\hat{\Lambda}$ has the form

$$\hat{\Lambda}(4, 2; 3, 1) = \begin{pmatrix} \Lambda_{(-,-;-,-)} & \Lambda_{(-,-;+,-)} & \Lambda_{(+,-;-,-)} & \Lambda_{(+,-;+,-)} \\ \Lambda_{(-,+;-,-)} & \Lambda_{(-,+;+,-)} & \Lambda_{(+,+;-,-)} & \Lambda_{(+,+;+,-)} \\ \Lambda_{(-,-;-,+)} & \Lambda_{(-,-;+,+)} & \Lambda_{(+,-;-,+)} & \Lambda_{(+,-;+,+)} \\ \Lambda_{(-,+;-,+)} & \Lambda_{(-,+;+,+)} & \Lambda_{(+,+;-,+)} & \Lambda_{(+,+;+,+)} \end{pmatrix}. \quad (12)$$

The formulas (9) and (10) comprise a system of equations which is closed with respect to Γ and makes it possible to find the exact vertex function $\Gamma(4, 2; 3, 1)$ and the two-particle Green's function $K(4, 2; 3, 1)$ in a nonequilibrium medium. We note that in contrast to the equilibrium situation (see, for example, [25]) the nonequilibrium nature of the medium has the effect that the interaction of the particles in matter is determined by the set of exact vertex functions which satisfy the system of equations (10).

4. EQUATIONS FOR THE TWO-PARTICLE GREEN'S FUNCTIONS

Although Eqs. (6), (9), and (10) solve the problem of finding the two-particle Green's function in a nonequilibrium medium, it is very important to obtain equations for $K(4, 2; 3, 1)$ directly without first calculating the vertex functions Γ.

For this we introduce the antichronologically ordered $\tilde{K}$, nonchronologically ordered K', and the partially chronologically ordered two-particle Green's functions. We shall determine the first two functions by the equations

$$\tilde{K}(4, 2; 3, 1) = \langle \tilde{T}\{\hat{\Psi}_3\hat{\Psi}_4\hat{\Psi}_1^+\hat{\Psi}_2^+\}\rangle, \quad K'(4, 2; 3, 1) = \langle\{\hat{\Psi}_3\hat{\Psi}_4\hat{\Psi}_1^+\hat{\Psi}_2^+\}\rangle. \quad (13)$$

The partially chronologically ordered Green's function is, once again, a product of four Ψ functions. However, this product is such that in it either only two Ψ functions (given, for definiteness, by even or odd indices) are chronologically or antichronologically ordered, and the remaining two functions are not chronologically ordered at all, or the Ψ functions are chronologically and antichronologically ordered in pairs. In other words, the partially chronologically ordered two-particle Green's functions are correlators of the type $\langle\hat{\Psi}_4\hat{\Psi}_2^+\tilde{T}\{\hat{\Psi}_3\hat{\Psi}_1^+\}\rangle$, $\langle\hat{\Psi}_4\hat{\Psi}_2^+T\{\hat{\Psi}_3\hat{\Psi}_1^+\}\rangle$, $\langle T\{\hat{\Psi}_4\hat{\Psi}_2^+\}\hat{\Psi}_3\hat{\Psi}_1^+\rangle$, $\langle T\{\hat{\Psi}_4\hat{\Psi}_2^+\}\tilde{T}\{\hat{\Psi}_3\hat{\Psi}_1^+\}\rangle$, and so on.

To introduce consistent notation for all types of two-particle Green's functions, we denote the latter by the number of the corresponding variable and by a + or – in front of it:

$$K(4, (s_4); 2, (s_2); 3, (s_3); 1, (s_1)) \equiv K(4; 2; 3; 1) \equiv$$

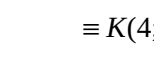

(14)

where s_1, s_2, s_3, and s_4 assume the values + or –. If all four signs are the same in the diagram, then this is a chronologically or antichronologically ordered Green's function. In the opposite case such a function is par-

tially chronologically ordered with respect to the variables corresponding to even or odd indices of the dynamical variables.

It follows from Eqs. (6) and (7) that

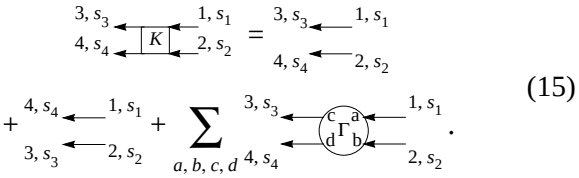

(15)

Summing in Eq. (9) over all possible different values of the parameters a, b, c, and d and then substituting the sum of the exact vertex functions from the relation (13) into the expression obtained after the summation indicated above (9), we find

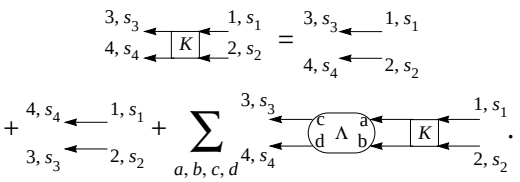

(16)

The latter expression can be written analytically in the form

$$\hat{K}(4,2;3,1) = \hat{K}^{(0)}(4,2;3,1) + \hat{K}^{0}(3,2;4,1) - \int dX_5 dX_6 dX_7 dX_8 \hat{K}^{0}(4,6;3,5) \times \hat{\Lambda}(6,8;5,7)\hat{K}(8,2;7,1), \quad (17)$$

where X_i denotes the collection of 4-coordinates and the spin variable of a particle, and all symbols with an overheat denote 4×4 matrices constructed similarly to the matrices in Eq. (10). The elements of the matrix $\hat{K}$ are the corresponding two-particle Green's functions K determined by the expression (14).

The equations (16) and (17) form a closed system of equations which makes it possible to find the two-particle Green's functions in a nonequilibrium medium. Just as for the equations for the exact vertex functions (10), the structure of the irreducible diagrams Λ completely determines the properties of the solutions of the system (17). We note that in contrast to the equilibrium situation [25], in an equilibrium medium there exists a variety of two-particle Green's functions which satisfy the closed system of equations (17).

We note that if the averaging in Eq. (3) is performed not over an arbitrary state but rather the vacuum, then all diagrams containing a sign + vanish. In this case Eqs. (17) become the well-known Bethe–Salpeter equation [26].

5. TWO-PARTICLE GREEN'S FUNCTIONS IN THE TRANSPORT APPROXIMATION

It follows from Eqs. (1), (2), and (14) that the correlator consisting of four Ψ operators and determining the probability dw of photon production in matter, is a nonchronologically ordered two-particle Green's function $K(2(+); 2(-)|1(-); 1(+))$. Then the problem of calculating dw reduces to finding $K(4(+); 2(-)|3(-); 1(+))$ for $X_1 = X_3$ and $X_2 = X_4$.

Let us consider the transport approximation for describing particles in matter: we assume that all particles, with the exception of one, occupy fixed stationary states (static medium), and the distinguished particle undergoes elastic multiple collisions with them. Let the interaction of a particle with static scattering centers be described by the potential $U(\mathbf{R}_j - \mathbf{r})$, where $\mathbf{r}$ is the radius vector of the particle and $\mathbf{R}_j$ is the radius vector of the jth scattering center. We introduce the functions $U_+(X)$ and $U_-(X)$:

$$iU_+(X) \equiv iU(\mathbf{R}_j - \mathbf{r}) = \overset{+}{\bullet}\cdots\cdots$$
$$iU_-(X) \equiv -iU(\mathbf{R}_j - \mathbf{r}) = \overset{-}{\bullet}\cdots\cdots \quad (18)$$

Then, to a first approximation in the interaction of a particle in the medium, we have for the function $K(4(+); 2(-)|3(-); 1(+))$ from Eqs. (16)

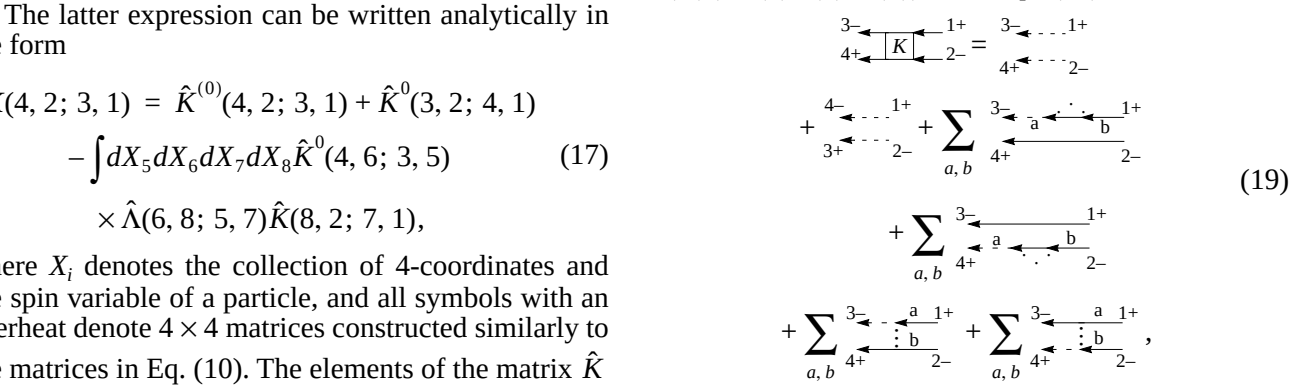

(19)

where the dashed lines denote free single-particle Green's functions, and the dotted lines without free ends imply summation over the scattering centers.

The expression (19), after switching to the mixed coordinate-momentum representation and standard (see [24]) transformations, leads to a system of two kinetic equations for the variables

$$t_1, \quad p = (p_1 + p_3)/2, \quad \mathbf{r} = (\mathbf{r}_1 + \mathbf{r}_3)/2$$

and

$$t_2, \quad p = (p_2 + p_4)/2, \quad \mathbf{r} = (\mathbf{r}_2 + \mathbf{r}_4)/2,$$

determining the evolution of a two-time distribution function in a scattering medium in the transport approximation. The third and fourth terms in Eq. (19) determine the probability of "arrival" and "departure" of a particle in the phase volumes $\Gamma(\mathbf{p}, \mathbf{r})$ and $\Gamma(\mathbf{p}', \mathbf{r}')$, respectively. The last two terms in the expression (19) correspond to the probability of "arrival" and "departure" in the phase volume $\Gamma(\mathbf{p}, \mathbf{r})\Gamma(\mathbf{p}', \mathbf{r}')$ and determine the temporal correlations in the scattering medium. We note that since the four-momentum is conserved at each vertex, the last terms in Eq. (19) make a large contribu-

tion to the collision integral, when the particle energies $E(\mathbf{p})$ and $E(\mathbf{p}')$ at the times t_1 and t_2, respectively, are essentially the same.

Let the emitting particle be a spin-1/2 fermion. We operate with the operator $\hat{p} - m$, which is the left-hand side of the Dirac equation for the function Ψ (m is the particle mass), on the variables 3 and 4 in Eq. (19). This gives two equations.

We note that the dashed lines, denoting single-particle free Green's functions, can be represented on the right in each term on the right-hand side of Eq. (19) and will correspond to the variables 1 and 4. Then, acting with the operator $\hat{p} + m$ on the variables 1 and 4 in the expression (19) rewritten in this manner, we obtain two additional equations. Next, we subtract the third from the first equation and the fourth from the second equation. Then, neglecting the "mixing" of the spin variables, as a result of multiple scattering of a particle in the medium, we obtain

$$\left(\frac{\partial}{\partial t_1} - i\mathbf{k}\cdot\mathbf{v}\right)F_{\mathbf{k}}(\mathbf{p}';\,\mathbf{p}';\,t_2;\,\mathbf{p};\,\mathbf{p};\,t_1) =$$

$$\frac{\pi nm}{2E(\mathbf{p})}\int d\mathbf{q}|U(\mathbf{q})|^2\{(F_{\mathbf{k}}(\mathbf{p}';\,\mathbf{p}';\,t_2;\,\mathbf{p}+\mathbf{q};\,\mathbf{p}+\mathbf{q};\,t_1)$$
$$- F_{\mathbf{k}}(\mathbf{p}';\,\mathbf{p}';\,t_2;\,\mathbf{p};\,\mathbf{p};\,t_1))\delta(E(\mathbf{p}+\mathbf{q}) - E(\mathbf{p}))$$
$$+ [F_{\mathbf{k}}(\mathbf{p}';\,\mathbf{p}'+\mathbf{q};\,t_2;\,\mathbf{p}+\mathbf{q};\,\mathbf{p};\,t_1)\delta(E(\mathbf{p}') - E(\mathbf{p}'+\mathbf{q})) \quad (20)$$
$$- F_{\mathbf{k}}(\mathbf{p}';\,\mathbf{p}'-\mathbf{q};\,t_2;\,\mathbf{p};\,\mathbf{p}+\mathbf{q};\,t_1)\delta(E(\mathbf{p}') - E(\mathbf{p}'-\mathbf{q}))]$$
$$\times\cos(t_1(E(\mathbf{p}+\mathbf{q}) - E(\mathbf{p})))\},$$

$$\left(\frac{\partial}{\partial t_2} + i\mathbf{k}\cdot\mathbf{v}'\right)F_{\mathbf{k}}(\mathbf{p}';\,\mathbf{p}';\,t_2;\,\mathbf{p};\,\mathbf{p};\,t_1) =$$

$$\frac{\pi nm}{2E(\mathbf{p})}\int d\mathbf{q}|U(\mathbf{q})|^2\{(F_{\mathbf{k}}(\mathbf{p}'+\mathbf{q};\,\mathbf{p}'+\mathbf{q};\,t_2;\,\mathbf{p};\,\mathbf{p};\,t_1)$$
$$- F_{\mathbf{k}}(\mathbf{p}';\,\mathbf{p}';\,t_2;\,\mathbf{p};\,\mathbf{p};\,t_1))\delta(E(\mathbf{p}'+\mathbf{q}) - E(\mathbf{p}'))$$
$$+ [F_{\mathbf{k}}(\mathbf{p}';\,\mathbf{p}'+\mathbf{q};\,t_2;\,\mathbf{p}+\mathbf{q};\,\mathbf{p};\,t_1)\delta(E(\mathbf{p}) - E(\mathbf{p}+\mathbf{q})) \quad (21)$$
$$- F_{\mathbf{k}}(\mathbf{p}';\,\mathbf{p}'+\mathbf{q};\,t_2;\,\mathbf{p};\,\mathbf{p}-\mathbf{q};\,t_1)\delta(E(\mathbf{p}) - E(\mathbf{p}-\mathbf{q}))]$$
$$\times\cos(t_2(E(\mathbf{p}'+\mathbf{q}) - E(\mathbf{p}')))\},$$

where $E(\mathbf{p})$ is the energy of a particle with momentum $\mathbf{p}$ (the dispersion law is assumed to be known), $\mathbf{v} = \mathbf{p}/E(\mathbf{p})$ and $\mathbf{v}' = \mathbf{p}'/E(\mathbf{p}')$ are the particle velocities, $U(\mathbf{q})$ is the Fourier component of the interaction of the particle with an individual scattering center in the medium, and n is the scatterer density. In deriving the last equations it was assumed that the photon momentum k is small compared to the energy E of the emitting particle; this corresponds to neglecting the effect of photon production on particle collisions in the medium.

The function $F_{\mathbf{k}}(\mathbf{p}';\,\mathbf{p}';\,t_2;\,\mathbf{p};\,\mathbf{p};\,t_1)$ is related with the two-particle Green's function $K(p_4(+);\,p_2(-)|\,p_3(-);\,p_1(-))$ by the relation

$$F_{\mathbf{k}}(\mathbf{p}';\,\mathbf{p}';\,t_2;\,\mathbf{p};\,\mathbf{p};\,t_1)$$
$$= F(\mathbf{p}' - \mathbf{k}/2;\,\mathbf{p}' + \mathbf{k}/2;\,t_2;\,\mathbf{p} + \mathbf{k}/2;\,\mathbf{p} - \mathbf{k}/2;\,t_1)$$
$$= \int dX_1 dX_2 dX_3 dX_4 \delta(X_1 - X_3)\delta(X_2 - X_4)$$
$$\times\int dp_1^0 dp_2^0 d^4p_3 d^4p_4 \delta(\mathbf{p}_3 - \mathbf{p}_1 - \mathbf{k})\delta(\mathbf{p}_2 - \mathbf{p}_4 - \mathbf{k}) \quad (22)$$
$$\times\exp(i(p_3^0 - p_1^0)t_1)\exp(-i(p_2^0 - p_4^0)t_2)$$
$$\times K(p_4(+);\,p_2(-)|\,p_3(-);\,p_1(+)) \equiv F_{\mathbf{k}}(\mathbf{p};\,\mathbf{p}';\,t_1;\,t_2).$$

The terms with the cosines on the right-hand sides of Eqs. (20) and (21) correspond to connected diagrams in Eq. (19) and determine the contribution of the two-time correlations in the collision integral. The remaining terms are the standard terms of the kinetic equation in the transport approximation.

Actually, Eqs. (20) and (21) can be solved analytically only in limiting cases. These are, specifically, the situation of an isotropically scattering medium, where $U(\mathbf{q})$ does not depend on the transferred momentum $\mathbf{q}$ (this situation is of interest for studying photon production in a hadronic medium) and small-angle scattering of particles in matter ($\mathbf{q}$ is small compared with the momentum of the emitting particle). Bremsstrahlung in the s-scattering case in a medium is investigated in detail in [27, 28].

6. BREMSSTRAHLUNG WITH SMALL-ANGLE SCATTERING OF PARTICLES IN MATTER

Let us consider a fast ($E \gg \omega$; ω is the photon energy) ultrarelativistic particle ($m \ll E$, m is the particle mass, and E is the particle energy), entering at time $t = 0$ a scattering medium and undergo multiple elastic collisions there.

Then the direct calculation of the matrix elements of the operators $\langle i|(\hat{O}^{\mu})_{\alpha,\beta}((\hat{O}^{\dagger})^{\nu})_{\gamma,\delta}|j\rangle$ (see Eqs. (1) and (2)) and summing and averaging the formulas for the probability of photon production over the final and initial states give for the spectral energy density of the radiation

$$dE_{\omega} = \omega\overline{d^4w} = \frac{\alpha}{4\pi^2E^2}\int_0^T dt_1\int_0^T dt_2$$
$$\times\int d\mathbf{p}\int d\mathbf{p}'(\mathbf{k}\times\mathbf{p})\cdot(\mathbf{k}\times\mathbf{p}')$$
$$\times\{\exp(i(t_1 - t_2))[F_{\mathbf{k}}(\mathbf{p},\,\mathbf{p}',\,t_1,\,t_2)$$
$$+ F_{\mathbf{k}}(\mathbf{p} = \mathbf{p}_0,\,\mathbf{p}' = \mathbf{p}_0,\,t_1,\,t_2)] \quad (23)$$
$$- 2\mathrm{Re}[F_{\mathbf{k}}(\mathbf{p},\,\mathbf{p}' = \mathbf{p}_0,\,t_1,\,t_2;\,a;\,b = 0)$$
$$\times\exp(i(t_1 - t_2))]\}d\mathbf{k},$$

where the function $F_{\mathbf{k}}(\mathbf{p}, \mathbf{p}', t_1, t_2)$ is determined by the relations (19)–(21); $\mathbf{p}_0$ is the particle momentum at the moment the particle enters the matter; the overbar in Eq. (23) denotes summation and averaging over the spin states of the particles. The separation of the integration interval [5] is due to the fact that the particle starts to move in the medium at $t = 0$, and in the time $-\infty < t < 0$ it moves as a free particle with momentum $\mathbf{p}_0$ without scattering.

Let the scattering in the medium be such that

$$\begin{aligned} &t_{1,2}|E(\mathbf{p}+\mathbf{q}) - E(\mathbf{p}' \pm \mathbf{q})| \\ &\sim T|E(\mathbf{p}-\mathbf{q}) - E(\mathbf{p}' \pm \mathbf{q})| \ll 1. \end{aligned} \tag{24}$$

Then the cosines on the right-hand sides of the equations are equal to one. In addition, in the small-angle approximation, which is valid for ultrarelativistic particles moving in a medium [1–3], the momentum transferred as a result of an individual collision of a particle with a scatterer $|\mathbf{q}|$ is small compared with the particle momentum $|\mathbf{p}|$. Setting the exponentials in Eqs. (20) and (21) equal to one and expanding the collision integrals obtained in powers of the small ratio $q/p \ll 1$, we obtain for the function $F_{\mathbf{k}}$

$$\begin{aligned} &\frac{\partial F_{\mathbf{k}}(\mathbf{p}, \mathbf{v}', t_1, t_2)}{\partial t_1} - i\mathbf{k}\cdot\mathbf{p}F_{\mathbf{k}}(\mathbf{p}, \mathbf{p}', t_1, t_2) \\ &= \frac{\langle\Theta_s^2\rangle}{4}\left\{\frac{\partial^2}{\partial\boldsymbol{\eta}^2} + \frac{\partial^2}{\partial\boldsymbol{\eta}\partial\boldsymbol{\zeta}}\right\}F_{\mathbf{k}}(\mathbf{p}, \mathbf{p}', t_1, t_2), \end{aligned} \tag{25}$$

$$\begin{aligned} &\frac{\partial F_{\mathbf{k}}(\mathbf{p}, \mathbf{p}', t_1, t_2)}{\partial t_1} + i\mathbf{k}\cdot\mathbf{v}'F_{\mathbf{k}}(\mathbf{p}, \mathbf{p}', t_1, t_2) \\ &= \frac{\langle\Theta_s^2\rangle}{4}\left\{\frac{\partial^2}{\partial\boldsymbol{\zeta}^2} + \frac{\partial^2}{\partial\boldsymbol{\eta}\partial\boldsymbol{\zeta}}\right\}F_{\mathbf{k}}(\mathbf{p}, \mathbf{p}', t_1, t_2). \end{aligned} \tag{26}$$

In Eqs. (25) and (26)

$$\begin{aligned} &\mathbf{p} = p_0\mathbf{e}_z\left(1 - \frac{\boldsymbol{\eta}^2}{2}\right) + p_0\boldsymbol{\eta}, \quad \boldsymbol{\eta} \perp \mathbf{e}_z, \quad |\boldsymbol{\eta}| \ll 1, \\ &\mathbf{p}' = p_0\mathbf{e}_z\left(1 - \frac{\boldsymbol{\zeta}^2}{2}\right) + p_0\boldsymbol{\zeta}, \quad \boldsymbol{\zeta} \perp \mathbf{e}_z, \quad |\boldsymbol{\zeta}| \ll 1, \\ &\langle\Theta_s^2\rangle = 2nm_0p_0^{-2}E^{-1}\int d\mathbf{q}q|U(\mathbf{q})|^2\delta(E(\mathbf{p}) - E(\mathbf{p}+\mathbf{q})), \\ &\mathbf{v} = \frac{\mathbf{p}}{E}, \quad \mathbf{v}' = \frac{\mathbf{p}'}{E}, \quad |\mathbf{v}| = |\mathbf{v}'| = v_0, \end{aligned} \tag{27}$$

where $\langle\Theta_s^2\rangle$ is the average squared angle of multiple scattering of a particle per unit length.

We introduce the variables $\tau = t_1 - t_2$ and $t \equiv t_2$ and add Eqs. (25) and (26). Since the photon formation time $\tau \ll t \sim T$, the characteristic scattering angles of a radiating particle in time τ are small compared with the scattering angles in the time interval $t \sim T$. Then τ can be neglected in the equation describing the evolution of the function $F_{\mathbf{k}}$ on times of the order of $t \sim T \gg \tau$, and in the equation determining the change in $F_{\mathbf{k}}$ in the photon formation time—the derivative with respect to the variable $\boldsymbol{\zeta}$.

As a result, we have

$$\begin{aligned} &\frac{\partial F_{\mathbf{k}}(\mathbf{p}, \mathbf{p}', t, \tau)}{\partial\tau} - i\mathbf{k}\cdot\mathbf{v}F_{\mathbf{k}}(\mathbf{p}, \mathbf{p}', t, \tau) \\ &= \frac{\langle\Theta_s^2\rangle}{4}\left\{\frac{\partial^2}{\partial(\boldsymbol{\eta} - \boldsymbol{\zeta})^2}\right\}F_{\mathbf{k}}(\mathbf{p}, \mathbf{p}', t, \tau), \end{aligned} \tag{28}$$

$$\begin{aligned} &\frac{\partial F_{\mathbf{k}}(\mathbf{p}, \mathbf{p}', t, \tau = 0)}{\partial\tau} - i(\mathbf{k}\cdot\mathbf{v} - \mathbf{k}\cdot\mathbf{v}')F_{\mathbf{k}}(\mathbf{p}, \mathbf{p}', t, \tau = 0) \\ &= \frac{\langle\Theta_s^2\rangle}{4}\left(\frac{\partial}{\partial\boldsymbol{\eta}} + \frac{\partial}{\partial\boldsymbol{\zeta}}\right)^2 F_{\mathbf{k}}(\mathbf{p}, \mathbf{p}', t, \tau = 0), \end{aligned} \tag{29}$$

Solving the obtained equations with the initial condition

$$F_{\mathbf{k}}(\mathbf{p}, \mathbf{p}', t_1 = 0, t_2 = 0) = \frac{\delta(p - p_0)}{p^2}\delta(\boldsymbol{\eta})\delta(\boldsymbol{\zeta}), \tag{30}$$

we find the function $F_{\mathbf{k}}(\mathbf{p}, \mathbf{p}', t, \tau)$. Substituting the expression obtained for $F_{\mathbf{k}}(\mathbf{p}, \mathbf{p}', t, \tau)$ into Eq. (23) for the radiation energy, we arrive at the spectral energy distribution $dE_\omega/d\omega$ of the radiation, obtained by A.B. Migdal,

$$\begin{aligned} \frac{dE_\omega}{d\omega} &= \frac{\alpha\omega T}{\pi\gamma^2}\int_0^{+\infty} dz \exp\left(-\frac{z(\omega/\langle\Theta_s^2\rangle)^{1/2}}{2\gamma^2}\right) \\ &\times\left\{\sin\left(\frac{z(\omega/\langle\Theta_s^2\rangle)^{1/2}}{2\gamma^2}\right)\coth z - \frac{\pi}{4}\right\}, \end{aligned} \tag{31}$$

where $\gamma = E/m$ is the Lorentz factor of an ultrarelativistic particle, $k = \omega$. In Eq. (31) the terms corresponding to radiation at the boundary of the medium [5] are dropped because they are small compared to $dE_\omega/d\omega$, given by the expression (31) and proportional to the macroscopic parameter T—the time over which the particle moves in the matter.

A distinguishing feature of Migdal's results is the linear dependence of the radiation energy on the motion time T of a particle in the medium. Formally, this was the consequence of the "decoupling" of the system of equations (25) and (26). From the physical standpoint such a dependence of $dE_\omega/d\omega$ on T signifies that the effect of scattering of a particle in matter on the formation of a photon in the time preceding photon emission is neglected.

Thus, the limits of applicability of the results obtained in [1, 4] are determined by the inequality

$$t_{1,2}|E(\mathbf{p}+\mathbf{q})-E(\mathbf{p}'+\mathbf{q})| \sim \langle\Theta_s^2\rangle^{1/2}\langle l\rangle^{1/4}ET^{5/4} \ll 1, \tag{32}$$

where $\langle l\rangle$ is the average mean free path length of particles in matter. Since the right-hand side of the inequality is proportional to $\langle l\rangle^{-1/4}$ (the average squared multiple scattering angle $\langle\Theta_s^2\rangle \sim \langle l\rangle^{-1}$), the expression (32) corresponds to the condition of weak scattering of the medium.

In the opposite limiting case of a strongly scattering medium,

$$\langle\Theta_s^2\rangle^{1/2}\langle l\rangle^{1/4}ET^{5/4} \gg 1,$$

the cosines which depend on t_1 and t_2 in Eqs. (20) and (21), respectively, are rapidly oscillating functions, and the terms which contain them are equal to zero. Then we find from Eqs. (20) and (21) for the function $F_{\mathbf{k}}(\mathbf{p}, \mathbf{p}', t_1, t_2)$

$$\frac{\partial F_{\mathbf{k}}(\mathbf{p},\mathbf{p}',t_1,t_2)}{\partial t_1} - i\mathbf{k}\cdot\mathbf{v}F_{\mathbf{k}}(\mathbf{p},\mathbf{p}',t_1,t_2) = \frac{\langle\Theta_s^2\rangle}{4}\left\{\frac{\partial^2}{\partial\boldsymbol{\eta}^2}\right\}F_{\mathbf{k}}(\mathbf{p},\mathbf{p}',t_1,t_2), \tag{33}$$

$$\frac{\partial F_{\mathbf{k}}(\mathbf{p},\mathbf{p}',t_1,t_2)}{\partial t_1} + i\mathbf{k}\cdot\mathbf{v}'F_{\mathbf{k}}(\mathbf{p},\mathbf{p}',t_1,t_2) = \frac{\langle\Theta_s^2\rangle}{4}\left\{\frac{\partial^2}{\partial\boldsymbol{\zeta}^2}\right\}F_{\mathbf{k}}(\mathbf{p},\mathbf{p}',t_1,t_2). \tag{34}$$

Solving the obtained equations with the initial condition (30) and substituting the function $F_{\mathbf{k}}$ found above into Eq. (22), we obtain after the required integrations

$$\frac{dE_\omega}{d\omega} = \frac{\alpha\omega^2}{2\pi\gamma^2}\mathrm{Re}\left\{\int_0^T dt_1\int_0^T dt_2\exp\left(-\frac{i(t_1-t_2)\omega}{2\gamma^2}\right)\times\left[\frac{2}{\left(\frac{a}{q}\tanh(at_1)-\frac{i\omega t_2}{2}\right)\cosh^2(at_1)} - \frac{1}{\left(\frac{a}{q}\tanh(at_1)+\frac{b}{q}\tanh(bt_2)\right)\cosh^2(at_1)}\right]\right\} \tag{35}$$

$$+\frac{2\alpha\omega}{\pi}\int_0^{+\infty}dz\exp\left(-\frac{z(\omega/\langle\Theta_s^2\rangle)^{1/2}}{2\gamma^2}\right)\times\cos\left(\frac{z(\omega/\langle\Theta_s^2\rangle)^{1/2}}{2\gamma^2}\right)\left[\frac{1}{z}-\frac{1}{\sinh z\cosh z}\right],$$

where

$$a = (1+i)\sqrt{\omega v_0\langle\Theta_s^2\rangle/2}, \quad b = a^*,$$

$$\gamma = E/m, \quad v_0 = p_0/E(\mathbf{p}_0).$$

Let us analyze the spectrum found for bremsstrahlung in matter.

For $\langle\Theta_s^2\rangle T\gamma^2 \ll 1$, which corresponds to quite thin layers of a scattering medium, the formula (35) goes into the spectral distribution (31). In the more realistic situation $\langle\Theta_s^2\rangle T\gamma^2 \gg 1$, we have the following.

In the region of quite small $\omega \ll \langle\Theta_s^2\rangle^{-1}T^{-2}$, the frequency distribution of the bremsstrahlung energy has the form

$$\frac{dE_\omega}{d\omega} = \frac{\alpha T}{\pi}\sqrt{\langle\Theta_s^2\rangle\omega}. \tag{36}$$

The latter expression is identical to Migdal's formula [1, 4] in the long-wavelength region of the spectrum. This is due to the fact that extremely soft photons ($\omega \longrightarrow 0$) are actually formed over the entire trajectory of the particle in matter. Consequently, the effect of scattering in the medium during a time preceding the creation of a photon is negligibly small, and $dE_\omega/d\omega \propto T$.

In the intermediate region of the spectrum

$$\langle\Theta_s^2\rangle^{-1}T^{-2} \ll \omega \ll \langle\Theta_s^2\rangle\gamma^4$$

we find

$$\frac{dE_\omega}{d\omega} = \frac{2\alpha}{\pi}\int_0^{+\infty}dz\left\{\frac{z}{(z^2+1)\cosh^2 z} + \frac{\exp(-z)}{z} - \frac{1}{\sinh z\cosh z}\right\} \simeq \frac{0.48\alpha}{\pi}. \tag{37}$$

If the radiation frequency $\omega \gg \langle\Theta_s^2\rangle\gamma^4$, then the energy density of the bremsstrahlung is determined by the expression

$$\frac{dE_\omega}{d\omega} = \alpha\Gamma\left(\frac{1}{3}\right)\left\{\frac{2\omega}{9\langle\Theta_s^2\rangle\gamma^4}\right\}^{1/3}, \tag{38}$$

where $\Gamma(z)$ is the standard gamma function [29].

It follows from Eqs. (35)–(38) that for a strongly scattering medium,

$$\langle \Theta_s^2 \rangle^{1/2} \langle l \rangle^{1/4} ET^{5/4} \gg 1,$$

the radiation spectrum is restructured compared with the situation where scattering in matter is quite weak, i.e.,

$$\langle \Theta_s^2 \rangle^{1/2} \langle l \rangle^{1/4} ET^{5/4} \ll 1.$$

This is manifested as a dependence of the radiation energy on the frequency and on the motion time of a particle in matter. Specifically, the radiation energy is found to be a strongly nonlinear function of the time T and, moreover, $dE_\omega/d\omega$ increases as $\omega^{1/3}$ in the short-wavelength region of the spectrum for strongly scattering medium and $dE_\omega/d\omega \propto T$ in the situation where scattering in the matter is weak.

7. CONCLUSIONS

In this paper a systematic method for calculating the two-particle Green's functions in a nonequilibrium medium was developed. Closed system of equations (7) and (14) were obtained for the exact vertex functions Γ and for the two-particle Green's functions K. The structure of the irreducible diagrams Λ completely determines the properties of the solutions of the systems obtained.

Bremsstrahlung of ultrarelativistic charged particles undergoing multiple elastic scattering in a static medium was investigated on the basis of the method developed for finding the two-particle Green's function in matter. The spectral distribution of the bremsstrahlung energy for such particles was found. It was shown that for sufficiently weak particle scattering in the medium, when

$$\langle \Theta_s^2 \rangle^{1/2} \langle l \rangle^{1/4} ET^{5/4} \ll 1,$$

the radiation spectrum is identical to the frequency dependence obtained in [1, 4] for the bremsstrahlung energy. For a strongly scattering medium, when

$$\langle \Theta_s^2 \rangle^{1/2} \langle l \rangle^{1/4} ET^{5/4} \gg 1,$$

the spectrum is restructured. This is manifested as a dependence of the bremsstrahlung energy on the radiation frequency and on the motion time of a particle in matter.

REFERENCES

1. A. B. Migdal, Dokl. Akad. Nauk SSSR **96**, 49 (1954).
2. L. D. Landau and I. Ya. Pomeranchuk, Dokl. Akad. Nauk SSSR **92**, 535 (1953).
3. L. D. Landau and I. Ya. Pomeranchuk, Dokl. Akad. Nauk SSSR **92**, 735 (1953).
4. A. B. Migdal, Phys. Rev. **103**, 1811 (1956).
5. I. I. Gol'dman, Zh. Éksp. Teor. Fiz. **38**, 1866 (1960) [Sov. Phys. JETP **11**, 1341 (1960)].
6. V. M. Galitskiĭ and V. V. Yakimets, Zh. Éksp. Teor. Fiz. **46**, 1066 (1964) [Sov. Phys. JETP **19**, 723 (1964)].
7. V. A. Bazylev, A. A. Varfolomeev, and N. I. Zhevago, Zh. Éksp. Teor. Fiz. **66**, 464 (1974) [Sov. Phys. JETP **39**, 222 (1974)].
8. N. V. Laskin, A. S. Mazmanishvili, N. N. Nasonov, and N. F. Shul'ga, Zh. Éksp. Teor. Fiz. **89**, 763 (1985) [Sov. Phys. JETP **62**, 438 (1985)].
9. A. I. Akhiezer and N. F. Shul'ga, Usp. Fiz. Nauk **151**, 385 (1987) [Sov. Phys. Usp. **30**, 197 (1987)].
10. A. V. Koshelkin, Zh. Éksp. Teor. Fiz. **100**, 1724 (1991) [Sov. Phys. JETP **73**, 951 (1991)].
11. A. V. Koshelkin, Zh. Éksp. Teor. Fiz. **102**, 791 (1992) [Sov. Phys. JETP **75**, 433 (1992)].
12. X.-N. Wang and M. Gyulassy, Phys. Rev. D **51**, 3436 (1995).
13. V. G. Zakharov, Pis'ma Zh. Éksp. Teor. Fiz. **63**, 906 (1996) [JETP Lett. **63**, 952 (1996)].
14. V. G. Zakharov, Pis'ma Zh. Éksp. Teor. Fiz. **64**, 737 (1996) [JETP Lett. **64**, 781 (1996)].
15. R. Baier, Yu. L. Dokshitzer, A. H. Muller, and D. Schiff, Nucl. Phys. B **478**, 577 (1996).
16. J. Schwinger, J. Math. Phys. **2**, 407 (1961).
17. L. P. Kadanoff and G. Baym, *Quantum Statistical Mechanics* (Bejamin, New York, 1962).
18. L. V. Keldysh, Zh. Éksp. Teor. Fiz. **47**, 1515 (1964) [Sov. Phys. JETP **20**, 1018 (1964)].
19. S. Fujita, *Introduction to Non-Equilibrium Statistical Mechanics* (Saunders, Philadelphia, 1966).
20. P. Danielewicz, Ann. Phys. **197**, 154 (1990).
21. J. Rammer and H. Smith, Rev. Mod. Phys. **58**, 323 (1986).
22. J. Knoll and D. N. Voskresensky, Ann. Phys. **249**, 532 (1996).
23. V. B. Berestetskii, E. M. Lifshitz, and L. P. Pitaevskii, *Quantum Electrodynamics* (Nauka, Moscow, 1980; Pergamon, Oxford, 1982).
24. E. M. Lifshitz and L. P. Pitaevskiĭ, *Physical Kinetics* (Nauka, Moscow, 1979; Pergamon, Oxford, 1981).
25. A. A. Abrikosov, L. P. Gor'kov, and I. E. Dzyaloshinskii, *Quantum Field Theoretical Methods in Statistical Physics* (Pergamon, Oxford, 1965).
26. C. Itzykson and J. B. Zuber, *Introduction to Quantum Field Theory* (McGraw-Hill, New York, 1980; Mir, Moscow, 1984).
27. A. V. Koshelkin, Pis'ma Zh. Éksp. Teor. Fiz. **63**, 911 (1996) [JETP Lett. **63**, 958 (1996)].
28. A. V. Koshelkin, Phys. Rev. D **56**, 2778 (1997).
29. I. S. Gradshteyn and I. M. Ryzhik, *Table of Integrals, Series, and Products* (Fizmatgiz, Moscow, 1963; Academic, New York, 1980).

Translation was provided by AIP

Journal of Experimental and Theoretical Physics, Vol. 91, No. 2, 2000, pp. 273–286.
Translated from Zhurnal Éksperimental'noĭ i Teoreticheskoĭ Fiziki, Vol. 118, No. 2, 2000, pp. 312–327.

ATOMS, SPECTRA, RADIATION

Effect of Quantum Interference Processes on the Angular Distribution of the Spontaneous Radiation in the *D* Line of Alkali-Metal Vapors in a Laser Wave Field

A. A. Panteleev* and Vl. K. Rerikh**

Troitsk Institute for Innovational and Thermonuclear Research,
Troitsk, Moscow oblast, 142092 Russia
**e-mail: mediana@mail.ru*
***e-mail: vroerieh@fly.triniti.ru*

Received February 24, 2000

Abstract—The resonance fluorescence of a degenerate *V*-type three-level atom in the field of an intense monochromatic wave with arbitrary polarization composition is investigated. The equations of motion, the general form of the radiation relaxation operator, and the analytical expressions for the angular distribution of the intensity of the spontaneous radiation from atoms, and the total intensity of the resonance fluorescence for such systems are obtained. The angular distribution of the spontaneous radiation from atoms for the *D* line of alkali-metal vapors is investigated. It is predicted theoretically that the intensity of the resonance fluorescence will decrease as the intensity of the pump wave increases in observations in a direction of the electric field vector of the laser wave. © *2000 MAIK "Nauka/Interperiodica"*.

1. INTRODUCTION

The study of the properties of the interaction of intense laser radiation with a resonant medium is one of the fundamental problems of modern optics. The study of interference phenomena accompanying spontaneous emission from the atom has a special place in these investigations. This interest is due to the great importance of these phenomena for many practical applications, such as the development of lasers without population inversion, generation of squeezed states, the study of laser-induced transparency, the suppression of absorption and emission, and others. Interference phenomena influencing the properties of spontaneous radiation have been known for a long time: the change in the polarization characteristics of the spontaneous emission from atoms in a magnetic field (Hanle effect), level crossing, quantum resonances, and nonstationary quantum beats [1]. These phenomena are linear. Nonlinear interference phenomena, due to parametric processes, are also widely investigated: the Stark effect, the dynamic Stark effect, two- and multiphoton scattering, generation of multiple harmonics, saturation effects, and others [2–10]. In the last few years many investigations have been performed of the influence of interference processes on the rate and structure of radiation relaxation. The effect of these processes on the decay of excited states of nondegenerate three-level systems for various parameters and conditions of excitation has been studied in [7, 11, 12]. In [13] the change in the radiation relaxation constants was taken into account in an analysis of the quasienergy states of molecules, and in [14] in a study of the properties of spontaneous Raman scattering for two close-lying states. The interference phenomena in spontaneous emission can appear only in systems containing at least three levels. At least two correlated paths are required in order for interference to arise. For three-level systems interference effects influencing the spontaneous relaxation rate can occur only for *V*-type schemes. Resonance fluorescence for a nondegenerate three-level *V*-type system was investigated in [15], where it is shown that for most real physical systems no changes in the character of the relaxation processes will occur under ordinary conditions. This is due to the fact that the interference terms vanish on integration over angles. In [15] the conditions under which interference contributions must be taken into account were indicated, and the effect of interference processes on the dynamics of level populations, the total intensity, and the resonance fluorescence spectra was investigated in detail. It should be noted that in [7, 11–14] the off-diagonal terms of the radiation relaxation operator, which correspond to the interference phenomena, were introduced formally. The properties of resonance fluorescence have been investigated theoretically and experimentally in [16], where it was shown that the spectra of these systems contain up to seven peaks. In [17] the characteristic features of quantum interference accompanying spontaneous emission from a three-level atom in a cavity and the characteristic features of the scattered radiation were investigated.

The present paper is devoted to a study of the resonance fluorescence of a degenerate *V*-type three-level atom in the field of an intense monochromatic wave with arbitrary polarization composition (see also [15, 18]).

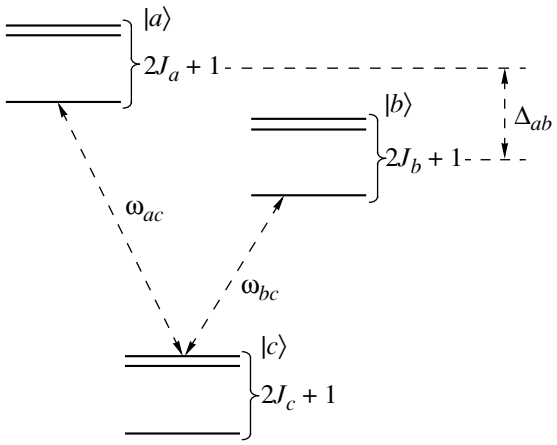

Fig. 1. Scheme of a degenerate *V*-type three-level atom.

This paper is organized as follows. In Section 2 the approximation employed is described and the basic dynamical equations for an atom are presented. A model in which the total angular momentum of the levels is assumed to be arbitrary is considered. In Section 3 analytical expressions are obtained for the angular distribution of the intensity of the spontaneous radiation from atoms. Section 4 is devoted to a detailed analysis of the angular distribution of the resonance fluorescence intensity for the *D* line of alkali-metal vapors; here it is discovered that the intensity of the spontaneous radiation from an atom decreases in a distinguished direction as the intensity of the pump wave field increases. This effect is based on interference quenching of photons emitted from various levels in a definite direction. The possibility of observing this effect experimentally is investigated in Section 5. The Appendix gives the derivation of the explicit form of the radiation relaxation operator for degenerate *V*-type three-level systems. The general form of the radiation relaxation constants for such systems is presented taking into account the off-diagonal relaxation due to interference processes.

2. BASIC EQUATIONS

Let us consider the interaction of a *V*-type three-level atom (see Fig. 1) with a monochromatic electromagnetic wave, resonant with respect to the transitions $a \longrightarrow c$ and $b \longrightarrow c$. Assuming that the electromagnetic wave has an arbitrary polarization composition, and using the rotating-wave approximation, we represent it in the form

$$\mathbf{E} = \sum_{\sigma = 0, \pm 1} \mathbf{e}^{\sigma} E_{\sigma} (e^{i\omega t} + e^{-i\omega t}),$$
$$E_{\pm 1} = \mp \frac{1}{\sqrt{2}} (E_x \pm i E_y), \quad E_0 = E_z. \tag{1}$$

Here, $\mathbf{E}$ is the electromagnetic field vector, $\mathbf{e}^{\sigma}$ is the unit σ-polarization vector, E_x, E_y, and E_z are the amplitudes of the oscillations of the field along the corresponding axes, and $E_{\pm 1}$ and E_0 are the corresponding amplitudes of the polarized radiation. Using the dipole and resonance approximations, we shall represent the Hamiltonian of the system in the form of a sum

$$\hat{H} = \hat{H}_0 + \hat{H}_f + \hat{V}_L + \hat{V}_q. \tag{2}$$

In Eq. (2), $\hat{H}_0$ describes the unperturbed atomic system and has the form

$$\hat{H}_0 = \sum_{j = a, b} \sum_{M_j} \frac{\epsilon(J_j, M_j)}{\hbar} |j, M_j\rangle\langle M_j, j|, \tag{3}$$

where $\epsilon(J_j, M)$ is the energy of the atomic state with total angular momentum J_j and projection of the angular momentum M_j on the quantization axis (z). Since in what follows we neglect the fine-structure splitting of the levels and other effects which cause the level energies to depend on the magnetic quantum number or other quantum numbers, the Hamiltonian of the free atom can be rewritten in the form

$$\hat{H}_0 = \sum_{j = a, b} \sum_{M_j} \omega_{jc} |j, M_j\rangle\langle M_j, j|, \tag{4}$$

where ω_{jc} is the frequency of the transition $j \longrightarrow c$ for any pair of sublevels.

The next term in Eq. (2) is the Hamiltonian of the quantum radiation field

$$\hat{H}_f = \sum_{\mathbf{k}\sigma} \omega_k \hat{a}^+_{\mathbf{k}\sigma} \hat{a}_{\mathbf{k}\sigma}, \tag{5}$$

where ω_k is the frequency of photons with wave vector $\mathbf{k}$ and σ-polarization, and $\hat{a}^+_{\mathbf{k}\sigma}$ and $\hat{a}_{\mathbf{k}\sigma}$ are creation and annihilation operators for the corresponding photons.

The interaction of the pump wave with the atomic system can be described by the expression

$$\hat{V}_L = \sum_{j = a, b} \sum_{M_j M_c} [V_{jc}(M_j M_c) \exp(-i\omega_L t) |j M_j\rangle\langle M_c c| + V_{cj}(M_c M_j) \exp(i\omega_L t) |c M_c\rangle\langle M_j j|], \tag{6}$$

$$V_{jc}(M_j M_c) = V^*_{cj}(M_c M_j) = \sum_{\sigma = 0, \pm 1} -\frac{d_{jc}(M_j M_c) E_{\sigma}}{2\hbar}, \tag{7}$$

where $d_{jc}(M_j M_c)$ is the dipole-moment matrix element. Using the Wigner–Eckart theorem [19], we represent the expression (7) in the form

$$V_{jc}(M_j M_c) = \sum_{\sigma = 0, \pm 1} (-1)^{j_j - M_j} C^{1-\sigma}_{J_j M_j J_c - M_c} V_{jc}(\sigma),$$
$$V_{jc}(\sigma) = -\frac{(-1)^{\sigma} \| d_{jc} \| E_{\sigma}}{2\sqrt{3}\hbar}, \tag{8}$$

where $C^{1-\sigma}_{J_j M_j J_c - M_c}$ are the Clebsch–Gordan coefficients [19] and $\|d_{jc}\|$ is the irreducible value of the dipole moment matrix element.

The interaction of atoms with a quantum radiation field is described by the expression

$$\hat{V}_q = \sum_{j=a,b}\sum_{\mathbf{k}\sigma}\sum_{M_j M_c}(g^{\mathbf{k}\sigma}_{jc}(M_j M_c)\hat{a}_{\mathbf{k}\sigma}|cM_c\rangle\langle M_j j| - g^{\mathbf{k}\sigma}_{cj}(M_c M_j)\hat{a}^{+}_{\mathbf{k}\sigma}|jM_j\rangle\langle M_c c|). \quad (9)$$

Here

$$g^{\mathbf{k}\sigma}_{jc}(M_j M_c) = d_{jc}(M_j M_c)\sqrt{\frac{2\pi\omega_k}{\hbar W}},$$

where W is the quantization volume. Using the Wigner–Eckart theorem, we obtain finally

$$g^{\mathbf{k}\sigma}_{cj}(M_c M_j) = g^{\mathbf{k}\sigma}_{jc}(M_j M_c) = (-1)^{\sigma}C^{1-\sigma}_{J_j M_j J_c - M_c}\|d_{jc}\|\sqrt{\frac{2\pi\omega_k}{\hbar W}}. \quad (10)$$

We shall use the atomic density matrix formalism to describe our system [18]. The equation for the atomic density matrix assumes the form

$$i\dot{\rho} = [\hat{H}_0 + \hat{V}_L, \rho] + i\hat{\Gamma}_a(\rho), \quad (11)$$

where $\hat{\Gamma}_a$ describes radiation relaxation processes. Three terms can be distinguished in this operator:

$$\hat{\Gamma}_a = -\hat{r}^{(1)} - \hat{r}^{(2)} + \hat{r}^{(3)}. \quad (12)$$

The first two terms correspond to radiation damping of the density matrix and transitions to lower-lying levels, and the third term corresponds to arrivals in the lower levels:

$$\hat{r}^{(1)}_{ms}(M_m M_s) = \frac{1}{2}\sum_{j=1,b}\sum_{M_j}\sum_{M_c}(L_{mj}(M_m M_j M_c)\rho_{js}(M_j M_s) + \rho_{mj}(M_m M_j)L_{js}(M_j M_s M_c)),$$

$$\hat{r}^{(2)}_{mc}(M_m M_c) = \frac{1}{2}\sum_{M'}(L_{mm}(M_m M_m M_c)\rho_{mc}(M_m M_c)), \quad (13)$$

$$\hat{r}^{(2)}_{cm}(M_c M_m) = \frac{1}{2}\sum_{M'}(L_{mm}(M_m M_m M_c)\rho_{cm}(M_c M_m)),$$

$$\hat{r}^{(3)}_{cc}(M_c M_c) = \sum_{m,s=a,b}\sum_{M_m, M_s}L_{ms}(M_m M_s M_c)\rho_{sm}(M_s M_m),$$

where

$$L_{ms}(M_m M_s M_c) = \sum_{\sigma,\sigma'}\int\langle\hat{a}^{+}_{\mathbf{k}\sigma'}\hat{a}_{\mathbf{k}\sigma}\rangle g^{\mathbf{k}c}_{mc}(M_m, M_c) \times g^{\mathbf{k}\sigma'}_{cs}(M_c, M_s)a_{ms}\frac{d\mathbf{k}}{(2\pi)^3} = \frac{2\pi\|d_{mc}\|\|d_{sc}\|}{\hbar\sqrt{(2J_m+1)(2J_s+1)}}\sum_{\sigma,\sigma'}C^{J_m M_m}_{J_c M_c 1\sigma}C^{J_s M_s}_{J_c M_c 1\sigma'} \times\int\sum_{\lambda=\pm1}U_{\mathbf{k}\sigma}U_{\mathbf{k}\sigma'}(D^{1}_{\lambda\sigma'})^{*}D^{1}_{\lambda\sigma}\omega a_{js}\frac{d\mathbf{k}}{(2\pi)^3}, \quad (14)$$

where $U_{\mathbf{k}\sigma}$ is the spatial-mode factor for photons with σ-polarization, $a_{js} = a_{js}(\omega_k)$ is the complex contour of the line, and $D^{2}_{\lambda\sigma}(\alpha, \beta, \gamma)$ is the Wigner function [20]. A detailed exposition of the method for obtaining the structure (13) and (14) of the radiation relaxation operator, taking account of the interference processes accompanying spontaneous emission, for degenerate V-type three-level systems is given in the Appendix.

The expressions (13) and (14) completely determine the radiation relaxation processes for the model under study. We note certain features of the definition of the quantities $L_{ms}(M_m M_s M_c)$ and the related properties of the operators $\hat{r}^{(1)}$, $\hat{r}^{(2)}$, and $\hat{r}^{(3)}$. The difficulty in calculating $L_{ms}(M_m M_s M_c)$ is due to the indefiniteness of the integrand, which contains Wigner functions. Generally speaking, the Wigner functions depend on three Euler angles (α, β, γ), while the direction on which the photon wave function can depend is determined only by two spherical angles: $\alpha \equiv \phi$ and $\beta \equiv \theta$. Following [21], we shall set $\gamma = 0$, i.e., $D^{1}_{\lambda\sigma} = D^{1}_{\lambda\sigma}(\phi, \theta, 0)$, since in this case the Wigner functions for the space (ϕ, θ) possess the familiar properties of orthogonality and normalization:

$$\int D^{J_1}_{\lambda_1\sigma_1}D^{J_2}_{\lambda_2\sigma_2}\frac{dO}{4\pi} = \frac{1}{2J+1}\delta_{J_1 J_2}\delta_{\sigma_1\sigma_2}. \quad (15)$$

By virtue of the orthogonality property (15) the value of $L_{ms}(M_m M_s M_c)$ is different from zero only for $M_m = M_s$. Using the summation property [19]

$$\sum_{M_1}C^{J_i M}_{J_1 M_1 1\sigma}C^{J_s M}_{J_1 M_1 1\sigma} = \delta_{J_j, J_s}, \quad (16)$$

the operator for radiative departures can be rewritten in the form

$$\hat{r}^{(1)}_{ms}(M_m M_s) = \frac{1}{2}\sum_{j=a,b}\sum_{M_j}\sum_{M_c}[L_{mj}(M_m M_j M_c)\rho_{js}(M_j M_s) + \rho_{mj}(M_m M_j)L_{js}(M_j M_s M_c)]\delta_{M_m M_s}\delta_{J_m J_s}. \quad (17)$$

It follows from Eq. (17) that the damping of the density matrix has a diagonal structure. It should be especially underscored that in deriving the structure of the relaxation operator of the form (17) we implicitly assumed that the density of states of the electromagnetic field is isotropic. The situation is different, for example, near the surface of a metal. Here the normalization and orthogonality properties (15) in the general case do not hold and the operator $\hat{r}^{(1)}_{ms}(M_mM_s)$ will not possess a diagonal structure. Moreover, the explicit form of these operators and their specific values can depend on the choice of the direction of the z-axis with respect to the surface.

The following equations describe the dynamics of our system in the rotating-wave approximation:

$$\begin{aligned}
i\dot{\rho}_{ms}(M_mM_s) &= [\Delta_{ms} - i\hat{r}^{(1)}_{ms}(M_mM_s) \\
&\quad - i\nu_{ms}(M_mM_s)]\rho_{ms}(M_mM_s) \\
&+ \sum_{M_c}[\tilde{V}_{mc}(M_mM_c)\tilde{\rho}_{cs}(M_cM_s) - \tilde{\rho}_{mc}(M_mM_c)\tilde{V}_{cs}(M_cM_s)], \\
i\dot{\tilde{\rho}}_{mc}(M_mM_c) &= [\Delta^m_L - i\hat{r}^{(2)}_{mc}(M_mM_c) \\
&\quad - i\nu_{mc}(M_mM_c)]\tilde{\rho}_{mc}(M_mM_c) \\
&\quad + \sum_{M'_c}\tilde{V}_{mc}(M_mM'_c)\tilde{\rho}_{cc}(M'_cM_c) \\
&\quad - \sum_{j=a,b}\sum_{M_i}\rho_{mj}(M_mM_j)\tilde{V}_{jc}(M_jM_c), \\
i\dot{\rho}_{cc}(M^1_cM^2_c) &= [i\hat{r}^{(3)}_{cc}(M^1_cM^2_c) \\
&\quad - i\nu_{cc}(M^1_cM^2_c)]\rho_{cc}(M^1_cM^2_c) \\
&\quad + \sum_{j=a,b}\sum_{M_c}[\tilde{V}_{cj}(M^1_cM_j)\tilde{\rho}_{jc}(M_jM^2_c) \\
&\quad - \tilde{\rho}_{mc}(M^1_cM_j)\tilde{V}_{jc}(M_jM^2_c)], \\
\rho_{mc}(M_mM_c) &= \rho^*_{mc}(M_cM_m),
\end{aligned} \tag{18}$$

where

$$\begin{aligned}
\tilde{V}_{mc}(M_mM_c) &= (\tilde{V}_{cm}(M_sM_m))^* \\
&= V_{mc}(M_mM_c)\exp(-i\omega_L t), \\
\tilde{\rho}_{mc}(M_mM_c) &= \rho_{mc}(M_mM_c)\exp(-i\omega_L t), \\
\Delta^m_L &= \omega_{mc} - \omega_L, \quad \Delta_{ms} = \Delta^m_L - \Delta^s_L,
\end{aligned}$$

$\nu_{ms}(M_mM_s)$ is the decay rate due to collisions. The constants $\nu_{ms}(M_mM_s)$ are, in the general case, complex and can lead not only to depolarization of coherence between states but also to a shift of the levels. A complete analysis of the influence of collisional relaxation falls outside the scope of the present paper, and in what follows the constants $\nu_{ms}(M_mM_s)$ will be introduced phenomenologically in the numerical simulation. Since we neglect the effect of other, external levels, Eqs. (18) must be supplemented by the normalization condition

$$\sum_{j=a,b}\sum_{M_j}\rho_{jj}(M_jM_j) = 1. \tag{19}$$

3. PROPERTIES OF THE SCATTERED RADIATION: ANGULAR AND POLARIZATION CHARACTERISTICS OF THE RESONANCE FLUORESCENCE INTENSITY

The study of the properties of resonance fluorescence is of great practical value in laser spectroscopy and its applications. One of the main characteristics of the interaction of laser radiation with an optically thin medium is resonance fluorescence. In this connection angular and polarization characteristics of the spontaneous radiation are of special interest. Following [18], the density matrix of the photon field of the spontaneous emission from atoms in the direction **k** can be defined as follows:

$$\begin{aligned}
S_{\lambda\lambda'} &= \sum_{j_1,j_2=a,b}\sum_{M_{j_1}M_{j_2}}\sum_{M_c} g^{\mathbf{k}\lambda}_{j_1c}(M_{j_1}M_c) \\
&\quad \times g^{\mathbf{k}\lambda'}_{cj_2}(M_cM_{j2})\rho^k_{j_1j_2}(M_{j_1}M_{j_2}),
\end{aligned} \tag{20}$$

where λ and $\lambda' = \pm 1$ are the elements of the atomic density matrix, obtained from Eqs. (18) and (19) for the case where the quantization axis z is directed along the direction of emission of the photon. To obtain the matrix $\rho^k_{j_1j_2}(M_{j_1}M_{j_2})$ in a unified coordinate system, the elements of the atomic density matrix $S_{\lambda\lambda'}$ must be expressed in terms of the analogous quantities determined in the unified system.

This transformation is performed in the standard manner [20]:

$$\begin{aligned}
\rho_{j_1j_2}(M_{j_1}M_{j_2}) &= \sum_{M'_{j_1}M'_{j_2}}\left(D^{J_{j_1}}_{M'_{j_1}M_{j_1}}\right)^* \\
&\quad \times D^{J_{j_2}}_{M'_{j_2}M_{j_2}}\rho^k_{j_1j_2}(M'_{j_1}M'_{j_2}),
\end{aligned} \tag{21}$$

where $D^{J_j}_{M'_jM_j}(\alpha = \phi, \beta = \theta, \gamma = 0)$ is a Wigner function, and ϕ and θ are spherical angles determining the direction of the photon. The choice $\gamma \neq 0$ will result in rotation of the polarization axes for the density matrix of the scattered radiation in a plane perpendicular to the

vector **k**. After substituting the expression (21), the matrix $S_{\lambda\lambda'}$ in the unified coordinate system becomes

$$S_{\lambda\lambda'} = \sum_{j_1, j_2 = a, b} \sum_{M_{j_1} M_{j_2}} \sum_{M_c} g^{\mathbf{k}\lambda}_{j_1 c}(M_{j_1} M_c) g^{\mathbf{k}\lambda'}_{c j_2}(M_c M_{j_2}) \times \sum_{M'_{j_1} M'_{j_2}} \left(D^{J_{j_1}}_{M'_{j_1} M_{j_1}} \right)^* D^{J_{j_2}}_{M'_{j_2} M_{j_2}} \rho^k_{j_1 J_2}(M'_{j_1} M'_{j_2}). \quad (22)$$

It can be shown that the substitution (21) in Eqs. (18) and (19) leads directly to the expression (20) for spontaneous emission in the direction of the vector **k**, which coincides with the *z*-axis in the new, rotated, coordinate system.

Taking this into account, two methods can be used to calculate the polarization matrix $S_{\lambda\lambda'}$ for spontaneous radiation in the case where there is only one distinguished direction—the polarization vector of the electromagnetic field of the pump wave. The first method consists of performing calculations directly using Eq. (22). This is the most general method, and it does not depend on the type of symmetry which the system possesses. The idea of the other method is to apply the transformation (21) to Eqs. (18) and (19). First it is necessary to perform a transformation of the polarization vector of the laser wave in a manner so that the *z*-axis coincides with the direction of observation. Then, solving Eqs. (18) and (19), it is necessary to find the matrix $S_{\lambda\lambda'}$, using Eq. (20). The advantage of this method is that explicit expressions are not required for the Wigner functions, which even for small values of the total angular momentum acquire a complicated form. The drawback of this method is that it is inapplicable in the case where the quantities appearing in Eq. (18) depend on the choice of the direction of the *z*-axis, for example, in the study of the resonance fluorescence near the surface of a metal.

The form of the expression for the intensity of spontaneous emission from atoms with a definite linear polarization, perpendicular to the axis of observation (see Fig. 2), is of interest for describing experimental results. As shown previously, rotation of the polarization axes in this plane can be performed using Eq. (22) with an appropriate choice of the angle γ. This can be done directly for the matrix $S_{\lambda\lambda'}$:

$$S'_{\lambda_1\lambda'_1} = \sum_{\lambda\lambda'} (D^1_{\lambda\lambda_1})^* D^1_{\lambda'\lambda'_1} S_{\lambda\lambda'}. \quad (23)$$

The intensity of the spontaneous radiation linearly polarized in the direction of the corresponding axes of the rotated coordinate system is determined in the form [22]

$$I^{\mathbf{k}}_\theta = S'_{11} + S'_{-1-1} - S'_{-11} - S'_{1-1},$$
$$I^{\mathbf{k}}_\phi = S'_{11} + S'_{-1-1} + S'_{-11} + S'_{1-1}. \quad (24)$$

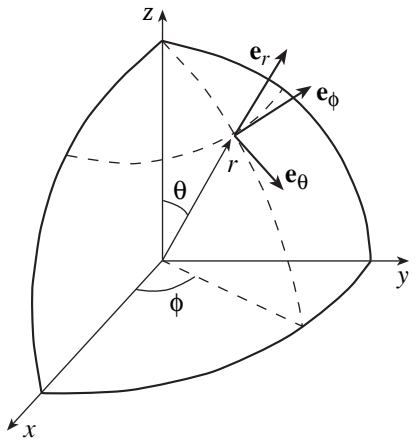

Fig. 2. Spherical coordinate system.

Using Eq. (22), the expression for the total resonance fluorescence intensity can be written in the form

$$I_{\text{total}} = \sum_{\lambda = \pm 1} \left(\int S_{\lambda\lambda} dO \right), \quad (25)$$

where *dO* is the solid angle element. If the density of states of the electromagnetic field is isotropic, then the expression for the total intensity (25) can be simplified substantially. Using the orthogonality property of Wigner functions (15), we have

$$I_{\text{total}} = \sum_{j = a, b} \sum_{M_j} \Gamma_{jj}(M_j, M_j) \rho_{jj}(M_j M_j). \quad (26)$$

The coefficients of proportionality $\Gamma_{jj}(M_j M_j)$ are radiation relaxation constants of the corresponding magnetic sublevels. It is evident that the expression (26) is similar to the formulas for the total intensity, which we obtained in [15, 18]. Thus, the expression (17) for the radiation relaxation operator, just as the expression (26) for the total intensity, does not contain off-diagonal elements of the density matrix. In other words, in contrast to the degenerate three-level atom model, studied in [15] and in [7, 11, 12], quantum interference effects for a degenerate *V*-type three-level atom do not influence the dynamics of the atom for most real physical systems. This result was noted in [15]. However, the interference effects must be taken into account when studying the angular distribution of the spontaneous radiation. The expression (22) contains off-diagonal elements of the density matrix with nonzero coefficients. In the next section we shall examine in greater detail the influence of quantum-interference effects on the properties of the angular distribution of the resonance fluorescence of the *D*-line doublet of alkali-metal vapors.

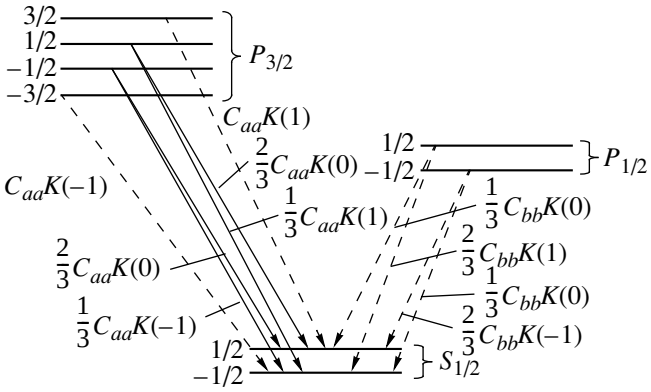

Fig. 3. Scheme of spontaneous transitions for the *D* line of alkali-metal vapors.

4. ANGULAR DISTRIBUTION OF RESONANCE FLUORESCENCE OF THE *D* LINE OF ALKALI-METAL VAPORS

Using the formalism developed in preceding sections of this paper, we shall examine the resonance fluorescence of the *D* line of alkali-metal vapors. We introduce the following correspondence for the levels: $a \longrightarrow P_{3/2}$, $b \longrightarrow P_{1/2}$, and $c \longrightarrow S_{1/2}$ and $J_a = 3/2$, $J_b = 1/2$, and $J_c = 1/2$. The level scheme is shown in Fig. 3. The radiation relaxation constants for the magnetic sublevels, calculating using Eq. (17) have the form

$$\begin{aligned}
\Gamma_{aa}\left(\frac{3}{2}, \frac{3}{2}\right) &= C_{aa}K(1),\\
\Gamma_{aa}\left(-\frac{3}{2}, -\frac{3}{2}\right) &= C_{aa}K(-1),\\
\Gamma_{aa}\left(\frac{1}{2}, \frac{1}{2}\right) &= C_{aa}\frac{K(1) + 2K(0)}{3},\\
\Gamma_{aa}\left(-\frac{1}{2}, -\frac{1}{2}\right) &= C_{aa}\frac{K(-1) + 2K(0)}{3},\\
\Gamma_{bb}\left(\frac{1}{2}, \frac{1}{2}\right) &= C_{aa}\frac{2K(1) + K(0)}{3},\\
\Gamma_{bb}\left(-\frac{1}{2}, -\frac{1}{2}\right) &= C_{aa}\frac{2K(-1) + K(0)}{3},
\end{aligned} \tag{27}$$

where

$$C_{j_1j_2} = \frac{2\pi\|d_{j_1c}\|\|d_{j_2c}\|\omega_{jc}^3}{\hbar\sqrt{(2J_{j_1}+1)(2J_{j_2}+1)}c^3}, \quad j_1, j_2 = a, b,$$

$$K(\sigma) = \int \sum_{\lambda = \pm 1} D^1_{\lambda\sigma}(D^1_{\lambda\sigma})^* dO = \frac{2}{3}, \quad \sigma = 0, \pm 1.$$

We note that

$$\frac{\|d_{ac}\|}{\sqrt{2J_a + 1}} = \frac{\|d_{bc}\|}{\sqrt{2J_b + 1}}, \tag{28}$$

and then we arrive at the well-known result: all radiation relaxation constants for the magnetic sublevels are equal to one another to within Δ_{ab}/ω_{jc}. Figures 4a and 4c show the dependences of the nonzero density matrix elements, appearing in the expression (22), of the form $\rho_{j_1j_2}(M_{j_1}M_{j_2})$, $j_1, j_2 = a, b$, on the pump wave intensity. As follows from the calculations, the density matrix elements are different from zero only for $M_{j_1} = M_{j_2}$. Taking this fact into account, we obtain directly from the expression (22) that $S_{\lambda\lambda'}$ will be different from zero only for $\lambda = \lambda'$, and this indicates that the spontaneous emission will be absolutely unpolarized. The following circumstance should be underscored: the quantities $S_{\lambda\lambda'}$ are integrals over a spectrum, and their behavior is different from that of the corresponding correlators $\langle a^+_{\mathbf{k}\lambda'}a_{\mathbf{k}\lambda}\rangle$, whose contribution becomes substantial in the calculation of the spectra and will influence the polarization characteristics of individual sections of the spectrum. This result was obtained in [18] in the two-level approximation for the transition $(J_a = 1) \longrightarrow (J_c = 0)$ in the neon atom.

We shall present the explicit expressions for S_{11} and S_{-1-1} for observation of spontaneous emission in the direction of the *z*-axis:

$$\begin{aligned}
S_{11} &= C_{aa}\rho_{aa}\left(\frac{3}{2}, \frac{3}{2}\right) + \frac{C_{aa}}{3}\rho_{aa}\left(\frac{1}{2}, \frac{1}{2}\right) + \frac{2C_{bb}}{3}\rho_{aa}\left(\frac{1}{2}, \frac{1}{2}\right)\\
&\quad - \frac{C_{ab}\sqrt{2}}{3}\left[\rho_{ab}\left(\frac{1}{2}, \frac{1}{2}\right) + \rho_{ba}\left(\frac{1}{2}, \frac{1}{2}\right)\right],\\
S_{-1-1} &= C_{aa}\rho_{aa}\left(-\frac{3}{2}, -\frac{3}{2}\right) + \frac{C_{aa}}{3}\rho_{aa}\left(-\frac{1}{2}, -\frac{1}{2}\right)\\
&\quad + \frac{2C_{bb}}{3}\rho_{aa}\left(-\frac{1}{2}, -\frac{1}{2}\right) + \frac{C_{ab}\sqrt{2}}{3}\\
&\quad \times\left[\rho_{ab}\left(-\frac{1}{2}, -\frac{1}{2}\right) + \rho_{ba}\left(-\frac{1}{2}, -\frac{1}{2}\right)\right].
\end{aligned} \tag{29}$$

As shown in the preceding section, using Eq. (29) and changing the direction of the intensity vector of the electromagnetic field of the laser wave, we can obtain the total angular distribution of the spontaneous radiation. We shall use this fact, since the expressions (29) are more convenient for analysis than the generalized formulas of the form (22). In what follows, unless otherwise stated, we shall analyze the intensity of the resonance fluorescence for observations in the direction of the *z*-axis for various configurations of the laser field. We shall consider two distinguished cases:

(1) The pump wave has the form $E_{\pm 1} = 0$, $E_0 = E_A$ ($E_x = E_y = 0$, $E_z = E_A$). Figure 4a shows the dependences of the density matrix elements appearing in Eqs. (29) on the field intensity E_A. As expected, sublevels with projections ±3/2 are not excited, and only the sublevels with $M_j = \pm 1/2$, $j = a, b$, contribute to the spontaneous emission from the atoms. The numerical calculations show that the quantity $\mathrm{Im}(\rho_{ab}(\pm 1/2, \pm 1/2))$ is always small, and moreover, in the case considered in a strong field ($E_A \gg \Delta_{ab}$)

$$\mathrm{Re}(\rho_{ab}(1/2, 1/2)) \approx \sqrt{\rho_{aa}(1/2, 1/2)\rho_{bb}(1/2, 1/2)},$$
$$\mathrm{Re}(\rho_{ab}(-1/2, -1/2)) \approx -\sqrt{\rho_{aa}(-1/2, -1/2)\rho_{bb}(-1/2, -1/2)}. \quad (30)$$

Taking this into consideration, the formulas (29) can be written in the form

$$S_{11} \approx \frac{C}{3}\left(\left|\psi_a\left(\frac{1}{2}\right)\right| - \sqrt{2}\left|\psi_b\left(\frac{1}{2}\right)\right|\right)^2,$$
$$S_{-1\,-1} \approx \frac{C}{3}\left(\left|\psi_a\left(-\frac{1}{2}\right)\right| - \sqrt{2}\left|\psi_b\left(-\frac{1}{2}\right)\right|\right)^2, \quad (31)$$

where $\psi_{j_1}(M_{j_1})\psi^*_{j_2}(M_{j_2}) = \rho_{j_1 j_2}(M_{j_1} M_{j_2})$ are the amplitudes of the wave functions of the corresponding sublevels, $C = C_{aa} = C_{bb} = C_{ab}$. The expressions (31) show that interference attenuation of spontaneous emission can be expected in a strong laser field. Figure 4b shows the total dependence of the intensity of resonance fluorescence on the intensity of the pump wave field. The dependence obtained confirms the arguments presented above; moreover, it follows from this dependence that as the field intensity increases, the intensity of the spontaneous emission tends to zero.

(2) The opposite result—an increase of the spontaneous emission intensity of atoms—can be obtained if the intensity vector of the pump wave is directed in the *xy* plane, for example, $E_x = E_A$, $E_y = 0$, and $E_z = 0$ (any other direction will lead to the same results). Figure 4c shows the dependences of the populations of the magnetic sublevels and $\mathrm{Re}(\rho_{ab}(\pm 1/2, \pm 1/2))$ on the intensity of the laser wave E_A. In contrast to the preceding case, levels with projections of the magnetic moments ±3/2 are excited and contribute to the spontaneous emission. In a strong field a relation similar to Eq. (30) is also satisfied:

$$\mathrm{Re}(\rho_{ab}(1/2, 1/2)) \approx -\sqrt{\rho_{aa}(1/2, 1/2)\rho_{bb}(1/2, 1/2)},$$
$$\mathrm{Re}(\rho_{ab}(-1/2, -1/2)) \approx \sqrt{\rho_{aa}(-1/2, -1/2)\rho_{bb}(-1/2, -1/2)}, \quad (32)$$

which leads to the formulas for the spontaneous emission:

$$S_{11} \approx C\rho_{aa}\left(\frac{3}{2}, \frac{3}{2}\right) + \frac{C}{3}\left(\left|\psi_a\left(\frac{1}{2}\right)\right| + \sqrt{2}\left|\psi_b\left(\frac{1}{2}\right)\right|\right)^2,$$
$$S_{-1\,-1} \approx C\rho_{aa}\left(-\frac{3}{2}, -\frac{3}{2}\right) + \frac{C}{3}\left(\left|\psi_a\left(-\frac{1}{2}\right)\right| + \sqrt{2}\left|\psi_b\left(-\frac{1}{2}\right)\right|\right)^2. \quad (33)$$

The expressions (33) show that for this consideration of the field interference amplification of resonance fluorescence will be observed (see Fig. 4d).

It will be shown below that the configuration of the field analyzed last can be interpreted as spontaneous emission in the *xy* plane for the field configuration $E_x = 0$, $E_y = 0$, and $E_z = E_A$. This makes it possible to draw the qualitative conclusion that when observing in the direction of the pump wave intensity vector the resonance fluorescence intensity in a strong field will be low and will increase as the angle between the direction of observation and the field intensity vector increases. Figure 5 shows such a dependence for laser field intensity $E_A = 10\Delta_{ab}$.

The conclusion that the resonance fluorescence becomes weaker in a strong field for observation in a direction of the intensity vector of the electromagnetic field is of interest for experimental verification. It should be underscored that this effect is a three-level effect and is possible only for *V*-type systems. It is due to interference quenching of photons from magnetic sublevels with different values of the total angular momentum. It does not occur in two-level systems because $\rho_{jj}(M_1 M_2) = 0$ for $M_1 \neq M_2$. In Λ-type three-level systems the effect is impossible because when a system decays it arrives in different final states. In the next section we shall analyze the possibility of observing the effect experimentally.

5. POSSIBILITY OF EXPERIMENTAL OBSERVATION

In the preceding sections we investigated an idealized system and neglected a variety of physical processes which could influence the dynamics of an atom in a laser field. Examples of such phenomena are collisional relaxation, collisional mixing with respect to the magnetic sublevels, and two-photon processes. In addition, geometric factors will influence the observed spontaneous emission intensity of atoms: the intensity distribution of the field in the cross section of the beam, the magnitude of the solid angle in which the observation is performed. Figure 6 shows plots of the resonance fluorescence intensity for $\gamma_{st} = \Gamma$, $\gamma_{st} = 0.1\Gamma$, where γ_{st} is the collisional relaxation, introduced phenomenologically, and Γ is the radiation relaxation con-

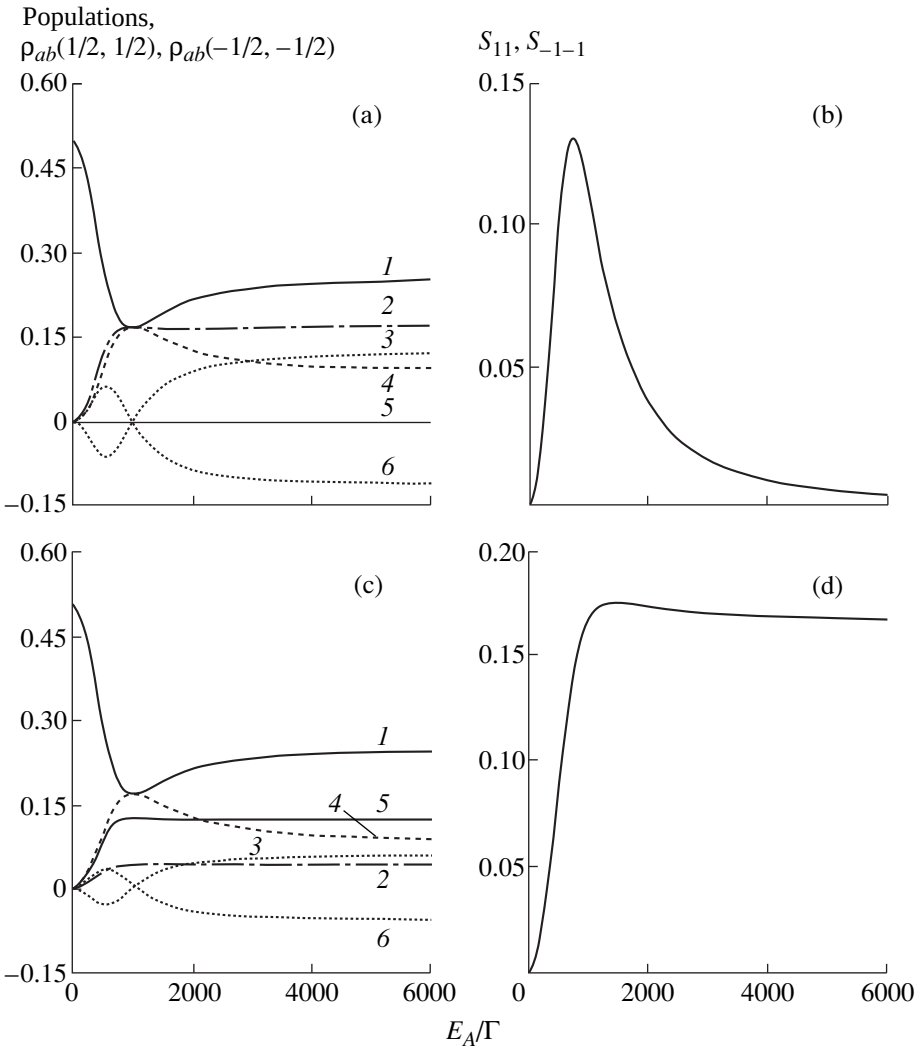

Fig. 4. The following quantities as functions of the intensity of the pump wave field: (a) and (c), populations and off-diagonal density matrix elements $\mathrm{Re}(\rho_{ab}(1/2, 1/2))$, $\mathrm{Re}(\rho_{ab}(-1/2, -1/2))$; (b) and (d), resonance fluorescence intensity for both polarizations for observation along the *z*-axis. The calculation is performed for detunings $\Delta_L^a = 250\Gamma$ and $\Delta_L^b = -250\Gamma$ and laser field configuration $E_x = 0$, $E_y = 0$, $E_z = E_A$ (a, b) and $E_y = 0$, $E_z = 0$, $E_x = E_A$ (c, d). Designations of the curves: *1*—$\rho_{cc}(1/2, 1/2)$, $\rho_{cc}(-1/2, -1/2)$; *2*—$\rho_{aa}(1/2, 1/2)$, $\rho_{aa}(-1/2, -1/2)$; *3*—$\rho_{ab}(1/2, 1/2)$; *4*—$\rho_{bb}(1/2, 1/2)$, $\rho_{bb}(-1/2, -1/2)$; *5*—$\rho_{aa}(3/2, 3/2)$, $\rho_{aa}(-3/2, -3/2)$; *6*—$\rho_{ab}(-1/2, -1/2)$.

stant (it was shown in the preceding section that the magnetic sublevels all have the same lifetime). It is evident in the figure that for $\gamma_{st} \geq \Gamma$ the spontaneous emission intensity of atoms increases. This is due to breakdown of the coherence between the levels *a* and *b* and, in consequence, results in a decrease of the interference quenching.

The effect of the geometric factors appears in the fact that we observed fluorescence from the entire section of the beam and from a quite extended section. Figure 5 reflects the characteristic angular distribution of the spontaneous emission, whence it can be concluded that if the observation angle is less than 0.1 rad and the laser beam is sufficiently thin, then the angular distribution can be neglected. This simplification makes it possible to express the observed intensity as

$$I_{\mathrm{exp}} \sim \int_0^{R_a} 2\pi r \sum_{\lambda = \pm 1} S_{\lambda\lambda}\left(E_L\left(\frac{r^2}{r_0^2}\right)\right) dr, \qquad (34)$$

where r is the distance to the beam center, r_0 is the characteristic beam size, E_L is the field intensity at a given location of the cross section, and R_a is the aperture of the laser beam. Assuming that the beam has a Gaussian profile, $E_L = E_a \exp(-r^2/r_0^2)$, the expression (34) simplifies:

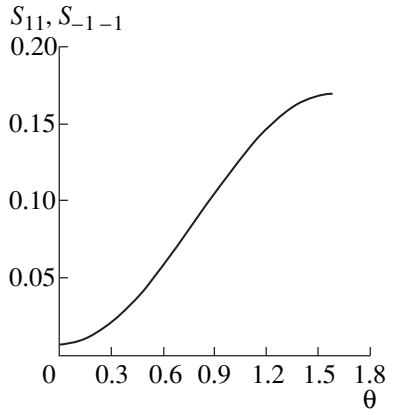

Fig. 5. Spontaneous emission intensity of atoms for both polarizations versus the angle between the direction of observation and the electric field intensity vector of the laser wave for the laser field $E_A = 10\Delta_{ab} = 5000\Gamma$. The values of all other parameters are the same as for the Fig. 4b.

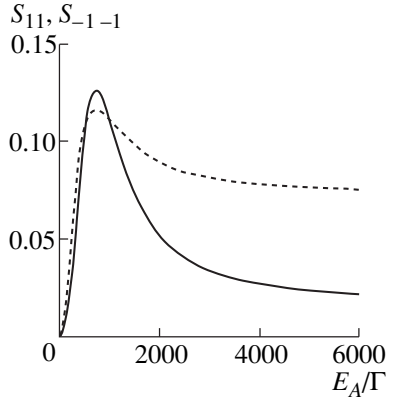

Fig. 6. Spontaneous emission intensity of atoms for observation along the *z*-axis for both polarizations as a function of the intensity of the pump wave field for collisional relaxation constants $\gamma_{st} = 0.1\Gamma$ (solid line) and $\gamma_{st} = \Gamma$ (dashed line). The values of all other parameters are the same as for Fig. 4b.

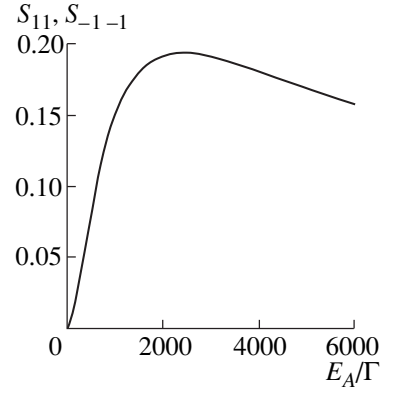

Fig. 7. Effect of the distribution (Gaussian profile) of the laser field intensity in the beam cross section on the experimentally measured spontaneous emission intensity of atoms for observation along the *z*-axis. The aperture radius $R_a = 2r_0$, and $\gamma_{st} = 0.5\Gamma$. The values of all other parameters are the same as for Fig. 4b.

$$I_{\exp} \sim \pi r_0^2 \int_{E_a \exp(-R_a^2/r_0^2)}^{E_a} \sum_{\lambda=\pm 1} \frac{S_{\lambda\lambda}(E_L)}{E_L} dE_L. \qquad (35)$$

It is evident from Eq. (35) that the "wings" of the beam, where the intensity is much lower than at beam center, will make the main contribution to the observed intensity. Figure 7 shows the resonance fluorescence intensity obtained taking account of the collisional relaxation and using Eq. (35). As one can see from the plot, even for quite stringent parameters $R_a = 2r_0$ and $\gamma_{st} = 0.5\Gamma$, substantial decrease of the spontaneous emission can be expected only for $E_a \approx 10\Delta_{ab}$. This means that if the experiment is performed using sodium, then the required power density for laser radiation will be $P \approx 1$ GW/cm^2. This condition is difficult to satisfy for 10 ns and longer duration pulses. In this connection it is of interest to perform investigations with lithium, for which $40\Delta_{ab}^{\mathrm{Li}} = \Delta_{ab}^{\mathrm{Na}}$, and a 1600 times lower power density is required to satisfy the condition $E_a \approx 10\Delta_{ab}$.

6. CONCLUSIONS

In this work the resonance fluorescence of a degenerate *V*-type three-level atom in the field of an intense monochromatic wave with arbitrary polarization composition was investigated. The general form of the radiation relaxation operator for the systems considered was obtained. The influence of interference effects accompanying spontaneous emission on the radiation relaxation structure was analyzed. It was shown that for most real physical systems the interference processes do not change the population dynamics of the atomic sublevels; the conditions under which the influence of interference effects on the structure of relaxation processes and the population dynamics must be taken into account were indicated. Analytical expressions were obtained for the resonance fluorescence intensity in a chosen direction, the polarization composition of the radiation, and the total intensity of the spontaneous emission of the atoms. It was shown that even though no changes occur in the equations of motion for the atomic density matrix because of interference effects, they must be taken into account when analyzing the angular distribution of the resonance fluorescence intensity. The angular distribution of the spontaneous emission from atoms was investigated in detail for the *D* line of alkali-metal vapors. It was predicted theoretically that the spontaneous emission intensity of atoms will decrease as the pump wave intensity increases, when observations are made in the direction of the electric field intensity vector of the laser wave. It should be underscored that this effect is due to interference quenching of photons from the upper levels in the direction indicated. The difficulties of observing this effect experimentally and the various factors which change substantially the physically measured intensity of resonance fluorescence were analyzed. The most important factor is the influence of

the intensity distribution in the cross section of the laser beam exciting the medium.

ACKNOWLEDGMENTS

We thank A.N. Starostin, A.G. Leonov, D.I. Chekhov, and A.A. Rudenko for a discussion of this work and for remarks. This work was supported by the Russian Foundation for Basic Research (projects nos. 99-02-17063, 00-15-96539).

APPENDIX

Radiation Relaxation Operator for a Degenerate V-type Three-Level Atom

We shall present one possible method for obtaining the explicit form of the radiation relaxation operator for a degenerate *V*-type three-level atom. The general form of atomic systems of this class with arbitrary values of the total angular momentum of the levels is studied. To simplify the exposition, we shall consider the decay of an excited state of the atom. A method for obtaining the radiation relaxation constants for a two-level atom in the field of a monochromatic wave is presented in [22]. The application of this method, described in [22], together with the technique described below makes it possible to obtain the radiation relaxation operator for our atomic system in the presence of a laser field.

Here we shall employ the notations for the indices and characteristics of magnetic sublevels similar to the notations adopted in preceding sections of this paper: j, j_1, and j_2 are the indices for the levels (see Fig. 1) assuming the values a, b, and c; J_j is the total angular momentum of level j; M_j is the projection of the angular momentum of the j level on the z-axis, taking on the values $J_j, J_j - 1, \ldots, -J_j$; $\mathbf{k}$ and $\mathbf{k}'$ are the wave vector of the emitted photon, $\sigma, \sigma' = 0, \pm 1$ is the polarization of the emitted photon in the chosen coordinate system. Just as in the preceding sections, if the range of values of the indices is not specially stipulated for the formulas presented, it is assumed that the expression is correct for any admissible values.

To describe our system we shall employ the Scully–Lamb atomic-photon density matrix formalism [23]. We introduce the following set of atomic-photon states:

$$|J_a M_a\rangle, |J_b M_b\rangle, |J_c M_c\rangle, |J_c M_c \mathbf{k}\sigma\rangle.$$

The corresponding atomic-photon density matrix elements have the form

$$\rho_{j_1 j_2}(M_{j_1}, M_{j_2}), \quad \rho^{\mathbf{k}}_{j_1 c}(M_{j_1}, M_c \mathbf{k}\sigma),$$

$$\rho^{\mathbf{k}}_{c j_1}(M_c \mathbf{k}\sigma, M_{j_1}), \quad \rho^{\mathbf{k}\mathbf{k}'}_{cc}(M_c \mathbf{k}\sigma, M'_c \mathbf{k}'\sigma').$$

For computational convenience, we shall employ the matrix notation

$$\rho_{j_1 j_2} = \begin{pmatrix} \rho_{j_1 j_2}(J_{j_1}, J_{j_2}) & \rho_{j_1 j_2}(J_{j_1}, J_{j_2} - 1) & \ldots & \rho_{j_1 j_2}(J_{j_1}, -J_{j_2}) \\ \ldots & \ldots & \ldots & \ldots \\ \rho_{j_1 j_2}(-J_{j_1}, J_{j_2}) & \rho_{j_1 j_2}(-J_{j_1}, J_{j_2} - 1) & \ldots & \rho_{j_1 j_2}(-J_{j_1}, -J_{j_2}) \end{pmatrix}, \tag{A.1}$$

$$\rho^{\mathbf{k}}_{c j_2} = \begin{pmatrix} \rho_{c j_2}(J_c \mathbf{k}\ 1, J_{j_2}) & \rho_{j_1 j_2}(J_c \mathbf{k}\ 1, J_{j_2} - 1) & \ldots & \rho_{j_1 j_2}(J_c \mathbf{k}\ 1, -J_{j_2}) \\ \rho_{c j_2}(J_c \mathbf{k}\ 0, J_{j_2}) & \rho_{j_1 j_2}(J_c \mathbf{k}\ 0, J_{j_2} - 1) & \ldots & \rho_{j_1 j_2}(J_c \mathbf{k}\ 0, -J_{j_2}) \\ \rho_{c j_2}(J_c \mathbf{k} - 1, J_{j_2}) & \rho_{j_1 j_2}(J_c \mathbf{k} - 1, J_{j_2} - 1) & \ldots & \rho_{j_1 j_2}(J_c \mathbf{k} - 1, -J_{j_2}) \\ \ldots & \ldots & \ldots & \ldots \\ \rho_{c j_2}(-J_c \mathbf{k}\ 1, J_{j_2}) & \rho_{j_1 j_2}(-J_c \mathbf{k}\ 1, J_{j_2} - 1) & \ldots & \rho_{j_1 j_2}(-J_c \mathbf{k}\ 1, -J_{j_2}) \\ \rho_{c j_2}(-J_c \mathbf{k}\ 0, J_{j_2}) & \rho_{j_1 j_2}(-J_c \mathbf{k}\ 0, J_{j_2} - 1) & \ldots & \rho_{j_1 j_2}(-J_c \mathbf{k}\ 0, -J_{j_2}) \\ \rho_{c j_2}(-J_c \mathbf{k} - 1, J_{j_2}) & \rho_{j_1 j_2}(-J_c \mathbf{k} - 1, J_{j_2} - 1) & \ldots & \rho_{j_1 j_2}(-J_c \mathbf{k} - 1, -J_{j_2}) \end{pmatrix}, \tag{A.2}$$

$$\rho^{\mathbf{k}}_{j_2 c} = \rho^{\mathbf{k}*}_{c j_2}, \tag{A.3}$$

$$\rho^{\mathbf{k}\mathbf{k}'}_{cc} = \begin{pmatrix} \tilde{\rho}^{\mathbf{k}\mathbf{k}'}_{cc}(J_c, J_c) & \tilde{\rho}^{\mathbf{k}\mathbf{k}'}_{cc}(J_c, J_c - 1) & \ldots & \tilde{\rho}^{\mathbf{k}\mathbf{k}'}_{cc}(J_c, -J_c) \\ \ldots & \ldots & & \\ \tilde{\rho}^{\mathbf{k}\mathbf{k}'}_{cc}(-J_c, J_c) & \tilde{\rho}^{\mathbf{k}\mathbf{k}'}_{cc}(-J_c, J_c - 1) & \ldots & \tilde{\rho}^{\mathbf{k}\mathbf{k}'}_{cc}(-J_c, -J_c) \end{pmatrix}, \tag{A.4}$$

where

$$\tilde{\rho}_{cc}^{\mathbf{k}\mathbf{k}'}(M_{c_1}, M_{c_2}) = \begin{pmatrix} \rho_{cj_2}(M_{c_1}\mathbf{k}\ 1, M_{c_2}\mathbf{k}'\ 1) & \rho_{cj_2}(M_{c_1}\mathbf{k}\ 1, M_{c_2}\mathbf{k}'\ 0) & \rho_{cj_2}(M_{c_1}\mathbf{k}\ 1, M_{c_2}\mathbf{k}'-1) \\ \rho_{cj_2}(M_{c_1}\mathbf{k}\ 0, M_{c_2}\mathbf{k}'\ 1) & \rho_{cj_2}(M_{c_1}\mathbf{k}\ 0, M_{c_2}\mathbf{k}'\ 0) & \rho_{cj_2}(M_{c_1}\mathbf{k}\ 0, M_{c_2}\mathbf{k}'-1) \\ \rho_{cj_2}(M_{c_1}\mathbf{k}-1, M_{c_2}\mathbf{k}'\ 1) & \rho_{cj_2}(M_{c_1}\mathbf{k}-1, M_{c_2}\mathbf{k}'\ 0) & \rho_{cj_2}(M_{c_1}\mathbf{k}-1, M_{c_2}\mathbf{k}'-1) \end{pmatrix}.$$

Using the notations (A.1)–(A.4), the atomic-photon density matrix assumes the form

$$\rho_{a-ph} = \begin{pmatrix} \rho_{aa} & \rho_{ab} & \rho_{ac} & \rho_{ac}^{\mathbf{k}} & \rho_{ac}^{\mathbf{k}'} & \cdots \\ \rho_{ba} & \rho_{bb} & \rho_{bc} & \rho_{bc}^{\mathbf{k}} & \rho_{bc}^{\mathbf{k}'} & \cdots \\ \rho_{ca} & \rho_{cb} & \rho_{cc} & \rho_{cc}^{\mathbf{k}} & \rho_{cc}^{\mathbf{k}'} & \cdots \\ \rho_{ca}^{\mathbf{k}} & \rho_{cb}^{\mathbf{k}} & \rho_{cc}^{\mathbf{k}} & \rho_{cc}^{\mathbf{k}\mathbf{k}} & \rho_{cc}^{\mathbf{k}\mathbf{k}'} & \cdots \\ \rho_{ca}^{\mathbf{k}'} & \rho_{cb}^{\mathbf{k}'} & \rho_{cc}^{\mathbf{k}'} & \rho_{cc}^{\mathbf{k}'\mathbf{k}} & \rho_{cc}^{\mathbf{k}'\mathbf{k}'} & \cdots \\ \cdots & \cdots & \cdots & \cdots & \cdots & \cdots \end{pmatrix}. \quad \text{(A.5)}$$

Using the dipole approximation, we represent the Hamiltonian of our system as a sum

$$\hat{H}_r = \hat{H}_0 + \hat{H}_f + \hat{V}_q, \quad \text{(A.6)}$$

where the operators $\hat{H}_0$, $\hat{H}_f$, and $\hat{V}_q$ are presented in Section 2. In the notations associated with Eqs. (A.1)–(A.4) the Hamiltonian H_r can be written as the following matrix:

$$\hat{H}_r = \begin{pmatrix} i\frac{\Delta_{ab}}{2}I & 0 & 0 & -G_a^{\mathbf{k}*} & -G_a^{\mathbf{k}'*} & \cdots \\ 0 & -i\frac{\Delta_{ab}}{2}I & 0 & -G_b^{\mathbf{k}*} & -G_b^{\mathbf{k}'*} & \cdots \\ 0 & 0 & -i\omega_u I & 0 & 0 & \cdots \\ G_a^{\mathbf{k}} & G_b^{\mathbf{k}} & 0 & i\nu_{\mathbf{k}}I & 0 & \cdots \\ G_a^{\mathbf{k}'} & G_b^{\mathbf{k}'} & 0 & 0 & i\nu_{\mathbf{k}'}I & \cdots \\ \cdots & \cdots & \cdots & \cdots & \cdots & \cdots \end{pmatrix}, \quad \text{(A.7)}$$

$$\nu_{\mathbf{k}} = \omega_{\mathbf{k}} - \omega_u, \quad \omega_u = -\frac{\omega_{ac} + \omega_{bc}}{2},$$

where I is a unit matrix with the required dimension; the matrices $G_j^{\mathbf{k}}$ describe the interaction of the transition $j \longleftrightarrow c$ with the $\mathbf{k}$ mode:

$$G_j^{\mathbf{k}} = \begin{pmatrix} \hat{a}_{\mathbf{k}1}g_{cj}^{\mathbf{k}1}(J_c, J_j) & \cdots & \hat{a}_{\mathbf{k}1}g_{cj}^{\mathbf{k}1}(J_c, -J_j) \\ \hat{a}_{\mathbf{k}0}g_{cj}^{\mathbf{k}0}(J_c, J_j) & \cdots & \hat{a}_{\mathbf{k}0}g_{cj}^{\mathbf{k}0}(J_c, -J_j) \\ \hat{a}_{\mathbf{k}-1}g_{cj}^{\mathbf{k}-1}(J_c, J_j) & \cdots & \hat{a}_{\mathbf{k}-1}g_{cj}^{\mathbf{k}-1}(J_c, -J_j) \\ \cdots & \cdots & \cdots \\ \hat{a}_{\mathbf{k}1}g_{cj}^{\mathbf{k}1}(-J_c, J_j) & \cdots & \hat{a}_{\mathbf{k}1}g_{cj}^{\mathbf{k}1}(-J_c, -J_j) \\ \hat{a}_{\mathbf{k}0}g_{cj}^{\mathbf{k}0}(-J_c, J_j) & \cdots & \hat{a}_{\mathbf{k}0}g_{cj}^{\mathbf{k}0}(-J_c, -J_j) \\ \hat{a}_{\mathbf{k}-1}g_{cj}^{\mathbf{k}-1}(-J_c, J_j) & \cdots & \hat{a}_{\mathbf{k}-1}g_{cj}^{\mathbf{k}-1}(-J_c, -J_j) \end{pmatrix}. \quad \text{(A.8)}$$

It should be underscored that because of the properties of the Clebsch–Gordan coefficient [19] and the explicit form of the coupling constants $g_{cj}^{\mathbf{k}\sigma}(M_c, M_j)$ (10) most matrix elements $G_j^{\mathbf{k}}$ are zero. The equation of motion for the atom–photon density matrix has the form

$$\frac{dH_r}{dt} = [H_r, \rho_{a-ph}]. \quad \text{(A.9)}$$

Using the substitution of variables $\rho_{a-ph} = C(t)YC^{-1}(t)$, where

$$C(t) = \begin{pmatrix} \exp\left(i\frac{\Delta_{ab}}{2}\right)I & 0 & 0 & 0 & \cdots \\ 0 & \exp\left(-i\frac{\Delta_{ab}}{2}\right)I & 0 & 0 & \cdots \\ 0 & 0 & \exp(-i\omega_u)I & 0 & \cdots \\ 0 & 0 & 0 & \exp(i\nu_k)I & \cdots \\ \cdots & \cdots & \cdots & \cdots & \cdots \end{pmatrix}, \quad \text{(A.10)}$$

we obtain from Eq. (A.6) the equation for the Y matrix

$$\frac{dY}{dt} = [H', Y]. \tag{A.11}$$

The operation

$$H' = C^{-1}\left(H - \frac{dC}{dt}C^{-1}\right)C$$

can be expressed explicitly as

$$H' = \begin{pmatrix} 0 & 0 & 0 & -\exp(i\mathcal{H}t)G_a^{\mathbf{k}*} & -\exp(i\mathcal{H}t)G_a^{\mathbf{k}'*} & \dots \\ 0 & 0 & 0 & -\exp(i\mathcal{H}'t)G_b^{\mathbf{k}*} & -\exp(i\mathcal{H}'t)G_b^{\mathbf{k}'*} & \dots \\ 0 & 0 & 0 & 0 & 0 & \dots \\ \exp(-i\mathcal{H}t)G_a^{\mathbf{k}} & \exp(-i\mathcal{H}'t)G_b^{\mathbf{k}} & 0 & 0 & 0 & \dots \\ \exp(-i\mathcal{H}t)G_a^{\mathbf{k}'} & \exp(-i\mathcal{H}'t)G_b^{\mathbf{k}'} & 0 & 0 & 0 & \dots \\ \dots & \dots & \dots & \dots & \dots & \dots \end{pmatrix}, \tag{A.12}$$

where $\mathcal{H} = \nu_k - \Delta_{ab}/2$ and $\mathcal{H}' = \nu_k + \Delta_{ab}/2$. The equation (A.11), taking account of the explicit form of the operator H', leads to the following equations for the matrix elements Y:

$$\frac{dY_{j_1j_2}}{dt} = -\sum_{\mathbf{k}}(\tilde{G}_{j_1}^{\mathbf{k}*}Y_{cj_2}^{\mathbf{k}} + Y_{j_1c}^{\mathbf{k}}\tilde{G}_{j_2}^{\mathbf{k}}), \tag{A.13}$$

$$\frac{dY_{cc}^{\mathbf{kk}}}{dt} = \sum_{j_1}(\tilde{G}_{j_1}^{\mathbf{k}}Y_{j_1c}^{\mathbf{k}} + Y_{cj_1}^{\mathbf{k}}\tilde{G}_{j_1}^{\mathbf{k}*}), \tag{A.14}$$

$$\frac{dY_{cj_1}^{\mathbf{k}}}{dt} = \sum_{j_2}(\tilde{G}_{j_2}^{\mathbf{k}}Y_{j_2j_1}) + Y_{cc}^{\mathbf{kk}}\tilde{G}_{j_1}^{\mathbf{k}}, \tag{A.15}$$

$$Y_{j_1c}^{\mathbf{k}} = Y_{cj_1}^{\mathbf{k}*}, \tag{A.16}$$

where

$$\tilde{G}_a^{\mathbf{k}} = \exp\left[-i\left(\nu_k - \frac{\Delta_{ab}}{2}\right)t\right]G_a^{\mathbf{k}},$$

$$\tilde{G}_b^{\mathbf{k}} = \exp\left[-i\left(\nu_k + \frac{\Delta_{ab}}{2}\right)t\right]G_b^{\mathbf{k}},$$

and moreover we have set formally $\tilde{G}_c^{\mathbf{k}} = 0$. Neglecting $Y_{cc}^{\mathbf{kk}}$ in Eq. (A.15) compared with $Y_{j_2j_1}$, we integrate this equation. Using the result obtained in Eqs. (A.13) and (A.14) and taking account of Eq. (A.16), we have

$$\frac{dY_{j_1j_2}}{dt} = -\sum_{\mathbf{k}}\left[\tilde{G}_{j_1}^{\mathbf{k}*}\left(\int_0^t\sum_{j_3}\tilde{G}_{j_3}^{\mathbf{k}}Y_{j_3j_2}d\tau\right) + \left(\int_0^t\sum_{j_3}Y_{j_3c}^{\mathbf{k}}\tilde{G}_{j_3}^{\mathbf{k}*}d\tau\right)\tilde{G}_{j_2}^{\mathbf{k}}\right], \tag{A.17}$$

$$\frac{dY_{cc}^{\mathbf{kk}}}{dt} = \sum_{j_1}\left[\tilde{G}_{j_1}^{\mathbf{k}}\left(\int_0^t\sum_{j_3}Y_{j_1j_3}^{\mathbf{k}}\tilde{G}_{j_3}^{\mathbf{k}*}d\tau\right) + \left(\int_0^t\sum_{j_3}\tilde{G}_{j_3}^{\mathbf{k}}Y_{j_1j_3}^{\mathbf{k}}d\tau\right)\tilde{G}_{j_1}^{\mathbf{k}*}\right]. \tag{A.18}$$

The atomic density matrix $\rho^{(a)}$ is determined from the operator ρ_{a-ph} by summing over the photon variables $\rho^{(a)} = \mathrm{Tr}(\rho_{a-ph})_{\mathbf{k}\sigma}$; since $\rho_{a-ph} = C(t)YC^{-1}(t)$, we have

$$\begin{aligned}\rho^{(a)} &= \mathrm{Tr}(C(t)YC^{-1}(t))_{\mathbf{k}\sigma} \\ &= C^{(a)}(t)\mathrm{Tr}(Y)_{\mathbf{k}\sigma}C^{(a)-1}(t) \\ &= C^{(a)}(t)Y^{(a)}C^{(a)-1}(t).\end{aligned} \tag{A.19}$$

The matrix elements $Y_{j_1j_2}^{(a)} = Y_{j_1j_2}$ for all j_1 and j_2, except $j_1 = j_2 = c$, for which

$$Y_{cc}^{(a)} = \sum_{\mathbf{k}}Y_{cc}^{\mathbf{kk}}.$$

The other terms appearing in the expression for the matrix elements $Y^{(a)}$ are zero. The operator for the substitution of the variables $C^{(a)}(t)$ for the atomic density matrix corresponding to the transformation $C(t)$ for the atomic-photon density matrix has the form

$$C^{(a)}(t) = \begin{pmatrix} \exp\left(i\frac{\Delta_{ab}}{2}t\right)I & 0 & 0 \\ 0 & \exp\left(-i\frac{\Delta_{ab}}{2}t\right)I & 0 \\ 0 & 0 & \exp(i\omega_u)I \end{pmatrix}. \tag{A.20}$$

Applying the Wigner–Weisskopf procedure to Eqs. (A.17) and (A.18) and neglecting the Lamb shift of the levels, we obtain the following equation for the matrix elements $Y^{(a)}$:

$$\frac{dY^{(a)}}{dt} = \sum_{\mathbf{k}} (UY^{(a)}U_\delta^* + U_\delta Y^{(a)}U^* - U^*U_\delta Y^{(a)} - Y^{(a)}U_\delta^* U), \tag{A.21}$$

where

$$U(t) = \begin{pmatrix} 0 \\ 0 \\ I \end{pmatrix} \times \left(G_a^{\mathbf{k}} \exp\left(i\frac{\Delta_{ab}}{2}t \right) \;\; G_b^{\mathbf{k}} \exp\left(-i\frac{\Delta_{ab}}{2}t \right) \;\; 0 \right),$$

$$U_\delta(t) = \begin{pmatrix} 0 \\ 0 \\ I \end{pmatrix} \left(G_a^{\mathbf{k}} \exp\left(i\frac{\Delta_{ab}}{2}t \right) \delta\left(\nu_k - \frac{\Delta_{ab}}{2} \right) \right.$$

$$\left. \times\, G_b^{\mathbf{k}} \exp\left(-i\frac{\Delta_{ab}}{2}t \right) \delta\left(\nu_k + \frac{\Delta_{ab}}{2} \right) \;\; 0 \right).$$

Performing the inverse transformation for the transformation to the atomic density matrix, we obtain from Eq. (A.21)

$$\frac{d\rho^{(a)}}{dt} = \sum_{\mathbf{k}} [Q\rho^{(a)}Q_\delta^* + Q_\delta \rho^{(a)} Q^* - (Q^*Q_\delta + iW)\rho^{(a)} - \rho^{(a)}(Q_\delta^* Q - iW)], \tag{A.22}$$

$$Q(t) = \begin{pmatrix} 0 \\ 0 \\ I \end{pmatrix} \left(G_a^{\mathbf{k}} \;\; G_a^{\mathbf{k}} \;\; 0 \right),$$

$$Q_\delta(t) = \begin{pmatrix} 0 \\ 0 \\ I \end{pmatrix} \times \left(\begin{array}{ccc} G_a^{\mathbf{k}} \delta\left(\nu_k - \frac{\Delta_{ab}}{2} \right) & G_b^{\mathbf{k}} \delta\left(\nu_k + \frac{\Delta_{ab}}{2} \right) & 0 \end{array} \right),$$

$$W = \begin{pmatrix} \frac{\Delta_{ab}}{2} I & 0 & 0 \\ 0 & -\frac{\Delta_{ab}}{2} I & 0 \\ 0 & 0 & -\omega_u I \end{pmatrix}.$$

The equation (A.22) completely determines the character of the radiative decay of an excited state of a degenerate *V*-type three-level atom. However, we cannot use this equation directly to obtain the radiation relaxation constants by analogy with the model for a nondegenerate case. The transverse character of the electromagnetic field of the emitted photon must be taken into account explicitly. The transversality condition can be expressed in the form of the identity

$$\sum_{\sigma = 0, \pm 1} D^1_{0\sigma}(\phi, \theta, 0) \hat{a}_{\mathbf{k}\sigma} g_{cj}^{\mathbf{k}\sigma}(M_c M_j) \equiv 0, \tag{A.23}$$

where ϕ and θ are the spherical angles determining the direction of the wave vector $\mathbf{k}$ of the emitted photon. Using the condition (A.23) in summing over $\mathbf{k}$ the products $G_{j_1}^{\mathbf{k}*} G_{j_2}^{\mathbf{k}}$ in Eq. (A.22) in the rotated coordinate system and neglecting the doublet splitting compared with ω_{jc}, we represent the radiative relaxation constants for arbitrary magnetic sublevels (including the off-diagonal elements) in the form

$$\Gamma_{j_1 j_2}(M_{j_1} M_{j_2}) = \int \sum_{M_c \sigma\sigma'} \langle \hat{a}_{\mathbf{k}\sigma'}^+ \hat{a}_{\mathbf{k}\sigma} \rangle g_{j_1 c}^{\mathbf{k}c}(M_{j_1} M_c) \times g_{c j_2}^{\mathbf{k}\sigma'}(M_c M_{j_2}) \delta(\nu_k) \frac{d\mathbf{k}}{(2\pi)^3}$$

$$= \frac{2\pi \| d_{j_1 c} \| \| d_{j_2 c} \|}{\hbar \sqrt{(2J_{j_1}+1)(2J_{j_2}+1)}} \sum_{M_c \sigma, \sigma'} C^{J_{j_1} M_{j_1}}_{J_c M_c 1\sigma} C^{J_{j_2} M_{j_2}}_{J_c M_c 1\sigma'} \times \int \sum_{\lambda = \pm 1} (D^1_{\lambda\sigma'})^* D^1_{\lambda\sigma} \omega \delta(\nu_k) \frac{d\mathbf{k}}{(2\pi)^3}. \tag{A.24}$$

Taking account of the possible inhomogeneity and nonisotropicity of the density of states of the electromagnetic field and the line contour different from a delta function, we arrive at the expressions (13) and (14).

REFERENCES

1. E. B. Aleksandrov, G. I. Khvostenko, and M. P. Chaĭka, *Interference of Atomic States* (Nauka, Moscow, 1991).
2. S. G. Rautian, G. I. Smirnov, and A. I. Shalagin, *Nonlinear Resonances in Atomic and Molecular Spectra* (Nauka, Novosibirsk, 1990).
3. S. Stenholm, Foundations of Laser Spectroscopy (Wiley, New York, 1984).
4. S. G. Rautian, Pis'ma Zh. Éksp. Teor. Fiz. **61**, 461 (1995) [JETP Lett. **61**, 473 (1995)].

5. F. A. Lomaya and A. A. Panteleev, Zh. Éksp. Teor. Fiz. **103**, 1970 (1993) [JETP **76**, 976 (1993)].
6. É. G. Pestov, Tr. Fiz. Inst. Akad. Nauk SSSR **187**, 60 (1988).
7. D. Agassi, Phys. Rev. A **30**, 2449 (1984).
8. É. A. Manykin and A. M. Afanas'ev, Zh. Éksp. Teor. Fiz. **48**, 931 (1965) [Sov. Phys. JETP **21**, 619 (1965)].
9. É. A. Manykin and A. M. Afanas'ev, Zh. Éksp. Teor. Fiz. **52**, 1246 (1967) [Sov. Phys. JETP **25**, 828 (1967)].
10. Ce Chen, Yi-Yian Yin, and D. S. Elliot, Phys. Rev. Lett. **64**, 507 (1990).
11. S. Y. Zhu, R. C. F. Chan, and C. P. Lee, Phys. Rev. A **52**, 710 (1995).
12. E. Paspalakis, C. H. Keitel, and P. L. Knight, quant-ph/9810072.
13. A. Z. Devdariani, V. N. Ostrovskiĭ, and Yu. N. Sebyakin, Zh. Éksp. Teor. Fiz. **71**, 909 (1976) [Sov. Phys. JETP **44**, 477 (1976)].
14. S. Y. Zhu and M. O. Scully, Phys. Rev. Lett. **76**, 388 (1996).
15. A. A. Panteleev, Vl. K. Rerikh, and A. N. Starostin, Zh. Éksp. Teor. Fiz. **117**, 57 (2000) [JETP **90**, 50 (2000)].
16. A. G. Leonov, A. A. Panteleev, A. N. Starostin, and D. I. Chekhov, Zh. Éksp. Teor. Fiz. **105**, 1536 (1994) [JETP **78**, 827 (1994)].
17. V. I. Savchenko, N. J. Fisch, A. A. Panteleev, and A. N. Starostin, Phys. Rev. A **59**, 708 (1999).
18. A. A. Panteleev, Zh. Éksp. Teor. Fiz. **111**, 440 (1997) [JETP **84**, 241 (1997)].
19. D. A. Varshalovich, A. N. Moskalev, and V. K. Khersonskii, *Quantum Theory of Angular Momentum* (Nauka, Leningrad, 1975; World Scientific, Singapore, 1988).
20. L. D. Landau and E. M. Lifshitz, *Course of Theoretical Physics*, Vol. 3: *Quantum Mechanics: Non-Relativistic Theory* (Nauka, Moscow, 1989, 4th ed.; Pergamon, New York, 1977, 3rd ed.).
21. L. D. Landau and E. M. Lifshitz, *Course of Theoretical Physics*, Vol. 8: *Electrodynamics of Continuous Media* (Nauka, Moscow, 1989; Pergamon, New York, 1984).
22. I. S. Osad'ko, Zh. Éksp. Teor. Fiz. **113**, 1606 (1998) [JETP **86**, 875 (1998)].
23. M. O. Scully and W. E. Lamb, Jr., Phys. Rev. **159**, 208 (1967).

Translation was provided by AIP

Journal of Experimental and Theoretical Physics, Vol. 91, No. 2, 2000, pp. 287–297.
Translated from Zhurnal Éksperimental'noĭ i Teoreticheskoĭ Fiziki, Vol. 118, No. 2, 2000, pp. 328–339.

ATOMS, SPECTRA, RADIATION

Nonlinear Resonances Free of Field and Doppler Broadenings

Yu. I. Belousov*, E. V. Podivilov, M. G. Stepanov, and D. A. Shapiro

Institute of Automatics and Electrometry,
Siberian Division, Russian Academy of Sciences, Novosibirsk, 630090 Russia
**e-mail: yura@uic.nsu.ru*
Received March 7, 2000

Abstract—For the case where the Rabi frequencies of the guiding fields are much larger than the relaxation constants but much smaller than the Doppler broadening, it is shown that resonances which are neither field nor Doppler broadened can appear in the absorption (or gain) spectrum of the probe field. A classification of four-level systems according to the number of resonances is made for cases where two strong fields interact either with opposite or adjoining transitions. The conditions under which the number of resonances reaches eight, while for stationary atoms the maximum number is four, are found. A method is proposed for calculating the number of resonances in a multilevel system with several strong fields using analysis of the extremum points of the frequency branches in the velocity–frequency plane. *© 2000 MAIK "Nauka/Interperiodica".*

1. INTRODUCTION

One of the basic problems of nonlinear optics is to develop methods for increasing the frequency of coherent radiation in gases. Among continuous-conversion schemes with an appreciable decrease of wavelength which have been developed, the three-level scheme of an anti-Stokes Raman laser [1, 2] and the four-level scheme of resonant four-wave mixing [3, 4] are of special interest. Doppler broadening decreases the conversion efficiency, but it can be compensated in many cases. It is important to know the resonance nonlinear susceptibility in gases in order to estimate the light conversion efficiency. Moving away from problems of propagation of an electromagnetic wave in a medium and making the assumption that the gas layer is optically thin, the calculation of the nonlinear susceptibility of n-level system reduces to solving an algebraic equation of degree n and averaging the absorbed power over the particle velocities [5]. Such averaging in calculation of the spectrum of the probe field in a three-level system interacting with a strong field on an adjoining transition was performed in the 1970s (see, for example, [6]). A characteristic feature of the spectrum found was that if the probe field was the longer wavelength field, then a doublet of narrow resonances remained after averaging.

In the absence of a strong field the resonance frequency is a linear function of the particle velocity because of the Doppler shift. To each group of particles moving with the same velocity there corresponds a unique resonance frequency. A strong field splits these resonances, and the magnitude of the splitting is also found to depend on the velocity. The split resonances are shifted from Bohr transition frequency to the Rabi frequencies, which become nonlinear functions of the velocity. Integration over the velocities signifies summation of "group spectra," each of which is a response of a group of particles moving with a prescribed velocity. In [7] it was discovered that the velocity-averaged susceptibility grows rapidly when the detuning of the probe-field frequency is equal to the Rabi frequency Ω_R at the extremum points of its velocity dependence. These spectral peaks are due to the fact that the susceptibility is proportional to the number of particles interacting resonantly with the field. The number of particles with the same shift of the resonance frequency is maximum at the extremal points. We shall call these extrema the turning points.

The contribution of an individual turning point to the probe-field spectrum in a three-level system has been calculated in [9] taking account of weak collisions with a change in the velocity. In [10] a scheme with resonant four-wave mixing with two strong fields on opposite transitions of a four-level system and two weak fields was examined. The asymptotic behavior of the velocity integral was found for the symmetric case of equal wave numbers of the weak fields and zero detunings of the strong fields. It was found that the number of peaks in the spectrum can increase compared with the case of stationary atoms. It was also shown that merging of the turning points leads to a large increase in the radiation conversion coefficient [11].

Numerical averaging over the velocities in a multilevel system (see, for example, [12, 13]) does not permit analyzing the dependence of the conversion coefficient on the relaxation constants, detunings, wave numbers, wave intensities, and spontaneous decay probability, since the problem is multiparametric. It is virtually impossible to obtain a general analytical expression for the work performed by the probe field in a multilevel system. The absorbed power can be written in a relatively compact form only for certain cases, spe-

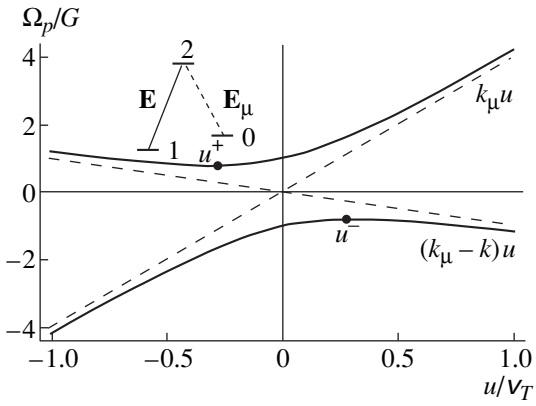

Fig. 1. Frequency branches of a three-level system in the (u, Ω_p) plane: $kv_T = 5G$, $k_\mu v_T = 4G$, $\Omega = 0$. Dashed straight lines—asymptotes of the frequency branches. The inset shows the level scheme; the solid line denotes the strong field **E**; the dashed line denotes the probe field $\mathbf{E}_\mu$. The turning points are shown on the frequency branches.

cifically, for a four-level system with strong fields on opposite transitions. In more complicated cases the problem reduces to solving a cubic or higher-degree equation. However, these difficult calculations can be avoided if one is interested only in the qualitative behavior of the spectrum of the probe field. The most informative part of the spectrum are the narrow resonance peaks. The problem becomes solvable if attention is confined only to the calculation of these peaks.

In the present paper we present a method for determining the number of narrow peaks in the probe-field spectrum for four-level systems with large Doppler and small homogeneous broadenings. For this the concept of frequency branches and turning points are presented in Section 2 for a three-level system interacting resonantly with one strong and one probe field. Four-level schemes with two strong fields on opposite or adjoining transitions in Section 3 are analyzed and the conditions for the existence of narrow resonances in the probe-field spectrum, when all waves are codirectional, are found. A classification of these schemes according to the number of peaks is presented. The results of the numerical calculation of a spectrum with eight peaks are presented in Section 4. The results obtained are discussed and compared with data obtained by other authors. Brief recommendations for checking the predicted effects experimentally are contained in the conclusions. An approximate expression for the work performed by the probe field in multilevel systems with large Doppler broadening is presented in the Appendix.

2. THREE-LEVEL SYSTEM

We shall consider a three-level system exposed to a strong electromagnetic wave $\mathrm{Re}\,\mathbf{E}\exp[i(kx - \omega t)]$ in resonance with a transition between levels 1 and 2. The energy, absorbed by such a system, of a probe wave $\mathrm{Re}\,\mathbf{E}_\mu\exp[i(k_\mu x - \omega_\mu t)]$ in resonance with a transition between levels 2 and 0 can be written as a sum of two terms resonant with respect to ω_μ. If the upper level is denoted by the index 2, $E_2 > E_1$ and E_0 (see inset in Fig. 1), then the expression for the work performed by the field $P_\mu(\omega_\mu)$ per unit time [5] can be written as a sum of elementary fractions:

$$P_\mu(\omega_\mu) = 2\hbar\omega_{20}|G_\mu|^2 \int_{-\infty}^{\infty}\frac{du}{2\Omega_R}\mathrm{Re}\left[\frac{\lambda^- N_{20}(u) + |G|^2 N_{21}(u)/(2\Omega_R - i\Gamma)}{\Gamma - i(\Omega'_\mu - \lambda^+)} - \frac{\lambda^+ N_{20}(u) - |G|^2 N_{21}(u)/(2\Omega_R + i\Gamma)}{\Gamma - i(\Omega'_\mu - \lambda^-)}\right], \quad (1)$$

where $\omega_{20} = (E_2 - E_0)/\hbar$, $\omega_{21} = (E_2 - E_1)/\hbar$ are the Bohr transition frequencies,

$$N_{ij}(u) = \frac{1}{\sqrt{\pi}v_T}(N_i - N_j)\exp\left(-\frac{u^2}{v_T^2}\right)$$

is the equilibrium distribution of the population difference with temperature $T = mv_T^2/2$, m is the mass of the particles, v_T is the thermal velocity, u is the projection of the particle velocity on the direction of propagation of a strong wave, and N_j is the population of the jth level, $G = \mathbf{E}\cdot\mathbf{d}_{21}/2\hbar$ and $G_\mu = \mathbf{E}_\mu\cdot\mathbf{d}_{20}/2\hbar$ are the Rabi frequencies, which are proportional to the field amplitudes, $\Omega_\mu = \omega_\mu - \omega_{20}$ and $\Omega = \omega - \omega_{21}$ are the detunings of the frequencies of the electromagnetic fields from the Bohr transition frequencies, and Γ are the relaxation constants, which we have chosen, for simplicity, to be the same for all levels and which we assume to be small. The quantities $\lambda^\pm$ are related with the splitting of the energy of level 2 by a strong electromagnetic field (so-called energies of dressed states):

$$\lambda^\pm = \frac{\Omega'}{2} \pm \Omega_R, \quad \Omega_R = \sqrt{\frac{\Omega'^2}{4} + |G|^2},$$

where Ω_R is the generalized Rabi frequency of the strong field taking account of the Doppler shift $\Omega' = \Omega - ku$ and $\Omega'_\mu = \Omega_\mu - k_\mu u$. Both terms in the integrand in Eq. (1) describe a resonance of the probe field with a transition between one of the dressed states of the subsystem 1–2 and the state 0.

We are interested in the qualitative form of the spectrum of the probe field in nondegenerate systems with large Doppler broadening and located in strong fields. We shall consider the situation where the Rabi frequency is much larger than the relaxation constants but much smaller than the Doppler width of a line:

$$\Gamma \ll G \ll kv_T. \quad (2)$$

The work performed by the probe field in resonance with a transition between two levels, which belong to different (not coupled with one another by strong fields) subsystems of a multilevel system, can always be written as a sum of resonant, with respect to Ω_μ, terms, similarly to the expression (1) (see Appendix). Consequently, it is convenient to start the explanation of the turning-point method, used below for analyzing the spectrum in multilevel systems, for a three-level system for which the work performed by the field can be calculated explicitly.

Since the conditions of a maximum of the integrand in Eq. (1),

$$\Omega_\mu = \Omega_p^\pm(u) \equiv \lambda^\pm(u) + k_\mu u, \tag{3}$$

depend on the particle velocity u, in the general case velocity averaging decreases the amplitude P_μ by the factor Γ/kv_T. The decrease in the work performed by the field is due to the fact that only a negligible fraction of particles ($\sim\Gamma/kv_T$) interacts resonantly with the probe field. The only exception is the case where the condition (3) holds simultaneously with the condition for an extremum of the function

$$\frac{d\Omega_p^\pm}{du} = k_\mu - \frac{k}{2} \pm \frac{k(ku_p - \Omega)}{2\sqrt{(\Omega - ku_p)^2 + 4|G|^2}} = 0, \tag{4}$$

which means that when the particle velocity varies near u_p the condition (3) continues to hold to within the terms which are quadratic in the deviation $(u - u_p)$. The number of points interacting with the field increases rapidly and hence sharp peaks should be observed in the spectrum of the probe field $P_\mu(\omega_\mu)$ at $\Omega_\mu = \Omega_p^\pm(u_p^\pm)$. From Eq. (4) we find the velocity

$$ku_p^\pm = \Omega \pm |G|\frac{k - 2k_\mu}{\sqrt{k_\mu(k - k_\mu)}}, \tag{5}$$

and substituting it into Eq. (3) we find the position of the resonances in the spectrum [6, 7]

$$\Omega_\mu^\pm = \Omega_p^\pm(u_p^\pm) = \frac{k_\mu}{k}\Omega \pm 2|G|\frac{\sqrt{(k - k_\mu)k_\mu}}{k}. \tag{6}$$

In multilevel systems the functions $\Omega_p(u)$, which determine the value of the resonance frequency as a function of the particle velocity, have a form which makes it impossible to solve Eqs. (3) and (4) analytically. We shall formulate a graphical method for calculating the peaks in the spectrum of the probe field. We plot in the (u, Ω_p) plane the curves $\Omega_p^\pm(u)$ (3), which we call frequency branches (Fig. 1). The condition (4) gives in the plane $(u_p^\pm, \Omega_p^\pm(u_p^\pm))$ the "turning points" where the frequency branch possesses an extremum. Thus, in order to determine the position of resonances in the probe-field spectrum, it is sufficient to represent the frequency branches $\Omega_p(u)$ in the (u, Ω_p) plane and find the turning points where $d\Omega_p/du = 0$. For a three-level system there are only two frequency branches, $\Omega_p^\pm(u)$, each of which is a branch of a hyperbola, and consequently there can be no more than one turning point on each of them. It is evident from Fig. 1 that resonances in the spectrum which are associated with the turning points can be observed only if the slopes of the asymptotes of the frequency branches, $\Omega_p(u) \sim k_\mu u$ and $\Omega_p(u) \sim (k_\mu - k)u$, have different signs, i.e., $k_\mu(k_\mu - k) < 0$. This result also follows from the expression (6), which gives a real frequency only for $k_\mu(k - k_\mu) > 0$. The asymptotic values of the slopes of the frequency branches are related with the relative arrangement of the energy levels in the three-level system:

$$k_\mu \propto \frac{\omega_{20}}{c} = \frac{E_2 - E_0}{\hbar c}, \quad k_\mu - k \propto \frac{\omega_{10}}{c} = \frac{E_1 - E_0}{\hbar c}.$$

Analyzing the expression (1) for the probe-field spectrum for an arbitrary scheme of levels, it is evident that the slopes of the asymptotes have different signs if

$$(E_2 - E_0)(E_1 - E_0) < 0. \tag{7}$$

In other words, the energy E_0 must fall between the levels E_1 and E_2: these are the so-called Stokes Λ and V schemes. If the condition (7) does not hold (anti-Stokes schemes), then the expression (6), determining the position of the turning points, is imaginary and therefore there will be no narrow resonances in the spectrum. The conditions for the existence of narrow resonances when electromagnetic waves propagate opposite to one another can be found similarly:

$$k_\mu(k_\mu + k) < 0, \quad |2E_0 - 3E_2 + E_1| < |E_2 - E_1|.$$

The shape of the spectrum near the resonance $\Omega_\mu^\pm$ can be found in the approximation (2), using only the fact that the first derivative of $\Omega_p^\pm(u)$ vanishes at the point $u = u_p$. Neglecting all terms which are small to the extent that G/kv_T and Γ/G are small, we obtain

$$P_\mu(\Omega_\mu) \approx 2\pi\hbar\omega_{20}|G_\mu|^2 \times \left[\frac{I^+(\Omega_\mu)}{2\Omega_R(u_p^+)}\left(\lambda^-(u_p^+)N_{20}(u_p^+) + \frac{|G|^2 N_{21}(u_p^+)}{2\Omega_R(u_p^+)}\right) - \frac{I^-(\Omega_\mu)}{2\Omega_R(u_p^-)}\left(\lambda^+(u_p^-)N_{20}(u_p^-) - \frac{|G|^2 N_{21}(u_p^-)}{2\Omega_R(u_p^-)}\right)\right], \tag{8}$$

where

$$I^\pm(\Omega_\mu) = \frac{1}{\pi}\mathrm{Re}\int_{-\infty}^{\infty}\frac{du}{\Gamma - i(\Omega_\mu - k_\mu u - \lambda^\pm(u))}. \tag{9}$$

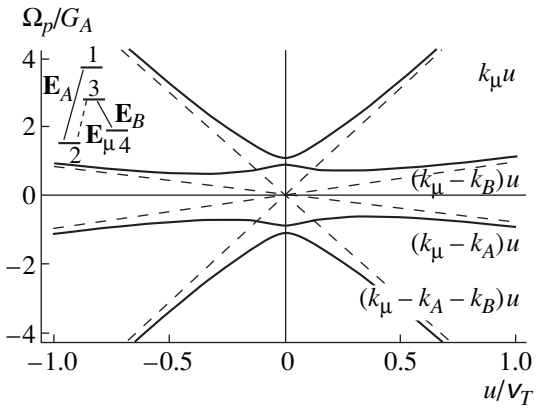

Fig. 2. Frequency branches of a four-level system in the (u, Ω_p) plane: $k_A v_T = 7G_A$, $k_B v_T = 5G_A$, $k_\mu v_T = 6G_A$, $G_B = 0.1G_A$, $\Omega_A = \Omega_B = 0$. Dashed straight lines—asymptotes of the frequency branches. The inset shows the four-level system with two strong fields on opposite transitions; the solid lines denote the strong fields $\mathbf{E}_A$ and $\mathbf{E}_B$; the dashed lines denote the probe field $\mathbf{E}_\mu$.

The derivation of the expression (8) used the fact that the width of the integrand in Eq. (1) of order Γ is determined by the denominator, and consequently the remaining expression can be removed from the integral at the points $u = u_p^+$ or $u = u_p^-$ in accordance with the indices + or – in Eq. (9).

Expanding the function $\Omega_p^\pm(u)$ in the power series in $u - u_p^\pm$ near the turning points $u = u_p^\pm$ and retaining quadratic terms

$$\Omega_p^\pm = \Omega_\mu^\pm + a^\pm(u - u_p)^2 + \ldots, \qquad (10)$$

where the letters $a^\pm \neq 0$ denote second derivatives at the turning points

$$a^\pm = \frac{1}{2}\frac{d^2\Omega_p^\pm}{du^2}\bigg|_{u = u_p^\pm} = \pm\frac{k_\mu^{3/2}(k - k_\mu)^{3/2}}{|G|k},$$

we obtain the profile of an isolated peak, which was first found in [6]:[1]

$$I^\pm(\Omega_\mu) = \mathrm{Re}\sqrt{\frac{\pm k|G|}{k_\mu^{3/2}(k - k_\mu)^{3/2}(\Omega_\mu - \Omega_\mu^\pm + i\Gamma)}}. \qquad (11)$$

The spectral peaks given by Eq. (11) have a width of the order of Γ, their amplitude is proportional to $\sqrt{|G|/\Gamma}$, and they have a characteristic asymmetric shape.

As $k_\mu \longrightarrow k$ the formula (11) becomes inapplicable. Consequently, the condition (2) must be replaced by a more stringent condition $G\sqrt{k_\mu(k - k_\mu)}/k \gg \Gamma$, which means a large field-induced splitting (6) compared with the relaxation constant. The condition that the field splitting is small compared with the Doppler width (2) is also replaced by a stronger condition, following from Eq. (5). The velocities at the turning points $u_p^\pm$ must be less than the thermal velocity v_T: $|u_p^\pm| \ll v_T$.

[1] The Eq. (54) of [6] contains a misprint: instead of 1/2 the exponent is written as 2.

3. FOUR-LEVEL SYSTEM

3.1. Four-Level System 2 + 2

Let us consider a four-level system interacting with two strong electromagnetic fields, G_A and G_B. If the fields are in resonance with opposite transitions, then the system can be represented in the form of two independent two-level subsystems (we shall call such a system 2 + 2). However, if the fields interact with neighboring transitions, then the system consists of a three-level system and an individual level (we shall call such a system 3 + 1). We begin by analyzing the first case (see inset in Fig. 2). The work performed by the probe field $\mathrm{Re}\,\mathbf{E}_\mu \exp[i(\omega_\mu t - k_\mu x)]$ in resonance with the transition 2–3 can be written as a sum

$$P_\mu(\Omega_\mu) = \sum_{I, J = 1, 2} P^{IJ}(\Omega_\mu), \qquad (12)$$

where

$$P^{IJ}(\Omega_\mu) = \mathrm{Re}\int_{-\infty}^{\infty}\frac{C^{IJ}(u)du}{\Gamma - i(\Omega_\mu - k_\mu u - \lambda_A^I(u) + \lambda_B^J(u))},$$

$$\lambda_A^{1,2} = \frac{1}{2}(\Omega_A - k_A u \pm \sqrt{(\Omega_A - k_A u)^2 + 4|G_A|^2}), \qquad (13)$$

$$\lambda_B^{1,2} = -\frac{1}{2}(\Omega_B - k_B u \pm \sqrt{(\Omega_B - k_B u)^2 + 4|G_B|^2}),$$

and λ_A^I and λ_B^J are the energies of the "dressed" states of independent two-level systems. The designations I and J of the frequency branches are introduced in the Appendix. The derivation of the formula (12) and the determination of the coefficients C^{IJ} are also presented in the Appendix.

To find the number of resonances in the probe-field spectrum, we represent the frequency branches in the (u, Ω_p) plane, for example, at $\Omega_A = \Omega_B = 0$ (Fig. 2). Since the position of the resonances in the spectrum is determined by the values of the extrema of the frequency branches, we shall analyze the condition for vanishing of the derivatives:

$$2\frac{d\Omega_p^{IJ}(u)}{du} = \Delta k + \kappa^{IJ}(u) = 0, \qquad (14)$$

$$\kappa^{12}(u) = -\kappa^{21}(u)$$
$$= \frac{k_B(\Omega_B - k_B u)}{\sqrt{(\Omega_B - k_B u)^2 + 4|G_B|^2}} + \frac{k_A(\Omega_A - k_A u)}{\sqrt{(\Omega_A - k_A u)^2 + 4|G_A|^2}},$$
$$\kappa^{11}(u) = -\kappa^{22}(u)$$
$$= \frac{k_B(\Omega_B - k_B u)}{\sqrt{(\Omega_B - k_B u)^2 + 4|G_B|^2}} - \frac{k_A(\Omega_A - k_A u)}{\sqrt{(\Omega_A - k_A u)^2 + 4|G_A|^2}},$$

where $\Delta k = 2k_\mu - k_A - k_B$. The values of the function $\kappa^{IJ}(u)$ are limited by the region $|\kappa^{IJ}(u)| < k_A + k_B$, and consequently Eq. (14) does not possess any solutions for $|\Delta k| > k_A + k_B$. The function $\kappa^{12}(u)$ (and also the function $-\kappa^{21}(u)$) is monotonic and in the limit $u \longrightarrow \pm\infty$ approaches the asymptotic values $\mp(k_A + k_B)$. Consequently, when

$$|\Delta k| < k_A + k_B \tag{15}$$

the frequency branches Ω_p^{12} and Ω_p^{21} each possess a turning point. The function $\kappa^{11}(u)$ (just as $-\kappa^{22}(u)$) approaches $\pm(k_A - k_B)$ in the limit $u \longrightarrow \pm\infty$ but it is not monotonic. It possesses two extrema, which can be found from the condition $d^2\Omega_p^{11}/du^2 = d\kappa^{11}/du = 0$:

$$u_\pm = \frac{\Omega_A}{k_A} - \frac{\gamma k_B}{k_A}\Delta \pm \sqrt{\Delta^2 + Q}. \tag{16}$$

Here

$$\kappa^{11}(u_\pm) = -\kappa^{22}(u_\pm)$$
$$= \frac{k_A k_B \Delta(1-\gamma) \pm (k_A^2 - \gamma k_B^2)\sqrt{\Delta^2 + Q}}{\sqrt{\Delta^2(k_A^2 + \gamma^2 k_B^2) + M \mp 2\gamma k_A k_B \Delta\sqrt{\Delta^2 + Q}}}, \tag{17}$$

where

$$\Delta = \gamma\frac{k_A\Omega_B - k_B\Omega_A}{k_A^2 - \gamma^2 k_B^2}, \quad M = 4\gamma^2\frac{|G_B|^2 k_A^2 - |G_A|^2 k_B^2}{k_A^2 - \gamma^2 k_B^2},$$
$$Q = 4\frac{\gamma^2|G_B|^2 - |G_A|^2}{k_A^2 - \gamma^2 k_B^2}, \quad \gamma = \left(\frac{|G_A|k_A}{|G_B|k_B}\right)^{2/3}.$$

Hence it follows that the frequency branch $\Omega_p^{11}(u)$ (or the branch $\Omega_p^{22}(u)$) possesses a turning point for $u < u_-$, if Δk lies in the interval between $k_A - k_B$ and $\kappa^{11}(u_-)$ (or between $k_B - k_A$ and $\kappa^{22}(u_-)$). If Δk falls between $\kappa^{11}(u_-)$ and $\kappa^{11}(u_+)$ (or between $\kappa^{22}(u_-)$ and $\kappa^{22}(u_+)$), then the frequency branch $\Omega_p^{11}(u)$ ($\Omega_p^{22}(u)$) possesses an extremum in the range $u_- < u < u_+$. Finally, for Δk between $\kappa^{11}(u_+)$ and $k_B - k_A$ (or between $\kappa^{22}(u_+)$ and $k_A - k_B$) a turning point arises $u > u_+$.

The ranges of Δk enumerated above can intersect, so that each frequency branch, $\Omega_p^{11}(u)$ and $\Omega_p^{22}(u)$, can have up to three turning points. Thus, the total number of turning points on all frequency branches and hence the maximum number of resonances in the spectrum of the probe field can reach 8. For $\Delta^2 + Q < 0$ the expression (16) is complex, i.e., the functions $\kappa^{11}(u)$ and $\kappa^{22}(u)$ become monotonic. In this case the frequency branches $\Omega_p^{11}(u)$ and $\Omega_p^{22}(u)$ each contain one extremum for $|\Delta k| < |k_A - k_B|$.

We shall investigate two limiting cases in greater detail: $\Delta^2 \gg |Q|$—the difference of the detunings of strong fields is large compared with their Rabi frequencies—and the opposite limit $\Delta^2 \ll |Q|$. In the limit $|Q| \ll \Delta^2$ it follows from the expression (17) and Eq. (14) that for $|\Delta k| < |k_A - k_B|$ the frequency branches $\Omega_p^{11}(u)$ and $\Omega_p^{22}(u)$ each possess one extremum. In the interval $|k_A - k_B| < |\Delta k| < k_A + k_B$ either $\Omega_p^{11}(u)$ or $\Omega_p^{22}(u)$ possesses two extrema. Thus, in the limit of a large difference of the detunings $\Delta\Omega = \Omega_A - \Omega_B k_A/k_B$ for strong fields the probe-field spectrum contains four resonances if the inequality (15) is satisfied. This condition can be formulated in an invariant form which is valid for any level scheme: if the energy of at least one level of the second subsystem lies between the energies of the levels of the first subsystem, then the number of resonances is 4. In the opposite case there will be no narrow resonances.

When the detunings of strong fields are in resonance with one another, $\Delta = 0$, the expressions (16) and (17) simplify substantially:

$$u_\pm = \frac{\Omega_A}{k_A}$$
$$\pm 2\sqrt{\frac{(|G_B|k_A^2)^{2/3} - (|G_A|k_B^2)^{2/3}}{(|G_B|^2 k_A)^{2/3} - (|G_A|^2 k_B)^{2/3}}}\left(\frac{|G_A G_B|}{k_A k_B}\right)^{2/3},$$
$$\kappa^{11}(u_\pm) = -\kappa^{22}(u_\pm) = \pm\kappa, \tag{18}$$
$$\kappa = ((|G_B|k_A^2)^{2/3} - (|G_A|k_B^2)^{2/3})$$
$$\times\sqrt{\frac{(|G_B|k_A^2)^{2/3} - (|G_A|k_B^2)^{2/3}}{|G_B|^2 k_A^2 - |G_A|^2 k_B^2}}.$$

The extremal values of the function $\kappa^{11}(u_\pm)$ depend on the ratios of the Rabi frequencies of strong fields: $|G_A/G_B|$. For definiteness we shall assume $k_A > k_B$. For $|G_A/G_B| < \sqrt{k_A/k_B}$ we find $\kappa^{11}(u_-) < k_B - k_A$ and $\kappa^{11}(u_+) > k_A - k_B$. Recall that as $u \longrightarrow \pm\infty$ the function $\kappa^{11}(u)$ approaches the asymptotic values $\pm(k_A - k_B)$, respectively. Consequently, the equation $\Delta k = \kappa^{11}(u)$ possesses two solutions with

$$k_A - k_B < |\Delta k| < \kappa, \quad |G_A/G_B| < \sqrt{k_A/k_B} \tag{19}$$

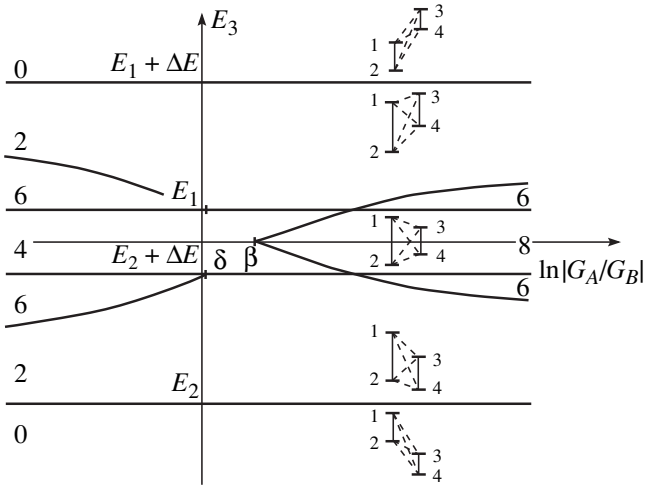

Fig. 3. The parameter ranges corresponding to different numbers of nonlinear resonances in the probe field spectrum in the ($\ln|G_A/G_B|$, E_3) plane for four-level systems with strong fields on opposite transitions, shown in the insets (the dashed lines denote examples of the arrangement of the probe field). $\Omega_A/k_A = \Omega_B/k_B$, $E_1 - E_2 > \Delta E \equiv E_3 - E_4$, $\beta = (1/2)\ln[(E_1 - E_2)/\Delta E]$, $\delta = 2\ln[(E_1 - E_2)/\Delta E]$. The large numbers denote the number of resonances in the corresponding regions separated by the heavy lines.

or one solution if

$$|\Delta k| < k_A - k_B. \tag{20}$$

Similarly, the frequency branch Ω_p^{22} possesses two extrema if the condition (19) is satisfied and one solution if the inequality (20) is satisfied.

For $\sqrt{k_A/k_B} < |G_A/G_B| < k_A^2/k_B^2$ the expression (18) is complex, so that $\kappa^{11}(u)$ and $\kappa^{22}(u)$ are monotonic functions and hence the frequency branches $\Omega_p^{11}(u)$ and $\Omega_p^{22}(u)$ each possess one extremum, while the condition (20) is satisfied. Finally, for $k_A^2/k_B^2 < G_A/G_B$ we find $\kappa^{11}(u_-) > 0$ and $\kappa^{11}(u_+) < 0$, so that the frequency branches $\Omega_p^{11}(u)$ and $\Omega_p^{22}(u)$ each possess three turning points for

$$|\Delta k| < \min(|\kappa|, k_A - k_B), \quad |G_A/G_B| > k_A^2/k_B^2,$$

and two turning points for

$$k_A - k_B < |\Delta k| < |\kappa|,$$

or one turning point each if

$$|\kappa| < |\Delta k| < k_A - k_B.$$

Figure 3 illustrates the usual rearrangement of the probe-field spectrum as a function of the parameters of the four-level system in the plane ($\ln|G_A/G_B|$, E_3) for $\Omega_A k_B = \Omega_B k_A$. Here we employ the following notations: E_1 and E_2 are the energies of the upper and lower levels of the transition in resonance with the field G_A, E_3 and E_4 are the energies of the upper and lower levels of the transition in resonance with the field G_B. For definiteness we assume $\Delta E = E_3 - E_4 < E_1 - E_2$. In this case the expression $\Delta k = \kappa$ for the boundaries between the regions with a different number of resonances can be written in a form valid for an arbitrary level scheme:

$$|E_4 + E_3 - E_1 - E_2| = \frac{(|G_B|^{2/3}(E_1 - E_2)^{4/3} - |G_A|^{2/3}(E_3 - E_4)^{4/3})^{3/2}}{\sqrt{|G_B|^2(E_1 - E_2)^2 - |G_A|^2(E_3 - E_4)^2}}. \tag{21}$$

The level schemes are shown in the insets. The large numbers denote the number of narrow resonances in the corresponding regions of the parameters. Thus, the number of resonances in the probe-field spectrum depends on the level scheme and on the relative detuning of the frequencies and intensities of the strong fields, and in general it can assume the values 0, 2, 4, 6, and 8. An odd number occurs in degenerate cases, specifically, if the condition (21) is satisfied.

3.2. Four-Level System 3 + 1

We now consider a four-wave system interacting with two strong fields ($\mathbf{E}_1$ and $\mathbf{E}_2$) on neighboring transitions; see inset in Fig. 4. In zeroth order perturbation theory in the probe field this four-level system decomposes into three- and one-level subsystems. The energies of the dressed states λ_A^I, $I = 1, 2, 3$, of the three-level system interacting resonantly with two electromagnetic fields ($\mathbf{E}_1$ and $\mathbf{E}_2$), can be determined in principle using the Cardano formula from the equation

$$\lambda_A^I(\lambda_A^I + \Omega_1')(\lambda_A^I + \Omega_2') - |G_1|^2(\lambda_A^I + \Omega_2') - |G_2|^2(\lambda_A^I + \Omega_1') = 0, \tag{22}$$

where $\Omega_{1,2}' = \Omega_{1,2} - k_{1,2}u$ are the detunings of the fields taking account of the Doppler shift and $G_{1,2} = \mathbf{E}_{1,2}\mathbf{d}_{1,2}/2\hbar$ is the Rabi frequency of the fields. The energy of a dressed state of the subsystem consisting of one level is $\lambda_B = 0$. To find the number of turning points we shall investigate the frequency branches $\Omega_p^I = k_\mu u + \lambda_B - \lambda_A^I = k_\mu u - \lambda_A^I$ (see Appendix). Substituting $\lambda_A^I = k_\mu u - \Omega_p^I$ into Eq. (22) we obtain a cubic polynomial of Ω_p^I and u, implicitly giving the form of the frequency branches,

$$P_3(\Omega_p^I, u) = \Omega_p'^I(\Omega_p'^I - \Omega_1')(\Omega_p'^I - \Omega_2') - (\Omega_p'^I - \Omega_2')|G_1|^2 - (\Omega_p'^I - \Omega_1')|G_2|^2 = 0. \tag{23}$$

If G_1, $G_2 = 0$, then all three frequency branches are linear functions of the velocity ($I = 1, 2, 3$):

$$\Omega_p^I(u) = k_\mu u, \quad \Omega_1 + (k_\mu - k_1)u,$$
$$\Omega_2 + (k_\mu - k_2)u,$$

which intersect at the points $u_1^* = \Omega_1/k_1$, $u_2^* = \Omega_2/k_2$, and $u_3^* = (\Omega_1 - \Omega_2)/(k_1 - k_2)$. When G_1, $G_2 \neq 0$ the frequency branches $\Omega_p^I(u)$ do not intersect, but rather they repel one another by an amount of the order of G_1 and G_2. If the difference of the detunings of the strong fields is large, $\Delta\Omega = |\Omega_1 - \Omega_2 k_1/k_2| \gg G_1, G_2$, then near the points u_ν^*, $\nu = 1, 2, 3$ the frequency branches pass smoothly from one linear asymptote to another. If u_ν^* is a point of intersection of the asymptotes, whose slopes have different signs, then there are two turning points near this point, similarly to the case of a three-level system (Fig. 4). The maximum number of such points of intersection is 2, so that the maximum number of extrema of the function Ω_p^I is 4. However, if the slopes of all three asymptotes have the same sign, then all frequency branches are monotonic functions and there are no narrow resonances in the probe-field spectrum. The conditions found can be formulated in terms of the energy: if the energy level of the second subsystem (in this case this is an individual level) lies outside the levels of the three-level subsystem, then there are no narrow resonances in the probe-field spectrum and conversely, if a solitary level lies between the levels of the three-level system, the maximum possible number of resonances is 4.

Two turning points can merge as the difference $\Delta\Omega$ of the detunings of strong fields decreases. The condition for merging of two extrema of the function Ω_p^I is determined by solving simultaneously the equations

$$P_3(\Omega_\mu, u) = 0, \quad \frac{dP_3(\Omega_\mu, u)}{du} = 0, \quad \frac{d^2P_3(\Omega_\mu, u)}{du^2} = 0.$$

Solving the system and eliminating Ω_μ and u we obtain an expression for the boundary separating the region of parameters for which 4 or 2 resonances exist for a level scheme shown in the inset in Fig. 4:

$$\Delta\Omega^2 = \frac{|G_1|^2(1+z)}{k_2^2 k_\mu(k_1 - k_\mu)} \times [2k_2k_\mu - k_1(k_2 + k_\mu) + (2k_1k_\mu - k_2(k_1 + k_\mu))z]^2, \quad (24)$$

where

$$z^3 = \frac{|G_2|^2 k_1 - k_\mu}{|G_1|^2 k_2 - k_\mu}.$$

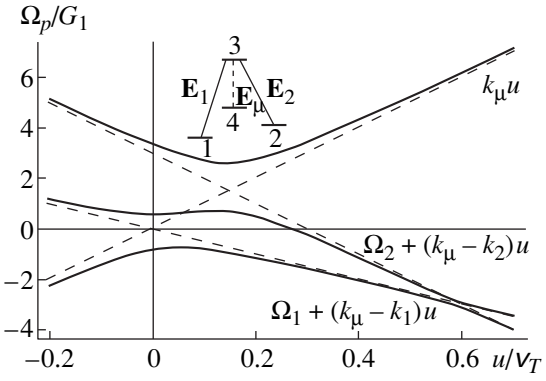

Fig. 4. Frequency branches of a four-wave system in the (u, Ω_p) plane: $k_1v_T = 20G_1$, $k_2v_T = 15G_1$, $k_\mu v_T = 10G_1$, $G_2 = 0.7G_1$, $\Omega_1 = 3G_1$, and $\Omega_2 = 0$. Dashed straight lines—asymptotes of the frequency branches. The inset shows a four-level system with two strong fields on adjoining transitions; the solid lines denote the strong fields $\mathbf{E}_1$ and $\mathbf{E}_2$; the dashed line denotes the probe field $\mathbf{E}_\mu$.

The equation (24) possesses a real solution only if

$$|G_1|^2 \frac{k_\mu}{k_1 - k_\mu} > |G_2|^2 \frac{k_\mu}{k_\mu - k_2}. \quad (25)$$

A classification of four-level systems with two strong fields on neighboring transitions with respect to the number of resonances with $\Delta\Omega = 0$ is presented in the parameter plane $(\ln|G_2/G_1|, E_4)$ in Fig. 5. For an arbitrary level scheme we introduce the following notations: E_1 and E_3 are the energies of the levels of the transition in resonance with the field G_1; E_2 and E_3 are the energies of the levels of a transition in resonance with the field G_2; the probe field is in resonance with the transition between level 4 and one of the levels which are coupled by strong fields. For definiteness we assume $|E_1 - E_3| > |E_2 - E_3|$. Then the condition (25), determining the region of parameters for which two resonances exist, can be written in a form valid for an arbitrary level scheme:

$$|G_1|^2 \frac{E_3 - E_4}{E_4 - E_1} + |G_2|^2 \frac{E_3 - E_4}{E_4 - E_2} > 0.$$

The level schemes are shown in the insets in Fig. 5. The large numbers in Fig. 5 denote the number of resonances in the corresponding regions of the parameters. Figures 5a, 5b, and 5c refer to the schemes in which a pair of strong fields forms. Respectively, *V*, Λ, and the cascade Ξ configurations.

4. DISCUSSION

In summary, it is found that a four-wave system behaves similarly to a three-level system. A pair of narrow resonances appears in the probe-field spectrum of a three-level system (Fig. 1) if the level which is coupled with the system by the probe field falls between

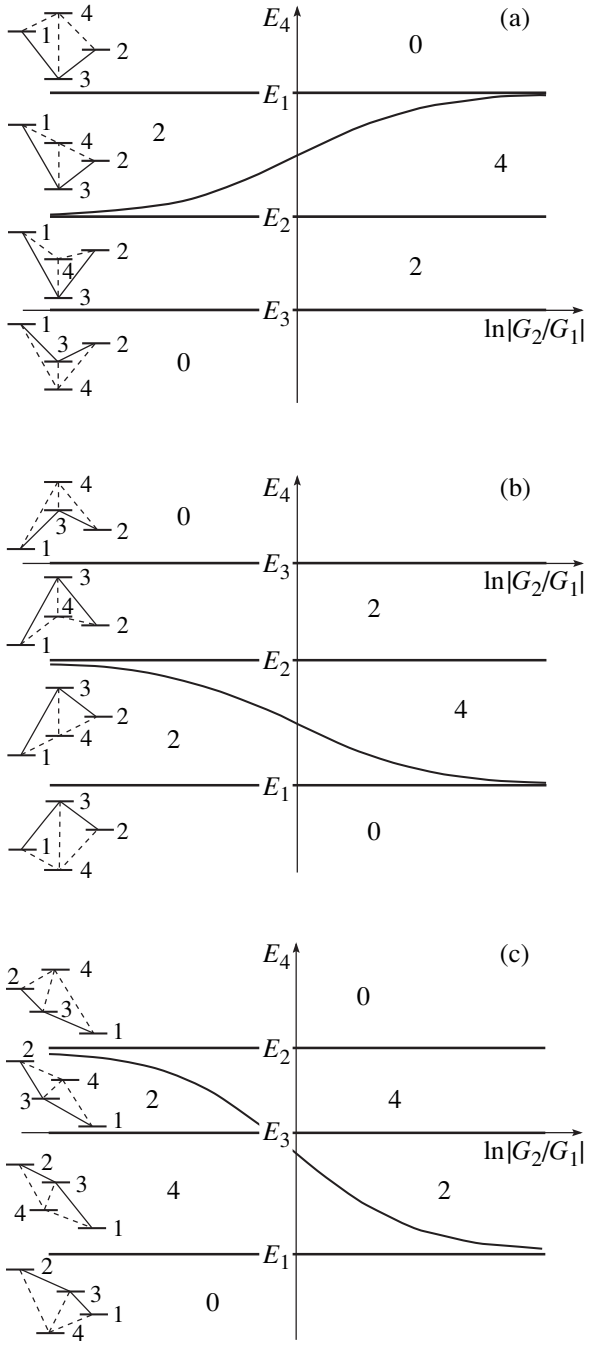

Fig. 5. The parameter regions corresponding to different numbers of nonlinear resonances in the probe-field spectrum in the ($\ln|G_2/G_1|$, E_4) plane with $\Omega_1/k_1 = \Omega_2/k_2$ for four-level systems with strong fields on adjoining transitions shown in the insets (the dashed lines show the examples of the arrangement of the probe field). The large numbers denote the number of resonances in the corresponding regions separated by the heavy curves: (a) *V* schemes; (b) Λ schemes; (c) Ξ schemes.

the levels coupled by the strong field. The Autler-Townes doublet in the anti-Stokes component vanishes in the *V* or Λ scheme with codirected waves. Similarly, in a four-level system with strong fields on neighboring

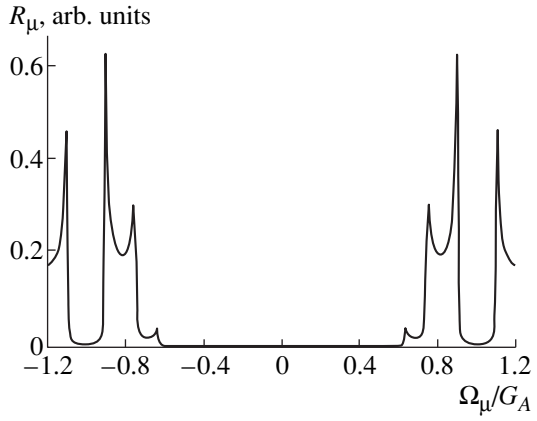

Fig. 6. The work performed by the probe field on the transition 2–3 as a function of the detuning Ω_μ for the scheme shown in the inset in Fig. 2: $G_B = 0.1G_A$, $k_A v_T = 7G_A$, $k_\mu v_T = 5.8G_A$, $k_B v_T = 5G_A$, and $\Gamma = 0.001G_A$.

transitions the maximum number of narrow peaks in the spectrum (up to four) is possible when a level coupled by the probe field with a three-level subsystem falls between its levels. For stationary atoms the number of resonances is three. Thermal motion increases this number to four. If the strong fields are applied on opposite transitions (see inset in Fig. 3), then the number of peaks is also sensitive to the relative arrangement of the two-level subsystems. There are no resonances if the subsystems lie at a different height on the energy scale. There will be more peaks if the intervals of the energies of the subsystems overlap. The number of resonances is maximum when both levels of one subsystem fall between the levels of another subsystem. In the latter case the number of peaks in the spectrum reaches 8, while for stationary atoms only four peaks are possible in a four-level system.

An example of a probe-field spectrum with the maximum number of peaks is presented in Fig. 6. It was obtained numerically using a simple program which inverts the matrix of the system using Gauss' method and integrates over velocities using Simpson's rule. In previous works on the experimental and theoretical investigation of the spectra of multilevel systems, the number of peaks observed was smaller probably because the parameter range that had to be reached in order for the maximum number to be obtained was quite narrow.

We shall now indicate some recent works devoted to three- and four-level systems with large Doppler broadening and interacting with strong fields. A four-wave mixing scheme was studied in [14]. The energies of dressed states, differing from the frequency branches by an added linear function of the velocity, were found. The dependences of the mixing ratio on the ratio of the Rabi frequencies were obtained. In [15] and [16], which are devoted to coherent effects in Doppler-broadened medium, cascade and *V*-like three-level sys-

tems, respectively, were studied. In these works the frequency branches with no turning points and with two turning points were represented, and the group spectra were calculated. A numerical calculation gave two resonant peaks in accordance with the concepts expounded above.

In [11] a four-level system with two strong fields on opposite transitions was studied. A so-called down-conversion scheme, shown in the inset in Fig. 2, was analyzed. Only six peaks were found in the calculation, though there were eight turning points, which is explained by the symmetry of the system studied ($k_\mu = (1/2)(k_A + k_B)$, $\Omega_A = \Omega_B = 0$). Two pairs of turning points contributed to the same peaks.

The effect of nonlinear interference processes on Doppler-broadened transitions in the scheme shown in Fig. 3 (second scheme at the top) was investigated in [12]. In this scheme six peaks can in principle be observed, and up to five peaks were found numerically. A "ladder" four-level scheme with two strong fields on adjoining transitions was investigated in [17]. The directions of propagation of the waves on successive transitions of a cascade alternated, so that the scheme reduces to the one shown in Fig. 5b (third scheme from the top). Up to four resonant peaks can exist in this scheme. However, the authors confine their attention to the case where the Rabi frequency of the strong field is much larger than the Doppler width. Then the neighborhood of only one turning point contributes to the probe-field spectrum, so that only one peak is found in this work. Narrow peaks in a degenerate four-wave mixing in Rb vapors were found in the experimental work [18]. The Doppler shifts were compensated, so that up to three peaks were observed.

5. CONCLUSIONS

The multipeak structures predicted for the probe-field spectrum are not confirmed experimentally. It would be especially interesting to check the degenerate cases where turning points merge, leading to a sharp increase of the nonlinear susceptibility. Considering the sensitivity of the number of peaks to the parameters of the problem, the experiment should be designed in accordance with the recommendations presented: (1) the lasers should be stable enough so that random frequency drifts do not destroy the assumption that the relaxation constants are small; (2) the medium should be rarefied, so that collisions do not increase the relaxation; (3) the angular momenta of the levels and the polarization of the fields must be chosen so that the effect does not disappear on averaging over the projections of the angular momenta; and (4) the medium should be thin compared with the absorption length of strong fields, which can smear the peaks.

ACKNOWLEDGMENTS

We thank S.A. Babin, S.G. Rautian, and A.M. Shalagin for helpful discussions. This work was supported by the Russian Foundation for Basic Research (projects no. 97-02-00016 and 96-15-96642) and the programs of the Ministry of Science and Technology: optics, laser physics (1.53) and fundamental spectroscopy (08.02.32). One of us (M.G.S.) is grateful to INTAS for support: 96-0457 as part of a program of the International Center for Fundamental Physics in Moscow.

APPENDIX

Let us consider a n-level system interacting resonantly with several monochromatic electromagnetic waves. The evolution of the atomic wave functions satisfies the Schrödinger equation

$$i\frac{d\mathbf{a}}{dt} = \hat{\mathcal{H}}\mathbf{a}, \quad \hat{\mathcal{H}} = \hat{\mathcal{H}}_0 + \hat{\mathcal{H}}_{\text{int}}(t), \tag{26}$$

where $\mathbf{a} = (a_1, \ldots, a_n)^T$ is a column vector of the probability amplitudes of the states $|i\rangle$, $i = 1, \ldots, n$; $\hat{\mathcal{H}}_0$ is the atomic Hamiltonian, and $\hat{\mathcal{H}}_{\text{int}}(t)$ describes the interaction of an atom with the electromagnetic field.

In the present work we shall confine our attention to interaction schemes for which Eq. (26) can be put into a form with a time-independent Hamiltonian $\hat{H}$ using a unitary transformation

$$A_j = a_j \exp(i\delta_j t), \quad j = 1, \ldots, n.$$

A sufficient condition for the existence of such a transformation is simultaneous satisfaction of the relations $\delta_j - \delta_i = \omega_\nu$, where ω_ν is the frequency of the wave in resonance with the transition $i \longrightarrow j$, and $E_i < E_j$. Let us consider a collection of levels coupled with one another by strong fields whose Rabi frequencies are much larger than the relaxation constants of the levels, $G \gg \Gamma$. The energies of the dressed states of such a subsystem "repel" one another by an amount of the order of the Rabi frequencies G. To obtain narrow spectral structures the probe field must couple levels belonging to two different subsystems.

Let us consider the absorption spectrum $P_\mu(\Omega_\mu)$ of a probe field with frequency ω_μ, which couples the levels i and j from the first and second subsystems, respectively, where $\Omega_\mu = \omega_\mu - (E_j - E_i)/\hbar$ is the detuning of the probe wave from resonance and $E_i < E_j$. The Hamiltonian $\hat{H}$ can be written in the form

$$\hat{H} = \begin{pmatrix} \hat{H}_A & \delta\hat{H} \\ \delta\hat{H}^\dagger & \hat{H}_B + \Omega_\mu \hat{I} \end{pmatrix}, \tag{27}$$

where $\hat{I}$ is a unit matrix and $\delta\hat{H}$ is a small perturbation proportional to the amplitude of the probe field. The matrices $\hat{H}_A$ and $\hat{H}_B$ do not contain the parameters of the weak field. Neglecting the amplitude of the weak

field, the secular equation $|\hat{H} - \Lambda\hat{I}| = 0$ separates into two equations

$$|\hat{H}_A - \Lambda\hat{I}| = 0, \quad |\hat{H}_B + \Omega_\mu\hat{I} - \Lambda\hat{I}| = 0.$$

We denote the normalized eigenvectors and eigennumbers of these two subsystems as $\mathbf{A}^I$, λ_A^I, and $\mathbf{B}^J$, $\Omega_\mu + \lambda_B^J$, respectively, where the superscripts enumerate the eigenvectors and the subscripts denote the subsystem.

For example, for a four-wave system (see inset in Fig. 2) the Hamiltonian has the form (27), where

$$\hat{H}_A = \begin{pmatrix} \Omega_A & -G_A \\ -G_A^* & 0 \end{pmatrix},$$
$$\hat{H}_B = \begin{pmatrix} 0 & -G_B \\ -G_B^* & -\Omega_B \end{pmatrix}, \quad \delta\hat{H} = \begin{pmatrix} 0 & 0 \\ -G_\mu^* & 0 \end{pmatrix}. \tag{28}$$

The eigenvalues of the matrices $\hat{H}_A$ and $\hat{H}_B$ can be written in the form

$$\lambda_A^{1,2} = \frac{1}{2}(\Omega_A \pm \sqrt{\Omega_A^2 + 4|G_A|^2}),$$
$$\lambda_B^{1,2} = -\frac{1}{2}(\Omega_B \pm \sqrt{\Omega_B^2 + 4|G_B|^2}). \tag{29}$$

Let one level in the subsystem, described by the operator $\hat{H}_A$, be occupied initially. Then the time dependence of the wave function $\mathbf{A}(t)$ can be represented in the form

$$\mathbf{A}(t) = \sum_{I=1}^{n_A} \mathbf{A}^I \exp(-i\lambda_A^I t)(\mathbf{A}^I, \mathbf{A}^0), \tag{30}$$

where

$$(\mathbf{X}, \mathbf{Y}) = \sum_{\nu=1}^{n} X_\nu^* Y_\nu$$

is the scalar product of the vectors $\mathbf{X}$ and $\mathbf{Y}$, $\mathbf{A}^0 = \mathbf{A}(t)|_{t=0}$ is the initial wave function normalized to one, and n_A is the number of levels in the subsystem A. Substituting the solution obtained into the equation for $\mathbf{B}$ in first-order perturbation theory in the amplitude of the probe field we obtain

$$i\frac{d\mathbf{B}}{dt} = \delta\hat{H}^\dagger\mathbf{A} + (\hat{H}_B + \Omega_\mu\hat{I})\mathbf{B}. \tag{31}$$

Solving the system of equations we obtain

$$\mathbf{B} = -\sum_{I=1}^{n_A}\sum_{J=1}^{n_B} \mathbf{B}^J \exp[-i(\lambda_B^J + \Omega_\mu)t]$$
$$\times (\mathbf{B}^J, (\lambda_A^I - (\Omega_\mu + \hat{H}_B))^{-1}\delta\hat{H}^\dagger\mathbf{A}^I)(\mathbf{A}^I, \mathbf{A}^0)$$
$$+ \sum_{I=1}^{n_A} \exp(-i\lambda_A^I t)[(\lambda_A^I - (\Omega_\mu + \hat{H}_B))^{-1}\delta\hat{H}^\dagger\mathbf{A}^I](\mathbf{A}^I, \mathbf{A}^0),$$

where n_B is the number of levels in the subsystem B.

The work performed by the probe field can be calculated using the formula (see, for example, [5])

$$R_\mu(\Omega_\mu) = -2\hbar\omega_\mu \mathrm{Re}\left[iG_\mu^* \int_0^\infty dt e^{-\Gamma t} A_i^*(t) B_j(t)\right]$$
$$= -2\hbar\omega_\mu \mathrm{Re}\left[G_\mu^* \sum_{I,I'=1}^{n_A}\sum_{J=1}^{n_B} B_j^J (A_i^I)^* (\mathbf{A}^0, \mathbf{A}^I)(\mathbf{A}^{I'}, \mathbf{A}^0)\right.$$
$$\times (\mathbf{B}^J, \delta\hat{H}^\dagger\mathbf{A}^{I'})[\Gamma + i(\Omega_\mu - \lambda_A^I + \lambda_B^J)]^{-1}$$
$$\left.\times [\Gamma - i(\lambda_A^I - \lambda_A^{I'})]\right]^{-1}.$$

In this sum the terms with $I = I'$ contain the small parameter Γ in the denominator, since the difference $\lambda_A^I - \lambda_A^{I'}$ vanishes. The other terms in the sum (for $I \neq I'$) can be neglected, since they are small to the extent that the parameter Γ/G is small. In this approximation the power absorption wave per unit volume $P_\mu(\Omega_\mu) = \Gamma N R_\mu(\Omega_\mu)$ can be written in the form

$$P_\mu(\Omega_\mu) = 2\hbar\omega_\mu$$
$$\times \mathrm{Re}\sum_{I=1}^{n_A}\sum_{J=1}^{n_B} \frac{N|G_\mu|^2 |B_j^J A_i^{*I}(\mathbf{A}^0, \mathbf{A}^I)|^2}{\Gamma + i(\Omega_\mu - \lambda_A^I + \lambda_B^J)}, \tag{32}$$

where N is the equilibrium population.

To take account of the Doppler effect for particles moving with velocity u, the detuning Ω_ν of all fields must be replaced by $\Omega_\nu - k_\nu u$ and the expression obtained must be averaged over the velocities. We shall now use the graphical method, formulated in Section 2, to calculate the peaks in the probe-field spectrum. The condition $\Delta^{IJ}(u, \Omega_\mu) = 0$, where

$$\Delta^{IJ}(u, \Omega_\mu) = \Omega_\mu - k_\mu u - \lambda_A^I(u) + \lambda_B^J(u) \tag{33}$$

determines the frequency branches $\Omega_\mu = \Omega_p^{IJ}(u) = k_\mu u + \lambda_A^J(u) - \lambda_B^J(u)$. The conditions for an extremum of the frequency branches give the turning points (u, Ω_p) in the $(u_p^{IJ}, \Omega_p^{IJ}(u_p^{IJ}))$ plane. For detunings $\Omega_\mu = \Omega_p^{IJ}(u_p^{IJ})$ narrow resonances are observed in the probe-field spectrum. The number of such resonances is determined by

the number of turning points. In the limit of small Γ the contribution of each turning point to the work performed by the field can be studied independently:

$$P_\mu(\Omega_\mu) = \sum_I^{n_A}\sum_J^{n_B} P^{IJ}(\Omega_\mu),$$
$$P^{IJ}(\Omega_\mu) = \mathrm{Re}\int_{-\infty}^{\infty} \frac{C^{IJ}(u)du}{\Gamma + i[\Omega_\mu - k_\mu u - \lambda_A^I(u) + \lambda_B^J(u)]}, \quad (34)$$

where $C^{IJ}(u)$ is the numerator in the expression (32). Since there can be several turning points for a fixed frequency branch, we shall enumerate them with the index m. Then $P^{IJ}(\Omega_\mu)$ can be written approximately as a sum over all turning points:

$$P^{IJ}(\Omega_\mu) \approx \pi\sum_m C^{IJ}((u_p^{IJ})_m)$$
$$\times \mathrm{Re}\sqrt{\frac{1}{a_m^{IJ}[\Omega_\mu - (\Omega_p^{IJ}((u_p^{IJ})_m) + i\Gamma)]}},$$
$$a_m^{IJ} = \frac{1}{2}\frac{d^2\Omega_p^{IJ}(u)}{du^2}\bigg|_{u=(u_p^{IJ})_m}.$$

The total number of narrow resonances in the spectrum can be determined by summing over the frequency branches and over the turning points of each branch.

REFERENCES

1. A. Feitisch, D. Schnier, T. Müller, and B. Wellegehausen, IEEE J. Quantum Electron. **24**, 507 (1988).
2. A. A. Apolonsky, S. A. Babin, A. I. Chernykh, *et al.*, Phys. Rev. A **55**, 661 (1997).
3. J. C. Petch, C. H. Keitel, P. L. Knight, and J. P. Marangos, Phys. Rev. A **53**, 543 (1996).
4. A. Apolonsky, S. Baluschev, U. Hinze, *et al.*, Appl. Phys. B **64**, 435 (1997).
5. S. G. Rautian, G. I. Smirnov, and A. M. Shalagin, *Nonlinear Resonances in Atomic and Molecular Spectra* (Nauka, Novosibirsk, 1979).
6. B. J. Feldman and M. S. Feld, Phys. Rev. A **5**, 899 (1972).
7. O. G. Bykova, V. V. Lebedeva, N. G. Bykova, and A. V. Petukhov, Opt. Spektrosk. **53**, 171 (1982) [Opt. Spectrosc. **53**, 101 (1982)].
8. N. G. Bykova, O. G. Bykova, V. V. Lebedeva, *et al.*, Preprint No. 26-84, ITPM SO AN SSSR (Novosibirsk, 1984).
9. M. G. Stepanov and D. A. Shapiro, Pis'ma Zh. Éksp. Teor. Fiz. **68**, 27 (1998) [JETP Lett. **68**, 29 (1998)].
10. S. A. Babin, E. V. Podivilov, and D. A. Shapiro, Pis'ma Zh. Éksp. Teor. Fiz. **66**, 777 (1997) [JETP Lett. **66**, 816 (1997)].
11. S. A. Babin, E. V. Podivilov, D. A. Shapiro, *et al.*, Phys. Rev. A **59**, 1355 (1999).
12. A. K. Popov and S. A. Myslivets, Kvantovaya Élektron. (Moscow) **24**, 1033 (1997).
13. M. D. Lukin, P. R. Hemmer, M. Löffer, and M. O. Scully, Phys. Rev. Lett. **81**, 2675 (1998).
14. C. H. Keitel, Phys. Rev. A **57**, 1412 (1998).
15. S. Shepherd, D. J. Fulton, and M. H. Dunn, Phys. Rev. A **54**, 5394 (1996).
16. J. R. Boon, E. Zekou, D. McGloin, and M. H. Dunn, Phys. Rev. A **58**, 2560 (1998).
17. A. K. Popov and V. M. Shalaev, Phys. Rev. A **59**, R946 (1999).
18. Jun Lin, A. I. Rubiera, and Yifu Zhu, Phys. Rev. A **52**, 4882 (1995).

Translation was provided by AIP

Journal of Experimental and Theoretical Physics, Vol. 91, No. 2, 2000, pp. 298–306.
Translated from Zhurnal Éksperimental'noĭ i Teoreticheskoĭ Fiziki, Vol. 118, No. 2, 2000, pp. 340–350.

ATOMS, SPECTRA, RADIATION

Phase and Group Synchronization in Second-Harmonic Generation of Ultrashort Light Pulses in One-Dimensional Photonic Crystals

A. M. Zheltikov*, A. V. Tarasishin, and S. A. Magnitskiĭ

International Center for Lasers, Moscow State University, Moscow, 119899 Russia
**e-mail: zheltikov@nlsl.ilc.msu.su*

Received March 14, 2000

Abstract—It is shown, on the basis of an analysis of the dispersion relation for an infinite one-dimensional periodic multilayer structure and direct numerical integration of Maxwell's equations by the finite-difference method, that structures with photonic band gaps (PBGs) make it possible to provide simultaneously conditions for phase and group synchronizations for second-harmonic generation with participation of extremely short light pulses. The phase and group detunings, which arise as a result of the dispersion of the nonlinear medium, are compensated by the dispersion of the PBG structure. The use of this regime of nonlinearly optical interactions opens up the possibility of attaining high frequency conversion efficiencies irrespective of the synchronization length in the interior volume of a nonlinear material. © *2000 MAIK "Nauka/Interperiodica".*

1. INTRODUCTION

Despite the impressive progress made in the last few years in understanding the properties of photonic crystals, or structures with photonic band gaps (PBGs), many fundamental physical aspects of nonlinearly optical interactions in photonic crystals and many possibilities which open up in this promising and interesting field of modern physics [1], once again remain little studied. One of the main applications of photonic crystals in nonlinear optics is associated with new possibilities for increasing the efficiency of second-harmonic generation (SHG) for extremely short light pulses, which at present are of special interest in connection with the widespread use of compact and economic solid-state femtosecond laser systems and substantial difficulties in doubling the frequency of ultrashort laser pulses. Providing phase and group synchronizations is one of the main problems of second-harmonic generation using ultrashort light pulses. Periodically nonuniform crystals [2–4], where the condition for quasisynchronous, with respect to the phase, interaction are attained by modulation of the quadratic susceptibility of the medium with a spatial period of the order of the coherent length of the nonlinearly optical interaction, are now being used widely to increase the second harmonic generation efficiency (the idea of phase quasisynchronization was proposed in one of the pioneering works on nonlinear optics [5] back in 1962).

In contrast to crystals for quasisynchronous interaction, PBG structures are characterized by a spatially periodic modulation not of the nonlinearly optical susceptibility but rather the refractive index. The characteristic spatial scale of the variation of the refractive index in PBG structures is of the order of the optical wavelength, i.e., much shorter than the modulation period of the nonlinearly optical susceptibility in structures for quasisynchronous interaction. The idea of using dispersion of periodic structures to compensate the material dispersion of the medium in order to provide phase synchronization conditions during second-harmonic generation and nonlinearly optical frequency mixing was advanced quite a long time ago [6]. Experimental investigations [7] have confirmed that this approach is promising. However, at the present stage of development of laser technology the problem of effective conversion of the frequency of short light pulses becomes urgent. Experiments on SHG in one-dimensional PBG structures [10] with a lattice defect [8], three-dimensional colloidal photonic crystals [9], and porous silicon PBG structures have demonstrated the possibility of controlling the phase-matching conditions in nonlinear optical interaction of short light pulses as a result of using the dispersion of the periodic structure.

Most works performed thus far on nonlinearly optical frequency conversion in photonic crystals are based on the idea of increasing the efficiency of frequency conversion by improving the phase matching conditions and a local increase in the field in the PBG structure. This approach is substantially limited by the fact that the width of the spectral region, where substantial increase of the second harmonic generation efficiency can be achieved, under these conditions is limited by the width of the resonance in the transmission spectrum of the one-dimensional PBG structure with a finite number of periods (see [11, 12]). As the number of periods of the PBG structure increases, the width of the transmission resonance decreases; this imposes increasingly more stringent requirements on the pulse duration.

1063-7761/00/9102-0298$20.00

The objective of the present work is to show that such an approach by no means exhausts the possibilities of PBG structures for increasing the efficiency of nonlinearly optical frequency conversion processes. Analysis of the dispersion relation for an infinite one-dimensional PBG structure and direct numerical integration of Maxwell's equations by the finite-difference method makes it possible to conclude that one-dimensional PBG structures make it possible to implement a new type of synchronization for the second harmonic generation process with participation of extremely short light pulses. In the process conditions are ensured not only for phase but also group synchronization; this makes it possible to increase the growth rate of the second-harmonic signal as a function of the nonlinearly optical interaction length as compared with the structures for quasisynchronous interactions and they open up the possibility of attaining high frequency-doubling efficiencies irrespective of the synchronization length in the interior volume of the nonlinear material.

In Section 2 we shall investigate the dispersion relation for the model of an infinite one-dimensional PBG structure and we shall obtain the conditions for phase and group synchronizations for the second harmonic generation process. The conditions for phase and group synchronizations are investigated for PBG structures without dispersion of the refractive indices of the layers comprising the structure (Subsection 2.1) and for PBG structures with material dispersion (Subsection 2.2). In Section 3 the SHG process with participation of ultrashort pulses in one-dimensional PBG structures is investigated by solving Maxwell's equations numerically; this method makes it possible to do away with the limitations associated with the approximation of slowly varying amplitudes. The method used to solve the problem is described in Subsection 3.1. The results of the investigation of the dependence of the second harmonic generation efficiency on the pulse duration and the pumping wavelength as well as the nonlinearly optical interaction length are presented in Subsection 3.2. In the Conclusions the basic results of the investigation are briefly summarized and the possibilities of practical applications of PBG structures for doubling the frequency of ultrashort laser pulses are discussed.

2. INFINITE PERIODIC STRUCTURE MODEL

To illustrate the idea of second harmonic generation in the field of ultrashort pulses in photonic crystals under conditions of phase and group synchronizations we shall examine the dispersion properties of an infinite model PBG structure consisting of periodically alternating layers with dimensions a and b and refractive indices n_a and n_b, respectively. The infinite PBG structure model, as will be shown below on the basis of a comparison of the results of analytical calculations and the data from numerical calculations, makes it possible to reproduce adequately the basic properties of nonlinearly optical interactions with the participation of quite short pulses, when the number of field periods in a pulse is much smaller than the number of periods of the PBG structure. We shall assume that layers with a refractive index n_b possess quadratic nonlinearity, leading to second-harmonic generation. We shall examine first the case of SHG in a one-dimensional PBG structure without dispersion of the constituent materials and then we shall extend these results to the case of PBG structures with the participation of material dispersion.

2.1. Period Structure without Material Dispersion

2.1.1. Phase synchronization. The phase synchronization condition for wave vectors $k(\omega)$ and $k(2\omega)$ of the pump and second-harmonic radiations participating in the SHG process is written in the form

$$k(2\omega) = 2k(\omega). \tag{1}$$

The wave vectors of the radiation at the fundamental frequency and at the second-harmonic frequency can be obtained from the dispersion relation for the infinite one-dimensional PBG structure considered (the thick line in Fig. 1) [13]:

$$\cos(k(\omega_0)d) = \cos\left(\frac{\omega_0}{c}n_a a\right)\cos\left(\frac{\omega_0}{c}n_b b\right) - \frac{n_a^2 + n_b^2}{2n_a n_b}\sin\left(\frac{\omega_0}{c}n_a a\right)\sin\left(\frac{\omega_0}{c}n_b b\right), \tag{2}$$

$$\cos(k(2\omega_0)d) = \cos\left(\frac{2\omega_0}{c}n_a a\right)\cos\left(\frac{2\omega_0}{c}n_b b\right) - \frac{n_a^2 + n_b^2}{2n_a n_b}\sin\left(\frac{2\omega_0}{c}n_a a\right)\sin\left(\frac{2\omega_0}{c}n_b b\right), \tag{3}$$

where $d = a + b$ is the period of the PBG structure.

Using the relations (2) and (3), the phase synchronization condition (1) can be written as

$$\cos^2(Ak_0) + \cos^2(Bk_0) - \cos^2(Ak_0)\cos^2(Bk_0) = 1, \tag{4}$$

where $k_0 = \omega_0/c$ and

$$A = n_a a, \quad B = n_b b, \quad N = \frac{n_a^2 + n_b^2}{2n_a n_b}.$$

The Eq. (4) is satisfied when one of the squared cosines is 1. We shall assume for definiteness that $\cos^2(Ak_0) = 1$, which is equivalent to the relation

$$a = \frac{\lambda l}{2n_a}, \tag{5}$$

where l is an integer.

Thus, when one of the subsystems of an infinite one-dimensional PBG structure without material dispersion is a collection of half-wave plates, i.e., the parameter a

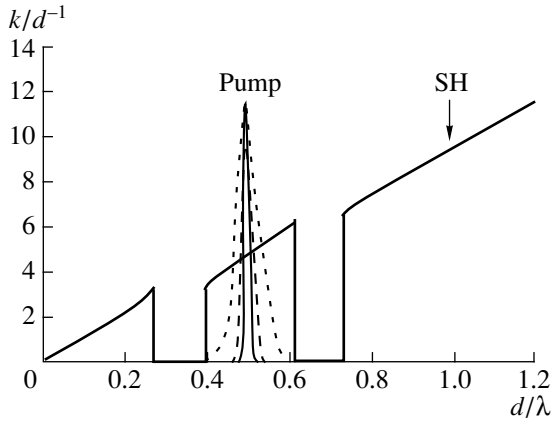

Fig. 1. Dispersion of an infinite one-dimensional PBG structure with parameters $a = \lambda/2n_a$, $b = \lambda/4n_b$, $n_a = 2$, and $n_b = 1$ (heavy curve). The fine solid, dashed, and dotted curves show the spectrum of a pump pulse with duration $10T_0$, $5T_0$, and $2T_0$ (T_0 is the period of the optical field), respectively. The arrow indicates the wave number of the second harmonic.

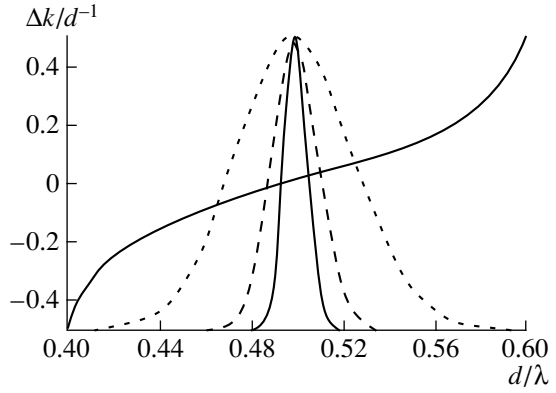

Fig. 2. Phase detuning Δk versus the wave number of the pump radiation for a one-dimensional PBG structure with the parameters $n_a = 2$, $a = \lambda/2n_a$, $n_b = 1$, $b = \lambda/4n_b$ (heavy line). The fine solid, dashed, and dotted curves show the spectrum of a pump pulse with duration $10T_0$, $5T_0$, and $2T_0$, respectively.

is chosen in accordance with Eq. (5), phase synchronization is always attained for second-harmonic generation (Fig. 1). The physical meaning of the condition (5) is that when this condition is satisfied, one of the subsystems of the PBG structure leads a phase shift of the light wave by a multiple of π. The phase of the radiation propagating in the PBG structure changes since it would change in a medium with a uniform distribution of the refractive index. In other words, the condition (5) means that the fundamental and second-harmonic frequencies lie in the range where the dispersion of the structure can be approximated by a linear function (Fig. 1). Since at this stage of the analysis we neglect material dispersion, this condition means that the phase synchronization condition is satisfied.

To understand the characteristic features of the second harmonic generation process for extremely short light pulses, it is also important to note that the phase synchronization conditions (5) for this process in a PBG structure can be satisfied only in a finite spectral range (Figs. 1 and 2). For a quantitative description of phase synchronization in second harmonic generation with participation of ultrashort pulses in a PBG structure, we introduce a phase detuning Δk as the difference of the wave vector of the second harmonic and the doubled pump wave vector with the pump frequency detuned by an amount equal to the half-width $\Delta\omega_0$ of the pulse spectra with respect to the e^{-1} level:

$$\Delta k = 2k(\omega_0 + \Delta\omega_0/2) - k(2\omega_0 + \Delta\omega_0).$$

Analysis of the dispersion relation for a one-dimensional PBG structure with refractive index $n_a = 2$, $a = \lambda/2n_a$, $n_b = 1$, $b = \lambda/4n_b$, detuning of the wave vectors for a pulse with duration $10T_0$ (where T_0 is the duration of a period of the light field, and the pulse duration is determined according to the level equal to e^{-1} times the maximum intensity) reaches $3.4 \times 10^{-2}\lambda^{-1}$ (Fig. 2). The synchronization length $l_{ph} = \pi/\Delta k$ in a PBG structure can be estimated as $184d$. As the pulse duration decreases, the phase detuning increases, since the width of the spectrum increases and the synchronization length decreases (Figs. 1 and 2). The data obtained in numerical calculations performed for the second harmonic generation process in a finite one-dimensional PBG structure by the method of integrating Maxwell's equations (see Section 3) confirm the results of this qualitative analysis.

The phase detuning and together with it the synchronization length for the SHG process in a one-dimensional PBG structure for pulses with a prescribed duration depends on the contrast n_a/n_b of the refractive indices of the layers comprising the PBG structure. This dependence is illustrated in Fig. 3. It is obvious that the dispersion of the PBG structure increases as the contrast n_a/n_b of the refractive indices increases. In the absence of material dispersion this means that decreasing the contrast of the refractive indices makes it possible to attain large synchronization lengths for the second harmonic generation process with the participation of ultrashort pulses. Specifically, for a pulse with duration $10T_0$ we obtain

$$\Delta k = 3.4 \times 10^{-2}\lambda^{-1}, \quad l_{ph} = 184d \text{ for } n_a/n_b = 2;$$

$$\Delta k = 1.0 \times 10^{-2}\lambda^{-1}, \quad l_{ph} = 538d \text{ for } n_a/n_b = 1.5;$$

$$\Delta k = 2.6 \times 10^{-3}\lambda^{-1}, \quad l_{ph} = 1857d \text{ for } n_a/n_b = 1.25;$$

$$\Delta k = 7 \times 10^{-4}\lambda^{-1}, \quad l_{ph} = 6461d \text{ for } n_a/n_b = 1.125.$$

To perform these calculations the period of the structure was not a fixed quantity, but rather it was chosen in accordance with the formula

$$d = \frac{\lambda}{4n_b}\left(1 + \frac{2n_b}{n_a}\right)$$

in a manner so that the subsystems of the PBG structure would consist of collections of half-wave and quarter-wave plates.

In real PBG structures with dispersion of the refractive indices of the materials of the layers, changing the ratio n_a/n_b makes it possible to compensate the phase detuning of the pulses of the fundamental radiation and the second harmonic arising as a result of the material dispersion. In the process, the PBG structure with a large contrast of the refractive index make it possible to compensate large phase detunings associated with the material dispersion (see Fig. 3 and Section 3).

2.1.2. Group synchronization. We shall show that when the condition (5) holds in a PBG structure without material dispersion the condition of group synchronization automatically holds for the SHG process:

$$\left.\frac{\partial k(\omega)}{\partial \omega}\right|_{\omega=\omega_0} = \left.\frac{\partial k(\omega)}{\partial \omega}\right|_{\omega=2\omega_0}. \tag{6}$$

Using the relations (2) and (3) we obtain

$$\begin{aligned}\left.\frac{\partial k(\omega)}{\partial \omega}\right|_{\omega=\omega_0} &= \frac{1}{cd\sin(k(\omega_0)d)}\\ &\times((B+AN)\cos(Ak_0)\sin(Bk_0)\\ &+(A+BN)\sin(Ak_0)\cos(Bk_0)).\end{aligned} \tag{7}$$

When the condition (5) is satisfied, the reciprocal of the group velocity at the fundamental frequency and the second harmonic frequency can be written in the form

$$\left.\frac{\partial k(\omega)}{\partial \omega}\right|_{\omega=\omega_0,\,2\omega_0} = \frac{\pm(B+AN)}{cd}. \tag{8}$$

Since the radiation passing through a PBG structure corresponds to positive values of the group velocity, we obtain that the conditions of group synchronization are also satisfied for a PBG structure without dispersion with parameters satisfying the relation (5). From the physical standpoint, the attainment of group of synchronization for the SHG process in one-dimensional PBG structures under the condition (5) is due, similarly to phase synchronization, to the fact that the phase of the radiation propagating in a PBG structure changes in the same way that it would change in a medium with a uniform distribution of the refractive index. The dispersion of such a structure is described by a linear function of the frequency; this means that the condition for group synchronization is satisfied.

2.1.3. Dispersion of the group velocity. Questions concerning the spreading of pulses in a PBG structure on account of dispersion of the group velocity are extremely important for the SHG process with the participation of extremely short pulses. To study the spreading of pump and second-harmonic pulses in a PBG structure, we shall calculate the second derivatives of the wave vectors for these pulses in an infinite one-dimensional PBG structure, using the expressions (2) and (3). After uncomplicated but laborious calculations we obtain

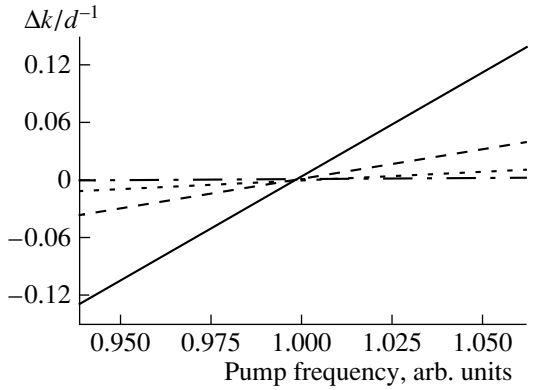

Fig. 3. Phase detuning versus the frequency of the pump radiation for the second-harmonic generation process in a one-dimensional PBG structure with various values of the refractive index contrast n_a/n_b of the layers for pulses with duration $10T_0$: $n_a/n_b = 2.0$ (solid line), 1.5 (dashed line), 1.25 (dotted line), and 1.125 (dash–dotted line).

$$\left.\frac{\partial^2 k(\omega)}{\partial \omega^2}\right|_{\omega=\omega_0} = \frac{\cos(Bk_0)\sin(Bk_0)}{\sin^2(Bk_0)}\frac{A^2(1-N^2)}{c^2 d}, \tag{9}$$

$$\begin{aligned}&\left.\frac{\partial^2 k(\omega)}{\partial \omega^2}\right|_{\omega=2\omega_0}\\ &= \frac{\cos(2Bk_0)\sin(2Bk_0)}{\sin^2(2Bk_0)}\frac{A^2(1-N^2)}{c^2 d}.\end{aligned} \tag{10}$$

It is easy to see that the right-hand sides of Eqs. (9) and (10) vanish when

$$\begin{aligned}\cos(Bk_0) = 0,\quad Bk_0 &= \frac{\pi}{2}+\pi m,\\ b &= \frac{\lambda}{4n_b}(1+2m),\end{aligned} \tag{11}$$

where m is an integer.

When this condition is satisfied, the dispersion of the group velocity at the fundamental frequency and at the second-harmonic frequency vanishes, i.e., in the second approximation of the dispersion theory the pulses propagate with constant envelopes through the structure. Thus, when the dispersion of the layers comprising the PBG structure is small compared with the dispersion of the periodic structure, there exist conditions for which the phase and group synchronization conditions are satisfied simultaneously and the dispersion of the group velocity at the fundamental and second-harmonic frequencies is small (or zero for zero material dispersion). In the absence of material dispersion these conditions are satisfied for one-dimensional PBG structures consisting of alternating half- and quarter-wave plates. Evidently, such PBG structures give

optimal conditions for doubling the frequency of extremely short pulses. This conclusion is confirmed by the results of numerical calculations, which are presented in Section 3, and is important for understanding the results of these calculations.

2.2. Periodic Structure with Frequency Dispersion of the Nonlinear Layer

In the present section we shall extend the results obtained above for SHG in an infinite one-dimensional PBG structure to a PBG structure where, aside from dispersion of the structure, it is also necessary to take into account the dispersion of the medium, and we shall find the conditions for phase and group synchronization for this case. For simplicity, we shall consider a PBG structure consisting of layers with thickness a and refractive index n_a with no nonlinearity and negligibly small dispersion and quadratically nonlinear layers of thickness b and with frequency-dependent refractive index $n_b(\omega)$. Then the wave vectors at the pump frequency and the second-harmonic frequency can be written in the form

$$\cos(k(\omega_0)d) = \cos\left(\frac{\omega_0}{c}n_a a\right)\cos\left(\frac{\omega_0}{c}n_{1b}b\right) - \frac{n_a^2 + n_{1b}^2}{2n_a n_{1b}}\sin\left(\frac{\omega_0}{c}n_a a\right)\sin\left(\frac{\omega_0}{c}n_{1b}b\right), \quad (12)$$

$$\cos(k(2\omega_0)d) = \cos\left(\frac{2\omega_0}{c}n_a a\right)\cos\left(\frac{2\omega_0}{c}n_{2b}b\right) - \frac{n_a^2 + n_{2b}^2}{2n_a n_{2b}}\sin\left(\frac{2\omega_0}{c}n_a a\right)\sin\left(\frac{2\omega_0}{c}n_{2b}b\right). \quad (13)$$

Here n_{1b} and n_{2b} are the refractive indices of the nonlinear medium at the pump and second-harmonic frequencies, respectively. The phase synchronization condition can be written, once again, in the form (1).

The reciprocals of the group velocities of the pump and second-harmonic pulses are given by the following expressions:

$$\left.\frac{\partial k(\omega)}{\partial\omega}\right|_{\omega=\omega_0} = \frac{1}{cd\sin(k(\omega_0)d)} \times ((B_1 + AN_1)\cos(Ak_0)\sin(B_1k_0) + (A + B_1N_1)\sin(Ak_0)\cos(B_1k_0)), \quad (14)$$

$$\left.\frac{\partial k(\omega)}{\partial\omega}\right|_{\omega=2\omega_0} = \frac{1}{cd\sin(k(2\omega_0)d)} \times ((B_2 + AN_2)\cos(Ak_0)\sin(B_2k_0) + (A + B_2N_2)\sin(Ak_0)\cos(B_2k_0)), \quad (15)$$

where

$$A = n_a a, \quad B_{1,2} = n_{1b,2b}b, \quad N_{1,2} = \frac{n_a^2 + n_{1b,2b}^2}{2n_a n_{1b,2b}}.$$

The condition for group synchronization can be written in the form (6).

Thus, the condition for effective second-harmonic generation in a one-dimensional PBG structure, taking account of material dispersion and neglecting the dispersion of the group velocity, is that the equalities (1) must be satisfied simultaneously for the quantities (12) and (13) and the equality (6) must be satisfied for the quantities (14) and (15). At a prescribed pump wavelength and for prescribed values of the refractive indices n_a, n_{1b}, and n_{2b} this system of two Eqs. (1) and (6) can be solved for the parameters a and b. Thus the conditions for phase and group synchronizations can be satisfied simultaneously. It is obvious, however, that the transcendental system of Eqs. (1) and (6) does not have solutions for all values of the refractive indices n_a, n_{1b}, and n_{2b}. Specifically, an illustrative example is a PBG structure where one of the subsystems is a collection of half-wave plates, so that the condition (5) is satisfied. As shown above, in the absence of frequency dispersion of the media comprising the PBG structure, satisfaction of this condition makes it possible to attain phase and group synchronizations simultaneously. However, as can be easily verified by direct substitution of the values of the parameter a, determined by the condition (5), into Eqs. (12) and (13), if the nonlinear medium possesses dispersion of the refractive index $n_b(\omega)$, phase synchronization is impossible.

Physically, the condition of phase and group synchronizations for the SHG process in a PBG structure, where the nonlinear material is characterized by dispersion of the refractive index, is achieved by compensation of the dispersion of the material by the dispersion of the periodic structure. Consequently, as the dispersion of the nonlinear medium increases, increasingly higher values of the contrast of the refractive indices of the constituent media of the PBG structure are required in order to compensate the increasing, in this case, phase and group detunings. Solving the system of equations numerically using the gradient method makes it possible to establish the dependence of the minimum value of the contrast n_{1b}/n_a for which a simultaneous solution of the system of Eqs. (1) and (6) still exists on the quantity $(n_{2b} - n_{1b})/n_{1b}$, which is the difference of the refractive indices of the nonlinear medium at the second-harmonic and fundamental frequencies, normalized to the refractive index of this medium at the fundamental frequency. This dependence for a PBG structure with $n_{1b} = 1.5$ is displayed in Fig. 4. As one can see from the computational results presented in this figure, the dispersion of PBG structures with contrast of refractive indices which can be easily attained using existing technologies makes it possible to compensate

the detuning of the phase in group velocities for the SHG process in a quite wide range of dispersion of the nonlinear medium.

The possibility of attaining the conditions for phase and group synchronizations for the SHG process in a PBG structure, taking account of the material dispersion with an appropriate choice of the parameters of the PBG structure, is illustrated in Fig. 5 for a one-dimensional PBG structure for which $a \simeq 0.214\lambda$, $b \simeq 0.397\lambda$, $n_a = 1$, $n_{1b} = 1.5$, and $n_{2b} = 1.53$. In this case, to obtain synchronous SHG the pump frequency must be shifted into the short-wavelength region (closer to the band gap) compared with the case of a PBG structure with no material dispersion (Fig. 1), and the second harmonic frequency lies in the fourth band of allowed energies. The group velocity at the pump frequency is then approximately 1.63 times smaller than the velocity of light and therefore 1.09 times smaller than in the interior volume of a nonlinear medium with the same refractive index. Consequently, the second-harmonic generation efficiency can be expected to increase by 18%. The results of the numerical calculations presented in Section 3 agree, to a high degree of accuracy, with the results based on an infinite one-dimensional PBG structure model.

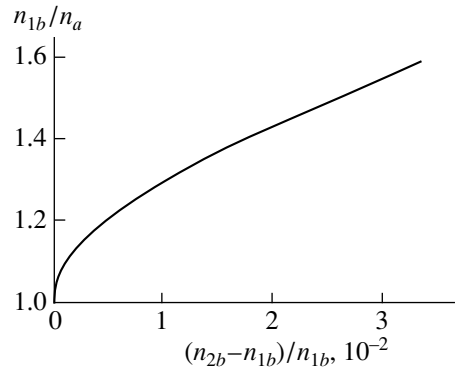

Fig. 4. The minimum value of the refractive index contrast n_{1b}/n_a for which the conditions of phase and group synchronization (1) and (6) can be satisfied simultaneously as a function of $(n_{2b} - n_{1b})/n_{1b}$.

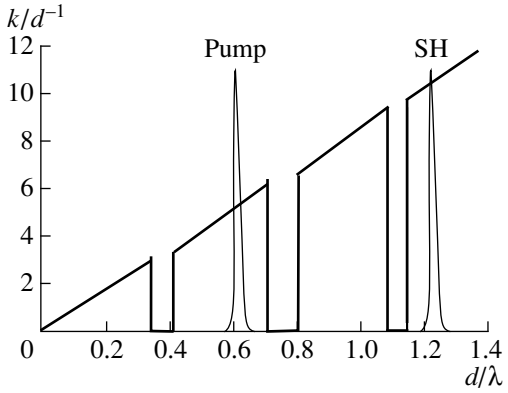

Fig. 5. Dispersion of an infinite one-dimensional PBG structure with the parameters $a \simeq 0.214\lambda$, $b \simeq 0.397\lambda$, $n_a = 1$, $n_{1b} = 1.5$, and $n_{2b} = 1.53$ (heavy line). The solid line shows the spectra of a pump pulse with duration $10T_0$ and the second harmonic.

3. NUMERICAL SIMULATION OF THE SECOND-HARMONIC GENERATION PROCESS

The calculation of the amplitude of the second harmonic arising as a result of the SHG process in a PBG structure is a complicated physical problem. As a rule, various modifications of the method of slowly varying amplitudes are used to solve it [11]. It is obvious that the approaches based on this approximation are inapplicable for ultrashort laser pulses [14–16]. In this connection, we performed a numerical calculation of the amplitude of the second harmonic, arising as a result of the SHG process, by solving Maxwell's equations numerically by the finite-difference method (finite difference time domain (FDTD) algorithm) [17]. As shown in [18–23], this approach is an effective method for analyzing the propagation of light and nonlinearly optical interactions with the participation of ultrashort light pulses in photonic crystals.

3.1. Computational Method

The FDTD method for a dispersive medium with cubic nonlinearity is described in [24]. We implemented the FDTD algorithm for a quadratically nonlinear medium with local response of nonlinearity and dispersion of the permittivity, as described by a Lorentzian line,

$$\varepsilon(\omega) = \varepsilon_\infty + \frac{\varepsilon_s - \varepsilon_\infty}{1 - \omega^2/\omega_L^2}, \tag{16}$$

where ω_L is the resonance frequency, ε_∞ is the permittivity of the medium in the high-frequency limit, and ε_s is the permittivity of the medium in the low-frequency limit.

Representing the induced polarization as a sum of linear and nonlinear components, we shall write the relation between the electric field intensity E_z and the electromagnetic induction D_z as

$$E_z = D_z - (P_{zL} + P_{zNL}), \tag{17}$$

where

$$P_{zL}(x, t) = \int_0^t \varepsilon(x, t - t')E_z(x, t')dt'. \tag{18}$$

Using zero initial conditions at $t = 0$ in the integral (18) and introducing the Fourier transform $\varepsilon(x, \omega)$ of the function $\varepsilon(x, t)$ we obtain

$$P_{zNL}(x, t) = \chi^{(2)}(x)E_z^{(2)}(x, t), \tag{19}$$

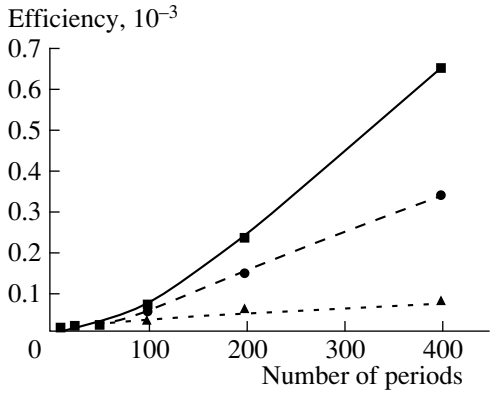

Fig. 6. Second-harmonic generation efficiency versus the number of periods of the PBG structure for pulses of different duration: $\tau = 10T_0$ (solid line), $5T_0$ (dashed line), $2T_0$ (dotted line) (T_0 is the period of the pump field).

where $\chi^{(2)}(x)$ is the dimensionless second-order nonlinear susceptibility of the medium. As a result, we obtain the differential equation

$$\frac{1}{\omega_L^2}\frac{d^2P_{zL}(x,t)}{dt^2} + \left[1 + \frac{\varepsilon_s - 1}{1 + \chi^{(2)}(x)E_z(x,t)}\right]P_{zL}(x,t) = \frac{\varepsilon_s - 1}{1 + \chi^{(2)}(x)E_z(x,t)}D_z(x,t). \quad (20)$$

We shall represent this equation in the finite difference form as

$$\frac{1}{\omega_L^2}\frac{P_i^{n+1} + P_i^{n-1} - 2P_i^{n-2}}{\Delta t^2} + \left[1 + \frac{\varepsilon_s - 1}{1 + \chi_i^{(2)}E_i^n}\right]\left(\frac{P_i^{n+1} + P_i^{n-1}}{2}\right) = \frac{\varepsilon_s - 1}{1 + \chi_i^{(2)}E_i^n}\frac{D_i^{n+1} + D_i^{n-1}}{2}. \quad (21)$$

Here the symbols i and n correspond to discrete variables of the coordinate x and time, respectively. Calculating the value of P_i^{n+1}, we can find the electric field intensity at $(n + 1)$st moment in time according to the formula

$$E_i^{n+1} = \frac{-1 + \sqrt{1 + 4(D_i^{n+1} - P_i^{n+1})\chi^{(2)}}}{2\chi^{(2)}}. \quad (22)$$

The procedure described above is performed only for sections of the PBG structure with frequency dispersion. In the absence of frequency dispersion the relation between E_i^{n+1} and D_i^{n+1} can be established according to the general FDTD scheme [17].

3.2. Discussion of the Computational Results

In the absence of frequency dispersion the maximum second-harmonic generation efficiency is attained in a PBG structure with the parameters

$$a = \frac{\lambda}{2n_a}, \quad b = \frac{\lambda}{4n_b}. \quad (23)$$

This result is in complete accord with the analytical analysis, performed above, for an infinite one-dimensional PBG structure. The first relation in Eqs. (23) ensures phase and group synchronization, and the second condition, as shown in Subsection 2.1.3, ensures that the dispersion of the group velocity at the fundamental frequency and the second-harmonic frequency is zero. Numerical simulation performed for Gaussian pulses of extremely short duration, propagating in PBG structure with $n_a = 2$ and $n_b = 1$, $\chi_a^{(2)} = \chi_b^{(2)} = 10^{-4}$, showed that when the conditions (23) are satisfied the dependence of the second-harmonic generation efficiency (defined as the ratio of the second-harmonic pulse energy at the exit from the PBG structure to the pump radiation energy at the entrance) on the length of the structure is close to quadratic for lengths of the order of 10^3d periods of the structure for pulse duration $10T_0$ (the solid line in Fig. 6). For shorter durations, when the pump pulse spectrum becomes of the order of or greater than the size of the region of allowed photon energies, the efficiency of the second harmonic generation process increases much more slowly than the squared length of the PBG structure (dashed and dotted lines in Fig. 6). This phenomenon is due to the fact that the conditions for phase and group matching cannot be satisfied in such a wide spectral region (Fig. 1). The dispersion spreading of a pulse also plays a large role for short pulses, since the dispersion of high orders near the band edge reaches large values.

As already mentioned above, the method for achieving synchronization for nonlinearly optical interactions in PBG structures is fundamentally different from the nature of the synchronization in structures for quasisynchronous interactions. A quasisynchronous interaction regime is achieved by changing the sign of the squared susceptibility of the nonlinear material on a characteristic spatial scale of the order of the coherence length. The characteristic dependence of the second harmonic generation efficiency on the length of a nonlinear crystal for this frequency conversion regime is presented in Fig. 7 (dot-dashed curve). The synchronous second-harmonic generation in PBG structures is obtained by modulation of the refractive index on a characteristic spatial scale less than the optical wavelength; this makes it possible to attain phase and group

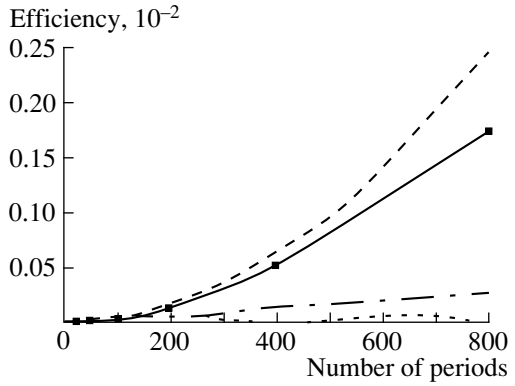

Fig. 7. Second harmonic generation efficiency versus the length of a nonlinear medium (expressed in the number of periods of the PBG structure) for a PBG structure (solid line), structures for quasisynchronous interaction (dashed-dotted line), nonlinear medium with uncompensated phase and group detunings (dotted line). The dashed line shows the quadratic dependence on the wavelength, corresponding to synchronous generation of the second harmonic. The parameters of the PBG structure are: $a \simeq 0.214\lambda$, $b \simeq 0.397\lambda$, $n_a = 1$, $n_{1b} = 1.5$, $n_{2b} = 1.53$, $\chi_a^{(2)} = 0$, $\chi_b^{(2)} = 10^{-4}$.

synchronization and to open up the possibility of attaining high second-harmonic generation efficiencies irrespective of the synchronization length in the interior volume of the nonlinear material. The latter circumstance is extremely important for practical applications.

As one can see from Figs. 1 and 4, dispersion and the length of the PBG structure as well as the pump pulse duration determine the region of pump radiation wavelengths where high SHG efficiency is attained. The numerical results presented in Figs. 8a–8c illustrate the effect of the material dispersion and length of the PBG structure on the form of the dependence of the second-harmonic generation efficiency on the pump radiation wavelength. Figure 8a shows the dependence of the SHG efficiency on the pump radiation wave number in a PBG structure with parameters $n_a = 2$, $a = \lambda/2n_a$, $n_b = 1$, $b = \lambda/4n_b$, $\chi_a^{(2)} = \chi_b^{(2)} = 10^{-4}$, and length $400d$ with no frequency dispersion for a pump pulse duration $10T_0$. As one can see from Fig. 8b, the maximum second harmonic generation efficiency in the PBG structure decreases, and the dependence of the second-harmonic generation efficiency on the pump wavelength becomes asymmetric with respect to the wavelength for which the phase and group synchronization conditions are satisfied simultaneously. This effect is due to the fact that for a PBG structure with material dispersion the wavelength corresponding to phase synchronization is shifted relative to the center of the band into the short-wavelength region. For a small increase in the frequency relative to the frequency of phase synchronization, the increase in the second harmonic generation efficiency associated with the decrease in the group velocity of the pulse near the band gap (see Fig. 4) compensates the decrease in the second-harmonic generation efficiency due to phase and group detunings. As the length of the PBG structure increases to values greater than the synchronization length ($400d$ in Fig. 8c), the width of the region of efficient second-harmonic generation decreases as a result of the large influence of phase and group detunings.

The large difference of the synchronous second-harmonic generation regime, proposed in the present work, in PBG structures from the second harmonic generation regime in photonic crystals, which was discussed in [11, 12], lies in the fact that in our case the width of the resonance in the transmission spectrum of a one-dimensional PBG structure with a finite number of periods does not limit the width of the spectral region of efficient second-harmonic generation. Since the one-dimensional PBG structures for the conditions considered above make it possible to satisfy simultaneously

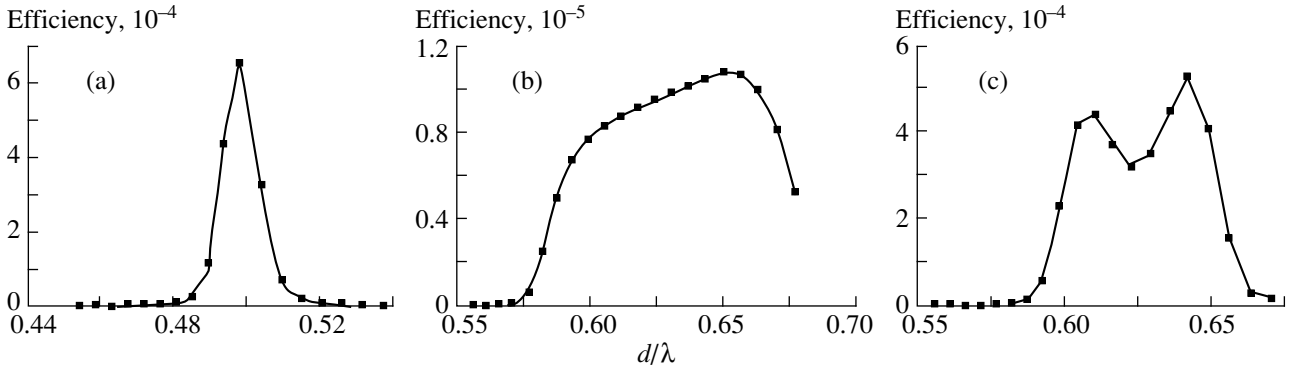

Fig. 8. Second harmonic generation efficiency versus the wave number of the pump radiation in a PBG structure for a pump pulse with duration $10T_0$: (a) no material dispersion for $n_a = 2$, $a = \lambda/2n_a$, $n_b = 1$, $b = \lambda/4n_b$, $\chi_a^{(2)} = \chi_b^{(2)} = 10^{-4}$, length of the structure—$400d$; (b) taking account of material dispersion with $a \simeq 0.214\lambda$, $b \simeq 0.397\lambda$, $n_a = 1$, $n_{1b} = 1.5$, $n_{2b} = 1.53$, $\chi_a^{(2)} = 0$, $\chi_b^{(2)} = 10^{-4}$, length of the structure—$50d$; (c) taking account of material dispersion for the same parameters, length of the structure—$400\,d$.

the conditions for phase and group synchronization, a synchronous second-harmonic generation regime can be realized for extremely short (several periods of the light field) pulses with sufficiently long PBG structures.

4. CONCLUSIONS

In summary, analysis of the dispersion relation for an infinite one-dimensional PBG structure and direct numerical integration of Maxwell's equations by the finite-difference method show that one-dimensional PBG structures make it possible to satisfy the conditions not only of phase but also group synchronization for laser pulses with duration of several periods of the light field. The dispersion of the PBG structure compensates the phase and group detunings due to the dispersion of the nonlinear medium. Choosing appropriate parameters of the PBG structure also makes it possible to decrease the influence of dispersion of the group velocity and reduce to a minimum the effect of the spreading of the pump pulses and the second-harmonic pulses due to the nonlinearly optical interaction. When these conditions are satisfied, optical frequency doublers based on PBG structures make it possible to increase the rate of growth of the second-harmonic signal as a function of the length of the nonlinearly optical interaction compared with structures for quasisynchronous interactions and they open up the possibility of achieving high frequency doubling efficiencies irrespective of the synchronization length in the interior volume of a nonlinear material.

ACKNOWLEDGMENTS

We thank K.N. Drabovich for fruitful discussions and the referee for helpful remarks.

These investigations were supported by the Constellation Group GmbH, a grant from the President of the Russian Federation no. 00-15-99304, and INTAS grant no. 97-0369.

REFERENCES

1. J. Joannopoulos, R. Meade, and J. Winn, *Photonic Crystals* (Princeton Univ. Press, Princeton, 1995).
2. M. M. Fejer, G. A. Magel, D. H. Jundt, and R. L. Byer, IEEE J. Quantum Electron. **28**, 2631 (1992).
3. R. L. Byer, Nonlinear Opt. **7**, 235 (1994).
4. R. L. Byer, J. Nonlinear Opt. Phys. Mater. **6**, 549 (1997).
5. J. A. Armstrong, N. Bloembergen, J. Ducuing, and P. S. Pershan, Phys. Rev. **127**, 1918 (1962).
6. N. Bloembergen and A. J. Sievers, Appl. Phys. Lett. **17**, 483 (1970).
7. J. P. van der Ziel and M. Ilegems, Appl. Phys. Lett. **28**, 437 (1976).
8. J. Trull, R. Vilaseca, J. Martorell, and R. Corbalan, Opt. Lett. **20**, 1746 (1995).
9. J. Martorell, R. Vilaseca, and R. Corbalan, Appl. Phys. Lett. **70**, 702 (1997).
10. L. A. Golovan', A. M. Zheltikov, P. K. Kashkarov, *et al.*, Pis'ma Zh. Éksp. Teor. Fiz. **69**, 274 (1999) [JETP Lett. **69**, 300 (1999)].
11. M. Scalora, M. J. Bloemer, A. S. Manka, *et al.*, Phys. Rev. A **56**, 3166 (1997).
12. M. Centini, C. Sibilia, M. Scalora, *et al.*, Phys. Rev. E **60**, 4891 (1999).
13. A. Yariv and P. Yeh, *Optical Waves in Crystals* (Wiley, New York, 1980).
14. A. M. Zheltikov, N. I. Koroteev, S. A. Magnitskiĭ, and A. V. Tarasishin, Kvantovaya Élektron. (Moscow) **25**, 885 (1998).
15. N. I. Koroteev, S. A. Magnitskiĭ, A. V. Tarasishin, and A. M. Zheltikov, Opt. Commun. **159**, 191 (1999).
16. A. M. Zheltikov, N. I. Koroteev, S. A. Magnitskiĭ, and A. V. Tarasishin, Izv. Ross. Akad. Nauk, Ser. Fiz. **63**, 717 (1999).
17. A. Taflove, *Computational Electrodynamics: The Finite-Difference Time-Domain Method* (Artech House, Norwood, 1995).
18. P. Tran, Opt. Lett. **21**, 1138 (1996).
19. P. Tran, J. Opt. Soc. Am. B **14**, 2589 (1997).
20. S. Scholz, O. Hess, and R. Ruhle, Opt. Express **3** (1), (1998).
21. A. M. Zheltikov, S. A. Magnitskiĭ, and A. V. Tarasishin, Pis'ma Zh. Éksp. Teor. Fiz. **70**, 323 (1999) [JETP Lett. **70**, 323 (1999)].
22. S. A. Magnitskiĭ, A. V. Tarasishin, and A. M. Zheltikov, Appl. Phys. B **69**, 497 (1999).
23. A. M. Zheltikov, S. A. Magnitskiĭ, and A. V. Tarasishin, Zh. Éksp. Teor. Fiz. **117**, 691 (2000) [JETP **90**, 600 (2000)].
24. A. Taflove, Opt. Lett. **17**, 180 (1992).

Translation was provided by AIP

Journal of Experimental and Theoretical Physics, Vol. 91, No. 2, 2000, pp. 307–313.
Translated from Zhurnal Éksperimental'noĭ i Teoreticheskoĭ Fiziki, Vol. 118, No. 2, 2000, pp. 351–358.

PLASMA, GASES

Formation of Ordered Structures of Charged Macroparticles in a Photoemission Trap

O. S. Vaulina, A. P. Nefedov, O. F. Petrov*, and V. E. Fortov

Research Center for Thermal Physics of Pulse Effects, Russian Academy of Sciences, Moscow, 127412 Russia
**e-mail: ipdustpl@redline.ru*

Received December 31, 1999

Abstract—The possibility of confining positively charged macroscopic dust particles in a unique photoemission trap was studied. The spatial distributions of the potentials for a cylindrical geometry of a phototrap were obtained (by the particles in a cell method) and the dynamics of the formation of ordered structures of dust particles in the potential field of the trap was studied (by the molecular-dynamics method). The dependence of the number of dust particles confined by a phototrap on the particle energies and sizes and the buffer-gas pressure were obtained. © *2000 MAIK "Nauka/Interperiodica".*

1. INTRODUCTION

The advancement of space studies has shown that dust and dust structures play a large role in the formation of stars, planetary systems, planetary rings, in processes occurring in the upper layers of the atmosphere (magnetosphere, ionosphere), and so on [1–3]. One mechanism leading to charging of dust particles under conditions of space in the presence of intense fluxes of ultraviolet radiation is photoemission. Macroparticles, several microns in size, can acquire a positive charge of the order of 10^2–10^5 elementary charges [4]. As is well known, in a low-pressure gas discharge, because of the large magnitudes of the charge of the macroparticles (of the order of 10^2–10^4e) a strong interparticle correlation results in the formation of ordered structures in the arrangement of the macroscopic particles, similar to the structures in a liquid or solid [5–8]. The main mechanism leading to charging of the particles placed in an hf or dc discharge are electron and ion fluxes. The particles are negatively charged because of the higher temperature and mobility of the electrons. The observed ordered structures of macroparticles are confined by the electric field of the strata (in a dc glow discharge) or electrodes (in an hf discharge) in the Earth's gravitational field [5–8].

Among the well-known works on ordered systems of particles charged by thermal and photoemission, we call attention to experiments on the observation of ordered structures of positively charged cerium oxide particles in a laminar jet of a weakly-ionized thermal plasma [8–10] and experiments on the observation of the behavior of macroparticles charged by solar radiation, which were performed onboard the *Mir* space station [11]. In both cases the type of observed ordered structure, analyzed according to the measured correlation function, was close to a liquid, even though the interparticle interaction parameter was quite large. A feature common to these works is that charged particles were observed as they move in a gas-dynamic flow, which even for the quite high positive charge of macroparticles does not give stationary conditions required for the formation of stable ordered dust structures, and does not make it possible to study reliably the electrophysical parameters of the structures. The lack of effective electric traps is one of the main reasons why it is impossible to obtain experimental data on the formation of strongly correlated ordered structures of positively charged particles.

In the present paper we study the formation of ordered structures of macroparticles in a novel photoemission-type electron trap in application to microgravity conditions.

As is well known, the existence of electrostatic traps for systems of identically charged macroparticles contradicts the basic Maxwell relations. To confine a system of macroparticles it is necessary to have and maintain a compensating background due to charges of the opposite sign, for example, electrons. Since the system is open, a large fraction of the emitted electrons will leave the particle cloud from the boundaries as well as from the interior region of the cloud. Consequently, an additional influx of electrons is necessary from regions outside the dust cloud in order for the Laplacian of the potential in our system (macroparticles plus electrons) to remain positive. Then, in the presence of a constant source of ionization and under certain conditions (particle sizes and density, wavelength and intensity of the radiation, work function for a photoelectron), crystalline structures can arise in such a system [4, 8]. Such conditions are entirely possible in space [12] and can be obtained by an artificial method using electron traps with thermal or photocathodes, emitting the "missing" electrons.

1063-7761/00/9102-0307$20.00

2. DISTRIBUTION OF THE ELECTRIC POTENTIAL IN A CYLINDRICAL TRAP WITH A PHOTOCATHODE

Let us find the distribution of the electric potential for a photoemission trap (Fig. 1), consisting of a cylinder, one face of which is a photocathode and the other, as well as the walls, are transparent to light and to the emitted photoelectrons (for example, they are metal grids). For simplicity, we shall neglect the thermal distribution of the initial velocities of the electrons. We shall assume that the initial velocity vectors of the emitted electrons are directed perpendicular to the photocathode, and the geometric dimensions of the trap are less than the mean-free path length of the electrons colliding with the buffer-gas atoms.

This problem was solved in several steps by the "particles in cells" method [13]. The solution of the one-dimensional Poisson equation was used as the initial approximation for solving the problem in a cylindrical r–z geometry. We introduce the new variable

$$U(z) = T_0 - e\varphi(z),$$

where $T_0 = m_e V_0^2/2$ is the initial energy of electrons with mass m_e and velocity V_0 and $\varphi(z)$ is the potential.

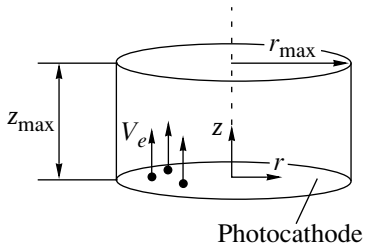

Fig. 1. Schematic representation of a cylindrical phototrap.

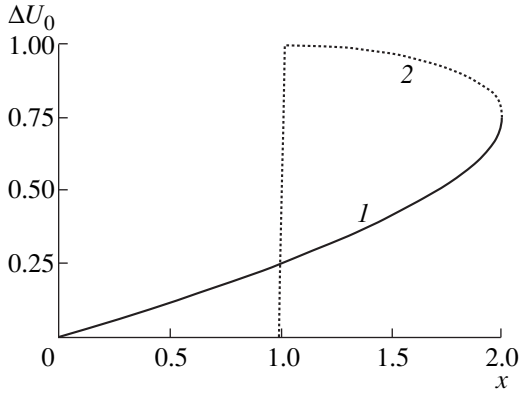

Fig. 2. Two branches of real solutions of the one-dimensional Poisson problem for $\Delta U_0 = \{T_0 - U(z_{max}/2)\}/T_0$ as a function of the parameter $X = (9z_{max}^2/8D^2)$.

Then the Poisson equation can be written in the form

$$\frac{d^2U}{dz^2} = \frac{B}{\sqrt{U}}, \tag{1}$$

where $B = 4\pi n_0 e^2 \sqrt{T_0}$ is a constant, which depends on the density of the electrons emitted by the photocathode:

$$n_0 \equiv n(z = 0) = \frac{j_0^{phe}}{\sqrt{2e^2 T_0/m_e}}. \tag{2}$$

Here $j_0^{phe} = j^{phe}(0)$ is the current density at the surface of the photocathode ($z = 0$), and it is constant as a function of z for the one-dimensional geometry under consideration ($j^{phe}(z) = \text{const}$). In the new variables the boundary conditions of the problem are

$$\begin{aligned} &U(z = 0) \equiv U(z = z_{max}) \equiv T_0, \\ &\partial U/\partial z = 0 \text{ at } z = z_{max}/2. \end{aligned} \tag{3}$$

The symmetry condition for the problem reflects the requirement that the extremum of the potential (minimum of the potential well for dust particles) be located at the center of the trap. The problem (1)–(3) has a single particular solution

$$U \sim |z - z_{max}/2|^{4/3}$$

with $U(z_{max}/2) \equiv 0$. The photocurrent $j_0^{phe} = j_{lim}$ will be determined by the well-known relation

$$j_{lim} = \frac{4(2e/m_e)^{1/2}(T_0/e)^{3/2}}{9\pi z_{max}^2}. \tag{4}$$

In a different case, where $U(z_{max}/2) \neq 0$, the problem (1)–(3) possesses an analytical solution only at the center of the trap $U(z_{max}/2)$. For

$$\Delta U_0 = (T_0 - U(z_{max}/2))/T_0,$$

which determines the depth of the potential well, there are two branches of real solutions (Fig. 2):

$$\Delta U_0 = \sin^2\{\arccos(1 - X)/3\}, \quad 0 \le X \le 2, \tag{5a}$$

$$\Delta U_0 = \sin^2\{\arccos(1 - X)/3 + 2\pi/3\}, \quad 1 \le X \le 2, \tag{5b}$$

where $X = 9z_{max}^2/8D^2$ is a parameter, and $D^2 = T_0/4\pi n_0 e^2$ is equivalent to the squared Debye radius.

The shooting method [13] was used to find the solution of the problem (1)–(3) for the entire range of the variable z. The results of the calculation of the distributions $U(z)$ in a one-dimensional trap for various values of the parameter X showed that only one of the solutions is stable—(5a) (Fig. 2, curve *1*). Analysis of the numerical solution of the one-dimensional problem shows that under certain conditions ($0 \le X \le 2$, correspondingly, $0 \le j_0^{phe} \le 2j_{lim}$) a potential well for posi-

tively charged particles will exist at the center of a phototrap. The depth $\varphi_{max} = \varphi(z_{max}/2)$ of the potential well will be maximum and equal to $0.75T_0/e$, when the parameter $X = 2$ ($j_0^{phe} = 2j_{lim}$). For $X > 2$ Eq. (1) with the boundary conditions (3) has no real solutions. This imposes a limit on the admissible photocurrent density $j_0^{phe} \le 2j_{lim}$.

To solve the problem in a two-dimensional r–z geometry the Poisson equation and the boundary conditions of the problem were represented in the variables $U(z, r) = T_0 - e\varphi(z, r)$:

$$\frac{1}{r}\frac{\partial}{\partial r}r\frac{\partial U}{\partial r} + \frac{\partial^2 U}{\partial z^2} = 4\pi e^2 n_e,$$
$$U(z = 0, r) \equiv U(z = z_{max}, t) \equiv U(z, r = r_{max}) \equiv T_0, \quad (6)$$
$$\partial U/\partial r = 0 \text{ at } r = 0,$$

where $n_e = n_e(z, r)$ is the photocurrent density in the trap ($n_e(0, r) = n_0$). The computational region of the problem was covered with a uniform grid

$$\Delta z = z_{max}/N_z, \quad \Delta r = r_{max}/N_r.$$

The derivatives in Eq. (6) were replaced by second-order difference relations. Seidel's iteration method was used to solve the system of equations obtained [14]. The distribution $U(z)$ obtained in solving the one-dimensional problem was used as the initial approximation ($t = 0$), and the right-hand side of Eq. (6) was assumed to be $B/\sqrt{U}$. The solution of Eq. (6) was included in the general numerical algorithm, which was based on the "particles in a cell" method. After the spatial distribution $U(z, r)$ was calculated for each "large" particle, which corresponded to 10^5 electrons, the equation of motion

$$\frac{d^2\mathbf{V}_k}{dt^2} = -\nu_e\mathbf{V}_k + \frac{e\mathbf{E}}{m_e}, \quad (7)$$

$$\mathbf{E} = \text{grad}\{U(z, r)\}, \quad (8)$$

where ν_e is the frequency of collisions between electrons and buffer-gas atoms and $\mathbf{V}_k$ is the velocity of the kth particle, was solved. In the course of the calculation the constant flux

$$j_0^{phe}(0, r) = Q_{M_e}n_0V_0^z$$

of large particles with charge $Q_{M_e} = 500e$, mass $M_e = 500m_e$, and the same initial velocities

$$V_0^z = \sqrt{2T_0/M_e}, \quad V_0^r = 0$$

is given in several layers of the cells near the surface of the photocathode. The free-effuse condition was used for particles which reached the cathode, grid, or wall (see Fig. 1). At the final step the electron density distribution $n_e(z, r)$ and the current density $j^{phe}(z, r)$ were determined for all computational cells (the motion of large particles at a given moment in time was assumed to be steady), after which a Poisson Eq. (6) was solved anew.

The parameters for the numerical solution of the problem (6) were chosen to be as follows:

$$T_0 = 2 \text{ eV}, \quad z_{max} = 2 \text{ cm}, \quad r_{max} = 1.5 \text{ cm}.$$

The initial energy T_0 of the emitted electrons depends on the energy of the induced-emission photons and the material of the photocathode. The temperature of the electrons leaving the surface of the photocathode under the action of solar radiation ranges from 1 to 2 eV in most cases [15, 16]. The geometric parameters of the trap z_{max} and r_{max}, on the one hand, must permit confinement of a large number of charged dust particles and, on the other, are bounded by the electron mean free path length l_e in the buffer gas, which must be comparable to or greater than the dimensions of the system. Thus, for neon l_e (cm) $\simeq 0.12/P$ (torr), where P is the gas pressure [17]. Consequently, in order for Eqs. (1) and (7) with $\nu_e = 0$ (in the collisionless regime) to remain valid, the neon pressure should not exceed 0.05 torr.

About 30 thousand large particles were taken into account in establishing the quasistationary regime in the computational region. The problem reaches a stationary solution in about 70 ns—the spatial distribution of the potential inside the trap no longer changes. The maximum depth of the potential well ~0.8 V is attained with $j_0^{phe} \approx 2j_{lim}$. The distributions of the functions $U(z/z_{max}, 0)$ and $U(z_{max}/2, r/r_{max})$ at the center of the trap ($r = 0$, $z = z_{max}/2$) are presented in Fig. 3. The data on the distribution $U(z, r)$ at the center of the trap for other initial electron energies ($T_0 \neq 2$ eV) can be obtained by simply scaling the curves in Fig. 3. The calculations were performed for two different buffer-gas (neon)

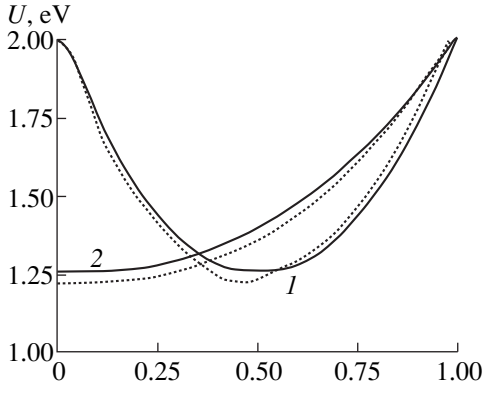

Fig. 3. $U(z/z_{max}, r = 0)$ versus z/z_{max} (*1*) and $U(z_{max}/2, r/r_{max})$ versus r/r_{max} (*2*) at the center of a trap for two different buffer-gas pressures $P_1 = 0.01$ torr (solid lines) and $P_2 = 0.1$ torr (dotted lines).

pressures: $P_1 = 0.01$ torr ($\nu_e = 10^7$ s^{-1}) and $P_2 = 0.1$ torr ($\nu_e = 10^8$ s^{-1}). The solution obtained in the case $P_1 = 0.01$ torr was identical to the solution obtained in the collisionless regime with $\nu_e = 0$. As pressure increases $P > 0.05$ torr, the depth of the potential well increases, and the center of the well shifts rapidly toward the photocathode, so that already for $P = 0.2$ torr the center of the potential well is located essentially on the photocathode. The observed picture is qualitatively similar to the case of calculations for high photocurrents $j_0^{phe} > 2j_{\lim}$ ($X > 2$).

3. PHOTOEMISSION CHARGING OF MACROPARTICLES

Let us consider macroparticles in a neutral gas irradiated with monochromatic source of light with wavelength λ. When particles in a buffer gas are irradiated with a flux of photons with energy higher than the photoelectron work function W of the surface of the particles, the macroparticles will acquire a positive charge. The characteristic photoelectron work function for most substances does not exceed 6 eV. Consequently photons with energy ≤12 eV can charge particles without at the same time ionizing the buffer gas, such as He or Ar. The maximum charge $Q_{\max} = \phi_s R_p$ of a spherical particle with radius R_p can be determined from the condition that the surface potential ϕ_s equal $(h\nu - W)/e$:

$$Q_{\max} = (h\nu - W)R_p/e, \tag{9}$$

where $h\nu$ is the photon energy. A more accurate estimate of the equilibrium charge of a dust particle can be obtained by using the bounded orbital motion approximation, which is valid for a rarefied plasma, where the mean free path length l_e of photoelectrons before collisions with neutrals is much larger than the particle radius R_p ($l_e \gg R_p$). Then the cross section σ_e for inelastic collisions (recombination cross section) of an electron with a spherical dust particle can be obtained from the energy and momentum conservation laws as

$$\sigma_e = \pi R_p^2(1 + 2e\phi_s/m_e V_e^2), \tag{10}$$

and the electron current onto an isolated dust particle can be written as

$$I_e = en_e\langle V_e\sigma_e\rangle_v, \tag{11}$$

where $\langle\ \rangle_v$ denotes averaging over the electron velocities V_e. In the general case, $\langle V_e\sigma_e\rangle_v$ for a macroparticle placed in a photoelectron trap is a complicated function of the thermal velocity $V_{Te} = \sqrt{2T_0/m_e}$ and the drift velocity of the electrons. A positive potential of the particles is established as a result of the balance between the recombination of electrons on the surface of the particle and the photoemission (electronic) current from the surface of the particle. For effective charging of particles and effective illumination of the photocathode of a trap, the external inducing radiation must be satisfy the condition for transparency of a dispersed medium:

$$\tau \approx 2\pi R_p^2 n_p L \ll 1, \tag{12}$$

where n_p is the particle density and L is the geometric length of the particle cloud in the direction of the incident radiation. Since the system is open, a large fraction of the emitted electrons will leave the cloud of particles, both from the boundary of the cloud and from the interior region, since for spherical dust particles the absorption cross section for photons and electrons are close. We shall neglect the density of the electrons emitted by dust particles, and we shall assume that the inducing radiation is directed and the radiation absorption efficiency is close to 1 ($2\pi R_p/\lambda \gg 1$). Then the charge $Q = \phi_s R_p$ acquired by a dust particle in a photoemission trap can be estimated by determining the surface potential ϕ_s from the equation [4]

$$j(z, r)\left(1 + \frac{e\phi_s}{U(z, r)}\right) \simeq Y_p J \exp\left(-\frac{e\phi_s}{T_{pe}}\right), \tag{13}$$

where J is the photon flux, Y_p is the quantum yield of photoelectrons for the particle material, T_{pe} is the temperature of the electrons leaving the surface of the particles in the process of photoemission (which, as already mentioned, depends on the particle material and ranges from 1 to 2 eV), and $U(z, r)$ is the kinetic energy of the electrons emitted by the photocathode assuming that the recombination rate of electrons on the particles is higher than the rate of thermal energy losses due to electron-neutrals collisions.

The electron current density of the photocathode $j(z, r) = j^{phe}(z, r)$, on the one hand, must provide a maximum depth of the potential well (see Section 2, $j_0^{phe} \approx 2j_{\lim}$), while on the other hand it is a function of $j^{phe} \sim Y_k J$, where Y_k is the quantum yield of photoelectrons for the photocathode material. Hence it follows that for equal illumination of the particles and equal photocathode surface area, the condition $Y_k < Y_p$ must be satisfied for positive charging of the particles. The equilibrium charge, obtained from Eq. (13), on a particle surface must be much less than the maximum charge determined by the relation (9) [11]. It should be noted that the quantum yield depends strongly on the material and the direction of the incident radiation. For irradiation of metals with radiation with wavelength $\lambda < 100$ nm the quantum yield of photocurrents is close to 1.

4. DYNAMICS OF THE FORMATION OF A STRUCTURE OF CHARGED MACROPARTICLES IN A CYLINDRICAL PHOTOTRAP

Let us consider the conditions for the formation of a crystalline structure of dust particles in the proposed phototrap. One of the main parameters of the problem

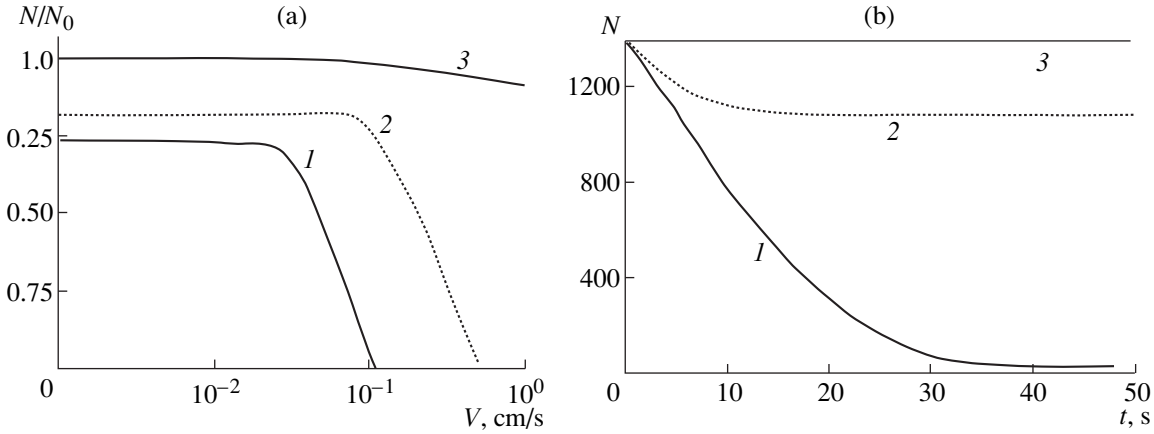

Fig. 4. The number of trapped particles as a function of the initial velocity V of the particles for two different pressures (a) and as a function of time (b) for $V = 0.1$ cm/s: (*1*) $\nu_{fr} = 0.02$ s^{-1}, $Q = 5000e$, $R_p = 37.5$ μm; (*2*) $\nu_{fr} = 0.2$ s^{-1}, $Q = 5000e$, $R_p = 37.5$ μm; (*3*) $\nu_{fr} = 5$ s^{-1}, $Q = 1000e$, $R_p = 7.5$ μm.

is the initial energy and size of the particles, which under otherwise the same conditions (conditions of illumination, particle material, and type and pressure of the buffer gas) is the main parameter determining the charge of the particles and the viscosity of the surrounding gas. A low pressure, which is required for operation of a phototrap, may not give efficient braking of dust particles. Hence the number of trapped particles may not be sufficient to observe the formation of a plasma-dust crystal.

The three-dimensional equation of motion

$$m_p \frac{d^2\mathbf{l}_k}{dt^2} = \sum_j \frac{Q^2}{l^2}\bigg|_{l=|\mathbf{l}_k-\mathbf{l}_j|} \frac{\mathbf{l}_k-\mathbf{l}_j}{|\mathbf{l}_k-\mathbf{l}_j|} - m_p\nu_{fr}\frac{d\mathbf{l}_k}{dt} + Q\mathbf{E}, \tag{14}$$

where l is the interparticle distance, m_p is the mass of a dust particle, and ν_{fr} is the friction coefficient, was solved for each macroparticle. The interparticle interaction potential is determined by Coulomb's law [11]. The data from calculations of the electric field of a trap, which are presented in the preceding section for a trap with the same geometric dimensions, were used to solve the system of Eqs. (14) numerically. The depth of the potential well

$$\varphi_{\max} \equiv |U(z_{\max}/2, 0) - U(0, 0)| = 0.4 \text{ V},$$
$$T_0 \simeq 1 \text{ eV},$$

and the spatial distribution of the field was found by simple scaling of the computed potential. The parameters of the system of particles were chosen to be close to the condition of the experiments on observation of the dynamical behavior of macroparticles under the action of solar radiation under zero-gravity conditions onboard the *Mir* space station: particle density $\rho = 6.7$ g/cm^3, particle radius $R_p = 37.5$ μm, friction coefficient $\nu_{fr} = 0.02$ s^{-1} (pressure $P = 0.01$ torr), and $\nu_{fr} = 0.2$ s^{-1} (for $P = 0.1$ torr) [11]. The initial particle density $n_p = 10^2$ cm^{-3} was chosen from the condition that the dispersed medium be transparent for the external photoinducing radiation (the initial number of particles in the trap $N_0 \approx 1500$). The final particle density in the trap changes when an ordered structure of particles is formed, depending on the magnitude of the charge acquired by the particles. Taking account of the decrease in the charge Q of dust particles as a result of absorption of electrons emitted from the photocathode (see Section 3, Eq. (13)), we shall take the particle charge to be $Q = 5000e$, which is approximately an order of magnitude smaller than its maximum estimate (9) for wavelength $\lambda \sim 0.3$ μm, and the value given in the experiment of [11]. For $\lambda \sim 0.3$ μm the quantum yield of bronze is $Y_p \sim 10^{-4}$, and the photoelectron work function W of the surface of cesium-coated bronze particles is determined by the cesium work function $W = 1.5$ eV.

The calculations were also performed for particles with a smaller radius $R_p = 7.5$ μm for buffer-gas pressure $P = 0.1$ torr. The friction coefficients for calculations was correspondingly increased to $\nu_{fr} = 5$ s^{-1} ($\nu_{fr} \propto R_p^{-2}$), and the charge was decreased to $Q = 1000e$ (since $Q \propto R_p$).

The problem was solved for monoenergetic particles with two initial conditions. In the first case the particles were fed in a strictly distinguished direction to the photocathode with velocity V, simulating the injection of particles through the top grid of the trap. In the second case the initial arrangement of the macroparticle was random over the entire volume of the trap, and the initial velocities of the particles were equal in magnitude but random in direction, simulating the behavior

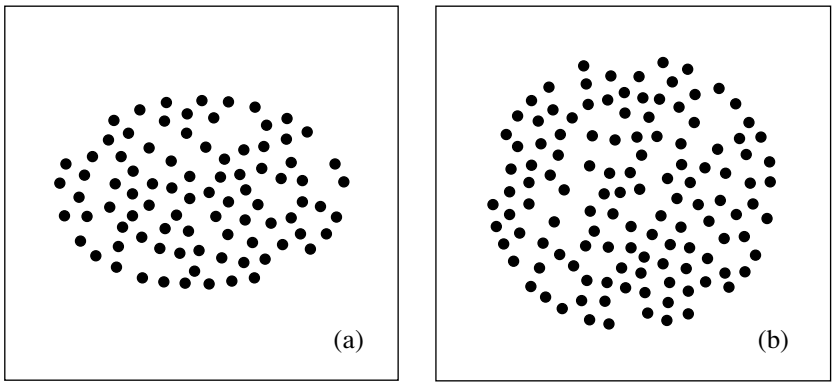

Fig. 5. Longitudinal (a) and transverse (b) sections of a phototrap for particles with radius $R_p = 37.5$ μm ($\nu_{fr} = 0.02$ s^{-1}).

of particles after shaking, analogously to the experiments of [11]. In both cases the formation times of an ordered structure of particles and the number of particles trapped in a phototrap were close. The results of the calculations of the dependence of the number of trapped particles on the initial velocity of the particles are presented in Fig. 4a for two different values of the pressure, and the time dependence of the number of particles for $V = 0.1$ cm/s, close to the threshold velocity of a particle with passage of a potential barrier $V_{th} = (2Q\varphi_{max}/m_p)^{1/2}$, is shown in Fig. 4b. Thus, for conditions close to those of [11], where the initial velocities of bronze particles with average diameter 75 μm reached, after shaking, 0.1–0.3 cm/s at buffer-gas pressure of about 0.01 torr, formation of stable order dust structures is virtually impossible, since the macroparticles leave toward the walls even in the presence of the electric field of a phototrap. In order for the number of trapped particles to be sufficient to observe the formation of dust structures under given conditions, the rate of particle injection into the trap should not exceed 0.01 cm/s (see Fig 4a). An illustration of the arrangement of particles for longitudinal and transverse sections of a trap and the pair correlation functions $g(l)$ for low initial velocities ($V < 0.01$ cm/s) and different radii of the macroparticles are presented in Figs. 5–7. The formation time of crystalline structures ranged from ~10 s for large particles up to ~500 s for small particles at $P = 0.1$ torr.

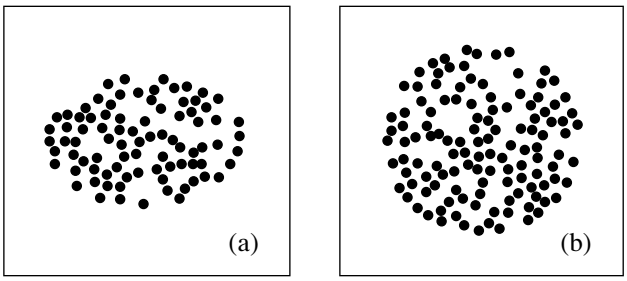

Fig. 6. Longitudinal (a) and transverse (b) sections of a phototrap for particles with radius $R_p = 7.5$ μm ($\nu_{fr} = 0.02$ s^{-1}).

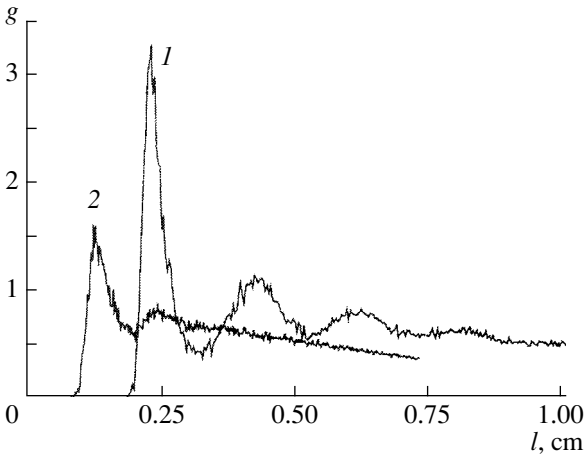

Fig. 7. Pair correlation functions $g(l)$ for particles with radius R_p = (*1*) 37.5 and (*2*) 7.5 μm.

Analysis of the computational results shows that for successful formation of strongly correlated dust structures in the working region of the proposed phototrap the ratios of parameters such as the size of the dust particles, their initial velocity, and the buffer-gas pressure must be optimized.

5. CONCLUSIONS

In the present paper a unique phototrap with a simple configuration, which makes it possible to form a potential well for confinement of particles with positive charges, is proposed. The distributions of the potentials of the external electric field of the trap were obtained and the dynamics of the formation of dust structures in the field of the trap was investigated as a function of the initial energies and sizes of the dust particles and the buffer-gas pressure. The calculations were performed for conditions close to those of the experiment on studying photoemission charging of particles by solar radiation onboard the *Mir* space station. Nonetheless,

many of the results presented can be easily transferred to the case of confinement of positively charged particles in any trap of the electron-emission type.

ACKNOWLEDGMENTS

This work was supported by the Russian Foundation for Basic Research (project no. 98-02-16828) and the INTAS Foundation (project no. YSF 99-215).

REFERENCES

1. S. A. Kaplan, *Interstellar Medium and Orgin of Stars* (Znanie, Moscow, 1977).
2. N. N. Gor'kavyĭ and A. M. Fridman, Usp. Fiz. Nauk **160**, 169 (1990) [Sov. Phys. Usp. **33**, 95 (1990)].
3. F. Melands and O. Havnes, J. Geophys. Res. **95**, 5837 (1991).
4. M. Rosenberg and D. A. Mendis, IEEE Trans. Plasma Sci. **23**, 177 (1995).
5. V. E. Fortov, A. P. Nefedov, V. M. Torchinsky, *et al.*, Phys. Lett. A **229**, 317 (1997).
6. J. H. Chu and Lin I, Phys. Rev. Lett. **72**, 4009 (1994).
7. H. Thomas, G. E. Morfill, V. Demmel, *et al.*, Phys. Rev. Lett. **73**, 652 (1994).
8. A. P. Nefedov, O. F. Petrov, and V. E. Fortov, Usp. Fiz. Nauk **167**, 1215 (1997) [Phys. Usp. **40**, 1163 (1997)].
9. V. E. Fortov, A. P. Nefedov, O. F. Petrov, *et al.*, Phys. Rev. E **54**, R2236 (1996).
10. V. E. Fortov, A. P. Nefedov, O. F. Petrov, *et al.*, Phys. Lett. A **219**, 89 (1996).
11. V. E. Fortov, A. P. Nefedov, O. S. Vaulina, *et al.*, Zh. Éksp. Teor. Fiz. **114**, 2004 (1998) [JETP **87**, 1087 (1998)].
12. T. Nitter, Plasma Sources Sci. Technol. **5**, 93 (1996).
13. E. S. Oran and J. P. Boris, *Numerical Simulation of Reactive Flow* (Elsevier, New York, 1987; Mir, Moscow, 1990).
14. S. K. Godunov and V. S. Ryaben'kiĭ, in *Difference Schemes* (Nauka, Moscow, 1973), p. 400.
15. C. K. Goertz, Geophys. Rev. **27**, 271 (1989).
16. V. A. Grilikhis, P. P. Orlov, and L. B. Popov, *Solar Energy and Space Flightes* (Nauka, Moscow, 1986).
17. Yu. P. Raĭzer, *The Physics of Gas Discharge* (Nauka, Moscow, 1987).

Translation was provided by AIP

Journal of Experimental and Theoretical Physics, Vol. 91, No. 2, 2000, pp. 314–323.
Translated from Zhurnal Éksperimental'noĭ i Teoreticheskoĭ Fiziki, Vol. 118, No. 2, 2000, pp. 359–369.

SOLIDS
Structure

Theory of an $Fm3m \longrightarrow I4/m$ Structural Phase Transition in an Rb_2KScF_6 Crystal

V. I. Zinenko* and N. G. Zamkova

Kirenskii Institute of Physics, Siberian Division, Russian Academy of Sciences, Krasnoyarsk, 660036 Russia
**e-mail: zvi@post.krascience.rssi.ru*

Received December 30, 1999

Abstract—An Rb_2KScF_6 crystal having an elpasolite structure undergoes a sequence of $Fm3m \longrightarrow I4/m \longrightarrow P12_1/n1$ structural phase transitions where the transition to the tetragonal phase is associated with "rotation" of the ScF_6 octahedron. An effective Hamiltonian is constructed to describe the $Fm3m \longrightarrow I4/m$ transition using the approximation of a local mode for which we selected a "soft mode" whose eigenvector corresponds to the rotation of the octahedron. The effective Hamiltonian also includes the relationship between the local mode and the homogeneous elastic strains. The parameters of the effective Hamiltonian were determined using the generalized Gordon–Kim model of an ionic crystal which allows for the deformability and polarizability of the ions. The thermodynamic properties of a system with this model Hamiltonian were investigated using the Monte Carlo method. The calculated phase transition temperature of 250 K is almost the same as the experimental value (252 K). The tetragonal phase remains stable as far as $T = 0$ K and a second transition (to the monoclinic phase) cannot be obtained using this effective Hamiltonian. This suggests that if the transition to the tetragonal phase is mainly associated with "rotations" of the octahedrons, in order to describe the phase transition to the monoclinic phase the effective Hamiltonian must allow for additional degrees of freedom mainly associated with the motion of rubidium ions. © *2000 MAIK "Nauka/Interperiodica".*

1. INTRODUCTION

Crystals having an $A_2BB^{3+}X_6$ elpasolite structure exhibit a wide range of structural phase transitions associated with the instability of the lattice of the high-symmetry cubic phase relative to specific vibration modes of the crystal lattice. In most crystals in this family, structural distortions are merely associated with rotations of $B^{3+}X_6$ octahedrons or a combination of octahedron rotations and displacements of A ions, and the problem of phase transitions in these crystals is related to the general problem of the soft mode and displacement-type phase transitions [1]. Instability of the crystal lattice relative to normal vibrations corresponding to octahedron rotations is clearly a characteristic feature of perovskite-like compounds. In most halide crystals and in some oxide crystals having a perovskite structure this instability leads to structural phase transitions to low-symmetry phases with an increase in the unit cell volume compared with the volume of the initial cubic phase. The problem of instability of a perovskite structure with respect to the ferroelectric mode of lattice vibrations and with respect to the vibration mode associated with octahedron rotations has been discussed in experimental and theoretical studies for several decades. Recent years have seen the publication of many studies in which the density functional method has been used in various approaches to calculate the band structure, the lattice vibration frequencies, and the phase transition temperatures for various representatives of the perovskite family and the temperature dependences of their physical properties have been determined. As a result of these calculations we now have a fairly good understanding of the reasons for instability of the crystal lattice and the reasons for the appearance of ferroelectricity and antiferroelectricity in oxides having perovskite structure (see, for example, [2–5]).

For crystals having an elpasolite structure very few calculations have been made of the spectrum of crystal lattice vibrations. However, these crystals have been studied intensively by various experimental methods and for many crystals in this family data are now available on the structures of low-symmetry phases, the physical properties, and their changes accompanying phase transition (see, for example, the review [6]).

The Rb_2KScF_6 crystal belongs to the elpasolite family and its crystal structure in the high-symmetry phase is cubic with the $Fm3m$ space group and a single molecule per unit cell (Fig. 1). As the temperature decreases, Rb_2KScF_6 undergoes two successive structural phase transitions: at $T_{c1} = 252$ K it undergoes a transition to the tetragonal phase with the $I4/m$ space group without any change in the cell volume compared with that in the cubic phase and at $T_{c2} = 220$ K it undergoes a transition to the monoclinic phase with the $P12_1/n1$ space group and two molecules per unit cell. Structural analyses of low-symmetry phases [6] indicate that the distortions of the cubic structure in the tetragonal phase are mainly caused by rotations of the ScF_6 octahedrons which are

uniform over the entire crystal volume. The distortions in the low-temperature monoclinic phase are caused by nonuniform rotations of ScF_6 octahedrons and displacements of rubidium atoms from the equilibrium positions of the tetragonal phase. The authors of the present study calculated the complete spectra of lattice vibrations in an Rb_2KScF_6 crystal in the unstable cubic and tetragonal phases and in the stable monoclinic phase [7] using the generalized Gordon–Kim method proposed by Ivanov and Maksimov [8] which allows for the deformability and polarizability of the ions. We established that the vibration spectra of the cubic and tetragonal phases contain soft vibration modes (negative values of the squares of the normal vibration frequencies).

The aim of the present study is to construct an effective Hamiltonian to describe the $Fm3m \longrightarrow I4/m$ phase transition in Rb_2KScF_6, to determine the parameters of this Hamiltonian from calculations of the lattice dynamics and the total energy of the distorted phases, and also to study the thermodynamic behavior of the crystal described by this model Hamiltonian. In Section 2 we give the effective Hamiltonian which allows for the minimum number of degrees of freedom and specifically the local mode corresponding to rotation of the ScF_6 octahedron and uniform elastic strains. In Section 3 we briefly describe the method of calculating the frequencies of the normal lattice vibrations and the total energy which is used to determine the parameters of the model Hamiltonian. Some details of a Monte Carlo analysis of the thermodynamic behavior of a system with the constructed model Hamiltonian are presented in Section 4. The results are presented and discussed in the final section.

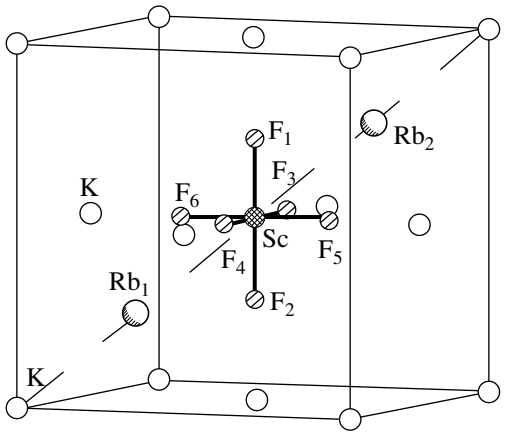

Fig. 1. Crystal structure of Rb_2KScF_6 in the cubic phase. The diagram shows a single molecule and the face-centered potassium lattice. The six rubidium ions of the other three molecules are positioned on the 1/4 and 3/4 three spatial diagonals. The remaining scandium ions occupy the centers of the cube edges. Each scandium ion is surrounded by six fluorine ions.

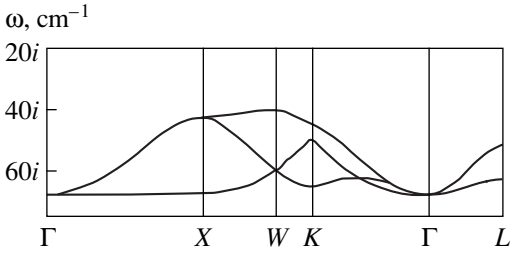

Fig. 2. Dispersion dependence of unstable vibration modes in the cubic phase of an Rb_2KScF_6 crystal.

2. CONSTRUCTION OF EFFECTIVE HAMILTONIAN

The local mode approximation [9] to formulate the equivalent model Hamiltonian was used by several authors to describe ferroelectric and structural phase transitions in the diatomic compound GeTe [10] and in oxides having a perovskite structure [2–5]. We used the scheme for construction of the model Hamiltonian proposed in [4, 5, 10] to formulate the Hamiltonian.

As we noted in the Introduction, the spectrum of lattice vibrations of a Rb_2KScF_6 crystal was calculated in an earlier study [7]. Figure 2 gives part of the total spectrum which shows the dispersion dependences of the unstable vibration modes. It can be seen that the most unstable modes are those belonging to the vibration branch between the points $\Gamma(q = 0)$ and $X(q = 2\pi/a_0, 0, 0)$ in the Brillouin zone. At point Γ the T_{1g} mode of this branch is threefold degenerate whereas in the directions Γ–X, Γ–Y, and Γ–Z including the boundary points, the lowest modes are nondegenerate. The threefold degenerate mode at $q = 0$ and the nondegenerate modes in the Γ–X, Γ–Y, and Γ–Z directions correspond to vibrations in which fluorine ions are displaced and their displacements v_k^{F} in these modes are related by:

$$\begin{aligned}
-v_{1y}^{\mathrm{F}} &= v_{2y}^{\mathrm{F}} = v_{5z}^{\mathrm{F}} = -v_{6z}^{\mathrm{F}},\\
T_{1g}\colon -v_{1x}^{\mathrm{F}} &= v_{2x}^{\mathrm{F}} = -v_{3z}^{\mathrm{F}} = v_{4z}^{\mathrm{F}},\\
-v_{3y}^{\mathrm{F}} &= v_{4y}^{\mathrm{F}} = -v_{5x}^{\mathrm{F}} = v_{6x}^{\mathrm{F}},\\
X_3\colon -v_{1y}^{\mathrm{F}} &= v_{2y}^{\mathrm{F}} = v_{5z}^{\mathrm{F}} = -v_{6z}^{\mathrm{F}},\\
Y_3\colon -v_{1x}^{\mathrm{F}} &= v_{2x}^{\mathrm{F}} = -v_{3z}^{\mathrm{F}} = v_{4z}^{\mathrm{F}},\\
Z_3\colon -v_{3y}^{\mathrm{F}} &= v_{4y}^{\mathrm{F}} = -v_{5x}^{\mathrm{F}} = v_{6x}^{\mathrm{F}}.
\end{aligned} \tag{1}$$

These fluorine displacements lead to rotation of the ScF_6 octahedrons. In order to formulate the model Hamiltonian we use a local-mode approximation in which we only allow for those degrees of freedom associated with the modes (1), assuming that the other degrees of freedom are insignificant for a structural

Table 1

	Rb_1	Rb_2	F_1	F_2	F_3	F_4	F_5	F_6	K	Sc
ξ_x	000	000	$0-\frac{1}{2}0$	$0\frac{1}{2}0$	000	000	$00\frac{1}{2}$	$00-\frac{1}{2}$	000	000
ξ_y	000	000	$-\frac{1}{2}00$	$\frac{1}{2}00$	$00-\frac{1}{2}$	$00\frac{1}{2}$	000	000	000	000
ξ_z	000	000	000	000	$0-\frac{1}{2}0$	$0\frac{1}{2}0$	$-\frac{1}{2}00$	$\frac{1}{2}00$	000	000

phase transition from the cubic to the tetragonal phase. Thus, for Rb_2KScF_6 the local mode has the form

$$S_\alpha = \frac{1}{a_0}\sum_k \xi_{\alpha k} v_k^{\mathrm{F}}, \qquad (2)$$

where $\alpha = x, y, z$; v_k^{F} is the amplitude of the displacement of the kth F atom from (1); $a_0 = 16.26$ au is the calculated lattice parameter in the cubic phase, and $\xi_{\alpha k}$ are the eigenvectors of the lattice vibration mode (Table 1).

Under the action of the symmetry operations of the high-symmetry cubic phase the local mode (S_x, S_y, S_z) is transformed as a pseudovector.

At this point it should be noted that the local mode corresponding to rotation of the octahedron was used to construct the model Hamiltonian to describe the structural phase transition in a perovskite structure $SrTiO_3$ crystal [5]. However, in a perovskite structure the SrO_6 octahedron is not isolated as a structural unit, each oxygen is assigned to two neighboring octahedrons, and additional, slightly artificial assumptions are made to formulate the effective Hamiltonian with this local mode [5]. In this particular case of crystals having an elpasolite structure this problem does not arise since in this structure the $B^{3+}F_6$ octahedron belongs to a single unit cell. It is also important to note that the local mode (2) is not polar, i.e. dipole moments do not appear in the vibrations, and when formulating the model Hamiltonian there is no need to allow for long-range dipole–dipole interactions.

Thus, in order to describe the $Fm3m \longrightarrow I4/m$ structural phase transition we write the effective Hamiltonian using the following scheme. A three-component local mode (pseudovector) is positioned at the sites of a face-centered-cubic lattice. For simplicity the effective Hamiltonian only includes anharmonic terms for the single-site potential. In this case we allow for all terms of the second and fourth orders and some anisotropic terms of the sixth order. Pair interactions between local modes at different lattice sites are only taken into account within the first and second coordination spheres. Finally, we allow for interaction of the local mode with uniform elastic strains over the lattice.

The microscopic model Hamiltonian allowing for the transformational properties of the local mode and the fcc lattice under the action of cubic symmetry operations has the form

$$H = \sum_i (H_i^{anh} + H_i^{SS}) + H^{Se} + H^{ee}, \qquad (3)$$

where

$$H_i^{anh} = B(S_{ix}^4 + S_{iy}^4 + S_{iz}^4) + C(S_{ix}^2 S_{iy}^2 + S_{iy}^2 S_{iz}^2 + S_{iz}^2 S_{ix}^2) + D(S_{ix}^6 + S_{iy}^6 + S_{iz}^6),$$

$$H_i^{SS} = S_{ix}\Bigg[AS_{ix} + a_1 \sum_{\mathbf{d}=(0,\pm1,\pm1)} S_x\left(\mathbf{R}_i + \frac{a_0\mathbf{d}}{2}\right) + a_2 \sum_{\mathbf{d}=\binom{\pm1,\pm1,0}{\pm1,0,\pm1}} S_x\left(\mathbf{R}_i + \frac{a_0\mathbf{d}}{2}\right) + a_3 \sum_{\mathbf{d}=(\pm1,0,\pm1)} (\mathbf{d}\cdot\mathbf{z})(\mathbf{d}\cdot\mathbf{x}) S_z\left(\mathbf{R}_i + \frac{a_0\mathbf{d}}{2}\right) + a_3 \sum_{\mathbf{d}=(\pm1,\pm1,0)} (\mathbf{d}\cdot\mathbf{y})(\mathbf{d}\cdot\mathbf{x}) S_y\left(\mathbf{R}_i + \frac{a_0\mathbf{d}}{2}\right)\Bigg]$$

$$+ S_{iy}\Bigg[AS_{iy} + a_1 \sum_{\mathbf{d}=(\pm1,0,\pm1)} S_y\left(\mathbf{R}_i + \frac{a_0\mathbf{d}}{2}\right) + a_2 \sum_{\mathbf{d}=\binom{\pm1,\pm1,0}{0,\pm1,\pm1}} S_y\left(\mathbf{R}_i + \frac{a_0\mathbf{d}}{2}\right) + a_3 \sum_{\mathbf{d}=(0,\pm1,\pm1)} (\mathbf{d}\cdot\mathbf{z})(\mathbf{d}\cdot\mathbf{y}) S_z\left(\mathbf{R}_i + \frac{a_0\mathbf{d}}{2}\right) + a_3 \sum_{\mathbf{d}=(\pm1,\pm1,0)} (\mathbf{d}\cdot\mathbf{x})(\mathbf{d}\cdot\mathbf{y}) S_x\left(\mathbf{R}_i + \frac{a_0\mathbf{d}}{2}\right)\Bigg]$$

$$+ S_{iz}\Bigg[AS_{iz} + a_1 \sum_{\mathbf{d} = (\pm 1, \pm 1, 0)} S_z\Big(\mathbf{R}_i + \frac{a_0\mathbf{d}}{2}\Big) + a_2 \sum_{\mathbf{d} = \binom{\pm 1, 0, \pm 1}{0, \pm 1, \pm 1}} S_z\Big(\mathbf{R}_i + \frac{a_0\mathbf{d}}{2}\Big) + a_3 \sum_{\mathbf{d} = (0, \pm 1, \pm 1)} (\mathbf{d}\cdot\mathbf{y})(\mathbf{d}\cdot\mathbf{z}) S_x\Big(\mathbf{R}_i + \frac{a_0\mathbf{d}}{2}\Big) + a_3 \sum_{\mathbf{d} = (\pm 1, 0, \pm 1)} (\mathbf{d}\cdot\mathbf{x})(\mathbf{d}\cdot\mathbf{z}) S_y\Big(\mathbf{R}_i + \frac{a_0\mathbf{d}}{2}\Big)\Bigg]$$

$$+ S_{ix}\Bigg[b_1 \sum_{\mathbf{d} = (\pm 1, 0, 0)} S_x(\mathbf{R}_i + a_0\mathbf{d}) + b_2 \sum_{\mathbf{d} = \binom{0, \pm 1, 0}{0, 0, \pm 1}} S_x(\mathbf{R}_i + a_0\mathbf{d})\Bigg]$$

$$+ S_{iy}\Bigg[b_1 \sum_{\mathbf{d} = (0, \pm 1, 0)} S_y(\mathbf{R}_i + a_0\mathbf{d}) + b_2 \sum_{\mathbf{d} = \binom{\pm 1, 0, 0}{0, 0, \pm 1}} S_y(\mathbf{R}_i + a_0\mathbf{d})\Bigg]$$

$$+ S_{iz}\Bigg[b_1 \sum_{\mathbf{d} = (0, 0, \pm 1)} S_z(\mathbf{R}_i + a_0\mathbf{d}) + b_2 \sum_{\mathbf{d} = \binom{\pm 1, 0, 0}{0, \pm 1, 0}} S_z(\mathbf{R}_i + a_0\mathbf{d})\Bigg],$$

$$H^{Se} = g_1(e_1 + e_2 + e_3)\sum_i (S_{ix}^2 + S_{iy}^2 + S_{iz}^2)$$

$$+ g_2\Bigg[(e_1 + e_2 - 2e_3)\sum_i (S_{ix}^2 + S_{iy}^2 - 2S_{iz}^2) + 3(e_1 - e_2)\sum_i (S_{ix}^2 - S_{iy}^2)\Bigg]$$

$$+ g_3\Bigg(e_4\sum_i S_{iy}S_{iz} + e_5\sum_i S_{ix}S_{iz} + e_6\sum_i S_{ix}S_{iy}\Bigg),$$

$$H^{ee} = C_{11}(e_1^2 + e_2^2 + e_3^2) + C_{12}(e_1e_2 + e_2e_3 + e_3e_1) + C_{44}(e_4^2 + e_5^2 + e_6^2),$$

where $\mathbf{R}_i$ is the position vector of the ith crystal lattice site, **x**, **y**, and **z** are the unit vectors along the axes of the Cartesian coordinates, and C_{ij} are the elastic constants of the crystal.

The elastic strains e_i are given in Voigt notation:

$$e_1 = u_{11}, \quad e_2 = u_{22}, \quad e_3 = u_{33},$$

$$e_4 = 2u_{23}, \quad e_5 = 2u_{13}, \quad e_6 = 2u_{12},$$

$$u_{\alpha\beta} = \frac{1}{2}\Big(\frac{\partial u_\alpha}{\partial x_\beta} + \frac{\partial u_\beta}{\partial x_\alpha}\Big),$$

where u_α is the displacement along the x_α axis.

3. CALCULATION OF THE PARAMETERS OF THE EFFECTIVE HAMILTONIAN

In order to determine the numerical values of the coefficients in the effective Hamiltonian (3) we made nonempirical calculations of the total energy and the crystal lattice dynamics using a generalized Gordon–Kim model of an ionic crystal proposed by Ivanov and Maksimov [8] which allows for the deformability and polarizability of the ions. In this model an ionic crystal is represented as consisting of individual overlapping spherically symmetric ions. The total electron density of the crystal at point **r** is then written as

$$\rho(\mathbf{r}) = \sum_i \rho_i(\mathbf{r} - \mathbf{R}_i),$$

where summation is performed over all the crystal ions.

The total crystal energy using the density functional method allowing only for pair interaction has the form

$$E_{cr} = \frac{1}{2}\sum_{i \neq j} \frac{Z_iZ_j}{|\mathbf{R}_i - \mathbf{R}_j|} + \sum_i E_i^{self}(R_w^i) + \frac{1}{2}\sum_{i \neq j} \Phi_{ij}(R_w^i, R_w^j, |\mathbf{R}_i - \mathbf{R}_j|), \tag{4}$$

Table 2. Parameters of the effective Hamiltonian (eV)

	Single-site		Interstitial		Coefficients of coupling with uniform strains		Elastic constants
A	4.096	a_1	–4.333	g_1	118.5	C_{11}	50.0
B	2.438×10^3	a_2	–0.028	g_2	–23.6	C_{12}	12.8
C	2.628×10^3	a_3	1.866			C_{44}	18.2
D	-40.700×10^3	b_1	–0.001				
		b_2	–2.166				

where Z_i is the charge of the ith ion,

$$\Phi_{ij}(R_w^i, R_w^j, |\mathbf{R}_i - \mathbf{R}_j|) = E\{\rho_i(\mathbf{r} - \mathbf{R}_i) + \rho_j(\mathbf{r} - \mathbf{R}_j)\} - E\{\rho(\mathbf{r} - \mathbf{R}_i)\} - E\{\rho(\mathbf{r} - \mathbf{R}_j)\}, \quad (5)$$

the energy $E\{\rho\}$ is calculated by the density functional method using a local approximation for the kinetic and exchange-correlation energies, and $E_i^{self}(R_w^i)$ is the ion self-energy. The electron density of an isolated ion and its natural energy are calculated taking into account the crystal potential V approximated by a charged sphere (Watson sphere):

$$V(r) = \begin{cases} Z_i/R_w, & r < R_w \\ Z_i/r, & r > R_w, \end{cases}$$

where R_w is the radius of the Watson sphere. The radii of the Watson sphere for isolated ions R_w^i are obtained from the condition for minimum total energy of the crystal. An expression for the dynamic matrix allowing for the electron polarizability and the deformability of the ions in the crystal neighborhood for crystals of arbitrary symmetry was given in [11]. Results of a group-theory analysis of the vibrational spectrum of crystals having an elpasolite structure were also presented there. The Coulomb contribution to the dynamic matrix was calculated using the Ewald method. The ion calculations were made using the Liberman program [12], the pair interaction energy and the ion polarizability were calculated using the Ivanov–Maksimov program [8] using the Thomas–Fermi approximation for the kinetic energy and the Hedin–Lundquist approximation for exchange and correlation. The derivatives appearing in the dynamic matrix were calculated using a technique of approximations of the energy dependences on the distances **R** and potentials V of the Watson sphere. Chebyshev polynomials were used for the approximations [8].

Table 3. Expressions for the eigenvalues λ_i of the force matrix for various phonon modes and for the distortion energies ΔE_i of various phases

λ_i	T_{1g}	$4a_1 + 8a_2 + 2b_1 + 4b_2 + A$	–22.125
	X_2^+	$4a_1 - 8a_2 + 2b_1 + 4b_2 + A$	–21.677
	$\mathbf{q} = \frac{\pi}{a_0}(1, 0, 0)$	$4a_1 - 2b_1 + 4b_2 + A$	–21.900
$\Delta E_L = E_L - E_0 - E_{anh}$		$-24a_3 - 6b_1 - 12b_2 + 3A$	–6.496
$\Delta E_{zx} = E_{zx} - E_0 - E_{anh}$		$-4a_1 + 2b_1 + 4b_2 + A$	12.762

The values of the elastic constants C_{11}, C_{12}, and C_{44} were determined from calculated dependences of the frequencies of the longitudinal and transverse acoustic vibrations for small q for three symmetric directions: [001], [110], and [111]. The calculated values of the elastic constants $C_{ij} = c_{ij}\Omega$, where Ω is the unit cell volume, are given in Table 2 for an Rb_2KScF_6 crystal. Unfortunately we are not aware of any experimental values of the elastic constants for this crystal and we can only make a rough comparison between the calculated values of C_{ij} and those measured for the isomorphic compound of similar chemical composition Rb_2NaHoF_6, for which C_{11} = 59.5 eV, C_{12} = 18.9 eV, C_{44} = 19.2 eV [13] and, as can be seen from Table 2, these constants are of the same order of magnitude as those calculated for an Rb_2KScF_6 crystal.

The coefficients of the second-order terms in (3) were determined from the calculated eigenvalues λ_i of the vibrational force constant matrix with the wave vector **q** in the [100] direction and from the total energies E_i of the two distorted phases. The second column in Table 3 gives the relationships between the linear combinations of coefficients in (3) and the eigenvalues λ_i and distortion energies $\Delta E_i = E_i - E_0 - E_{anh}$ [where E_0 = –216960 eV is the total crystal energy in the cubic phase, and E_{anh} is the numerical value of H_i^{anh} in (3) in the corresponding distorted phase], and the third column gives the values of λ_i and ΔE_i in electronvolts calculated from first principles. In this case, the energy ΔE_L corresponds to the distorted rhombohedral phase where the unit cell is twice the size of the cubic phase. This distortion corresponds to rotation of the octahedron about the spatial diagonal of a cube, i.e., the following distribution of $S_\alpha(\mathbf{R}_i)$:

$$S_x(\mathbf{R}_i) = S_y(\mathbf{R}_i) = S_z(\mathbf{R}_i) = |S| \exp(-i\mathbf{q}_L \cdot \mathbf{R}_i),$$

where $|S|$ is the amplitude of the local mode and $\mathbf{q}_L = \frac{\pi}{a_0}(1, 1, 1)$. The amplitude of this local mode was determined from the minimum of the total energy E_L of the distorted phase. We note that although this distorted phase cannot be obtained by condensation of any single phonon mode, in the crystal being discussed there is an unstable mode at the boundary point L of the Brillouin zone in which displacements lead to rotation of the octahedron accompanied by some slight distortion [11]. We also calculated the total energy E_{zx} of the distorted phase obtained as a result of rotation of the ScF_6 octahedron about the [001] axis with doubling of the unit cell along the [100] axis and the distribution $S_\alpha(\mathbf{R}_i)$ given by

$$S_z(\mathbf{R}_i) = |S|\exp(-i\mathbf{q}_X \cdot \mathbf{R}_i), \quad S_x = S_y = 0,$$

where $\mathbf{q}_X = \frac{2\pi}{a_0}(1, 0, 0)$. This distorted structure does not correspond to condensation of the phonon mode. Other homogeneous distorted structures with doubled unit cells associated with rotation of the octahedron do not yield new relationships between the linear combinations of coefficients so that we could not separate the isolated terms in the combination $4a_1 + 4b_2 + A$. We therefore assumed that the constant of interaction with the second neighbors b_2 in (3) is half the interaction constant between the nearest neighbors a_1. The basis for using this assumption was that, as calculations of the thermodynamic properties of a system with the Hamiltonian (3) have shown (see below), these properties were barely sensitive to the ratio b_2/a_1 for a certain value of a_1 (at least for three values of $b_2/a_1 = 1/4, 1/2, 3/4$ the results of the numerical modeling are indistinguishable).

The coefficients B, C, D before the anharmonic terms of the single-site potential were determined from the dependence of the total energy of a "squeezed" crystal (i.e., with the lattice parameter of the cubic phase $a_0 = 16.26$ au) on the angle of rotation of the ScF_6 octahedron about the [001]($S_x = S_y = 0$, $S_z = |S|$), [110] ($S_x = S_y = |S|$, $S_z = 0$), and [111] axes ($S_x = S_y = S_z = |S|$). These dependences are plotted in Fig. 3 and the values of the coefficients B, C, and D obtained by least squares fitting are given in Table 2.

We shall now determine the coefficients of coupling between the uniform elastic strains and the local mode. Since no shear strains are formed as a result of an $Fm3m \longrightarrow I4/m$ phase transition in the tetragonal phase, the coefficient g_3 in (3) was not determined. The coefficients g_1 and g_2 were determined as follows. The dependence of the total energy of a "free" crystal on the angle of rotation of the octahedron about the [001]-axis was calculated and for every angle the energy was minimized with respect to the unit cell parameters and the radii of the Watson spheres of the ions. This dependence is given by the open circles in Fig. 3a. The total energy of the squeezed crystal was then subtracted from this dependence and the coefficients g_1 and g_2, whose values are given in Table 2, were least-squares fitted to this energy difference using the values of the elastic constants already determined (Fig. 3d). As a check on the accuracy of determining these coefficients, Fig. 3e gives the dependence of the elastic strains in the tetragonal phase on the angle of rotation of the octahedron obtained by calculating the total energy of the free crystal and calculated from the condition for minimum of the model Hamiltonian:

$$\begin{aligned} e_1 &= -\frac{g_1(S_1^2 + S_2^2 + S_3^2)}{C_{11} + 2C_{12}} + \frac{2g_2(S_2^2 + S_3^2 - 2S_1^2)}{C_{11} - C_{12}}, \\ e_2 &= -\frac{g_1(S_1^2 + S_2^2 + S_3^2)}{C_{11} + 2C_{12}} + \frac{2g_2(S_3^2 + S_1^2 - 2S_2^2)}{C_{11} - C_{12}}, \\ e_3 &= -\frac{g_1(S_1^2 + S_2^2 + S_3^2)}{C_{11} + 2C_{12}} + \frac{2g_2(S_1^2 + S_2^2 - 2S_3^2)}{C_{11} - C_{12}}. \end{aligned} \quad (6)$$

The calculated and fitted values of $e_1 = e_2$ differ almost twofold. This is because the accuracy of the method used by us to calculate the total energy, the vibration frequencies, and thus the Hamiltonian parameters is inadequate to calculate values of e_i having small absolute values.

4. INVESTIGATION OF THERMODYNAMIC PROPERTIES

Despite its simplicity, the constructed effective Hamiltonian contains many parameters and it is difficult to make analytic calculations of the free energy and other thermodynamic quantities by self-consistent field methods. Thus, we used the Monte Carlo numerical method to study the thermodynamic properties of a system having the effective Hamiltonian (3). We used a classical Monte Carlo method with the Metropolis algorithm [14] for an $L \times L \times L$ fcc lattice with periodic boundary conditions. At each lattice site there is a three-component pseudovector (S_x, S_y, S_z). The entire lattice is located in a field of uniform strains e_1, e_2, e_3.

The Monte Carlo method was used to investigate two cases: a squeezed crystal, i.e., neglecting elastic strains ($e_1 = e_2 = e_3 = 0$) and a free crystal when e_1, e_2, and e_3 were calculated in the Monte Carlo process. In the first case a single Monte Carlo step was as follows. At each lattice site an increment in the pseudovector components (S_{ix}, S_{iy}, S_{iz}) was systematically selected at random and the possibility of taking this increment was checked. At this point it should be noted that our calculations of the total energy of the distorted phases and numerical simulation of the effective Hamiltonian show that distorted phases with unequal pseudovector components $S_x \neq S_y \neq S_z$ have energies substantially higher than phases with equal pseudovector components. Thus, to economize on machine time for the Monte Carlo procedure we took pseudovectors having

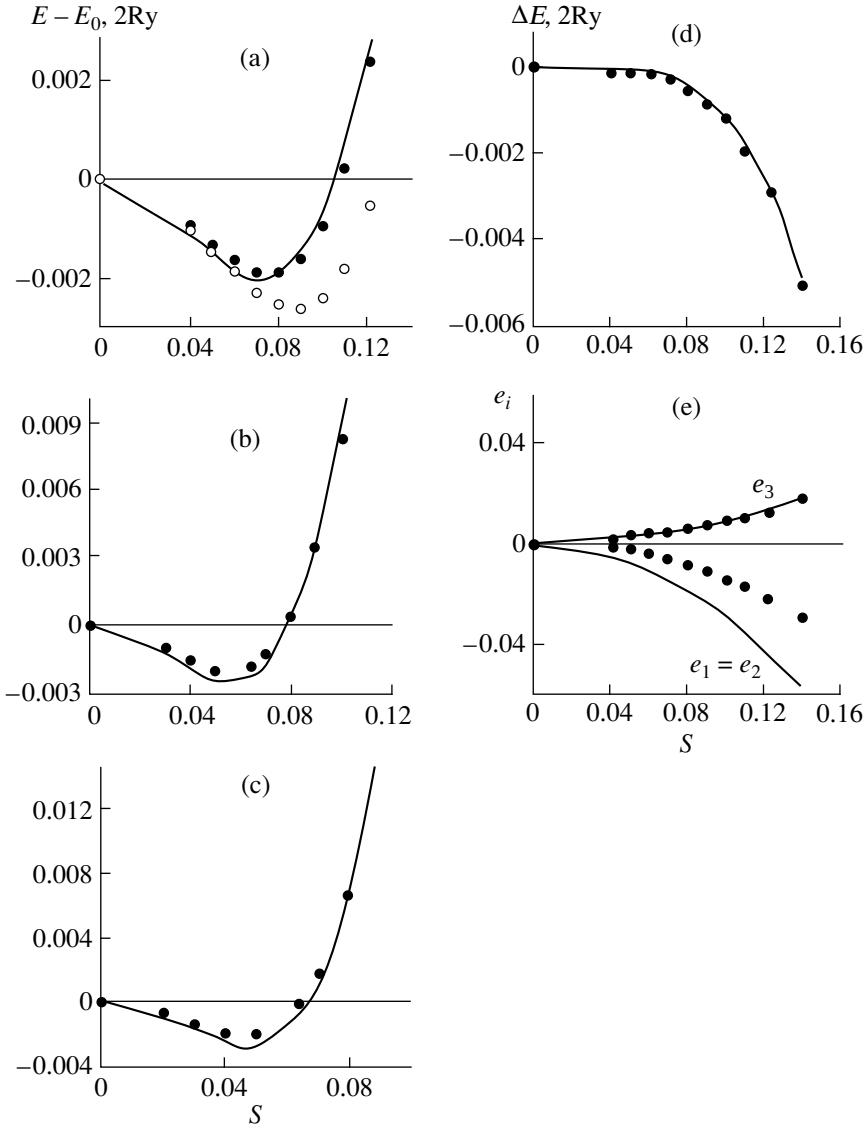

Fig. 3. Dependences of the total energy of a squeezed crystal on the angle of rotation of the octahedron. The solid curves give the calculations and the symbols give the energies obtained from the effective Hamiltonian with least squares fitted coefficients: (a) rotation about the [001]-axis, $S_x = S_y = 0$, $S_z = S$, open circles—total energy of free crystal; (b) rotation about the [110]-axis, $S_x = S_y = S$, $S_z = 0$; (c) rotation about the [111]-axis, $S_x = S_y = S_z = S$; (d) difference between the total energies ΔE of free and squeezed crystals; (e) dependence of the elastic strains in the tetragonal phase on the angle of rotation of the octahedron [the symbols give values of the elastic strains calculated from (6)].

the following three relationships between the components:

$$\text{(a) } S_z,\ S_x = S_y = 0;\ \text{(b) } S_z = \pm S_x,\ S_y = 0;$$
$$\text{(c) } S_z = \pm S_x = \pm S_y.$$

It can be seen from Fig. 3 that from $|S| \simeq 0.08$ the energy increases abruptly and thus the values of the components S_α and their increments were confined to the interval [–0.09; 0.09]. For each temperature we made 50000 Monte Carlo steps and averaging to find the thermodynamic quantities was performed over the last 10000 steps by a standard technique [14].

For the case of a free crystal after each Monte Carlo step described above we attempted to give an increment to each component of the stress tensor. The increment was selected randomly from the range [–0.03; 0.03]. For each component we made 1000 attempts and then averaged over these. The average values of the strain components and the pseudovector configuration obtained at each Monte Carlo step were the initial values for the next step.

Both high (500 K) and low (≃50 K) temperatures were taking as the starting temperatures. The Monte Carlo procedure from high temperatures was performed in parallel from two initial configurations corre-

sponding to the high-symmetry cubic phase ($S_x^i = S_y^i = S_z^i = 0$) and the distorted tetragonal phase ($S_z^i = 0.08$, $S_x^i = S_y^i = 0$). An initial configuration corresponding to the tetragonal phase was selected when starting from low temperatures. The calculations were made for $L = 10$ (4000 pseudovectors). As a check several temperatures were calculated for a larger lattice ($L = 20$, 32000 pseudovectors). The results of the calculations for a $20 \times 20 \times 20$ lattice differ negligibly from the results for a $10 \times 10 \times 10$ lattice and thus only the results obtained for a $10 \times 10 \times 10$ lattice are considered subsequently.

5. DISCUSSION OF RESULTS

Results of calculations of the temperature dependences of the pseudovector components S_x^i, S_y^i, S_z^i of the internal energy $E - E_0$ (E_0 is the total crystal energy in the cubic phase) and the components of the strain tensor e_1, e_2, e_3 are plotted in Fig. 4. We extracted the phase transition temperature from the point of inflection in the temperature dependence of the internal energy (Fig. 4a) and from the peak on the temperature dependence of the specific heat C_V determined by a standard method [14]. We do not give the curve of $C_V(T)$ here because, although this dependence has an abrupt peak at $T = 250$ K the value of C_V in the phase transition region and even at low temperatures is anomalously high (for example, $C_V/R = 2.5$, 20.1, 1.5, and 0.6, where R is the universal gas constant, at $T = 50$, 250, 300, and 500 K respectively). This is evidently because although the system reaches a steady state fairly rapidly at this temperature (after approximately 1000–5000 Monte Carlo steps), in this state small oscillating changes in energy and the lattice-averaged components of the pseudovector are observed in subsequent Monte Carlo steps (Fig. 5). For a given temperature the character and amplitude of the oscillations does not change over several tens of thousands of steps and for temperatures near T_c the amplitudes of these oscillations increases slightly. These energy oscillations (evidently due to some as yet unexplained procedural error) lead to anomalously high values of C_V.

At $T_c = 250$ K a free crystal undergoes a second-order phase transition to a distorted phase having the pseudovector $S_z^i = S$, $S_x^i = S_y^i = 0$. This is a tetragonal symmetry phase with no change in the unit cell volume relative to the volume of the cubic phase with the $I4/m$ space group which is observed experimentally in an Rb_2KScF_6 crystal below 252 K [6]. The accuracy of the calculations of the phase transition temperature is determined by the accuracy of the vibration frequencies and the total energy of the distorted phases. In our approach these values are calculated to within around 5%. The transition temperature obtained from the Monte Carlo calculations is almost the same as the experimental value.

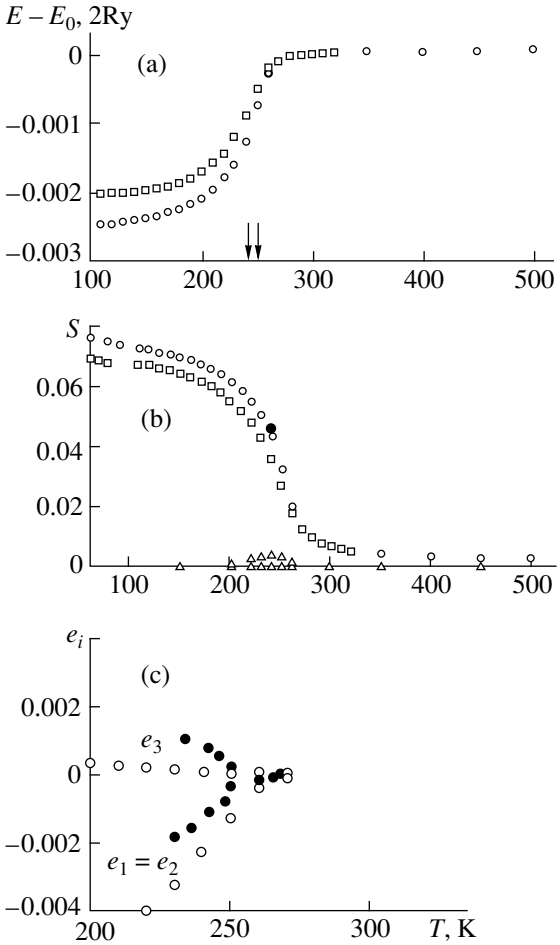

Fig. 4. Temperature dependences of: (a) internal energy using Monte Carlo data (the circles refer to the free crystal, the squares refer to the squeezed crystal); (b) the order parameter using Monte Carlo data (b) (open circles give the component S_z for a free crystal, squares give the component S_z for a squeezed crystal, triangles give the components S_x, S_y, the filled circle gives the experimental value of S_z from data on the structure of Rb_2KScF_6 in the tetragonal phase at $T = 240$ K [6]); (c) components of the strain tensor e_i in the tetragonal phase (open circles—Monte Carlo data, filled circles—experimental data [15]).

It follows from the experimental results of a structural study [6] that in the tetragonal phase the main distortions of the cubic structure are caused by equal displacements of four of the six fluorine ions from the equilibrium positions in the cubic phase (rotation of the octahedron). The experimental value of these displacements at $T = 240$ K is plotted in Fig. 4b. It can be seen that this shows very good agreement with the value of S_z at $T = 240$ K obtained from the Monte Carlo calculations. Figure 4c gives the experimental values and Monte Carlo calculations of the components of the elastic strain tensor $e_1 = e_2$ and e_3 in the tetragonal phase. Here the quantitative agreement between the calculated and experimental values is fairly poor but, as has already been discussed, the actual values of e_i are very low and the method of cal-

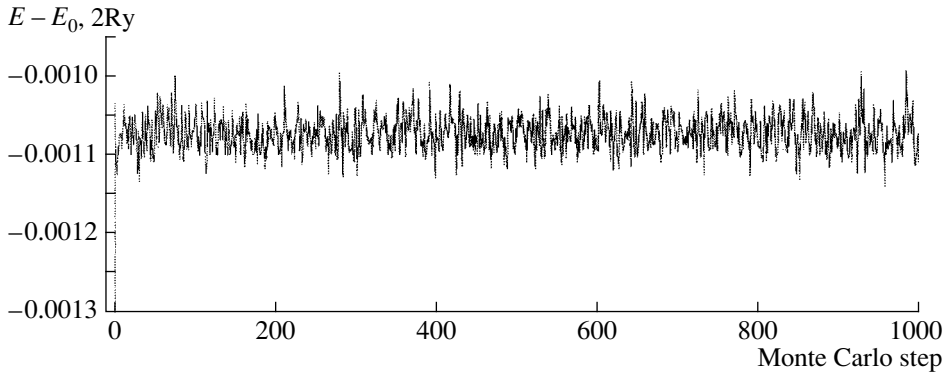

Fig. 5. Dependence of the internal energy on the number of Monte Carlo steps at $T = 230$ K.

culating the total crystal energy, vibration frequencies, and parameters of the model Hamiltonian used by us is not very accurate.

For a squeezed crystal, i.e., for zero values of the strain tensor components the phase transition temperature extracted from the Monte Carlo calculations is ten degrees lower than the transition temperature for a free crystal $T_c = 240$ K (Fig. 4).

In the Monte Carlo calculations the tetragonal phase remains stable as far as zero temperature and the other components of the pseudovector (S_x and S_y) do not appear which contradicts the experiment in which a second structural phase transition to the monoclinic phase with unit cell doubling is observed in an Rb_2KScF_6 crystal at $T_{c2} = 220$ K. It follows from the results of structural investigations of the monoclinic phase [6] that this transition is associated with the appearance of a second nonuniform pseudovector component over the crystal below T_{c2} and with displacements of rubidium ions from equilibrium positions. These Monte Carlo results confirm the result of a previous study made by the authors [7] in which it was shown by calculating the total energy of the monoclinic phase at $T = 0$ that if the monoclinic phase is obtained as a result of distortions associated only with rotations of ScF_6 octahedrons, the energy of this phase will be higher than the energy of the tetragonal phase. The monoclinic phase becomes favorable if the experimental values of the atomic coordinates are used in the calculations. This indicates that displacements of rubidium ions play a fundamental role in stabilizing the monoclinic phase in this crystal and in order to describe the second structural phase transition when constructing the model Hamiltonian, we need to consider the degrees of freedom corresponding to these displacements in addition to pure rotation.

6. CONCLUSIONS

Thus, we have constructed a nonempirical effective Hamiltonian to describe an $Fm3m \longrightarrow I4/m$ structural phase transition in an Rb_2KScF_6 crystal. The parameters of the Hamiltonian were determined from calculations of the total energy and the lattice vibration frequencies using a model of an ionic crystal which takes into account the deformability and polarizability of the ions. The model Hamiltonian was studied by the numerical Monte Carlo method. The temperature of the phase transition from the cubic to the tetragonal phase extracted from the Monte Carlo calculations $T_c = 250$ K is the same as the experimental value. This agreement may be random because the method of calculating the total energy and lattice vibration frequencies used in this study is not very accurate. In particular, the calculated equilibrium cell parameter in the cubic phase is 4.5% lower than the experimental value [7]. Nevertheless, it follows from the results obtained in this study that in an Rb_2KScF_6 crystal the $Fm3m \longrightarrow I4/m$ phase transition is mainly caused by uniform rotations of the ScF_6 octahedron over the lattice and the other degrees of freedom do not make any significant contribution to the mechanism or the thermodynamics of this phase transition.

In addition, the fairly successful description of this phase transition may indicate that the approach [2–5, 7, 8] used in the present study for microscopic studies of structural phase transitions in ionic crystals is fruitful and promising.

ACKNOWLEDGMENTS

The authors are grateful to the Russian Foundation for Basic Research (project no. 97-02-16277) and INTAS (grant no. 97-10-177) for financial support. We also thank O.V. Ivanov and E.G. Maksimov for allowing us to use their programs to calculate the total energy and polarizability of ions.

REFERENCES

1. V. G. Vaks, *Introduction to the Microscopic Theory of Ferroelectrics* (Nauka, Moscow, 1973).
2. R. D. King-Smith and D. Vanderbilt, Phys. Rev. B **49**, 5828 (1994).

3. K. M. Rabe and U. V. Waghmare, Ferroelectrics **164**, 15 (1995).
4. U. V. Waghmare and K. M. Rabe, Phys. Rev. B **55**, 6161 (1997).
5. D. Vanderbilt and W. Zhong, Ferroelectrics **206**, 181 (1998); W. Zhong, D. Vanderbilt, and K. M. Rabe, Phys. Rev. B **52**, 6301 (1995).
6. I. N. Flerov, M. V. Gorev, K. S. Aleksandrov, *et al.*, Mater. Sci. Eng. **R24**, 81 (1998).
7. V. I. Zinenko and N. G. Zamkova, Fiz. Tverd. Tela (St. Petersburg) **41**, 1297 (1999) [Phys. Solid State **41**, 1185 (1999)].
8. O. V. Ivanov and E. G. Maksimov, Zh. Éksp. Teor. Fiz. **108**, 1841 (1995) [JETP **81**, 1008 (1995)].
9. H. Thomas and K. A. Muller, Phys. Rev. Lett. **21**, 1256 (1968).
10. K. M. Rabe and J. D. Joannopoloulos, Phys. Rev. B **36**, 6631 (1987).
11. V. I. Zinenko, N. G. Zamkova, and S. N. Sofronova, Zh. Éksp. Teor. Fiz. **114**, 1742 (1998) [JETP **87**, 944 (1998)].
12. D. A. Liberman, D. T. Cromer, and J. J. Waber, Comput. Phys. Commun. **2**, 107 (1971).
13. P. Selgert, C. Lingner, and B. Luthi, Z. Phys. B **55**, 219 (1984).
14. *Monte Carlo Methods in Statistical Physics*, Ed. by K. Binder (Springer-Verlag, Berlin, 1979; Mir, Moscow, 1982).
15. I. N. Flerov, M. V. Gorev, S. V. Mel'nikova, *et al.*, Fiz. Tverd. Tela (St. Petersburg) **34**, 2185 (1992) [Sov. Phys. Solid State **34**, 1168 (1992)].

Translation was provided by AIP

Journal of Experimental and Theoretical Physics, Vol. 91, No. 2, 2000, pp. 324–331.
Translated from Zhurnal Éksperimental'noĭ i Teoreticheskoĭ Fiziki, Vol. 118, No. 2, 2000, pp. 370–379.

SOLIDS
Structure

Characteristics of the Thermodynamic and Kinetic Properties of $NbH_{0.83}$ in the Phase Transition Region

N. A. Sorokina*, D. Wlosewicz, T. Plackowski**, H. Misiorek**, and Ch. Sulkowski****

** Institute of High-Pressure Physics, Russian Academy of Sciences, Troitsk, Moscow oblast, 142092 Russia*

*** Institute of Low Temperature and Structure Research, Polish Academy of Sciences, P.O. Box 937, 50-950 Wroclaw, Poland*

Received February 25, 2000

Abstract—Measurements were made of the specific heat (in the temperature range 80–400 K), electrical resistivity (4.2–300 K), thermo-emf (4.2–300 K), thermal conductivity (7–300 K), magnetic susceptibility (4.2–400 K), and lattice parameters (30–300 K) of the alloy $NbH_{0.83}$. The $\lambda' \longrightarrow \lambda \longrightarrow \beta$ phase transitions were studied. It was established that the structure of the niobium matrix of the hydride remains unchanged as a result of these transitions. It is shown that the $\beta \longrightarrow \lambda$ phase transition (one-dimensional hydrogen ordering) is a three-stage one and is accompanied by a substantial change in the shear modulus of the hydride. The λ' phase existing at $T < 110$ K was determined. The electron thermal conductivity κ_{el} calculated for the λ' phase in the range $T < 23$ K is 25% higher than the measured thermal conductivity. In order to explain this fact and also the discontinuity in the concentration dependence of the coefficient of thermal expansion of NbH_x for $x \simeq 0.83$–0.84 and the approximately 1.5% compression of the $NbH_{0.84}$ volume it is assumed that in the region of x_c in the λ' phase the topology of the Fermi surface of the NbH_x interstitial alloy changes substantially. © *2000 MAIK "Nauka/Interperiodica".*

1. INTRODUCTION

On the basis of the "rigid band" model it has been suggested that niobium hydride NbH, having six electrons per cell, may be considered to be the electronic analog of molybdenum. The Fermi surface of niobium is open whereas that of molybdenum is closed and it is quite possible that at certain critical hydrogen concentrations the Fermi surface topology of the interstitial alloy NbH_x changes substantially [1]. Strictly speaking, the Fermi surface of an alloy has not been formally defined although various studies indicate that in many alloys of metals having similar properties the smearing of the Fermi surface is small [2]. Band calculations of stoichiometric NbH indicate that the density of electronic states has an abrupt minimum near the Fermi level [3], which correlates with the minimum at $x \simeq 0.82$–0.85 in the concentration dependences of the electron specific heat γ_{el} and the magnetic susceptibility χ of niobium hydrides NbH_x [4, 5]. However, insufficient experimental data were available to assess whether it is possible to talk of an electron-topological transition in the interstitial alloy NbH.

In order to obtain reliable data in this range of hydrogen concentrations, $x \sim 0.82$–0.85, we need to study the thermodynamic, kinetic, and structural properties of NbH_x hydrides at $T < 300$ K since no such data are available at present. For this purpose we investigated the little-studied part of the NbH phase diagram at $x > 0.75$ and $T < 230$ K using methods not previously used for such a study. The following properties of NbH_x were measured: specific heat, thermal expansion, thermal and electrical conductivity, thermo-emf, and structure of the niobium matrix. It should be noted that all the measurements were made for niobium hydride samples obtained from the same single-crystal niobium.

Our data indicate various anomalous dependences of the thermal and kinetic properties of NbH_x in various phases at $x \simeq 0.82$–0.85. For example, for the NbH_x niobium hydride samples studied, we obtained a concentration dependence of the thermo-emf of the cubic α' phase ($T \geq 400$ K) whose volume depends linearly on the hydrogen concentration [6]. This had an anomalously low value of –22 μV/K for the composition $NbH_{0.83}$ [7]. In accordance with theoretical estimates of the dependence of the electronic properties of the α and α' phases on the hydrogen concentration [8], it was suggested that in the region of this hydrogen concentration the Fermi level may pass through a minimum in the NbH density of states [7].

In the β-phase of NbH_x ($T = 300$ K) the concentration dependence of the specific heat had anomalies at $x = 0.8$–0.9 [9]. The volume of the β phase also depends linearly on the hydrogen concentration [6, 10].

The low-temperature λ' phase ($T \leq 100$ K) $NbH_{0.84}$ has a face-centered rhombic (fcr) structure and according to our estimate, its coefficient of thermal expansion is negative, $\beta = -58 \times 10^{-6}$ K^{-1} [11]. The Grüneisen parameter of the λ' phase $NbH_{0.84}$ is also negative [12].

The low-temperature γ phase ($T < 190$ K) of the hydride having a higher hydrogen concentration $NbH_{0.86}$ has a bcc lattice and its coefficient of thermal expansion is negative [13, 14].

In this context it was interesting to determine the structure of the niobium matrix $NbH_{0.83}$ at $T < 230$ K and the temperature dependence of its volume. It was also interesting to study the λ ⟶ β and λ ⟶ ? (unknown phase) phase transitions at $x = 0.83$. The present paper is devoted to clarifying these issues.

According to the generalized phase diagram of NbH [15] the niobium hydride $NbH_{0.83}$ when cooled below 420 K undergoes various phase transitions α' ⟶ β ⟶ λ ⟶ ?, attributable to ordering processes of the implanted hydrogen atoms over tetrahedral interstitial sites of the niobium matrix. Hydrogen in the α' phase is randomly distributed over tetrahedral interstitial sites of the bcc matrix. When the α' phase is cooled, the "hydrogen liquid" crystallizes, i.e. forms its own hydrogen sublattice. In this case the symmetry of the niobium matrix is reduced; the β phase lattice has a fcr structure [6]. When cooled below 230 K, the β phase $NbH_{0.83}$ is converted to the incommensurate λ phase. Since it is almost impossible to determine the type of modulation by purely structural studies, the terms "modulated structure" and "incommensurate structure" (or "disproportionate") are usually used as synonyms in the literature. Hydrogen in the λ phase forms a long-period structure modulated in the [001] direction and the β ⟶ λ phase transition is attributable to one-dimensional ordering of hydrogen and hydrogen vacancies [16, 17]. Studies of the λ ⟶ β phase transition in $NbH_{0.84}$ using calorimetry and x-ray structural analysis have shown that on the whole this is a first-order phase transition with a volume jump of the order of 1% and is isostructural relative to the niobium matrix; in the region of this phase transition ($T \simeq 227$ K) the $C_p(T)$ curve revealed three distinct peaks in the temperature range $\Delta T \simeq 1.5$ K [11] although it was unclear whether these peaks in the specific heat were merely attributable to hydrogen ordering. In a study of the acoustic properties of niobium hydrides the temperature dependence of the dynamic shear modulus G was plotted for $NbH_{0.83}$. This exhibited various anomalies in the λ ⟶ β phase transition region ($T \simeq 218$ K) and at $T \simeq 100$ K (λ ⟶ ?) which were interpreted as second-order phase transitions [18].

It was therefore interesting to study the λ ⟶ β and λ ⟶ ? phase transitions of $NbH_{0.83}$ hydride using the methods mentioned above and to compare the results with the data for $NbH_{0.84}$ [11] and $NbH_{0.83}$ [18]. We also measured the magnetic susceptibility $\chi(T)$ of the hydride since the phase diagram of NbH constructed using the measured dependences of $\chi(T, x)$ [5] differed appreciably from the generalized phase diagram from [15].

2. EXPERIMENT

A sample of $NbH_{0.83}$ was prepared from single-crystal niobium with $\Gamma = \rho_{300\ K}/\rho_{10\ K} \simeq 56$ by saturating through with hydrogen at $T \simeq 1120$ K, hydrogen pressure ≤5 atm, holding for 2 h and slowly cooling to $T \simeq 300$ K. For niobium hydride we find $\Gamma = \rho_{300\ K}/\rho_{4.2\ K} \simeq 11.8$. The pycnometric sample density is 7.69 ± 0.02 g/cm^3 while density calculations using x-ray data give 7.66 ± 0.09 g/cm^3. The hydrogen concentration is accurate to within 1% [14]. The specific heat was measured using an adiabatic calorimeter to within 1.5% [19]. The thermo-emf was determined with a temperature gradient of ≃1 K. The resistivity was measured by a dc four-contact method to within 3%, the magnetic susceptibility was measured in a field $H = 5$ kOe using a Quantum Design MPMS-5 SQUID magnetometer, the thermal conductivity was measured using a static method, and the averaged error in the determination of the thermal conductivity was 3%. An x-ray diffraction analysis of the hydride powder was made using a Siemens D5000 diffractometer at 30–300 K. The electrical resistivity, thermo-emf, thermal conductivity, and magnetic moment of $NbH_{0.83}$ were measured in a direction approximately 7° from the [001] fourfold axis.

3. RESULTS AND DISCUSSION

Figure 1 gives temperature dependences of the specific heat, parameters of the niobium matrix, hydride volume, magnetic susceptibility, and kinetic properties (thermal conductivity, electrical resistivity, thermo-emf) of the $NbH_{0.83}$ sample.

The curve of $C_p(T)$ in Fig. 1a shows anomalies whose temperatures correspond to ? ⟶ λ ⟶ β ⟶ α' phase transitions in $NbH_{0.83}$ according to the generalized phase diagram [15]. Table 1 gives data on the temperature boundaries of the phase transitions deter-

Table 1

T, K*	T, K**	Type of Nb sublattice	ΔS, J/(mol K)
385.1–392.7 β ⟶ α'	382–384.2 β ⟶ α'	fcr ⟶ bcc	≃8.07
179.3–229.8 λ ⟶ β	184–221 λ ⟶ β	fcr ⟶ fcr	≃1.85
93.4–141.4 ? ⟶ λ	116–142 λ' ⟶ λ	fcr ⟶ fcr	≃0.22

* Using phase diagram data [15], ** our data.

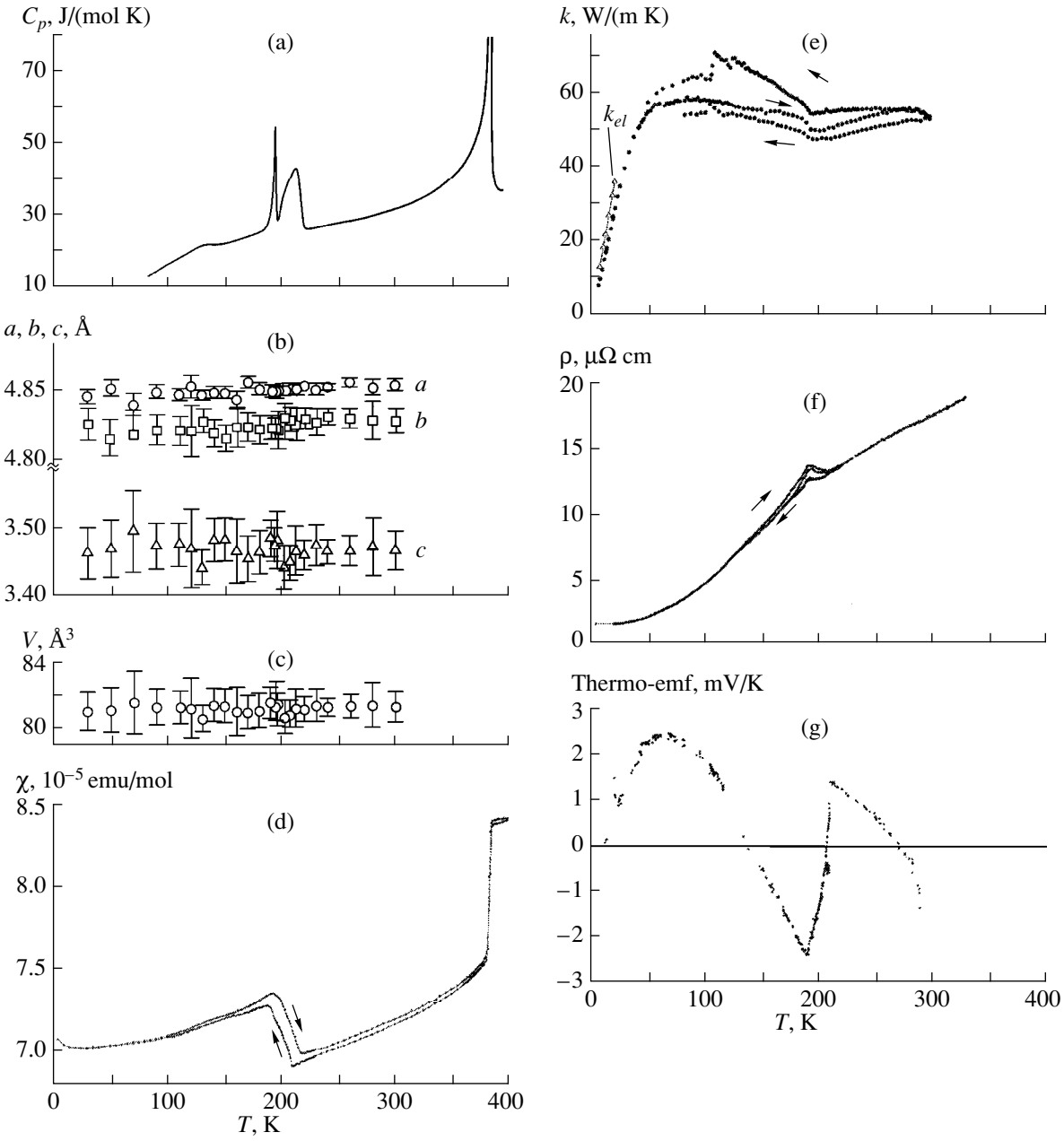

Fig. 1. Temperature dependences of the thermodynamic, structural, and kinetic properties of niobium hydride $NbH_{0.83}$: (a) specific heat at 80–400 K; (b) unit cell parameters of Nb sublattice at 30–300 K; (c) volume of hydride unit cell at 30–300 K; (d) magnetic susceptibility of hydride at 4.2–400 K; (e) thermal conductivity of hydride at 7–300 K; (f) electrical resistivity of hydride at 4.2–300 K; (g) thermo-emf of hydride at 4.2–300 K.

mined from calorimetric measurements, the entropy jumps ΔS accompanying the phase transitions, and the structure of the niobium matrix in the λ and λ' phases of $NbH_{0.83}$.

According to the x-ray data plotted in Fig. 1b, the structure of the niobium matrix in $NbH_{0.83}$ remains unchanged for $T < 300$ K and all the low-temperature conversions in this hydride are isostructural relative to the metal matrix. By analogy with the low-temperature phase ($T < 110$ K) $NbH_{0.84}$, having an fcr structure and denoted by us as λ', we shall assume that the phase of the $NbH_{0.83}$ hydride which exists at $T < 116$ K and also has an fcr structure, is the λ' phase. It is fairly difficult to determine exactly whether a volume jump is present or absent in these low-temperature phase transitions in $NbH_{0.83}$ because the error in determining the volume (of the order of 2%) is greater than in $NbH_{0.84}$ hydride where volume jumps of the order of 1% were clearly visible for $\lambda \longrightarrow \beta$ and $\lambda' \longrightarrow \lambda$ transitions where the error in determining the volume of this hydride was less than 1% [11].

The curve of $\chi(T) = M(T)/H$, where $M(T)$ is the magnetic moment of the sample and H is a static magnetic field (Fig. 1d), also clearly reveals anomalies corresponding to $\lambda \longrightarrow \beta$ transitions at 190–210 K and $\beta \longrightarrow \alpha'$ transitions at 382–384 K. The temperature dependence of the thermal conductivity $\kappa(T)$ in Fig. 1e exhibits a kink at 190–200 K associated with a $\lambda \longrightarrow \beta$ transition and a very weak singularity in the region of the $\lambda' \longrightarrow \lambda$ transition. The resistivity $\rho(T)$ in Fig. 1f has a kink at 193 K and the thermo-emf (Fig. 1g) increases in the region of the $\lambda \longrightarrow \beta$ transition (190–211 K). We shall examine these phase transitions in greater detail.

3.1. High-Temperature $\beta \longrightarrow \alpha'$ Phase Transition

The high-temperature peak on the curve of $C_p(T)$ in Fig. 2 corresponding to an order–disorder ($\beta \longrightarrow \alpha'$) phase transition, is fairly narrow. This is a first-order phase transition [6] with a large entropy jump. We can assume that the transition begins at 382 K, then has a singularity at 382.8 K, the maximum specific heat is observed at 383.6 K, and the transition ends at 384.2 K. The width of the transition is $\simeq$1.6 K. For $NbH_{0.84}$ the width of the $\beta \longrightarrow \alpha'$ transition according to our specific heat data is less than 0.6 K [11].

It is fairly interesting to note that in this narrow temperature range ($\simeq$1.6 K) two singularities are observed at the peak of the dependence $C_p(T)$ associated with a transition across the two-phase ($\beta + \alpha'$) region. For $NbH_{0.825}$ which has a similar concentration to the hydride under study, neutron diffraction data revealed an extremely narrow two-phase region: for the $\beta \longrightarrow \alpha'$ transition the intensity $I(T)$ of the (011) superstructural reflex dropped sharply in the temperature range 383.7–386.7 K [15].

A volume jump of approximately 0.3% for $NbH_{0.83}$ for the $\beta \longrightarrow \alpha'$ transition was determined from precision measurements of the NbH_x lattice parameters in the β and α' phases [10]. We note the good agreement between the unit cell volume of $NbH_{0.83}$ from this study ($V_{313\,K} = 81.278$ Å^3) and the average volume $V_{300\,K} = 81.28 \pm 1.56$ Å^3 for $NbH_{0.83}$. Knowing the hydride density and having determined the volume jump for the $\beta \longrightarrow \alpha'$ transition, $\Delta V \simeq 0.036$ cm^3/mol, we estimated the pressure dependence of this phase transition temperature $dT/dP = \Delta V/\Delta S \simeq 0.45$ K/kbar using the Clausius–Clapeyron law.

The magnetic susceptibility of $NbH_{0.83}$ increases abruptly by approximately 11% for the $\beta \longrightarrow \alpha'$ transition, i.e., in the hydrogen-disordered α' phase it is higher than that in the ordered phase. Singularities of the Knight shift of niobium hydride observed for ^{93}Nb in $^{93}NbD_{0.82}$ are strongly broadened in the β-phase compared with the α' phase [20]. A possible reason for this broadening and also for the reduction in susceptibility in the β phase is the nonuniform hydrogen neighborhood of the niobium atoms: the β phase has a layered structure with alternating (011) planes filled with hydrogen and without hydrogen. However, it is not yet possible to determine exactly what contribution is responsible for the change in the magnetic susceptibility accompanying the $\beta \longrightarrow \alpha'$ transition. The resistivity of $NbH_{0.83}$ increases approximately 1.6 times for the $\beta \longrightarrow \alpha'$ transition ($\Delta T \simeq 3.2$ K), the temperature at the center of the transition is 378.2 K and at the end it is 380.6 K, and the thermo-emf of the hydride decreases abruptly and in the α' phase is –22 μV/K [7].

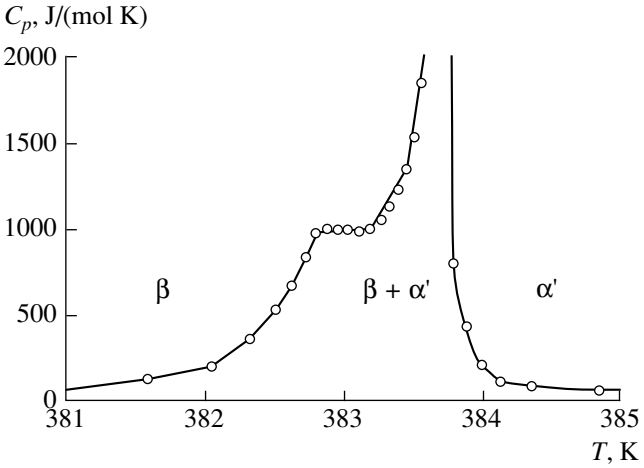

Fig. 2. Specific heat of $NbH_{0.83}$ near the $\beta \longrightarrow \alpha'$ phase transition.

3.2. Properties of the β Phase of $NbH_{0.83}$

The β phase of NbH_x has a polydomain structure. Division of the single crystal into domains of up to several hundred micron reduces the elastic energy of the crystal [6]. Curves of the magnetic susceptibility, electrical resistivity, and thermal conductivity clearly reveal hysteresis which is evidently associated with some irreproducibility of the domain structure of the hydride for the $\beta \longrightarrow \alpha'$ transition. The magnetic susceptibility of β-$NbH_{0.83}$ at $T = 300$ K is 71.8×10^{-6} emu/mol which shows good agreement with the data from [21, 22] and is three times lower than the susceptibility of niobium. The reduction in the susceptibility of niobium hydrides with increasing hydrogen concentration observed even at low temperatures is attributed to a decrease in the density of electron states obtained in the NbH band calculations [3]. This correlates with a decrease in γ_{el} for $NbH_{0.83}$ by a factor of 3.5 compared with γ_{el} for Nb [4]. The Debye temperature Θ_D of the β phase of the $NbH_{0.83}$ sample, 301 K, was measured from the ultrasound velocities measured at room temperature. This differs from the value of $\Theta_D = 360$ K for the λ' phase obtained from calorimetric data at 1.5–16 K [4]. The specific heat of the hydride in the β phase increases for $T > T/\Theta_D \simeq 0.8$, i.e., the Dulong

Table 2

No.	T_{peak}, K	Peak width ΔT, K	ΔS, J/(mol K)
1	193.4	2 ± 0.2	0.44 ± 0.03
2	205.1	11.5 ± 1.7	1.16 ± 0.22
3	212.5	6 ± 1	0.607 ± 0.16

and Petit law is not satisfied. In the region of the β-phase the thermo-emf changes sign from negative to positive at 280 K. The thermal conductivity of this hydride phase is the same as that of niobium, 55 W/mK [23].

3.3. λ ⟶ β Phase Transition

The λ phase typically exhibits an ordered distribution of hydrogen atoms and vacancies in the hydrogen sublattice along the *z* axis at a distance of approximately 14 lattice periods. The wave vector of the superstructure of the $NbH_{0.83}$ λ phase is $(3/14)2\pi/a[001]$ and the incommensurability parameter is $\delta \simeq 1 - x \simeq 0.16$ [16]. Figure 3 gives temperature dependences of the specific heat and the dynamic shear modulus $G(T)$ [18] of niobium hydride in the phase transition region. The

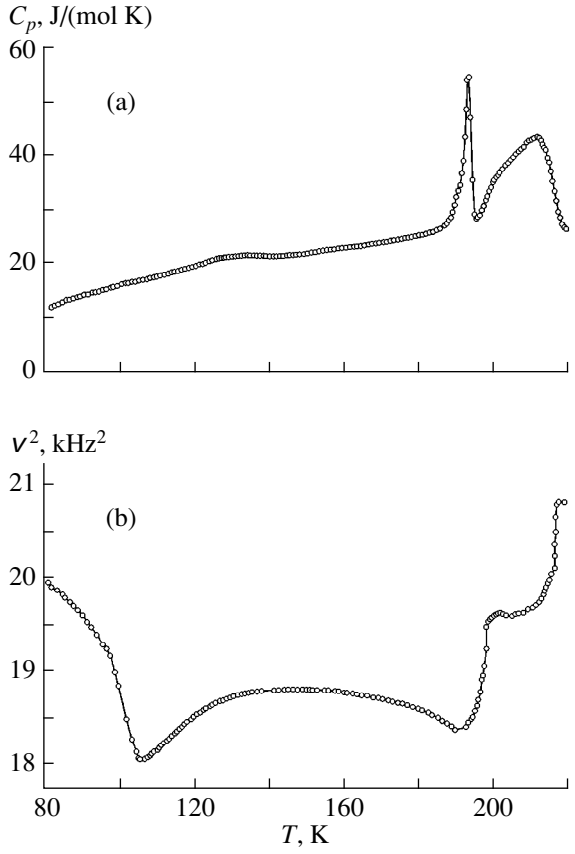

Fig. 3. Specific heat (a) and square of the resonant transverse frequency (b) of $NbH_{0.83}$ [18] for the low-temperature phases transitions λ' ⟶ λ and λ ⟶ β.

$C_p(T)$ curve has two peaks: a narrow one and a broad one with a shoulder. For $NbH_{0.84}$ this transition has three specific heat peaks in the interval $\Delta T \simeq 1.5$ [11]. Thus, we decided to separate the broad peak with a shoulder at $T \simeq 205$ K into two peaks using a Lorentz function. Data on the temperatures of the specific heat peaks and the entropy jumps are presented in Table 2.

The magnetic susceptibility $\chi = M(T)/H$ of the hydride decreases by approximately 6% for the λ ⟶ β transition [the beginning of the decrease (≃190 K) and the end (≃211 K under heating) show good agreement with the calorimetric data]. The curve of $\chi(T)$ (see Fig. 1d) exhibits hysteresis in this transition region, $\Delta T \simeq 10$ K. Since the magnetic moment is a thermodynamic quantity and possesses hysteresis, it can be assumed that the λ ⟶ β transition in a magnetic field is more likely first-order than three-stage as for $NbH_{0.84}$. We note that unlike the resistivity, the thermo-emf of the hydride has three singularities in this transition region: a minimum at 190.6 K, a change in slope at 202.6 K, and a maximum at 211 K. These temperatures show reasonable agreement with the temperatures of the specific heat peaks and also with the singularities in the temperature dependence of the dynamic shear modulus $G(T)$ of $NbH_{0.83}$. The elastic modulus has a minimum at 191.05 K and increases by approximately 6.5% to $T \simeq 200$ K. Near 202 K there is a small area with a kink ($\Delta T \simeq 4$–5 K) and then $G(T)$ increases by approximately 6% until the end of the transition at ≃218 K, Fig. 3b. It has been noted that no time dependence of the shear modulus of $NbH_{0.8}$ is observed even at 79 K which indicates that the niobium matrix rearranges rapidly with the hydrogen redistribution and the hydrogen mobility is high even at $T \simeq 100$ K [18].

The intensity $I(T)$ of the (011) superstructural reflex associated with the order parameter in the hydrogen sublattice in the (011) plane of $NbH_{0.825}$ decreases almost to zero as the temperature decreases from 236.7 to 183.7 K [15]. This indicates that the order in the hydrogen distribution in the (011) plane disappears in the λ phase compared with the β phase, i.e., the formation of a disproportionate structure in the hydrogen sublattice in the (001) plane is accompanied by the disappearance of order in the (011) plane.

We are not completely clear why the $C_p(T)$ curve for $NbH_{0.84}$ exhibits three peaks in such a narrow temperature range, these being most likely broadened as for $NbH_{0.86}$ [13] and for $NbH_{0.83}$. However, we can assume that the configurational entropy of these peaks is evidently associated with redistribution of hydrogen atoms and changes in the shear modulus of the metal matrix since the electron contribution to the entropy is small because of the low density of states at $x = 0.83$ and the vibrational contribution is also small, i.e., the specific heat of this hydride is approximately the same before and after the transition.

The resistivity $\rho(T)$ of $NbH_{0.83}$ only increases by 14% near the first stage of the phase transition (184.8–196.7 K), see Fig. 1f. For various cooling and heating cycles the resistivity of the sample in the transition region differs but the temperature of this transition remains the same. The thermal conductivity also has a jump near the first stage of the transition at $T \simeq 193$ K, whose temperature also remains constant for different cycles (cooling, heating, and recooling) but the thermal conductivities in the transition region differ. We can assume that the different values of the thermal conductivity and the electrical resistivity are caused by scattering at domains which, as was noted in electron diffraction studies of NbH_x foils, had different patterns under cooling and heating [16]. It may be noted that the period c of the niobium sublattice along the z axis along which hydrogen atoms and vacancies undergo ordering according to [16], decreases at the given temperature, i.e., the metal matrix is compressed in the [001] direction.

The ratio of the entropy jumps of the peaks on the $C_p(T)$ curve for $NbH_{0.83}$ obtained by separating the large peak with a shoulder, using the Lorentz–Gauss method, is approximately the same, being 1 : 2.6 : 1.4.

On comparing these data we can state that when hydrogen atoms undergo one-dimensional ordering along the z axis, substantial changes take place in the hydrogen sublattice and these are associated with changes in the shear modulus of the hydride. Unfortunately in [18] the authors do not indicate how the $NbH_{0.83}$ sample is cut and thus we do not know in which crystallographic direction the shear modulus changes. However, we can postulate that the niobium atoms are displaced in the [001] direction in the (110) planes not filled with hydrogen atoms [24].

According to electron diffraction data for niobium hydride foils [16], the domain walls of the β-phase disappeared as a result of a $\lambda \longrightarrow \beta$ transition and stripes appeared perpendicular to the [001] direction characteristic of the incommensurate λ phase, the spacing between them (≃50 Å) corresponding to the unit cell dimension of the long-period phase. The shear modulus of the λ phase is approximately 12% lower than that of the β phase.

3.4. $\lambda' \longrightarrow \lambda$ Phase Transition

The $C_p(T)$ curve at 110–138 K has a weak anomaly as a result of the $\lambda' \longrightarrow \lambda$ phase transition with an entropy jump $\Delta S \simeq 0.22 \pm 0.01$ J/(mol K). An anomalous increase in the shear modulus by approximately 4% is observed in this temperature range but no specific heat anomalies are detected for this $NbH_{0.83}$ sample at $T \simeq 105$ K where a minimum in $G(T)$ was observed for $NbH_{0.83}$ which was interpreted as a second-order phase transition [18]. The magnetic properties in this temperature range do not reveal any singularities but the curve of $\kappa(T)$ shows a slight change in slope at 110–138 K. The parameter c (see Fig. 1b) also decreases in this range of anomalies.

In $NbH_{0.84}$ an anomaly on the $C_p(T)$ curve with an entropy jump $\Delta S \simeq 0.05$ J/(mol K) and a volume jump of around 1% was also observed for the $\lambda' \longrightarrow \lambda$ transition ($T \simeq 115$–138 K), i.e., this was a first-order phase transition. The $NbH_{0.83}$ volume jump for this transition cannot be determined exactly because the error in determining the volume is larger than that for $NbH_{0.84}$, possibly due to the higher lattice stress at a given hydrogen concentration. However, the specific heat anomaly of $NbH_{0.83}$ may be compared with the specific heat and electrical resistivity anomalies of $PdH_x(D_x)$ at 50 K [6]. A neutron-diffraction analysis of $PdD_{0.65}$ powder [25] showed that the specific heat anomaly is attributable to a transition of deuterium atoms in octapores from a random distribution over nearest-neighbor sites to an ordered distribution over second coordination sphere sites. In this case the crystal structure of $PdD_{0.65}$ remains the same, cubic, and only the space group changes. In an NbH system in the range of hydrogen concentrations $x \simeq 0.83$–0.84 the type of $\lambda' \longrightarrow \lambda$ phase transition depends on the change in the electronic structure of the hydrides.

3.5. Properties of the λ' Phase

Despite the large error in its determination, the degree of tetragonalness of the λ' phase $c - \sqrt{a^2 + b^2}/2$ is positive and constant for $NbH_{0.83}$ at $T \leq 110$ K unlike $NbH_{0.84}$ for which it is negative and decreases linearly at $T \leq 110$ K. The magnetic susceptibility curve has a positive slope. The shear modulus increases anomalously as far as $T \simeq 65$ K as the temperature decreases. At $T < 65$ K the hysteresis in the kinetic and magnetic properties of $NbH_{0.83}$, i.e., $\rho(T)$, $\kappa(T)$, and $\chi(T)$ disappears.

The thermal conductivity of the λ' phase of $NbH_{0.83}$ has a broadened maximum with $T_{max} \simeq 92$ K caused by phonon scattering at hydride lattice defects and most likely, hydrogen sublattice defects and is similar to the broadened maximum of $NbH_{0.78}$ [23]. The residual resistivity of $NbH_{0.83}$ $\rho_{res} = 1.35$ μΩ cm is constant as far as $T \simeq 23$ K and is higher than $\rho_{res} = 0.63$ μΩ cm for $NbH_{0.84}$. At low temperatures ($T \leq 0.1\Theta_D$, elastic scattering) the thermal conductivity κ is proportional to temperature. The electron contribution to the thermal conductivity of $NbH_{0.83}$ calculated using the Wiedemann–Frantz formula: $\kappa_{el} = L_0 T/\rho$, where L_0 is the Lorentz constant, is approximately 25% higher than the measured value in this temperature range unlike $NbH_{0.78}$ and $NbH_{0.86}$ for which κ_{el} was 0.9κ and 0.42κ, respectively at $T = 10$ K [23]. The situation for $NbH_{0.83}$ may be explained by the fact that for $x \simeq 0.83$–0.84 there are two groups of carriers having different relax-

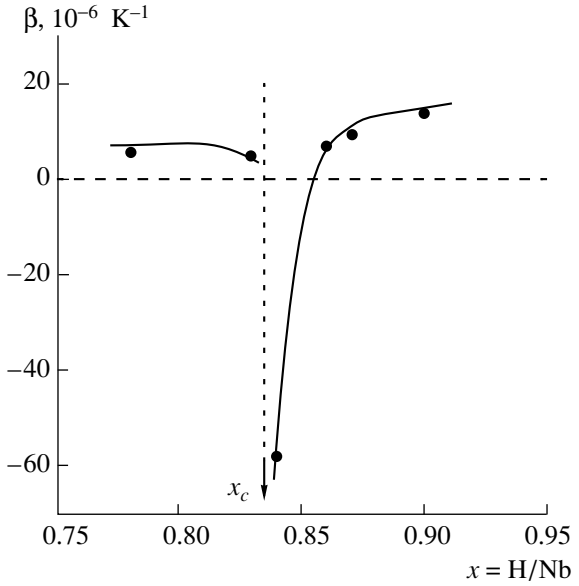

Fig. 4. Behavior of the coefficient of thermal expansion of NbH_x (t = 100 K) near the critical hydrogen concentration $x_c \simeq 0.83$–0.84.

ation times as a result of an electron-topological transition near these hydrogen concentrations.

4. NbH SYSTEM—INTERSTITIAL ALLOY

It is appropriate to recall that the chemical potential and the Fermi surface can change by applying pressure or varying the concentration of the alloy components [26]. As we noted in the Introduction, various studies have shown that in many substitutional alloys the smearing of the Fermi surface is small [2]. Unlike substitutional alloys, the interstitial NbH alloy has a regular metal matrix which can easily be seen from the Laue diffraction pattern of β-$NbH_{0.83}$ which reveals slight splitting of the reflexes as a result of a reduction in the symmetry of the niobium matrix (fcr).

The assumption that the Fermi surface topology of NbH_x changes substantially near $x \simeq 0.83$–0.84 is based on the following two factors: (1) the coefficient of thermal expansion of these NbH_x niobium hydrides has a discontinuity at 100 K and $x \simeq 0.83$–0.84; (2) the density of electronic states of stoichiometric NbH has an abrupt minimum near the Fermi level as for molybdenum. The Fermi surface of molybdenum is closed whereas that of niobium is open and for certain values of x_c for interstitial alloys, as for substitutional alloys of the Nb_xMo_{1-x} type, the hole surface centered at point Γ in the Brillouin zone characteristic of Nb may well be compressed and disappear completely and an electron sheet may appear at the center of the Brillouin zone characteristic of molybdenum [27]. For NbH_x the behavior of the dependence $\beta(x)$ for $x_c \simeq 0.83$–0.84 is similar to the behavior of $\beta(P)$ near the critical pressure P_c if the number of cavities at the Fermi surface increases for $P = P_c$ [26, Fig. 40]. Thus, we shall assume that a new surface, most probably an electron sheet, appears in the region of x_c for NbH_x, as shown in Fig. 4.

We shall make a more detailed analysis of the behavior of the volume coefficient of thermal expansion for NbH_x

$$\beta = \frac{1}{V}\frac{\partial V}{\partial T},$$

using data on the linear expansion of hydrides,

$$\alpha = \frac{1}{l_0}\frac{\partial L}{\partial T},$$

for x = 0.78, 0.86, 0.87, and 0.9 at T = 100 K [14, 28]. This temperature was selected because the dilatometric measurements of the hydrides were made at $T > 77$ K and at $T \leq 110$ K no phase transitions take place in an NbH system. Since according to preliminary x-ray data hydrides having these compositions have a bcc lattice at $T < 120$ K (data for $NbH_{0.86}$ were published in [13]), we can take $\beta \simeq 3\alpha$. For $NbH_{0.84}$ the values of β were obtained from x-ray data. For $NbH_{0.83}$ we estimated $\beta \simeq 4.86 \times 10^{-6}$ K^{-1} from x-ray data for two points at 90 and 110 K having the same error, bearing in mind that the overall $NbH_{0.83}$ volume remains constant at 30–100 K, as can be seen from Fig. 1c. Note that the lattice of the niobium matrix for $NbH_{0.83}$ and $NbH_{0.84}$ compositions has an fcr structure.

The volume of the $NbH_{0.83}$ unit cell at 30 K is 81.03 ± 1.38 Å^3 which is 0.5% larger than the volume of $NbH_{0.84}$, V = 80.61 ± 0.79 Å^3. The compression of the $NbH_{0.84}$ volume can also be attributed to an electron-topological transition near this hydrogen concentration.

Thus, the assumption that an electron-topological transition takes place in an NbH_x alloy at x_c can explain three experimental observations in the λ' phase: (1) the calculated value of κ_{el} for $NbH_{0.83}$ at $T < 23$ K is 25% higher than the measured value of κ; (2) the discontinuity in the concentration dependence $\beta(x)$ at 100 K; (3) the compression of the $NbH_{0.84}$ volume by approximately 1.5% at 100 K. Quite clearly, information on the galvanomagnetic properties of $NbH_{0.83}$ is required to explain this assumption.

5. CONCLUSIONS

1. We have refined the NbH phase diagram for $NbH_{0.83}$. We studied α' ⟶ β ⟶ λ ⟶ λ' phase transitions and determined the temperature boundaries, entropy jumps, and lattice parameters of the β, λ, and λ' phases. We determined the λ' phase which exists at $T <$ 110 K and the degree of tetragonalness of this phase was positive.

2. The $\lambda \longrightarrow \beta$ phase transition for $NbH_{0.83}$ is more likely of the first order but three-stage as for $NbH_{0.84}$. The one-dimensional ordering of the hydrogen atoms is closely related to a substantial change in the elastic moduli of the niobium matrix.

3. From an analysis of our data and the published data we put forward the assumption that in an NbH_x interstitial alloy in the vicinity of hydrogen concentrations $x \simeq 0.83$–0.84 in the λ' phase the Fermi surface most likely changes substantially and the appearance of a new surface, possibly an electron sheet, is most probable. The smearing of the Fermi surface of this interstitial alloy is clearly small at 100 K.

ACKNOWLEDGMENTS

In conclusion the authors are deeply grateful to E.G. Maksimov for interest in this work, discussions of the results, and critical comments. Thanks are also due to O.V. Stal'gorova for measurements of the ultrasound velocities, M.I. Baneeva for recording and analyzing the Laue diffraction patterns, and V.A. Ventsel', I.M. Kaganova, and E.M. Dizhur for valuable advice during discussion of the results.

REFERENCES

1. P. V. Gel'd, R. A. Ryabov, and L. P. Mokhracheva, *Hydrogen and Physical Properties of Metals and Alloys* (Nauka, Moscow, 1985).
2. V. G. Vaks, A. V. Trefilov, and S. V. Fomichev, Zh. Éksp. Teor. Fiz. **80**, 1613 (1981) [Sov. Phys. JETP **53**, 830 (1981)].
3. D. J. Peterman, D. K. Misemer, J. H. Weaver, and D. T. Peterson, Phys. Rev. B **27**, 799 (1983); K. M. Ho, H. J. Tao, and X. Y. Zu, Phys. Rev. Lett. **53**, 1586 (1984); P. Vargas and A. Pisanty, Z. Phys. Chem., Neue Folge **163**, 521 (1989).
4. D. Ohlendorf and E. Wicke, J. Phys. Chem. Solids **40**, 721 (1979).
5. U. Kobler and J. M. Welter, J. Less-Common Met. **84**, 225 (1982).
6. *Hydrogen in Metals*, Ed. by G. Alefeld and J. Volkl (Springer-Verlag, New York, 1978; Mir, Moscow, 1981).
7. N. I. Sorokina, Fiz. Tverd. Tela (Leningrad) **31**, 123 (1989) [Sov. Phys. Solid State **31**, 1545 (1989)].
8. V. G. Vaks and V. G. Orlov, J. Phys. F **18**, 883 (1988); V. G. Vaks and V. I. Zinenko, J. Phys.: Condens. Matter **1**, 9085 (1989).
9. T. Plackowski, D. Wlosewicz, and N. I. Sorokina, Physica B (Amsterdam) **212**, 119 (1995).
10. G. Mair, K. Bickmann, and K. Wenzl, Z. Phys. Chem., Neue Folge **114**, 29 (1979).
11. D. Wlosewicz, T. Plackowski, and N. I. Sorokina, Physica B (Amsterdam) **212**, 113 (1995).
12. N. I. Sorokina and V. V. Evdokimova, Fiz. Tverd. Tela (Leningrad) **29**, 218 (1987) [Sov. Phys. Solid State **29**, 122 (1987)].
13. T. Plackowski, N. I. Sorokina, and D. Wlosewicz, J. Phys.: Condens. Matter **10**, 1259 (1998).
14. N. I. Sorokina, O. V. Basargin, and V. I. Savin, Fiz. Tverd. Tela (Leningrad) **33**, 3565 (1991) [Sov. Phys. Solid State **33**, 2003 (1991)].
15. J.-M. Welter and F. Schondube, J. Phys. F **13**, 529 (1983).
16. B. J. Makenas and H. K. Birnbaum, Acta Metall. **30**, 469 (1982).
17. T. O. Brun, T. Kajitani, M. H. Mueller, *et al.*, in *Proceedings of the Modulated Structures Meeting, Kailua-Kona, Hawaii*, AIP Conf. Proc. **53**, 397 (1979).
18. V. A. Melik-Shakhnazarov, I. N. Bydlinskaya, I. A. Naskidashvili, *et al.*, Zh. Éksp. Teor. Fiz. **81**, 314 (1981) [Sov. Phys. JETP **54**, 168 (1981)].
19. D. Wlosewicz, T. Plackowski, and K. Rogacki, Cryogenics **32**, 265 (1992).
20. Y. S. Hwang, D. R. Torgeson, and R. G. Barnes, Solid State Commun. **24**, 773 (1977).
21. V. Tzhebyatovski and B. Stalinski, Acad. Pol. Sci., Ser. III **1** (7), 317 (1953).
22. S. Kasama and Y. Fukai, J. Less-Common Met. **53**, 25 (1977).
23. H. Misiorek, N. I. Sorokina, J. Mucha, and A. Jezowski, J. Alloys Compd. **176**, 233 (1991).
24. O. V. Gurin, V. N. Syromyatnikov, and W. Sikora, J. Less-Common Met. **101**, 529 (1984).
25. S. J. Kennedy, E. Wu, E. H. Kisi, *et al.*, J. Phys.: Condens. Matter **7**, L33 (1995).
26. I. M. Lifshits, M. Ya. Azbel', and M. I. Kaganov, *Electron Theory of Metals* (Nauka, Moscow, 1971; Consultants Bureau, New York, 1973).
27. K. M. Katachara, M. H. Menghnani, and E. S. Fisher, J. Phys. F **9**, 773 (1979).
28. N. I. Sorokina, O. V. Basargin, and V. I. Savin, Fiz. Tverd. Tela (St. Petersburg) **35**, 2958 (1993) [Phys. Solid State **35**, 1453 (1993)].

Translation was provided by AIP

Journal of Experimental and Theoretical Physics, Vol. 91, No. 2, 2000, pp. 332–337.
Translated from Zhurnal Éksperimental'noĭ i Teoreticheskoĭ Fiziki, Vol. 118, No. 2, 2000, pp. 380–387.

SOLIDS
Structure

Improved Phenomenological Renormalization Schemes

M. A. Yurishchev

*Radiophysical Research Institute, Nizhni Novgorod, 606263 Russia**
e-mail: yur@nirfi.sci-nnov.ru

Received March 22, 2000

Abstract—An analysis is made of various methods of phenomenological renormalization based on finite-dimensional scaling equations for inverse correlation lengths, the singular part of the free energy density, and their derivatives. The analysis is made using two-dimensional Ising and Potts lattices and the three-dimensional Ising model. Variants of equations for the phenomenological renormalization group are obtained which ensure more rapid convergence than the conventionally used Nightingale phenomenological renormalization scheme. An estimate is obtained for the critical finite-dimensional scaling amplitude of the internal energy in the three-dimensional Ising model. It is shown that the two-dimensional Ising and Potts models contain no finite-dimensional corrections to the internal energy so that the positions of the critical points for these models can be determined exactly from solutions for strips of finite width. It is also found that for the two-dimensional Ising model the scaling finite-dimensional equation for the derivative of the inverse correlation length with respect to temperature gives the exact value of the thermal critical index. *© 2000 MAIK "Nauka/Interperiodica".*

1. INTRODUCTION

As we know [1], the renormalization group method lies at the basis of modern phase transition theory. In this approach, the critical points of a system are identified with the fixed points of renormalization group mappings. By linearizing the renormalization group transformations near a fixed point it is possible to find the critical indices of the system of interest.

Many different specific realizations of the renormalization group procedure now exist. One of these realizations is the so-called phenomenological renormalization group proposed by Nightingale [2, 3] (see also the reviews [4, 5]). In this approach the scaling functional relationship between the correlation lengths of partially finite subsystems is interpreted as a renormalization group transformation. Combining this with expressions for the correlation lengths in terms of eigenvalues of the transfer matrices reduces the initial functional equation to a transcendental one and its solution gives an estimate for the critical temperature.

Dos Santos and Sneddon [6] noted that a phenomenological renormalization group can be constructed using not only the correlation length but any quantity having a power divergence at the phase transition point.

Binder [7, 8] suggested a variant of the phenomenological renormalization group based on using the moments of the distribution function of the order parameter; the moments can be expressed directly in terms of the susceptibility of the system. This method has been widely used in calculations using the Monte Carlo method. Recently, Itakura [9] expanded the Binder phenomenological renormalization scheme using linear combinations of different-order moments.

In the present study various phenomenological renormalization variants using a wide range of physical quantities (such as the free and internal energy, ordinary and nonlinear susceptibility, and so on) are used to calculate the critical coupling in the two-dimensional Ising and Potts models and also in the three-dimensional Ising model. An analysis can reveal the best renormalization strategies. Increasing the convergence is fundamentally important for three-dimensional systems because as a result of the giant orders of the transfer matrices, the eigenvalue problem can only be solved for subsystems having extremely small transverse dimensions.

However, a study of the convergence of various types of renormalizations revealed equations which can be used to find exact values of the parameters of infinite systems (critical temperatures and in one case, critical index) using the characteristics of partially finite subsystems.

This article is constructed as follows. Section 2 contains equations for different variants of the phenomenological renormalization group. In Section 3 these equations are applied to the two-dimensional Ising and Potts models and in Section 4 they are applied to the three-dimensional Ising lattice. The conclusions reached are summarized briefly in the final section.

2. EQUATIONS FOR THE PHENOMENOLOGICAL RENORMALIZATION GROUP

In accordance with finite-dimensional scaling theory [10–13], the inverse correlation length κ_L and the singular part of the reduced free energy density f_L^s ($f_L^s = f_L - f_\infty$, where f_L and f_∞ are the free energy densities of

* This work was partly carried out at the Landau Institute of Theoretical Physics, Russian Academy of Sciences, Chernogolovka, Moscow oblast, 142432 Russia.

the subsystem and the total system, respectively) near the critical point $t = h = 0$ ($t = K - K_c$ is the "temperature" or more accurately the deviation from the critical coupling, and h is the external field) satisfy the functional relationships

$$\kappa_L(t, h) = b^{-1}\kappa_{L/b}(t', h'), \quad (1)$$

$$f_L^s(t, h) = b^{-d} f_{L/b}^s(t', h'). \quad (2)$$

Here d is the space dimension, L is the characteristic linear dimension of the subsystem, $b = L/L'$ is the coefficient of the scaling transformation. The renormalization group equations $t' = t'(t, h)$ and $h' = h'(t, h)$ linearized near the fixed point $t = h = 0$ have the form

$$t' = b^{y_t}t + O(t^2), \quad (3)$$

$$h' = b^{y_h}h + O(h^2), \quad (4)$$

where y_t and y_h are the thermal and magnetic critical indices of the system.

In the Nightingale approach [2–5] the relationship (1) is treated as a renormalization group mapping $(t, h) \longrightarrow (t', h')$. In this case, the inverse correlation length of the spin–spin correlation function is given by the standard expression

$$\kappa_L = \ln(\lambda_1^{(L)}/\lambda_2^{(L)}), \quad (5)$$

where $\lambda_1^{(L)}$ and $\lambda_2^{(L)}$ are the largest and second largest eigenvalues of the transfer matrix of the subsystem, respectively. As a result, for systems with phase diagram symmetry $h \longrightarrow -h$ (and thus $h_c = 0$; we only consider these systems here) the only unknown coordinate of the critical point can be determined from the transcendental equation

$$L\kappa_L(K_c) = (L-1)\kappa_{L-1}(K_c) \quad (6)$$

(in order to maximize the accuracy of the estimate K_c it is usually assumed that $L' = L - 1$). Nightingale described his renormalization method as "phenomenological" [3] (see also [14]) since it uses a scaling finite-dimensional equation which is not derived microscopically using the method.

Quite clearly, the phenomenological renormalization $(t, h) \longrightarrow (t', h')$ can be made with equal justification using relation (2). In this case, we obtain the following equation to determine the critical coupling K_c

$$L^d f_L^s(K_c) = (L-1)^d f_{L-1}^s(K_c). \quad (7)$$

The free energy density of the partially finite subsystem $L^{d-1} \times \infty$ is then calculated using the formula

$$f_L = L^{1-d}\ln\lambda_1^{(L)}, \quad (8)$$

and the "background" f_∞ is taken from outside.

Differentiating expressions (1) and (2) m times with respect to temperature and n times with respect to the field allowing for Eqs. (3) and (4), we obtain [15]

$$L^{1-my_t-ny_h}\kappa_L^{(m,n)}(t, h) = (L')^{1-my_t-ny_h}\kappa_{L'}^{(m,n)}(t', h'), \quad (9)$$

$$L^{d-my_t-ny_h}f_L^{s(m,n)}(t, h) = (L')^{d-my_t-ny_h}f_{L'}^{s(m,n)}(t', h'). \quad (10)$$

These relationships or some combinations thereof can also be considered as implicit renormalization group transformations. For large subsystem dimensions all equations of this type should give the same results. However, for small L which we need to deal with in practice, the various renormalization group equations yield estimates of different accuracy. As we shall see, this circumstance means that it is possible to construct phenomenological renormalization schemes which give faster convergence than that achieved in conventionally used realizations of the phenomenological renormalization group method.

In addition to Eqs. (6) and (7) in the present study we also give estimates of the critical coupling obtained from the following renormalization group equations [taking those ratios (9) and (10) from which the unknown indices y_t and y_h are dropped *a priori*]:

$$\left.\frac{\chi_L^{(4)}}{L^d\chi_L^2}\right|_{K_c} = \left.\frac{\chi_{L-1}^{(4)}}{(L-1)^d\chi_{L-1}^2}\right|_{K_c}, \quad (11)$$

where $\chi_L = \partial^2 f_L/\partial h^2|_{h=0} = f_L^{s(0,2)}$ is the susceptibility and $\chi_L^{(4)} = \partial^4 f_L/\partial h^4|_{h=0} = f_L^{s(0,4)}$ is the nonlinear susceptibility (Eq. (11) corresponds to the Binder phenomenological renormalization [7, 8]);

$$L^{2-d}(\kappa_L^{(1)})^2/\chi_L = (L-1)^{2-d}(\kappa_{L-1}^{(1)})^2/\chi_{L-1}, \quad (12)$$

$$L^{1-d}\kappa_L^{(2)}/\chi_L = (L-1)^{1-d}\kappa_{L-1}^{(2)}/\chi_{L-1}, \quad (13)$$

$$L^{1-2d}\kappa_L^{(4)}/\chi_L^2 = (L-1)^{1-2d}\kappa_{L-1}^{(4)}/\chi_{L-1}^2. \quad (14)$$

Here we have $\kappa_L^{(n)} = \partial^n\kappa_L/\partial h^n|_{h=0} = \kappa_L^{(0,n)}(K, 0)$. Formulas for the derivatives of the inverse correlation length and the free energy with respect to h, expressed in terms of the eigenvalues and eigenvectors of the transfer matrices, suitable for programming are given in [16, 17].

For better clarity, Eqs. (6), (7), (11), (12), (13), and (14) will be denoted by the mnemonic symbols κ, f^s, $\chi^{(4)}/\chi^2$, $(\kappa^{(1)})^2/\chi$, $\kappa^{(2)}/\chi$, and $\kappa^{(4)}/\chi^2$, respectively when the numerical data are given in the tables.

Table 1. Estimates of K_c for a two-dimensional square Ising lattice; $K_c^{exact} = 0.440686\ldots$

Equation	(2, 3)	(3, 4)	(4, 5)
κ	0.42236	0.43088 (–2.23%)	0.43595
$\chi^{(4)}/\chi^2$	0.42593	0.43242 (–1.88%)	0.43672
$\kappa^{(4)}/\chi^2$	0.42596	0.43243 (–1.87%)	0.43673
f^s	0.44324	0.44168 (+0.23%)	0.44105
$\kappa^{(2)}/\chi$	0.47420	0.45153 (+2.64%)	0.44626

3. TWO-DIMENSIONAL SYSTEMS

We shall first test various types of phenomenological renormalization group equations on the two-dimensional Ising and Potts models, for which the positions of the critical points are known in exact analytic form [18, 19].

3.1. Ising Model

We shall start with the most studied system, the Ising model. Table 1 gives results of our calculations of the critical coupling for a simple square Ising lattice. The calculations were made for $L \times \infty$ strips having a periodic boundary condition in the transverse direction. Estimates are given for $(L-1, L)$ pairs with $L \le 5$. For a (3, 4) pair the relative errors of the estimates are also given in parentheses; their sign indicates whether they are lower (–) or upper (+) estimates. The types of renormalization group equations used are indicated in the first column. We recall that in this model we have

$$K_c = \frac{1}{2}\ln(1+\sqrt{2}), \quad f_\infty = \frac{2G}{\pi} + \frac{1}{2}\ln 2$$

(G is the Catalan constant) [20].

It can be seen from the data presented in Table 1 that the best lower estimate of K_c is obtained from Eq. (14). The Binder scheme gives slightly inferior results. This approach, which is usually used for Monte Carlo simulations, as we noted in the Introduction [because it does not have formulas of the type (5) for the inverse correlation length], was used in the transfer matrix variant in [21]. The Nightingale renormalization (first row in Table 1) which is almost universal (except perhaps for the study just mentioned [21]) is used for calculations using the transfer matrix method and is only third in terms of accuracy among the lower estimates.

It is worth noting that we also succeeded in obtaining phenomenological renormalization group equations which also yield upper estimates of K_c (the two lower rows in Table 1). Of these two estimates the renormalization scheme using the singular part of the free energy density [Eq. (7)] gives better-quality results. The values obtained using this scheme are at the same time the best in terms of absolute value among all the lower and upper estimates.

Unfortunately the renormalization procedure using the singular part of the free energy requires an advance knowledge of the critical free energy of the system f_∞. In order to overcome this constraint, instead of the two strips required to construct the renormalization group equation, we take three. In other words we shall take the triads (L_1, L_2, L_3); an additional relationship can eliminate the parameter f_∞. For the free energy densities of the three subsystems at the critical point we have

$$f_{L_1} = f_\infty + \frac{A_f}{L_1^d}, \quad f_{L_2} = f_\infty + \frac{A_f}{L_2^d}, \quad f_{L_3} = f_\infty + \frac{A_f}{L_3^d}. \tag{15}$$

Here $A_f = L^d f_L^s(0, 0)$ is the critical finite-dimensional scaling amplitude of the singular part of the free energy density. Eliminating the parameters f_∞ and A_f from the system (15), we arrive at the equation

$$\mathcal{F}(K) = F(K) - \frac{L_2^d - L_1^d}{L_3^d - L_2^d}\left(\frac{L_3}{L_1}\right)^d = 0, \tag{16}$$

where

$$F(K) = \frac{f_{L_1} - f_{L_2}}{f_{L_2} - f_{L_3}}. \tag{17}$$

Equation (16) can apparently be used to determine the position of the critical point but it has no real roots.

All the eigenvalues of the transfer matrix of an $L \times \infty$ Ising cylinder are known in exact analytic form for any L [20, 22]. The largest eigenvalue is

$$\lambda_1^{(L)} = (2\sinh 2K)^{L/2} \times \exp[(\gamma_1 + \gamma_3 + \ldots + \gamma_{2L-1})/2], \tag{18}$$

where γ_r are the positive solutions of the equations

$$\cosh\gamma_r = \cosh 2K \cosh 2K - \cos(\pi r/L). \tag{19}$$

Using formula (8) we then obtain expressions for the free energy densities f_{L_i} ($i = 1, 2, 3$) contained in Eq. (17).

Subsequent calculations using these formulas show that the curves $\mathcal{F}(K)$ do not intersect the abscissa and thus the equation $\mathcal{F}(K) = 0$ has no real solutions (see figure). However, it is noticeable that for various choices of parameters L_1, L_2, and L_3 the function $\mathcal{F}(K)$ [and therefore $\mathcal{F}(K)$] has an extremum positioned at the exact value of the critical coupling. Differentiating relation (17) with respect to K, we arrive at the equation

$$(u_{L_1} - u_{L_2})(f_{L_2} - f_{L_3}) = (u_{L_2} - u_{L_3})(f_{L_1} - f_{L_2}), \tag{20}$$

where $u_L = \partial f_L/\partial K$ is the internal energy of the subsystem. By using this equation or finding the extremum of the function $F(K)$ we can extract exact values of the

critical temperatures for infinite systems (at any rate for some) from the characteristics of their finite subsystems. (This is the desired aim of any finite-dimensional theory.)

Equation (20) can be approached from several positions. We shall analyze expression (10) in the first derivative with respect to K ($m = 1$, $n = 0$). For a fixed point this renormalization group transformation gives

$$L^{d-y_t}u_L^s(K_c) = (L')^{d-y_t}u_{L'}^s(K_c), \qquad (21)$$

where $u_L^s = u_L - u_\infty$ is the singular part of the internal energy density. It follows from Eq. (19) that

$$\partial\gamma_r/\partial K|_{K=K_c} = 0 \quad (r \neq 0) \qquad (22)$$

(in this context see Fig. 118 in [23]). After differentiating we find that $u_L(K_c) = \sqrt{2}$ regardless of L. In other words, all the finite-dimensional corrections to the background u_∞ ($=\sqrt{2}$ [20]) are zero, i.e., the singular part of the internal energy is completely absent. Consequently, we obtain

$$u_L^s(K_c) = 0. \qquad (23)$$

This property of the model leads to Eqs. (20) and (21) being satisfied.

We shall now analyze the first derivative with respect to temperature of the other fundamental equation in finite-dimensional scaling theory, i.e., Eq. (1).

The second eigenvalue of the transfer matrix of the Ising model in terms of value is given by

$$\lambda_2^{(L)} = (2\sinh 2K)^{L/2} \times \exp[(\gamma_0 + \gamma_2 + \ldots + \gamma_{2L-2})/2]. \qquad (24)$$

Equations (5), (18), (19), and (24) can be used to find an analytic expression for the inverse correlation length. Taking the first derivative with respect to K we obtain the dependences $\dot{\kappa}_L(K) \equiv \partial\kappa_L/\partial K$ for various L. All these dependences have a common point of self-intersection and this is positioned at the exact value of the critical coupling: $\dot{\kappa}_L(K_c) = -2$ for all $L = 1, 2, \ldots$ (i.e. in an infinite lattice $\dot{\kappa}_\infty = -2$). Thus we have

$$\dot{\kappa}_L(K_c) = \dot{\kappa}_{L'}(K_c). \qquad (25)$$

Reversing this reasoning, we conclude that Eq. (25) can also be used to determine the exact position of the critical point of an infinite two-dimensional Ising lattice using the solutions for strips of finite width.

Moreover, in accordance with relation (9) for $m = 1$ and $n = 0$ we have

$$y_t = 1 + \frac{\ln(\dot{\kappa}_L/\dot{\kappa}_{L'})}{\ln(L/L')}. \qquad (26)$$

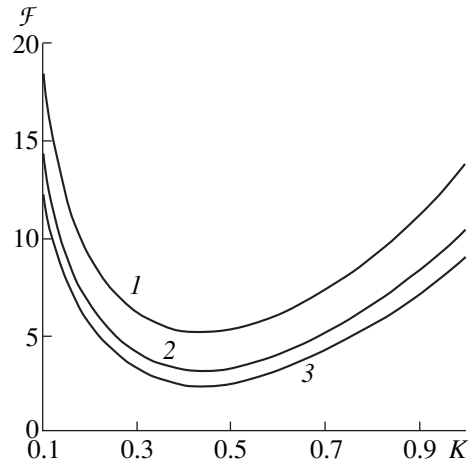

Behavior of the function $\mathcal{F}(K)$ for triads of Ising strip clusters (1, 2, 3), (2, 3, 4), and (3, 4, 5) given by curves *1*, *2*, and *3*, respectively. In all cases the minimum of the function is positioned at the exact value $K_c = 0.5\ln(1 + \sqrt{2}) = 0.440686\ldots$.

Consequently, this finite-dimensional expression taking into account condition (25) gives an exact value for the thermal critical index of the two-dimensional Ising model: $y_t = 1$.

For the Ising model Eq. (25) can be generalized to the form

$$(\dot{\kappa}_{L_1} - \dot{\kappa}_{L_2})(\kappa_{L_2} - \kappa_{L_3}) = (\dot{\kappa}_{L_2} - \dot{\kappa}_{L_3})(\kappa_{L_1} - \kappa_{L_2}) \qquad (27)$$

and the problem of determining K_c can be reduced to searching for the extremum of the function

$$\Phi(K) = \frac{\kappa_{L_1} - \kappa_{L_2}}{\kappa_{L_2} - \kappa_{L_3}}. \qquad (28)$$

3.2. Potts Model

In the two-dimensional q-position Potts model for an isotropic square-cell lattice the critical coupling is $K_c = \ln(1+\sqrt{q})$ [24]. Table 2 contains estimates of K_c obtained by us using various constructions of the phenomenological renormalization group for the Potts model with three node states ($q = 3$). The free energy background in this model is given by [25, 26]

$$f_\infty = \frac{4G}{3\pi} + \ln(2\sqrt{3}) + \frac{1}{3}\ln(2 + \sqrt{3}). \qquad (29)$$

An analysis of the data given in Table 2 shows that Eqs. (7) and (12) give substantially better-quality estimates than the Nightingale approach (first row in the table). The renormalization group equation based on the scaling relationship for the singular part of the free

Table 2. Estimates of K_c for a two-dimensional square three-position Potts lattice: $K_c^{exact} = 1.005052\ldots$

Equation	(2, 3)	(3, 4)	(4, 5)
κ	0.96248	0.98350 (–2.1%)	0.99467
$\kappa^{(1)^2}/\chi$	0.99311	0.99920 (–0.6%)	1.00380
f^s	1.00927	1.00667 (+0.2%)	1.00565

Table 3. Estimates of K_c for a three-dimensional simple cubic Ising lattice; $K_c^{exact} = 0.22165459(10)$

Equation	(2, 3)	(3, 4)
κ	0.21340	0.21826 (–1.53%)
$\chi^{(4)}/\chi^2$	0.21823	0.22002 (–0.74%)
$\kappa^{(4)}/\chi^2$	0.21824	0.22006 (–0.72%)
f^s	0.22354	0.22236 (+0.32%)
$\kappa^{(2)}/\chi$	0.22658	0.22323 (+0.71%)

energy again gives the smallest errors in terms of absolute value.

Calculations made for $L \times \infty$ strips with a periodic boundary condition in the transverse direction then uniquely indicate that in the two-dimensional q-position Potts model all finite-dimensional corrections to the internal energy ($u_\infty = 1 + 1/\sqrt{q}$ [18]) are also absent at the critical point. Consequently, the equation

$$u_L(K_c) = u_{L'}(K_c) \tag{30}$$

gives the exact value of K_c. Satisfying condition (30) then has the result that Eq. (20) is valid and thus the extremum of the function (17) is positioned strictly at the exact value of the critical coupling. It should be noted that in computer calculations it is more logical to search directly for the extremum of the function than to differentiate the free energy numerically and then solve the transcendental Eq. (30) numerically.

Equation (30) for the pair (1, 2) was first obtained by Wosiek from his postulated maximum principle for the normalized moments of transfer matrices [27] (see also [28]). In [29] the Wosiek equation was then generalized to the form (30). Our Eq. (20) is a further generalization of Eq. (30).

Note that in the Potts model the curves $\dot{\kappa}_L(K)$ also intersect. However, unlike the Ising model the points of intersection are not now positioned at the exact value of K_c. At the exact value of the critical coupling the functions $\dot{\kappa}_L(K)$ have different values for various L. Unfortunately the scaling formula (26) then only gives approximate estimates of the thermal critical index which, for example for the three-node Potts model is $y_t = 6/5$.

Returning to the two-dimensional Ising model we can confirm that a complete system of equations of the type (30) is in fact obtained for this model:

$$u_L^j(K_c) = u_{L'}^j(K_c), \tag{31}$$

where $u_L^j = \partial f_L^j/\partial K$ are internal energy levels; this term was taken by analogy with the "free energy levels" $f_L^j = L^{1-d}\ln\lambda_j^{(L)}$, $j = 1, 2, \ldots$ (see, for example [30]).

4. THREE-DIMENSIONAL ISING LATTICE

We shall now consider a three-dimensional Ising model for a simple cubic lattice. Unlike the two-dimensional Ising model, which is solved analytically over the entire temperature range, or the two-dimensional Potts model which is solved exactly at a single point, the critical point, for the three-dimensional Ising model we are forced to confine ourselves to numerical estimates. The highest-quality estimates for the critical coupling and the free energy background have now been obtained by Monte Carlo simulation for $L \times L \times L$ cubes: $K_c = 0.22165459(10)$ [31] and $f_\infty = 0.77790(2)$ [32].

Table 3 gives our results for the three-dimensional Ising model. The renormalizations were made for $L \times L \times \infty$ parallelepipeds with periodic boundary conditions in both transverse directions. The calculations were made for subsystems with side lengths $L \le 4$, i.e., for transfer matrices having dimensions up to 65536×65536.

We can see from Table 3 that as in the two-dimensional case, the best lower estimates of K_c are provided by the renormalization group Eq. (14). On comparing the lower and upper estimates we can conclude that the best of all the results is again given by renormalizing the singular part of the free energy.

In the three-dimensional case the amplitudes of the finite-dimensional corrections to the internal energy at the critical point are no longer zero. In accordance with the scaling Eq. (21) we have

$$u_L(K_c) = u_\infty + A_u L^{-d+y_t}, \tag{32}$$

where A_u is the amplitude of the principal finite-dimensional correction to the internal energy density of the system at the critical point. Calculations using formula (32) for a $4 \times 4 \times \infty$ cluster using the values $u_\infty = 0.990637(47)$ [33, 34] and $y_t = 1.5865(14)$ [31] give $A_u \simeq 1.19$.

Since $A_u \neq 0$, Eq. (30) now only reproduces an approximate value of K_c. Also Eq. (20) is not satisfied exactly. Calculations of the position of the minimum of the function (17) for the triad (2, 3, 4) yield the estimate $K_c = 0.233003$. Unfortunately, the accuracy of this estimate (5.1%) is significantly inferior to the errors of the

estimates obtained from the other renormalization schemes (see Table 3).

5. CONCLUSIONS

Nontrivial models with known values of the critical coupling have been used to study phenomenological renormalization schemes which for the same subsystem dimensions give more accurate results than those used so far. We established that for Ising models the renormalization group equations using combinations $L^{1-2d}\kappa_L^{(4)}/\chi_L^2$ and $L^{1-d}\kappa_L^{(2)}/\chi_L$ give uniformly converging bilateral estimates of K_c where the errors (in the three-dimensional, most important case) are less than half those obtained in the Nightingale method.

Another result of this study is related to the exact results. We have shown that by making the amplitudes of the finite-dimensional corrections to the internal energy vanish, exact values of the critical temperatures can be determined for the infinite two-dimensional Ising and Potts models from the solutions for their partially finite subsystems. In addition, we have observed that for the two-dimensional Ising model the temperature derivative of the inverse correlation length has absolutely no finite-dimensional corrections. This means that it is also possible to find the exact value of the thermal crisis index for this model from the finite-dimensional equation.

Both the conclusions reached from these results have practical applications but separate analyses are required to develop them.

ACKNOWLEDGMENTS

The author thanks A.A. Belavin for useful discussions and valuable comments. Thanks are also due to J. Wosiek for showing interest in this work. This work was supported financially by the Russian Foundation for Basic Research (project no. 99-02-16472).

REFERENCES

1. S. Ma, *Modern Theory of Critical Phenomena* (Benjamin, Reading, Mass., 1976; Mir, Moscow, 1980).
2. M. P. Nightingale, Physica A (Amsterdam) **83**, 561 (1976).
3. M. P. Nightingale, Proc. K. Ned. Akad. Wet., Ser. B: Paleontol., Geol., Phys., Chem., Anthropol. **82**, 235 (1979).
4. P. Nightingale, J. Appl. Phys. **53**, 7927 (1982).
5. M. P. Nightingale, in *Finite Size Scaling and Numerical Simulation of Statistical Systems*, Ed. by V. Privman (World Scientific, Singapore, 1990), p. 287.
6. R. R. dos Santos and L. Sneddon, Phys. Rev. B **23**, 3541 (1981).
7. K. Binder, Phys. Rev. Lett. **47**, 693 (1981).
8. K. Binder, Z. Phys. B **43**, 119 (1981).
9. M. Itakura, cond-mat/9611174.
10. M. Fisher, in *International School of "Enrico Fermi" on Critical Phenomena, 1970*, Ed. by M. S. Green (Academic, New York, 1971); F. J. Dyson, E. W. Montroll, M. Kac, and M. Fisher, *Stability and Phase Transition* (Mir, Moscow, 1973), p. 245.
11. M. E. Fisher and M. N. Barber, Phys. Rev. Lett. **28**, 1516 (1972).
12. M. N. Barber, in *Phase Transitions and Critical Phenomena*, Ed. by C. Domb and J. L. Lebowitz (Academic, London, 1983), Vol. 8, p. 145.
13. V. Privman, in *Finite Size Scaling and Numerical Simulation of Statistical Systems*, Ed. by V. Privman (World Scientific, Singapore, 1990), p. 1.
14. W. Kinzel and M. Schick, Phys. Rev. B **23**, 3435 (1981).
15. M. A. Yurishchev, hep-lat/9908019; submitted to Nucl. Phys. B (Proc. Suppl.) (2000).
16. M. A. Yurishchev, Phys. Rev. B **50**, 13533 (1994).
17. M. A. Yurishchev, Phys. Rev. E **55**, 3915 (1997).
18. R. J. Baxter, *Exactly Solved Models in Statistical Mechanics* (Academic, New York, 1982; Mir, Moscow, 1985).
19. F. Y. Wu, Rev. Mod. Phys. **54**, 235 (1982).
20. L. Onsager, Phys. Rev. **65**, 117 (1944).
21. H. Saleur and B. Derrida, J. Phys. (Paris) **46**, 1043 (1985).
22. B. Kaufman, Phys. Rev. **76**, 1232 (1949).
23. K. Huang, *Statistical Mechanics* (Wiley, New York, 1963; Mir, Moscow, 1966).
24. R. B. Potts, Proc. Cambridge Philos. Soc. **48**, 106 (1952).
25. R. J. Baxter, J. Phys. A **6**, L445 (1973).
26. R. J. Baxter, Proc. R. Soc. London, Ser. A **383**, 43 (1982).
27. J. Wosiek, Phys. Rev. B **49**, 15023 (1994).
28. Z. Burda and J. Wosiek, Nucl. Phys. B (Proc. Suppl.) **34**, 677 (1994).
29. A. Pelizzola, Phys. Rev. B **51**, 12005 (1995).
30. V. Privman and M. E. Fisher, Phys. Rev. B **30**, 322 (1984).
31. H. W. J. Blöte, L. N. Shchur, and A. L. Talapov, Int. J. Mod. Phys. C **10**, 437 (1999).
32. K. K. Mon, Phys. Rev. B **39**, 467 (1989).
33. M. Hasenbusch and K. Pinn, Nucl. Phys. B (Proc. Suppl.) **63**, 619 (1998).
34. M. Hasenbusch and K. Pinn, J. Phys. A **31**, 6157 (1998).

Translation was provided by AIP

Journal of Experimental and Theoretical Physics, Vol. 91, No. 2, 2000, pp. 338–345.
Translated from Zhurnal Éksperimental'noĭ i Teoreticheskoĭ Fiziki, Vol. 118, No. 2, 2000, pp. 388–396.

SOLIDS
Electronic Properties

Influence of Phonon Dispersion and Exciton Spectrum on the Energy Spectrum of Magnetopolarons in a Quantum Well

L. I. Korovin[1, *], I. G. Lang [1], and S. T. Pavlov[2, **]

[1] *Ioffe Physicotechnical Institute, Russian Academy of Sciences, St. Petersburg, 194021 Russia*
[2] *Lebedev Physical Institute, Russian Academy of Sciences, Moscow, 117924 Russia*
**e-mail: korovin@masha.shuv.pti.spb.su*
***e-mail: pavlov@sci.lpi.ac.ru*

Received October 6, 1999

Abstract—An analysis is made of the influence of the spatial dispersion of *LO* phonons and the exciton effect on the energy spectrum of magnetopolarons in a quantum well. It is shown that in optical experiments where light is incident normally on the plane of the quantum well, a discrete spectrum of magnetopolarons is observed. Both the phonon dispersion and the Coulomb attraction of an electron and a hole may lead to a shift of the discrete magnetopolaron energy levels and additional contributions to the broadening of various levels. © *2000 MAIK "Nauka/Interperiodica".*

1. INTRODUCTION

We shall analyze the energy spectrum of the electronic excitations in a quantum well positioned in a strong magnetic field perpendicular to the plane of the well. Since the system is homogeneous in the quantum well plane (*xy* plane), any excitation, be it an exciton or a magnetopolaron–hole pair allowing for Coulomb electron–hole interaction, may be characterized by the quasi-momentum $\mathcal{K}_\perp$ in the quantum well plane if the wave functions are suitably selected. For excitons in a strong magnetic field these functions were obtained in [1] and for magnetopolaron–hole pairs they were obtained in [2]. The quasi-momentum $\mathcal{K}_\perp$ can be a quantum number since any excitation consisting of an electron and a hole is neutral. (We recall that in a strong magnetic field states in which the vector $\mathcal{K}_\perp$ is a quantum number do not exist separately for an electron or a hole.) The aim of the present study is to determine in principle how magnetopolaron theory changes when allowance if made for the dispersion of *LO* phonons and the exciton effect, i.e., Coulomb interaction between an electron forming a polaron and a hole which interacts weakly with *LO* phonons.

If the excitations are generated in a quantum well as a result of exposure to light, the condition $\mathcal{K}_\perp = \kappa_\perp$ is satisfied where $\kappa_\perp$ is the projection of the light wave vector on the plane *xy*. For normal irradiation, i.e., $\kappa_\perp = 0$ we obtain $\mathcal{K}_\perp = 0$. Quite clearly, for $\mathcal{K}_\perp = 0$ and finite motion of excitations along the *z* axis it is only possible to have a discrete energy spectrum. In particular, this implies that for normally incident light neither allowance for the dispersion of the *LO* phonons nor Coulomb interaction between an electron and a hole can lead to smearing of the excited energy levels in the band. These factors can only cause a shift of the discrete levels and change the reciprocal lifetimes γ corresponding to these levels. The results of the present study confirm this general assumption. It will be shown that allowance for the exciton effect leads to a dependence of the energy of a magnetopolaron–hole pair on the energy of the quasi-momentum $\mathcal{K}_\perp$ of the total motion which may be observed experimentally including cases where the light is obliquely incident on the quantum well plane.

The magnetopolaron effect, also known as the Johnson–Larsen effect, was first described in [3–5] (see also the reviews [6–8]). Magnetopolarons are formed in three-dimensional (3D) and in quasi-two-dimensional (2D) systems, for example, in quantum wells. The spacing between the magnetopolaron levels in 3D systems is approximately $\alpha^{2/3}\hbar\omega_{LO}$ [9] where α is the dimensionless Fröhlich coupling constant of electrons with *LO* phonons [10] and in 2D systems this spacing is approximately $\alpha^{1/2}\hbar\omega_{LO}$ [11–24].

2. INFLUENCE OF THE DISPERSION OF *LO* PHONONS ON THE MAGNETOPOLARON SPECTRUM

A theory of magnetopolarons in a quantum well was constructed in [19] neglecting the phonon dispersion, i.e., using an approximation in which all the phonons involved in the formation of polarons have the same frequency ω_{LO}. The electrons interact with trapped and interface phonons. In the continuum approximation [25], i.e. in the limit $a \longrightarrow 0$, where a is a lattice constant, the trapped phonons have the frequency ω_{LO} with no dispersion whereas the interface phonons possess dispersion, i.e., the frequency depends on the modulus $q_\perp$ of the phonon wave vector in the plane of the quan-

tum well. The frequency of the interface phonons depends on the parameter $q_\perp d$ where d is the width of the quantum well. Outside the limits of the continuum approximation we need to allow in particular for the dependence of the *LO* phonon frequency on the variable $q_\perp a$. In [23] we showed that in cases of fairly wide quantum wells we can use an approximation in which the interaction with trapped phonons is replaced by interaction with bulk phonons and the interaction with interface phonons can be neglected. Quite clearly, only the dispersion caused by the departure from the continuum model remains in this case. Polarons allowing for interaction with interface phonons were considered in [14].

Magnetopolarons in a quantum well were classified in [2, 23]. By way of example we consider the most well-studied magnetopolaron which is denoted by *A*. This occurs as a result of the crossing of two levels of the electron–phonon system having indices m, $n = 0$, $N = 1$ and m, $n = 1$, $N = 0$, where m is the quantum number of the electron size quantization, n is the Landau quantum number, and N is the number of *LO* phonons. The energy of the first level is $\varepsilon_m^e + \Sigma_0 + \hbar\omega_{LO}$ and that of the second is $\varepsilon_m^e + \Sigma_1$ where ε_m^e is the energy of the size-quantized level m measured from the bottom of the quantum well. For example, for a well having infinitely high barriers we have

$$\varepsilon_m^e = \frac{\hbar^2\pi^2 m^2}{2m_e d^2}, \tag{1}$$

where m_e is the effective electron mass, $m = 1, 2, 3, \ldots$. We also introduce the notation

$$\Sigma_0 = \frac{\hbar\omega_{eH}}{2}, \quad \Sigma_1 = \frac{3\hbar\omega_{eH}}{2}, \quad \omega_{eH} = \frac{|e|H}{m_e c} \tag{2}$$

(where e is the electron charge, H is the magnetic field, and c is the velocity of light in vacuum). We shall neglect the phonon dispersion for now. Quite clearly the levels cross at the magnetic field where

$$\omega_{eH} = \omega_{LO}. \tag{3}$$

If the resonance condition (3) is satisfied, the role of the electron–phonon interaction increases sharply, leading to repulsion of the levels of the electron–phonon system and thus to the formation of a magnetopolaron.

The theory developed in [19] can be applied if the widths of the quantum wells are not too great when the spacing between the magnetopolaron levels (polaron splitting) is small compared with the distance from the next size-quantized level. It was shown in [23] that this last condition is satisfied for a well in the AlSb/GaAs/AlSb system where $d \le 500$ Å. We assume low temperatures, at which optical phonons are not excited.

We consider a square quantum well of type I having the band gap E_g. The magnetic field is directed perpendicular to the plane of the quantum well (along the z-axis) and the vector potential is selected in the gauge $\mathbf{A} = (0, xH, 0)$. The wave functions of the electrons in the quantum well have the form

$$\Psi^e_{n,k_y,m}(x, y, z) = \Phi_n(x + a_H^2 k_y)\frac{1}{\sqrt{L_y}}e^{ik_y y}\varphi^e_m(z), \tag{4}$$

where

$$\Phi_n(x) = \frac{H_n(x/a_H)\exp(-x^2/2a_H^2)}{\sqrt{\pi^{1/2}2^n n!\, a_H}},$$

$$a_H = \sqrt{\frac{c\hbar}{|e|H}},$$

$H_n(t)$ is a Hermite polynomial, L_y is the normalization length, $\varphi^e_m(z)$ is the real electron wave function normalized to unity, corresponding to the mth size-quantized level (see, for example, [19]). We write the electron–*LO* phonon interaction in the form

$$V = \sum_\nu [\mathscr{C}_\nu(\mathbf{r}_\perp, z)b_\nu + \mathscr{C}^*_\nu(\mathbf{r}_\perp, z)b^+_\nu], \tag{5}$$

where ν is a set of indices consisting of the vector $\mathbf{q}_\perp$ and other indices j characterizing the trapped and interface phonons, b^+_ν (b_ν) is the phonon creation (annihilation) operator,

$$\mathscr{C}_\nu(\mathbf{r}_\perp, z) = C_\nu e^{i\mathbf{q}_\perp\mathbf{r}_\perp}\eta_\nu(z), \tag{6}$$

where the values of $C_\nu\eta_\nu(z)$ for interaction of electrons with other species of phonons in the quantum well were determined in [25]. We showed in [23] that for $d \ge 200$ Å, in the case of GaAs we can use interaction with bulk phonons, which gives a good approximation. In this approximation the set of indices ν is converted into $\mathbf{q}$ where $\mathbf{q} = (\mathbf{q}_\perp, q_z)$ is the three-dimensional phonon wave vector and according to [10] we have

$$\eta_\nu(z) = e^{iq_z z},$$
$$C_\nu = C_q = -i\hbar\omega_{LO}\left(\frac{4\pi\alpha l^3}{V_0}\right)^{1/2}\frac{1}{ql}, \tag{7}$$

$l = \sqrt{\hbar/2m_e\omega_{LO}}$, $\alpha = (e^2/2\hbar\omega_{LO}l)(1/\varepsilon_\infty - 1/\varepsilon_0)$, V_0 is the normalization volume, and $\varepsilon_0(\varepsilon_\infty)$ is the static (RF) permittivity [10]. For GaAs we have $l \simeq 40$ Å, $\alpha \simeq 0.071$. Using Eqs. (4) and (6) we find that the matrix elements of the interaction are given by

$$\int d^3r \Psi^{e*}_{n',k'_y,m}\mathscr{C}^*_\nu(\mathbf{r}_\perp, z)\Psi^e_{n,k_y,m}$$
$$= \delta_{k'_y, k_y - q_y}U^*_{n,n'}(\nu)\exp\frac{ia_H^2 q_x(k_y + k'_y)}{2}, \tag{8}$$

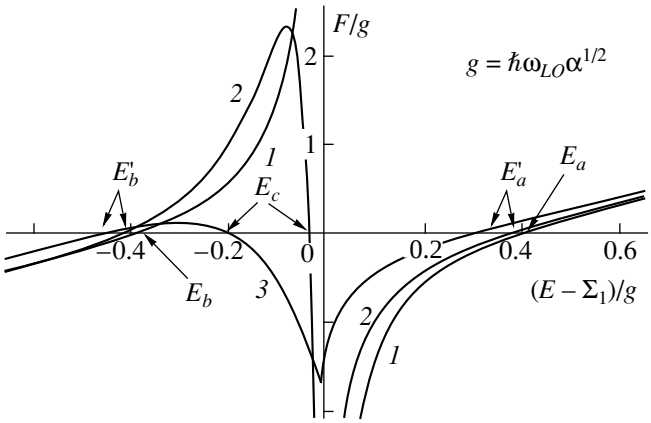

Fig. 1. Dependences of the function $F(E)$ determining the position of the magnetopolaron levels [formula (19)] on the energy E when the resonance condition (3) is satisfied; $\beta_0 = d/l = 7.5$, $l = (\hbar/2m_e\omega_{LO})^{1/2}$, size quantization quantum number $m = 1$, (*1*) $c = 0$, (*2*) $c = 0.04gl^2$, (*3*) $c = 0.2gl^2$, $g = \hbar\omega_{LO}\alpha^{1/2}$, E'_a, E'_b, and E_c denote the position of the levels in the presence of dispersion, E_a and E_b denote the position in the absence of dispersion.

where we introduce the notation:

$$U^*_{n,n'}(\nu) = C^*_\nu \mathcal{H}_{n,n'}(a_H \mathbf{q}_\perp \times \mathbf{H}/H)\mathcal{M}^*(\nu), \tag{9}$$

$$K_{n,n'}(\mathbf{s}) = \sqrt{\frac{\min(n!, n'!)}{\max(n!, n'!)}} i^{|n-n'|}\left(\frac{s}{\sqrt{2}}\right)^{|n-n'|} \times \exp\left(-\frac{s^2}{4}\right)\exp\left[i\left(\phi - \frac{\pi}{2}\right)\right](n-n')L^{|n-n'|}_{\min(n,n')}\left(\frac{s^2}{2}\right), \tag{10}$$

$$\mathcal{M}(\nu) = \int_{-\infty}^{\infty} dz[\varphi^e_m(z)]^2 \eta_\nu(z), \tag{11}$$

$\mathbf{s}$ is a two-dimensional vector, $s = \sqrt{s_x^2 + s_y^2}$, $\phi = \arctan(s_y/s_x)$, and $L^n_m(t)$ is a Laguerre polynomial.

Neglecting the phonon dispersion, the authors of [19] obtained the following equation for the energy E of magnetopolaron A:

$$E - \Sigma_1 - \frac{\sum_\nu |U(\nu)|^2}{E - \Sigma_0 - \hbar\omega_{LO}} = 0, \tag{12}$$

where the notation $U(\nu) = U_{1,0}(\nu)$ was introduced. Using Eqs. (10) and (11) we obtain

$$|U(\nu)|^2 = |C_\nu|^2 \frac{a_H^2 q_\perp^2}{2}\exp\left(-\frac{a_H^2 q_\perp^2}{2}\right)|\mathcal{M}(\nu)|^2. \tag{13}$$

Solving Eq. (12) we find that

$$E_p = \frac{\Sigma_1 + \Sigma_0 + \hbar\omega_{LO}}{2} \pm \sqrt{\frac{(\Sigma_1 - \Sigma_0 - \hbar\omega_{LO})^2}{4} + \sum_\nu |U(\nu)|^2}, \tag{14}$$

where the index p denotes one of two polaron levels: $p = a$ conventionally refers to the upper level [plus sign on the right-hand side of Eq. (14)] and $p = b$ refers to the lower level [minus sign on the right-hand side of Eq. (14)]. The solution (14) is valid near the resonance (3), exactly at the resonance

$$E_p^{\text{res}} = \Sigma_1 \pm \sqrt{\sum_\nu |U(\nu)|^2}, \tag{15}$$

so that the polaron splitting is

$$\Delta E^{\text{res}} = E_a^{\text{res}} - E_b^{\text{res}} = 2\sqrt{\sum_\nu |U(\nu)|^2}. \tag{16}$$

In [19] calculations were also made of the wave functions of magnetopolaron A in states $p = a$ and $p = b$.

Neglecting the phonon dispersion, i.e., the dependence of the frequency ω_{LO} on the indices ν, using the method described in [19] we obtain instead of Eq. (12)

$$E - \Sigma_1 - \sum_{\mathbf{q}_\perp, j} \frac{|U(\mathbf{q}_\perp, j)|^2}{E - \Sigma_0 - \hbar\omega_j(\mathbf{q}_\perp)} = 0. \tag{17}$$

By way of example we consider the case of a fairly wide quantum well when the approximation of electron interaction with bulk phonons can be used. Neglecting the anisotropy of the phonon spectrum, we define the phonon dispersion as

$$\omega_{LO}(\mathbf{q}) = \omega_{LO} - \Delta\omega_{LO}(q), \quad \Delta\omega_{LO}(q = 0) = 0. \tag{18}$$

Then Eq. (17) is transformed to give

$$F(E) \equiv E - \Sigma_1 - \sum_{\mathbf{q}} \frac{|U(\mathbf{q}_\perp, q_z)|^2}{E - \Sigma_0 - \hbar\omega_{LO} + \hbar\Delta\omega_{LO}(q)} = 0, \tag{19}$$

where in accordance with Eqs. (7), (11), and (13) we have

$$|U(\mathbf{q}_\perp, q_z)|^2 = (\hbar\omega_{LO})^2 \times \frac{4\pi\alpha l}{V_0 q^2}\frac{a_H^2 q_\perp^2}{2}\exp\left(-\frac{a_H^2 q_\perp^2}{2}\right)|\mathcal{M}(q_z)|^2, \tag{20}$$

$$\mathcal{M}(q_z) = \int_{-\infty}^{\infty} dz[\varphi^e_m(z)]^2 \exp(iq_z z). \tag{21}$$

The function $F(E)$ is calculated for the case of quadratic dispersion

$$\Delta\omega_{LO}(q) = cq^2 \tag{22}$$

and when the resonance condition (3) is satisfied. For those values of the energy E when the denominator may

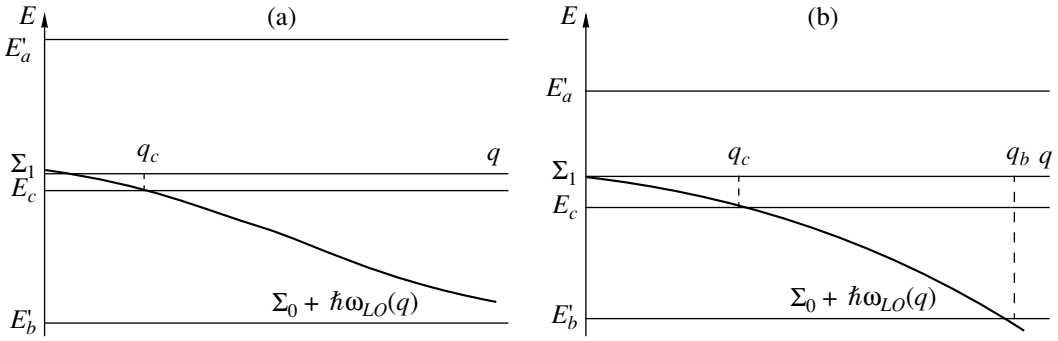

Fig. 2. Schematic diagram of the magnetopolaron levels E'_a, E'_b, and E_c and dependences $\Sigma_0 + \hbar\omega_{LO}(q)$. Figure 2a corresponds to a lower phonon dispersion than Fig. 2b.

go to zero, the integral was taken in the sense of the principal value. Figure 1 gives the function $F(E)$ for the case of zero dispersion: $c = 0$ (curve *1*), $c/gl^2 = 0.04$ (curve *2*), $c/gl^2 = 0.2$ (curve *3*), and $g = \hbar\omega_{LO}\alpha^{1/2}$. Curves *2* and *3* intersect the abscissa at the points E'_b, E_c and E'_a obtained allowing for the dispersion of *LO* phonons. The points $E_b = \Sigma_1 - \sqrt{\sum_\nu |U(\nu)|^2}$ and $E_a = \Sigma_1 + \sqrt{\sum_\nu |U(\nu)|^2}$ of intersection of curves *1* with the abscissa are consistent with the theory, neglecting the *LO* phonon dispersion. It can be seen from Fig. 1 that as the dispersion parameter increases, the differences $E_a - E'_a$ and $E'_b - E_b$ increase. If the dispersion is weak, the deviations are small, i.e., we obtain small shifts of the polaron levels. The third point of intersection corresponding to the energy E_c only occurs when the dispersion is taken into account. This last result will be discussed below.

Phonon dispersion may lead to additional contributions to the reciprocal lifetimes of the polaron states.[1] This can be explained using Fig. 2 which gives the energy levels E'_b, E_c and E'_a and also the schematic curves describing the dependence of $\Sigma_0 + \hbar\omega_{LO}(q)$ on the absolute value q of the three-dimensional phonon wave vector when the resonance condition (3) is satisfied. Figure 2b corresponds to higher phonon dispersion than in Fig. 2a. In Fig. 2a the curve $\Sigma_0 + \hbar\omega_{LO}(q)$ does not intersect the energy levels E'_a and E'_b. This means that the denominators $E'_a - \Sigma_0 - \hbar\omega_{LO}(q)$ and $E'_b - \Sigma_0 - \hbar\omega_{LO}(q)$ on the left-hand side of Eq. (19) do not go to zero and the real solutions E'_a and E'_b are exact.

Using the method developed in [19], we can show that the wave functions of a magnetopolaron corresponding to the exact solutions E'_a and E'_b near the resonance (3) have the form

$$\Theta_{p,k_y}|0\rangle = \left[1 + \sum_\nu \frac{|U(\nu)|^2}{E'_p - \Sigma_0 - \hbar\omega_{LO}(\nu)}\right]^{-1/2} \times \left[\Psi^e_{1,k_y,m} + \sum_\nu \frac{\exp[ia_H^2 q_x(k_y - q_y/2)]}{E'_p - \Sigma_0 - \hbar\omega_{LO}(\nu)} \times U^*(\nu)\Psi^e_{0,k_y-q_y,m} b^+_\nu\right]|0\rangle, \quad (23)$$

where $|0\rangle$ is a function describing the phonon vacuum, and p is equal to a or b. The functions (23) differ from the corresponding functions neglecting the phonon dispersion merely by replacing E_p with E'_p and ω_{LO} with $\omega_{LO}(\nu)$ [19]. The wave functions are orthonormalized, i.e.,

$$\int d^3r \left\langle 0\left|\Theta^+_{p'k'_y}\Theta_{pk_y}\right|0\right\rangle = \delta_{p,p'}\delta_{k_y,k'_y}. \quad (24)$$

The condition for orthogonality of the wave functions (23) having the indices a and b is easily checked if we bear in mind that the following relationship is satisfied

$$\sum_\nu \frac{|U(\nu)|^2}{[E'_a - \Sigma_0 - \hbar\omega_{LO}(\nu)][E'_b - \Sigma_0 - \hbar\omega_{LO}(\nu)]} = -1, \quad (25)$$

which is easily obtained if first E'_a and then E'_b are substituted on the left-hand side of Eq. (19) and one expression is subtracted from the other.

With reference to the energy E_c, it can be seen from Fig. 2 that the curve $\Sigma_0 + \hbar\omega_{LO}(q)$ always intersects the E_c level since this level is closer to the energy $\Sigma_1 = \Sigma_0 + \hbar\omega_{LO}$, the weaker the dispersion. This implies that the denominator $E_c - \Sigma_0 - \hbar\omega_{LO}(q)$ on the left-hand side of Eq. (19) goes to zero for a certain value q_c of the absolute value of the *LO* phonon wave vector. Consequently, the real value of E_c is not an exact solution of Eq. (19).

[1] The main, radiative and nonradiative, contributions were calculated in [2].

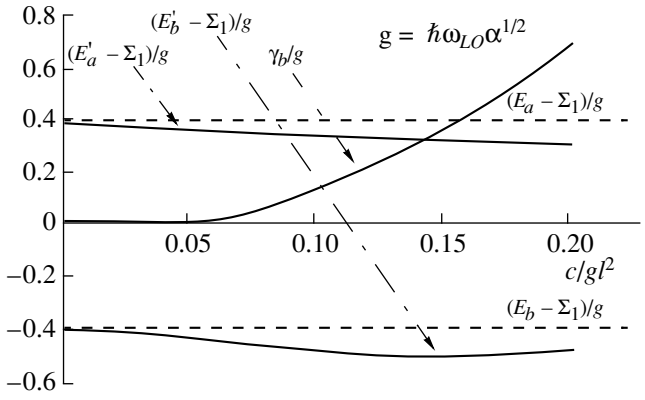

Fig. 3. Position and broadening of the magnetopolaron levels under resonance conditions caused by the phonon dispersion as a function of the dispersion parameter c: $\beta_0 = 7.5$, $m = 1$, $g = \hbar\omega_{LO}\alpha^{1/2}$, E_a and E_b are the level positions in the absence of dispersion, E'_a and E'_b are the level positions allowing for dispersion, and γ_b is the reciprocal lifetime of the lower level caused by the spatial dispersion.

In Fig. 2b the curve $\Sigma_0 + \hbar\omega_{LO}(q)$ not only intersects the energy level E_c but also the lower polaron level E'_b. From this it follows that only the real solution E'_a is exact and the solutions corresponding to levels c and b should contain imaginary parts. This implies that states c and b have finite lifetimes, which are denoted as γ_c^{-1} and γ_b^{-1}. We shall attempt to calculate the values of γ_c and γ_b. For this we need to generalize Eq. (19) so that it can have a complex solution. This generalization involves replacing the true energy E by $E + i\delta$ where $\delta \longrightarrow +0$. An imaginary correction then appears in Eq. (19) associated with going round the pole of the integrand expression [in fact the function $F(E + i\delta)$ is the denominator of the single-particle retarded electron Green function]. We shall assume that the reciprocal lifetime γ_p of the magnetopolaron state p is very short. Then, assuming $\tilde{E}_p = E'_p - i\hbar\gamma_p/2$, where E'_p is real and using an expansion as a series in terms of small γ_p in the zeroth approximation we obtain from Eq. (19)

$$E'_p - \Sigma_1 - \mathrm{Re}\sum_{\mathbf{q}} \frac{|U(\mathbf{q}_\perp, q_z)|^2}{E'_p - \Sigma_0 - \hbar\omega_{LO}(q) + i\delta} = 0, \quad (26)$$

where $\delta \longrightarrow +0$ and in the next approximation

$$\gamma_p = -2\mathrm{Im}\frac{1}{\hbar}\sum_{\mathbf{q}} \frac{|U(\mathbf{q}_\perp, q_z)|^2}{E'_p - \Sigma_0 - \hbar\omega_{LO}(q) + i\delta} = \frac{2\pi}{\hbar}\sum_{\mathbf{q}} |U(\mathbf{q}_\perp, q_z)|^2 \delta[E'_p - \Sigma_0 - \hbar\omega_{LO}(q)]. \quad (27)$$

Having calculated γ_p, we find that these values are actually small and thus we check whether the method that reduces to the equalities (26) and (27) is valid. We can say a priori that the method can be applied to level b for fairly weak dispersion but not to level c.

We substitute Eq. (20) into the right-hand side of Eq. (27) and use the dispersion (22). We calculate the functions $\mathcal{M}(q_z)$ using the wave functions

$$\varphi^e_m(z) = (2/d)^{1/2}\sin(m\pi z/d), \quad 0 < z < d \quad (28)$$

(and $\varphi^e_m(z) = 0$ outside this interval, which corresponds to a well with infinite barriers). We then obtain

$$|\mathcal{M}(q_z)|^2 \equiv f_m(Q) = \frac{2(2\pi m)^4(1 - \cos Q)}{Q^2[Q^2 - (2\pi m)^2]^2}, \quad (29)$$

where $Q = q_z d$, m is the number of the size-quantized level. Integrating on the right-hand side of Eq. (27) over $q_\perp$ using a δ-function, we express γ_p as an integral in terms of the variable Q:

$$\gamma_p = \frac{2\alpha l\hbar\omega^2_{LO}}{d(\Sigma_0 + \hbar\omega_{LO} - E'_p)}\int_0^{q_p d} dQ e^{-x} x f_m(Q), \quad (30)$$

where E'_p is the energy of the polaron level p calculated in accordance with Eq. (26) allowing for the LO phonon dispersion:

$$q_p = \sqrt{\frac{\Sigma_0 + \hbar\omega_{LO} - E_p}{c}}, \quad (31)$$

$$x = \frac{a_H^2 q_p^2}{2} - \frac{Q^2}{\beta_0^2}, \quad (32)$$

$$\beta_0 = \frac{\sqrt{2}d}{a_H}. \quad (33)$$

If condition (3) is satisfied, we find $\beta_0 = d/l$. For any values of the number m we have

$$\int_0^\infty dQ f_m(Q) = 3\pi/2. \quad (34)$$

Thus, the integral on the right-hand side of Eq. (30) is always smaller than $3\pi/2$. For very weak dispersion

$$dq_p \gg 1, \quad a_H q_p \gg 1, \quad (35)$$

the integral is

$$\int_0^{q_p d} dQ e^{-x} x f_m(Q) \ll 1. \quad (36)$$

This implies that for the $p = b$ level we find $\gamma_p \longrightarrow 0$ as the dispersion parameter c tends to zero since $\Sigma_0 + \hbar\omega_{LO} - E'_p$ in the denominator on the right-hand side of Eq. (30) tends to $\Sigma_0 + \hbar\omega_{LO} - E_b$. Figure 3 shows the position of the E'_a level and also the position and broad-

ening of the E_b' level as a function of the dispersion parameter c. It can be seen that for low values of the parameter c the broadening is weak and the approximate expression (30) obtained above for γ_b is valid. However, as the parameter c increases, the value of γ_b increases to such an extent that the solutions (26) and (27) cannot be considered to be correct. For comparison we give the formula for the magnetopolaron splitting ΔE^{res} obtained in [23] for broad wells in the limit $\beta_0 \gg 2\pi m$. This formula has the form

$$\Delta E^{\text{res}} = \alpha^{1/2}\hbar\omega_{LO}\sqrt{6l/d}. \quad (37)$$

Comparing Eq. (30) with Eq. (37), we find that $\hbar\gamma_b \gg \Delta E^{\text{res}}$ in cases of fairly weak dispersion.

For level c we find in accordance with Eq. (30) that as the dispersion decreases, the reciprocal lifetime γ_c of this level increases. In fact the denominator on the right-hand side of Eq. (30) contains the value $\Sigma_0 + \hbar\omega_{LO} - E_c$ which tends to zero as the dispersion parameter decreases, whereas γ_c tends to infinity. The fact that the reciprocal lifetime γ_c is high in cases of weak dispersion indicates that the method of successive approximations (26) and (27) cannot be applied to analyze level c. The question of the existence of this level still remains unresolved.

3. INFLUENCE OF THE EXCITON EFFECT ON THE MAGNETOPOLARON SPECTRUM

In the previous section we studied a magnetopolaron formed by an electron. In this section we consider a magnetopolaron–hole pair. We shall assume that Coulomb forces have a weak influence on the spectrum of an electron–hole pair which is satisfied under the conditions

$$a_{\text{exc}}^2 \gg a_H^2, \quad a_{\text{exc}} \gg d, \quad (38)$$

where $a_{\text{exc}} = \hbar^2\varepsilon_0/\mu e^2$ is the Vanier–Mott exciton radius for zero magnetic field, $\mu = m_e m_h/(m_e + m_h)$ is the reduced mass. For GaAs using the parameters $m_e/m_0 = 0.065$, $m_h/m_0 = 0.16$, $\varepsilon_0 = 12.55$, $\hbar\omega_{LO} = 0.0367$ eV we obtain

$$a_{\text{exc}} = 146\ \text{Å}, \quad a_H^{\text{res}} = 57.2\ \text{Å}, \quad (39)$$

$a_H^{\text{res}} = \sqrt{c\hbar/(|e|H_{\text{res}})}$, H_{res} is the magnetic field corresponding to the magnetopolaron resonance (3), and m_0 is the free electron mass. For GaAs we have $H_{\text{res}} = 20.2$ T. From Eq. (39) we find that $(a_H^{\text{res}}/a_{\text{exc}})^2 \simeq 0.154$, i.e., the first of the two conditions (38) is satisfied although the second requires us to analyze wells of width $d \ll 146$ Å, i.e., narrower than those considered in Section 2.

The first of the two inequalities (38) is equivalent to the following:

$$\hbar\omega_{\mu H}/2 \gg \Delta E_{\text{exc}}, \quad (40)$$

where $\omega_{\mu H} = |e|H/\mu c$ is the cyclotron frequency, and $\Delta E_{\text{exc}} = \hbar^2/\mu a_{\text{exc}}^2$ is the exciton binding energy in zero magnetic field. If the conditions (38) are satisfied, the Coulomb electron–hole interaction may be considered to be a small perturbation and we can calculate the first-order corrections to the energy of the electron–hole pair (see [1] where the purely one-dimensional case was considered). In [2] the unperturbed wave functions of an electron–hole pair were taken as functions having the index $\mathcal{K}_\perp$ and the indices n and n' referring to the relative motion of the electrons and the holes [26]. Note that the indices n and n' are uniquely related to the Landau quantum numbers n_e and n_h of the electrons and holes, respectively, and for $n_e > n_h$ we have $n = n_h$, $n' = n_h - n_e < 0$ whereas if $n_e < n_h$ we have $n = n_e$, $n' = n_h - n_e > 0$. Electron–hole pairs allowing for Coulomb forces, which may be called excitons, are characterized by the same sets of indices $\mathcal{K}_\perp, n, n'$ or $\mathcal{K}_\perp, n_e, n_h$. It was shown in [1] that the corrections to the energy of an electron–hole pair caused by Coulomb interaction depend on the quasi-momentum $\mathcal{K}_\perp$ in the quantum well plane, i.e., the Coulomb forces lead to dispersion of the excitons.

The corrections to the energy caused by the exciton effect may divided into two parts. The first part depends only on the indices n_e and n_h and corresponds to $\mathcal{K}_\perp = 0$. The second part (residue) depends on $\mathcal{K}_\perp$, n_e, and n_h and describes the exciton dispersion. The energy of an exciton characterized by the quasi-momentum $\mathcal{K}_\perp$ and consisting of an electron having indices n_e and m_e and a hole having indices n_h and m_h, where $m_e(m_h)$ is the number of the electron (hole) size-quantized level, is given by

$$\mathcal{E}_{n_e, n_h, m_h}(\mathcal{K}_\perp) = E_g + \varepsilon_{m_e}^e + \varepsilon_{m_h}^h + \left(n_e + \frac{1}{2}\right)\hbar\omega_{eH} + \left(n_h + \frac{1}{2}\right)\hbar\omega_{hH} + \Delta\mathcal{E}_{n_e, n_h}(\mathcal{K}_\perp), \quad (41)$$

where $\Delta\mathcal{E}_{n_e, n_h}(\mathcal{K}_\perp)$ is the Coulomb correction to the exciton energy in which we isolate the contribution $\mathcal{K}_\perp = 0$:

$$\Delta\mathcal{E}_{n_e, n_h}(\mathcal{K}_\perp) = \Delta\mathcal{E}_{n_e, n_h}(\mathcal{K}_\perp = 0) + \Delta_1\mathcal{E}_{n_e, n_h}(\mathcal{K}_\perp). \quad (42)$$

The exciton states having indices n_e, n_h, m_e, m_h, and $\mathcal{K}_\perp$ are described by unperturbed (neglecting Coulomb forces) wave functions which are not given here.

We shall consider a pair consisting of a magnetopolaron and a hole. For the case of a magnetopolaron A the following levels cross: an exciton having the indices $n_e = 1$, $n_h = 1$, m and an exciton having indices $n_e = 0$,

$n_h = 0$, m plus a phonon of frequency ω_{LO}. We selected $n_h = 1$, $m_h = m_e = m$ since this electron–hole combination may be generated by light in the case of an infinitely deep quantum well. If we neglect the correction $\Delta_1\mathcal{E}_{n_e, n_h}(\mathcal{H}_\perp)$ which depends on $\mathcal{H}_\perp$, the resonance condition has the form

$$\begin{aligned}\hbar\omega_{eH} &= \hbar\omega_{LO} \\ &+ \Delta\mathcal{E}_{0,1}(\mathcal{H}_\perp = 0) - \Delta\mathcal{E}_{1,1}(\mathcal{H}_\perp = 0).\end{aligned} \tag{43}$$

Since the exciton corrections $\Delta\mathcal{E}_{0,1}(\mathcal{H}_\perp = 0)$ and $\Delta\mathcal{E}_{1,1}(\mathcal{H}_\perp = 0)$ have different values, the resonance condition (43) differs from the resonance condition (3) obtained neglecting Coulomb forces. Using [19] we can obtain the following equation for the energy $\mathcal{E}$ of a magnetopolaron–hole pair:

$$\begin{aligned}&\mathcal{E} - \mathcal{E}_{1,1}(\mathcal{H}_\perp) \\ &- \sum_\nu \frac{|U(\nu)|^2}{\mathcal{E} - \mathcal{E}_{0,1}(\mathcal{H}_\perp - \mathbf{q}_\perp) - \hbar\omega_{LO}} = 0.\end{aligned} \tag{44}$$

The inequalities (38) and the estimates (39) give fairly stringent upper constraints on the quantum well width which makes it difficult to use the approximation of bulk phonons, at least for GaAs. Thus, the index ν in Eq. (44) is taken to mean the indices $\mathbf{q}_\perp$ and j, where j refers to trapped and interface phonons, as noted above. Since the dispersion of any phonons is neglected in this section, the denominator in equation Eq. (44) does not depend on the index j.

Measuring the energy from the level $E_g + \varepsilon_m^e + \varepsilon_m^h + 3\hbar\omega_{hH}/2$ we obtain

$$\begin{aligned}\mathcal{E}_{1,1}(\mathcal{H}_\perp) &= \Sigma_1 + \Sigma\mathcal{E}_{1,1}(\mathcal{H}_\perp), \\ \mathcal{E}_{0,1}(\mathcal{H}_\perp) &= \Sigma_0 + \Sigma\mathcal{E}_{0,1}(\mathcal{H}_\perp).\end{aligned} \tag{45}$$

Quite clearly the corrections $\Delta_1\mathcal{E}_{n_e, n_h}(\mathcal{H}_\perp)$ to the energy yield two important results. First the energy of a magnetopolaron–hole pair begins to depend on the vector $\mathcal{H}_\perp$. For normally incident light we have $\Delta_1\mathcal{E}_{n_e, n_h}(\mathcal{H}_\perp) = 0$ but a dependence of the energy on $\mathcal{H}_\perp$ should be observed for obliquely incident light on the surface of the quantum well. Second, the denominator on the left-hand side of Eq. (44) contains the term $\mathcal{E}_{0,1}(\mathcal{H}_\perp - \mathbf{q}_\perp)$ and this should give the same qualitative results as allowance for the phonon dispersion, i.e., additional shifts of the energy $\mathcal{E}_p$ of the upper and lower polaron levels and additional contributions to the reciprocal lifetimes of the polaron states. In order to obtain more accurate results we also need to allow for the dispersion of the *LO* phonons and the influence of Coulomb forces.

ACKNOWLEDGMENTS

One of the authors (S.T.P.) is grateful to the Zacatecas Autonomous University, Zac., Mexico and the Mexican National Council for Physics and Technology (CONACyt) for financial support and hospitality.

This work was partly financed by the Russian Foundation for Basic Research and the MNTK program "Physics of Solid-State Nanostructures."

REFERENCES

1. I. V. Lerner and Yu. E. Lozovik, Zh. Éksp. Teor. Fiz. **78**, 1167 (1980) [Sov. Phys. JETP **51**, 588 (1980)].
2. I. G. Lang, L. I. Korovin, D. A. Contreras-Solorio, and S. T. Pavlov, cond-mat/0001248 (2000).
3. D. M. Larsen and E. J. Johnson, in *Proceedings of 8th International Conference on Physics of Semiconductors, Kyoto, 1966*, J. Phys. Soc. Jpn. Suppl. **21**, 443 (1966).
4. E. J. Johnson and D. M. Larsen, Phys. Rev. Lett. **16**, 655 (1966).
5. D. M. Larsen, in *Proceedings of X International Conference on the Physics of Semiconductors, Cambridge, Mass., 1970*, Ed. by S. P. Keller, J. C. Hensel, and F. Stern (US AEC, Oak Ridge, 1970).
6. A. Petron and B. D. McComb, in *Landau Level Spectroscopy*, Ed. by G. Landwer and E. I. Rashba, Modern Problems in Condensed Matter Sciences (1988), Vol. 27.2.
7. R. J. Nicholas, D. J. Barnes, D. R. Seadly, *et al.*, in *Spectroscopy of Semiconductor Microstructures*, Ed. by G. Fasel, A. Fasolino, and P. Lugli (Plenum, New York, 1980), NATO Adv. Study Inst. Ser., Ser. B: Phys. **206**, 451 (1980).
8. R. J. Nicholas, in *Handbook of Semiconductors*, Ed. by M. Balkanski (North-Holland, Amsterdam, 1994), Vol. 2.
9. L. I. Korovin and S. T. Pavlov, Zh. Éksp. Teor. Fiz. **53**, 1708 (1967) [Sov. Phys. JETP **26**, 979 (1968)]; Pis'ma Zh. Éksp. Teor. Fiz. **6**, 525 (1967) [JETP Lett. **6**, 50 (1967)].
10. H. Fröhlich, Adv. Phys. **3**, 325 (1954).
11. L. I. Korovin, S. T. Pavlov, and B. É. Éshpulatov, Fiz. Tverd. Tela (Leningrad) **20**, 3594 (1978) [Sov. Phys. Solid State **20**, 2077 (1978)].
12. Das Sarma and O. Madhucar, Phys. Rev. B **22**, 2823 (1980).
13. Das Sarma and O. Madhucar, Phys. Rev. Lett. **52**, 859 (1984).
14. G. O Hai, F. M. Peeters, and J. T. Devreese, Phys. Rev. B **47**, 10358 (1993).
15. A. O. Govorov, Solid State Commun. **92**, 977 (1994).
16. R. J. Nicholas, S. Sasaki, N. Niura, *et al.*, Phys. Rev. B **50**, 7596 (1994).
17. J. M. Shi, F. M. Peeters, and J. T. Devreese, Phys. Rev. B **50**, 15182 (1994).

18. L. I. Korovin, S. T. Pavlov, and B. É. Éshpulatov, Fiz. Tverd. Tela (St. Petersburg) **35**, 1562 (1993) [Phys. Solid State **35**, 788 (1993)].

19. I. G. Lang, V. I. Belitsky, A. Cantarero, *et al.*, Phys. Rev. B **54**, 17768 (1996).

20. L. I. Korovin, I. G. Lang, and S. T. Pavlov, Zh. Éksp. Teor. Fiz. **111**, 2194 (1997) [JETP **84**, 1197 (1997)].

21. L. I. Korovin, I. G. Lang, and S. T. Pavlov, Pis'ma Zh. Éksp. Teor. Fiz. **65**, 511 (1997) [JETP Lett. **65**, 532 (1997)].

22. I. G. Lang, V. I. Belitsky, A. Cantarero, *et al.*, Phys. Rev. B **56**, 6880 (1997).

23. L. I. Korovin, I. G. Lang, and S. T. Pavlov, Zh. Éksp. Teor. Fiz. **115**, 187 (1999) [JETP **88**, 105 (1999)].

24. L. I. Korovin, I. G. Lang, and S. T. Pavlov, Zh. Éksp. Teor. Fiz. **116**, 1419 (1999) [JETP **89**, 764 (1999)].

25. N. Mori and T. Ando, Phys. Rev. B **40**, 6175 (1989).

26. L. D. Landau and E. M. Lifshitz, *Quantum Mechanics: Non-Relativistic Theory* (Nauka, Moscow, 1974; Pergamon, Oxford, 1977).

Translation was provided by AIP

Journal of Experimental and Theoretical Physics, Vol. 91, No. 2, 2000, pp. 346–352.
Translated from Zhurnal Éksperimental'noĭ i Teoreticheskoĭ Fiziki, Vol. 118, No. 2, 2000, pp. 397–403.

SOLIDS
Electronic Properties

Influence of Inelastic Subbarrier Impurity Scattering on the Nonresonant Tunneling Transmission of a Quasi-One-dimensional Tunneling Junction with Weak Structural Disorder

V. Ya. Kirpichenkov
South-Russian State Technical University, Novocherkassk, 346400 Russia
e-mail: kirp@srstu.novoch.ru
Received December 27, 1999

Abstract—The contribution of inelastic subbarrier impurity scattering of tunneling electrons to the nonresonant transmission of a quasi-one-dimensional tunneling junction with weak (low impurity concentrations) structural disorder at temperature $T = 0$ is determined. It is shown that this contribution leads to an increase in the tunneling transmission and conditions are determined for which this increase may be appreciable. © *2000 MAIK "Nauka/Interperiodica".*

1. INTRODUCTION

The influence of elastic subbarrier impurity scattering of electrons on the tunneling transmission and current–voltage characteristic of a quasi-one-dimensional dielectric layer with weak structural disorder was investigated in [1, 2] in resonant and nonresonant tunneling regimes.

In the present study we consider an additional channel for subbarrier scattering of tunneling electrons, i.e., inelastic scattering by impurities at $T = 0$, and in the first order in terms of impurity concentration we calculate its contribution to the tunneling transmission of this junction in the nonresonant tunneling regime.

We shall show that at $T = 0$ this contribution leads to an increase in the nonresonant tunneling transmission compared with the case of purely elastic impurity scattering. Conditions are obtained for which this increase may be appreciable and, for example, for the typical parameters of a tunneling junction may be severalfold.

2. MODEL: BASIC EQUATIONS

We shall solve the problem of calculating the tunneling transmission of a quasi-one-dimensional dielectric layer containing randomly distributed identical impurities for electrons incident normally to the layer and having the energy $\varepsilon_0 > 0$ on entry to the layer.

We assume that the dielectric layer consists of a fairly large number [2] of dielectric filaments of length L with noninteracting impurities situated in the ground state at $T = 0$. The regular (not perturbed by impurities) barrier potential of the filament is uniform: $U_0 = \text{const} > \varepsilon_0$. The electron density in the incident flux is so small that all interelectron interactions and statistical correlations attributable to the Pauli principle may be neglected over the entire barrier region. This means that we can in fact consider a single-electron problem in which a tunneling electron can undergo either elastic or inelastic scattering by impurities. The relaxation time of an impurity, i.e., the time taken for it to be transferred from an excited state to the ground state is assumed to be much shorter than the time interval between successive collisions and the excitation energy is "dumped" into a thermostat situated at $T = 0$. The tunneling takes place by a nonresonant mechanism, i.e., at energies ε_0 some distance, first from the spectrum of resonant tunneling transmission [1, 2] (in the case of attractive impurities) and second from the "ceiling" of the barrier U_0 so that quantum transitions of a tunneling electron into the energy range of the resonant spectrum and into the subbarrier energy range may be neglected. The mean free path for electron hopping from filament to filament is assumed to be large compared to the filament length L and thus the one-dimensional tunneling dynamics for each filament does not depend on the others. The one-dimensional impurity concentration n per filament is low so that the following relationships are satisfied between the characteristic parameters having the dimensions of length

$$r_0 \ll \alpha_0^{-1} \ll n^{-1} < L, \tag{1}$$

where r_0 is the radius of the electron–impurity interaction, $\alpha_0^{-1} = (U_0 - \varepsilon_0)^{-1/2}$ is the characteristic attenuation length of an electron state having the energy ε_0 in a homogeneous barrier ($\hbar = 1$, $m = 1/2$ is the electron mass).

Since in cases of weak disorder the principal contribution of subbarrier impurity scattering effects to the specific coefficient of attenuation factor of the nonresonant tunneling transmission is determined by first-

order terms with respect to the dimensionless impurity concentration $c = n\alpha_0^{-1} \ll 1$, in order to find these, as in cases of purely elastic scattering [1], it is sufficient to consider the scattering of a tunneling electron at an isolated impurity situated as an arbitrary point x_i in the dielectric filament ($0 < x_i < L$).

The Schrödinger equation describing a system containing an interacting electron and impurity has the form

$$[\hat{H}_0^x + \hat{H}_0^\xi + \hat{H}_{\text{int}}^{x,\xi}]\Psi(x,\xi) = E\Phi(x,\xi), \quad 0 < E < U_0, \tag{2}$$

where $\Psi(x, \xi)$ and E are the wave function and the total energy of the system

$$\hat{H}_0^x = -\frac{\partial^2}{\partial x^2} + U(x) \tag{3}$$

is the Hamiltonian of a free (not interacting with an impurity) electron,

$$U(x) = \begin{cases} U_0, & 0 \le x \le L, \\ 0, & x < 0, x > L \end{cases} \tag{4}$$

is the regular potential of the barrier,

$$\hat{H}_0^\xi = -\frac{1}{2M}\frac{\partial^2}{\partial \xi^2} + \frac{\gamma\xi^2}{2} \tag{5}$$

is the Hamiltonian of a free impurity. The quantity ξ can either be taken to be the internal vibrational degree of freedom of the impurity or the overall vibrational degree of freedom of the entire impurity. In this last case $\xi = x_i - x_i^{(0)}$ is the deviation of the impurity coordinate x_i from the equilibrium position $x_i^{(0)}$. In both cases the free impurity is modeled by a one-dimensional harmonic oscillator having the mass M and elastic coupling constant γ. The model Hamiltonian of the electron–impurity interaction,

$$\hat{H}_{\text{int}}^{x,\xi} = \beta\delta(\xi)\delta(x - x_i^{(0)}), \tag{6}$$

is the simplest generalization to the case of inelastic scattering of the operator of the local ($r_0 \longrightarrow 0$) single-impurity perturbation of the δ-function type used in the one-dimensional case [1]. Attractive impurities correspond to the "interaction" constant $\beta < 0$ and repulsive impurities correspond to $\beta > 0$.

We shall seek a solution $\Psi(x, \xi)$ of Eq. (2) in the form of an expansion in terms of the eigenfunctions $\varphi_k(\xi)$ [3] of the Hamiltonian $\hat{H}_0^\xi$ satisfying the equation

$$\hat{H}_0^\xi\varphi_k(\xi) = \omega(k)\varphi_k(\xi), \quad k = 0, 1, 2, \ldots, \tag{7}$$

where

$$\omega(k) = \left(k + \frac{1}{2}\right)\Omega, \quad \Omega = \sqrt{\frac{\gamma}{M}},$$

$$\varphi_k(\xi) = (2^k k!\sqrt{\pi}\xi_0)^{-1/2}\exp\left(-\frac{\xi^2}{2\xi_0^2}\right)H_k\left(\frac{\xi}{\xi_0}\right),$$

$$\xi_0 = (M\Omega)^{-1/2},$$

$$H_k(z) = (-1)^k\exp(z^2)\frac{d^k\exp(-z^2)}{dz^k}$$

are Hermite polynomials.

To the left of the barrier ($x < 0$) $\Psi(x, \xi)$ is a superposition of waves incident on the barrier and reflected waves:

$$\Psi(x,\xi) = \varphi_{k_0}(\xi)\exp(iq_0x) + \sum_k b_k\varphi_k(\xi)\exp(-iq_kx), \tag{8}$$

where $q_k = \sqrt{\varepsilon(k)}$, $\varepsilon(k) = E - \omega(k)$, $q_0 = q_{k_0}$, $k_0 = 0$ is the quantum number of the oscillator before scattering.

To the right of the barrier ($x > 0$) $\Psi(x, \xi)$ is a superposition of transmitted waves:

$$\Psi(x,\xi) = \sum_k c_k\varphi_k(\xi)\exp[iq_k(x - L)]. \tag{9}$$

The object of the calculations is the tunneling transmission of the barrier averaged over the impurity coordinates:

$$D(\varepsilon_0) = \frac{\langle j_x^{\text{out}}\rangle}{j_x^{\text{in}}(\varepsilon_0)}, \tag{10}$$

where

$$\langle j_x^{\text{out}}\rangle = \sum_k 2\sqrt{\varepsilon(k)}\langle c_k^* c_k\rangle \tag{11}$$

is the transmitted flux (per filament), the angular brackets denote averaging over the impurity coordinates,

$$j_x^{\text{in}}(\varepsilon_0) = 2\sqrt{\varepsilon_0} \tag{12}$$

is the incident flux.

Substituting Eqs. (11) and (12) into Eq. (10), we find

$$D(\varepsilon_0) = \sum_k\sqrt{\frac{\varepsilon(k)}{\varepsilon_0}}\langle c_k^* c_k\rangle, \tag{13}$$

or, going over here from summation over k to integration over $\varepsilon = E - (k + 1/2)\Omega$, we finally obtain

$$D(\varepsilon_0) = \int \sqrt{\frac{\varepsilon}{\varepsilon_0}} \langle c^*(\varepsilon) c(\varepsilon) \rangle \frac{d\varepsilon}{\Omega}, \tag{14}$$

where integration is performed over all subbarrier energies $0 \le \varepsilon \le U_0$.

3. DERIVATION OF THE SUBBARRIER "KINETIC" EQUATION

Here the method proposed in [1] is generalized to the case where inelastic scattering at impurities is also taken into account and the subbarrier "kinetic" equation is derived to within terms of the first order with respect to the impurity concentration.

We write Eq. (2) in the barrier region $0 \le x \le L$ in the form

$$\frac{\partial^2 \Psi}{\partial x^2} - \hat{\alpha}^2 \Psi = \beta \delta(\xi) \delta(x - x_i^{(0)}) \Psi, \tag{15}$$

where $\hat{\alpha}^2 = U_0 - E + \hat{H}_0^{\xi}$. We seek its solution in the form

$$\Psi(x, \xi) = \sum_k g_k(x) \varphi_k(\xi). \tag{16}$$

Substituting Eq. (16) into Eq. (15), we obtain an equation for $g_k(x)$:

$$\frac{d^2 g_k(x)}{dx^2} - \alpha_k^2 g_k(x) = \beta \sum_{k'} f_{kk'} \delta(x - x_i) g_{k'}(x_i), \tag{17}$$

where $\alpha_k^2 = U_0 - \varepsilon(k)$, $\varepsilon(k) = E - \omega(k)$,

$$f_{kk'} = \int \varphi_k^*(\xi) \delta(\xi) \varphi_{k'}(\xi) d\xi = \varphi_k^*(0) \varphi_{k'}(0). \tag{18}$$

We write the solution $g_k(x)$ in the form of a sum:

$$g_k(x) = g_k^+(x) + g_k^-(x), \tag{19}$$

where the functions $g_k^{\pm}(x)$ are defined so that outside an impurity they satisfy the equation

$$\frac{dg_k^{\pm}}{dx} = \pm \alpha_k g_k^{\pm}. \tag{20}$$

Introducing the Green function $h_k(x - x') = (2\alpha_k)^{-1} \exp(-\alpha_k |x - x'|)$ of Eq. (17), we express $g_k(x)$ and $g_k^{\pm}(x)$ as follows:

$$\begin{aligned} g_k(x) &= \exp(-\alpha_k x) g_k^-(0) \\ &+ \exp[\alpha_k(x - L)] g_k^+(L) - h_k(x - x_i) \beta \sum_{k'} f_{kk'} g_{k'}(x_i), \end{aligned} \tag{21}$$

$$g_k^-(x) = \begin{cases} \exp(-\alpha_k x) g_k^-(0), & x < x_i \\ \exp(-\alpha_k x) g_k^-(0) - h_k(x - x_i)\beta \\ \times \sum_{k'} f_{kk'} g_{k'}(x_i), & x > x_i, \end{cases} \tag{22}$$

$$g_k^+(x) = \begin{cases} \exp[\alpha_k(x - L)] g_k^+(L) - h_k(x - x_i) \\ \times \beta \sum_{k'} f_{kk'} g_{k'}(x_i), & x < x_i \\ \exp[\alpha_k(x - L)] g_k^+(L), & x > x_i. \end{cases} \tag{23}$$

Note that the functions $g_k^{\pm}(x)$ have a discontinuity at the point $x = x_i$.

The conditions of continuity $\Psi(x, \xi)$ and $\partial\Psi(x, \xi)/\partial x$ with respect to the variable x expressed in terms of the functions $g_k^{\pm}(x)$ at the barrier interfaces $x = 0$, $x = L$, have the form

$$\begin{aligned} \delta_{k_0 k} + b_k &= g_k^+(0) + g_k^-(0), \\ iq_k[\delta_{k_0 k} - b_k] &= \alpha_k[g_k^+(0) - g_k^-(0)], \\ g_k^+(L) + g_k^-(L) &= c_k, \\ \alpha_k[g_k^+(L) - g_k^-(L)] &= iq_k c_k. \end{aligned} \tag{24}$$

From this we obtain two relationships necessary for the following calculations:

$$g_k^-(0) = -\frac{2iq_0}{\alpha_0 - iq_0} \delta_{k_0 k} + \frac{\alpha_k + iq_k}{\alpha_k - iq_k} g_k^+(0), \tag{25}$$

$$c_k = \frac{2\alpha_k}{\alpha_k - iq_k} g_k^-(L). \tag{26}$$

It follows from Eq. (26) that

$$\langle c_k^* c_k \rangle = \frac{4\alpha_k^2}{\alpha_k^2 + q_k^2} \langle g_k^{-*}(L) g_k^-(L) \rangle. \tag{27}$$

Thus, in accordance with Eq. (27), in order to find the average $\langle c_k^* c_k \rangle$ contained in the formula for the tunneling transmission (13), we need to find the correlation function $G_k(x) = \langle g_k^{-*}(x) g_k^-(x) \rangle$ at the point $x = L$.

We obtain the subbarrier kinetic equation for $G_k(x)$ following the ideology adopted in [1]. For this we first note that, as in the case of pure elastic subbarrier scattering at low impurity concentrations ($c = n\alpha_0^{-1} \ll 1$) the second terms on the right-hand sides of Eqs. (21) and (25) for nonresonant tunneling are exponentially small compared with the other terms with the probability $1 - c$ and may be neglected. Physically, this corresponds to neglecting waves reflected from the interfaces $x = 0$,

$x = L$ from the inner region of the barrier $0 < x < L$. To within exponential accuracy we then have from Eqs. (21) and (25)

$$g_k(x) = \exp(-\alpha_k x)\bar{g}_k(0) - h_k(x - x_i)\beta\sum_{k'} f_{kk'}g_{k'}(x_i), \quad (28)$$

$$\bar{g}_k(0) = -\frac{2iq_0}{\alpha_0 - iq_0}\delta_{k_0 k}. \quad (29)$$

Assuming in Eq. (28) $x = x_i$ and taking into account Eq. (22), we find

$$g_k(x_i) = \bar{g}_k(x_i - 0) - \frac{\beta}{2\alpha_k}\sum_{k'} f_{kk'}g_{k'}(x_i). \quad (30)$$

Equation (30) is a discrete variant of the Fredholm second-order integral equation for the function $g_k(x_i)$. For the model interaction Hamiltonian (6) the kernel $f_{kk'}$ [Eq. (18)] is degenerate [4] and an exact solution (30) is easily found:[1]

$$g_k(x_i) = \bar{g}_k(x_i - 0) - \mu_k\sum_{k'} f_{kk'}\bar{g}_{k'}(x_i - 0), \quad (31)$$

where

$$\mu_k = \frac{\beta}{2\alpha_k}\left[1 + \beta\sum_k \frac{f_{kk}}{2\alpha_k}\right]^{-1}.$$

Substituting Eq. (31) into Eq. (22) and systematically assuming $x = x_i - \delta x/2$ and $x = x_0 + \delta x/2$, we obtain in the limit $\delta x \longrightarrow 0$ an equation for the smoothed function $G_k(x) = \langle \bar{g}_k^*(x)\bar{g}_k(x)\rangle$ averaged over the impurity coordinates:

$$\frac{\partial G_k(x)}{\partial x} = -2\alpha_k^{\mathrm{el}}G_k(x) + \sum_{\substack{k' \\ (k' \neq k)}} w_{kk'}G_{k'}(x), \quad (32)$$

where

$$\alpha_k^{\mathrm{el}} = \alpha_k + n\mu_k f_{kk} - \frac{w_{kk}}{2} \quad (33)$$

is the attenuation coefficient for purely elastic scattering,

$$w_{kk'} = n\mu_k^2|f_{kk'}|^2. \quad (34)$$

Equation (32) was derived using an approximation of random phases of the quantities $\bar{g}_k(x)$ in accordance with which [5] for scattering at a macroscopic system of impurities randomly distributed in space we have

$$\sum_{k'} f_{kk'}\langle \bar{g}_k^*(x)\bar{g}_{k'}(x)\rangle \simeq f_{kk}\langle \bar{g}_k^*(x)\bar{g}_k(x)\rangle,$$

$$\sum_{k', k''} f_{kk'}^* f_{kk''}\langle \bar{g}_{k'}^*(x)\bar{g}_{k''}(x)\rangle \simeq \sum_{k'}|f_{kk'}|^2\langle \bar{g}_{k'}^*(x)\bar{g}_{k'}(x)\rangle.$$

Note that in the limit of purely elastic scattering (when $k = k_0$ and $f_{kk'} = \delta_{k_0 k'}$) Eq. (32) yields the corresponding Eq. (2.12) from [1].

Converting in Eq. (32) from summation over k to integration over ε, we obtain the subbarrier kinetic equation on the εx plane:

$$\frac{\partial G(\varepsilon, x)}{\partial x} = -2\alpha^{\mathrm{el}}(\varepsilon)G(\varepsilon, x) + I(\varepsilon, x), \quad (35)$$

where

$$\alpha^{\mathrm{el}}(\varepsilon) = \alpha(\varepsilon) + n\mu(\varepsilon)f(\varepsilon, \varepsilon) - \frac{w(\varepsilon, \varepsilon)\Omega}{2},$$
$$I(\varepsilon, x) = \int_0^{\varepsilon_0} w(\varepsilon, \varepsilon')G(\varepsilon', x)d\varepsilon', \quad (36)$$

$$w(\varepsilon, \varepsilon') = n\mu^2(\varepsilon)|f(\varepsilon, \varepsilon')|^2\Omega^{-1}. \quad (37)$$

Note that in the "collision" integral $I(\varepsilon, x)$ the section $\varepsilon - \Omega < \varepsilon' < \varepsilon + \Omega$ is "cut out."

Equation (35) is solved with the boundary condition derived from Eq. (29):

$$G(\varepsilon, 0) = \eta(\varepsilon_0)\delta(\varepsilon - \varepsilon_0), \quad \eta(\varepsilon_0) = \frac{4q_0^2\Omega}{\alpha_0^2 + q_0^2}. \quad (38)$$

4. FOKKER–PLANCK EQUATION

Assuming (as a result of the smallness of the impurity concentration and the nonresonance of the scattering) that the energy exchange process between a tunneling electron and impurities is slow [the x coordinate plays the role of time in Eq. (35)], we find a solution of Eq. (35) in the diffusion approximation. For this purpose, acting in the spirit of the procedure for deriving the Fokker–Plank equation from the kinetic equation [6, 7], we convert from the integrodifferential Eq. (35) to the corresponding differential equation.

[1] Note that for more "realistic" interaction when the kernel $f_{kk'}$ is nondegenerate equation (30) can be solved by an iterative method for a fairly small interaction constant β and the first iteration has the form (31) where $\mu_k = \beta(2\alpha_k)^{-1}$.

Writing the function in the integrand in $I(\varepsilon, x)$ as a dependence on the energy transfer $\delta = \varepsilon - \varepsilon'$ and the energy $\varepsilon' = \varepsilon - \delta$, we express the integral in the form

$$I(\varepsilon, x) = \int_{\varepsilon - \varepsilon_0}^{\varepsilon} w(\varepsilon - \delta, \delta) G(\varepsilon - \delta, x) d\delta. \quad (39)$$

In accordance with the assumption that the energy exchange process is slow, the function $w(\varepsilon - \delta, \delta)$, being a "slow" function of the first argument $\varepsilon - \delta$, decreases rapidly as the second argument δ departs from zero since the principal term in the integral (39) gives very low values of $|\delta| \ll \varepsilon_0$. Taking this into account, we expand in powers of δ in the argument $\varepsilon - \delta$ of the integrand function $w(\varepsilon - \delta, \delta)G(\varepsilon - \delta, x)$ to within terms $\sim\delta^2$ and then reduce Eq. (35) to the form

$$\frac{\partial G(\varepsilon, x)}{\partial x} = -2\alpha^{\text{inel}}(\varepsilon) G(\varepsilon, x) - \frac{\partial}{\partial \varepsilon}[v(\varepsilon) G(\varepsilon, x)] + \frac{\partial^2}{\partial \varepsilon^2}[d(\varepsilon) G(\varepsilon, x)], \quad (40)$$

where

$$\alpha^{\text{inel}}(\varepsilon) = \alpha^{\text{el}}(\varepsilon) - \Delta(\varepsilon),$$
$$\Delta(\varepsilon) = \frac{1}{2}\int_{\varepsilon - \varepsilon_0}^{\varepsilon} w(\varepsilon, \delta) d\delta,$$
$$v(\varepsilon) = \int_{\varepsilon - \varepsilon_0}^{\varepsilon} w(\varepsilon, \delta)\delta d\delta, \quad (41)$$
$$d(\varepsilon) = \frac{1}{2}\int_{\varepsilon - \varepsilon_0}^{\varepsilon} w(\varepsilon, \delta)\delta^2 d\delta.$$

Bearing in mind the boundary condition (38), the slow variation of the functions $v(\varepsilon)$, $d(\varepsilon)$, and the boundedness of x ($0 \le x \le L$), Eq. (40) can be further simplified by replacing the functions $v(\varepsilon)$, $d(\varepsilon)$ with their values at $\varepsilon = \varepsilon_0$ and writing Eq. (40) in he form

$$\frac{\partial G(\varepsilon, x)}{\partial x} = -2\alpha^{\text{inel}}(\varepsilon) G(\varepsilon, x) - v\frac{\partial G(\varepsilon, x)}{\partial \varepsilon} + d\frac{\partial^2 G(\varepsilon, x)}{\partial \varepsilon^2}, \quad (42)$$

where

$$v = v(\varepsilon_0) = \int_{\Omega}^{\varepsilon_0} w(\varepsilon, \delta)\delta d\delta,$$
$$d = d(\varepsilon_0) = \frac{1}{2}\int_{\Omega}^{\varepsilon_0} w(\varepsilon, \delta)\delta^2 d\delta. \quad (43)$$

Equation (42) is the Fokker–Planck equation for the tunneling process being considered. The first term on the right-hand side of Eq. (42) describes the attenuation, the second describes the drift, and the third describes the diffusion of the spectral component $G(\varepsilon, x)$ on the plane εx.

5. TUNNELING TRANSMISSION

An approximate solution of Eq. (42) with the boundary condition (38) for a small diffusion coefficient $\sqrt{dx} \ll \alpha_0^2 \sim \varepsilon_0$ (asymptotically exact in the limit $d \longrightarrow 0$) has the form

$$G(\varepsilon, x) = \frac{\eta(\varepsilon_0)}{\sqrt{4\pi dx}} \exp\left[-\frac{(\varepsilon - \varepsilon_0 - vx)^2}{4dx}\right] \times \exp\left[-2\int_0^x \alpha^{\text{inel}}(\varepsilon_0 + vy) dy\right], \quad (44)$$

where

$$\alpha^{\text{inel}}(\varepsilon_0 + vy) = \alpha^{\text{el}}(\varepsilon_0 + vy) - \Delta(\varepsilon_0),$$
$$\Delta(\varepsilon_0) = \frac{1}{2}\int_{\Omega}^{\varepsilon_0} w(\varepsilon_0, \delta) d\delta,$$
$$\alpha^{\text{el}}(\varepsilon_0 + vy) = \alpha(\varepsilon_0 + vy) + n\mu(\varepsilon_0) f(\varepsilon_0, \varepsilon_0) - \frac{w(\varepsilon_0, \varepsilon_0)\Omega}{2}, \quad (45)$$
$$\alpha(\varepsilon_0 + vy) = \sqrt{U_0 - (\varepsilon_0 + vy)}.$$

We note that only terms of the order n were retained in the calculations of $\alpha^{\text{inel}}(\varepsilon_0 + vy)$ in accordance with the accuracy of the model.

It can be seen from Eq. (44) that the trajectory of the maximum of the function $G(\varepsilon, x)$ with respect to ε on the εx plane is described by the equation $\varepsilon_m = \varepsilon_0 + vx$ and its characteristic width is of the order of magnitude of $\sqrt{dx}$. In this case, the procedure for converting from Eq. (40) to Eq. (42) implies that the conditions $vx \ll \varepsilon_0$ are satisfied for all $0 \le x \le L$.

Now assuming that Eq. (27) yields the inequality

$$\langle c^*(\varepsilon) c(\varepsilon)\rangle = \frac{4\alpha^2(\varepsilon)}{\alpha^2(\varepsilon) + q^2(\varepsilon)} G(\varepsilon, L), \quad (46)$$

and substituting Eq. (46) into Eq. (14), we obtain a formula for the tunneling transmission in the form

$$D^{\text{inel}}(\varepsilon_0) = \sigma(\varepsilon_0) \exp\left[-2\int_0^L \alpha^{\text{inel}}(\varepsilon_0 + vy) dy\right], \quad (47)$$

where

$$\sigma(\varepsilon_0) = \frac{16\alpha^2(\varepsilon_0)q^2(\varepsilon_0)}{[\alpha^2(\varepsilon_0)+q^2(\varepsilon_0)]^2}.$$

When calculating the preexponential factor $\sigma(\varepsilon_0)$ in Eq. (47) we neglected small terms $\sim vL/\varepsilon_0 \ll 1$ compared with unity.

In order to estimate the contribution of inelastic scattering effects to the tunneling transmission we find

$$\lambda(\varepsilon_0) = \ln\left[\frac{D^{\text{inel}}(\varepsilon_0)}{D^{\text{el}}(\varepsilon_0)}\right], \tag{48}$$

where

$$D^{\text{el}}(\varepsilon_0) = \sigma(\varepsilon_0)\exp\left[-2\int_0^L \alpha^{\text{el}}(\varepsilon_0)dy\right] \tag{49}$$

is the tunneling transmission for purely inelastic scattering.

Substituting Eqs. (49) and (47) into Eq. (48), we obtain

$$\lambda(\varepsilon_0) = 2\int_0^L [\alpha^{\text{el}}(\varepsilon_0) - \alpha^{\text{inel}}(\varepsilon_0 + vy)]dy. \tag{50}$$

Taking into account that $vy/\alpha_0^2 \ll 1$ for all $0 \le y \le L$, we find from Eq. (50) taking into account Eq. (45),

$$\lambda(\varepsilon_0) = \frac{vL^2}{2\alpha(\varepsilon_0)} + 2\Delta(\varepsilon_0)L. \tag{51}$$

Thus, since $v > 0$, $\Delta(\varepsilon_0) > 0$, it follows that $\lambda(\varepsilon_0) > 0$, i.e., inelastic subbarrier scattering at $T = 0$ leads to an increase in the tunneling transmission compared with the case of purely elastic scattering at impurities.

This at first glance unexpected effect can be explained qualitatively as follows.

Allowance for inelastic processes in nonresonant subbarrier scattering of tunneling electrons by impurities at $T = 0$ not only leads to the appearance of additional (in relation to purely inelastic scattering) "inelastic" tunneling channels where the energies of the transmitted electrons are $\varepsilon_n < \varepsilon_0$ [these correspond to terms with $n \neq 0$) in formula (13)] but also leads to changes of the tunneling transmission in the input, "elastic" channel [the term with $n = 0$ in Eq. (13)].

A specific feature of subbarrier (with imaginary momenta $i\alpha_k$) scattering is that allowance for inelastic processes in the input channel leads to an increase in the real part of the amplitude S_{00} of the elastic propagation of an impurity determined by

$$g_0^-(x_i + 0) = S_{00}g_0^-(x_i - 0). \tag{52}$$

In fact, substituting Eq. (31) into Eq. (22), we obtain the following expression for S_{00} in the second order of perturbation theory in terms of the interaction constant β:

$$S_{00} = 1 + F_{00}, \tag{53}$$

where

$$F_{00} = F_{00}^{\text{el}} + F_{00}^{\text{inel}} \tag{54}$$

is the amplitude of the subbarrier forward scattering in the input channel,

$$F_{00}^{\text{el}} = -\frac{\beta f_{00}}{2\alpha_0} + \frac{\beta^2|f_{00}|^2}{(2\alpha_0)^2} \tag{55}$$

is the amplitude of the elastic forward scattering in the absence of inelastic processes,

$$F_{00}^{\text{inel}} = \frac{\beta^2}{2\alpha_0}\sum_{\substack{k\\k\neq 0}} \frac{|f_{0k}|^2}{2\alpha_k} > 0 \tag{56}$$

is the contribution of inelastic process ("virtual" $\varepsilon_0 \rightleftharpoons \varepsilon_k$ electron transitions) to the amplitude of the forward elastic scattering.

The fact that F_{00}^{inel} is positive ultimately leads to an increase in the tunneling transmission of the layer in the input channel compared with the case of purely elastic scattering [the term containing $n = 0$ in Eq. (13)] while the presence of inelastic tunneling channels [terms with $n \neq 0$ in Eq. (13)] gives an additional increase in the tunneling transmission.

Note that in the case of "above-barrier" (with real momenta q_k) scattering allowance for inelastic processes leads to the opposite effect, a reduction in the transmission coefficient of the layer [3]. The corresponding formulas for the input channel in the quasi-one-dimensional case considered here may be obtained by substituting $i\alpha_k \longrightarrow q_k$ in formulas (55) and (56) after which it can be seen that for above-barrier scattering $F_{00}^{\text{inel}} < 0$, which leads to a decrease in the real part of the amplitude S_{00} and ultimately reduces the coefficient of above-barrier transmission of the quasi-one-dimensional layer.

We shall now estimate the right-hand side of Eq. (51). For small energy transfers, $\delta \ll \varepsilon_0$, when oscillator transitions from the $k_0 = 0$ ground state to the lower excited states with low values of $k = \delta/\Omega$ are important, for $w(\varepsilon_0, \delta)$ ((Eq. 37)) taking into account Eq. (18) and the explicit form of the functions $\varphi_k(\varepsilon)$ ((Eq. 7)) we obtain the estimate

$$w(\varepsilon_0, \delta) \sim n\mu_0^2\Omega^{-1}(\delta/\Omega)^{-p}, \quad p \approx 1, \tag{57}$$

where $\mu_0 = \mu(\varepsilon_0)/\xi_0$. Then we have

$$\Delta(\varepsilon_0) = \frac{1}{2}\int_{\Omega}^{\varepsilon_0} w(\varepsilon_0, \delta)d\delta \sim n\mu_0^2 \ln\left(\frac{\varepsilon_0}{\Omega}\right), \quad (58)$$

$$\nu(\varepsilon_0) = \int_{\Omega}^{\varepsilon_0} w(\varepsilon_0, \delta)\delta d\delta = \Delta(\varepsilon_0)\langle\delta\rangle \sim n\mu_0^2\varepsilon_0, \quad (59)$$

where $\langle\delta\rangle \sim \varepsilon_0 \ln^{-1}(\varepsilon_0/\Omega)$ is the average energy transfer.

Substituting Eqs. (58) and (59) into Eq. (51), we obtain the estimate

$$\lambda(\varepsilon_0) \sim c\mu_0^2 \mathcal{L}\left[\frac{\varepsilon_0}{\alpha_0^2}\mathcal{L} + 4\ln\left(\frac{\varepsilon_0}{\Omega}\right)\right], \quad (60)$$

where $c = n\alpha_0^{-1} \ll 1$, $\mathcal{L} = \alpha_0 L \gg 1$ are the dimensionless impurity concentrations and the barrier length, respectively.

The estimate (60) should be made subject to the constraint

$$\frac{\nu L}{\varepsilon_0} \sim c\mu_0^2 \mathcal{L} \ll 1. \quad (61)$$

The inelasticity of the subbarrier impurity scattering strongly influences the tunneling transmission if

$$\lambda(\varepsilon_0) \gtrsim 1. \quad (62)$$

From Eqs. (60)–(62) we then obtain the corresponding condition:

$$\left[\frac{\varepsilon_0}{\alpha_0^2}\mathcal{L}^2 + 4\mathcal{L}\ln\left(\frac{\varepsilon_0}{\Omega}\right)\right]^{-1} \lesssim c\mu_0^2 \ll \mathcal{L}^{-1}. \quad (63)$$

For nonresonant energies ε_0 the value of μ_0^2 is no greater than unity. Then, for example, for the typical parameters of a tunneling junction $\mathcal{L} \sim 10$, $\varepsilon_0/\alpha_0^2 \sim 1$, $\varepsilon_0/\Omega \sim 10$–$100$ we find that for concentrations c such that $c\mu_0^2 \sim 10^{-2}$ the inequalities (63) are satisfied, $\lambda(\varepsilon_0) \sim 1$.

Consequently, even at low impurity concentrations $c \ll 1$ and nonresonant energies ε_0 inelastic subbarrier scattering of electrons at impurities at $T = 0$ in fairly long barriers $\mathcal{L} \gg 1$ may increase the tunneling transmission severalfold.

REFERENCES

1. I. M. Lifshits and V. Ya. Kirpichenkov, Zh. Éksp. Teor. Fiz. **77**, 989 (1979) [Sov. Phys. JETP **50**, 499 (1979)].
2. V. Ya. Kirpichenkov, Zh. Éksp. Teor. Fiz. **113**, 1522 (1998) [JETP **86**, 833 (1998)].
3. L. D. Landau and E. M. Lifshitz, *Quantum Mechanics: Non-Relativistic Theory* (Nauka, Moscow, 1974; Pergamon, Oxford, 1977).
4. S. G. Mikhlin, *Lectures on Linear Integral Equations* (Fizmatgiz, Moscow, 1959).
5. L. van Hove, Physica (Amsterdam) **21**, 517 (1955).
6. E. M. Lifshitz and L. P. Pitaevskiĭ, *Physical Kinetics* (Nauka, Moscow, 1979; Pergamon, Oxford, 1981).
7. A. G. van Kampen, *Stochastic Processes in Physics and Chemistry* (North-Holland, Amsterdam, 1984; Vysshaya Shkola, Moscow, 1990).

Translation was provided by AIP

Journal of Experimental and Theoretical Physics, Vol. 91, No. 2, 2000, pp. 353–360.
Translated from Zhurnal Éksperimental'noĭ i Teoreticheskoĭ Fiziki, Vol. 118, No. 2, 2000, pp. 404–412.

SOLIDS
Electronic Properties

Microscopic Model of the Coexistence of Superconductivity and Ferromagnetism in the Hybrid Ruthenate-Cuprate Oxide $RuSr_2GdCu_2O_8$

E. V. Kuz'min[1, *], S. G. Ovchinnikov[2, **], I. O. Baklanov[2], and E. G. Goryachev[1]

[1] *Krasnoyarsk State University, Krasnoyarsk, 660062 Russia*
[2] *Kirenskii Institute of Physics, Siberian Division, Russian Academy of Sciences, Krasnoyarsk, 660036 Russia*
**e-mail: evk@iph.krasn.ru*
***e-mail: sgo@iph.krasn.ru*
Received December 30, 1999

Abstract—A microscopic *t–J–I* model with competing antiferromagnetic (*J*) and ferromagnetic (*I*) exchange interactions is proposed for strongly correlated electrons in $RuSr_2GdCu_2O_8$. It is assumed that $J \gg I$ for CuO_2 layers and $J \ll I$ for RuO_2 layers. A superconducting solution of $d_{x^2-y^2}$ symmetry was obtained for the CuO_2 layers while competition between ferromagnetism and *p*-type triplet superconducting pairing is obtained for RuO_2 layers. It is shown that the RuO_2 layers have a lower carrier concentration in the Hubbard subband formed by coupled $((d_{xy}–p)–\pi)$ orbitals compared with a bulk Sr_2RuO_4 crystal, which leads to stabilization of the ferromagnetic state in the RuO_2 layer. © *2000 MAIK "Nauka/Interperiodica".*

1. INTRODUCTION

In the present paper we propose a microscopic model of the electronic structure, electrical and magnetic properties of recently synthesized $RuSr_2GdCu_2O_8$ layered oxides in which the coexistence of ferromagnetism and superconductivity is observed [1, 2].

As a result of the structural similarity of ruthenate Sr_2RuO_4 and copper oxides, it has been possible to construct a hybrid compound $RuSr_2GdCu_2O_8$ in which the RuO_2 and CuO_2–Gd–CuO_2 bilayer are separated by SrO buffer layers where the RuO_2 layers are responsible for ferromagnetism below the Curie point $T_C = 133$ K and the superconductivity below $T_c = 46$ K is attributed to the CuO_2 layers. However, the bulk Sr_2RuO_4 crystal does not exhibit magnetic properties and is a superconductor with a low value of $T_c \approx 1$ K [3] and *p*-type pairing [4]. A characteristic feature of Sr_2RuO_4 is its closeness to ferromagnetic instability which is observed in the ferromagnetism of $Sr_2Ir_{1-x}Ru_xO_4$ [5] and the Ruddelsdon–Popper series $Sr_{n+1}Ru_nO_{3n+1}$ with $n \geq 2$ [6, 7].

The coexistence of ferromagnetism and superconductivity has been discussed on many occasions, beginning with [8, 9]. There are two factors which destroy the superconductivity in a ferromagnetic medium: first, exchange splitting lifts the energy degeneracy of the partners of a spin-up and spin-down Cooper pair; second, magnon exchange leads to repulsion for a singlet pair [10] (although for triplet pairs this exchange gives attraction additional to the phonon mechanism [11]). In the compound being discussed, $RuSr_2GdCu_2O_8$, coexistence occurs below T_c and the superconductivity is not destroyed in the ferromagnetic state because of the spatial separation of the CuO_2 and RuO_2 layers by SrO buffer layers which suppress the relative influence of the magnetic and superconducting layers. This means that to a first approximation the superconductivity in the CuO_2 layers and the ferromagnetism in the RuO_2 layers can be considered independently. In this approach the main question to explain the properties of $RuSr_2GdCu_2O_8$ is as follows: why does the RuO_2 layer exhibit ferromagnetic properties while the Sr_2RuO_4 is a superconductor?

Band calculations of Sr_2RuO_4 using the density functional method in the local density approximation (LDA) give a nonmagnetic ground state [12, 13] whereas GGA calculations using gradient corrections to the density functional yield a ferromagnetic Sr_2RuO_4 ground state [14]. The effective masses obtained in the band calculations differ by almost an order of magnitude from the masses observed in experiments on the de Haas–van Alfven effect [15] which suggests that we need to allow for strong electron correlations in the RuO_2 layers. For cuprates the important role of strong electron correlation effects is also widely known (see, for example, the review [16]). Thus, in the present study we shall use the *t–J–I* model which explicitly allows for strong electron correlations and was proposed in [17] to compare the superconductivity in cuprates and ruthenates. This model is generalized to the case of $RuSr_2GdCu_2O_8$ by having one set of parameters (*t*, *J*, *I*) for the CuO_2 layer and another set of the same parameters for the RuO_2 layer.

The study has the following structure: in Section 2 we describe the *t–J–I* model and its specific characteristics for $RuSr_2GdCu_2O_8$, in Section 3 we describe the superconductivity of CuO_2 layers, in Section 4 we analyze the competing ferromagnetic and superconducting states of the RuO_2 layer, and Section 5 contains a discussion of the results.

2. GENERALIZATION OF *t–J–I* MODEL FOR $RuSr_2GdCu_2O_8$

This compound, like oxides of copper and ruthenium, is characterized by a mixed type of chemical bond, with an ionic bond predominating in which all ions entering the lattice participate. The weaker metallic bond can be described using the multiband *p–d* model which allows for the e_g ($d_{x^2-y^2}$ and d_{z^2}) orbitals of copper, the t_{2g} (d_{xy}, d_{yz}, d_{zx}) orbitals of ruthenium, all the *p*-orbitals of the oxygen ions, *p–d* hopping between them, and also for the Coulomb matrix elements at copper U_{Cu} and ruthenium U_{Ru}. In this model the Cd^{3+} and SrO layers all play a passive role.

In the weak correlation regime $U_{Cu} \ll W_{Cu}$, $U_{Ru} \ll W_{Ru}$, where W_i is the band half-width in the layers i = Cu, Ru, a single-electron approach works and the band structure can be calculated from first principles. Such calculations were recently made in [18, 19] which confirmed that Gd^{3+} having the magnetic moment $\mu \approx 7\mu_B$ does not influence the band structure of the CuO_2 and RuO_2 layers. In these studies it was shown that the electronic structure of the CuO_2 layer is almost independent of the magnetic state of the RuO_2 layer; despite the strong exchange splitting (~1 eV) of the spin subbands in the ferromagnetic RuO_2 layer, the induced exchange splitting in the CuO_2 layer is small, $\Delta_{ex} \approx 25$ eV, which is attributed to characteristics of the crystal, magnetic, and electronic structures of $RuSr_2GdCu_2O_8$. In fact the magnetic moment of Ru is produced by the t_{2g} orbitals which are bound to the p_x, p_y orbitals of apical oxygen by an extremely weak $pd\pi$ bond and have a zero overlap with the p_z orbitals of apical oxygen. In turn, the $p\pi$ orbitals of apical oxygen are not bound to the copper $d_{x^2-y^2}$ and 4*s* orbitals. All these factors have the result that the electronic structures of the CuO_2 and RuO_2 layers may be considered as isolated layers to a first approximation.

The electron correlations in the band approach [18, 19] were taken into account using a generalized gradient approximation which cannot be used to describe the electronic structure of CuO_2 and RuO_2 layers over a wide range of concentrations, including the dielectric in the undoped CuO_2 layer in addition to the metallic phases. It is therefore interesting to consider a model for the case of strong intraatomic correlations $U_{Cu} \gg W_{Cu}$, $U_{Ru} \gg W_{Ru}$. Although both layers (CuO_2 and RuO_2) are metallic in this compound, the carrier concentration in these layers, as will be shown below, corresponds to weakly doped compositions in which strong electron correlation effects give substantial deviations from Fermi liquid behavior [16].

In the strong correlation regime the three-band *p–d* model at low quasiparticle energies reduces to an effective *t–J* model [20–23]. The correlations raise the energies of the two-particle polar states, eliminating these from the low-energy range. Mathematically this elimination leads to the constraint that part of the Hilbert space is inaccessible as a result of the zero occupation numbers of the polar states. As a result for the CuO_2 layer we obtain the effective *t–J* Hamiltonian (additional hopping between second neighbors *t*' and third neighbors *t*'' can also be taken into account in this approach, but from the point of view of a qualitative comparison of CuO_2 and RuO_2 layers they are unimportant in the present study):

$$H_{CuO_2} = \sum_{\mathbf{f}\sigma}(\varepsilon_{Cu} - \mu)X_{\mathbf{f}}^{\sigma\sigma} - t_{Cu}\sum_{\mathbf{f}\boldsymbol{\delta}\sigma}X_{\mathbf{f}}^{\sigma 0}X_{\mathbf{f}+\boldsymbol{\delta}}^{0\sigma} + J_{Cu}\sum_{\mathbf{f}\boldsymbol{\delta}}\left(\mathbf{S}_{\mathbf{f}}\cdot\mathbf{S}_{\mathbf{f}+\boldsymbol{\delta}} - \frac{1}{4}\hat{n}_{\mathbf{f}}n_{\mathbf{f}+\boldsymbol{\delta}}\right). \quad (1)$$

Here $\mathbf{f}$ are the lattice sites, $\boldsymbol{\delta}$ is a vector joining the nearest neighbors of the site, $X_{\mathbf{f}}^{mn} = |m\rangle\langle n|$ are the Hubbard operators, $\mathbf{S}_{\mathbf{f}}$ is the spin operator, $\hat{n}_{\mathbf{f}}$ is the electron number operator, ε_{Cu} is the energy of the single-hole state, μ is the chemical potential, t_{Cu} is the hopping integral between nearest neighbors, and $J_{Cu} = 4t_{Cu}^2/U_{Cu}$ is the indirect antiferromagnetic exchange. For hole-doped superconductors the local basis of the *t–J* model includes the states: $|0\rangle$, a Zhang–Rice singlet consisting of two holes (number of electrons $n_e = 0$) and the single-hole states $|\sigma\rangle$, $\sigma = \pm 1/2$ (number of electrons $n_e = 1$). The constraint which eliminates local two-electron states has the form

$$X_{\mathbf{f}}^{00} + \sum_{\sigma}X_{\mathbf{f}}^{\sigma\sigma} = 1. \quad (2)$$

Typical values of the model parameters for the CuO_2 layer are: $(J/t)_{Cu} = 0.4$, and the parameter t is numerically small compared with the copper–oxygen *p–d* hopping integral $t \sim 0.1t_{pd}$ [21]. For the typical value t_{pd} = 1 eV we obtain $t_{Cu} \sim 0.1$ eV. For these values of t_{Cu} and J_{Cu} in the exchange pairing mechanism [24, 25] we obtain $T_c \sim 100$ K.

No similar derivation of the effective Hamiltonian for the RuO_2 layer where the Ru layers have a d^4 electron configuration has been reported in the literature although it is qualitatively clear from a general approach to the derivation of the effective spin Hamil-

tonian eliminating polar states as a result of strong correlations that the hopping part of the Hamiltonian has a form similar to the term containing t_{Cu} in Eq. (1) and the exchange interaction for a d^4 configuration is determined by two contributions: ferromagnetic 180° cation–anion–cation superexchange I (Fig. 1) and antiferromagnetic cation–cation exchange $J \sim 4t_{Ru}^2/U_{Ru}$ [26]. As a result, we arrive at the Hamiltonian of the t–J–I model introduced in [17]:

$$H_{RuO_2} = \sum_{\mathbf{f}\sigma}(\varepsilon_{Ru}-\mu)X_{\mathbf{f}}^{\sigma\sigma} - t_{Ru}\sum_{\mathbf{f}\delta\sigma}X_{\mathbf{f}}^{\sigma 0}X_{\mathbf{f}+\delta}^{0\sigma} + J_{Ru}\sum_{\mathbf{f}\delta}\left(\mathbf{S}_{\mathbf{f}}\cdot\mathbf{S}_{\mathbf{f}+\delta}-\frac{1}{4}\hat{n}_{\mathbf{f}}\hat{n}_{\mathbf{f}+\delta}\right) - I_{Ru}\sum_{\mathbf{f}\delta}\left(\mathbf{S}_{\mathbf{f}}\cdot\mathbf{S}_{\mathbf{f}+\delta}+\frac{1}{4}\hat{n}_{\mathbf{f}}\hat{n}_{\mathbf{f}+\delta}\right). \quad (3)$$

For the RuO_2 layer the Hamiltonian (3) describes strongly correlated γ-band electrons formed by intraplanar hybridized (d_{xy}–p)–π states. Here $|0\rangle$ and $|\sigma\rangle$ are local (d_{xy}–p)–π states of the RuO_4 cell having the numbers of holes $n_h = 9$ and $n_h = 1$, and two-hole states of the form $|\uparrow,\downarrow\rangle$ do not fall within the low-energy range. Since the d^4 configuration contains two holes (measured from the vacuum term of the d^6 configuration), the second hole is situated in a different orbital state. According to band calculations [12, 13] for Sr_2RuO_4 this hole belongs to the half-filled β-band. For a periodic multilayer superlattice such as $RuSr_2GdCu_2O_8$ essentially is, tunneling across layers involving α- and β-band electrons formed by hybrid (d_{yz}–p) and (d_{zx}–p) orbitals is very weak and the role of strong correlation effects for these states and also for their localization is enhanced compared with a three-dimensional Sr_2RuO_4 crystal.

Typical values of the parameters for an RuO_2 layer are as follows: $t_{Ru} \sim 0.1$ eV for the same reasons as t_{Cu} (independent confirmation of this value of t_{Ru} is obtained from the value of the effective mass $m_\gamma \sim 10m_0$ in the Hubbard I approximation for the lattice parameter of the RuO_2 layer). For $U_{Ru} = 4$ eV the antiferromagnetic exchange value is $(J/t)_{Ru} = 0.1$ or $J_{Ru} = 0.01$ eV. The ferromagnetic exchange parameter can be estimated using the spin-wave formula for the Curie temperature of a quasi-two-dimensional magnetic substance:

$$T_C \sim zI/\ln(I/I_\perp), \quad (4)$$

where z is the number of nearest neighbors and for the unknown ratio of the exchanges within the RuO_2 layer (I) and between the layers ($I_\perp$) we can assume on the basis of the crystal chemistry similarity of the structures of ruthenates and cuprates that by analogy with cuprates $I/I_\perp \sim 10^4$ [quite clearly as a result of the logarithm in formula (4) the exponent in this ratio very weakly influences the result of the estimate). For $I_{Ru}/t_{Ru} \sim 0.4$ we obtain $T_C \sim 100$ K which is in good agreement with the experimental value of $T_C = 133$ K. According to the Goodenough rules [26] for indirect 180° exchange d^4–anion–d^4 ferromagnetic exchange predominates over antiferromagnetic $I_{Ru} > J_{Ru}$ as was obtained in our estimate of the parameters. The value of I_{Ru} can also be estimated independently using the temperature of the superconducting transition in Sr_2RuO_4, $T_c \sim 1$ K which is obtained for $(I/t)_{Ru} = 0.4$ and $t_{Ru} = 0.1$ eV within the limits of the triplet pairing mechanism [17].

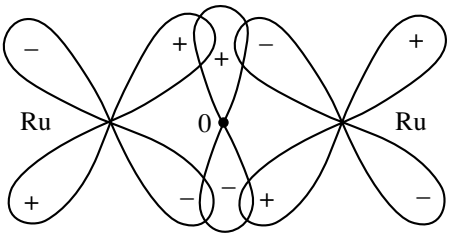

Fig. 1. Diagram of (d_{xy}–p)–π coupling in RuO_2 layer.

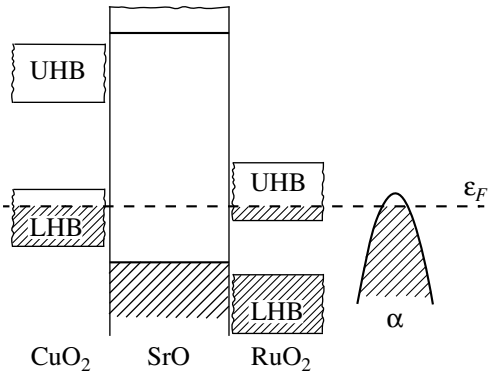

Fig. 2. Diagram of the band structure of a CuO_2/SrO/RuO_2 superlattice in the paramagnetic phase. Here UHB and LHB denote the upper and lower Hubbard subbands. The hole α band is also shown for RuO_2. Carriers are holes at the LHB top for CuO_2 layers and electrons at the UHB bottom for RuO_2 layers.

Interaction between the CuO_2 and RuO_2 layers not contained in the Hamiltonians (1) and (3) is small although important from the fundamental point of view since it ensures thermodynamic stability and determines the macroscopic symmetry of the superconducting and magnetic phases. We shall make a qualitative analysis of the role of these interactions in Section 5. Figure 2 shows a diagram of the electronic structure of the CuO_2/SrO/RuO_2 superlattice in the paramagnetic state. The carriers in the CuO_2 layer are holes in the lower Hubbard subband (LHB) and in RuO_2 they are electrons at the bottom of the upper Hubbard subband

(UHB) obtained by correlation splitting of the γ band responsible for the superconductivity in Sr_2RuO_4 [27]. The α hole band in the RuO_2 layer (and also the β band not shown in the diagram) plays the role of an electron reservoir and leads to the presence of carriers in the RuO_2 layer without doping. A general chemical potential is established as a result of the interlayer tunneling. The carrier concentration n_0 in the RuO_2 layer is a parameter of the model. For Sr_2RuO_4 we have $n_0 = 0.28$ [17]. The carriers in the CuO_2 and RuO_2 layers are spin polarons, i.e. quasiparticles surrounded by local spin fluctuations where both ferro- and antiferromagnetic correlations make a contribution in the RuO_2 layers.

The Hamiltonians (1)–(3) can be used to analyze two fundamentally different scenarios for the behavior of the system.

1. If $J > I$, which is the case for cuprates, for $n = 1$ ($n_0 = 0$, completely filled LHB) the ground state possesses long-range antiferromagnetic (AF) order. We know that the antiferromagnetic state is destroyed at fairly low hole concentrations $n_{AF} \approx 0.03$. In the range $n_0 > n_{AF}$ superconductivity may occur as a result of antiferromagnetic (J) exchange interactions.

2. If $I > J$, which is the case for ruthenates, for $n = 1$ ($n_0 = 0$ completely filled LHB), the ground dielectric state is ferromagnetic (F). In the presence of carriers, competition occurs between the saturated ferromagnetic state and the normal (nonmagnetic) N state. As a result of this competition, at concentrations $n_0 > n_F$ the system is converted to the N state and in this range superconductivity may also occur as a result of ferromagnetic (I) exchange interactions. We observe different results of this competition between the ferromagnetic and superconducting states in Sr_2RuO_4 (triplet superconductivity in RuO_4 layers) and $RuSr_2GdCu_2O_8$ (ferromagnetism in the RuO_2 layers) and thus we shall make a detailed analysis of this competition.

Omitting the index "Ru" in the Hamiltonian of the t–J–I model (3), we normalize this to the half-width of the initial electron band $W = zt$. After a Fourier transformation of the Hubbard operators

$$X_{\mathbf{k}\sigma} = \frac{1}{\sqrt{N}}\sum_{\mathbf{f}} e^{i\mathbf{k}\cdot\mathbf{f}} X_{\mathbf{f}}^{0\sigma},$$
$$X_{\mathbf{q}}^{\sigma\sigma'} = \frac{1}{\sqrt{N}}\sum_{\mathbf{f}} e^{i\mathbf{q}\cdot\mathbf{f}} X_{\mathbf{f}}^{\sigma\sigma'}, \tag{5}$$

where the vectors $\mathbf{k}$ and $\mathbf{q}$ belong to the first Brillouin band, we obtain the model Hamiltonian in the form

$$H/zt \equiv h = h_{\mathrm{kin}} + h_{\mathrm{int}}, \tag{6}$$

$$h_{\mathrm{kin}} = \sum_{\mathbf{k}\sigma} (\omega_{\mathbf{k}} - \tilde{\mu}) X_{\mathbf{k}\sigma}^{+} X_{\mathbf{k}\sigma},$$
$$\omega_{\mathbf{k}} = -\frac{1}{z}\sum_{\boldsymbol{\delta}} e^{i\mathbf{k}\cdot\boldsymbol{\delta}} = -\gamma_{\mathbf{k}}, \tag{7}$$

$$h_{\mathrm{int}} = \frac{1}{2}\sum_{\mathbf{q}\sigma} \gamma_{\mathbf{q}} \{ g(X_{\mathbf{q}}^{\sigma\bar{\sigma}} X_{-\mathbf{q}}^{\bar{\sigma}\sigma} - X_{\mathbf{q}}^{\sigma\sigma} X_{-\mathbf{q}}^{\bar{\sigma}\bar{\sigma}}) - r(X_{\mathbf{q}}^{\sigma\bar{\sigma}} X_{-\mathbf{q}}^{\bar{\sigma}\sigma} + X_{\mathbf{q}}^{\sigma\sigma} X_{-\mathbf{q}}^{\sigma\sigma}) \}, \tag{8}$$

where $g = J/t$, $r = I/t$, and $\mu/zt = \tilde{\mu}$ is the dimensionless chemical potential. The Hamiltonian h_{kin} (7) describes the electron kinetic energy and forms part of the Hubbard model for $U = \infty$.

3. SUPERCONDUCTIVITY IN CuO_2 LAYERS

In order to describe the magnetic and superconducting states of the model we use the mean-field approximation for strongly correlated systems in the formulation of the method of irreducible Green's functions [24, 28, 29] in which the higher Green's functions are projected onto the subspace of the normal $\langle\langle X_{\mathbf{k}}^{0\sigma} | X_{\mathbf{k}}^{0\sigma}\rangle\rangle$ and anomalous $\langle\langle X_{-\mathbf{k}}^{-\sigma 0} | X_{\mathbf{k}}^{\sigma 0}\rangle\rangle$ Green's functions coupled by a system of Gorkov equations [24, 25]. Fluctuations of the charge and spin states outside the limits of the mean-field theory were recently explicitly taken into account in [30] where the authors showed that the solutions for the superconducting phase obtained in the mean-field approximation are stable. The main difference between the carrier dispersion law allowing for fluctuations and the Hubbard I approximation according to [30] is that the spin correlation functions χ_1 and χ_2 between the first and second nearest neighbors are taken into account. This leads to some refinement of the Fermi surface and the appearance of satellites in the spectral density but from the qualitative point of view has little influence on the thermodynamic properties of the system and consequently in the range of parameters studied $J_{Cu}/t_{Cu} \approx 0.4$, $I_{Ru}/t_{Ru} \approx 0.4$, $J_{Ru}/t_{Ru} \approx 0.1$ we shall confine ourselves to the mean-field approximation.

In the superconducting phase the anomalous averages $B_{\mathbf{p}\sigma} = \langle X_{-\mathbf{p},-\sigma} X_{\mathbf{p}\sigma}\rangle$ determining the superconducting gap $\Delta_{\mathbf{k}\sigma}$ are nonzero:

$$\Delta_{\mathbf{k}\sigma} = \frac{1}{N}\sum_{\mathbf{p}} \{ \omega_{\mathbf{p}} (B_{\mathbf{p},-\sigma} - B_{\mathbf{p}\sigma}) + \omega_{\mathbf{k}-\mathbf{p}} [(r-g) B_{\mathbf{p},-\sigma} + g B_{\mathbf{p}\sigma}] \}. \tag{9}$$

An analysis of the symmetry of the possible solutions showed that three types of solution are possible [17].

(1) *s*-Type singlet pairings, $l = 0$,

$$\Delta_{\mathbf{k},0} = 2\Delta_0 + \lambda_s \omega_{\mathbf{k}} \Delta_0, \tag{10}$$

where the coupling constant is $\lambda_s = 2g - r$ and the dimensionless order parameter is

$$\Delta_0 = \frac{1}{2N}\sum_{\mathbf{k}} \omega_{\mathbf{k}} (B_{\mathbf{k}\uparrow} + B_{-\mathbf{k}\downarrow}). \tag{11}$$

The first term in Eq. (10) originates from the kinematic pairing mechanism [31] while the second originates from the exchange pairing mechanisms.

(2) *p*-Type triplet pairing, $l = 1$,

$$\begin{aligned} \Delta_{\mathbf{k},1} &= \lambda_p \psi_p(\mathbf{k}) \Delta_p, \\ \psi_p(\mathbf{k}) &= \frac{1}{2}(\sin k_x + i \sin k_y), \quad \lambda_p = r, \end{aligned} \tag{12}$$

the coupling constant in the *p*-pairing channel $\lambda_p = r$ is only determined by ferromagnetic exchange; this state cannot be achieved in CuO_2 layers with antiferromagnetic Cu–Cu interaction.

(3) $d_{x^2-y^2}$-Type singlet pairing, $l = 2$,

$$\begin{aligned} \Delta_{\mathbf{k},2} &= \lambda_d \psi_d(\mathbf{k}) \Delta_d, \\ \psi_d(\mathbf{k}) &= \frac{1}{2}(\cos k_x - \cos k_y), \quad \lambda_d = 2g - r. \end{aligned} \tag{13}$$

The coupling constant for the $d_{x^2-y^2}$ gap, $\lambda_d \approx 2g$ is determined by the antiferromagnetic Cu–Cu interaction (the ferromagnetic interaction $I = rt$ for the CuO_2 layers discussed in Section 2 can be neglected because of its smallness).

Expressions for the gap and the chemical potential are usually obtained from the corresponding self-consistent equations. In addition, in a strongly correlated system we also have another constraint, i.e., the constraint (2) which forbids the population of two-particle states at a single site. This condition may be written in the form [24]

$$\frac{1}{N}\sum_{\mathbf{k}} B_{\mathbf{k}\sigma} = 0, \tag{14}$$

and it is easy to see that an *s*-type solution does not satisfy this. Thus, neglecting electron–phonon interaction assuming only magnetic pairing mechanisms for the CuO_2 planes we obtain the only possible $d_{x^2-y^2}$-type state.

The gap Δ_d is determined self-consistently from the equation (for $l = 2$)

$$\frac{1}{\lambda_l} = \frac{1}{N}\sum_{\mathbf{p}} \frac{|\psi_l(\mathbf{p})|^2}{2E_{\mathbf{p}l}} \tanh\frac{E_{\mathbf{p}l}}{2\tau}, \tag{15}$$

where $\tau = k_B T/zt$ is the dimensionless temperature, $E_{\mathbf{p}l}$ is the quasiparticle energy in the superconducting phase,

$$E_{\mathbf{p}l} = \sqrt{c^2(n)(\omega_{\mathbf{p}} - m)^2 + \frac{\Delta_{\mathbf{p}l}^2}{c^2(n)}}. \tag{16}$$

Here we have $c(n) = 1 - n/2$ and m is the renormalized dimensionless chemical potential,

$$m = [\tilde{\mu} + (g + r)n/4]/c(n).$$

A similar self-consistent equation for the gap (15) was obtained earlier using a diagram technique for the *X* operators in the *t*–*J* model [32].

The solution of the equation at T_c for $d_{x^2-y^2}$ pairing shows that at moderate values of the coupling constant $\lambda_d = 0.5$ we can obtain $T_c \sim 100$ K and the high values of T_c are attributable to the closeness of the chemical potential for the optimum doped layers to the Van Hove singularity. A similar conclusion on the increase in T_c as a result of the Van Hove singularity in the superconducting state having $d_{x^2-y^2}$ symmetry caused by antiferromagnetic fluctuations was reached in an earlier study using the *t*–*J* model based on the Monte Carlo quantum method [33].

In order to estimate T_c we need to clarify the carrier concentration in the CuO_2 layers. We express the $RuSr_2GdCu_2O_8$ unit cell in the form of the successive layers:

$$\begin{aligned} &(Cu^{+2.5}O_2^{-2} - Gd^{+3} - Cu^{+2.5}O_2^{-2}) \\ &- Sr^{+2}O^{-2} - Ru^{+4}O_2^{-2} - Sr^{+2}O^{-2}, \end{aligned} \tag{17}$$

from which it follows that the number of holes per CuO_4 cell in the layer is $n_h = 1.5$. This concentration is obtained for weakly doped $YBa_2Cu_3O_{6+x}$ for $x \approx 0.5$ for we know that the $T_c(x)$ curve has a plateau at $T_c \approx 55$ K. Thus, the value of $T_c = 46$ K obtained in [1] for $RuSr_2GdCu_2O_8$ is not surprising and suggests that this compound falls within the range of weakly doped compositions. The jump in the specific heat at the transition point $\Delta\gamma(T_c) \equiv C_p/T \approx 0.35$ mJ/(g-at. K^2) is also typical of weakly doped superconductors [1].

4. COMPETITION BETWEEN FERROMAGNETIC AND SUPERCONDUCTING STATES IN THE RuO_2 LAYER

As we have noted for RuO_2 layers (and also in Sr_2RuO_4) we find $I_{Ru} \gg J_{Ru}$. The $d_{x^2-y^2}$ superconducting state with *d*-type pairing cannot be achieved in RuO_2 as a result of the antiferromagnetic correlations J_{Ru} since the coupling constant is $\lambda_d = (2J_{Ru} - I_{Ru})/t_{Ru} < 0$ [see $d_{x^2-y^2}$(13)]. Subsequently we show that $J_{Ru} = 0$

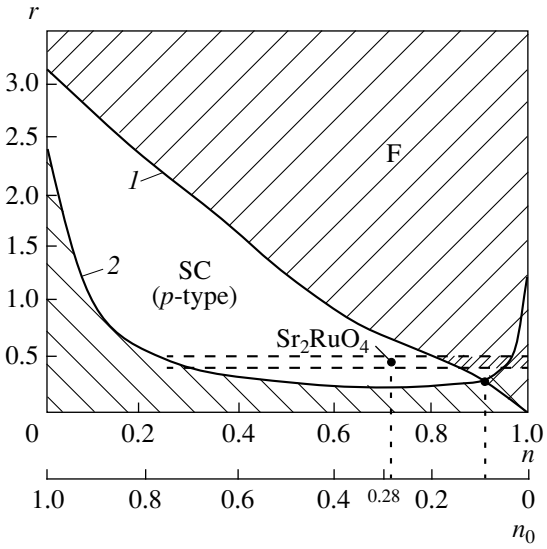

Fig. 3. *n–r* phase diagram ($T = 0$), n is the concentration, and r is the dimensionless parameter of ferromagnetic exchange interaction. Curve *1* was obtained by comparing the energies of the F and N states and the region above curve *1* corresponds to the ferromagnetic F state. Curve *2* was obtained from the equation ($T = 0$) for the superconducting gap with the minimum $\Delta_{\min} \sim 5 \times 10^{-4}$. The region above curve *2* corresponds to the *p*-type superconducting (SC) state, that below the curve is the normal N region, and the region bounded by curves *2* and *1* corresponds to the SC state.

and we retain the possibility of *p*-type superconductivity (triplet pairing) occurring as a result of ferromagnetic exchange $r = I_{\mathrm{Ru}}/t_{\mathrm{Ru}}$. The description of a system having the carrier concentration n_0 in the UHB is equivalent to its description having the hole concentration n_0 in the LHB. Using this procedure we determine the states of the system for various values of the ferromagnetic exchange parameter r and concentration $n = 1 - n_0$, i.e., we construct the *n–r* phase diagram at $T = 0$.

For fairly high values of the exchange parameter r and concentrations n in the RuO_2 layer our model gives long-range ferromagnetic order. We can establish a range of r and n values for which the ground state is ferromagnetic by comparing the energies of the normal (N) and ferromagnetic (F) states since the energy of the superconducting triplet states differs from the normal state energy by a very small relative quantity $\Delta E \sim \Delta_p^2 \rho(\varepsilon_F) \sim 10^{-2}$ eV ($\rho(\varepsilon_F)$ is the density of states at the Fermi level).

In the normal (nonmagnetic) state in the mean-field approximation [34] the distribution function at $T = 0$ has the form of a Fermi step: $f_{\mathbf{k}}^0 = \theta(m - \omega_{\mathbf{k}})$ and then the interrelation between the electron concentration n and the effective chemical potential m is written as follows:

$$n = \frac{1}{N}\sum_{\mathbf{k}\sigma} n_{\mathbf{k}\sigma} = 2c(n)\frac{1}{N}\sum_{\mathbf{k}} f_{\mathbf{k}}^0. \tag{18}$$

From this it follows that

$$\frac{n}{2-n} = \frac{1}{N}\sum_{\mathbf{k}} \theta(m - \omega_{\mathbf{k}}) = \int_{-1}^{m} \rho(\omega)\,d\omega \equiv g(m), \tag{19}$$

where $\rho(\omega) = \rho(-\omega)$ is the density of states corresponding to the $\omega_{\mathbf{k}}$ dispersion law. The energy of the N-state (at the lattice site) allowing for ferromagnetic exchange is given by

$$\epsilon_0 = \frac{1}{N}\sum_{\mathbf{k}\sigma} \omega_{\mathbf{k}}\left(1 - \frac{n}{2}\right) f_{\mathbf{k}}^0 - \frac{rn^2}{4} = (2-n)\,v(m) - \frac{rn^2}{4}, \tag{20}$$

$$v(m) \equiv \int_{-1}^{m} \omega\rho(\omega)\,d\omega,$$

and the energy of the saturated F-state is

$$\epsilon_F(n, r) = v(m_F) - \frac{rn^2}{2}, \tag{21}$$

where n is the electron concentration and m_F is the chemical potential in the F-state which is related to n by the following equation:

$$n = g(m_F) = \int_{-1}^{m_F} \rho(\omega)\,d\omega.$$

Equating the energies of the F and N states we obtain an expression for the values of the parameter r above which ferromagnetism occurs at a given concentration and below which normal or superconducting phases are possible:

$$r_{\mathrm{F}}(n) = \frac{4}{n^2}[v(m_F) - (2-n)\,v(m)]. \tag{22}$$

In order to establish a criterion for the occurrence of superconductivity (SC) outside the region of ferromagnetism, we set a very small fixed energy gap $D_{\min} \approx 10^{-3}$ outside the entire range of concentrations. For this gap we obtain for $\tau \longrightarrow 0$ the corresponding parameter r using formulas (15) and (16) for $l = 1$ (*p*-type solution):

$$r_{\mathrm{SC}}(n) = \left[\frac{1}{N}\sum_{\mathbf{k}} \frac{\psi_p^2(\mathbf{k})}{\sqrt{(\omega_{\mathbf{k}} - m)^2 + \psi_p^2(\mathbf{k})\dfrac{D_{\min}^2}{c^2(n)}}}\right]^{-1}. \tag{23}$$

This function $r_{\mathrm{SC}}(n)$ depends very weakly on the value of $D_{\min}$ and thus we shall assume that above this value of r, if no ferromagnetism occurs, the exchange param-

eter is sufficient for superconductivity to occur whereas below this value no superconductivity occurs.

Figure 3 gives the n–r phase diagram of the system where the curves $r_F(n)$ and $r_{SC}(n)$separate the regions of existence of the various phases. The right-hand point of intersection of the curves corresponds to the hole concentration $n_0 \approx 0.09$ and the parameter $r \approx 0.26$. The three-dimensional superconductor Sr_2RuO_4 has the hole concentration $n_0 \approx 0.28$ and the dimensionless parameter lies in the range $r \approx 0.4$–0.5 which leads to superconducting transition temperatures of ≈ 1–3 K [17]. The RuO_2 layers lie in this range of r values but since they are antiferromagnetic the hole concentrations in them are considerably lower (in Fig. 3 this range is shown by the closer shading).

5. DISCUSSION OF RESULTS

We shall compare the parameters of the model for RuO_2 in $RuSr_2GdCu_2O_8$ and for Sr_2RuO_4. The value of the exchange interaction I_{Ru} is determined by the overlap of the planar molecular $(d_{xy}$–$p)$–π orbitals, which is the same in both these cases so we shall assume that the parameter I_{Ru} remains the same. The parameter t_{Ru}, the effective Ru–Ru hopping parameter, also varies little since it is caused by overlap of the same $(d_{xy}$–$p)$–π orbitals. Thus, the dimensionless coupling constant r can be considered to be the same. The hole concentration n_0 undergoes the largest changes. As we discussed in Section 2, as a result of the narrowing of the α and β bands involving z-oriented orbitals of ruthenium and oxygen, the parameter n_0 should decrease. It can be seen from Fig. 3 that for $0.4 < r < 0.5$ the range of n_0 values where the superconducting triplet phase is replaced by a ferromagnetic one is $0.15 < n_0 < 0.20$. Consequently, a comparatively small reduction of the hole concentration in the RuO_2 layer compared with the three-dimensional Sr_2RuO_3 leads to stabilization of the ferromagnetic phase. Note that a similar conclusion on the stabilization of the ferromagnetic phase in Sr_2RuO_4 was obtained in [14] where allowance was made for gradient corrections to the local density functional whereas calculations using the density functional method in the local functional approximation give a paramagnetic Sr_2RuO_4 state [12, 13].

Direct information on the carrier concentration in the upper Hubbard subband of the RuO_2 layer could be obtained, for example, from experiments on the de Haas–van Alfven effect although such data are not available at present. In the present study the value of n_0 thus remains an undetermined parameter. At the same time, some predictions for experiments to study the influence of pressure on the thermodynamics of the system can be made from the phase diagram. For example, when pressure is applied perpendicular to the layers the Ru–Ru spacing in the layer increases and the bands become narrower whereas the ratio I/t changes little, and all these factors should lead to a reduction in n_0 and further stabilization of the ferromagnetic phase. However, pressure applied parallel to the layers reduces the Ru–Ru spacing, broadens the bands, and increases n_0 so that the ferromagnetic phase may become unstable and the RuO_2 layer will be converted to the superconducting triplet state with $T_c \sim 1$ K.

So far we have considered ferromagnetic RuO_2 layers and CuO_2 superconducting layers separately, whereas in $RuSr_2GdCu_2O_8$ they form a ferromagnetic metal/dielectric/superconductor/dielectric superlattice with atomic-scale layer thicknesses. Interlayer influences and tunneling effects were discussed in [18]. The exchange splitting t_{2g} of the Ru bands obtained in [18] is large, ~1 eV but the exchange splitting induced by them in the CuO_2 layer is two orders of magnitude smaller as a result of the absence of direct overlap of the d_{xy} states of Ru and the $d_{x^2-y^2}$ states of copper and the weak indirect interaction via the chain of oxygen ions O_{Ru}–O_{apex}–O_{Cu}. Thus, the splitting of the electron states at the Fermi surface is small and

$$Q = k_{F\uparrow} - k_{F\downarrow} \sim 0.01 k_F.$$

Under these conditions the superconductivity of the CuO_2 layer is not destroyed by exchange splitting but instead of the spatially uniform superconducting order parameter, an inhomogeneous state [35, 36] with a nonzero pair momentum Q and modulation length $\lambda = 2\pi/Q$ forms preferentially.

Coupling between the neighboring superconducting layers via the ferromagnetic layer will not destroy the superconductivity if the phase of the superconducting order parameter changes by π between the neighboring layers. Then the phase within the ferromagnetic layer will be close to zero which substantially reduces the loss of Cooper pairs in the magnetic layer [37].

To conclude we note that the coexistence of superconductivity and ferromagnetism in $RuSr_2GdCu_2O_8$ in our model is associated with a change in the ground state of the RuO_2 layer compared with Sr_2RuO_4. Both systems are close to the interface between the ferromagnetic and triplet superconducting phases and small changes in carrier concentration are responsible for a transition between these phases.

ACKNOWLEDGMENTS

The authors are grateful to N.M. Plakide for useful discussions. This work was partly financed by the "Integration" Federal Target Program (grant A0019), the Russian Foundation for Basic Research (project no. 00-02-16110), and the Krasnoyarsk District Science Foundation (grant 9F0039).

REFERENCES

1. C. Bernard, J. L. Tallon, Ch. Niedermayer, *et al.*, Phys. Rev. B **59**, 14099 (1999).

2. D. J. Pringle, J. L. Tallon, B. G. Walker, and H. J. Trodahl, Phys. Rev. B **59**, 11679 (1999).
3. Y. Maeno, H. Hasimoto, K. Yoshida, *et al.*, Nature **372**, 532 (1994).
4. T. M. Rice and H. Sigrist, J. Phys.: Condens. Matter **7**, L643 (1995).
5. R. J. Cava, B. Batlogg, K. Kiyono, *et al.*, Phys. Rev. B **49**, 11890 (1994).
6. A. Callaghan, C. W. Moeller, and R. Ward, Inorg. Chem. **5**, 1572 (1966).
7. G. Gao, S. McCall, and J. E. Crow, Phys. Rev. B **55**, 672 (1997).
8. V. L. Ginzburg, Zh. Éksp. Teor. Fiz. **31**, 202 (1956) [Sov. Phys. JETP **4**, 153 (1956)].
9. S. V. Vonsovskiĭ and M. S. Svirskiĭ, Dokl. Akad. Nauk SSSR **122**, 204 (1958) [Sov. Phys. Dokl. **3**, 949 (1959)].
10. S. V. Vonsovskiĭ and M. S. Svirskiĭ, Zh. Éksp. Teor. Fiz. **40**, 1677 (1961) [Sov. Phys. JETP **13**, 1182 (1961)].
11. A. I. Akhiezer and I. Ya. Pomeranchuk, Zh. Éksp. Teor. Fiz. **36**, 859 (1959) [Sov. Phys. JETP **9**, 605 (1959)].
12. T. Oguchi, Phys. Rev. B **51**, 1385 (1995).
13. D. J. Singh, Phys. Rev. B **52**, 1358 (1995).
14. P. K. de Boer and R. A. de Groot, Phys. Rev. B **59**, 9894 (1999).
15. P. Mackenzie, S. R. Julian, A. J. Diver, *et al.*, Phys. Rev. Lett. **76**, 3786 (1996).
16. S. G. Ovchinnikov, Usp. Fiz. Nauk **167**, 1043 (1997) [Phys. Usp. **40**, 993 (1997)].
17. E. V. Kuz'min, S. G. Ovchinnikov, and I. O. Baklanov, Zh. Éksp. Teor. Fiz. **116**, 655 (1999) [JETP **89**, 349 (1999)].
18. W. E. Pickett, R. Weht, and A. B. Shik, Phys. Rev. Lett. **83**, 3713 (1999).
19. R. Weht, A. B. Shick, and W. E. Pickett, in *High Temperature Superconductivity*, Ed. by S. E. Barnes, J. Ashkenazi, J. L. Cohn, and F. Zuo (American Inst. of Physics, New York, 1999), AIP Conf. Proc. **483**, 141 (1999).
20. F. C. Zhang and T. M. Rice, Phys. Rev. B **37**, 3759 (1988).
21. S. V. Lovtsov and V. Yu. Yushanhai, Physica C (Amsterdam) **179**, 159 (1991).
22. J. H. Jefferson, H. Eshes, and L. F. Feiner, Phys. Rev. B **45**, 7959 (1992).
23. V. I. Belinicker, A. I. Chernyshev, and V. A. Shubin, Phys. Rev. B **53**, 335 (1996).
24. N. M. Plakida, V. Yu. Yushanhai, and I. V. Stasyuk, Physica C (Amsterdam) **160**, 80 (1989).
25. V. Yu. Yushanhai, N. M. Plakida, and P. Kalinay, Physica C (Amsterdam) **174**, 401 (1991).
26. J. B. Goodenough, *Magnetism and the Chemical Bond* (Interscience, New York, 1963; Metallurgiya, Moscow, 1968).
27. T. M. Riseman, P. G. Kealey, E. M. Forgan, *et al.*, Nature **396**, 242 (1998).
28. S. V. Tyablikov, *Methods in the Quantum Theory of Magnetism* (Nauka, Moscow, 1975; Plenum, New York, 1967).
29. E. V. Kuz'min and S. G. Ovchinnikov, Teor. Mat. Fiz. **31**, 379 (1977).
30. N. M. Plakida and V. S. Oudovenko, Phys. Rev. B **59**, 11949 (1999).
31. R. O. Zaĭtsev and V. A. Ivanov, Fiz. Tverd. Tela (Leningrad) **29**, 2554 (1987) [Sov. Phys. Solid State **29**, 1475 (1987)].
32. Yu. A. Izyumov and B. M. Letfulov, J. Phys.: Condens. Matter **3**, 5373 (1991).
33. E. Dagotto, A. Nazarenko, and A. Moreo, Phys. Rev. Lett. **74**, 310 (1995).
34. E. V. Kuz'min and I. O. Baklanov, Zh. Éksp. Teor. Fiz. **144**, 2130 (1998) [JETP **87**, 1159 (1998)].
35. A. I. Larkin and Yu. N. Ovchinnikov, Zh. Éksp. Teor. Fiz. **47**, 1136 (1964) [Sov. Phys. JETP **20**, 762 (1964)].
36. P. Fulde and R. A. Ferrel, Phys. Rev. A **135**, 550 (1964).
37. V. Prokic, A. I. Buzdin, and L. Dobrosavljevic-Grujic, Phys. Rev. B **59**, 587 (1999).

Translation was provided by AIP

Journal of Experimental and Theoretical Physics, Vol. 91, No. 2, 2000, pp. 361–368.
Translated from Zhurnal Éksperimental'noĭ i Teoreticheskoĭ Fiziki, Vol. 118, No. 2, 2000, pp. 413–421.

SOLIDS
Electronic Properties

Fano Resonances and Electron Localization in Heterobarriers

C. S. Kim [1], A. M. Satanin[2, *], and V. B. Shtenberg [2, **]

[1]*Department of Physics, Chonnam National University, Kwangju, Korea*
[2]*Nizhni Novgorod State University, Nizhni Novgorod, 603600 Russia*
**e-mail: satanin@phys.unn.runnet.ru*
***e-mail: shten@phys.unn.runnet.ru*
Received January 3, 2000

Abstract—A study is made of electron tunneling in semiconductor heterostructures having a complex dispersion law. A generalized Fabry–Perot approach is used to describe tunneling across the barrier. Mixing of electron states at the heterojunctions is responsible for the asymmetric resonant structure of the transmission which is characterized by a resonance–antiresonance pair. The resonance corresponds to a pole while the antiresonance corresponds to a zero of the scattering amplitude in the complex energy plane, i.e., near the pole and the zero the transmission of the heterobarrier has a Fano resonance structure. It is shown that for certain barrier parameters the resonances may collapse and localized states may appear in the heterobarrier, which is observed on the current–voltage characteristics of the barriers. The two-valley model of a GaAs/Al_xGa_{1-x}As/GaAs heterostructure is considered as an example. An analysis is made of the resonance structure in the barrier as a function of the type of boundary conditions used for the heterojunctions. The low-temperature current–voltage characteristic of the barrier is calculated. © *2000 MAIK "Nauka/Interperiodica".*

1. INTRODUCTION

Studies of resonant electron tunneling in heterostructures have recently attracted increased interest [1]. From the application point of view this problem has attracted attention because resonance states are responsible for the operation of various quantum electronic devices such as the resonant tunnel diode and the resonant transistor. Theoretical studies of resonances in heterostructures were first reported in [2, 3]. In order to obtain a resonance level, we need to have at least two thin wide-gap semiconducting layers (barrier) separated by a narrow-gap semiconducting layer. The quasibound states formed between the barriers as a result of constructive wave interference are approximately characterized by two parameters: the position of the resonance E_R and its width Γ. The resonance width is determined by the electron oscillation frequency in the interbarrier region and by the probability of tunneling across the semiconductor layers. Quite clearly Γ is always finite since there is a finite probability that the electron will escape from the interbarrier region.

The aim of the present study is to show that in a semiconductor heterostructure with a complex dispersion law it is possible to have a fundamentally new situation where the resonance widths may go to zero, i.e., a unique type of resonance collapse may occur. It has been found that resonance collapse is accompanied by the appearance of localized states in barriers and by qualitative changes in their transmission. This effect becomes possible for asymmetric resonances (Fano resonances) which are characterized by another parameter which determines their asymmetry. The existence of asymmetric resonances was first noted by Fano [4] in a study on the autoionization of atoms. Recently Fano resonances were also observed in semiconductor structures. For example, in a numerical simulation of tunneling across an Al_xGa_{1-x}As layer the authors of [5] observed a transmission fine structure as a function of the barrier composition and width. Using various generalizations of the effective mass approximation to the case of a multivalley semiconductor, the authors of [6, 7] discussed the nature of the transmission dips and peaks.

In the present study we first use a generalized Fabry–Perot method to make a detailed study of the structure of an isolated Fano resonance in semiconductor layers having a complex dispersion law. We shall then study the resonance interaction and show that for certain parameters of the structure the resonances may collapse and discrete levels situated in the continuum may appear. We shall also discuss the consequences of the appearance of localized states for the tunnel transmission and current–voltage characteristic of the barrier.

2. MODEL OF THE STRUCTURE AND EQUATION

Figure 1 gives a schematic energy diagram of a heterostructure having a complex dispersion law. We shall assume that the z axis lies in the direction of tunneling and the equations for the heterojunction planes are determined by the expressions $z = \pm L/2$. Then using the

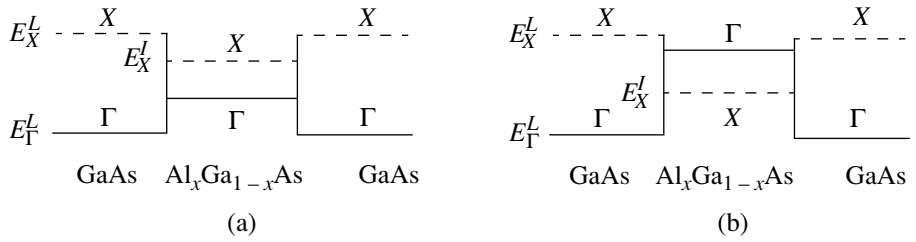

Fig. 1. Energy diagram of an GaAs/$Al_xGa_{1-x}As$/GaAs heterostructure. The position of the bands is shown schematically for the case when the Al concentration in the barrier layer corresponds to: (a) the direct position of the bands ($x < 0.45$) and (b) the inverted position.

effective mass model for systems with a complex dispersion law electron tunneling across the heterobarrier is described by

$$-\frac{\hbar^2}{2}\frac{\partial}{\partial z}\frac{1}{m_n}\frac{\partial \psi_n}{\partial z} + \sum_{n'} E_{n,n'}\psi_{n'} + \sum_{n'} V_{n,n'}\delta\left(z \pm \frac{L}{2}\right)\psi_{n'} = E\psi_n, \tag{1}$$

where m_n is the effective mass of an electron in the nth valley, $\delta(z)$ is a Dirac function defining the position of the heterojunctions, $E_{n,n'}$ is a matrix describing the intervalley electron interaction, and $V_{n,n'}$ is an off-diagonal matrix describing the mixing of states at the heterojunction.

By way of an example for specific calculations, we shall consider the two-valley model of a GaAs/$Al_xGa_{1-x}As$/GaAs heterostructures which was introduced by Liu [8] and also a more general situation developed by Ando and Akera [9], and by Aleiner and Ivchenko [10]. We also refer to the important study [11] which discusses the more general structure of the boundary conditions.

3. TRANSMISSION MATRIX

We are interested in the multichannel transmission matrix **t** which expresses the amplitudes of the waves transmitted by the barrier in terms of the amplitudes of the incident waves. The matrix **t** can be used to determine the barrier transmission, the tunnel current, and to study the resonance states in the barrier. In order to describe electron tunneling across the barrier, we use a generalized Fabry–Perot approach in which the transmission matrix is given by

$$\mathbf{t} = \mathbf{t}_R\left(\frac{1}{1-\mathbf{r}_L\mathbf{r}_R}\right)\mathbf{t}_L, \tag{2}$$

where $\mathbf{t}_L$, $\mathbf{r}_L$ and $\mathbf{t}_R$, $\mathbf{r}_R$ are the amplitude transmission and reflection matrices of the left and right boundaries, respectively. Using Eq. (1) we can easily find expressions for the transmission and reflection matrices of the heterojunctions. For the left boundary these matrices can be conveniently written in the form

$$\mathbf{t}_L = i\mathbf{d}_I\mathbf{l}_{IL}^{-1}\bar{\mathbf{k}}^L\mathbf{d}_L^{-1}, \quad \mathbf{r}_L = i\mathbf{d}_I\mathbf{l}_{IL}^{-1}\bar{\mathbf{k}}^I\mathbf{d}_I - \mathbf{d}_I^2, \tag{3}$$

and for the right boundary

$$\mathbf{t}_R = i\mathbf{d}_R^{-1}\mathbf{l}_{IR}^{-1}\bar{\mathbf{k}}^I\mathbf{d}_I, \quad \mathbf{r}_R = i\mathbf{d}_I\mathbf{l}_{IR}^{-1}\bar{\mathbf{k}}^I\mathbf{d}_I - \mathbf{d}_I^2, \tag{4}$$

where $\bar{\mathbf{k}}^\gamma = \mu^\gamma\mathbf{k}^\gamma$, $\mathbf{k}^\gamma$ are diagonal matrices whose nonzero elements determine the electron wave vectors in the nth valley: $k_n^\gamma = \sqrt{2m_n^\gamma(E-E_n^\gamma)}/\hbar$ (E_n^γ, being the position of the bottom of the band of the nth valley, are the solutions of (1) for the case of a corresponding bulk semiconductor), $\mu_n^\gamma = m_0/m_n^\gamma$ (m_0 is the free electron mass),

$$\mathbf{l}_{IL} = i\bar{\mathbf{k}}^{LI} - \mathbf{v}_L, \quad \mathbf{l}_{IR} = i\bar{\mathbf{k}}^{RI} - \mathbf{v}_R, \tag{5}$$

and $\mathbf{d}_L$, $\mathbf{d}_I$, and $\mathbf{d}_R$ are diagonal matrices having the elements

$$(\mathbf{d}_\gamma)_{n,n'} = \exp(i\theta_n^\gamma)\delta_{n,n'}, \quad \theta_n^\gamma = k_n^\gamma L/2.$$

The following notation is introduced in expression (5)

$$\bar{\mathbf{k}}^{LI} = \frac{1}{2}(\mu^I\mathbf{k}^I + \mu^L\mathbf{k}^L), \quad \bar{\mathbf{k}}^{RI} = \frac{1}{2}(\mu^I\mathbf{k}^I + \mu^R\mathbf{k}^R)$$

and

$$\mathbf{v}_{L(R)} = \frac{m_0}{\hbar^2}(V_{L(R)})_{n,n'}.$$

The matrices $\mathbf{d}_\gamma$ describe a change in the wave vector caused by a shift of the heterojunctions relative to the origin by $z = \pm L/2$. The index γ indicates the region on the left (L), right (R), or inside the barrier (I).

Substituting into (2) the expressions for the transmission matrices of the heterojunctions and the reflection R from them, we express **t** in the form

$$\mathbf{t} = \mathbf{d}_R^{-1}\mathbf{M}^{-1}\bar{\mathbf{k}}^L\mathbf{d}_L^{-1}, \tag{6}$$

where

$$\mathbf{M} = \mathbf{M}_s(\bar{\mathbf{k}}^I)^{-1}\mathbf{M}_a + i(\mathbf{v}_R - \mathbf{v}_L),$$
$$\mathbf{M}_a = (\mathbf{d}_I - \mathbf{d}_I^{-1})\mathbf{l}_{IR} - i\bar{\mathbf{k}}^I\mathbf{d}_I, \quad (7)$$
$$\mathbf{M}_s = \mathbf{l}_{IL}(\mathbf{d}_I + \mathbf{d}_I^{-1}) - i\bar{k}^I\mathbf{d}_I.$$

4. ANALYSIS OF ZEROS AND POLES OF THE TRANSMISSION MATRIX

The mixing effect between electronic states at the heterojunction determines the resonance structure of the transmission. It is found that the resonance structure depends strongly on the type of boundary conditions. We shall first consider a simplified situation assuming that Γ- and *X*-valley states play the main role in tunneling, and mixing of states at the boundaries is described by the matrix element $V_{\Gamma, X}$ [8], i.e., we shall consider the two-component function (ψ_Γ, ψ_X). The boundary conditions from [8] are obtained by integrating Eq. (1) over small vicinities near the boundaries (along the normal to the layer). For example, integrating (1) near $z = L/2$ gives

$$\psi_\Gamma(L/2+0) = \psi_\Gamma(L/2-0),$$
$$\psi_X(L/2+0) = \psi_X(L/2-0), \quad (8)$$
$$\mu_\Gamma^R\frac{\partial\psi_\Gamma(L/2+0)}{\partial z} - \mu_\Gamma^I\frac{\partial\psi_\Gamma(L/2-0)}{\partial z} = v\psi_X\left(\frac{L}{2}\right),$$
$$\mu_X^R\frac{\partial\psi_X(L/2+0)}{\partial z} - \mu_X^I\frac{\partial\psi_X(L/2-0)}{\partial z} = v\psi_\Gamma\left(\frac{L}{2}\right),$$

where $v = m_0V_{\Gamma, X}/\hbar^2$. The boundary conditions for $z = -L/2$ are written similarly. These boundary conditions can be used for a fairly wide $Al_xGa_{1-x}As$ layer when the discreteness of the barrier variation can be neglected. In this case the matrices $v_{L(R)}$ become real and the conditions for matching of the wave functions at the heterojunctions are the same, i.e., the barrier can be considered to be symmetric. It follows from (6) that the poles of the **t** matrix are determined by

$$\mathrm{Det}(\mathbf{M}) = 0. \quad (9)$$

According to (7) this equation is satisfied for a symmetric barrier when

$$\mathrm{Det}(\mathbf{M}_s) = 0 \text{ or } \mathrm{Det}(\mathbf{M}_a) = 0. \quad (10)$$

These equations correspond to the conditions for resonant tunneling across symmetric and antisymmetric states in a *X* well. The conditions for total reflection are determined from Eq. (6)

$$(\mathbf{M}^c)_{n,n'} = 0, \quad (11)$$

where $\mathbf{M}^c$ is the cofactor of the matrix **M**. The analysis of the resonant structure of the transmission is exactly the same as that used in [12–14] to study the interaction of resonances and localization in open multichannel systems. Assuming that the wave mixing is weak, using the first equation in (10) we find the position of the pole in the two-valley approximation

$$\tilde{E}^s = E_p^s - i\Gamma^s,$$
$$E_p^s = E_0^s + E_p^{s1}, \quad (12)$$

where

$$\Gamma^s \approx \frac{4\hbar^2v^2\bar{k}_\Gamma^L\cos\theta_\Gamma^I}{m_0\alpha K},$$
$$E_p^{s1} \approx \frac{4\hbar^2v^2\bar{k}_\Gamma^I\cos\theta_\Gamma^I\sin\theta_\Gamma^I}{m_0\alpha K}, \quad (13)$$

$$\alpha = (\bar{k}_\Gamma^I)^2\sin^2\theta_\Gamma^I + (\bar{k}_\Gamma^L)^2\cos^2\theta_\Gamma^I, \quad (14)$$

$$K = \frac{1}{|k_X^L|} + \frac{L}{2} + \frac{|\bar{k}_X^L|}{\bar{k}_X^I}\left(\frac{|\bar{k}_X^L|L}{2\bar{k}_X^I} + \frac{1}{k_X^I}\right). \quad (15)$$

The energy E_0^s in (12) is obtained from the condition

$$\tan\theta_X^I = |\bar{k}_X^L|/\bar{k}_X^I, \quad (16)$$

and the wave vectors, phases, and the factor *K* depend on E_0^s. For antisymmetric states the poles are determined by the expressions

$$\tilde{E}^a = E_p^a - i\Gamma^a,$$
$$E_p^a = E_0^a + E_p^{a1}, \quad (17)$$

where

$$\Gamma^a \approx \frac{4\hbar^2v^2\bar{k}_\Gamma^L\sin^2\theta_\Gamma^I}{m_0\beta K},$$
$$E_p^{a1} \approx -\frac{4\hbar^2v^2\bar{k}_\Gamma^I\cos\theta_\Gamma^I\sin\theta_\Gamma^I}{m_0\beta K}, \quad (18)$$

$$\beta = \sin^2\theta_\Gamma^I(\bar{k}_\Gamma^L)^2 + (\bar{k}_\Gamma^I)^2\cos^2\theta_\Gamma^I. \quad (19)$$

The energy E_0^a is obtained from the equation

$$\tan\theta_X^I = -\bar{k}_X^I/|\bar{k}_X^L|. \quad (20)$$

The conditions for total reflection (11) are satisfied at the energy E_0 for which we find

$$E_0 \approx E_0^s + \frac{4\hbar^2v^2\cos\theta_\Gamma^I\sin\theta_\Gamma^I}{m_0\bar{k}_\Gamma^IK} \quad (21)$$

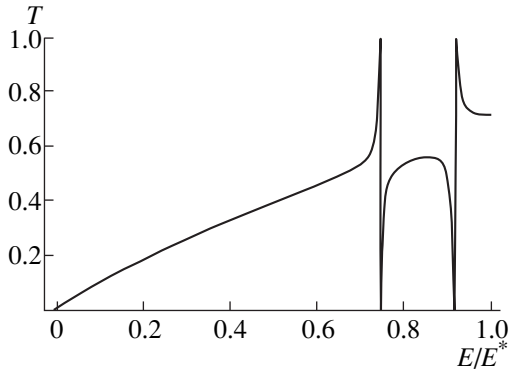

Fig. 2. Transmission of an $Al_xGa_{1-x}As$ barrier of thickness 2.1 nm in the energy range $0 < E < 1$, where E is in units of $E^* \equiv E_X^L$ ($E_X^I = 0.69$, $E_\Gamma^I = 0.58$). The calculations were made for an $Al_xGa_{1-x}As$ barrier with $x = 0.4$, $V_{\Gamma,x} = 0.01$ eV nm.

for symmetric states and

$$E_0 \approx E_0^a - \frac{4\hbar^2 v^2 \cos\theta_\Gamma^I \sin\theta_\Gamma^I}{m_0 \bar{k}_\Gamma^I K} \tag{22}$$

for antisymmetric states. The values of K, E_0^s, and E_0^a are determined by Eqs. (15), (16), and (20), respectively. It follows from this analysis that near the pole and the zero the transmission matrix has a universal structure of Fano resonances:

$$T = \frac{1}{(1+q^2)}\frac{(\epsilon+q)^2}{(\epsilon^2+1)}, \tag{23}$$

where $\epsilon = (E - E_p)/\Gamma$, $q = (E_p - E_0)/\Gamma$ are the dimensionless Fano resonance parameters.

In order to illustrate these results we used known dependences of the parameters of $Al_xGa_{1-x}As$ on the composition [16]. Figure 2 gives the transmission T of an $Al_xGa_{1-x}As$ barrier as a function of the energy E when $x = 0.4$, and the barrier thickness is $L = 2.1$ nm. In the energy range $E_X^I < E < E_X^L$ we can see a pair of Fano resonances having the parameters $E_p^s = 0.748$, $\Gamma^s = 0.0013$, $E_0^s = 0.75$, and $E_p^a = 0.917$, $\Gamma^a = 0.003$, $E_0^a = 0.915$ (the energy $E^* = E_X^L$ is taken as the unit of measurement).

Using (12), (17), (21), and (22), we can easily obtain

$$q = \pm\left(\frac{\bar{k}_\Gamma^L}{\bar{k}_\Gamma^I} - \frac{\bar{k}_\Gamma^I}{\bar{k}_\Gamma^L}\right)\cos\theta_\Gamma^I \sin\theta_\Gamma^I. \tag{24}$$

In this expression the "–" and "+" signs are taken for symmetric and antisymmetric states, respectively. The structure of (24) is such that the sign of q is determined by the sign of $\cos\theta_\Gamma^I$ or $\sin\theta_\Gamma^I$ (the expression in parentheses is positive for $E_X^I < E < E_X^L$). When the phase of the functions $\cos\theta_\Gamma^I$ or $\sin\theta_\Gamma^I$ changes, the parameter q changes sign and the pole and zero of the Fano resonance change places.

The structure of the resonances changes slightly if we take into account the dependence of the intervalley mixing on the parity of the layers and the barrier composition. To be specific we shall consider a $GaAs/(Al_xGa_{1-x}As)_N/GaAs$ barrier where the mixing of the electronic states at the heterojunctions is taken into account in the form

$$v_{L(R)} = \begin{pmatrix} 0 & v\exp(i\phi_{L(R)}) \\ v\exp(-i\phi_{L(R)}) & 0 \end{pmatrix}, \tag{25}$$

where the phase difference $\phi_R - \phi_L$ of the matrix elements responsible for Γ–X mixing is taken in the form πNx. This choice is justified by the fact that for pure AlAs the phase difference is the same as the result obtained by Aleiner and Ivchenko [10].

The position of the pole for symmetric states in the barrier is determined by Eq. (12) in which

$$\Gamma^s \approx \frac{2\hbar^2 v^2 \bar{k}_\Gamma^L \cos^2\theta_\Gamma^I}{m_0 \alpha\beta K}\left(2\beta + \Phi(\bar{k}_\Gamma^I)^2\left(\frac{\sin^2\theta_\Gamma^I}{\cos^2\theta_\Gamma^I} - 1\right)\right), \tag{26}$$

$$E_p^{s1} \approx \frac{2\hbar^2 v^2 \bar{k}_\Gamma^L \cos\theta_\Gamma^I \sin\theta_\Gamma^I}{m_0 \alpha\beta K}(2\beta + \Phi((\bar{k}_\Gamma^I)^2 + (\bar{k}_\Gamma^L)^2)),$$

$$\Phi = 1 - \cos(\phi_R - \phi_L). \tag{27}$$

For these boundary conditions the expression for the zero of the Fano resonance [which generalizes (21)] is written in the form

$$E_0 \approx E_0^s + \frac{4\hbar^2 v^2 \exp i(\phi_R - \phi_L)\cos\theta_\Gamma^I \sin\theta_\Gamma^I}{m_0 \bar{k}_\Gamma^I K}. \tag{28}$$

It can be seen from Eqs. (26) and (28) that the minimum resonance width and the position of the Fano resonance zero in the complex energy plane are determined by the phase difference $\phi_R - \phi_L$. Figure 3 gives the transmission of an $(Al_xGa_{1-x}As)_N$ barrier as a function of the energy ($x = 0.4$, $N = 7$, $E_X^I < E < E_X^L$). This figure demonstrates a pair of Fano resonances whose zeros are shifted in the complex plane. The expressions for the pole and the zero for the antisymmetric resonance have a similar structure and are not given here.

5. ELECTRON LOCALIZATION IN HETEROBARRIERS

It can be seen from the expressions for the pole (13) and the zero (21) in cases of symmetric states [and similar expressions (18) and (22) for antisymmetric states]

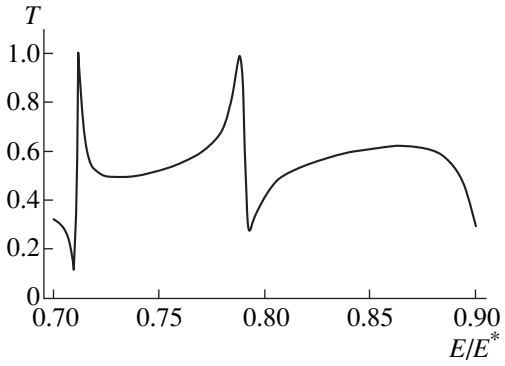

Fig. 3. Transmission of an $(Al_{0.4}Ga_{0.6}As)_7$ barrier as a function of energy E in the range $E_X^I < E < E_X^L$.

that as the parameters of the system vary, the poles and zeros of the transmission matrix move in the complex plane. As a result, the resonant structure of the barrier transmission may vary. Figure 4 shows the motion of the singularities (pole, zero) of the heterobarrier transmission in the complex energy plane during collapse of a Fano resonance. As the barrier width increases and approaches L_{cr} (Figs. 4a and 4b) the pole (light region in the figures) moves in the direction of the real energy axis and approaches the zero (dark region) of the Fano resonance. When the barrier width becomes equal to the critical value, the transmission singularities disappear in this energy range and the resonance disappears (Fig. 4c). A further increase in the barrier width leads to the appearance of a resonance (Fig. 4d). It can be seen that the pole and the zero have now changed places compared with those shown in Fig. 4a. The expressions obtained for a resonance–antiresonance pair indicate a possible scenario for resonance collapse in the barrier when the resonance width goes to zero and the pole goes over to the real axis and collides with the zero of the scattering amplitude. We take the barrier width as

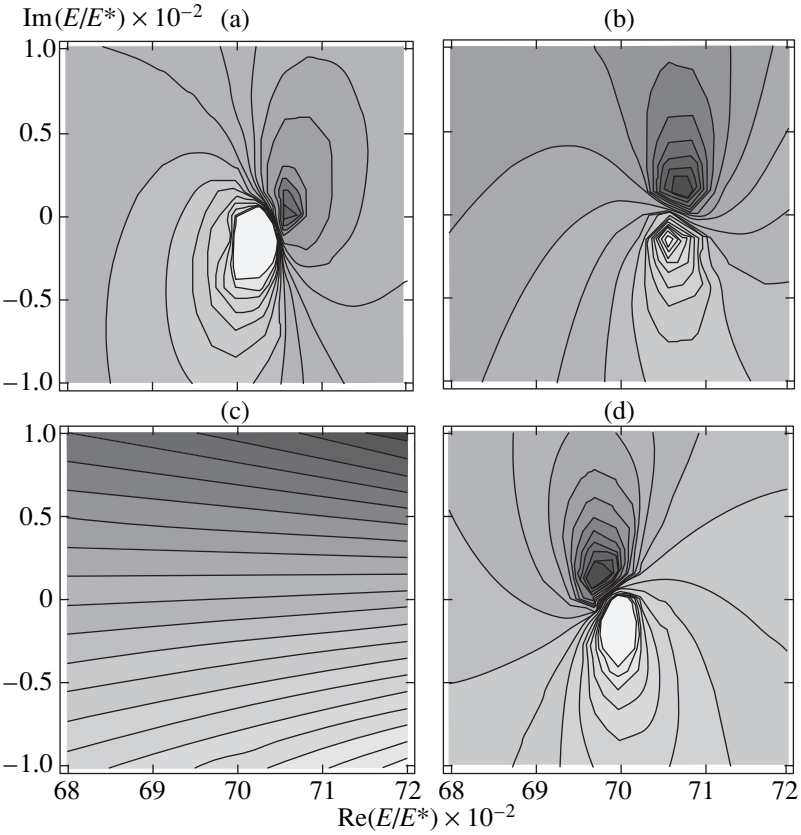

Fig. 4. Position of pole (light region) and zero (dark region) of the square of the modulus of the transmission amplitude $t_{\Gamma,\Gamma}(E)$ continued into the complex energy plane ($E = \mathrm{Re}E + i\,\mathrm{Im}E$): (a) for $L = 2.8$ nm when the pole is on the left of the zero, $\mathrm{Re}E_0 > \mathrm{Re}E_p$; (b) the pole and zero converge as the barrier width increases; (c) as a result of a "collision" between the pole and the zero at $L = L_{cr}$ the Fano resonance collapses; (d) as the barrier width increases further, the pole and the zero change places, $\mathrm{Re}E_0 < \mathrm{Re}E_p$. A transition from darker to lighter regions in the figure implies an increase in $T(E)$. The contours give isolines of the function $|t_{\Gamma,\Gamma}(\mathrm{Re}E, \mathrm{Im}E)|^2$. The calculations were made for an $Al_xGa_{1-x}As$ barrier for $x = 0.44$.

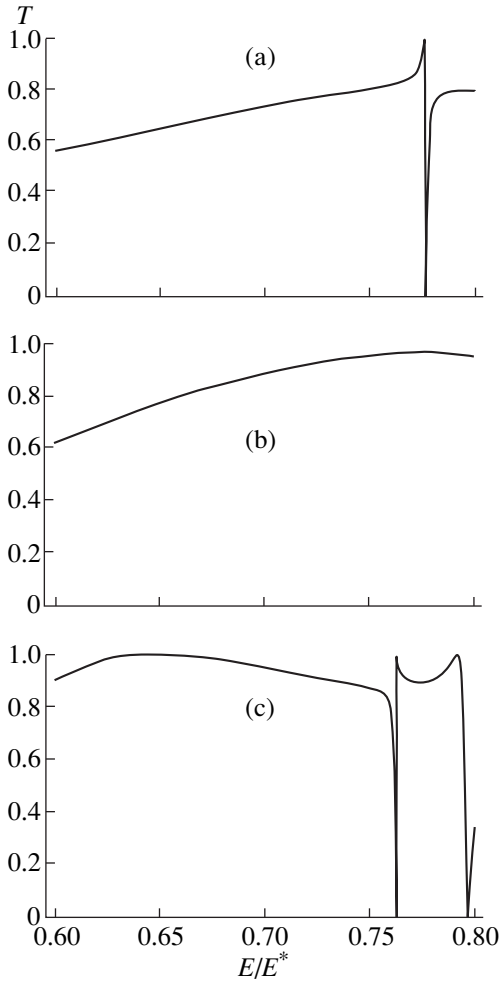

Fig. 5. Transmission of an $Al_xGa_{1-x}As$ barrier for $x = 0.3$, $V_{\Gamma, x} = 0.008$ eV nm as a function of energy E in the range $E_X^I < E < E_X^L$ ($E_X^I = 0.75$, $E_\Gamma^I = 0.44$) for various heterobarrier widths: L (a) = 4.7, (b) 4.8, (c) 7.6 nm.

the control parameter. Then, if the following conditions are satisfied

$$\begin{cases} \cos\theta_\Gamma^I = 0, \\ \tan\theta_\Gamma^I = \dfrac{|\bar{k}_X^L|}{\bar{k}_X^I} \end{cases} \tag{29}$$

the Fano resonance will collapse. We shall now discuss the physical reason for this effect in greater detail. The first equation in (29) determines a set of discrete states in the continuum above the Γ barrier having the energy

$$E = E_\Gamma^I + \frac{\hbar^2\pi^2(2j+1)^2}{2m_\Gamma^I L^2}, \quad j = 0, 1, 2\ldots \tag{30}$$

The second condition in (29) is equivalent to the equation determining the spectrum of even levels in a symmetric potential well. Quite clearly for a certain heterobarrier width (L_{cr}) these levels will be the same which leads to unique level degeneracy in the continuum. In this case, the particle is "trapped" in the heterobarrier. We give the explicit form of the wave function of the localized states:

$$\psi_\Gamma(z) = \begin{cases} D\cos(k_\Gamma^I z), & |z| < L/2, \\ 0, & |z| > L/2, \end{cases} \tag{31}$$

and

$$\psi_X(z) = \begin{cases} A\exp(ik_X^I z) + B\exp(-ik_X^I z), & |z| < L/2, \\ C\exp\{-|k_X^{L(R)}||z|\}, & |z| > L/2. \end{cases} \tag{32}$$

It is easy to see that this wave function will be a solution of Eq. (1) if condition (29) is satisfied. In fact, having substituted the symmetric solution ($A = B$) determined by (31) and (32) into the boundary conditions (8), we obtain

$$D\cos\theta_\Gamma^I = 0, \tag{33}$$

$$2A\cos\theta_X^I = Ce^{-|\theta_X^R|}, \tag{34}$$

$$\bar{k}_\Gamma^I D\sin\theta_\Gamma^I = vCe^{-|\theta_X^R|}, \tag{35}$$

$$-|\bar{k}_X^R|Ce^{-|\theta_X^R|} + 2\bar{k}_X^I A\sin\theta_X^I = vD\cos\theta_\Gamma^I. \tag{36}$$

An analysis of (33) shows that: (1) if Eq. (33) is satisfied ($\cos\theta_\Gamma^I = 0$], Eq. (36) will not contain the channel coupling parameter v; (2) the amplitudes A and C will be determined by the independent Eqs. (34) and (36) which yield the second relationship (29); (3) Eq. (35) gives the relationship between the amplitudes D and C. Note that the remaining amplitude is determined by the normalization condition. Thus, we have established that particles are trapped by the barrier and the resonance collapses.

Similarly, the same level crossing exists for the antisymmetric solutions (9) if the following conditions are satisfied

$$\begin{cases} \sin\theta_\Gamma^I = 0, \\ \tan\theta_X^I = -\dfrac{\bar{k}_X^I}{|\bar{k}_X^L|}. \end{cases}$$

Note that the energy of the localized states lies in the continuum of Γ states of the contact regions. Figure 5 shows the disappearance of the Fano resonance at $x = 0.3$ which is associated with the appearance of a localized state in the barrier. If the barrier width is less than critical ($L = 4.7$ nm), a Fano resonance occurs in the barrier (see Fig. 5a). It can be seen from Fig. 5b that this resonance disappears when the barrier width reaches the

critical value (L_{cr} = 4.8 nm). As the barrier width increases, the resonance reappears, as shown in Fig. 5c (L = 7.6 nm). In this case an effect occurs where the pole and zero of the Fano resonance change places.

Thus, resonances may collapse when the virtual levels lying above the barrier (in the Γ valley) cross levels in the well (X valley). The levels can cross if $E_\Gamma^I < E_X^{L(R)}$ (see Figs. 1a and 1b). From the experimentally determined dependence of E_Γ on x [15] we find that this is satisfied when $x < 0.63$.

The more complex boundary conditions for the heterojunctions require an additional condition to be satisfied for resonance collapse. In this case for symmetric states in the barrier in (29) we need to add another equation:

$$\begin{cases} \cos(\Delta\phi) = 1 \\ \cos\theta_\Gamma^I = 0 \\ \tan\theta_X^I = \dfrac{|\bar{k}_X^L|}{\bar{k}_X^I}, \end{cases} \tag{37}$$

where we introduce the notation $\Delta\phi = \phi_R - \phi_L$. It is easy to see that these conditions cannot be satisfied exactly as a result of the discreteness of the variation in the barrier width. Approximately satisfying the system (37) leads to narrowing of the resonance in the barrier. Figure 6 shows the transmission of a GaAs/$(Al_xGa_{1-x}As)_7$/GaAs barrier. The change in the Fano resonance structure as a function of the barrier composition can be seen from Figs. 6a–6c. Figure 6a corresponds to the case when the conditions (37) are approximately satisfied (N = 7, x = 0.287, $E_0 \approx$ 0.79). It can be seen that as the barrier composition varies, the resonance becomes broader, the zero shifts into the complex plane (Fig. 6b, x = 0.35), and the position of the Fano resonance zero gradually shifts relative to the pole (Fig. 6c, x = 0.44). An estimate of the resonance width in this case shows that it may be an order of magnitude narrower compared with the case when the system parameters are far from critical. However, the conditions (37) can be satisfied exactly if we introduce a new parameter controlling the width of the $Al_xGa_{1-x}As$ monolayer. This parameter may be the external electric field or the pressure [16].

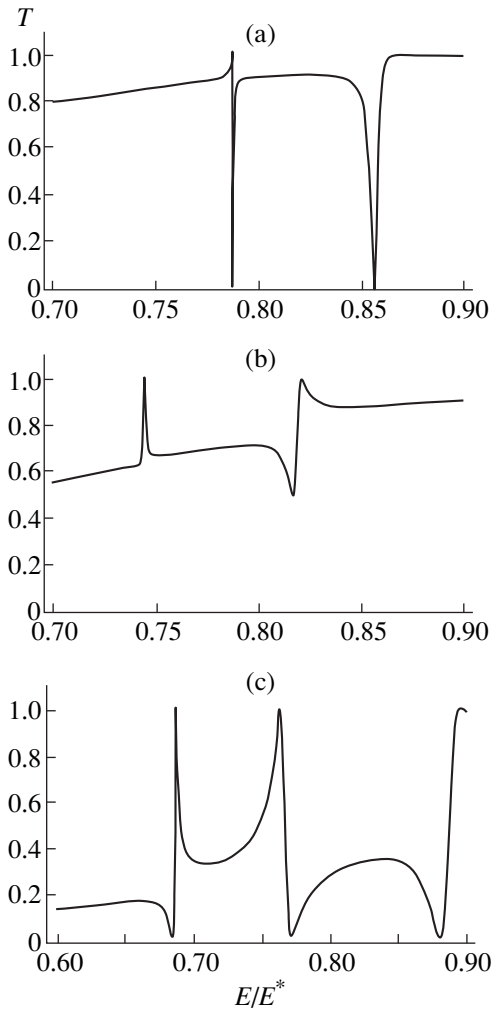

Fig. 6. Transmission of an $(Al_xGa_{1-x}As)_7$ barrier as a function of energy E in the range $E_X^I < E < E_X^L$: (a) x = 0.287 (E_X^I = 0.76, E_Γ^I = 0.42), (b) x = 0.35 (E_X^I = 0.72, E_Γ^I = 0.51), (c) x = 0.44 (E_X^I = 0.65, E_Γ^I = 0.64).

6. DISCUSSION OF RESULTS

Thus, we have studied electron tunneling in semiconductor heterobarriers having a complex dispersion law. We have show that the barrier transmission has a Fano resonance structure which may vary qualitatively as the system parameters vary. In particular, for critical system parameters the resonances collapse accompanied by the appearance of localized states inside the barrier. These states are doubly degenerate with one state belonging to the discrete spectrum and the other to the continuous spectrum.

The analytic expressions obtained above and the qualitative conclusions on the resonance structure are valid assuming weak interaction of Γ–X valley states. In order to illustrate the universal nature of these results we made direct numerical calculations for a realistic GaAs/$Al_xGa_{1-x}As$/GaAs heterostructure.

Using the Esaki–Tsu formula for the tunnel current [3], we constructed the resonant current–voltage characteristic of the heterobarrier. Figure 7 gives the dependence of the resonant current J on the applied voltage U. The unit of measurement of the current was $J^* = em^*E^*/2\pi^2\hbar^3$ and the energy $E^* = E_X^L$ was taken as the unit of measurement of eU. The parameters of the $Al_xGa_{1-x}As$ barrier are: L = 1.4 nm, x = 0.44, and E_F = 0.05 eV is the Fermi energy. Regions of negative differential resistance can

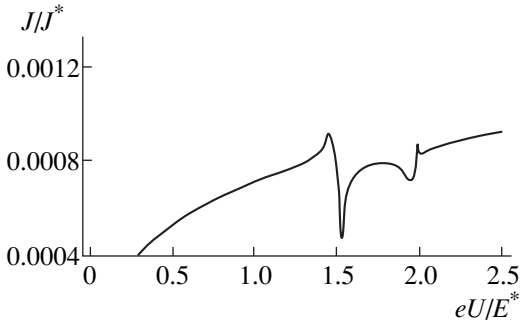

Fig. 7. Current–voltage characteristic of an $Al_xGa_{1-x}As$ barrier having the parameters: $x = 0.44$, $V_{\Gamma,X} = 0.011$ eV nm, $L = 1.4$ nm, $E_F = 0.05$ eV. The current is in units of $J^* = em^*E^*/2\pi^2\hbar^3$ and eU is in units of E^*.

be clearly seen on the current–voltage characteristic of the barrier. Quite clearly the profile of the current–voltage characteristic is the same as that of the barrier. As we have already discussed, a change in the barrier width leads to a change in the resonance width and in particular to collapse of the resonances. On the current–voltage characteristic this factor will be reflected in a change in the size of the region of negative differential resistance. In other words, it follows from this analysis that the section of negative differential resistance on the heterobarrier current–voltage characteristic can be modified, which may be used in nanoelectronics.

ACKNOWLEDGMENTS

The authors are grateful to A.A. Andronov, A.Ya. Aleshkin, V.A. Volkov, E.V. Demidov, and D.O. Filatov for useful observations and discussions of the results. This work was partially supported by the KISTEP program.

REFERENCES

1. *Quantum Transport in Ultrasmall Devices*, Ed. by D. K. Ferry, H. L. Grubin, C. Jacoboni, and A.-P. Jauho (Plenum, New York, 1995), NATO Adv. Study Inst. Ser., Ser. B, Vol. 342.
2. L. V. Iogansen, Zh. Éksp. Teor. Fiz. **47**, 270 (1964) [Sov. Phys. JETP **20**, 180 (1964)].
3. R. Tsu and L. Esaki, Appl. Phys. Lett. **22**, 562 (1973).
4. U. Fano, Phys. Rev. B **104**, 1866 (1961).
5. D. Y. K. Ko and J. C. Inkson, Semicond. Sci. Technol. **3**, 791 (1988).
6. E. Tekman and P. F. Bagwell, Phys. Rev. B **48**, 2553 (1993).
7. R. C. Bowen *et al.*, Phys. Rev. B **52**, 2754 (1995).
8. H. C. Liu, Appl. Phys. Lett. **51**, 1019 (1987).
9. T. Ando and H. Akera, Phys. Rev. B **40**, 11619 (1989).
10. I. L. Aleĭner and E. L. Ivchenko, Fiz. Tekh. Poluprovodn. (St. Petersburg) **27**, 594 (1993) [Semiconductors **27**, 330 (1993)].
11. V. A. Volkov and É. E. Takhtamirov, Zh. Éksp. Teor. Fiz. **116**, 1843 (1999) [JETP **89**, 1000 (1999)].
12. C. S. Kim and A. M. Satanin, Phys. Rev. B **58**, 15389 (1998).
13. C. S. Kim and A. M. Satanin, J. Phys: Condens. Matter **10**, 10587 (1998).
14. Ch. S. Kim and A. M. Satanin, Zh. Éksp. Teor. Fiz. **115**, 211 (1999) [JETP **88**, 118 (1999)].
15. S. Adachi, J. Appl. Phys. **58**, R1 (1985).
16. V. P. Dragunov and A. A. Shishkov, in *Proceedings of the IV Russia Conference on Physics of Semiconductors "Semiconductors'99," Novosibirsk, 1999.*

Translation was provided by AIP

Journal of Experimental and Theoretical Physics, Vol. 91, No. 2, 2000, pp. 369–383.
Translated from Zhurnal Éksperimental'noĭ i Teoreticheskoĭ Fiziki, Vol. 118, No. 2, 2000, pp. 422–437.

SOLIDS
Electronic Properties

Evolution of the Band Structure of Quasiparticles with Doping in Copper Oxides on the Basis of a Generalized Tight-Binding Method

V. A. Gavrichkov*, S. G. Ovchinnikov, A. A. Borisov, and E. G. Goryachev

Kirenskii Institute of Physics, Siberian Division, Russian Academy of Sciences, Krasnoyarsk, 660036 Russia
**e-mail: gav@ksc.krasn.ru*

Received January 18, 2000

Abstract—Two methods for stabilizing the two-hole $^3B_{1g}$ state as the ground state instead of the Zhang–Rice singlet are determined on the basis of an orthogonal cellular basis for a realistic multiband *pd* model of a CuO_2 layer and the dispersion relations for the valence band top in undoped and doped cases are calculated. In the undoped case, aside from the valence band, qualitatively corresponding to the experimental ARPES data for $Sr_2CuO_2Cl_2$ and the results obtained on the basis of the *t*–*t*'–*J* model, the calculations give a zero-dispersion virtual level at the valence band top itself. Because of the zero amplitude of transitions forming the virtual level the response corresponding to it is absent in the spectral density function. In consequence, the experimental ARPES data do not reproduce its presence in this antiferromagnetic undoped dielectric. A calculation of the doped case showed that the virtual level transforms into an impurity-type band and acquires dispersion on account of the nonzero occupation number of the two-hole states and therefore should be detected in ARPES experiments as a high-energy peak in the spectral density. The computed dispersion dependence for the valence band top is identical to the dispersion obtained by the Monte Carlo method, and the ARPES data for optimally doped $Bi_2Sr_2CaCu_2O_{8+\delta}$ samples. The data obtained also make it possible to explain the presence of an energy pseudogap at the symmetric *X* point of the Brillouin band of HTSC compounds. © *2000 MAIK "Nauka/Interperiodica".*

1. INTRODUCTION

Intense discussions about the choice of an effective model for describing the physical properties of CuO_2 planes in perovskite structures has been going on since the discovery of high-temperature superconductivity. Suggestions [1] that the single-band Hubbard model could be the key to understanding the nature of the unusual behavior of these materials were made back in 1987. In the strong correlations regime the Hubbard model reduces to the so-called *t*–*J* model with exchange interaction $J = 4t^2/U$, corresponding to second-order of perturbation theory. Following experimental evidence [2, 3] showing that the mobile charge carriers are primarily in the $2p_x$ and $2p_y$ orbitals, Emery proposed a three-band generalized Hubbard model [4] (the so-called Emery *p*–*d* model) for describing the electronic structure. In this approach there is no longer any obvious relation to the single-band Hubbard model. Considering the importance of charge-transfer processes, a similar approach was proposed in [5, 6]. Subsequently, Zhang and Rice showed [7] that at least for a strong Coulomb repulsion and high charge transfer energy the Emery model does indeed reduce to an effective single-band model, since the doped hole charge carriers are in a singlet state A_{1g}—the Zhang–Rice singlet state, separated well by an energy gap from the other possible two-hole states. The concept of a Zhang–Rice singlet has been found to be true in principle and productive, even though once again it was based on the perturbation theory for the tight-binding case, where the Coulomb interactions on oxygen, between oxygen and copper, as well as oxygen–oxygen charge transfer were neglected. Eskes and Jefferson demonstrated [8] that this approach is not always correct for realistic values of the model parameters. Nonetheless, calculations in Anderson's impurity model [9] as well as cluster calculations [10, 11] based on a three-band *pd* model indeed confirmed that the Zhang–Rice singlet is well separated in energy from the bulk of the two-hole states. Jefferson, Eskes, and Feiner [12] and, independently, Lovtsov and Yushankhaem [13] as well as Schutler and Fedro [14], using a cluster method of perturbation theory introduced previously by Ovchinnikov, Sandalov [15] and Jefferson [16], have given a more accurate derivation of the single-band model. The most complete derivation of the *t*–*J* model from the three-band *p*–*d* model, using a cluster perturbation theory, is contained in the work of Belinicher, Chernyshov, and Shubin [17]. The investigations have made it clear that hops not only between nearest neighbors, *t* (intersublattice hops), but also between the second neighbors, *t*' (intrasublattice hops), and third neighbors, *t*'', are important for the dispersion law for a hole moving against the background of antiferromagnetic (AFM) spin order. It is the terms *t*' that made it possible to

describe on the basis of the t–t'–J model the dispersion law at the valence band top in $Sr_2CuO_2Cl_2$ [18, 19], obtained experimentally by ARPES spectroscopy [20]. At the same time, there are a number of experimental and theoretical indications showing that the three-band p–d model is itself inadequate. Thus, the absorption spectra of polarized X-rays (XAS) [21] and electronic loss spectra (ELS) [2] have revealed an appreciable (10–15%) population of $d_{3z^2-r^2}$ copper orbitals in all p-type HTSCs. In [23, 24] the effect of Coulomb repulsion on oxygen and between oxygen and copper on the effective interactions in a single-band model was examined, and the main consequences of using a realistic $d_{x^2-y^2}$, $d_{3z^2-r^2}$, p_x, p_y, p_z orbital basis on the possibility of constructing an effective one-band model were indicated. Specifically, when the apical oxygen approaches the CuO_2 plane as the degree of doping increases, the two-hole triplet term $^3B_{1g}$ can compete with the Zhang–Rice singlet. As a result, the systematic description of the physics of the lower-lying excitations is no longer possible in the one-band effective model. A similar conclusion was obtained earlier on the basis of a generalized tight-binding method [15]. In this method all possible multihole terms as well as Coulomb and exchange interactions are taken into account. The method formulated using the equations of motion for the Green's functions makes it possible, in principle, to calculate in a unified approach the dispersion curves and the spectral density of states and their temperature, field, and concentration dependences.

The generalized tight-binding method has been used to calculate the dispersion laws and density of states of an undoped CuO_2 layer in the paramagnetic [25] and antiferromagnetic [26] states. The band structure of the quasiparticles was found to depend on the temperature, magnetic field, and particle density. Specifically, for doping with holes new states, similar to deep impurity levels in doped semiconductors, appear in the semiconductor gap [27, 28]. The results of the calculations of the dispersion law of the valence band top in undoped CuO_2 layer were found to be in good agreement with the experimental ARPES-spectroscopy data for $Sr_2CuO_2Cl_2$ [20]. However, the problem of the common oxygen was solved in [15, 25–28] by artificially dividing the CuO_2 layer into two sublattices with the triplets O–Cu–O as a unit cell in each sublattice. In addition, the unit cell in one of the sublattices is turned by 90° with respect to the unit cell in the other sublattice. Since all Cu–O distances in the planes are the same, there are no reasons for such a separation into two sublattices. It would be more systematic to use CuO_6 (CuO_5) cells and the Shastry canonical-fermion representations [29], as done in [12, 16, 17, 23, 24]. In what follows we shall combine the strong aspects of both methods into a single approach. Specifically, in the present paper a systematic formulation is given for the generalized tight-binding method, where a CuO_6 cluster will serve as the unit cell, and the problem of the nonorthogonality of the molecular orbitals of neighboring clusters will be solved in the obvious manner—by constructing the corresponding Wannier functions on the $d_{x^2-y^2}$, $d_{3z^2-r^2}$, p_x, p_y, p_z five-orbital initial basis of atomic states.

The single-cell part of the Hamiltonian factorizes in the new symmetric basis, making it possible to classify according to symmetry all possible effective single-particle excitations in a CuO_2 plane. A subsequent exact diagonalization of the Hamiltonian of a unit cell and a transition to the Hubbard operator representation make it possible to take account of the part of the Hamiltonian that corresponds to hops. The construction and analysis of the dispersion relations are performed using the generalized tight-binding method and the equations of motion for the corresponding Green's functions. The nature of the states at the valence band top of HTSC compounds and the behavior of the states as a function of temperature and hole density are analyzed in the Conclusions.

2. EFFECTIVE HAMILTONIAN OF A CuO_2 LAYER IN THE CELLULAR REPRESENTATION

The initial Hamiltonian of the model can be written in the standard manner:

$$H = H_d + H_p + H_{pd} + H_{pp}, \quad H_d = \sum_r H_d(r), \quad (1)$$

$$H_d(\mathbf{r}) = \sum_{\lambda\sigma}\Bigg[(\varepsilon_\lambda - \mu)d^+_{\lambda\mathbf{r}\sigma}d_{\lambda\mathbf{r}\sigma} + \frac{1}{2}U_\lambda n^\sigma_{\lambda\mathbf{r}}n^{-\sigma}_{\lambda\mathbf{r}}$$

$$+ \sum_{\lambda'\sigma'}\Bigg(-J_d d^+_{\lambda\mathbf{r}\sigma}d_{\lambda\mathbf{r}\sigma'}d^+_{\lambda'\mathbf{r}\sigma'} + \sum_{\mathbf{r}'}V_{\lambda\lambda'}n^\sigma_{\lambda\mathbf{r}}n^{\sigma'}_{\lambda'\mathbf{r}'}\Bigg)\Bigg],$$

$$H_p = \sum_{\mathbf{i}} H_p(\mathbf{i}),$$

$$H_p(\mathbf{i}) = \sum_{\alpha\sigma}\Bigg[(\varepsilon_\alpha - \mu)p^+_{\alpha\mathbf{i}\sigma}p_{\alpha\mathbf{i}\sigma} + \frac{1}{2}U_\alpha n^\sigma_{\alpha\mathbf{i}}n^{-\sigma}_{\alpha\mathbf{i}}$$

$$+ \sum_{\alpha'\mathbf{i}'\sigma'}V_{\alpha\alpha'}n^\sigma_{\alpha\mathbf{i}}n^{\sigma'}_{\alpha'\mathbf{i}'}\Bigg],$$

$$H_{pd} = \sum_{\langle\mathbf{i},\mathbf{r}\rangle} H_{pd}(\mathbf{i},\mathbf{r}),$$

$$H_{pd}(\mathbf{i},\mathbf{r}) = \sum_{\alpha\lambda\sigma\sigma'}(t_{\lambda\alpha}p^+_{a\mathbf{i}\sigma}d_{\mathbf{r}\lambda\sigma} + V_{\alpha\lambda}n^\sigma_{\alpha\mathbf{i}}n^{\sigma'}_{\lambda\mathbf{r}}),$$

$$H_{pp} = \sum_{\langle\mathbf{i},\mathbf{r}\rangle}\sum_{\alpha\beta\sigma}(t_{\alpha\beta}p^+_{\alpha\mathbf{i}\sigma}p_{\beta\mathbf{j}\sigma} + \text{H.c.}),$$

where

$$n^{\sigma}_{\lambda \mathbf{i}} = d^{+}_{\lambda \mathbf{i}\sigma} d_{\lambda \mathbf{i}\sigma}, \quad n^{\sigma}_{\alpha \mathbf{i}} = p^{+}_{\alpha \mathbf{i}\sigma} p_{\alpha \mathbf{i}\sigma}.$$

The indices **r** and **i** run through the positions $d_{x^2-y^2}$, $d_{3z^2-r^2}$, and p_x, p_y, p_z sets of localized atomic orbitals. Similarly, $\varepsilon_\lambda = \varepsilon_{d_x}$ ($\lambda = d_x$), ε_{d_x} ($\lambda = d_z$) and $\varepsilon_\alpha = \varepsilon_p$ ($\alpha = p_x, p_y$), ε_{p_x} ($\alpha = p_z$) are the energies of the corresponding atomic orbitals; $t_{\lambda\alpha} = t_{pd}$ ($\lambda = d_x$, $\alpha = p_x, p_y$); $t_{pd}/\sqrt{3}$ ($\lambda = d_z$, $\alpha = p_x, p_y$) are the matrix elements of a hop; $U_\lambda = U_d$ ($\lambda = d_x, d_z$) and $U_\alpha = U_p$ ($\alpha = p_x, p_y, p_z$) are intraatomic Coulomb interactions; $V_{\alpha\lambda} = V_{pd}$ ($\alpha = p_x, p_y$; $\lambda = d_x, d_z$) and V'_{pd} ($\alpha = p_z$; $\lambda = d_x, d_y$) are the copper-oxygen Coulomb repulsion energies. All matrix elements of the Coulomb and exchange interactions are assumed to be independent of the form of the *d* or *p* planar orbitals. A prime indicates an interaction with apical oxygen. The first step in converting our Hamiltonian to the cellular basis corresponds to the analogous step in the method of [23] and refers to the transformation of the hopping part of the Hamiltonian.

Depending on the elements between CuO_2 layers, the copper ion can have oxygen coordination 6 in La_2CuO_4 compounds, 1-2-0-1 and 2-2-0-1 (Bi and Tl), 5 in the compounds 1-2-3, 1-2-4, 1-2-1-2, 2-2-1-2 (Bi, Tl), and 4 in the compound Nd_2CuO_4. In what follows we shall work with a CuO_6 cluster as the most general case. All subsequent calculations are also valid, with minimal changes, for smaller coordination numbers. Figure 1 displays the unit cell of the CuO_2 plane with the accompanying apical oxygen. In accordance with the choice of phases in Fig. 1, the part of the Hamiltonian of a CuO_6 cell that takes account of the hops can be written as follows:

$$\begin{aligned} H^{c}_{pd} &= t_{pd} d^{+}_{x}(p_{x-1/2,\sigma} - p_{x+1/2,\sigma} + p_{y-1/2,\sigma} - p_{y+1/2,\sigma}) \\ &+ \frac{t_{pd} d^{+}_{z}}{\sqrt{3}}(-p_{x-1/2,\sigma} + p_{x+1/2,\sigma} + p_{y-1/2,\sigma} - p_{y_{+1/2,\sigma}}) + \text{h.c.}, \\ H^{c}_{pp} &= t_{pp}(p^{+}_{x-1/2,\sigma} p_{y+1/2,\sigma} - p^{+}_{x-1/2,\sigma} p_{y-1/2,\sigma} \\ &- p^{+}_{y+1/2,\sigma} p_{x+1/2,\sigma} + p^{+}_{x+1/2,\sigma} p_{y-1/2,\sigma}) + \text{h.c.} \end{aligned} \tag{2}$$

In the initial reducible representation the choice of phases can be made in any other manner, since the subsequent Fourier- and linear transformations are similar to using the method of projection operators in molecular-orbital theory to construct the functions belonging

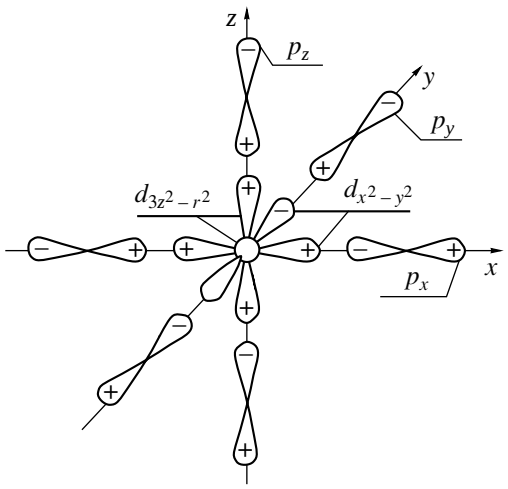

Fig. 1. Unit cell of a CuO_2 layer. The choice of phases corresponds to an initial reducible representation.

to irreducible representations and contained in the initial representation. We shall define the Fourier-transform as follows:

$$\begin{aligned} d_{\lambda \mathbf{k}\sigma} &= \frac{1}{\sqrt{N}} \sum_{\mathbf{f}} d_{\lambda \mathbf{f}\sigma} e^{-i\mathbf{k}\cdot\mathbf{f}}, \\ p_{\alpha \mathbf{k}\sigma} &= \frac{1}{\sqrt{N}} \sum_{\mathbf{m}} p_{\alpha \mathbf{m}\sigma} e^{-i\mathbf{k}\cdot\mathbf{m}}. \end{aligned} \tag{3}$$

Summing over all cells and performing the indicated Fourier transform, we arrive at

$$\begin{aligned} H_{pd} &= t_{pd} \sum_{\mathbf{k}\sigma} d^{+}_{x\mathbf{k}\sigma}(-2i)(s_x p_{x\mathbf{k}\sigma} + s_y p_{y\mathbf{k}\sigma}) \\ &+ \frac{t_{pd}}{\sqrt{3}} \sum_{\mathbf{k}\sigma} d^{+}_{z\mathbf{k}\sigma} 2i(s_x p_{x\mathbf{k}\sigma} - s_y p_{y\mathbf{k}\sigma}) + \text{h.c.}, \\ H_{pp} &= -4t_{pp} \sum_{\mathbf{k}\sigma} s_x s_y p^{+}_{x\mathbf{k}\sigma} p_{y\mathbf{k}\sigma} + \text{h.c.}, \\ s_x &= \sin\frac{k_x}{2}, \quad s_y = \sin\frac{k_y}{2}. \end{aligned} \tag{4}$$

Using the linear transformation $\hat{S}$, we introduce the new operators $a_{\mathbf{k}\sigma}$ and $b_{\mathbf{k}\sigma}$ annihilating a *p* hole in the molecular orbitals of oxygen:

$$\begin{aligned} \begin{pmatrix} b_{\mathbf{k}\sigma} \\ a_{\mathbf{k}\sigma} \end{pmatrix} &= \hat{S} \begin{pmatrix} p_{x\mathbf{k}\sigma} \\ p_{y\mathbf{k}\sigma} \end{pmatrix} \\ &= \begin{pmatrix} is_x/\mu_{\mathbf{k}} & is_y/\mu_{\mathbf{k}} \\ is_y/\mu_{\mathbf{k}} & -is_x/\mu_{\mathbf{k}} \end{pmatrix} \begin{pmatrix} p_{x\mathbf{k}\sigma} \\ p_{y\mathbf{k}\sigma} \end{pmatrix}, \end{aligned} \tag{5}$$

where

$$\mu_{\mathbf{k}}^2 = s_x^2 + s_y^2, \quad |\hat{S}| = 1.$$

The new operators satisfy the required commutation relations $\{b_{\mathbf{k}\sigma}^+, a_{\mathbf{p}\sigma}\} = 0$. Making the substitution

$$p_{x\mathbf{k}\sigma} = -\frac{\mathbf{i}}{\mu_{\mathbf{k}}}(s_x b_{\mathbf{k}\sigma} + s_y a_{\mathbf{k}\sigma}),$$

$$p_{y\mathbf{k}\sigma} = -\frac{\mathbf{i}}{\mu_{\mathbf{k}}}(s_y b_{\mathbf{k}\sigma} - s_x a_{\mathbf{k}\sigma}),$$

we find that H_{pd} and H_{pp} can be written as follows:

$$\begin{aligned} H_{pd} &= -2t_{pd}\sum_{\mathbf{k}\sigma}\mu_{\mathbf{k}} d_{x\mathbf{k}\sigma}^+ b_{\mathbf{k}\sigma} \\ &+ \frac{2t_{pd}}{\sqrt{3}}\sum_{\mathbf{k}\sigma}(\xi_{\mathbf{k}} d_{z\mathbf{k}\sigma}^+ b_{\mathbf{k}\sigma} + \lambda_{\mathbf{k}} d_{z\mathbf{k}\sigma}^+ a_{\mathbf{k}\sigma}) + \text{h.c.} \\ &= -2t_{pd}\sum_{\mathbf{ij}}\mu_{\mathbf{ij}} d_{x\mathbf{i}\sigma}^+ b_{\mathbf{j}\sigma} \\ &+ \frac{2t_{pd}}{\sqrt{3}}\sum_{\mathbf{ij}}(\xi_{\mathbf{ij}} d_{z\mathbf{i}\sigma}^+ b_{\mathbf{j}\sigma} + \lambda_{\mathbf{ij}} d_{z\mathbf{i}\sigma}^+ a_{\mathbf{j}\sigma}) + \text{h.c.}, \\ H_{pp} &= -2t_{pp}\sum_{\mathbf{k}\sigma}\nu_{\mathbf{k}} b_{\mathbf{k}\sigma}^+ b_{\mathbf{k}\sigma} + 2t_{pp}\sum_{\mathbf{k}\sigma}\nu_{\mathbf{k}} a_{\mathbf{k}\sigma}^+ a_{\mathbf{k}\sigma} \\ &- 2t_{pp}\sum_{\mathbf{k}\sigma}\chi_{\mathbf{k}}(b_{\mathbf{k}\sigma}^+ a_{\mathbf{k}\sigma} + \text{h.c.}) \\ &= -2t_{pp}\sum_{\mathbf{ij}\sigma}\nu_{\mathbf{ij}} b_{\mathbf{i}\sigma}^+ b_{\mathbf{j}\sigma} + 2t_{pp}\sum_{\mathbf{ij}\sigma}\nu_{\mathbf{ij}} a_{\mathbf{i}\sigma}^+ a_{\mathbf{j}\sigma} \\ &+ 2t_{pp}\sum_{\mathbf{ij}\sigma}\chi_{\mathbf{ij}}(a_{\mathbf{i}\sigma}^+ b_{\mathbf{j}c} + \text{h.c.}), \end{aligned} \tag{6}$$

where

$$\lambda_{\mathbf{k}} = \frac{2s_x s_y}{\mu_{\mathbf{k}}}, \quad \xi_{\mathbf{k}} = \frac{s_x^2 - s_y^2}{\mu_{\mathbf{k}}},$$

$$\nu_{\mathbf{k}} = \frac{4s_x^2 s_y^2}{\mu_{\mathbf{k}}^2}, \quad \chi_{\mathbf{k}} = \frac{2s_x s_y}{\mu_{\mathbf{k}}^2}(s_x^2 - s_y^2).$$

Inside a cell $\xi_{\mathbf{i}=\mathbf{j}} = 0$ and $\chi_{\mathbf{i}=\mathbf{j}} = 0$ in agreement with the fact that the $b_{\mathbf{k}\sigma}^+|0\rangle$ and $a_{\mathbf{k}\sigma}^+|0\rangle$ states belong to different b_1 and a_1 irreducible representations. Similar transformations for contributions from apical oxygen to the part of the Hamiltonian that takes account of hops,

$$\begin{aligned} H_{pp}^c &= t'_{pp}\{p_{z+1/2,\sigma}^+(p_{x-1/2,\sigma} - p_{x+1/2,\sigma} - p_{y-1/2,\sigma} \\ &+ p_{y+1/2,\sigma}) - p_{z-1/2,\sigma}^+(p_{x-1/2,\sigma} - p_{x+1/2,\sigma} \\ &- p_{y-1/2,\sigma} + p_{y+1/2,\sigma})\} + \text{h.c.}, \\ H_{pd}^{\prime c} &= -\frac{2t'_{pd}}{\sqrt{3}}(p_{z+1/2,\sigma}^+ d_{z\sigma} - p_{z-1/2,\sigma\Sigma}^+ d_{z\sigma} + \text{h.c.}), \end{aligned} \tag{7}$$

lead to the following result:

$$\begin{aligned} H'_{pp} &= -2t'_{pp}\sum_{\mathbf{k}\sigma}(\xi_{\mathbf{k}\sigma} p_{z\mathbf{k}\sigma}^+ b_{\mathbf{k}\sigma} + \lambda_{\mathbf{k}} p_{z\mathbf{k}\sigma}^+ a_{\mathbf{k}\sigma} + \text{h.c.}) \\ &= -2t'_{pp}\sum_{\mathbf{ij}\sigma}(\xi_{\mathbf{ij}\sigma} p_{z\mathbf{i}\sigma}^+ b_{\mathbf{j}\sigma} + \lambda_{\mathbf{ij}} p_{z\mathbf{i}\sigma}^+ a_{\mathbf{j}\sigma} + \text{h.c.}), \\ H'_{pd} &= -\frac{2t'_{pd}}{\sqrt{3}}\sum_{\mathbf{k}\sigma}(d_{z\mathbf{k}\sigma}^+ p_{z\mathbf{k}\sigma} + \text{h.c.}) \\ &= -\frac{2t'_{pd}}{\sqrt{3}}\sum_{\mathbf{ij}\sigma}(d_{z\mathbf{i}\sigma}^+ p_{z\mathbf{i}\sigma} + \text{h.c.}). \end{aligned} \tag{8}$$

As one can see from Eqs. (6) and (8), the dependences of the coefficients $\mu_{\mathbf{ij}}$, $\nu_{\mathbf{ij}}$, $\xi_{\mathbf{ij}}$, $\lambda_{\mathbf{ij}}$, and $\chi_{\mathbf{ij}}$ on the intersite distance $\Delta\mathbf{R}_{ij}$ completely determine in our approach the rules for and the magnitude of the hybridization of the oxygen molecular *a* and *b* orbitals with one another as well as with $d_{x^2-y^2}$ and d_{z^2} orbitals on different cells *i* and *j*. The functions are summarized in Table 1 [23]. In application to the Coulomb term, this procedure leads to three- and four-center contributions to the aggregate Hamiltonian:

$$\begin{aligned} H_{pd}^{\text{int}} &= \sum_{\mathbf{lij}}\sum_{\alpha\lambda\sigma\sigma'} V_{pd}\Phi_{\mathbf{lij}} n_{\lambda l}^{\sigma} p_{\alpha\mathbf{i}\sigma'}^+ p_{\alpha\mathbf{j}\sigma'}, \\ H_{pp}^{\text{int}} &= \sum_{\mathbf{ijkl}}\sum_{\alpha} U_p \Psi_{\mathbf{ijkl}} p_{\alpha\mathbf{i}\uparrow}^+ p_{\alpha\mathbf{j}\uparrow} p_{\alpha\mathbf{k}\downarrow}^+ p_{\alpha\mathbf{l}\downarrow}, \end{aligned} \tag{9}$$

where $p_{\alpha\mathbf{f}\sigma} = a_{\mathbf{f}\sigma}, b_{\mathbf{f}\sigma}$. Thus, aside from the standard single-center Coulomb interaction, we obtain additional contributions, for example, to the part of the aggregate Hamiltonian that takes account of hops $\sim V_{pd}\Phi_{\mathbf{ij}} n_{\lambda\mathbf{i}}^{\sigma} p_{\alpha\mathbf{i}\sigma'}^+ p_{\alpha\mathbf{j}\sigma'}$. Direct calculations of the coefficients $\Phi_{\mathbf{lij}}$ and $\Psi_{\mathbf{klij}}$ show that $\Phi_{000} = 0.918$, $\Phi_{001} = -0.13$, $\Phi_{002} = -0.02$, $\Psi_{0000} = 0.2109$, and $\Psi_{0001} = -0.03$. Since the computed coefficients depend strongly on the distance, we retain in what follows the strongest single-center interactions:

$$\begin{aligned} H_{pd}^{\text{int}} &= V_{pd}\Phi_{000}\sum_{\mathbf{i}\alpha\lambda\sigma\sigma'} n_{\lambda\mathbf{i}}^{\sigma} n_{\alpha\mathbf{i}}^{\sigma'}, \\ H_{pd}^{\text{int}} &= U_p \Psi_{0000}\sum_{\alpha\mathbf{i}} n_{\alpha\mathbf{i}}^{\uparrow} n_{\alpha\mathbf{i}}^{\downarrow}. \end{aligned} \tag{10}$$

Table 1. Dependence of the matrix elements on the distance (*ij*) [23]

	00	10	11	20	21	22
μ	0.95809	−0.14009	−0.02351	−0.01373	−0.00685	−0.00327
ν	0.72676	−0.27324	0.12207	−0.06385	0.01737	0.01052
λ	0.74587	−0.17578	0.06179	−0.07134	0.01703	0.00925
ξ	0.00000	0.25763	0.00000	0.03913	0.00886	0.00000
χ	0.00000	0.13397	0.00000	−0.04056	0.03043	0.00000

Thus, after this step our Hamiltonian becomes a sum of intracell and intercell terms:

$$H = H_c + H_{cc}, \quad H_c = \sum_{\mathbf{f}\sigma} H_{\mathbf{f}\sigma}, \tag{11}$$

$$H_{\mathbf{f}\sigma} = h^{(a)} + h^{(b)} + h^{(ab)},$$

$$h^{(a)} = (\varepsilon_a n_a^\sigma + \varepsilon_{d_z} n_{d_z}^\sigma + \varepsilon_{p_z} n_{p_z}^\sigma) + \frac{1}{2} U_d n_{d_z}^\sigma n_{d_z}^{-\sigma} + \frac{1}{2} U_a n_a^\sigma n_a^{-\sigma} + \frac{1}{2} U'_p n_{p_z}^\sigma n_{p_z}^{-\sigma} + \sum_{\sigma'} (V'_{pd} n_{d_z}^\sigma n_{p_z}^{\sigma'} + V_{pd} n_{d_z}^\sigma n_a^{\sigma'}) + \tau_a (d_{z\sigma}^+ a_\sigma + \text{h.c.}) - \tau'_{pd} (d_{z\sigma}^+ p_{z\sigma} + \text{h.c.}) - t'_{pp} (a_\sigma^+ p_{z\sigma} + \text{h.c.}),$$

$$h^{(b)} = (\varepsilon_b n_b^\sigma + \varepsilon_{d_x} n_{d_x}^\sigma) + \frac{1}{2} U_d n_{d_x}^\sigma n_{d_x}^{-\sigma} + \frac{1}{2} U_b n_b^\sigma n_b^{-\sigma} + \sum_{\sigma'} V_{pd} n_{d_x}^\sigma n_b^{\sigma'} - \tau_b \sum_\sigma (d_{x\sigma}^+ b_\sigma + \text{h.c.}),$$

$$h^{(ab)} = \sum_{\sigma'} U_d n_{d_x}^\sigma n_{d_x}^{\sigma'} + U_{ab} n_a^\sigma n_b^{\sigma'} + V_{pd} n_{d_x}^\sigma n_a^{\sigma'} + V_{pd} n_b^\sigma n_{d_x}^{\sigma'} + V'_{pd} n_{d_x}^\sigma n_{p_x}^{\sigma'},$$

$$H_{cc} = \sum_{(\mathbf{i} \neq \mathbf{j})} \sum_\sigma (h_{\text{hop}}^{(a)} + h_{\text{hop}}^{(b)} + h_{\text{hop}}^{(ab)}),$$

$$h_{\text{hop}}^{(a)} = \frac{2t_{pd}}{\sqrt{3}} \lambda_{\mathbf{ij}} (d_{\mathbf{i}z\sigma}^+ a_{\mathbf{j}\sigma} + \text{h.c.}) + 2t_{pp} \nu_{\mathbf{ij}} a_{\mathbf{i}\sigma}^+ a_{\mathbf{j}\sigma} - 2t'_{pp} \lambda_{\mathbf{ij}} (p_{\mathbf{i}z\sigma}^+ a_{\mathbf{j}\sigma} + \text{h.c.}),$$

$$h_{\text{hop}}^{(b)} = -2t_{pd} \mu_{\mathbf{ij}} (d_{\mathbf{i}x\sigma}^+ b_{\mathbf{j}\sigma} + b_{\mathbf{i}\sigma}^+ d_{\mathbf{i}x\sigma}) - 2t_{pp} \nu_{\mathbf{ij}} b_{\mathbf{i}\sigma}^+ b_{\mathbf{j}\sigma},$$

$$h_{\text{hop}}^{(ab)} = \frac{2t_{pd}}{\sqrt{3}} \xi_{\mathbf{ij}} (d_{\mathbf{i}z\sigma}^+ b_{\mathbf{j}\sigma} + \text{h.c.}) + 2t_{pp} \chi_{\mathbf{ij}} (a_{\mathbf{i}\sigma}^+ b_{\mathbf{j}\sigma} + \text{h.c.}) - 2t'_{pp} \xi_{\mathbf{ij}} (p_{\mathbf{i}z\sigma}^+ b_{\mathbf{j}\sigma} + \text{h.c.}),$$

where

$$\varepsilon_b = \varepsilon_p - 2t_{pp}\nu_{00}, \quad \varepsilon_a = \varepsilon_p + 2t_{pp}\nu_{00},$$

$$\tau_b = 2t_{pd}\mu_{00}, \quad \tau_a = \frac{2t_{pd}\lambda_{00}}{\sqrt{3}},$$

$$\tau'_{pd} = \frac{2t'_{pd}}{\sqrt{3}}, \quad \tau'_{pp} = 2t'_{pp}\lambda_{00}.$$

In what follows, as a simplification, we shall drop the coefficients Ψ_{000} and Φ_{000} when we write the Coulomb interaction parameters: $U_a = U_{ab} = U'_p = U_b = U_p\Psi_{000}$, $V_{pd} = V_{pd}\Psi_{000}$. Besides these parameters, which refer to the Coulomb interaction in a plane, there are also parameters characterizing the analogous interaction with the apical oxygen V'_{pd}. The coefficients μ_{ij}, ν_{ij}, and λ_{ij} refer to hybridization of states possessing the same symmetry and depend only on the distance between the i and j sites. The coefficients ξ_{ij} and χ_{ij} refer to the hybridization of the states belonging to different a_1 and b_1 representations, and they change sign on reflection along one of the x or y axes. The Hamiltonian (11) does not contain hops $d_z \longleftrightarrow d_z$, $p_z \longleftrightarrow p_z$, and $d_z \longleftrightarrow p_z$. The holes in these states are less "mobile" than in the planar d_x, b, and a states.

As the next step, we shall determine the eigenvalues and eigenstates of the single-cell Hamiltonian H_c that can be found exactly and we shall then rewrite the total Hamiltonian H in terms of these eigenstates. In the vacuum sector we have the proper state $d^{10}p^6$ or $|0\rangle$. In the single-hole b_1 sector in the basis of $|d_{x\sigma}^+|0\rangle$ and $|b_\sigma^+|0\rangle$ states the eigenvectors $|\tilde{b}_p\rangle = \beta_p(b)|b_\sigma^+|0\rangle + \beta_p(d_x)|d_{x\sigma}^+|0\rangle$ with energies $\varepsilon_{1\tilde{b}_p}$, $p = 1, 2$, can be found by exact diagonalization

$$\hat{h}^{(b)} = \begin{pmatrix} \varepsilon_{d_x} & -\tau_b \\ -\tau_b & \varepsilon_b \end{pmatrix}. \tag{12}$$

In the single-hole a_1 sector in the basis $|a_\sigma^+|0\rangle$, $|p_{z\sigma}^+|0\rangle$, and $|d_{z\sigma}^+|0\rangle$ states, the eigenvectors $|\tilde{a}_p\rangle = \alpha_p(a)|a_\sigma^+|0\rangle + \alpha_p(p_z)|p_\sigma^+|0\rangle + \alpha_p(d_z)|d_{z\sigma}^+|0\rangle$ with energies $\varepsilon_{1\tilde{a}_p}$, $p = 1, 2, 3$ can be found by exact diagonalization

$$\hat{h}^{(a)} = \begin{pmatrix} \varepsilon_{d_z} & \tau_a & -\tau'_{pd} \\ \tau_a & \varepsilon_a & -t'_{pp} \\ -\tau'_{pd} & -t'_{pp} & \varepsilon_{p_z} \end{pmatrix}. \tag{13}$$

The eigenstates of a cell in the two-hole A_1 sector $|\tilde{A}_q\rangle = \sum_i A_{qi}|A_i\rangle$, where the coefficients are the eigenvectors A_{qi} (i, q = 1–9), and the set of basis singlet functions $|A_i\rangle$ are presented in Table 2. The $|\tilde{A}_q\rangle$ eigenstates with energy $\varepsilon_{2\tilde{A}_q}$ can be found by exact diagonalization of the matrix

$$\hat{h}^{(A)} = \begin{pmatrix} \hat{h}_{11}^{(A)} & 0 \\ 0 & \hat{h}_{22}^{(A)} \end{pmatrix}, \tag{14}$$

$$\text{where } \hat{h}_{11}^{(A)} = \begin{pmatrix} \varepsilon_b + \varepsilon_{d_x} + V_{pd} & -\sqrt{2}\tau_b & \sqrt{2}\tau_b \\ -\sqrt{2}\tau_b & 2\varepsilon_b + U_b & 0 \\ -\sqrt{2}\tau_b & 0 & 2\varepsilon_{d_x} + U_d \end{pmatrix},$$

$$\hat{h}_{22}^{(A)} = \begin{pmatrix} \varepsilon_a + \varepsilon_{p_z} + V'_p & -\tau'_{pd} & \tau_a & -\sqrt{2}t'_{pp} & -\sqrt{2}t'_{pp} & 0 \\ -\tau'_{pd} & \varepsilon_{d_z} + \varepsilon_a + V_{pd} & -t'_{pp} & \sqrt{2}\tau_a & 0 & \sqrt{2}\tau_a \\ \tau_a & -t'_{pp} & \varepsilon_{d_z} + \varepsilon_{p_z} + V'_{pd} & 0 & -\sqrt{2}\tau'_{pd} & -\sqrt{2}\tau'_{pd} \\ -\sqrt{2}t'_{pp} & \sqrt{2}\tau_a & 0 & 2\varepsilon_a + U_a & 0 & 0 \\ -\sqrt{2}t'_{pp} & 0 & -\sqrt{2}\tau'_{pd} & 0 & 2\varepsilon_{p_z} + U'_p & 0 \\ 0 & \sqrt{2}\tau_a & -\sqrt{2}\tau'_{pd} & 0 & 0 & 2\varepsilon_{d_z} + U_d \end{pmatrix}. \tag{15}$$

In addition, the Zhang–Rice singlet $|ZR\rangle$ appears in it as one of the basis states. In the two-hole sector B_1 we seek the triplet eigenvectors in the form $|\tilde{B}_{qM}\rangle = \sum_i B_{qi}|B_{iM}\rangle$ (q = 1–6, M = –1, 0, 1), where the corresponding coefficients B_{qi} and the set of basis functions $|B_{qM}\rangle$ are presented in Table 3 with energies $\varepsilon_{2\tilde{B}_q}$ found by diagonalizing the matrix

$$\hat{h}^{(\tilde{B})} = \begin{pmatrix} \varepsilon_a + \varepsilon_{d_x} + V_{pd} & -\tau_b & \tau_a & 0 & -t'_{pp} & 0 \\ -\tau_b & \varepsilon_a + \varepsilon_b + V_b & 0 & \tau_a & 0 & -t'_{pp} \\ \tau_a & 0 & \varepsilon_{d_z} + \varepsilon_{d_x} + V_d & -\tau_b & -\tau'_{pd} & 0 \\ 0 & \tau_a & -\tau_b & \varepsilon_{d_z} + \varepsilon_b + V_{pd} & 0 & -\tau'_{pd} \\ -t'_{pp} & 0 & -\tau'_{pd} & 0 & \varepsilon_{d_x} + \varepsilon_{p_z} + V'_{pd} & -\tau_b \\ 0 & -t'_{pp} & 0 & -\tau'_{pd} & -\tau_b & \varepsilon_b + \varepsilon_{p_z} + V'_{pp} \end{pmatrix}. \tag{16}$$

Diagonalization of the Hamiltonian for a CuO_6 cluster is done separately in different sectors with n = 0, 1, and 2 holes. The vacuum section n = 0 corresponds to the $3d^{10}$ configuration of copper and the $2p^6$ configuration of oxygen. Figure 2 shows the energies of the competing singlet $|\tilde{A}_p\rangle$ (p = 1, 2) and triplet $|\tilde{B}_{1M}\rangle$ states as a function of the crystal field parameter $\Delta_d = \varepsilon_{d_z} - \varepsilon_{d_x}$, the difference in the energies of the $2p$ orbitals of the planar and apical oxygen $\Delta_{ap} = \varepsilon_p - \varepsilon_{p_z}$, and the ratio d_{ap}/d_{pl} of the distances from the copper atom to the apical and the planar oxygen atoms. The energy of the state $|\tilde{A}_1\rangle = A_1(d_x b)|ZR\rangle + A_3(d_x d_x)|A_3\rangle + A_2(bb)|A_2\rangle$ does not depend on the values of the parameters presented above. The contributions from the cell orbitals in

Table 2. Eigenvectors A_{qi} and the set of basis singlet functions $|A_i\rangle$

i	A_{qi}	$\lvert A_i\rangle$
1	$A_q(d_xb)$	$\lvert ZR\rangle = \frac{1}{\sqrt{2}}\lvert d^+_{x\downarrow}b^+_\uparrow - d^+_{x\uparrow}b^+_\downarrow\rvert 0\rangle$
2	$A_q(bb)$	$\lvert b^+_\downarrow b^+_\uparrow\rvert 0\rangle$
3	$A_q(d_xd_x)$	$\lvert d^+_{x\downarrow}d^+_{x\uparrow}\rvert 0\rangle$
4	$A_q(p_za)$	$\frac{1}{\sqrt{2}}\lvert p^+_{z\downarrow}a^+_\uparrow - p^+_{z\uparrow}a^+_\downarrow\rvert 0\rangle$
5	$A_q(d_za)$	$\frac{1}{\sqrt{2}}\lvert d^+_{z\downarrow}a^+_\uparrow - d^+_{z\uparrow}a^+_\downarrow\rvert 0\rangle$
6	$A_q(d_zp_z)$	$\frac{1}{\sqrt{2}}\lvert d^+_{z\downarrow}p^+_{z\uparrow} - d^+_{z\uparrow}p^+_{z\downarrow}\rvert 0\rangle$
7	$A_q(aa)$	$\lvert a^+_\downarrow a^+_\uparrow\rvert 0\rangle$
8	$A_q(p_zp_z)$	$\lvert p^+_{z\downarrow}p^+_{z\uparrow}\rvert 0\rangle$
9	$A_q(d_zd_z)$	$\lvert d^+_{z\downarrow}d^+_{z\uparrow}\rvert 0\rangle$

the other two states $|\tilde{A}_2\rangle$ and $|\tilde{B}_{1M}\rangle$ change strongly together with the values of the parameters, and they cannot be identified with any specific orbitals from the molecular orbitals with the same symmetry.

As the energy of the 2*p* orbital of apical oxygen decreases, the state $|\tilde{B}_{1M}\rangle$ is observed to approach the singlet $|\tilde{A}_1\rangle$ (Fig. 2b). Together with the tendency for crossover, there is also an appreciable increase in the fraction of the d_xp_z-symmetrized configuration in $|\tilde{B}_{1M}\rangle$. It is important to note that this is only the first main mechanism of stabilization of the $|\tilde{B}_{1M}\rangle$ state, and it is related with the large contribution from the d_xp_z-symmetrized configuration. The increase of this contribution is confirmed by this dependence as well as the dependence shown in Fig. 2a. Therefore, the same stabilization mechanism operates in both cases. However, in the first case its nature is associated with the decrease in the energy of the p_z orbital, whereas in the second case it is associated with the dependence of the corresponding hopping integral on the distance to the apical oxygen. A decrease in the energies of the p_z orbitals gives rise more effectively to an increase in the d_xp_z contribution in the ground two-hole state.

A decrease of the parameter $\Delta_d = \varepsilon_{d_z} - \varepsilon_{d_z}$ (Fig. 3c) results in an increase in the Hund state fraction and ultimately convergence of the ground $|\tilde{A}_1\rangle$ singlet and the $|\tilde{B}_{1M}\rangle$ states. This is the second basic mechanism for stabilization of the $|\tilde{B}_{1M}\rangle$ state. Since it is associated with a gain in the Hund interaction with an increasing contribution of the d_xd_z configuration, it is all the more effective the higher the energy of the 2*p* orbital of the planar oxygen and the lower the energy of the d_z orbital. For this method of stabilization of the $|\tilde{B}_{1M}\rangle$ state, the fraction of p_z states decreases in this state, and the fraction of the Hund configuration d_xd_z, through which the population of the d_z orbitals could be observed, increases.

Table 3. Eigenvectors B_{qi} and the set of basis functions $|B_{iM}\rangle$

i	B_{qi}	$\lvert B_{i-1}\rangle$	$\lvert B_{i0}\rangle$	$\lvert B_{i1}\rangle$
1	$B_q(d_xa)$	$\lvert d^+_{x\downarrow}a^+_\downarrow\rvert 0\rangle$	$\frac{1}{\sqrt{2}}\lvert d^+_{x\downarrow}a^+_\uparrow + d^+_{x\uparrow}a^+_\downarrow\rvert 0\rangle$	$\lvert d^+_{x\uparrow}a^+_\uparrow\rvert 0\rangle$
2	$B_q(ba)$	$\lvert b^+_\downarrow a^+_\downarrow\rvert 0\rangle$	$\frac{1}{\sqrt{2}}\lvert b^+_\downarrow a^+_\uparrow + b^+_\uparrow a^+_\downarrow\rvert 0\rangle$	$\lvert b^+_\uparrow a^+_\uparrow\rvert 0\rangle$
3	$B_q(d_xd_z)$	$\lvert d^+_{x\downarrow}d^+_{z\downarrow}\rvert 0\rangle$	$\frac{1}{\sqrt{2}}\lvert d^+_{x\downarrow}d^+_{z\uparrow} + d^+_{x\downarrow}d^+_{z\uparrow}\rvert 0\rangle$	$\lvert d^+_{x\uparrow}d^+_{z\uparrow}\rvert 0\rangle$
4	$B_q(d_xb)$	$\lvert d^+_{x\downarrow}b^+_\downarrow\rvert 0\rangle$	$\frac{1}{\sqrt{2}}\lvert d^+_{x\downarrow}b^+_\uparrow + d^+_{x\uparrow}b^+_\downarrow\rvert 0\rangle$	$\lvert d^+_{z\uparrow}b^+_\uparrow\rvert 0\rangle$
5	$B_q(d_xp_z)$	$\lvert d^+_{x\downarrow}p^+_{z\downarrow}\rvert 0\rangle$	$\frac{1}{\sqrt{2}}\lvert d^+_{x\downarrow}p^+_{z\uparrow} + d^+_{x\downarrow}p^+_{z\uparrow}\rvert 0\rangle$	$\lvert d^+_{x\uparrow}p^+_{z\uparrow}\rvert 0\rangle$
6	$B_q(bp_z)$	$\lvert b^+_\downarrow p^+_{z\downarrow}\rvert 0\rangle$	$\frac{1}{\sqrt{2}}\lvert b^+_\downarrow p^+_{z\uparrow} + b^+_\uparrow p^+_{z\downarrow}\rvert 0\rangle$	$\lvert b^+_\uparrow p^+_{z\uparrow}\rvert 0\rangle$

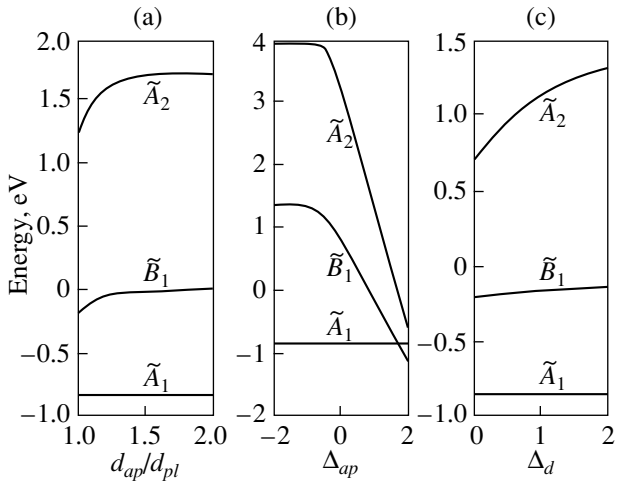

Fig. 2. Energies of $|\tilde{A}_1\rangle$, $|\tilde{A}_2\rangle$, and $|\tilde{B}_{1M}\rangle$ two-hole states versus the ratio d_{ap}/d_{pl} of the distances from the copper atom to the apical oxygen to the analogous distance to the planar oxygen, where $\Delta_d = 2$ eV and $\Delta_{ap} = 0.5$ eV (a) and versus the energy difference between the $2p$ orbitals of the planar and apical oxygen: $\Delta_{ap} = \varepsilon_p - \varepsilon_{p_z}$, where $d_{ap}/d_{pl} = 1.2$, $\Delta_d = 2$ eV (b), and versus the crystal field parameter $\Delta_d = \varepsilon_{d_z} - \varepsilon_{d_x}$, where $d_{ap}/d_{pl} = 1.2$, $\Delta_d = 0.5$ eV (c).

Thus, the energy splitting between the triplet and singlet states is $\Delta\varepsilon_2 \approx 0.5$ eV (Fig. 3a). Consequently, the presence of two states $|\tilde{A}_1\rangle$ and $|\tilde{B}_{1M}\rangle$, competing in energy, for realistic values of the parameters makes it necessary to take them into account simultaneously as basis states in our model and makes it impossible further reduction to an effective one-band Hubbard model. As a result of exact diagonalization, the Hamiltonian H_c for the antiferromagnetic phase becomes

$$H_c = \sum_{p\mathbf{f}_G\sigma} (\varepsilon_{1pG} - \mu) X^{pp}_{\mathbf{f}_G\sigma} + \sum_{q\mathbf{f}_G\sigma} (\varepsilon_{2qG} - 2\mu) X^{qq}_{\mathbf{f}_G\sigma}, \quad \text{where } f_G = \begin{cases} \mathbf{f}_A, & \mathbf{f} \in A \\ \mathbf{f}_B, & \mathbf{f} \in B. \end{cases} \tag{17}$$

Here p and q *e*numerate the single- and two-hole terms of a cell; $X^{pq}_{\mathbf{f}} = |p\rangle\langle q|$ are Hubbard operators constructed on the exact states of a cell. The sublattice levels are split by the field of the antiferromagnetic state: $\varepsilon_{1pA} = \varepsilon_{1p} - \sigma h$ and $\varepsilon_{1pB} = \varepsilon_{1p} + \sigma h$. The quantity $h \sim J\langle S_z\rangle$, where the effective exchange interaction of nearest neighbors $J \sim t'^2_{\text{eff}}/(\varepsilon_{20} - 2\varepsilon_{10})$ and t'_{eff} is determined below (see Eq. (29)); ε_{10} and ε_{20} are the energies of the bottom single- and two-particle terms. Doping decreases h, which vanishes in the paramagnetic phase. In the present work we confine our attention to a nonself-consistent calculation, in which the magnetic state is assumed to be given (antiferromagnetic or paramagnetic). On the other hand the role of the field h is to separate the sublattices, just as in Bogolyubov's method of quasiaverages. Effects due to the change in h taking account of doping give band shifts by an amount of the order of 10^{-3} eV, which is less than the resolution of modern photoelectronic methods; we shall neglect these effects. In the new basis the single-electron operators become

$$c_{\mathbf{f}\lambda\sigma} = \sum_m \gamma_{\lambda\sigma}(m) X^m_{\mathbf{f}\sigma}, \tag{18}$$

where $c_{\lambda\mathbf{f}\sigma} = d_{x\mathbf{f}\sigma}, d_{z\mathbf{f}\sigma}, a_{\mathbf{f}\sigma}, b_{\mathbf{f}\sigma}, p_{z\mathbf{f}\sigma}$ and m is the number of the root vector $\boldsymbol{\alpha}_m(pq)$. Here, to make it easier to work with Hubbard operators, we employ the notation of Zaitsev [30], where to each pair (initial–final) of states $|q\rangle \longrightarrow |p\rangle$ there is associated a root vector $\boldsymbol{\alpha}_m(pq)$, so that

$$X^{pq}_{\mathbf{f}\sigma} \longrightarrow X^{\boldsymbol{\alpha}_m(pq)}_{\mathbf{f}\sigma} \longrightarrow X^m_{\mathbf{f}\sigma}.$$

The matrix elements of the hopping amplitudes $\gamma_{\lambda\sigma}(m)$ ($m = 1, 2, \ldots, 32$), corresponding to these root vectors, can be calculated directly by performing an exact diagonalization of the Hamiltonian H_c and are presented in Tables 4–6. Only the two bottom terms (b_1 and a_1) are taken into account in the single-particle sector and $\tilde{A}_1$, $\tilde{B}_{1M}$ are taken into account in the two-particle sector. Therefore in Eq. (17) $|p\rangle = |\tilde{a}_1\rangle$, $|\tilde{b}_1\rangle$ and $|q\rangle = \tilde{A}_1$, $\tilde{B}_{1M}$. All other terms correspond to a higher energy and are of no significance for the physics of low-energy excitations.

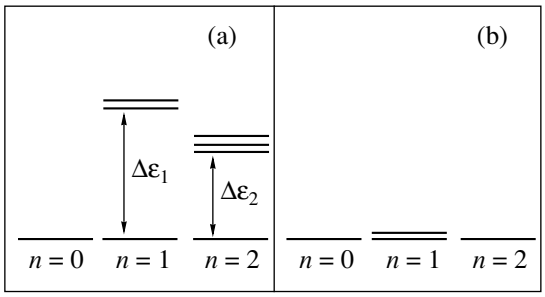

Fig. 3. Sets of basal states for realistic multiband *pd* model (a) and for a single-band Hubbard model (b).

Table 4. Matrix elements for quasiparticle excitations $\alpha_m(\tilde{b}_{1\sigma'}\tilde{A}_1)$. Here c_i denotes d_x or b

$\mathbf{f}_G$	$\mathbf{f}_A$		$\mathbf{f}_B$	
σ'	$\uparrow$	$\downarrow$	$\uparrow$	$\downarrow$
m	1	9	17	25
$\gamma_{d_x\sigma}$	$\eta(\sigma)(\delta_{\sigma\sigma'} - 1)\sum_i \beta_1(c_i) A_1(d_x c_i)$			
$\gamma_{b\sigma}$	$\eta(\sigma)(\delta_{\sigma\sigma'} - 1)\sum_i \beta_1(c_i) A_1(b c_i)$			

Let $\mathbf{R}_1$ in the two-sublattice case refer to the intrasublattice neighbors and $\mathbf{R}_2$ to the intersublattice neighbors. Then the Hamiltonian of intercell hops can be written in the matrix form

$$H_{cc} = \begin{pmatrix} H_{AA} & H_{AB} \\ H_{BA} & H_{BB} \end{pmatrix} = \sum_{\lambda\lambda'\sigma} \begin{pmatrix} \sum_{\mathbf{fR}_1} T_{\lambda\lambda'}(\mathbf{R}_1)(c^+_{\mathbf{f}\lambda\sigma} c_{\mathbf{f}+\mathbf{R}_1\lambda'\sigma} + \text{h.c.}) & \sum_{\mathbf{fR}_2} T_{\lambda\lambda'}(\mathbf{R}_2)(c^+_{\mathbf{f}\lambda\sigma} c_{\mathbf{f}+\mathbf{R}_2\lambda'\sigma} + \text{h.c.}) \\ \sum_{\mathbf{gR}_2} T_{\lambda\lambda'}(\mathbf{R}_2)(c^+_{\mathbf{g}\lambda\sigma} c_{\mathbf{g}+\mathbf{R}_2\lambda'\sigma} + \text{h.c.}) & \sum_{\mathbf{gR}_1} T_{\lambda\lambda'}(\mathbf{R}_1)(c^+_{\mathbf{g}\lambda\sigma} c_{\mathbf{g}+\mathbf{R}_1\lambda'\sigma} + \text{h.c.}) \end{pmatrix}$$

$$= \sum_{\lambda\lambda'\sigma kmn} \gamma^*_{\lambda\sigma}(m)\gamma_{\lambda'\sigma}(n) \begin{pmatrix} T^{AA}_{\lambda\lambda'}(\mathbf{k}) X^{+m}_{\mathbf{k}\sigma} X^n_{\mathbf{k}\sigma} & T^{AB}_{\lambda\lambda'}(\mathbf{k}) X^{+m}_{\mathbf{k}\sigma} Y^n_{\mathbf{k}\sigma} \\ T^{BA}_{\lambda\lambda'}(\mathbf{k}) X^{+m}_{\mathbf{k}\sigma} Y^n_{\mathbf{k}\sigma} & T^{BB}_{\lambda\lambda'}(\mathbf{k}) Y^{+m}_{\mathbf{k}\sigma} Y^n_{\mathbf{k}\sigma} \end{pmatrix} + \text{h.c.}, \tag{19}$$

where

$$T^{AA}_{\lambda\lambda'}(\mathbf{k}) = T^{BB}_{\lambda\lambda'}(\mathbf{k}) = \frac{2}{N}\sum_{\mathbf{R}_1} T^{AA}_{\lambda\lambda'}(\mathbf{R}_1) e^{i\mathbf{k}\cdot\mathbf{R}_1},$$

$$T^{AB}_{\lambda\lambda'}(\mathbf{k}) = T^{BA}_{\lambda\lambda'}(\mathbf{k}) = \frac{2}{N}\sum_{\mathbf{R}_2} T^{AB}_{\lambda\lambda'}(\mathbf{R}_2) e^{i\mathbf{k}\cdot\mathbf{R}_2},$$

$X^m_{\mathbf{k}\sigma}$ and $Y^n_{\mathbf{k}\sigma}$ are the Fourier transforms of the Hubbard operators, respectively, with respect to the A and B sublattices. In the basis d_x, d_z, b, a, and p_z the matrix for intercell hops has the form

$$T_{\lambda\lambda'}(\mathbf{R}) = \begin{pmatrix} 0 & 0 & -2t_{pd}\mu_{\mathbf{ij}} & 0 & 0 \\ 0 & 0 & \frac{2t_{pd}}{\sqrt{3}}\xi_{\mathbf{ij}} & \frac{2t_{pd}}{\sqrt{3}}\lambda_{\mathbf{ij}} & 0 \\ -2t_{pd}\mu_{\mathbf{ij}} & \frac{2t_{pd}}{\sqrt{3}}\xi_{\mathbf{ij}} & -2t_{pp}\nu_{\mathbf{ij}} & 2t_{pp}\chi_{\mathbf{ij}} & -2t'_{pp}\xi_{\mathbf{ij}} \\ 0 & \frac{2t_{pd}}{\sqrt{3}}\lambda_{\mathbf{ij}} & 2t_{pp}\chi_{\mathbf{ij}} & 2t_{pp}\nu_{\mathbf{ij}} & -2t'_{pp}\lambda_{\mathbf{ij}} \\ 0 & 0 & -2t'_{pp}\xi_{\mathbf{ij}} & -2t'_{pp}\lambda_{\mathbf{ij}} & 0 \end{pmatrix}. \tag{20}$$

Table 5. Matrix elements for quasiparticle excitations $\alpha_m(\tilde{a}_{1\sigma'}\tilde{B}_{1M})$. Here c_i denotes d_z, a, p_z

α_m	$\alpha_m(\tilde{a}_{1\sigma'}\tilde{B}_{1-1})$				$\alpha_m(\tilde{a}_{1\sigma'}\tilde{B}_{10})$				$\alpha_m(\tilde{a}_{1\sigma'}\tilde{B}_{11})$			
$\mathbf{f}_G$	$\mathbf{f}_A$		$\mathbf{f}_B$		$\mathbf{f}_A$		$\mathbf{f}_B$		$\mathbf{f}_A$		$\mathbf{f}_B$	
σ'	↑	↓	↑	↓	↑	↓	↑	↓	↑	↓	↑	↓
m	2	10	18	26	3	11	19	27	4	12	20	27
$\gamma_{d_x\sigma}$	$\delta_{\sigma\sigma'}\sum_i \alpha_1(c_i)B_1(d_x c_i)$				$\frac{1}{\sqrt{2}}(1-\delta_{\sigma\sigma'})\sum_i \alpha_1(c_i)B_1(d_x c_i)$				$\delta_{\sigma\sigma'}\sum_i \alpha_1(c_i)B_1(d_x c_i)$			
$\gamma_{b\sigma}$	$\delta_{\sigma\sigma'}\sum_i \alpha_1(c_i)B_1(b c_i)$				$\frac{1}{\sqrt{2}}(1-\delta_{\sigma\sigma'})\sum_i \alpha_1(c_i)B_1(b c_i)$				$\delta_{\sigma\sigma'}\sum_i \alpha_1(c_i)B_1(b c_i)$			

Table 6. Matrix elements for the quasiparticle excitations $\alpha_m(\tilde{b}_{1\sigma'}\tilde{B}_{1M})$. Here c_i denotes d_x or b

α_m	$\alpha_m(\tilde{b}_{1\sigma'}\tilde{B}_{1-1})$				$\alpha_m(\tilde{b}_{1\sigma'}\tilde{B}_{10})$				$\alpha_m(\tilde{b}_{1\sigma'}\tilde{B}_{11})$			
$\mathbf{f}_G$	$\mathbf{f}_A$		$\mathbf{f}_B$		$\mathbf{f}_A$		$\mathbf{f}_B$		$\mathbf{f}_A$		$\mathbf{f}_B$	
σ'	↑	↓	↑	↓	↑	↓	↑	↓	↑	↓	↑	↓
m	5	13	21	28	6	14	22	29	7	15	23	21
$\gamma_{a\sigma}$	$-\delta_{\sigma\sigma'}\sum_i \beta_1(c_i)B_1(a c_i)$				$-\frac{1}{\sqrt{2}}(1-\delta_{\sigma\sigma'})\sum_i \beta_1(c_i)B_1(a c_i)$				$-\delta_{\sigma\sigma'}\sum_i \beta_1(c_i)B_1(a c_i)$			
$\gamma_{d_z\sigma}$	$-\delta_{\sigma\sigma'}\sum_i \beta_1(c_i)B_1(p_z c_i)$				$-\frac{1}{\sqrt{2}}(1-\delta_{\sigma\sigma'})\sum_i \beta_1(c_i)B_1(p_z c_i)$				$-\delta_{\sigma\sigma'}\sum_i \beta_1(c_i)B_1(p_z c_i)$			
$\gamma_{p_z\sigma}$	$-\delta_{\sigma\sigma'}\sum_i \beta_1(c_i)B_1(d_z c_i)$				$-\frac{1}{\sqrt{2}}(1-\delta_{\sigma\sigma'})\sum_i \beta_1(c_i)B_1(d_z c_i)$				$-\delta_{\sigma\sigma'}\sum_i \beta_1(c_i)B_1(d_z c_i)$			

3. DERIVATION OF THE DISPERSION RELATIONS

Next, we shall derive the corresponding dispersion relations for the valence band of a CuO_2 layer. For this, as already done in the generalized tight-binding method [15], we employ the Green's functions method. The equations of motion for the operators $X^m_{\mathbf{f}\sigma}$ and $Y^n_{\mathbf{g}\sigma}$ have the form

$$i\dot{X}^m_{\mathbf{f}\sigma} = [X^m_{\mathbf{f}\sigma}, H] = \Omega_m X^m_{\mathbf{f}\sigma} + [X^m_{\mathbf{f}\sigma}, H_{cc}], \qquad (21)$$

where $\Omega^G_m = \Omega_G(\boldsymbol{\alpha}_m) = \varepsilon_{2qG} - \varepsilon_{1pG}$. For any radius vector $\mathbf{R}$ the corresponding commutator can be calculated in the Hubbard 1 approximation:

$$[X^m_{\mathbf{f}\sigma}, H_{cc}]$$
$$= \sum_{\lambda\lambda'\sigma}\sum_{nl}\sum_{\mathbf{iR}} T_{\lambda\lambda'}(\mathbf{R})\{\gamma^*_{\lambda\sigma}(n)\gamma_{\lambda'\sigma}(l)[X^m_{\mathbf{f}\sigma}, X^{+n}_{\mathbf{i}\sigma'}X^l_{\mathbf{i}+\mathbf{R}\sigma'}] \qquad (22)$$
$$+ \gamma^*_{\lambda'\sigma'}(l)\gamma_{\lambda\sigma'}(n)[X^m_{\mathbf{f}\sigma}, X^{+l}_{\mathbf{i}+\mathbf{R}\sigma'}X^n_{\mathbf{i}\sigma}]\} \approx \sum_{\lambda\lambda' n\mathbf{R}} T_{\lambda\lambda'}(\mathbf{R})$$
$$\times \gamma^*_{\lambda\sigma}(n)\gamma_{\lambda'\sigma}(n)F_{\mathbf{f}\sigma}(m)(X^n_{\mathbf{f}+\mathbf{R}\sigma} + X^n_{\mathbf{f}-\mathbf{R}\sigma}),$$

where $F_{G\sigma}(m) = F_{G\sigma}(\boldsymbol{\alpha}_m(pq)) = \langle X^{pp}_{f_{G\sigma}}\rangle + \langle X^{qq}_{f_{G\sigma}}\rangle$ is the filling factor [30]. Hence, taking account of the existence of the *A* and *B* sublattices, we obtain the system of equations

$$i\dot{X}^m_{\mathbf{f}\sigma} = \Omega^A_m X^m_{\mathbf{f}\sigma} + 2\sum_{\lambda\lambda' n}\gamma^*_{\lambda\sigma}(m)\gamma_{\lambda'\sigma}(n)F_{A\sigma}(m)$$
$$\times\left(\sum_{\mathbf{R}_1} X^n_{\mathbf{f}+\mathbf{R}_1\sigma}T_{\lambda\lambda'}(\mathbf{R}_1) + \sum_{\mathbf{R}_2} Y^n_{\mathbf{f}+\mathbf{R}_2\sigma}T_{\lambda\lambda'}(\mathbf{R}_2)\right), \qquad (23)$$
$$i\dot{Y}^m_{\mathbf{g}\sigma} = \Omega^B_m X^m_{\mathbf{g}\sigma} + 2\sum_{\lambda\lambda' n\mathbf{R}}\gamma^*_{\lambda\sigma}(m)\gamma_{\lambda'\sigma}(n)F_{B\sigma}(m)$$
$$\times\left(\sum_{\mathbf{R}_1} Y^n_{\mathbf{g}+\mathbf{R}_1\sigma}T_{\lambda\lambda'}(\mathbf{R}_1) + \sum_{\mathbf{R}_2} X^n_{\mathbf{g}+\mathbf{R}_2\sigma}T_{\lambda\lambda'}(\mathbf{R}_2)\right).$$

For the matrix Green's function,

$$\hat{D}_{\mathbf{ij}} = \begin{pmatrix} \hat{D}_{\mathbf{ij}\sigma}(AA) & \hat{D}_{\mathbf{ij}\sigma}(AB) \\ \hat{D}_{\mathbf{ij}\sigma}(BA) & \hat{D}_{\mathbf{ij}\sigma}(BB)\end{pmatrix},$$

where $D^{mn}_{\mathbf{ij}\sigma}(AB) = \langle\langle X^n_{\mathbf{i}\sigma} \big| Y^n_{\mathbf{j}\sigma}\rangle\rangle$, we have an analogous system of equations:

$$D^{mn}_{\mathbf{ij}\sigma}(AA) = D^0_{m\sigma}(A)\delta_{\mathbf{ij}}\delta_{mn}$$
$$+ 2D^0_m(A)\sum_{\lambda\lambda' l}\gamma^*_{\lambda\sigma}(m)\gamma_{\lambda'\sigma}(l)$$
$$\times\left(\sum_{\mathbf{R}_1} T_{\lambda\lambda'}(\mathbf{R}_1)D^{ln}_{\mathbf{i}+\mathbf{R}_1\mathbf{j}\sigma}(AA)\right.$$
$$\left. + \sum_{\mathbf{R}_2} T_{\lambda\lambda'}(\mathbf{R}_2)D^{ln}_{\mathbf{i}+\mathbf{R}_2\mathbf{j}\sigma}(BA)\right), \qquad (24)$$
$$D^{mn}_{\mathbf{ij}\sigma}(BA) = 2D^0_{m\sigma}(B)\sum_{\lambda\lambda' l}\gamma^*_{\lambda\sigma}(m)\gamma_{\lambda'\sigma}(l)$$
$$\times\left(\sum_{\mathbf{R}_1} T_{\lambda\lambda'}(\mathbf{R}_1)D^{ln}_{\mathbf{i}+\mathbf{R}_1\mathbf{j}\sigma}(BA)\right.$$
$$\left. + \sum_{\mathbf{R}_2} T_{\lambda\lambda'}(\mathbf{R}_2)D^{ln}_{\mathbf{i}+\mathbf{R}_2\mathbf{j}\sigma}(AA)\right).$$

Here $D^0_{m\sigma}(A) = F_{A\sigma}(m)/(E - \Omega^A_m + i\varepsilon)$, i.e., the zero-approximation Green's function is diagonal with respect to the matrix indices *m* and *n*. After Fourier transforming

$$D^{mn}_{\mathbf{ij}} = \frac{2}{N}\sum_{\mathbf{k}} D^{mn}_{\mathbf{k}\sigma}e^{i\mathbf{k}\cdot(\mathbf{R}_i - \mathbf{R}_j)}$$

the system of equations becomes

$$D^{mn}_{\mathbf{k}\sigma}(AA) = D^0_m(A)\delta_{mn} + 2D^0_m(A)$$
$$\times\sum_{\lambda\lambda' l}\gamma^*_{\lambda\sigma}(m)\gamma_{\lambda'\sigma}(l)$$
$$\times[T^{AA}_{\lambda\lambda'}(\mathbf{k})D^{ln}_{\mathbf{k}\sigma}(AA) + T^{AB}_{\lambda\lambda'}(\mathbf{k})D^{ln}_{\mathbf{k}\sigma}(BA)], \qquad (25)$$
$$D^{mn}_{\mathbf{k}\sigma}(BA) = 2D^0_m(B)\sum_{\lambda\lambda' l}\gamma^*_{\lambda\sigma}(m)\gamma_{\lambda'\sigma}(l)$$
$$\times[T^{BB}_{\lambda\lambda'}(\mathbf{k})D^{ln}_{\mathbf{k}\sigma}(BA) + T^{BA}_{\lambda\lambda'}(\mathbf{k})D^{ln}_{\mathbf{k}\sigma}(AA)].$$

In the matrix form the system of equations (25) is

$$\hat{A}_\sigma(\mathbf{k})\hat{D}_{\mathbf{k}\sigma} = \hat{D}^0_\sigma,$$
$$\hat{A}_\sigma(\mathbf{k}) = \begin{pmatrix} 1 - \hat{D}^0_\sigma(A)\hat{T}^{AA}_{\text{eff}}(\mathbf{k},\sigma) & -\hat{D}^0_\sigma(A)\hat{T}^{AB}_{\text{eff}}(\mathbf{k},\sigma) \\ -\hat{D}^0_\sigma(B)\hat{T}^{BA}_{\text{eff}}(\mathbf{k},\sigma) & 1 - \hat{D}^0_\sigma(B)\hat{T}^{BB}_{\text{eff}}(\mathbf{k},\sigma)\end{pmatrix}, \qquad (26)$$
$$\hat{T}_{\text{eff}}(\mathbf{k},\sigma) = \begin{pmatrix} \hat{T}^{AA}_{\text{eff}}(\mathbf{k},\sigma) & \hat{T}^{AB}_{\text{eff}}(\mathbf{k},\sigma) \\ \hat{T}^{BA}_{\text{eff}}(\mathbf{k},\sigma) & \hat{T}^{BB}_{\text{eff}}(\mathbf{k},\sigma)\end{pmatrix},$$

$$T^{PG}_{\text{eff}mn}(\mathbf{k},\sigma) = \sum_{\lambda\lambda'}\gamma^*_{\lambda\sigma}(m)T^{PG}_{\lambda\lambda'}(\mathbf{k})\gamma_{\lambda'\sigma}(n).$$

Thus, the dispersion relations are determined by the equation for the poles of the matrix Green's function $\hat{D}$:

$$\left\| \frac{(E-\Omega_m^G)\delta_{mn}}{F_\sigma^G(m)} - 2\sum_{\lambda\lambda'}\gamma^*_{\lambda\sigma}(m)T^{PG}_{\lambda\lambda}(\mathbf{k})\gamma_{\lambda'\sigma}(n)\right\| = 0. \quad (27)$$

The equation (27) is similar to the standard single-electron equation for the tight-binding method, differing from it in two respects. In the first place, the single-particle energies are determined as resonances between multielectron states taking account of strong correlations. In the second place, the filling factors $F_\sigma^G(m)$ lead to a concentration dependence of the band structure of the quasiparticles. In the next section we shall present and discuss the results obtained by solving Eq. (27). The order of the determinant presented above is determined by the 32×32 matrix Green's function, constructed on a $m \times m$ basis from the root vectors. The equation (27) is an equation for the generalized eigenvalue problem, where a diagonal matrix of the inverse sum of the filling numbers of the initial and final states participating in the transition with a m root vector appear instead of the usual "nonorthogonality matrix." Each root vector $\boldsymbol{\alpha}_m$ determines a charged spin-1/2 Fermi quasiparticle; their local energies are Ω_m^G. The intercell hops lead to dispersion of the local quasiparticles.

4. COMPUTATIONAL RESULTS: DISPERSION RELATIONS AND ENERGY GAP IN AN UNDOPED DIELECTRIC WITH $x = 0$

Figure 4 shows the computational results for the undoped case (hole density $n_h = 1 + x = 1$) and the set of parameters in units of t_{pd}:

$$\varepsilon_{d_z} = 2, \quad \varepsilon_p = 1.6, \quad \varepsilon_{p_z} = 0.5,$$
$$t_{pp} = 0.46, \quad t'_{pp} = 0.42, \quad U_d = 9, \quad U_p = 4, \quad (28)$$
$$V_{pd} = 1.5, \quad J_d = 1.$$

The directions of the Brillouin zone for calculating the dispersion relations were chosen in accordance with the directions along which the ARPES observations were performed for antiferromagnetic dielectric compound $Sr_2CuO_2Cl_2$ [20]. The valence band top with prescribed values of the parameters is formed by quasiparticle states with root vectors $\boldsymbol{\alpha}_m(\tilde{b}_{1\sigma}\tilde{A}_1)$. In addition, the interband transitions with t_{pd}—the largest of the possible hopping integrals—are responsible for the dispersion of the wide valence band. The form of the valence band corresponds quantitatively to the ARPES-spectroscopy results for $Sr_2CuO_2Cl_2$ (Fig. 4). In this respect our calculation reproduces existing results for

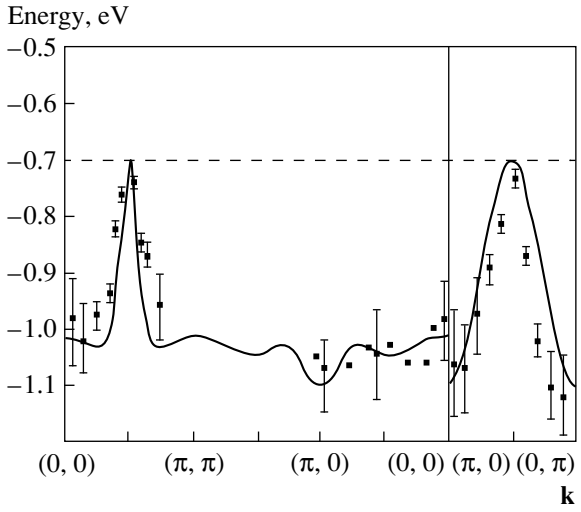

Fig. 4. Computed dispersion curves for $x = 0$ and directions of the Brillouin zone presented in the ARPES experiments (dots, $Sr_2CuO_2Cl_2$ [20]). The dashed line denotes the zero-dispersion virtual level with zero spectral density.

the dispersion of the valence band top on the basis of the t–t'–J model [19]. In contrast to the t–t'–J model, in our calculation there appears an additional zero-dispersion level at the valence band top, for which the filling factor and spectral weight ~x, i.e., they are zero in the undoped case. For $x = 0$ this level can be called virtual.

In the undoped antiferromagnetic case we are dealing with two quasiparticles at the valence band top: $\boldsymbol{\alpha}_m(\tilde{b}_{1\uparrow}\tilde{A}_1)$ and $\boldsymbol{\alpha}_m(\tilde{b}_{1\downarrow}\tilde{A}_1)$. At zero temperature, neglecting Coulomb fluctuations, the filling numbers of the $|\tilde{b}_{1\sigma}\rangle$ single-hole state for one spin projection are zero in the A and B sublattices. Consequently, for this spin projection a zero-dispersion level is present in the undoped case. Since transitions between empty states have zero amplitude, a peak corresponding to this transition is not observed in the spectral density, and only a peak corresponding to the valence band is detected. This is a typical effect of strong correlations. Similar effects have been observed previously for the density of states in the theory of magnetic semiconductors [31]. The valence band corresponds to a transition with the participation of a $|\tilde{b}_{1\sigma}\rangle$ state with nonzero filling numbers. A large effect of quasiparticles $\boldsymbol{\alpha}_m(\tilde{b}_{1\sigma}\tilde{B}_{1M})$ (with participation of a triplet) on the dispersion of the valence band is also observed. This is due to the small energy splitting, approximately 0.7 eV, between the triplet and ground singlet states in the two-hole sector of Hilbert space. The largest changes due to such a singlet-triplet hybridization are observed near the symmetry point $X = (\pi, 0)$. We reproduce the computational results obtained in the t–t'–J model [19] with $t'/t = -0.35$.

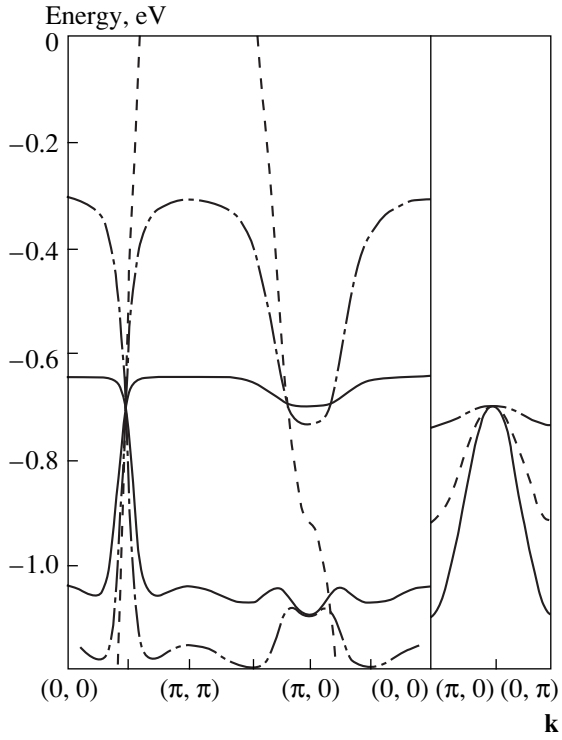

Fig. 5. Computed dispersion curves of the valence band of a CuO_2 layer in the antiferrophase: hole density $x = 0.01$ (solid line); hole density $x = 0.1$ (dot-dashed line); in the para phase the hole density $x = 0.2$ (dashed line).

In addition, in our case the ratio with a similar meaning

$$\frac{t'_{\text{eff}}}{t_{\text{eff}}} = \frac{t_{pd}\mu_{11}\varphi_d\varphi_p + t_{pp}\nu_{11}\varphi_p^2}{t_{pd}\mu_{10}\varphi_d\varphi_p + t_{pp}\nu_{10}\varphi_p^2} = -0.24, \qquad (29)$$

where

$$\varphi_d = \beta_1(d_x)A_1(d_xd_x) + \beta_1(b)A_1(d_xb),$$

$$\varphi_b = \beta_1(d_x)A_1(d_xb) + \beta_1(b)A_1(bb).$$

Contributions from intersublattice transitions to the dispersion of the valence band along the symmetric direction $X \longleftrightarrow Y$, i.e., along the boundary of the antiferromagnetic Brillouin zone, are forbidden. However, the width of the valence band in this direction and in $\Gamma = (0, 0) \longleftrightarrow M = (\pi, \pi)$, where intersublattice transitions contribute in the experiment [20], are approximately the same. In reality, because of the closeness of the triplet, the widths are determined not by the integral transfer, which is obviously much greater for intersublattice than for intrasublattice transitions, but rather by the hybridization of the singlet and lower-lying triplet valence bands. Neglecting the triplet, a much smaller dispersion was observed (just as in the *t–J* model [32]) in the direction $X \longleftrightarrow Y$ than in the direction $\Gamma \longleftrightarrow M$. The valence-band widths themselves, in this case, just as in the LDA calculations [33], were greater than the observed values.

The deeper valence bands are formed by quasiparticles $\boldsymbol{\alpha}_m(\tilde{a}_{1\sigma}\tilde{B}_{1M})$ and $\boldsymbol{\alpha}_m(\tilde{b}_{1\sigma}\tilde{B}_{1M})$. The former refer to transitions between empty excited states and have zero amplitude. In Fig. 4 these transitions correspond to a zero-dispersion level deep in the valence band. The second transitions form bands with much smaller dispersion than quasiparticles with $\boldsymbol{\alpha}_m(\tilde{b}_{1\sigma}\tilde{A}_1)$ root vectors, since they correspond only to hole transport with smaller hopping integrals t_{pd_z} or t_{pp}. This can be easily seen from the differences of Tables 4 and 6, where the amplitudes of the transitions $\gamma_{d_x\sigma}(m)$ and $\gamma_{b\sigma}(m)$ are zero for quasiparticles with vectors $\boldsymbol{\alpha}_m(\tilde{b}_{1\sigma'}\tilde{B}_{1M})$ and different from zero for $\boldsymbol{\alpha}_m(\tilde{b}_{1\sigma'}\tilde{A}_1)$ quasiparticles.

5. EFFECT OF DOPING ON THE BAND STRUCTURE OF THE QUASIPARTICLES OF A CuO_2 LAYER

The behavior of the zero-dispersions virtual level with doping is interesting. In the undoped case the filling numbers of both two-hole states $|\tilde{A}_1\rangle$ and $|B_{1M}\rangle$ are zero and correspond to a zero-dispersion virtual level. In the presence of doping the filling numbers of the two-hole state $|\tilde{A}_1\rangle$ are nonzero, $n_A = 1 + x$. In consequence, the initial virtual level acquires dispersion $\partial W/\partial x \sim 1$ eV. The wide valence band remains unchanged, since its filling factor $F = n_{\tilde{A}} + n_{\tilde{b}} = 1$ does not depend on the number of holes. Figure 5 shows the dispersion curves for $x = 0.01$ and for $x = 0.1$.

The largest changes with doping, as one can see by comparing Figs. 4 and 5, are due precisely to the dispersion of the previous virtual level; it is characterized by the wide maximum near the points Γ and M and minimum near the point X. At the same time the spectral density of the new valence band is proportional to the degree of doping x, i.e., this band is similar to the impurity bands in doped semiconductors. We underscore that in our approach there are no impurity effects in the form of fluctuations of the impurity potential or hopping integrals; doping influences only the hole density, and consequently the term "impurity" band signifies a band of quasiparticles whose spectral density for small $x \ll 1$ is proportional to the degree of doping. A mechanism, specific to strongly correlated systems, leading to the formation of impurity levels with doping has been discussed in detail on the basis of a two-orbital Hubbard model [27].

As the hole density increases with x changing from $x = 0.01$ to $x = 0.1$, the largest dispersion of the impurity band occurs near the points Γ and M with a further decrease of the minimum at the point X. However, a discussion of the high hole densities requires a special clarification. The point is that in principle the general approach formulated in Section 2 makes it possible to

study self-consistently the changes in the electronic and magnetic structures. However, our Hubbard 1 approximation for intercell hops leads to the fact that the magnetic system is described by an effective Heisenberg model, and its influence on the electronic system reduces to a redistribution of the filling numbers between the spin sublevels for a given sublattice. The applicability of such an approximation is analyzed in detail in [26], where it is shown that the results agree with the data obtained by exact diagonalization of small clusters by the Lanczos method for the Hubbard model and the *t–J* and three-band *p–d* models. Thus, comparing the perturbation theory for $J < t$ with the exact answers in the *t–J* model shows that the corrections to the vertices are small [34]. For the undoped case in the Hubbard model the spectral density of the quasiparticles, which is obtained by exact diagonalization, can be described in the mean-field theory (spin density waves) with a calculation of the magnetization of a sublattice in the spin-wave theory [35]. Consequently, we study the electronic structure against the background of a fixed magnetic order, which itself depends on the doping. Since on doping a *p*-type hole moves primarily along oxygen orbitals, additional exchange $J_{\text{Cu–O}} \gg J_{\text{Cu–Cu}}$ arises, resulting in frustrations in the Heisenberg antiferromagnet and rapid suppression of the three-dimensional antiferromagnetic long-range order. The critical densities [36, 37] and the concentration dependence of the Néel temperature $T_N(x)$ [38] were obtained in the *t–J* model in the spin-wave approach. Although there is no long-range antiferromagnetic order for $x > x_{cr}$, there does exist a two-dimensional short-range order with coherence length $x_{AFM} \gg a$ for lightly doped compositions, $x \ll 1$. Since the mean-free path length $l \sim a$ and $l \ll \xi_{AFM}$, the main effect of short-range order reduces to motion of an electron within an antiferromagnetic cluster, and the band structure can be interpreted similarly to a doped antiferromagnet even for $x > x_{cr}$ in the lightly doped range. The fluctuation character of a magnetic cluster introduces certain refinements in the picture described above. Specifically, instead of symmetry of bands with doubling of the Brillouin zone in an antiferromagnetic phase and the equivalence-coupled states k and $\mathbf{k} + \mathbf{Q}$ ($\mathbf{Q} = (\pi/a, \pi/a)$ is the nesting vector) which are equivalent because of Umpklapp processes, under conditions of short-range order the coupling of these states is of a dynamical character and is determined by the decay of the state $\mathbf{k}$, as a result of damping, into the final state $\mathbf{k} + \mathbf{Q}$ [39]. However, these differences are not fundamental, and a doped antiferromagnet with $x \sim 0.1$ will be studied in order to investigate the concentration evolution of the band structure. The transition from a doped antiferromagnet to an almost antiferromagnetic Fermi liquid seems to occur at $x \approx x_{\text{opt}}$, where $x_{\text{opt}} \approx 0.18$ is the optimal doping concentration for which $T_c(x)$ possesses a maximum. For optimal compositions $\xi_{AFM} \approx 2a$. Analysis of the concentration dependences of the two-magnon spectra of Bi-2212 led the authors of [40] likewise to the conclusion that crossover occurs between a doped antiferromagnet and an almost antiferromagnetic Fermi liquid at $x \approx x_{\text{opt}}$. In the paramagnetic phase the filling numbers of local terms do not depend on the spin index. Doubling of the Brillouin zone as compared with the antiferromagnetic phase removes the equivalence of the points Γ and M. Figure 5 shows (dashed lines) the band structure with $x = 0.2$ in the para phase. As one can see in Fig. 5, in the paramagnetic phase there is one valence band instead of two bands. The latter band reproduces well the dispersion curves calculated by the Monte Carlo method [19] and the dispersion curves observed for the optimally doped samples [41], including the Van Hove singularity near the symmetric point X.

6. DISCUSSION

The evolution of the band structure with doping can be traced by comparing Figs. 4 and 5. It is the dispersion of the impurity band and the merging of this band with the main band in the para phase that give the transition from an undoped structure with a maximum at the point $\overline{M} = (\pi/2, \pi/2)$ (Fig. 4) to the band structure of a doped system with a maximum at the point M and a saddlepoint X (Fig. 5). An important effect of magnetic order in the doped case is a gap between the impurity and the main valence bands at the point X. This gap is known as a pseudogap from NMR, inelastic neutron scattering, and ARPES experiments (see review [39]).

Spin fluctuations fall outside the scope of the present paper. Consequently, we cannot compare our results with the ARPES results and calculations of the spectral function on the basis of the quantum Monte Carlo method [19, 42] in the entire range of doped hole densities. However, for doping, an additional peak corresponding to a narrow impurity band and a high energy is added in our approach to the peak corresponding to a wide valence band and a quasiparticle state with wave vector $\mathbf{k}$. In addition, just as in [42], the behavior of the low-energy peak is identical to the behavior of the quasiparticle peak in the undoped case, since the dispersion of the wide valence band does not depend on the doping level. A high-energy peak is observed only in the doped variant, where the virtual level acquires dispersion. Indeed, as temperature decreases, for low degrees of doping, the Monte Carlo calculations for the *t–J* model [42] and calculations in the spin-bag model [43] show a similar splitting of the quasiparticle peak into two peaks—low and high energy. The splitting of the quasiparticle peaks in the spectral density occurs, according to [41] only near the symmetry point X. Calculations were performed for temperatures $T > 0.1t$. Lower temperatures are inaccessible because the influence of the finite size of the cluster in the analysis on the computational results cannot be controlled. This result becomes understandable if one keeps in mind the fact that, according to calcula-

tions in the theory of an almost antiferromagnetic liquid [44], hot regions, where quasiparticles are most sensitive to the short-range antiferromagnetic order, exist near the symmetry points X and Y on the Fermi surface. There is no splitting in the spectral function of the experimental ARPES investigations. Nonetheless, the presence of a pseudogap near X is indirect proof of the presence of a high-energy peak, lying above the Fermi level and consequently not observed in the ARPES experiment.

The mechanism for acquiring additional dispersion can be used to explain the ARPES-spectroscopy results concerning the opening of an energy gap along the line $X \longleftrightarrow M$ of the Brillouin zone [40] for $Bi_2Sr_2CaCu_2O_{8+\delta}$. Switching to dielectric samples, the form of the dispersion curves from Γ to $\overline{M}$ remains similar to the corresponding section of the dispersion curve of metallic samples. The dispersion curves near the point X behave completely differently. The transition from optimally doped metallic samples to lightly doped samples results in vanishing of the section of the Fermi surface on the line $X \longleftrightarrow M$. For samples with optimal doping (T_c = 85 K) large areas of the section of the Fermi surface were observed. If the rigid-band model were valid, then a decrease of hole density would result only in a decrease of the area of the section while its shape would remain unchanged. In addition, the intersections of the Fermi surface by the line $X \longleftrightarrow M$ should remain, which contradicts experiment, showing opening of an energy gap on the Fermi surface along the line $X \longleftrightarrow M$. In a dielectric sample the filling numbers of all two-hole states are zero, since transitions between empty states have zero amplitude, a peak corresponding to this transition is not observed in the spectral density (zero-dispersion virtual level), but rather a peak corresponding to the valence band for nonzero filling numbers of the state $|\tilde{b}_{1\sigma}\rangle$ for one of the spin projections is detected. For doping, the virtual level acquires dispersion but now according to the scenario described above and it is detected in ARPES experiments. The existence of an energy pseudogap is based on the difference in the dispersion laws between the valence and narrow impurity bands. Comparing the computed dispersion curves with the ARPES observations [40] we conclude that dispersion, characteristic for the para phase in all experimental samples, is observed in the experiment along the direction $\Gamma \longleftrightarrow \overline{M}$, while near X a similar dispersion is observed only for an optimally doped sample. The appearance of an energy gap near X is a consequence of the manifestation of an impurity band near energies above the Fermi energy with doping of antiferromagnetic CuO_2 layer. Our conclusions, just as the conclusions of [44], do not support the conclusions of [19] that it is impossible to describe in a unified approach the dispersion relations for an antiferromagnetic dielectric and doped samples.

Calculation of the evolution of the Fermi surface taking doping into account requires a self-consistent calculation of the Fermi level for each hole density. Since the band structure itself depends on the density and cannot be described by a rigid-band model, this problem requires a large volume of calculations and falls outside the scope of the present paper.

ACKNOWLEDGMENT

This work was supported by the Krasnoyarsk Krai Science Foundation (project no. 8F0032).

REFERENCES

1. P. W. Anderson, Science **235**, 196 (1987); R. O. Zaĭtsev and V. A. Ivanov, Fiz. Tverd. Tela (Leningrad) **29**, 2554 (1987) [Sov. Phys. Solid State **29**, 1475 (1987)].
2. P. Kuiper, G. Kruizinga, J. Chijsen, *et al.*, Phys. Rev. B **38**, 6483 (1988).
3. N. Nucker, J. Fink, J. C. Fugle, *et al.*, Phys. Rev. Lett. **58**, 2794 (1987).
4. V. J. Emery, Phys. Rev. Lett. **58**, 2794 (1987).
5. C. M. Varma, S. Schmitt-Rink, and E. Abrahams, Solid State Commun. **62**, 681 (1987).
6. Yu. B. Gaididei and V. M. Loktev, Phys. Status Solidi B **147**, 307 (1988).
7. F. C. Zhang and T. M. Rice, Phys. Rev. B **37**, 3759 (1988).
8. H. Eskes and J. H. Jefferson, Phys. Rev. B **48**, 9788 (1993).
9. H. Eskes and G. A. Sawatzky, Phys. Rev. Lett. **61**, 1415 (1988).
10. E. B. Stechel and D. R. Jennison, Phys. Rev. B **38**, 4632 (1988).
11. H. Eskes, G. A. Savatzky, and L. F. Feiner, Physica C (Amsterdam) **160**, 424 (1989).
12. J. H. Jefferson, H. Eskes, and L. F. Feiner, Phys. Rev. B **45**, 7959 (1992).
13. S. V. Lovtsov and V. Yu. Yushankhai, Physica C (Amsterdam) **179**, 159 (1991).
14. H.-B. Schutler and A. J. Fedro, Phys. Rev. B **45**, 7588 (1992).
15. S. G. Ovchinnikov and I. S. Sandalov, Physica C (Amsterdam) **198**, 607 (1989).
16. J. H. Jefferson, Physica B (Amsterdam) **165–166**, 1013 (1990).
17. V. I. Belinicher, A. L. Chernyshev, and V. A. Shubin, Phys. Rev. B **53**, 335 (1996).
18. A. Nazarenko, K. J. E. Vos, S. Haas, *et al.*, Phys. Rev. B **51**, 8676 (1995).
19. D. Daffy, A. Nazarenko, S. Haas, *et al.*, Phys. Rev. B **56**, 5597 (1997).
20. B. O. Wells, Z.-X. Shen, A. Matsuura, *et al.*, Phys. Rev. Lett. **74**, 964 (1995).
21. A. Bianconi *et al.*, Physica C (Amsterdam) **162–164**, 209 (1989).
22. H. Romberg *et al.*, Phys. Rev. B **41**, 2609 (1990).

23. L. F. Feiner, J. H. Jefferson, and R. Raimondi, Phys. Rev. B **53**, 8751 (1996).
24. R. Raimondi, J. H. Jeferson, and L. F. Feiner, Phys. Rev. B **53**, 8774 (1996).
25. S. G. Ovchinnikov, Phys. Rev. B **49**, 9891 (1994).
26. C. G. Ovchinnikov, Zh. Éksp. Teor. Fiz. **107**, 796 (1995) [JETP **80**, 451 (1995)].
27. S. G. Ovchinnikov, Zh. Éksp. Teor. Fiz. **102**, 534 (1992) [Sov. Phys. JETP **75**, 283 (1992)].
28. S. G. Ovchinnikov, Pis'ma Zh. Éksp. Teor. Fiz. **64**, 23 (1996) [JETP Lett. **64**, 25 (1996)].
29. B. S. Shastry, Phys. Rev. Lett. **63**, 1288 (1989).
30. R. O. Zaĭtsev, Zh. Éksp. Teor. Fiz. **68** (1), 207 (1975) [Sov. Phys. JETP **41**, 100 (1975)].
31. V. A. Gavrichkov, M. Sh. Erukhimov, S. G. Ovchinnikov, and I. S. Édel'man, Zh. Éksp. Teor. Fiz. **90**, 1275 (1986) [Sov. Phys. JETP **63**, 744 (1986)].
32. Z. Liu and E. Manousakis, Phys. Rev. B **45**, 2425 (1992).
33. O. K. Andersen, A. Liechtenstein, O. Jepsen, and F. Paulsen, J. Phys. Chem. Solids **56**, 1573 (1995).
34. G. Martinez and P. Horsch, Phys. Rev. B **44**, 317 (1991).
35. E. Daggotto, F. Ortolani, and D. Scalapino, Phys. Rev. B **46**, 3183 (1992).
36. G. Khaliullin and P. Horsch, Phys. Rev. B **47**, 463 (1993).
37. G. G. Khaliullin, Pis'ma Zh. Éksp. Teor. Fiz. **52**, 999 (1990) [JETP Lett. **52**, 389 (1990)].
38. J. L. Richard and V. Yu. Yushankhai, Phys. Rev. B **50**, 12927 (1994).
39. S. G. Ovchinnikov, Usp. Fiz. Nauk **167**, 1043 (1997) [Phys. Usp. **40**, 993 (1997)].
40. M. Guptasarma, D. G. Hinks, and M. V. Klein, Phys. Rev. Lett. **82**, 5349 (1999).
41. D. S. Marshall *et al.*, Phys. Rev. Lett. **76**, 4841 (1996).
42. P. Prelovsek, J. Jaklic, and K. Bedell, Phys. Rev. B **60**, 40 (1999).
43. A. P. Kampf and J. R. Schrieffer, Phys. Rev. B **41**, 6399 (1990).
44. J. Schmalian, D. Pains, and B. Stoykovich, Phys. Rev. B **60**, 667 (1999).

Translation was provided by AIP

Journal of Experimental and Theoretical Physics, Vol. 91, No. 2, 2000, pp. 384–392.
Translated from Zhurnal Éksperimental'noĭ i Teoreticheskoĭ Fiziki, Vol. 118, No. 2, 2000, pp. 438–447.

SOLIDS
Electronic Properties

Reconstruction of the Deformation Potential at the *N*-Ellipsoid of the Fermi Surface of Tungsten

A. V. Tkach

Institute of Metal Physics, Ural Division, Russian Academy of Sciences, Yekaterinburg, 620219 Russia
e-mail: ildan@imp.uran.ru; ildan@hotmail.com

Received February 1, 2000

Abstract—A simple model is used to reconstruct for the first time the distributions of local values of the deformation potential at one of the sheets of the Fermi surface of tungsten. © *2000 MAIK "Nauka/Interperiodica".*

1. INTRODUCTION

Studies of the Fermi surfaces of pure metals are now fairly well advanced. Nevertheless, the problem of the deformation potential characterizing the change in the energy of the electronic states accompanying a deformation of the lattice has not yet been fully resolved. The difficulty is that the deformation potential is a local characteristic of a state on the Fermi surface. This means that each point on the Fermi surface of this metal should have its own value of the deformation potential (in general it is desirable to know all six independent components of the deformation potential for each point on the Fermi surface). As far as the experimental possibilities are concerned, we can most frequently only record the response of a Fermi system to a deformation as an integrated process, for specific "effective" orbits. Examples are the de Haas–van Alfvén effect or the absorption of ultrasound in strong magnetic fields $\mathbf{H} \parallel \mathbf{q}$. Scope for local measurements in this scenario is limited.

In [1] the author noted possible methods for the practical reconstruction of local values of the deformation potential Λ on the Fermi surfaces of metals using experimental information. In the present publication we shall attempt for the first time to reconstruct patterns of local values of various components of the deformation potential for one of the sheets of the Fermi surface of tungsten (hole *N*-ellipsoids) using one of the methods proposed in [1], parametrization using a physically substantiated model. The main constraint is that without exception all known experimental data on the deformation dependence of the effective cross section areas (more than 40 experimentally determined values, for various effective cross sections and different deformations) should be exactly reconstructed on *N*-ellipsoids.

The data obtained subsequently may also be important for interpreting or detailed modeling of various magnetoacoustic effects associated with the Fermi surface sheet being discussed or with various sections of it (for example, quantum oscillations of the absorption and transverse ultrasound velocity in a longitudinal magnetic field [2], geometric oscillations of the absorption, Doppler-shifted cyclotron resonance at reference points, and so on).

Although ellipsoids constitute a very small part of the Fermi surface, this does not mean that they cannot make a significant contribution to integral kinetic effects. For example, according to estimates [3], ellipsoids give 30% of the total absorption of longitudinal ultrasound in a strong magnetic field which is almost equal to the contribution of an "electron jack." We also agree with [4] where the RF conductivity of molybdenum is estimated in a zero field and it is shown that the contribution of the *N*-ellipsoids is even greater than the contribution of the hole "octahedron." However, in those cases where the contribution of some sections of the Fermi surface was extremely small, it is quite possible to record this experimentally against a background of weakly varying contributions of the remaining carriers if there is a strong functional dependence (a peak, oscillations having a characteristic frequency, and so on) on the magnetic field for example.

We consider it very important to note that the term "deformation potential" can have more than one meaning. In different contexts this term denotes either a derivative (λ) of the energy of a given electronic state with respect to a small elastic distortion or a similar value $\Lambda = \lambda - \bar{\lambda}$ (the bar denotes averaging over all states at the undeformed Fermi surface of the metal). The analysis is made most easily using a special comoving coordinate system (for example, [5]) in which the mesh of allowed Bloch states remains the same after deformation. After deformation the initial Fermi surface is not longer isoenergetic, with the result that a new Fermi surface forms. However, in comoving $\mathbf{k}$ space the volume below the Fermi surface should not change ("charge conservation"). Ultimately it is found that the derivative of the Fermi energy with respect to the elastic distortion is $\bar{\lambda}$. Hence, the meaning of the deformation potential Λ is abundantly clear: Λ shows

how rapidly this state moves away (on the energy scale) from the Fermi surface as the metal is deformed.

The relationship between the deformation potentials λ and Λ does not require special comment; we merely note that if the complete pattern of local values of Λ_{ij} can be reconstructed on the entire Fermi surface, not much remains to be done to determine λ_{ij}: only one number needs to be determined. Quite clearly the first part of this "program" is immeasurably more complex than the second. When we talk of the deformation potential subsequently, we shall have in mind the potential Λ.

2. CHOICE OF MODEL

The Fermi surface of tungsten contains six hole "pockets" positioned at the center ("N" type point) of the rhombic faces of the Brillouin zone (tungsten has a bcc lattice). The pockets are converted from one to another in the symmetry operations of the lattice; the only difference is the different spatial orientation. A specific characteristic of these fragments of the Fermi surface of tungsten is that they are extremely small compared with the characteristic size of the Brillouin zone. Thus, we have a natural small parameter: the pocket size in **k** space. This means that we can confine ourselves to quadratic expansions of the carrier energy in terms of k_i, in the single-electron approximation

$$\varepsilon = \varepsilon_0 + \sum_{i \le j} b_{ij} k_i k_j. \tag{1}$$

Here and subsequently the vector **k** s plotted from the *N* type point at the center of the corresponding pocket. Linear and cubic elements of the expansion with respect to *k* do not appear in (1) since the *N* point is a center of inversion: $\varepsilon(\mathbf{k}) = \varepsilon(-\mathbf{k})$. Multiparticle effects slightly distort this dispersion law in the immediate vicinity of the Fermi energy and thus act completely independently of the smallness (or lack of smallness) of the *k* values, depending only on the single-particle energy ε. These effects are taken into account by introducing the phenomenological constant μ which describes the renormalization of the velocities and effective masses at the Fermi surface. This value of the Fermi energy can be considered to be constant compared with the single-particle ("band") model. The real dispersion law for the energy range near the Fermi energy is modeled by (see, for example [6])

$$E - E_F = \frac{\varepsilon - E_F}{1 + \mu}. \tag{2}$$

Combining expressions (1) and (2) (with a change in the energy origin) we can write

$$E^*(\mathbf{k}) = \sum_{i \le j} B_{ij} k_i k_j, \tag{3}$$

where $B_{ij} = b_{ij}/(1 + \mu)$. Expression (3) forms the essence of our model.

Three important factors should be noted. First, the energy E^* in this expression is not measured from the bottom of the band ε_0; in fact

$$E^* = (E - \varepsilon_0) - (E_F - \varepsilon_0)\frac{\mu}{1 + \mu}.$$

Second, the expression is only valid in the immediate vicinity of the Fermi surface. Third, the dispersion law (3) is written in comoving coordinates (see, for example [5]). In the absence of deformations the comoving system is the same as the laboratory one. In the presence of elastic deformations the comoving system is obtained by a geometric transformation to the initial (undistorted) Brillouin zone. Thus, **k** is the same as the electron wave vector only in an undeformed crystal [1].

Three mutually perpendicular planes of specular reflection intersect at the point *N* in the initial (undeformed) Brillouin zone. Ultimately a natural system of rectangular coordinates is formed: each coordinate axis is the intersection of a pair of planes. This system is used subsequently.

Since in the initial (undeformed) state all three coordinate planes $k_i = 0$ are specular, we have

$$B_{ij} \equiv 0, \quad \text{if } i \neq j. \tag{4}$$

Tension or compression along any of the natural axes conserves these symmetry elements. Relation (3) remains valid as before although the values of the diagonal elements B_{ii} and the Fermi energy E_F^* change.

Of greater interest are the consequences of shear distortions. For instance, a distortion of the type $u_{23} = \partial u_2/\partial x_3$ substantially changes the lattice symmetry. Two of the specular reflection planes are omitted, leaving only one: $k_1 = 0$. In this case, another nonzero element $B_{23} \neq 0$ may appear in the quadratic form (3). However, as a result of the symmetry of the problem it also follows (for example [5]) that in the linear approximation with respect to small distortions u_{23} the energy of states belonging to the $k_2 = 0$ and $k_3 = 0$ planes remains constant. This implies that all three diagonal elements B_{ii} remain the same. In addition, the value of the Fermi energy is conserved.

Ultimately it is found that the response of a hole *N*-ellipsoid to any small distortions of the lattice may be described by nine variations of the diagonal elements of the matrix $\mathbf{B}/E_F^*$ (three for each of the elementary tension–compression deformations) and by three variations of the off-diagonal elements (for three "shear" distortions in the principal axes), i.e., only 12 parameters.

At present we do not have a sufficient volume of experimental information to determine all 12 parameters independently. Hence it is desirable to introduce an additional constraint in the model. If the dimensions of

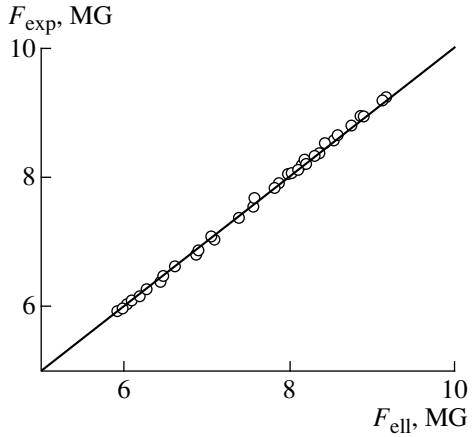

Fig. 1. Comparison of experimental and model values of the quantum oscillation frequencies associated with a hole pocket on the Fermi surface of tungsten.

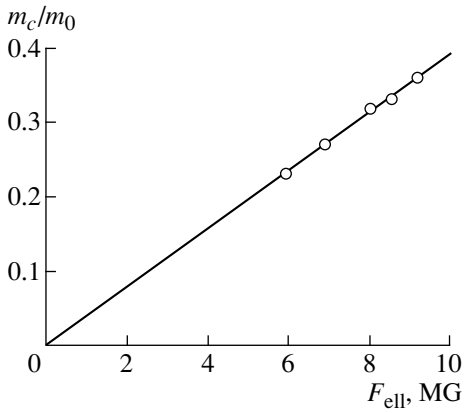

Fig. 2. Dependence of the cyclotron masses on the quantum oscillation frequency for the hole ellipsoid of the Fermi surface of tungsten.

the ellipsoid semiaxes a_i are compared, it is found that the values of a_2 and a_3 are similar but they are 1.5 times smaller than a_1. In this sense the direction k_1 is selected. We shall assume that the changes in the smaller semiaxes under tensile deformations can also be considered to be almost the same:

$$\frac{\partial a_2}{\partial u_{ii}} = \frac{\partial a_3}{\partial u_{ii}}. \quad (5)$$

Thus, the model can be reduced to two equations: (3) and (5). Of course this model must first be checked by a comparison with the experimental data.

3. VERIFICATION OF THE MODEL

3.1. Fermi Surface Geometry and Cyclotron Masses

The basic equation of the model shows that the hole pockets have the form of an ellipsoid. For the area S of the central cross section of any ellipsoid we have the simple relationship:

$$S^{-2} = \sum_{i=1}^{3} s_i^{-2} \cos\alpha_i, \quad (6)$$

where α_i are the direction cosines defining the orientation of the normal to the intersecting plane in the natural axes, and s_i are the areas of the principal cross sections of the ellipsoid. If this pocket is in fact an ellipsoid, there are three numbers s_i which invert (6) into an identity. The area of the effective cross sections is uniquely related to the frequency of the quantum oscillations. Consequently, the frequency of the quantum oscillations can easily be calculated for an ellipsoid as given by (6) for any orientation of the magnetic field and the calculated frequencies can be compared with those observed experimentally. The results of a comparison are plotted in Fig. 1 for all orientations of the field tabulated in [7], around 40 points in total. The calculated frequencies were determined for values of s_i^{-2} of 3971, 2190, and 1658 (au)$^{-2}$, respectively.

Another consequence of equation (3) is a universal relationship for the cyclotron masses m_c measured for various orientations of the field. Since in this particular case the dispersion law is $\partial S/\partial E^* \equiv S/E^*$, according to the definition of the cyclotron masses we have

$$m_c = \frac{\hbar^2}{2\pi E_F^*} S. \quad (7)$$

Another independent method of checking the model also emerges: the cyclotron masses should be proportional to the effective cross-sectional areas and the frequencies of the quantum oscillations. Figure 2 gives the cyclotron masses measured by Walsh [8] as a function of the quantum oscillation frequencies [7]. As we can see, a linear dependence is obtained. In addition, the graph in Fig. 2 can be used to determine $E_F^* = -0.297$ eV.

3.2. Response to Isotropic Tension–Compression

A considerable volume of the existing experimental data refers to changes in the areas of the effective cross sections under isotropic quasihydrostatic tension Ω. The strain achieved in these experiments may be represented as the sum of three numerically equal tensile strains along the three principal axes. Thus, the strain Ω having the numerical value β is expressed as $\sum u_{ii}$ where $u_{ii} = \beta/3$. Taking into account the symmetry analysis made above this means that the values of the elements B_{ii} change as a result; in addition it is possible to have a Fermi level shift. As a result the areas of the principal cross sections of the ellipsoid s_i change although

Variations of the reciprocal squares of the effective areas on the *N*-ellipsoid under isotropic tension–compression

h'k'l'	*S*, au	$\partial(S^{-2})/\partial\Omega$, 10^3 (au)$^{-2}$			
		value	references	weighted mean	model
0'0'1'	0.0159	71 ± 7 69 ± 7 56 ± 9 66 ± 13 58 ± 13	[10] [11] [12] [13] [13]	67 ± 4	66.9
0'1'1'	0.0184	53 ± 5	[11]	53 ± 5	51.3
1'1'1'	0.0188	49 ± 7	[10]	49 ± 7	49.4
1'0'0'	0.0228	31 ± 10 36 ± 5	[13] [13]	35 ± 4	35.8
$\bar{1}$' 1'1'	0.0205	42 ± 6	[10]	42 ± 6	41.5

the orientation of the principal axes is conserved. By directly differentiating equation (6) we obtain

$$-\frac{2}{S^2}\frac{\partial(\ln S)}{\partial\Omega} = \sum_{i=1}^{3}\frac{\partial(s_i^{-2})}{\partial\Omega}\cos\alpha_i. \qquad (8)$$

Experimental values of the derivative $\partial(\ln\tilde{S})/\partial\Omega$ determined in the laboratory coordinates (the areas measured are denoted here and subsequently by the tilde) are known [9] for various orientations of the magnetic field **H**. The transition to comoving coordinates is made by introducing special corrections, see [1]. Using these data a linear regression method was used to determine three values of $\partial(s_i^{-2})/\partial\Omega$ which are 66850, 41680, and 29820 (au)$^{-2}$, respectively. The experimental and calculated variations of the effective areas using (8) are compared in the table; again we note the good agreement between these values. Moreover, by knowing $\partial(s_i^{-2})/\partial\Omega$ we can also determine the derivatives $\partial a_i/\partial\Omega$ which were found to be –1.00, –0.57, and –0.56 Å^{-1}. We affirm that relation (5) is also confirmed in this case.

3.3. Response to Angular Shear

Another possible method of checking the model is provided by the results of experiments in which the response of the effective areas to shear deformations of the lattice [14, 4, 1] defined in the crystallographic axes is determined. However we first need to introduce some notation to simplify the following exposition.

All the experimental data used below are given in a system of crystallographic coordinate axes. These differ from the natural axes of the *N*-ellipsoid (see Fig. 3). We subsequently assume the following agreement: the orientations in the crystallographic axes are denoted by primed indices while those in the natural axes of the ellipsoid are denoted by those without primes. The distortions defined in the crystallographic axes *x'*, *y'*, *z'* can be written as a sum of elementary distortions in the natural axes (for example [15]. The notation can be simplified if this sum is represented symbolically as a square matrix. Thus, for example, the notation

$$\nu = \beta\begin{pmatrix} 1/2 & 1/3 & 0 \\ 0 & 0 & -1 \\ 0 & 0 & 0 \end{pmatrix} \equiv \beta\mathbf{M}_\nu$$

implies that the distortion ν whose magnitude is characterized by the number β, is expressed in the natural axes of the ellipsoid as the sum of the distortions $u_{11} = \beta/2$, $u_{12} = \beta/3$, and $u_{23} = -\beta$. Hence the derivative of any

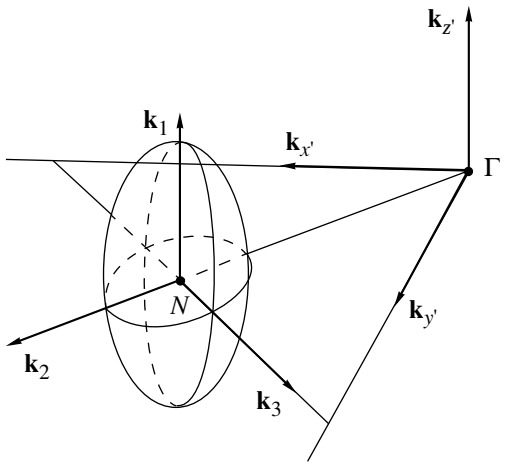

Fig. 3. Hole *N* ellipsoid of the Fermi surface of tungsten (arbitrary) showing systems of crystallographic and natural axes.

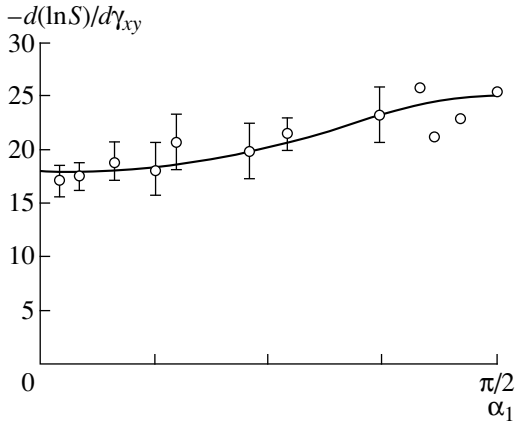

Fig. 4. Deformation variations in the effective areas for various directions of the magnetic field as a result of angular shear deformation. The solid curve gives the model.

scalar e in terms of β of this composite distortion (this is generally written as $\partial e/\partial\nu$) has the form

$$\frac{\partial e}{\partial \nu} \equiv \frac{\partial e}{\partial \beta} = \begin{pmatrix} \frac{1}{2}\frac{\partial e}{\partial u_{11}} & \frac{1}{3}\frac{\partial e}{\partial u_{12}} & 0 \\ 0 & 0 & -\frac{\partial e}{\partial u_{23}} \\ 0 & 0 & 0 \end{pmatrix}$$

and is represented symbolically using the same matrix $\mathbf{M}_\nu$ in the form

$$\frac{\partial e}{\partial \nu} = \mathbf{M}_\nu \frac{\partial e}{\partial}.$$

The deformation of the angular shear $\gamma_{x'y'} \equiv (u_{x'y'} + u_{y'x'})/2$ has the following representation in the natural axes of the ellipsoid

$$\gamma_{x'y'} = \beta \begin{pmatrix} 0 & 0 & 0 \\ 0 & 1/2 & 0 \\ 0 & 0 & -1/2 \end{pmatrix}. \quad (9)$$

It follows from the symmetry properties of the model in Section 2 that the only consequence of this lattice distortion will be a change in the diagonal elements of the matrix $\mathbf{B}/E_F^*$ which is equivalent to a change in the areas of the three principal ellipsoid cross sections. All the available experimental data on the variations of the effective cross sections have been obtained for orientations of the magnetic field perpendicular to [0'1'0'] ≡ (011). The direction of the field in this case is uniquely defined by the single angle α_1 [see equation (6)] and the dependence of the effective cross-sectional areas on the angle may be obtained by differentiating equation (6) and by means of subsequent simple transformations is reduced to the form

$$-\frac{2}{S^2}\frac{\partial(\ln S)}{\partial \gamma_{x'y'}} = a + b\cos^2\alpha_1 \quad (10)$$

with the constants a and b.

The validity of this relationship is checked in Fig. 4 which requires some explanation.

Most of the data presented here was obtained by a Canadian group [14]. The accuracy of the results published in [14] differs appreciably for the two ranges of angles. The random error of one measurement for the main range $0 \le \alpha_1 < 5\pi/12$ was estimated from the scatter of the experimental results relative to the mean (in those cases where several values of $\partial(\ln S)/\partial\gamma_{x'y'}$ were obtained for one angle and it was possible to determine the mean). The error Δ was ±2.55 with a 95% probability. Figure 4 gives the mean experimental value of the derivative for each angle α_1 with the value $\Delta_n = \Delta/\sqrt{n}$ plotted as the confidence interval, where n is the number of experimental points given in [14] for a particular angle. The correction taking into account the transition from laboratory to comoving coordinates [1] is zero for $\alpha_1 = 0$ and at the other end of the interval $\alpha_1 = \pi/2$ its value is approximately 1% and is negligible compared with the indeterminacy of the results plotted in the graph. Thus, in this case we can neglect this correction over the entire range of angles.

The authors of [14] show that a small range of angles (between $5\pi/12$ and $\pi/2$) cannot be measured reliably because of the superposition of stronger but similar-frequency oscillations from other extremal cross sections. The confidence interval is not given for these points but the errors in this case are far more appreciable. The graph plotted in Fig. 4 also gives the point $\alpha_1 = \pi/2$ determined in [1] from results of ultrasound experiments in a strong magnetic field [4].

The figure confirms that equality (10) is well satisfied for any angles α_1. Thus, the model completely agrees with the experimental data even in cases of angular shear deformation.

4. RECONSTRUCTION OF COMPONENTS OF THE DEFORMATION POTENTIAL

An analysis has shown that the assumed simple model is consistent with all the available experimental observations. Now we can reconstruct (using available experimental information) patterns of the spatial distribution of the deformation potentials over the surface of a hole N-ellipsoid. Using the notation from the present study the renormalized deformation potential Λ_{nl} [see, for example, [5], formulas (2.2.2) and (2.8.5)] can be written for states on the Fermi surface as follows:

$$\frac{\partial E^*(\mathbf{k})}{\partial u_{nl}} - \frac{\partial E_F^*}{\partial u_{nl}} = \Lambda_{nl}(\mathbf{k}). \quad (11)$$

The states on the Fermi surface are described by [see (3)]

$$k^{-2} = \frac{1}{E_F^*}\sum_{i\le j} B_{ij}\cos\alpha_i\cos\alpha_j, \quad (12)$$

where $k \equiv |\mathbf{k}|$. For a fixed triplet of direction cosines deformation leads to changes in the Fermi energy and the elements of the matrix $\mathbf{B}$:

$$\frac{d(k^{-2})}{du_{nl}}\frac{1}{k^{-2}} = -\frac{\partial E_F^*}{\partial u_{nl}}\frac{1}{E_F^*} + \frac{1}{E_F^*}\frac{\partial E_F^*(k=\text{const})}{\partial u_{nl}}, \quad (13)$$

whence

$$\Lambda_{nl} \equiv \frac{\partial E_F^*(k=\text{const})}{\partial u_{nl}} - \frac{\partial E_F^*}{\partial u_{nl}} = \frac{\partial(k^{-2})}{\partial u_{nl}}\frac{E_F^*}{k^{-2}}. \quad (14)$$

The energy E_F^* was determined earlier. In addition, for an undeformed crystal the dimensions of the principal semiaxes of the ellipsoid $a_i = \sqrt{E_F^*/B_{ii}}$ are well-known so that k^{-2} can be calculated at the Fermi surface of the undeformed metal:

$$k^{-2} = \sum_{i=1}^{3}\frac{\cos^2\alpha_i}{a_i^2}. \quad (15)$$

Thus, the last fraction in equation (14) is known for any angles.

Data on the deformation dependence of the effective ellipsoid areas have now been published for the following types of deformation (for a summary of the data see [9]):

(a) isotropic tension–compression Ω,

(b) tetragonal shear $\gamma_{x'}$, $\gamma_{y'}$, $\gamma_{z'}$,

(c) one form of angular shear $\gamma_{x'y'}$.

In our notation these deformations are written as follows [see also the equality (9)]:

$$\Omega = \beta\begin{pmatrix} 1/3 & 0 & 0 \\ 0 & 1/3 & 0 \\ 0 & 0 & 1/3 \end{pmatrix},$$

$$\gamma_{x'} = \beta\begin{pmatrix} -1/2 & 0 & 0 \\ 0 & 1/4 & -3/4 \\ 0 & -3/4 & 1/4 \end{pmatrix}, \quad (16)$$

$$\gamma_{y'} = \beta\begin{pmatrix} -1/2 & 0 & 0 \\ 0 & 1/4 & 3/4 \\ 0 & 3/4 & 1/4 \end{pmatrix},$$

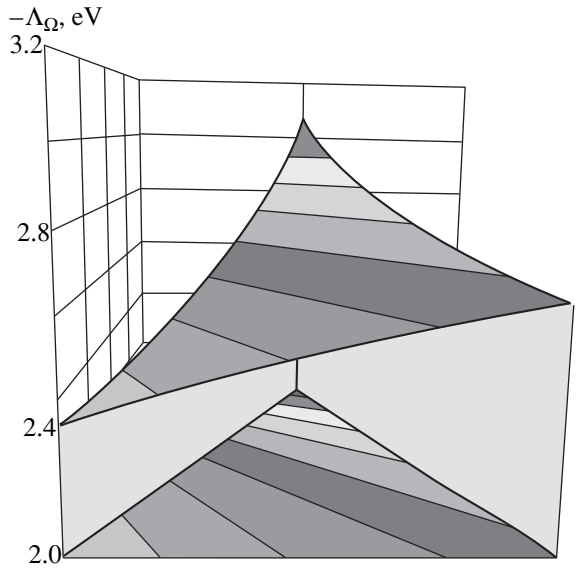

Fig. 5. Values of the deformation potential corresponding to deformation under isotropic tension–compression.

$$\gamma_{z'} = \beta\begin{pmatrix} 1 & 0 & 0 \\ 0 & -1/2 & 0 \\ 0 & 0 & -1/2 \end{pmatrix}.$$

4.1. Tension in Natural Axes

In the particular case of longitudinal deformations u_{nn} (or combinations of these deformations) only the three ellipsoid semiaxes vary with the result that the areas s_i of the three principal cross sections vary, see equality (8). Having determined the three values of $\partial(\ln a_i)/\partial u_{nn}$ from the experimental data we can calculate [see equations (14) and (15)] the corresponding component of the deformation potential for an arbitrary point on the ellipsoid surface:

$$\Lambda_{nn}(\alpha) = \frac{-2E_F^*\sum_i[\partial(\ln a_i)/\partial u_{nn}]a_i^{-2}\cos^2\alpha_i}{\sum_i a_i^{-2}\cos\alpha_i}. \quad (17)$$

We first applied this approach to the isotropic deformation Ω considered in Section 3.2 which allowed us to obtain for the first time the distribution pattern of the potential $\Lambda_\Omega = (\Lambda_{11} + \Lambda_{22} + \Lambda_{33})/3$ over the entire surface of the ellipsoid. This pattern is shown in Fig. 5.

We shall explain the principle of the graphical representation of the data on the deformation potential. The position of any point on the ellipsoid surface is uniquely defined by the three direction cosines α_i. In this case we have

$$\sum_i \cos^2\alpha_i \equiv 1.$$

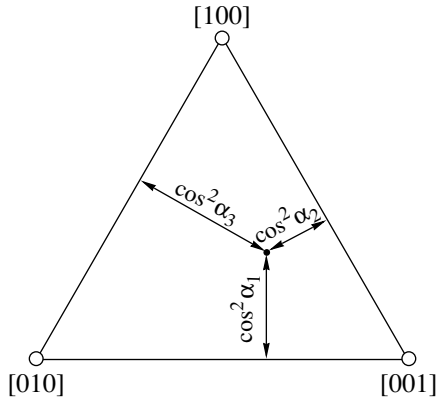

Fig. 6. Orientation triangle.

Then in our case it is sufficient to show the distribution of any component of the deformation potential merely in the principal octant ($\pi/2 \geq \alpha_1 \geq 0$, $\pi/2 \geq \alpha_2 \geq 0$, $\pi/2 \geq \alpha_3 \geq 0$) since the values in all the other octants can easily be obtained by applying simple symmetry concepts.

We shall take an equilateral triangle of unit height. The sum of the distances from any point inside the triangle to its three sides is one. Any direction from the principal octant may be represented by a point on the plane within this triangle of orientations, see Fig. 6. The distance from the corresponding side of the triangle should then be equal to the square of the direction cosine $\cos^2\alpha_i$. Thus, all the graphs of the deformation potential values are plotted above the orientation triangle.

Using this model we apply the same scheme to completely separate the patterns Λ_{ii} corresponding to the three elementary longitudinal deformations based on relationships derived from equalities (16) and (9), see Fig. 7:

$$\begin{aligned} u_{11} &\equiv \frac{2}{3}\gamma_{z'} + \Omega, \\ u_{22} &\equiv \gamma_{x'y'} - \gamma_{z'} + u_{11}, \\ u_{33} &\equiv u_{22} - 2\gamma_{x'y'}. \end{aligned} \tag{18}$$

For the parameters determining the complete pattern of tension–compression deformations in the principal axes we obtain the following sets of three values: $\partial(\ln a_i)/\partial u_{11}$ = –0.72, 1.49, 1.71, then $\partial(\ln a_i)/\partial u_{22}$ = –23.2, –14.5, –16.7, and finally $\partial(\ln a_i)/\partial u_{33}$ = 9.34, 1.35, 1.55. It should be noted that all four graphs demonstrate appreciable anisotropy.

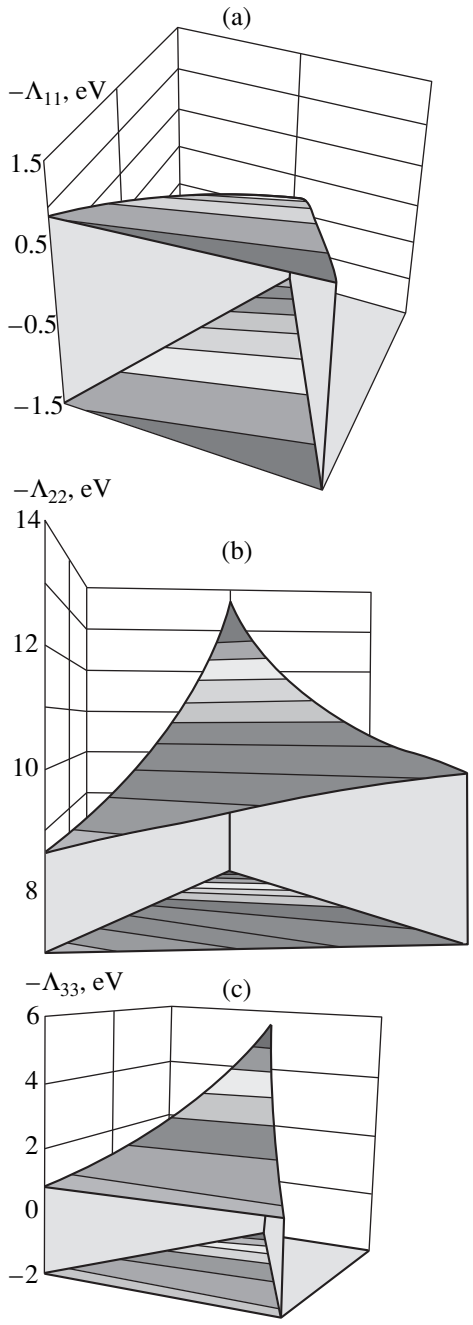

Fig. 7. Values of the deformation potentials corresponding to uniaxial tensile deformations u_{ii}.

4.2. Shear in Natural Axes

It follows from the relations (16) that the composite deformations $\gamma_{x'}$ and $\gamma_{y'}$ also contain information on the distortions u_{23} and u_{32}. In this case the difference $u_{23} - u_{32}$ is not a deformation and merely describes rotation of the body in space. Since rotation cannot lead to any change in the electronic spectrum, we obtain $\Lambda_{23} \equiv \Lambda_{32}$. Ultimately we can also determine the deformation potential corresponding to the distortion u_{23}.

We shall also assume that in this case the Fermi energy does not change. This statement may be substantiated by symmetry concepts. It is sufficient to assume for example that $(u_{23} + u_{32}) \sim (\gamma_{y'} - \gamma_{x'})$ and then bear in mind that the crystallographic directions x' and y' are equivalent. We also note that in this case it follows

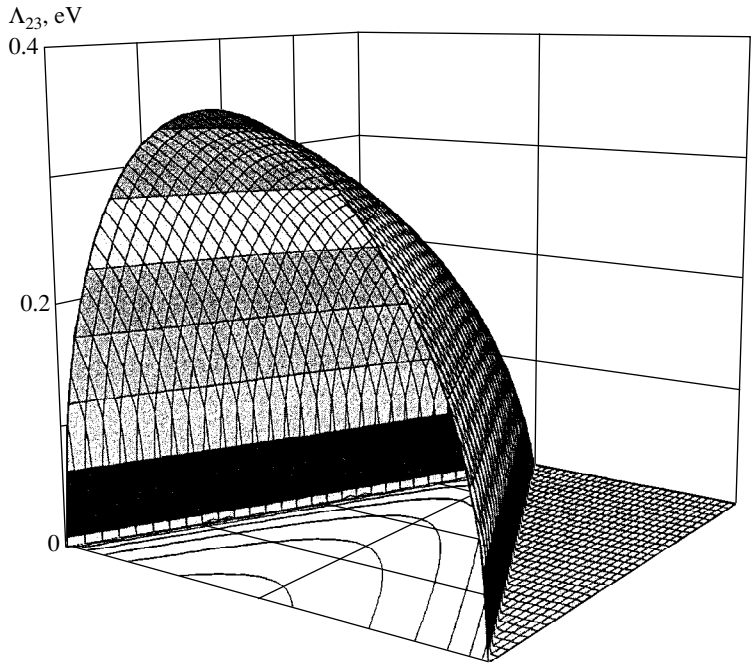

Fig. 8. Values of the deformation potential corresponding to the shear u_{23}.

from symmetry concepts that ε_0 remains constant and this implies that E_F^* also remains constant.

Effects associated with u_{23} can only be isolated from the experimental data for two ellipsoid cross sections: the cross section ρ_1 corresponds to the magnetic field orientation $\mathbf{H} \parallel [100]$ and ρ_2 is formed for $\mathbf{H} \parallel [011]$.

However, it follows from symmetry concepts (Section 2) that the outlines of the orbit ρ_1 cannot change in the presence of distortions of the type u_{23}. Thus, for a given orbit the experimentally measured changes in area for the deformations $\gamma_{x'}$ and $\gamma_{y'}$ are (a) the same and (b) form half of the deformation effect $\gamma_{z'}$ taken with the opposite sign.

The ρ_2 orbit has no symmetry constraints. As a result of the distortion u_{23} a change in area is observed which may be determined from the available data by one of two methods:

$$3\frac{\partial(\ln S)}{\partial u_{23}} = \frac{\partial(\ln S)}{\partial \gamma_{y'}} - \frac{\partial(\ln S)}{\partial \gamma_{x'}}, \tag{19}$$

$$3\frac{\partial(\ln S)}{\partial u_{23}} = 2\frac{\partial(\ln S)}{\partial \gamma_{y'}} + \frac{\partial(\ln S)}{\partial \gamma_{z'}}. \tag{20}$$

Both variants give the same value: $\partial(\ln S)/\partial u_{23} = 0.6$ for the ρ_2 orbit.

How is this value related to the parameters of the model (3), (12)? First, for any deformations every cross section has the form of an ellipse. Then, the distortion u_{23} conserves the diagonal elements of the matrix $\mathbf{B}$ although it leads to the appearance of a nonzero element B_{23}. Ultimately the cross section of the ellipsoid with the plane normal to $\mathbf{H} \parallel [011]$ conserves one of its semiaxes a_1. The second semiaxis $a_{\pi/4}$ changes. The energy of the state at the former Fermi surface satisfying the condition $\alpha_1 = 0$; $\alpha_2 = \alpha_3 = \pi/4$ increases by $(\partial B_{23}/\partial u_{23})u_{23}a_{\pi/4}^2/2$. This implies that after deformation the second semiaxis of the cross section of the isoenergy surface changes by

$$\partial a_{\pi/4} = -\frac{\partial B_{23}/\partial u_{23}}{2(B_{22} + B_{23})} u_{23} a_{\pi/4}.$$

Finally for the ρ_2 orbit we have

$$\frac{\partial(\ln S)}{\partial u_{23}} \equiv \frac{\partial(\ln a_{\pi/4})}{\partial u_{23}} = -\frac{\partial B_{23}/\partial u_{23}}{2(B_{22} + B_{33})}, \tag{21}$$

from which we obtain the following numerical value for the known parameters of the initial dispersion law

$$\partial B_{23}/\partial u_{23} = 40 \text{ (eV Å}^2\text{)}.$$

Now we can reconstruct the deformation potential Λ_{23} for any point on the model Fermi surface. Returning to equations (14) and (12), we obtain

$$\Lambda_{23}(\alpha) = \frac{(\partial B_{23}/\partial u_{23})\cos\alpha_2 \cos\alpha_3}{\sum_i a_i^{-2}\cos\alpha_i}. \tag{22}$$

Figure 8 gives the dependence of Λ_{23} on the position of the point on the N ellipsoid.

5. CONCLUSIONS

To conclude we have considered a very simple model of the dispersion law for small cavities on the Fermi surface of tungsten, known as hole ellipsoids. This contains a single fundamental assumption, that we can confine ourselves to elements no higher than third order in the expansion of the energy in terms of k_i. A comparison with the experimental data revealed no discrepancies between the model predictions and the experimental data.

The model was used for the first time to reconstruct the distribution of local values of the deformation potential for one of the sheets of the Fermi surface of the metal. The local values of Λ_{11}, Λ_{22}, and Λ_{33} and also the value of the potential Λ_Ω corresponding to isotropic expansion–compression were completely determined using the system of natural axes of the ellipsoid. Finally the values of Λ_{23} describing the shear were determined in terms of the natural axes.

It should be stressed that the patterns of Λ values obtained show complete agreement with the published experimental data on the deformation variations of the effective cross sections of the N ellipsoid without exception.

ACKNOWLEDGMENTS

This work was supported by the Russian Foundation for Basic Research.

REFERENCES

1. A. V. Tkach, Solid State Commun. **107**, 407 (1998).
2. V. V. Gudkov, I. V. Zhevstovskikh, N. A. Zimbovskaya, and V. I. Okulov, Zh. Éksp. Teor. Fiz. **100**, 1286 (1991) [Sov. Phys. JETP **73**, 711 (1991)].
3. A. V. Tkach, Physica B (Amsterdam) **263–264**, 236 (1999).
4. A. V. Tkach and A. B. Rinkevich, Fiz. Met. Metalloved. **84**, 79 (1977).
5. V. M. Kontorovich, Zh. Éksp. Teor. Fiz. **59**, 2116 (1970) [Sov. Phys. JETP **32**, 1146 (1970)].
6. N. W. Ashcroft and N. D. Mermin, in *Solid State Physics* (Holt, Rinehart and Winston, New York, 1976; Mir, Moscow, 1979), Vol. 2.
7. R. F. Girvan, A. V. Gold, and R. A. Phillips, J. Phys. Chem. Solids **29**, 1485 (1968).
8. D. Walsh, in *Solid State Physics: Simon Fraser University Summer School*, Vol. 1: *Electrons in Metals*, Ed. by J. F. Cochran, R. R. Haering, and R.H. Enns (Gordon and Breach, New York, 1968), Vol. 1, p. 127.
9. W. Joss, R. Griessen, and E. Fawsett, in *Landolt–Bornstein Numerical Data and Functional Relationships in Science and Technology. New Series* (Springer-Verlag, Berlin, 1983), Group III, 13(b),
10. J. E. Schirber, Phys. Lett. A **35**, 194 (1971).
11. I. V. Svechkarev and V. P. Pluzhnikov, Phys. Status Solidi B **5**, 315 (1973).
12. D. J. Stanley, J. M. Perz, and H. P. Au, Can. J. Phys. **54**, 1234 (1976).
13. D. J. Stanley, J. M. Perz, and M. J. G. Lee, Can. J. Phys. **55**, 344 (1977).
14. M. J. G. Lee, J. M. Perz, and D. J. Stanley, Phys. Rev. Lett. **37**, 537 (1976).
15. G. L. Bir and G. E. Pikus, *Symmetry and Stain-Induced Effects in Semiconductors* (Nauka, Moscow, 1972; Wiley, New York, 1975).

Translation was provided by AIP

Journal of Experimental and Theoretical Physics, Vol. 91, No. 2, 2000, pp. 393–398.
Translated from Zhurnal Éksperimental'noĭ i Teoreticheskoĭ Fiziki, Vol. 118, No. 2, 2000, pp. 448–454.

SOLIDS
Electronic Properties

Band Structure and CK_α Emission of Ultrathin Nanotubes

M. M. Brzhezinskaya[1, *], E. M. Baitinger[1], and V. I. Kormilets[2]

[1]*Chelyabinsk State Pedagogical University, Chelyabinsk, 454080 Russia*
[2]*Izhevsk Physicotechnical Institute, Ural Division, Russian Academy of Sciences, Izhevsk, 426000 Russia*
**e-mail: bmm@cpsi.urc.ac.ru*

Received February 8, 2000

Abstract—An attempt is made to calculate the energy bands and spectra of the characteristic CK_α emission of small-diameter carbon nanotubes. The calculated spectra for the nanotubes are compared with similar spectra for graphite monolayers used as a test object and with known experimental results for nanotubes. It is concluded that the x-ray emission spectra can be used to identify thin carbon nanotubes. A classification of solid-phase carbon is proposed which takes into account the position of carbon nanotubes in the family of allotropic carbon forms. The type of hybridization of the electrons in the carbon atom is used as the criterion for classification.

1. DESCRIPTION OF MODEL AND BAND STRUCTURE

The prediction of the various emission characteristics of carbon nanotubes is important not only for industrial applications but also for diagnostics during the synthesis process and at subsequent process stages [1]. Below we describe results of calculations of the band structure and the x-ray characteristics of the emission spectra of ultrathin carbon nanotubes.

Zigzag-shaped (3,3) and (4,4) nanotubes having diameters of 4.16 and 5.46 Å were modeled. The number of hexagons over the perimeter of the tubes is six in the first case and eight in the second. The *z*-axis is directed along the axis of the tube and the *x*-axis is directed along the radius inside the tube.

The energy band structure was determined at the first stage of the calculations The nanotube bands were calculated using the self-consistent method of full-potential linear muffin-tin orbitals (FP-LMTO) described in [2]. The method is based on density functional theory and belongs to a class of methods based on first principles. The exchange correlation potential was taken in the local density approximation in the Ceperley–Alder form [3] using the Perdeu–Zunger parametrization [4].

In order to use the band calculation method, a nanotube fragment was placed in an expanded cell whose height *z* was taken to be equal to the translation period in this direction ($\sqrt{3}\,a_0$; a_0 = 1.42 Å). In the (*x*, *y*) plane perpendicular to the nanotube axis the shape of the expanded cell was selected so that it corresponded to the rotational symmetry of the tube. For a (4,4) structure in which four units (a total of 16 atoms) are distributed on a circle we took a square. For a (3,3) structure in which three units (a total of 12 atoms) are distributed on a circle we took a hexagon.

The test object was a graphite monolayer (graphene sheet) whose band structure is well-known. The expanded cell in this case contained two atoms. The band dispersion for the test object (see Table 1) showed satisfactory agreement with the results of calculations made by other authors and also with the experimental results. Experimental and calculated data are only given in Table 1 for the Γ point in the two-dimensional Brillouin zone. However, satisfactory agreement was also obtained for other extreme points in the Brillouin zone. The band notation in Table 1 is conventional.

Results of calculations of the nanotube bands are plotted in Fig. 1. Figure 1a shows the band dispersion of a (3,3) nanotube while Fig. 1b gives that for a (4,4) nanotube. The number of valence bands in Figs. 1a and 1b is 24 and 32, respectively. The calculations were made for three mutually perpendicular directions (k_x, k_y, k_z). These results show that energy dispersion is only observed along the tube axis, which corresponds to the direction of the *z*-axis. The absence of dispersion in the other two directions is attributable to the choice of fairly large values of the translation parameters (or intertube spacings) $d_x = d_y = 15$ au, i.e., intertube interactions are in fact neglected. The translation period selected for the calculations along the *z* axis of the tube precisely corresponds to that actually observed for zigzag tubes (d_z = 4.65 au).

Figure 2 shows the dispersion of the *p*-bands along the axes of (3,3) (a) and (4,4) (b) nanotubes near the Fermi energy. The values of the wave number k_z from the center ($k_z = 0$) to the edge of the Brillouin zone in the *z* direction (point *A* or *X*) are plotted on the abscissa. The band edge lies at a distance of 1.614 $(\text{au})^{-1}$ from Γ for the (3,3) nanotube and 1.613 $(\text{au})^{-1}$ for the (4,4) nanotube. This choice of electron energy range (–3…–2 eV) is not arbitrary since this is the range in which the main distinguishing features of *p*-band dispersion are obtained.

Table 1. Comparison of experimental data and results of theoretical calculations of the energy bands of graphite (at the center of the Brillouin zone) from data given by various authors. The energy (in eV) is measured from the Fermi level

Subband notation	Calculations				Experiments	
	[6]	[7]	[5, 8]	present study	[9]	[10, 11]
Valence band						
σ	–20.8	–19.2	–19.2	–19.0		–20.75 [10]
σ	–20.2	–18.9		–18.86		
π	–8.2	–7.9	–7.8	–7.70	–8.65 ± 0.1	–7.75, –8.7 [11]
π	–6.7	–6.3	–6.4	–6.58	–7.25 ± 0.1	
σ	–4.7	–4.1	–3.4	–4.01	–4.95 ± 0.1	–3.75 [10]
Conduction band						
σ*	7.0	7.1	5.7	6.03		
σ*	7.3	7.3	7.9	6.64		7.2 [10]
σ*	7.7	7.3	8.0	8.79		
π*	10.5			12.20		10.7 [10]

The inset to Fig. 2b also shows the dispersion in the π-band of the graphene sheet. The Γ*K* direction in the hexagonal Brillouin zone of the graphene sheet specifically corresponds to the Γ*X* (Γ*A*) direction in the zigzag nanotubes.

Qualitative agreement is observed between the dispersion of the π-bands in the graphite monolayer and in the (4,4) nanotube; the bands intersect near the Fermi surface. However substantial differences are also found. First, the degeneracy of similar bands is lifted by 0.5 eV or more. In our opinion, this is attributable to the nonequivalent states of the neighboring carbon atoms in the zigzag tube as a result of the considerable curvature of the graphene sheet. This degeneracy lifting process should most probably decrease as the tube diameter increases. The point of intersection of the bands shown in Fig. 2b was shifted into the Brillouin zone by 1/3 from the Γ*X* direction compared with the results for the graphene sheet. This effect has already been described in the literature [12]. Another interesting observation is that the points of intersection of the bands are shifted downward on the energy scale by 0.2–0.9 eV. This shift leads to changes in the density of valence states and conduction-band states near the Fermi energy.

We shall now consider Fig. 2a. The *p*-band dispersion for the (3,3) nanotube differs substantially from that for the (4,4) nanotube and the graphene sheet.

For the (3,3) nanotube (Fig. 2a) there are eight subbands of which some are filled with electrons and some

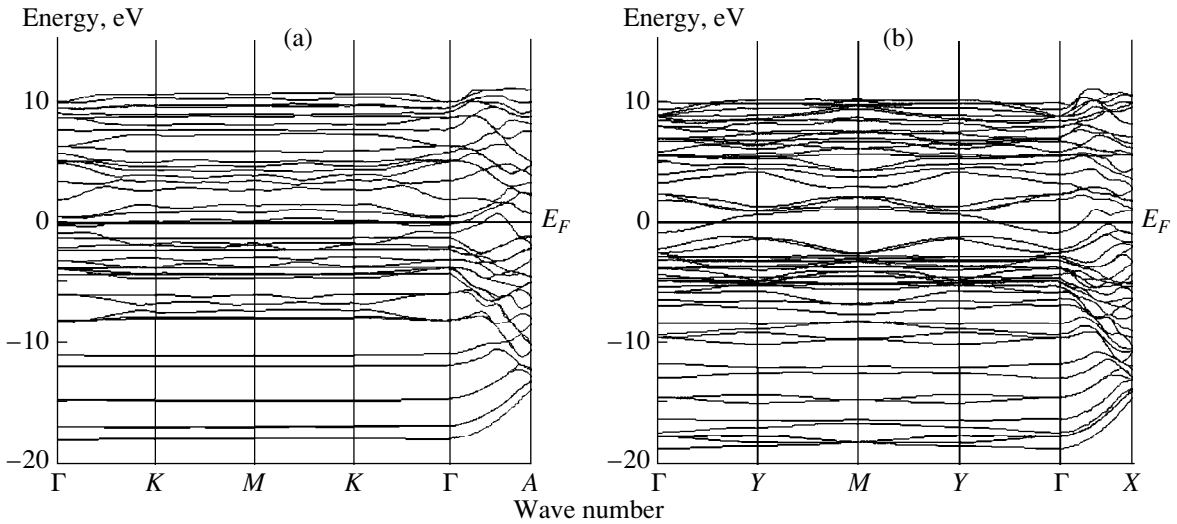

Fig. 1. Energy dispersion along the three characteristic directions of the Brillouin zone for (a) (3,3) and (b) (4,4) nanotubes.

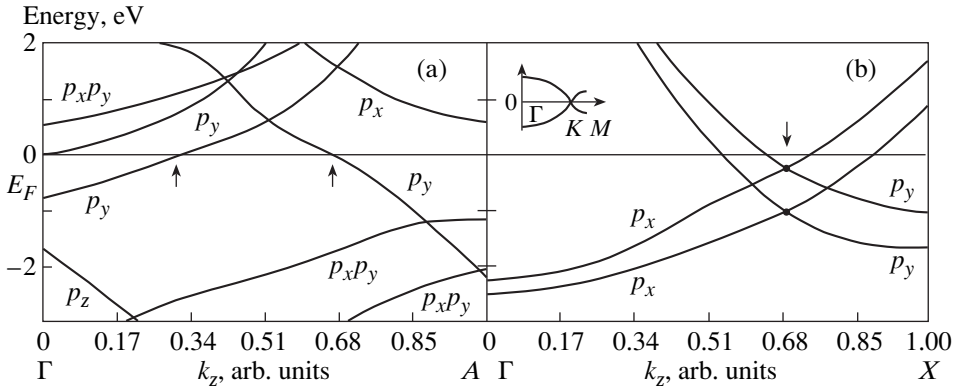

Fig. 2. Dispersion of *p*-bands along the k_z-axis near the Fermi level for (a) (3,3) and (b) (4,4) nanotubes. The inset shows the dispersion of the π band in a graphite monolayer. The letters on the curves indicate the preferential symmetry of the wave functions of these subbands.

are empty. Only one subband is formed by p_z electrons although this is situated fairly deep within the valence band. Its top can be seen at the point Γ at the energy −1.7 eV. Similar bands generally have wave functions of mixed p_x and p_y symmetry. The unusual behavior of the dispersion curves is, in our opinion, attributable to lifting of the degeneracy of similar bands, a reduction in their width, and also to inversion. Two subbands intersect the Fermi level, one intersecting it at a distance of 1/3 (Γ*A*) and the other at a distance of 2/3 (Γ*A*) (see vertical arrows in Fig. 2a). These subbands are most likely responsible for the electrophysical properties of the (3,3) nanotube. The sign and magnitude of the curvature of these subbands near the Fermi level differs. They may be sources of two types of carriers which not only have effective masses of different magnitude and sign but also different dispersion laws.

A comparison between the results for two nanotubes of different diameter shows that the thinner nanotubes are less stable because of the lower binding energy of the valence electrons. The bands become narrower and are expelled upward on the energy scale. In order to illustrate this Table 2 gives the band energy at the extreme points (band edges) for nanotubes and graphene sheet. Energy values for a (5,5) nanotube were taken from [13]. These data convincingly demonstrate that twisting of

Table 2. Comparison of results of theoretical calculations of the energy bands of nanotubes and graphene sheet. The energy (in eV) is measured from the Fermi level

Conventional subband notation	Points	Nanotubes			Graphene sheet
		(3, 3)	(4, 4)	(5, 5)	
σ_1	Γ	–17.76	–18.57	–20.0	–22.0
	*X**	–13.61	–14.37	–16.8	–14.6
σ_2	Γ	–7.92	–5.83	–3.0	–4.7
	X	–10.38	–9.44	–13.8	–14.6
σ_3	Γ		–5.39		–4.7
	X		–9.01		–10.6
π	Γ	–7.88	–9.24	–8.0	–6.7
	X	2.09	1.71	1.4	0
π*	Γ	8.79	12.40		12.20
	X	2.09	4.34		
σ_2^*	Γ		9.34		6.64
	X		15.40		
σ_1^*	Γ	8.12	8.80		8.79
	X	11.72	13.40		

* Point *X*, or *A*, or *K* depending on type of symmetry of the structure.

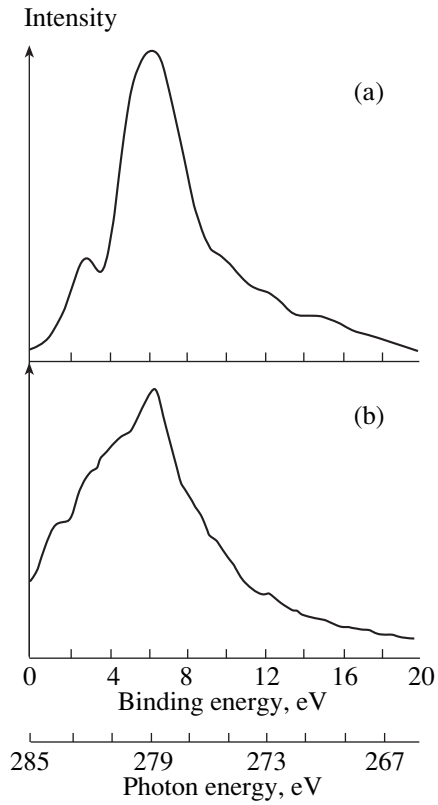

Fig. 3. Emission spectra (a) calculated for graphene sheet and (b) measured for pyrographite. Zero binding energy corresponds to the Fermi energy.

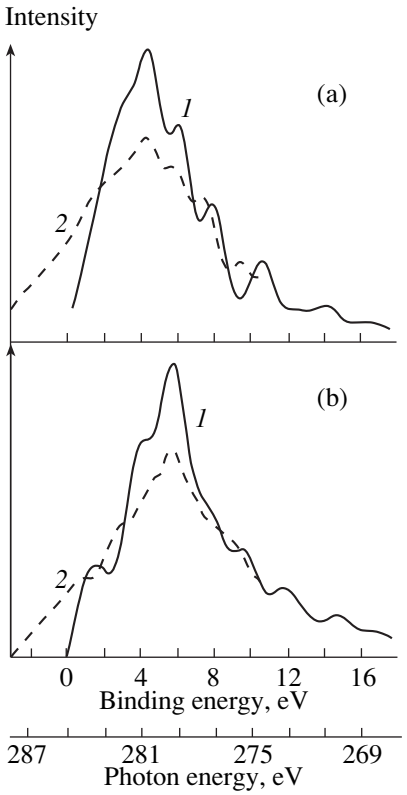

Fig. 4. Calculated spectra (solid curves) of (a) (3,3) and (b) (4,4) carbon nanotubes as compared with experimental spectra [15] (dashed curves) of (a) light soot and (b) multilayer nanotubes.

graphene sheet into a tube promotes narrowing of the subbands and shifts them toward lower binding energies. This conclusion also follows from an analysis of Fig. 2.

2. CALCULATIONS OF THE CK_α BAND AND COMPARISON WITH EXPERIMENT

Taking into account optical selection rules and the polarization of the characteristic radiation, the emission spectrum of carbon is determined only by the partial density of *p*-states in the valence band. The probability of photon emission cannot significantly change the shape of the emission band which extends over the wavelength range 4.3–4.7 nm. As a result, we identified the intensity distribution in the emission spectrum with the similar density distribution of the *p*-states $N_p(E)$, i.e.,

$$I(E) = \sum_p \omega \left|M^0_{p,\,1s}\right|^2 N_p = k \sum_p N_p(E),$$

where $\left|M^0_{p,\,1s}\right|^2$ is the probability of an optical transition from the valence band to the island level, and ω is the frequency of the characteristic radiation. Assuming for simplicity that *k* is one, we obtain the model X-ray emission spectrum. We assumed that the device used to analyze the radiation collimates rays leaving the sample not only perpendicular to the graphene sheet or the tube axis but also gliding along these. The only treatment of the calculated spectral curves involved smoothing the dependence $I(E)$.

The main results are plotted in Fig. 3 for the test object. The experimental X-ray emission spectrum was obtained for a sample of pyrographite [14]. For the test object the agreement between the calculated curve and the experiment should be taken to be satisfactory.

Figure 4 gives calculated CK_α spectra for carbon nanotubes (solid curves). The dashed curves give the experimental results obtained in [15]. The curves were matched according to the position of the principal maximum. The positions of the Fermi levels differed which is probably attributable to the experimental error of the measuring device.

Figure 4a contains two spectra: that calculated for a (3,3) nanotube and an experimental spectrum obtained for a sample of "light soot" which was assumed to contain predominantly single-layer carbon nanotubes. Figure 4b also shows two spectra: an experimental spec-

trum for multilayer nanotubes and a theoretical one calculated for a model (4,4) nanotube. In both cases the agreement between the calculations and the experiment can be considered to be satisfactory.

At low energies (0–3 eV) the CK_α emission spectrum of the (3,3) nanotube exhibits no significant singularities (Fig. 4a). We merely observe the presence of a small excess at a binding energy of around 3 eV. The dominant structure in the form of peaks and excesses is observed on the right shoulder of the spectral curve. We can identify at least three clearly distinguishable local maxima at binding energies of 6, 8, and 10 eV. The experimental spectrum exhibits the same peaks which are shifted negligibly toward lower binding energies.

In contrast, the calculated spectrum of the (4,4) nanotube typically exhibits spectral singularities at low binding energies on the left shoulder of the curve [16]. The spectrum of the multilayer nanotubes exhibits similar characteristics (Fig. 4b, dashed curve).

Another general dependence characteristic of the calculated spectra can also be identified: the principal peak shifts toward higher binding energies as we go over from the small-diameter to the large-diameter tube and then to the graphene sheet. For example, for the (3,3) nanotube this peak is observed at a binding energy of around 4.5 eV, for the (4,4) nanotube at 5.5 eV, and for the graphene sheet at 6 eV (see Fig. 3).

To conclude we note that according to the data plotted in Fig. 4, the profile of the CK_α spectra of carbon nanotubes is determined not so much by the number of layers as by the curved surface of the twisted graphene sheet.

3. ELECTRON HYBRIDIZATION IN NANOTUBES

When analyzing the electronic structure of carbon nanotubes we must not overlook the problem of the degree of hybridization of the atomic orbitals forming the valence wave functions.

By relating the densities of the *s*- and *p* states to the total density of states, we established that for (3,3) and (4,4) nanotubes the conventional formula determining the hybridization of the atomic orbitals may be expressed in the form $S^{1,4}p_z^1p^{1.6}$. Here *p* is taken to mean to total contribution of the p_x and p_y orbitals to the entire system of valence bonds. These valence states are oriented radially and probably play the role of π states in carbon tubes. As a result of bending the graphene sheet the π electrons become partially mixed with the σ system.

The curvature of the graphene sheet gives it a third dimension as it were. For this reason it is also appropriate to note that the (111) layer in diamond also has deflections in the form of holes or cells which are repeated periodically in space. The diameter of the spherical surface corresponding to this deflection in diamond is 4.62 Å. For condensed carbon this can be arbitrarily described as critical since it corresponds to the maximum hybridization of the valence electrons. The diameter of the (3,3) nanotube under study, 4.16 Å, is less than the critical value whereas the diameter of the (4,4) nanotube (5.46 Å) is larger than critical. This may well explain the substantial difference between the properties of these nanotubes.

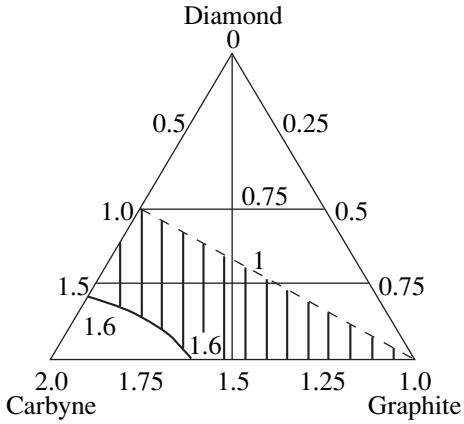

Fig. 5. Diagram showing the position of carbon nanotubes in the family of allotropic forms of carbon. The numbers on the diagram correspond to the number of π electrons (per atom) in a particular modification of carbon. The $i_\pi = 1.6$ line corresponds to the (3,3) and (4,4) nanotubes under study.

We attempted to determine the position of carbon nanotubes in the family of allotropic forms of carbon using the type of hybridization of the electrons in the carbon atom as the classification criterion. For this we used a qualitative three-component diagram (Fig. 5) described recently in [17]. In the opinion the authors [17] the three-component carbon phase has features of the three known allotropic modifications of carbon: graphite, carbyne, and diamond. In the variant of this scheme assumed by us each side of the equilateral triangle in Fig. 5 should correspond to the number axis i_π (i_π is the number of π electrons in the atom). In our view, the inner part of the triangle specifically corresponds to the situation where the atom simultaneously exhibits the features of three allotropic forms. For example, the dashed line in Fig. 5 ($i_\pi = 1$) not only corresponds to the phase state of graphite but also to some more complex formations having a single π electron. The number of nonhybrid π electrons in the ultrathin nanotubes studied here is 1.6. The line inside the triangle having this value is shown in heavy print. It corresponds to the phase state of a carbon medium consisting of ultrathin nanotubes. As the tube diameter increases, this line should shift toward the dashed line $i_\pi = 1$. Hence, the shaded part of the diagram corresponds to the phase state of nanotubular carbon.

4. CONCLUSIONS

The results of the band calculations presented above supplement the known information [18] on the electronic structure of carbon nanotubes. For very small diameters the distortion of the band spectrum is substantial, involving narrowing of the bands and lifting of the degeneracy of some of them. This leads to changes in the properties of the nanotubes. In particular the CK_α emission spectra were sensitive to distortion of the band structure. The experimental results available in the literature confirm this.

A general scheme for hybridization of all forms of carbon, including nonequilibrium ones, has been presented and the position of nanotubes in this scheme has been determined.

REFERENCES

1. A. V. Eletskiĭ, Usp. Fiz. Nauk **167**, 945 (1997) [Phys. Usp. **40**, 899 (1997)].
2. K. H. Weyrich, Phys. Rev. B **37**, 10269 (1988).
3. D. M. Ceperley and B. J. Alder, Phys. Rev. Lett. **45**, 566 (1980).
4. J. P. Perdeu and A. Zunger, Phys. Rev. B **23**, 5048 (1981).
5. R. Ahuja, S. Auluck, J. Trygg, *et al.*, Phys. Rev. B **51**, 4813 (1995).
6. R. F. Willis, B. Fitton, and G. S. Painter, Phys. Rev. B **9**, 1926 (1974).
7. R. C. Tatar and S. Rabii, Phys. Rev. B **25**, 4126 (1982).
8. R. Ahuja, S. Auluck, J. M. Wills, *et al.*, Phys. Rev. B **55**, 4999 (1997).
9. D. Marcand, C. Fretigny, M. Lagues, *et al.*, Phys. Rev. B **30**, 4788 (1984).
10. A. R. Law, M. T. Jonson, and H. P. Hughes, Phys. Rev. B **34**, 4289 (1986).
11. T. Takahashi, H. Tokailin, and T. Sagawa, Solid State Commun. **52**, 765 (1984).
12. N. Hamada, S. Sawada, and A. Oshiyama, Phys. Rev. Lett. **68**, 1579 (1992).
13. J. W. Mintmire and C. T. White, Carbon **33**, 893 (1995).
14. V. Yu. Karasov and S. N. Shamin, in *Physical Properties of Carbonaceous Materials* (Chelyabinsk, 1983), p. 65.
15. L. B. Bulusheva, Candidate's Dissertation in Chemistry (Institute of Inorganic Chemistry, Siberian Division, Russian Academy, Novosibirsk, 1998).
16. M. M. Brzhezinskaya, E. M. Baĭtinger, and V. I. Kormilets, Fiz. Tverd. Tela (St. Petersburg) **41**, 1511 (1999) [Phys. Solid State **41**, 1383 (1999)].
17. *Carbyne and Carbynoid Structures*, Ed. by R. B. Heimann, S. E. Evsyukov, and L. Kavan (Kluwer, Dordrecht, 1999).
18. A. L. Ivanovskiĭ, *Quantum Chemistry in Materiology: Nanotubular Forms of Substance* (Ural. Otd. Ross. Akad. Nauk, Yekaterinburg, 1999).

Translation was provided by AIP

Journal of Experimental and Theoretical Physics, Vol. 91, No. 2, 2000, pp. 399–406.
Translated from Zhurnal Éksperimental'noĭ i Teoreticheskoĭ Fiziki, Vol. 118, No. 2, 2000, pp. 455–464.

SOLIDS
Electronic Properties

Nature of the Low-Temperature Colossal Magnetoresistance of $La_{0.35}Nd_{0.35}Sr_{0.3}MnO_3$ Epitaxial Films

A. I. Abramovich[1], L. I. Koroleva[1,] *, A. V. Michurin[1], R. Shimchak[2], and S. Deev[2]

[1]*Moscow State University, Moscow, 119899 Russia*

[2]*Institute of Physics, Polish Academy of Sciences, Warsaw, 02-668 Poland*
**e-mail: koroleva@ofef343.phys.msu.su*

Received February 16, 2000

Abstract—The colossal negative magnetoresistance (approximately 12%) in a field of 8.4 kOe over a wide range of temperatures below the Curie point $T_C \approx 240$ K in a single-crystal $La_{0.35}Nd_{0.35}Sr_{0.3}MnO_3$ film on a single-crystal (001)$ZrO_2(Y_2O_3)$ wafer substrate is discussed. Isotherms of the magnetoresistance of this film reveal that its absolute value increases with the field, abruptly in the technical magnetization range and almost linearly in stronger fields. For three single-crystal films of the same composition on (001)$LaAlO_3$, (001)$SrTiO_3$, and (001)MgO substrates, colossal magnetoresistance only occurred near $T_C \approx 240$ K and at $T < T_C$ it increased weakly, almost linearly, with the field. In the film on a $ZrO_2(Y_2O_3)$ substrate the electrical resistivity was almost 1.5 orders of magnitude higher than that in the other three films. It is shown that this increase is attributable to the electrical resistance of the interfaces between microregions having four types of crystallographic orientations, while the magnetoresistance in the region before technical saturation of the magnetization is attributable to tunneling of polarized carriers across these interfaces which coincide with the domain walls (in the other three films there is one type of crystallographic orientation). The reduced magnetic moment observed for all four samples, being only 46% of the pure spin value, can be attributed to the existence of magnetically disordered microregions which originate from the large thickness of the domain walls which is greater than the size of the crystallographic microregions and is of the same order as the film thickness. The colossal magnetoresistance near T_C and the low-temperature magnetoresistance in fields exceeding the technical saturation level can be attributed to the existence of strong *s–d* exchange which is responsible for a steep drop in the carrier mobility (holes) and their partial localization at levels near the top of the valence band. Under the action of the magnetic field the carrier mobility increases and they become delocalized from these levels. © *2000 MAIK "Nauka/Interperiodica".*

1. INTRODUCTION

Although manganites having a perovskite structure have been known for some time [1, 2], they have attracted a new wave of interest since 1995 following the observation of colossal magnetoresistance in thin films of various compositions at room temperature. These compositions can be used as the basis to develop various sensors. The colossal magnetoresistance in these compounds is observed in a narrow temperature range near the Curie point T_C. Since any device should have stable characteristics in the operating temperature range, for practical applications it is important to extend the range of temperatures in which colossal magnetoresistance could occur. It has been noted in various studies using both bulk and thin-film polycrystalline samples that a high magnetoresistance is observed at low temperatures and the peak on the curve of the absolute magnetoresistance as a function of temperature broadens substantially near T_C [3–17]. In weak magnetic fields before technical saturation of the magnetization was achieved, colossal magnetoresistance was ascribed to spin-polarized tunneling between granules [9] or scattering of carriers within domain walls which generally coincide with intergranular boundaries [4]. However, in some of these studies it was noted that in stronger magnetic fields the absolute value of the magnetoresistance continued to increase almost linearly with the field. A similar almost linear increase in the absolute value of the magnetoresistance at low temperatures was also observed in single-crystal samples. This phenomenon has not been explained.

In an earlier study we observed that $La_{0.85}Sr_{0.15}MnO_3$ films on an (001)$ZrO_2(Y_2O_3)$ single-crystal wafer substrate exhibit colossal magnetoresistance over a wider temperature range than films on a (001)$LaAlO_3$ single-crystal wafer substrate [18]. The problem for the present study was to determine whether colossal magnetoresistance could be observed over a wide temperature range in single-crystal manganite films. For this purpose we studied thin single-crystal films of $La_{0.35}Nd_{0.35}Sr_{0.3}MnO_3$ on substrates of (001)$SrTiO_3$, (001)$LaAlO_3$, (001)MgO, and ($ZrO_2(Y_2O_3)$ single-crystal wafers. This composition is attractive because it is almost at the morphotropic boundary between the orthorhombic (*Pnma*) and rhombohedral (*R*3*c*) structures. Thus, the distortions of the

perovskite structure are so small that they cannot be detected by X-ray analysis. For this reason the lattice stresses typical of manganite films are very small in these films and need not be taken into account when discussing the reasons for the colossal magnetoresistance at low temperatures.

We established that the film on $ZrO_2(Y_2O_3)$ exhibits colossal magnetoresistance not only near T_C but also at $T < T_C$ as far as 80 K, the lowest temperature at which studies have been made.

Another problem for the present study was to describe the physical reasons for the colossal magnetoresistance observed by us over a wide range of temperature in the single-crystal film described above and also for the increase in the absolute value of the magnetoresistance with field at $T < T_C$ observed in all the films studied in magnetic fields exceeding the technical magnetization saturation level.

2. PREPARATION OF THIN FILMS AND EXPERIMENTAL METHOD

The films were prepared by metal organic chemical vapor deposition (MOCVD) using an aerosol source of vapor of metal organic compounds (La, Nd, Sr, and Mn dipivaloylmethanates [19]), The substrates were 1 mm thick single-crystal substrates of (001)$ZrO_2(Y_2O_3)$, (001)$LaAlO_3$, (001)$SrTiO_3$ (in a pseudocubic arrangement) and (001)MgO. The films were deposited in a vertical reactor with an inductively heated substrate. After deposition the films were additionally annealed in oxygen at the deposition temperature (750°C) for 30 min.

An X-ray diffraction analysis of the films, including determining the phase composition, the orientation and lattice parameters, was made using a Siemens D5000 four-circle diffractometer with a secondary graphite monochromator (CuK_α radiation). The composition of the films was determined by X-ray structural analysis (using a CASCAN scanning electron microscope).

The magnetization of the thin films was determined using a SQUID magnetometer and the electrical resistance was determined by a four-probe method. The magnetoresistance was measured in the plane of the film when the current through the film was parallel to the magnetic field **H**.

3. EXPERIMENTAL RESULTS

3.1. Crystallographic Properties

A θ–2θ sweep showed that the films on $LaAlO_3$, $SrTiO_3$, and MgO are (001) oriented while that on $ZrO_2(Y_2O_3)$ is (110) oriented. The planar orientation was determined using φ sweeping. The films on $LaAlO_3$, $SrTiO_3$, and MgO revealed epitaxial ordering with the substrate known as the "cube on cube" growth mode. The film on $ZrO_2(Y_2O_3)$ also exhibits planar orientation but this is more complex. In this case the bulk diagonals of the perovskite cubes are parallel to the diagonals of the faces of the fluorite cube in the $ZrO_2(Y_2O_3)$ structure and there are four equivalent orientational variants:

(1) $[1-11]_f \parallel [110]_s$, $[-112]_f \parallel [-110]_s$;

(2) $[1-11]_f \parallel [110]_s$, $[-112]_f \parallel [-1-10]_s$;

(3) $[1-11]_f \parallel [-110]_s$, $[-112]_f \parallel [110]_s$;

(4) $[1-11]_f \parallel [-110]_s$, $[-112]_f \parallel [-1-10]_s$;

where the indices *f* and *s* denote the film and the substrate, respectively. This has the result that in Mn–O–Mn–O⋯ chains angles of 19.5°, 70.5°, and 90° are formed on transition from one to another of the sections having the different crystallographic orientations listed above. A similar orientation was observed earlier in $La_{1-x}Sr_xMnO_3$ films on a $ZrO_2(Y_2O_3)$ substrate [18].

It can be seen from the table, which gives the lattice parameters of the films, that their crystal structure is close to pseudocubic: the interplane parameter is similar to the intraplane parameter and the latter cannot be resolved. These parameters do not vary for films on different substrates. No reflections other than those typical of a simple perovskite structure were observed. This is because the $La_{0.35}Nd_{0.35}Sr_{0.3}MnO_3$ composition under study for which the average ionic radius of the A cation is 1.225 A (tolerance factor 0.922) is positioned almost on the morphotropic boundary between the orthorhombic *Pnma* and rhombohedral *R*3*c* structures. The distortions of the perovskite structure are thus so small that they are below the experimental accuracy. This is evidently why the lattice stresses typical of manganite films almost relax in these films.

3.2. Magnetic Properties

The magnetization *M* of the films was measured in a magnetic field applied parallel to the plane of the film and corrections were introduced to the magnetization of the substrate. Figure 1 gives the dependence *M*(*H*) for all the films at $T = 5$ K. It can be seen that the magnetization of all the films, except that on MgO, saturates rapidly in a field of a few kilo-oersted. For the film on MgO saturation in the range 7–25 kOe is followed by an almost linear increase in *M* with further increasing field (the maximum measured field is $H = 50$ kOe) and the magnetic moment per chemical formula unit increases from $1.9\mu_B$ to $2.6\mu_B$. The limiting hysteresis loops of all the films are fairly narrow and the coercive force does not exceed 300 Oe. Curves of the temperature dependence of the initial magnetic susceptibility *M*/*H* ($H = 10$ and 100 Oe) were used to determine the Curie point T_C by extrapolating the steepest part of the curves (*M*/*H*)(*T*) to its intersection with the temperature axis. The values of T_C for all the films studied here are given in the table.

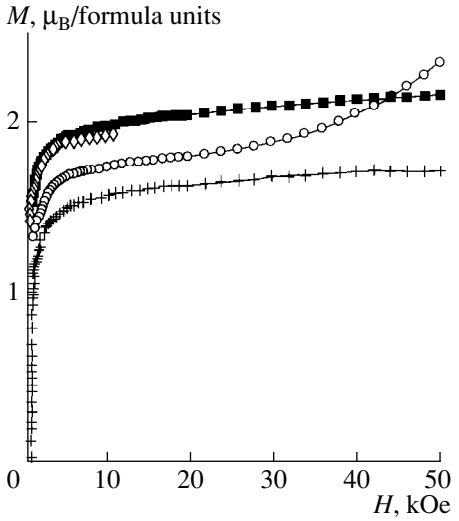

Fig. 1. Dependence of the magnetization M of $La_{0.35}Nd_{0.35}Sr_{0.3}MnO_3$ thin films on various substrates on the magnetic field H parallel to the surface of the film: (○) MgO; (■) $SrTiO_3$; (+) $LaAlO_3$; (◇) $ZrO_2(Y_2O_3)$ at $T = 5$ K.

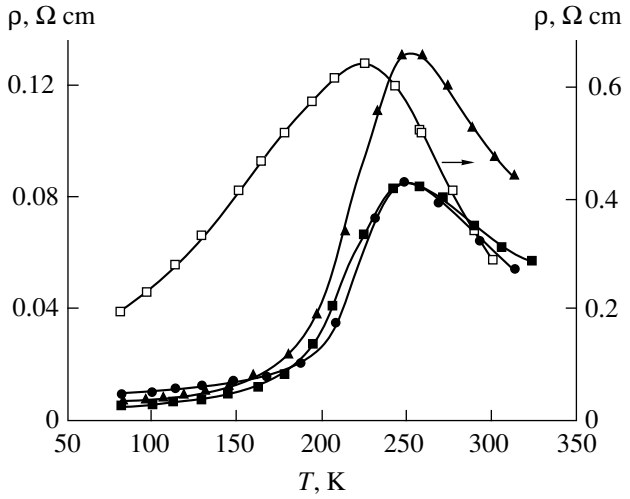

Fig. 2. Temperature dependence of the electrical resistivity ρ of $La_{0.35}Nd_{0.35}Sr_{0.3}MnO_3$ on various substrates: (□) $ZrO_2(Y_2O_3)$; (■) $SrTiO_3$; (●) MgO; (▲) $LaAlO_3$.

3.3. Electrical Properties

Figure 2 gives the temperature dependence of the electrical resistivity ρ for all the films studied. Figure 3 gives the temperature dependence of the magnetoresistance $\Delta\rho/\rho = (\rho_H - \rho_{H=0})/\rho_{H=0}$ for films on $SrTiO_3$ and $ZrO_2(Y_2O_3)$. Figure 4 shows Δρ/ρ isotherms at various temperatures for these films. The curves of $(\Delta\rho/\rho)(T)$ and $(\Delta\rho/\rho)(H)$ for films on MgO and $LaAlO_3$ are similar to those plotted in Figs. 3a and 4a for films on $SrTiO_3$. It can be seen from Figs. 3 and 4 that the magnetoresistance is negative. Our studies showed that Δρ/ρ does not depend on the direction of the electric current density in the plane of the film nor on the angle between this direction and the direction of the magnetic field, i.e., the magnetoresistance is isotropic in the plane of the film. The temperatures of the maxima on the curves $\rho(T)$ and the minima on the curves $(\Delta\rho/\rho)(T)$ are given in the table for all the films studied.

Magnetic, electrical, and crystallographic characteristics of $La_{0.35}Nd_{0.35}Sr_{0.3}MnO_3$

Characteristics	Substrate			
	MgO	$LaAlO_3$	$SrTiO_3$	$ZrO_2(Y_2O_3)$
T_C, K (H = 10 Oe)	242	231	219	
T_C, K (H = 100 Oe)		241	223	245
M, μ_B/formula units: magnetization	1.7	1.6	2	1.9
T_{max}, K: temperature of maximum resistivity ρ	252	252	252	225
T_{min}, K: temperature of minimum magnetoresistance Δρ/ρ (H = 8.4 kOe)	228	223	213	225
ρ_{max}, Ω cm: maximum ρ	0.085	0.13	0.084	0.63
$\rho_{82\ K}$, Ω cm: value of ρ at 82 K	0.0089	0.0059	0.0040	0.19
$\lvert\Delta\rho/\rho\rvert_{max}$: maximum absolute magnetoresistance (H = 8.4 kOe)	0.34	0.23	0.22	0.13
$\lvert\Delta\rho/\rho\rvert_{82\ K}$ (T = 82 K, H = 8.4 kOe)	0.04	0.03	0.03	0.11
Film thickness, Å	4100	5500	5500	5500
Interplane parameter, Å	3.882 ± 0.001	3.880 ± 0.002	3.872 ± 0.001	3.874 ± 0.001
Intraplane parameter, Å	3.876 ± 0.002	3.875 ± 0.002	3.878 ± 0.001	3.881 ± 0.002
Perovskite cell volume, $Å^3$	58.32 ± 0.08	58.26 ± 0.09	58.23 ± 0.05	58.25 ± 0.06

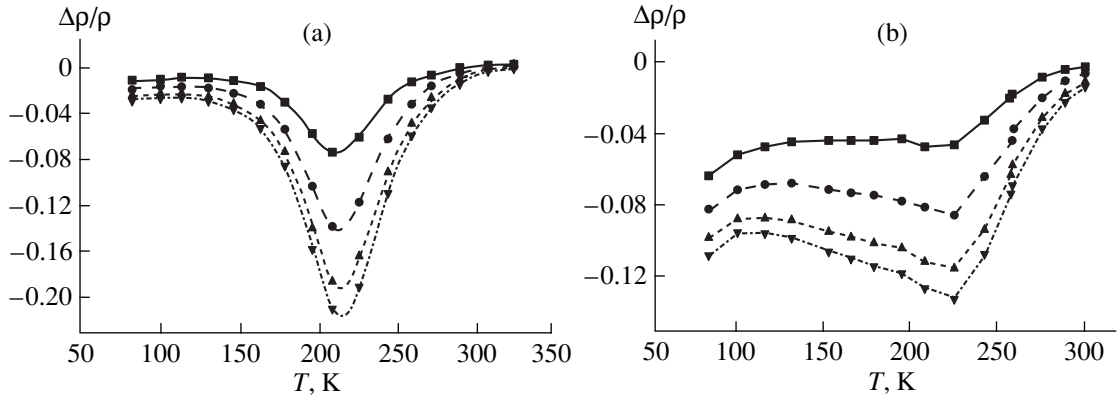

Fig. 3. Temperature dependences of the magnetoresistance $\Delta\rho/\rho$ of $La_{0.35}Nd_{0.35}Sr_{0.3}MnO_3$ thin films on (a) (001)$SrTiO_3$ and (b) (001) $ZrO_2(Y_2O_3)$ substrates at H = (■) 2.2, (●) 4.5, (▲) 6.7, and (▼) 8.4 kOe.

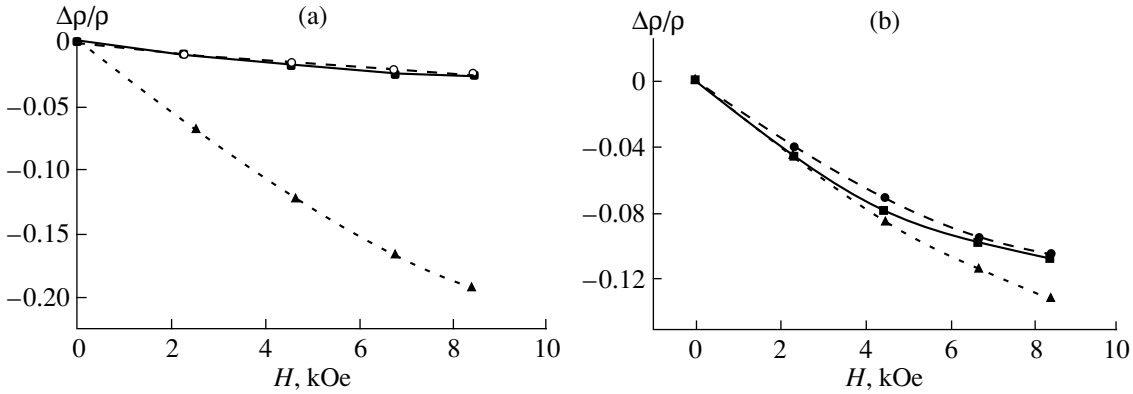

Fig. 4. Isotherms of the magnetoresistance $\Delta\rho/\rho$ of $La_{0.35}Nd_{0.35}Sr_{0.3}MnO_3$ thin films on (a) (001)$SrTiO_3$ and (b) (001) $ZrO_2(Y_2O_3)$ substrates at T = (■) 82, (◇) 100, (●) 152, and (▲) 225 K.

4. DISCUSSION OF RESULTS

It can be seen from Fig. 2 that the curves of $\rho(T)$ have a minimum and as can be seen from Table 1, the temperature T_{max} at the maximum of $\rho(T)$ for the film on $ZrO_2(Y_2O_3)$ is 20 K lower and that for the films on $SrTiO_3$, MgO, and $LaAlO_3$ is approximately 20 K higher than T_C. The magnetoresistance is negative and the curves $(\Delta\rho/\rho)(T)$ pass through a minimum near T_C (Fig. 3). The isotherms of the magnetoresistance do not saturate over the entire temperature range studied (Fig. 4). The magnetoresistance reaches 34% at H = 8.4 kOe for the film on MgO and is lower for the other films, being 23, 22, and 13% for the films on $LaAlO_3$, $SrTiO_3$, and $ZrO_2(Y_2O_3)$, respectively (see the table). Thus, for these films we observe colossal magnetoresistance near T_C similar to that obtained in manganites of different composition [20–22].

A comparison of the $\rho(T)$ curves for the film on the $ZrO_2(Y_2O_3)$ substrate and the other three films on the perovskite and MgO substrates (Fig. 2) shows that the value of ρ for the first film is much higher than that for the others. It can be seen from the table that the resistivities at 82 K differ by more than an order of magnitude and near the maximum of ρ they differ between four and eight times. The form of the curves also differs. For example, for the films on $SrTiO_3$, $LaAlO_3$, and MgO ρ increases abruptly with increasing temperature from $T \approx 180$ K whereas for the film on $ZrO_2(Y_2O_3)$ ρ begins to increases monotonically from 80 K, the lowest measurement temperature, i.e., the maximum on the $\rho(T)$ curve is broadened substantially. The curves $(\Delta\rho/\rho)(T)$ differ even more strikingly: for the first three films we observe an abrupt minimum at T_{min} which is slightly lower than T_C whereas for the last film this minimum, also positioned slightly below T_C, is strongly broadened and is barely observed on the low-temperature side (Fig. 3). The absolute value of $|\Delta\rho/\rho|$ for the last film at low temperatures is high, reaching almost 10% in a field of 8.4 kOe, and from 100 K, increases slightly with further increasing temperature. The curves $(\Delta\rho/\rho)(H)$ (Fig. 4) for the first three films and the last differ substantially: for the first three films we observe an almost linear increase in $|\Delta\rho/\rho|$ with increasing field at temperatures below the minimum on the $(\Delta\rho/\rho)(T)$ curve whereas for the last film in a weak field

up to 2 kOe we observe an abrupt increase in $|\Delta\rho/\rho|$ followed by an almost linear increase $|\Delta\rho/\rho|$ in stronger fields.

These dependences $\rho(T)$, $(\Delta\rho/\rho)(H)$, and $(\Delta\rho/\rho)(T)$ described above for the film on $ZrO_2(Y_2O_3)$ are similar to those observed earlier for polycrystalline bulk and thin-film manganese samples [3–17] whereas the dependences observed for the films on $SrTiO_3$, $LaAlO_3$, and MgO are similar to those observed for single-crystal samples [3–17]. The enhanced values of ρ in the polycrystalline samples can be attributed to spin-polarized tunneling between granules [9] or scattering of carriers within domain walls which generally coincide with the intergranular boundaries [4], whereas the enhanced values of $|\Delta\rho/\rho|$ at $T < T_C$ can be ascribed to the influence of the magnetic field on these processes. It was shown in [23] that the nuclear resonance data for an $La_{0.67}Ca_{0.33}MnO_3$ film indicate a reduced hole concentration within the domain walls.

However, all the films studied here are single-crystal, including that on $ZrO_2(Y_2O_3)$. The difference between this film and the others studied here is that, as we noted in Section 3.1, it consists of microregions having four different crystallographic orientations. This leads to the existence of magnetic domains having at least four different directions of easy magnetization axes, and the boundaries between them form different angles with the directions of magnetization in the domains. In films on perovskite and MgO substrates the axes of easy magnetization of their different parts are parallel and thus most of the film should be occupied by magnetic domains having 180° walls.

It can be seen from the values of ρ at $T < T_C$ for films on perovskite and MgO substrates (table) that their conductivity is metallic. From this it follows that exchange via carriers, i.e., holes predominates in $La_{0.35}Nd_{0.35}Sr_{0.3}MnO_3$. The Curie temperature in this case is given by [24]

$$T_C \propto zt\nu, \tag{1}$$

where t is the transport integral (the width of the conduction band W is proportional to t), z is the coordination number of the magnetic ion (Mn in this case), and ν is the number of carriers per magnetic ion. It can be seen from the table that the Curie temperature of the film on $ZrO_2(Y_2O_3)$ is approximately the same as that for the other films. This implies that exchange via carriers, i.e., holes, also takes place for this film and the increase in its electrical resistivity by more than an order of magnitude compared with the three other films is attributable to the boundaries between the regions having different crystallographic orientations. It has been noted that the other three films studied here do not have these boundaries. In this case, the electrical resistivity of the film on $ZrO_2(Y_2O_3)$, as in polycrystalline samples, consists of two components: the electrical resistivity ρ_1 within the crystallographic regions described in Section 3.1 having an average linear dimension L (or the electrical resistivity within isolated granules in the case of a polycrystal), i.e., the intrinsic electrical resistivity of the material, and the resistivity ρ_2 within the boundaries between regions of different crystallographic orientation, having the average thickness L' (or the electrical resistivity of the intergranular boundaries). The value of ρ is written in the form [25]

$$\rho \approx \rho_1 + (L'/L)\rho_2. \tag{2}$$

In the film on $ZrO_2(Y_2O_3)$ boundaries exist between the regions of different crystallographic orientation, the angles between these being 19.5°, 70.5°, and 90°. This implies that the angles θ in the Mn–O–Mn–O–Mn–$\cdots$ chains between lines connecting two manganese ions with an oxygen ion, which are close to 180° within the crystallographic regions, change abruptly to the values given above within the boundaries between these microregions.

We know that the width of the conduction band in manganites (single-electron approximation) is proportional to $\cos^2\theta$ [22] so that an abrupt decrease in θ within the boundary between microregions of different crystallographic orientation leads to a sharp drop in conductivity within this boundary. Electron microscopy of this film has shown that the thickness of the boundary is close to the lattice constant [26]. However, all the sections of the films on $SrTiO_3$, $LaAlO_3$, and MgO have the same crystallographic orientation and do not exhibit these boundaries. Consequently the increase in ρ in the film on $ZrO_2(Y_2O_3)$ is only attributable to the second term in expression (2). Assuming that the value of ρ_1 is the same in all four films and is approximately 6×10^{-3} Ω cm (table) and substituting this value and also $L' \approx 4$ Å and $L \approx 400$ Å [26] into expression (2), we find that $\rho_2 \approx 18.4$ Ω cm at 82 K. Hence, the electrical resistivity inside the boundary between microregions of different crystallographic orientation is more than three orders of magnitude higher than that inside the microregions and is of the same order of magnitude as the semiconductor value.

The small thickness of the boundary layer and the high value of ρ_2 suggest that the conduction here is achieved by tunneling through this boundary. It will be shown that some of these boundaries coincide with the domain walls. In this case, the tunneling has a specific feature associated with the fact that almost completely spin-polarized electrons tunnel. This case was described in [9] for polycrystalline bulk manganese samples. When the electron spin is conserved during tunneling and the magnetic moments of neighboring granules are not parallel, the magnetoresistance is described by the following expression [9]:

$$\frac{\Delta\rho}{\rho} = -\frac{JP}{4k_BT}[m^2(H, T) - m^2(0, T)], \tag{3}$$

where J is the intergranular exchange constant, P is the electron polarization, and m is the magnetization nor-

malized to the saturation value. This expression can evidently be used for the film on $ZrO_2(Y_2O_3)$. It can be seen from expression (3) that when technical saturation of the magnetization is reached, the absolute value of the magnetoresistance should also saturate.

However, Fig. 4 shows that for the film on $ZrO_2(Y_2O_3)$ no saturation is observed on the magnetoresistance isotherms at low temperatures although saturation of the magnetization had already been achieved (see Fig. 1). It can be seen from Fig. 4 that at low temperatures the magnetoresistance isotherms initially show an abrupt increase in $|\Delta\rho/\rho|$ in fields up to 2 kOe followed by a slower almost linear increase with further increasing H. Thus, we should assume that in addition to the spin-polarized tunneling noted above, some other processes are also responsible for the low-temperature magnetoresistance in fields exceeding the technical saturation field.

We have already noted that the enhanced low-temperature electrical resistivity and magnetoresistance in polycrystalline samples has also been attributed to scattering of carriers by disordering of the spin system inside the domain walls. However, this explanation is hardly applicable to manganites for which strong *s–d* exchange takes place and the domain wall thickness is considerable. It was noted in Section 3.2 that the coercive force is approximately 300 Oe in all these films. It follows from Fig. 1 that the saturation magnetization is $M \approx 300$ G for all the films. The effective magnetic anisotropy constant calculated from these data is $K_{\text{eff}} = 9 \times 10^4$ erg/cm^3. Hence the films considered here possess low magnetic anisotropy which is typical of manganites [27] so that the domain wall thickness is large. According to estimates [28] in similar magnetically soft materials this may reach 10^3a (a is the lattice constant) in bulk samples.

In thin-film samples, where the film thickness is of the same order as the domain wall thickness indicated for a bulk sample (the thickness of the films considered here is 4100–5500 Å), the domain structure is more complex. At present there is no common viewpoint on its structure [28]. Thus, to a rough approximation we assume that the domain wall thickness in thin films is the same as in the bulk sample. As has been noted, the size of the crystallographic microregions in the film on $ZrO_2(Y_2O_3)$ is approximately 400 Å or 10^2a which is an order of magnitude smaller than the possible domain wall thickness. Since long-range magnetic order is achieved in this film, each magnetic domain should contain more than ten crystallographic microregions. However, in some parts of the film long-range magnetic order may be absent because the domain wall thickness is larger than the size of the crystallographic microregions and is of the same order as the film thickness. It can be seen from Fig. 1 and the table that the magnetic moment per chemical formula unit for this film is severely underestimated compared with that predicted for the complete ferromagnetic ordering of all the ions (including the magnetic sublattice of Nd^{3+} ions) and is approximately 46% of this. In such a wide domain wall, spin flipping takes place gradually and as a result of the strong *s–d* exchange the carrier spin is aligned parallel to the spin of the ion at which it is located at any given moment and the carrier is not scattered [24].

It can be seen from Fig. 3 that the curves of $(\Delta\rho/\rho)(T)$ have a minimum near T_C for all four films studied. The absolute value of $\Delta\rho/\rho$ at the minimum, $|\Delta\rho/\rho|_{\max}$ is high: 34% for the film on MgO and 13% for the film on $ZrO_2(Y_2O_3)$; for the other two films we have 22.5% in a field of 8.4 kOe (table). For comparison we should note that in ordinary magnetic substances such as ferrites, the value of $|\Delta\rho/\rho|_{\max}$ near T_C is two or three orders of magnitude lower. The compound $La_{0.35}Nd_{0.35}MnO_3$ is a strongly strontium-doped antiferromagnetic semiconductor $La_{0.35}Nd_{0.35}MnO_3$ in which metallic conductivity is observed below T_C and a transition to semiconducting conductivity takes place near T_C (see Fig. 2). It was shown in [29] that in manganites of this type with strong *s–d* exchange there are two mechanisms by which impurity–magnetic interaction influences the resistance: carrier scattering which reduces their mobility and the formation of localized states near the top of the valence band. Near T_C the carrier mobility drops sharply and they are partially localized at a level near the top of the valence band. Under the action of a magnetic field the impurity–magnetic scattering of carriers diminishes and these become delocalized from the tail of the valence band.

It can be seen from Fig. 3b that for the film on $ZrO_2(Y_2O_3)$ the minimum on the curve $(\Delta\rho/\rho)(T)$ near T_C is barely distinguishable and the absolute value of $|\Delta\rho/\rho|$ in the low-temperature range is only 2–3% lower than that near T_C. This suggests that the nature of the magnetoresistance at low temperatures in fields above the technical saturation of the magnetization and near T_C is the same. At low temperatures in spin-disordered microregions occupying around 54% of the film area the carriers are situated under approximately the same conditions as near T_C: the spins are strongly disordered and strong *s–d* exchange takes place. However, this is only possible when the spin-disordered regions exist in fields higher than the technical saturation of the magnetization.

Thus, we can explain the behavior of the low-temperature magnetoresistance in fields above the technical saturation level in films on $SrTiO_3$, $LaAlO_3$, and MgO substrates since these films also contain spin-disordered microregions. This is evidenced by the excessively low magnetizations of the films on $SrTiO_3$, $LaAlO_3$, and MgO compared with the pure spin value for ferromagnetic ordering of all the ions (see table and Fig. 1). It can be seen from Fig. 1 that for the film on MgO saturation in fields between 10 and 25 kOe is followed by an almost linear increase in the magnetic moment with the field. We know that as a result of mis-

match between the crystal structures of the material and the substrate manganite films exhibit stresses which increase the magnetic anisotropy. However the stresses in films on a MgO substrate relax rapidly. As was noted in Section 3.1 in films having this composition the stresses are very weak because this composition is positioned near the morphotropic boundary between the orthorhombic and rhombohedral structures which further intensifies the relaxation of the film on MgO. This film is clearly the least stressed of all those studied and thus the field-induced spin ordering observed by us takes place in magnetically disordered microregions described above.

By replacing Nd with La in $Nd_{0.7}Sr_{0.3}MnO_3$ we hoped to increase the Curie temperature of the film. We based this on the following reasoning. We know that in an undistorted perovskite structure the Mn–O–Mn bond angle is 180°. When Nd ions are replaced with smaller Sr ions, the lattice becomes distorted. It could be predicted that partially replacing Nd ions with larger La ions will make the bond angle close to 180° resulting in broadening of the conduction band, and thus increasing the transport integral t and intensifying the exchange via the carriers. As a result, in accordance with expression (1), the Curie temperature increases. However, as can be seen from Table 1, replacing half the Nd ions with La did not give the predicted result: the value of T_C, 240 K for $Nd_{0.7}Sr_{0.3}MnO_3$ [30], remained the same for $La_{0.35}Nd_{0.35}Sr_{0.3}MnO_3$. This may be attributed to the crystallographic disordering of the A sites in ABO_3 perovskite described, for example, in [31]. As a result of this disordering the orthorhombic distortion of the perovskite lattice in this last compound is the same as in the first which leads to equal transport integrals t in both compositions and consequently their Curie points are the same in accordance with expression (1).

5. CONCLUSIONS

We have described a new possibility for the existence of colossal magnetoresistance over a wide temperature range in manganites, and specifically in single-crystal thin films in which microregions having different crystallographic orientations exist. These epitaxial films differ from polycrystalline films in that they contain several types of microregions with different crystallographic orientation and they have an ordered configuration in the plane of the film. Since the crystallographic orientations in neighboring microregions differ, boundaries exist between them at which the angles in Mn–O–Mn–O–⋯ chains differ from 180° so that the electrical resistivity of these boundaries ρ_2 is strongly enhanced compared with ρ_1 within the microregions. The existence of this possibility is described for an $La_{0.35}Nd_{0.35}Sr_{0.3}MnO_3$ epitaxial film on a $ZrO_2(Y_2O_3)$ substrate. The thickness of the boundaries between the microregions of different crystallographic orientation is 5 Å and the ratio is $\rho_2/\rho_1 \sim 10^3$, the conductivity within the microregions being metallic. The most probable mechanism for electroconduction across this boundary is carrier (hole) tunneling.

An estimate of the effective magnetic anisotropy constant K_{eff} showed that $K_{\text{eff}} \approx 9 \times 10^4$ erg/cm^3. This means that the wall thickness between the magnetic domains is very large (~10^3a), of the same order as the film thickness and an order of magnitude larger than the dimensions of the microregions of different crystallographic orientation. This has the result that some regions of the film are magnetically disordered, as is evidenced by the approximately halved magnetic moment per chemical formula unit. As a result of the absence of long-range magnetic order in these microregions, we can assume that the nature of the magnetoresistance in them is the same as that near T_C. For instance, the existence of strong *s–d* exchange leads to impurity–magnetic carrier interaction which causes scattering of the carriers, reducing their mobility, and leads to the formation of localized states near the top of the valence band. In the temperature ranges indicated above the mobility of the carriers diminishes abruptly and they are partially localized at levels near the top of the valence band. Under the action of a magnetic field the impurity-magnetic scattering of the carriers increases and they become delocalized from levels near the top of the valence band.

A sharp increase in the magnetoresistance with the field when technical magnetization has not yet been achieved can be attributed to spin-polarized tunneling across boundaries between microregions of different crystallographic orientation which coincide with the domain walls. The magnetoresistance in fields below the technical saturation of the magnetization can hardly be attributed to scattering of the charge by disordering the spin system within domain walls whose thickness is very large. In such a wide domain wall, spin flip takes place gradually and as a result of the strong *s–d* exchange the carrier spin is aligned parallel to the spin of that ion at which it is situated at a particular moment; in this case no carrier scattering occurs [24].

Spin-disordered microregions can exist in both bulk and thin-film polycrystalline manganite samples provided that the dimensions of some of the crystallites do not exceed the domain wall thickness.

ACKNOWLEDGMENTS

The authors are grateful to O.Yu. Gorbenko and A.R. Kaul' for preparing the samples for analysis. This work was partly supported by the Russian Foundation for Basic Research (project no. 00-02-017810) and INTAS (grant no. 97-open-30253).

REFERENCES

1. G. H. Jonker and J. H. van Santen, Physica (Amsterdam) **16**, 337 (1950).
2. C. Searle and S. Wang, Can. J. Phys. **48**, 2023 (1970).

3. H. L. Ju, J. Gopalakrishnan, J. L. Peng, *et al.*, Phys. Rev. B **51**, 6143 (1995).
4. P. Schiffer, A. P. Ramirez, W. Bao, and S.-W. Cheong, Phys. Rev. Lett. **75**, 3336 (1995).
5. A. Gupta, G. Q. Gong, G. Xiao, *et al.*, Phys. Rev. B **54**, R15629 (1996).
6. H. Y. Hwang, S.-W. Cheong, N. P. Ong, and B. Batlogg, Phys. Rev. Lett. **77**, 2041 (1996).
7. R. Shreekala, M. Rajeswari, K. Ghosh, *et al.*, Appl. Phys. Lett. **71**, 282 (1997).
8. R. Mahesh, R. Mahendiran, A. K. Raychaudhuri, and C. N. R. Rao, Appl. Phys. Lett. **68**, 2291 (1996).
9. J.-H. Park, C. T. Chen, S.-W. Cheong, *et al.*, Phys. Rev. Lett. **76**, 4215 (1996).
10. P. Raychaudhuri, T. K. Nath, A. K. Nigam, and R. Pinto, J. Appl. Phys. **84**, 2048 (1998).
11. E. S. Vlakhov, R. A. Chakalov, R. I. Chakalova, *et al.*, J. Appl. Phys. **83**, 2152 (1998).
12. D. K. Petrov, A. Gupta, J. R. Kirtley, *et al.*, J. Appl. Phys. **83**, 7061 (1998).
13. A. K. M. Akther Hossain, L. F. Cohen, F. Damay, *et al.*, J. Magn. Magn. Mater. **192**, 263 (1999).
14. T. Walter, K. Dorr, K.-H. Muller, *et al.*, Appl. Phys. Lett. **74**, 2218 (1999).
15. V. G. Bar'yakhtar, A. N. Pogorilyi, N. A. Belous, and A. I. Tovstolytkin, J. Magn. Magn. Mater. **207**, 118 (1999).
16. M. Ziese, S. P. Sena, and H. J. Blythe, J. Magn. Magn. Mater. **202**, 292 (1999).
17. Fu Yonglai and C. K. Ong, J. Magn. Magn. Mater. **208**, 69 (2000).
18. O. Yu. Gorbenko, R. V. Demin, A. R. Kaul', *et al.*, Fiz. Tverd. Tela (St. Petersburg) **40**, 290 (1998) [Phys. Solid State **40**, 263 (1998)].
19. O. Yu. Gorbenko, A. R. Kaul, N. A. Babushkina, and L. M. Belova, J. Mater. Chem. **7**, 747 (1997).
20. É. L. Nagaev, Usp. Fiz. Nauk **166**, 833 (1996) [Phys. Usp. **39**, 781 (1996)].
21. A. P. Ramirez, J. Phys.: Condens. Matter **9**, 8171 (1997).
22. Y. Tokura and Y. Tomioka, J. Magn. Magn. Mater. **200**, 1 (1999).
23. G. Papavassiliou, M. Fardis, F. Milia, *et al.*, Phys. Rev. B **58**, 12237 (1998).
24. É. A. Nagaev, in *Physics of Magnetic Semiconductors* (Nauka, Moscow, 1979), p. 431.
25. H. Berger, Phys. Status Solidi **1**, 739 (1961).
26. M. Bibes, O. Gorbenko, B. Martinez, *et al.*, J. Magn. Magn. Mater. **209**, 15 (2000).
27. Y. Suzuki, H. Y. Hwang, S.-W. Cheong, *et al.*, J. Appl. Phys. **83**, 7064 (1998).
28. A. Hubert, in *Theorie der Domanenwande in Geordneten Medien* (Springer-Verlag, Berlin, 1974; Mir, Moscow, 1977), p. 306.
29. E. L. Nagaev, Phys. Lett. A **211**, 313 (1996).
30. V. A. Bokov, N. A. Grigoryan, M. F. Bryzhina, and V. V. Tikhonov, Phys. Status Solidi **28**, 835 (1968).
31. L. M. Rodriguez and J. P. Attfield, Phys. Rev. B **58**, 2426 (1998).

Translation was provided by AIP

Journal of Experimental and Theoretical Physics, Vol. 91, No. 2, 2000, pp. 407–415.
Translated from Zhurnal Éksperimental'noĭ i Teoreticheskoĭ Fiziki, Vol. 118, No. 2, 2000, pp. 465–474.

SOLIDS
Electronic Properties

Quantum Hall Effect in Inhomogeneous Media: Effective Characteristics and Local Current Distribution

V. E. Arkhincheev

Buryat Science Center, Siberian Division, Russian Academy of Sciences, Ulan-Ude, 670047 Russia
e-mail: varkhin@bsc.buryatia.ru

Received March 10, 2000

Abstract—An analysis is made of the problem of current flow in heterophase inhomogeneous media in the quantum Hall effect regime. Duality relations are derived and expressions are obtained for the effective conductivity of inhomogeneous media over the entire range of concentrations. Local current distributions (fields) are determined in the quantum Hall effect regime. © *2000 MAIK "Nauka/Interperiodica".*

1. INTRODUCTION

In studies of current flow in inhomogeneous media we encounter the problem of determining the effective conductivity σ_e which is defined as the proportionality factor between the average current density **J** and the field **E**:

$$\mathbf{J} = \sigma_e \mathbf{E}. \tag{1}$$

For a medium consisting of two phases having conductivities σ_1 and σ_2 and corresponding concentrations x and $1 - x$ the expression for the effective conductivity may be written in the form

$$\sigma_e = \sigma_1 f(\epsilon, h), \tag{2}$$

where $\epsilon = x - x_c$ is the excess over the percolation threshold x_c, $h = \sigma_2/\sigma_1$ is the conductivity ratio, and f is a function to be determined. An expression for the effective conductivity of two-phase media was first obtained in the effective medium approximation [1]:

$$f(\epsilon, h) = (1 + h)\epsilon + \sqrt{(1 + h)^2\epsilon^2 + h}. \tag{3}$$

We know that this approximation is well satisfied for weakly inhomogeneous media. For strongly inhomogeneous media in the critical region $h \ll 1$, i.e., near the metal–insulator transition a similarity hypothesis is used [2]. According to this hypothesis, near the percolation threshold the conductivity of a strongly inhomogeneous two-phase medium may be written in the scaling form:

$$f(\varepsilon, h) = h_s f\left(\frac{\epsilon}{h^{s/t}}\right), \tag{4}$$

where s, t are the critical indices in percolation theory which describe the asymptotic power behavior of the function f. Nevertheless, these generally recognized methods are approximate. Due to the dual symmetry, in the two-dimensional case exact results were obtained: the Keller reciprocity theorem [3] and the Dykhne symmetry transformation [4]. It was shown that at the percolation threshold (equal phase concentrations) the effective conductivity of two-phase media is equal to the geometric mean:

$$\sigma_e = \sqrt{\sigma_1\sigma_2}, \tag{5}$$

whereas for arbitrary phase concentrations we obtain the duality relation:

$$\sigma_e(\epsilon)\sigma_e(-\epsilon) = \sigma_1\sigma_2. \tag{6}$$

(A medium having the same geometric distribution of phases as the initial one and differing only in position of the phases is called a dual medium.) These results were obtained as a result of the symmetry of the two-dimensional direct-current equations relative to linear rotation transformations. This macroscopic approach was used in [5] to study the stability of the Hall conductivity plateau relative to changes in the concentration of the metal phase in an inhomogeneous medium. It was shown that over a wide range of concentrations as far as the percolation threshold metal inclusions do not influence the Hall conductivity plateau. This approach was recently used to study the fractional quantum Hall effect in the two-phase approximation [6]. Expressions were obtained for the components of the conductivity tensor in a magnetic field, a phase diagram was constructed in the coordinate plane σ_{xx}, σ_{xy}, and it was established that regions of phase intersection have a substantial influence on the components of the conductivity tensor.

The aim of the present paper is to study current flow in inhomogeneous multiphase media in the quantum Hall effect regime ($\sigma_{xx} = 0$, $\sigma_{xy} = \text{const}$). Duality relations are obtained for effective multiphase systems and the effective characteristics of inhomogeneous media are determined over a wide range of concentrations. Some of the results for the three-phase case were published in [7]. The second part of the study is devoted to finding local current distributions for doubly periodic

systems with square inclusions using methods from the theory of functions of a complex variable. Following [8, 9], for a certain class of systems with inclusions we constructed corresponding conformal mappings and solved Riemann boundary-value problems. This allowed us to determine local current distributions (fields) for these systems in the quantum Hall effect regime.

The article is constructed as follows. In Section 2 we describe a general method for studying inhomogeneous two-dimensional media based on linear rotation transformations. In Section 3 we derive duality relations for two-phase media and these results are used to study the quantum Hall effect in a mixture of metal and Hall phases. An expression is derived for the effective Hall conductivity above the percolation threshold. A multiphase randomly inhomogeneous Hall medium is studied in Section 4. Duality relations are derived and expressions are obtained for the effective conductivity over a wide range of concentrations. In Section 5 we generalize the results of a phenomenological approach developed in [6] to the four-phase case. In this approach the influence of the regions near the phase boundaries is taken into account as a boundary condition. In Section 6 we introduce basic concepts required to solve two-dimensional problems using methods from the theory of functions of a complex variable and formulate the boundary conditions for current flow in the quantum Hall effect regime. In Sections 7 and 8 we construct conformal mappings for various classes of periodic systems, solve corresponding boundary-value problems, and obtain distributions of local currents and fields for these systems under conditions of the quantum Hall effect. The results are discussed in the Conclusions.

2. DESCRIPTION OF METHOD BASED ON ROTATION TRANSFORMATIONS

We shall briefly describe the method proposed in [4]. We shall consider a conducting medium. In the static case this is described by the direct-current equations and Ohm's law:

$$\mathrm{div}\mathbf{j} = 0, \quad \mathrm{rot}\mathbf{e} = 0, \quad \mathbf{j} = \sigma\mathbf{e}. \tag{7}$$

In the two-dimensional case the direct-current equations are invariant relative to linear transformations of the rotation:

$$\mathbf{j} = b[\mathbf{n}\times\mathbf{e}'], \quad \mathbf{e} = d[\mathbf{n}\times\mathbf{j}']. \tag{8}$$

Here $\mathbf{n}$ is the unit vector of the normal to the plane, b and d are constant coefficients. As a result of the linearity of these transformations Ohm's law is conserved:

$$\mathbf{j}' = \sigma'\mathbf{e}', \tag{9}$$

where the conductivity of the primed system is given by

$$\sigma' = \frac{b}{d\sigma}. \tag{10}$$

A similar relationship is obtained for the effective conductivity. If the coefficients b, d are taken in the form

$$b = \frac{1}{d} = \sqrt{\sigma_1\sigma_2} \tag{11}$$

the primed system will only differ from the initial one by the exchange of the phases, i.e., it is dual with respect to the initial system:

$$\sigma'_e(\epsilon) = \sigma_e(-\epsilon). \tag{12}$$

This then yields relation (6).

If the two-dimensional medium is placed in a perpendicular magnetic field $\mathbf{B}$, Ohm's law has the tensor form:

$$\mathbf{j} = \hat{\sigma}\mathbf{e}, \tag{13}$$

where $\hat{\sigma}$ is the conductivity tensor in the magnetic field having the components

$$\sigma_{xx} = \frac{\sigma}{1-\beta^2}, \quad \sigma_{xy} = -\sigma_{yx} = \frac{\sigma\beta}{1+\beta^2}, \quad \beta = \frac{\mu B}{c}$$

is the Hall factor, μ is the particle mobility, and c is the velocity of light.

In this case we need to use generalized rotation transformations:

$$\mathbf{j} = a\mathbf{j}' + b[\mathbf{n}\times\mathbf{e}'], \quad \mathbf{e} = c\mathbf{e}' + d[\mathbf{n}\times\mathbf{j}']. \tag{14}$$

For the primed system we also obtain Ohm's law in the tensor form:

$$\mathbf{j}' = \hat{\sigma}'\mathbf{e}', \tag{15}$$

where the conductivity tensor has the components

$$\begin{aligned}\sigma'_{xx} &= \frac{\sigma_{xx}(ac+bd)}{(\sigma_{xx}d)^2 + (\sigma_{xy}d+a)^2},\\ \sigma'_{xy} &= \frac{\sigma_{xx}^2 cd + (\sigma_{xy}c-b)(\sigma_{xy}d+a)}{(\sigma_{xx}d)^2 + (\sigma_{xy}d+a)^2}.\end{aligned} \tag{16}$$

3. HALL CONDUCTIVITY PLATEAU

We shall show that in a mixture of Hall and metal phases where the concentrations of the Hall phase exceed the percolation threshold, the effective Hall conductivity of the medium is constant and equal to the value for the Hall phase:

$$\sigma_{xy}^e = \sigma_{xy}^{(2)}. \tag{17}$$

In other words, the Hall conductivity plateau is stable relative to metal inclusions over a wide range of concentration as far as the percolation threshold. In order to solve this problem we consider the general case of a two-phase medium situated in a magnetic field, we derive some general relations, and then go over to the limit of the Hall phase of interest to us ($\sigma_{xx} = 0$, $\sigma_{xy} =$ const) in these formulas. It was noted earlier [10, 11]

that an initial two-phase system in a magnetic field may be transformed into a primed system having given (known) properties by at least three methods. In the first transformation the primed system is dual relative to the initial one:

$$\hat{\sigma}_1' = \hat{\sigma}_2, \quad \hat{\sigma}_2' = \hat{\sigma}_1, \tag{18}$$

$$\hat{\sigma}_e'(\epsilon) = \hat{\sigma}_e(-\epsilon). \tag{19}$$

This transformation is defined by the coefficients

$$a = -c, \quad d = \frac{\sigma_{xx}^{(1)} + \sigma_{xx}^{(2)}}{\sigma_{xx}^{(1)}\sigma_{xy}^{(2)} + \sigma_{xx}^{(2)}\sigma_{xy}^{(1)}}. \tag{20}$$

Here the following duality relation is obtained for the effective characteristics:

$$\frac{\sigma_{xx}^e(\epsilon)\sigma_{xy}^e(-\epsilon) + \sigma_{xx}^e(-\epsilon)\sigma_{xy}^e(\epsilon)}{\sigma_{xx}(\epsilon) + \sigma_{xx}(-\epsilon)} = \frac{\sigma_{xx}^{(1)}\sigma_{xy}^{(2)} + \sigma_{xx}^{(2)}\sigma_{xy}^{(1)}}{\sigma_{xx}^{(1)} + \sigma_{xx}^{(2)}}. \tag{21}$$

In the second transformation the primed system differs from the initial one by a exchange of the phases and by reversal of the direction of the magnetic field:

$$\sigma_{xx}'^{(1)} = \sigma_{xx}^{(2)}, \quad \sigma_{xx}'^{(2)} = \sigma_{xx}^{(1)}, \quad \sigma_{xy}' = -\sigma_{xy}. \tag{22}$$

In this case the tensor components of the primed system are

$$\sigma_{xx}^{e\prime} = \sigma_{xx}^e(-\epsilon), \quad \sigma_{xy}^{e\prime}(-\epsilon) = -\sigma_{xy}^e(\epsilon) \tag{23}$$

and the following duality relation is obtained

$$\frac{\sigma_{xx}^e(\epsilon)\sigma_{xy}^e(-\epsilon) - \sigma_{xx}^e(-\epsilon)\sigma_{xy}^e(\epsilon)}{\sigma_{xx}^e(\epsilon) - \sigma_{xx}^e(-\epsilon)} = \frac{\sigma_{xx}^{(1)}\sigma_{xy}^{(2)} - \sigma_{xx}^{(2)}\sigma_{xy}^{(1)}}{\sigma_{xx}^{(1)} - \sigma_{xx}^{(2)}}. \tag{24}$$

The third transformation reduces the initial system to a system which only differs by a change in the direction of the magnetic field:

$$\sigma_{xx}' = \sigma_{xx}, \quad \sigma_{xy}' = -\sigma_{xy}. \tag{25}$$

In this case we obtain the following relation linking the components of the effective conductivity tensor:

$$[(\sigma_{xx}^e(\epsilon))^2 + (\sigma_{xy}^e(\epsilon))^2]cd + \sigma_{xy}^e(\epsilon)(ac - bd) - ab = 0. \tag{26}$$

This is valid for any phase concentrations.

We shall apply these relations to the problem formulated above which is of interest to us. Let us assume that the concentration of the first metal phase is below the critical value $X_c = 1/2$, i.e., the diagonal component of the conductivity tensor is zero, $\sigma_{xx}^e(\epsilon) = 0$ since an infinite cluster forms from the Hall phase in this system. It can be seen from formulas (21) and (24) that over the entire range of concentrations, as long as flow takes place in the Hall phase, the effective Hall conductivity remains constant:

$$\sigma_{xy}^e = \sigma_{xy}^{(2)}. \tag{27}$$

This result also agrees with relation (26) according to which, over the entire range of concentrations where the diagonal component σ_{xx}^e vanishes, the effective Hall conductivity should have a constant value.

This result has a clear physical meaning. In an inhomogeneous medium, current flows such that the minimum Joule heat is released in the medium. In our case, it is only possible for current to flow in the Hall phase with the minimum, zero, heat release which is achieved. In addition, the electric field in the metal phase should be zero, otherwise dissipation will occur. We shall show that this is in fact the case. From the definition of the averages we have

$$\sigma_{xy}^{(1)}\langle[\mathbf{n}\times\mathbf{e}]\rangle_1 + \sigma_{xy}^{(2)}\langle[\mathbf{n}\times\mathbf{e}]\rangle_2 = \sigma_{xy}^e[\mathbf{n}\times\mathbf{E}], \quad \langle e\rangle_1 + \langle e\rangle_2 = E. \tag{28}$$

Solving this system of equations, we obtain

$$\langle e\rangle_1 = E\frac{\sigma_{xy}^e - \sigma_{xy}^{(2)}}{\sigma_{xy}^{(1)} - \sigma_{xy}^{(2)}}, \quad \langle e\rangle_2 = E\frac{\sigma_{xy}^{(1)} - \sigma_{xy}^e}{\sigma_{xy}^{(1)} - \sigma_{xy}^{(2)}}. \tag{29}$$

Thus, when an infinite cluster forms in the system from the Hall phase, which corresponds to $\sigma_{xy}^e = \sigma_{xy}^{(2)}$, the electric field in the metal phase goes to zero. When Hall currents flow around the metal clusters a surface charge appears at the interface, its field exactly compensating for the external field in the metal phase.

4. MULTIPHASE MEDIUM: DUALITY RELATIONS AND EFFECTIVE CONDUCTIVITY

Let us assume that four phases exist in the quantum Hall effect regime having different conductivities $\sigma_{xy}^{(i)}$. We shall also assume that the concentrations of the even and odd phases are equal

$$X_1 = X_3, \quad X_2 = X_4, \tag{30}$$

and are of arbitrary magnitude with the condition

$$2(X_1 + X_2) = 1. \tag{31}$$

For convenience we express the concentrations of phases 1 and 2 in the form

$$X_1 = \frac{1}{4} + \delta, \quad X_2 = \frac{1}{4} - \delta. \tag{32}$$

(Two- and three-phase media are particular cases of this problem.) Following a general method we establish possible exchange symmetries and corresponding duality relationships. We exchange the even and odd phases:

$$\sigma_1' = \sigma_2, \quad \sigma_2' = \sigma_1, \quad \sigma_3' = \sigma_4, \quad \sigma_4' = \sigma_3 \quad (1 \longleftrightarrow 2, 3 \longleftrightarrow 4). \tag{33}$$

According to the conditions (33) and formula (16), this transformation is defined by the coefficients

$$a_1 = -c_1, \quad b_1 = \frac{\sigma_1\sigma_2(\sigma_3 + \sigma_4) - \sigma_3\sigma_4(\sigma_1 + \sigma_2)}{\sigma_1\sigma_2 - \sigma_3\sigma_4}, \quad d_1 = \frac{\sigma_1 + \sigma_2 - \sigma_3 - \sigma_4}{\sigma_1\sigma_2 - \sigma_3\sigma_4}. \tag{34}$$

We stress that for arbitrary values of the conductivities, this transformation is only possible for media in the quantum Hall effect regime.

For arbitrary phase concentrations the primed system is dual relative to the initial one: $\sigma_e'(\delta) = \sigma_e(-\delta)$. Thus, we obtain the following duality relation for the effective conductivities of four-phase inhomogeneous media in the quantum Hall effect regime:

$$d_1\sigma_e(-\delta)\sigma_e(\delta) + b_1 = a_1[\sigma_e(-\delta) + \sigma_e(\delta)]. \tag{35}$$

In addition to this symmetry, this problem also has another possibility for exchange of the even and odd phases: $\sigma_1' = \sigma_4$, $\sigma_2' = \sigma_3$, $\sigma_3' = \sigma_2$, $\sigma_4' = \sigma_1$ ($1 \longleftrightarrow 4$, $2 \longleftrightarrow 3$). In this case, the coefficients a, b, d have the values

$$a_2 = -c_2, \quad b_2 = \frac{\sigma_1\sigma_4(\sigma_2 + \sigma_3) - \sigma_2\sigma_3(\sigma_1 + \sigma_4)}{\sigma_1\sigma_4 - \sigma_2\sigma_3}, \quad d_2 = \frac{\sigma_1 + \sigma_4 - \sigma_2 - \sigma_3}{\sigma_1\sigma_4 - \sigma_2\sigma_3}, \tag{36}$$

and another duality relation is obtained similar to (35) but having the coefficients a_2, b_2, d_2.

This system also possesses additional symmetry, exchange within the even and the odd phases:

$$\sigma_1' = \sigma_3, \quad \sigma_2' = \sigma_4, \quad \sigma_3' = \sigma_1, \quad \sigma_4' = \sigma_2 \quad (1 \longleftrightarrow 3, 2 \longleftrightarrow 4). \tag{37}$$

In this case, the primed system is macroscopically equivalent to the initial system $\sigma_e'(\delta) = \sigma_e(\delta)$ and the effective Hall conductivity is given by

$$d_3\sigma_e(\delta)^2 + b_3 - 2a_3\sigma_e(\delta) = 0. \tag{38}$$

Here the coefficients a_3, b_3, d_3 are obtained from the conditions (37). Hence, the effective conductivity of a four-phase system in the quantum Hall effect regime is given by

$$\sigma_{xy}^e(\pm\delta) = \frac{\sigma_1\sigma_3 - \sigma_2\sigma_4}{\sigma_1 + \sigma_3 - \sigma_2 - \sigma_4} \pm \left[\left(\frac{\sigma_1\sigma_3 - \sigma_2\sigma_4}{\sigma_1 + \sigma_3 - \sigma_2 - \sigma_4}\right)^2 + \frac{\sigma_2\sigma_4(\sigma_1 + \sigma_3) - \sigma_1\sigma_3(\sigma_2 + \sigma_4)}{\sigma_1 + \sigma_3 - \sigma_2 - \sigma_4}\right]^{1/2}. \tag{39}$$

A transition to media with fewer phases can be made quite easily: a three-phase medium corresponds to the limit $\sigma_2 = \sigma_4$ and a two-phase medium corresponds to $\sigma_1 = \sigma_3$, $\sigma_2 = \sigma_4$. We reemphasize that the Hall conductivity plateau does not depend on the phase concentration over a wide range. Another interesting factor is that the plateau height depends on the conductivities of all four phases down to low concentrations.

These unexpected results are attributable to the unusual nature of the current flow under the conditions of the quantum Hall effect. We know that the Hall current is always perpendicular to the electric field:

$$j = \sigma_{xy}[\mathbf{n} \times \mathbf{e}]. \tag{40}$$

From $\mathrm{div}\,\mathbf{j} = 0$ allowing for the potentiality of the electric field $\mathrm{rot}\,\mathbf{e} = 0$ we obtain

$$\mathbf{e} \times \nabla\sigma_{xy} = 0. \tag{41}$$

Consequently, the lines of flow cannot intersect the lines of constant σ_{xy}. In other words, the Hall current cannot flow from one phase to another and "freeze" in each phase. This explains why the σ_{xy} plateau is constant over a wide range of concentrations. We also note that our results indicate that the Hall conductivity at the percolation threshold depends strongly on which phases form the infinite cluster via which the threshold value of σ_{xy} was reached. Two phases are sufficient to form an infinite cluster so that six independent methods of forming an infinite cluster of different phases (there are six combinations) are possible in a four-phase system.

5. CHESSBOARD MODEL

The analysis of a multiphase system described above has shown that near the percolation threshold even a low concentration of inclusions of different phases can strongly influence the effective characteristics of inhomogeneous media. In order to understand this we shall consider a four-color chessboard model. Each colored box has its own conductivity $\sigma_{xy}^{(i)}$, $i = 1, \ldots, 4$. Following [6] where the two-phase case was considered, we shall assume that the odd-numbered phases 1 and 3 are separated in the corners by small gaps (see Fig. 1). For low values of σ_{xx} the current should be concentrated in the corner to flow through the entire system. We shall consider in greater detail the

node at which all four phases are adjacent. According to the charge conservation law, the sum of the inflowing currents is equal to the sum of the outflowing currents:

$$I_1 + I_4 = I_2 + I_3. \tag{42}$$

We also assume that because of their small width the effective transmittivity of the gaps can be simply replaced by the boundary condition

$$\frac{I_1 + I_3}{I_2 + I_4} = \alpha, \tag{43}$$

where α is the parameter of the problem. The main difference in the four-color model is that in order to find the average currents and field we need to analyze four cells of dimension a. Thus, the average current and field components will be

$$\begin{aligned} j_x &= \frac{I_1 + I_3 + I_2 + I_4}{4a}, \quad j_y = \frac{I_1 + I_3 - I_2 - I_4}{4a}, \\ E_x &= \frac{V_2 + V_4 - V_1 - V_3}{4a}, \quad E_y = \frac{V_2 + V_4 + V_1 + V_3}{4a}. \end{aligned} \tag{44}$$

After suitable calculations we find the components of the effective conductivity tensor for the four-phase case:

$$\sigma_{xx}^e = \frac{\alpha\left(\frac{\gamma}{\sigma_2} + \frac{1-\gamma}{\sigma_4} - \frac{\beta}{\sigma_1} - \frac{1-\beta}{\sigma_3}\right)}{\alpha^2\left(\frac{\beta}{\sigma_1} + \frac{1-\beta}{\sigma_3}\right)^2 + \left(\frac{\gamma}{\sigma_2} + \frac{1-\gamma}{\sigma_4}\right)^2}, \tag{45}$$

$$\sigma_{xy}^e = \frac{\frac{\gamma}{\sigma_2} + \frac{1-\gamma}{\sigma_4} + \alpha^2\left(\frac{\beta}{\sigma_1} + \frac{1-\beta}{\sigma_3}\right)}{\alpha^2\left(\frac{\beta}{\sigma_1} + \frac{1-\beta}{\sigma_3}\right)^2 + \left(\frac{\gamma}{\sigma_2} + \frac{1-\gamma}{\sigma_4}\right)^2}. \tag{46}$$

Here we introduce the parameters

$$\beta = \frac{J_1}{J_1 + J_3}, \quad \gamma = \frac{J_2}{J_2 + J_4}. \tag{47}$$

According to the current conservation law and the boundary condition (43), β and γ are interrelated by

$$\gamma = \frac{1}{2} + \alpha\left(\beta - \frac{1}{2}\right). \tag{48}$$

It is easy to see that the values of $\beta = \gamma = 1/2$ correspond to the two-phase case and the expressions obtained give the familiar ones:

$$\begin{aligned} \sigma_{xx}^e &= \frac{\alpha\sigma_1\sigma_2(\sigma_1 - \sigma_2)}{(\alpha\sigma_2)^2 + \sigma_1^2}, \\ \sigma_{xy}^e &= \frac{\sigma_1\sigma_2(\alpha^2\sigma_2 + \sigma_1)}{(\alpha\sigma_2)^2 + \sigma_1^2}. \end{aligned} \tag{49}$$

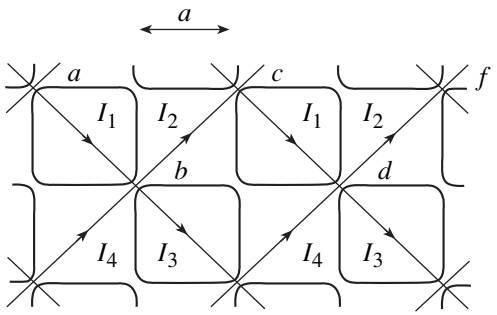

Fig. 1. Four-color chessboard model. The cell color is indicated by numbers.

Consequently an analysis of the four-color chessboard model confirms that at the percolation threshold (when the concentrations of all four concentrations are equal), the value of the effective characteristics depends strongly on the method of going to the limit. In this model it is defined by the permittivity of the nodes, the boundary condition (43).

6. COMPLEX REPRESENTATION IN TWO-DIMENSIONAL CONDUCTIVITY PROBLEMS

The macroscopic approaches described above can be used to find the average characteristics of inhomogeneous media although they cannot give the local distribution pattern of the currents and fields. Nevertheless, for some two-dimensional periodic systems the problem can be solved using methods from the theory of functions of a complex variable. For this purpose we reformulate the problem in terms of complex quantities [8]. We convert to the plane of the complex variable $Z = X + iY$ and introduce the complex values of the current density and electric field strength:

$$j^{(k)}(z) = j_x^{(k)}(x, y) - ij_y^{(k)}(x, y), \tag{50}$$

$$E^{(k)}(z) = E_x^{(k)}(x, y) - iE_y^{(k)}(x, y), \quad k = 1, 2. \tag{51}$$

We know that this representation is valid for functions satisfying the Cauchy–Riemann conditions. We shall check the validity of these conditions. The equation of current continuity gives one of these conditions

$$\frac{\partial j_x^{(k)}}{\partial x} = -\frac{\partial j_y^{(k)}}{\partial y}, \tag{52}$$

and the second follows from $\mathrm{rot}\,\mathbf{e} = 0$, which for cells having constant values of σ and β is equivalent to $\mathrm{curl}\,\mathbf{j} = 0$:

$$\frac{\partial j_x^{(k)}}{\partial y} = \frac{\partial j_y^{(k)}}{\partial x}. \tag{53}$$

Similarly, the equations $\mathrm{rot}\,\mathbf{e} = 0$ and $\mathrm{div}\,\mathbf{e} = 0$ (derived from $\mathrm{div}\,\mathbf{j} = 0$) yield the Cauchy–Riemann

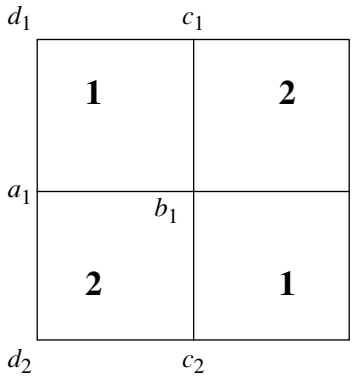

Fig. 2. Two-color doubly periodic chessboard structure.

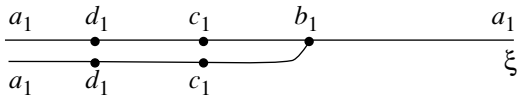

Fig. 3. Correspondence between points in conformal mapping of cells on half-planes.

conditions for the electric field. Ohm's law is written in complex form as

$$j(z) = \frac{\sigma}{1 + i\beta}E(z). \tag{54}$$

7. LOCAL CURRENT DISTRIBUTION UNDER CONDITIONS OF THE QUANTUM HALL EFFECT

We shall analyze a doubly periodic two-color structure (chessboard), see Fig. 2. As a result of the symmetry of the problem, the pattern of the fields and currents is doubly periodic so that it is sufficient to find the current distribution in two different-colored squares. We denote the physical values in these squares by the indices 1 and 2. For an Ohmic contact at the phase boundary the conditions of continuity of the normal current components and the tangential components of the field strength are satisfied:

$$j_n^+ = j_n^-, \quad E_r^+ = E_r^-. \tag{55}$$

In addition, we are interested in current flow in the quantum Hall effect regime:

$$j(z) = -i\frac{\sigma}{\beta}E(z). \tag{56}$$

Consequently, the boundary conditions at the phase boundary $0 < x < l$, $y = 0, l$ have the form

$$\begin{aligned} j_y^{(1)}(x, t) &= j_y^{(2)}(x, -y), \\ \frac{\beta_1}{\sigma_1}j_y^{(1)}(x, y) &= \frac{\beta_2}{\sigma_2}j_y^{(2)}(x, -y). \end{aligned} \tag{57}$$

It is easy to see that this system of equations is equivalent to the normal components of the current going to zero at the interface $0 < x < l$, $y = 0, l$:

$$j_y^{(1)}(x, y) = 0 = j_y^{(2)}(x, -y). \tag{58}$$

The boundary conditions for the sections $x = 0, l$ and $0 < y < l$ are written similarly:

$$j_x^{(1)}(x, y) = 0 = j_x^{(2)}(l - x, y - l). \tag{59}$$

Using the equalities between the currents and strengths in the same cell for points separated by a distance of half the perimeter, these boundary conditions for $0 < y < l$, $x = 0, l$ may be expressed in the more convenient standard form:

$$j_x^{(1)}(x, y) = 0 = j_x^{(2)}(x, -y). \tag{60}$$

We then map the inner regions of adjacent squares onto the plane $\zeta = \xi + i\eta$ using the Weierstrass function $P(z)$. Then square 1 is mapped onto the lower half-plane and square 2 onto the upper half-plane with a branch cut along the η-axis. The correspondence of the points in the mapping is shown in Fig. 3. Here we have $e_1 = P(l)$, $e_2 = P(l + il)$, $e_3 = P(il)$, and $e_1 = -e_3$. The boundary conditions in the ζ plane are conserved in the complex current notation $j^{(k)}(\zeta) = j_\xi^{(k)}(\xi, \eta) - i j_{(\eta)}^{(k)}(\xi, \eta)$ and have the form

$$\begin{aligned} &j_\eta^{(k)} + \bar{j}_\eta^{(k)} = 0, \quad -e_1 < \xi < 0, \quad e_1 < \xi < \infty, \\ &j_\xi^{(k)} - \bar{j}_\xi^{(k)} = 0, \quad -\infty < \xi < -e_1, \quad 0 < \xi < e_1. \end{aligned} \tag{61}$$

Here the bar above the function denotes complex conjugation.

We shall briefly explain the method of solving the problem (for further details see [9]). We introduce the piecewise analytic vector function:

$$\Phi(\zeta) = \begin{pmatrix} j_2(\zeta) \\ \bar{j}_1(\zeta) \end{pmatrix}.$$

On the ξ-axis this has the limiting values

$$\Phi^+(\xi) = \begin{pmatrix} j_2(\xi) \\ \bar{j}_1(\xi) \end{pmatrix},$$

$$\Phi^-(\xi) = \begin{pmatrix} \bar{j}_2(\xi) \\ j_1(\xi) \end{pmatrix}.$$

In this form the boundary conditions formulate a vector-matrix Riemann boundary-value problem:

$$\Phi^+(\xi) = G(\xi)\Phi^-(\xi), \tag{62}$$

where the G matrix is $G(\xi) = \mu E$, E is the unit matrix, and

$$\mu(\xi) = \begin{cases} 1, & -\infty < \xi < -e_1, \ 0 < \xi < e_1 \\ -1, & -e_1 < \xi < 0, \ e_1 < \xi < \infty. \end{cases}$$

The next step is to simplify the boundary conditions. We introduce a new piecewise-analytic function:

$$\Psi(\zeta) = \begin{pmatrix}\Psi_1(\zeta)\\ \Psi_2(\zeta)\end{pmatrix}.$$

This is related to the vector function $\Phi(\zeta)$ by

$$\Psi(\xi) = \begin{cases}\Phi(\xi), & \mathrm{Im}(\zeta) > 0\\ M\Phi(\xi), & \mathrm{Im}(\zeta) < 0.\end{cases}$$

Here M is a matrix which is the same as the matrix of the boundary conditions G on the sections $-\infty < \xi < -e_1$, $0 < \xi < -e_1$. On the remaining part of the real axis the boundary conditions have the form

$$\Psi^+(\xi) = M^{-1}\Psi^-(\xi). \tag{63}$$

Introducing the function $F(\zeta)$ using

$$\Psi(\zeta) = SF(\zeta), \tag{64}$$

we select the matrix S so as to diagonalize the matrix of the boundary conditions. As a result we obtain a system of independent boundary-value problems:

$$F_1^+(\xi) = \lambda_1 F_1^-(\xi), \quad F_2^+(\xi) = \lambda_2 F_2^-(\xi). \tag{65}$$

The solution is then constructed by a standard method using the theory of the Riemann scalar problem [12] and has the form

$$F_1(\zeta) = C_2 X(\zeta), \quad F_2(\zeta) = C_1 X^{-1}(\zeta),$$
$$X(\zeta) = \sqrt{\frac{\zeta^2 - e_1^2}{2e_1\zeta}}. \tag{66}$$

Returning to the initial vector function we can confirm that the values of C_1 and C_2 are real. We finally obtain expressions for the current distributions:

$$j_2 = C_2 X(\zeta), \quad j_1 = C_1 X^{-1}(\zeta),$$
$$X(\zeta) = \sqrt{\frac{\zeta^2 - e_1^2}{2e_1\zeta}}. \tag{67}$$

These formulas show that the current density distribution has a concentration at some opposite corners of the squares and goes to zero at the other corner points. This reflects the characteristics of current flow in the quantum Hall effect regime: it is impossible for current to flow from one phase to another across all interface points, except for those selected. The question of the effective Hall conductivity will be discussed in detail in the next section.

8. DOUBLY PERIODIC MEDIUM WITH INCLUSIONS IN THE QUANTUM HALL EFFECT REGIME

In this section we find the current distribution in a doubly periodic two-phase medium containing square inclusions of a third phase (see Fig. 4). This model allows for the influence of inclusions on the nature of the current flow and is useful since it can be solved exactly. As a result of the periodicity and symmetry of the problem, it is sufficient to consider a figure consisting of phases having the conductivities σ_1 and σ_2 and inclusions of a third phase (Fig. 5).

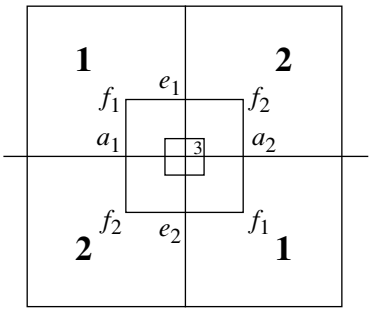

Fig. 4. Two-phase medium with square inclusions of a third phase. As a result of the symmetry it is sufficient to consider the square $f_1 f_2 f_1 f_2$.

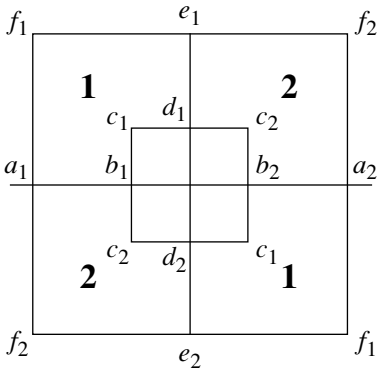

Fig. 5. The selected square is analyzed to construct a conformal mapping.

Let us assume that the electric field is directed along the x-axis. In this case the lines bounding the square under study will either be lines of equal potential ($f_1e_1f_2$, $f_1e_2f_2$) or lines of constant current ($f_1a_1f_2$, $f_1a_2f_2$). In Hall media the x component of the current goes to zero on these lines:

$$j_x^{(k)} = 0, \quad k = 1, 2. \tag{68}$$

(We also note that these lines were selected purely from the symmetry of the problem.) At the interfaces between the first and second phases the normal components of the current also go to zero. Allowance must also be made for the conditions at the interfaces with the third phase.

In order to simplify the calculations we shall assume that the inclusions are dielectric so that the conditions

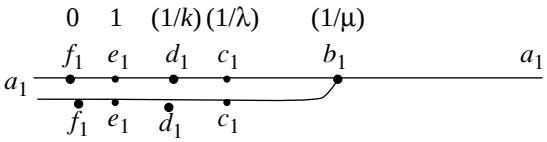

Fig. 6. Correspondence between points in conformal mapping of a figure on half-planes.

at the boundary with the third phase can be expressed in the same form: for $x = l - h$, $0 < y < h$

$$j_x^{(1)}(x, y) = 0 = j_x^{(2)}(x, -y) \tag{69}$$

and for $y = l - h$, $(l - h) < x < l$ we have

$$j_y^{(1)}(x, y) = 0 = j_y^{(2)}(x, -y). \tag{70}$$

We then construct conformal mappings of the regions of adjacent figures onto the plane $\zeta = \xi - i\eta$ using Jacobi elliptic functions [13]:

$$w = \int_0^z \frac{\partial t}{\sqrt{t(1-t)(1-\kappa t)(1-\lambda t)(1-\mu t)}}. \tag{71}$$

Then figure 1 is mapped onto the lower half-plane and figure 2 is mapped onto the upper half-plane with a branch cut along the ξ-axis. The correspondence of the points in the mapping is shown in Fig. 6. The boundary conditions have the form

$$\begin{aligned} j_\eta^{(k)} + \tilde{j}_\eta^{(k)} &= 0, \quad \xi \in L_1, \\ j_\xi^{(k)} - \tilde{j}_\xi^{(k)} &= 0, \quad \xi \in L_2. \end{aligned} \tag{72}$$

Here region L_1 includes the segments $[a_1, b_1]$, $[c_1, d_1]$ and region L_2 includes the remaining part of the ξ-axis.

Having made the necessary simplifications and calculations similar to those made above, we obtain a two-element Riemann problem with a diagonal matrix of boundary conditions. Using a standard method of constructing solutions, we obtain solutions over the entire range:

$$\begin{aligned} \Phi(\zeta) &= C_1 X(\zeta) + C_2 X^{-1}(\zeta), \quad \mathrm{Im}(\zeta) > 0, \\ \Phi(\zeta) &= C_3 X(\zeta) + C_4 X^{-1}(\zeta), \quad \mathrm{Im}(\zeta) < 0, \\ X(\zeta) &= \sqrt{\frac{(\zeta - \kappa^{-1})}{(\zeta - \lambda^{-1})(\zeta - \mu^{-1})}}. \end{aligned} \tag{73}$$

Since the current cannot penetrate into the dielectric phase, the constants C_2 and C_4 should be zero. These solutions imply that, in the quantum Hall effect regime, in a medium containing dielectric inclusions current flows from one phase to another at the joint between the phase interface and the dielectric inclusions. In this case the phases are connected in series, i.e., the reciprocal resistances are added:

$$2\sigma_e^{-1} = \sigma_1^{-1} + \sigma_2^{-1}. \tag{74}$$

A different situation arises if the inclusions are "superconducting": $\sigma_{xy}^{(3)} \longrightarrow \infty$. In order to solve this problem it is more convenient to search for the electric field distribution, since in superconducting inclusions the field goes to zero. Consequently we obtain boundary conditions for the electric fields which correspond to vanishing of the tangential components of the electric field, similar to (59) and (60). Thus, the solutions for the local electric field distributions will also have a similar form but will differ by the factor i (by the phase $\pi/2$). From physical reasoning current singularities should occur when current flows into highly conducting inclusions and thus the coefficients C_1 and C_3 should be zero. This corresponds to current flow from the first phase to the second via highly conducting inclusions by two independent methods which corresponds to parallel connection of the phases. Thus, the effective conductivity will be

$$\sigma_e = \frac{\sigma_1 + \sigma_2}{2}, \tag{75}$$

which agrees with formula (39).

In general current flows as a result of overflow near the join between three phases and as a result of flow across highly conducting inclusions of the third phase.

9. CONCLUSIONS

The main feature of current flow in inhomogeneous media in the quantum Hall effect regime is that the normal components of the current go to zero at the phase boundary, in other words current cannot flow from one phase to another. This factor explains the constant plateau of the Hall conductivity σ_{xy} over a wide range of concentrations as far as the percolation threshold since the current circulates enclosed in the phases forming an infinite cluster. This conclusion holds for a mixture of Hall and metal phases and for many-phase heterogeneous media. In four-phase media, various methods of forming a percolation cluster from two phases are possible: (1) odd–odd phases (1 + 3), (2) even–even phases (2 + 4), and (3) odd–even phases (1 + 2, 1 + 4, 3 + 2, 3 + 4).

In this case, according to our results (36), (38), (40), the values of the Hall conductivity plateau for each percolation cluster are the same.

The transition from one plateau to another is achieved by a jump at the percolation threshold. A solution for the local current distribution in a two-phase medium shows that even at the percolation threshold current only flows from one phase to another at corner points having the maximum current concentration and not over the entire phase boundary. Thus, small regions

near the corner points of the phase intersection have a substantial influence on the effective characteristics in the quantum Hall effect regime. This is confirmed by a phenomenological analysis using the chessboard model where the influence of other phases is taken into account as a boundary condition and by solving the problem for dielectric and superconducting inclusions.

The power behavior of the electric field and current densities near the corner points may be explained as follows. Near a corner at distances much smaller than the cell dimensions the problem has no characteristic spatial dimensions. Thus, the solution of the Laplace equation on these scales has a power form. The value of the exponent is obtained by solving the problem and is determined by the surface charge distribution at the boundaries of the region under conditions of the quantum Hall effect.

ACKNOWLEDGMENTS

This work was supported by the Russian Foundation for Basic Research (project no. 99-02-17355). The author also thanks Yu. P. Emets for kindly supplying a copy of his book.

REFERENCES

1. R. Landauer, J. Appl. Phys. **23**, 779 (1952).
2. B. I. Shklovskii and A. L. Efros, Phys. Status Solidi **76**, 475 (1976).
3. J. B. Keller, J. Math. Phys. **5**, 548 (1964).
4. A. M. Dykhne, Zh. Éksp. Teor. Fiz. **59**, 110 (1970) [Sov. Phys. JETP **32**, 63 (1970)]; Zh. Éksp. Teor. Fiz. **32**, 641 (1970) [Sov. Phys. JETP **32**, 348 (1970)].
5. V. E. Arkhincheev and E. G. Batyiev, Solid State Commun. **72**, 1059 (1989).
6. A. M. Dykhne and I. M. Ruzin, Phys. Rev. B **50**, 2369 (1994).
7. V. E. Arkhincheev, Zh. Éksp. Teor. Fiz. **116**, 2150 (1999) [JETP **89**, 1166 (1999)].
8. Yu. P. Emets, *Electrical Properties of Composites with Regular Structure* (Naukova Dumka, Kiev, 1986).
9. Yu. P. Emets, Zh. Éksp. Teor. Fiz. **96**, 701 (1989) [Sov. Phys. JETP **69**, 397 (1989)].
10. B. Ya. Balagurov, Zh. Éksp. Teor. Fiz. **82**, 1333 (1982) [Sov. Phys. JETP **55**, 774 (1982)].
11. V. E. Arkhincheev, Phys. Status Solidi **161**, 815 (1990).
12. M. A. Lavrent'ev and B. V. Shabat, *Methods of the Theory of Functions of a Complex Variable* (Nauka, Moscow, 1973).
13. A. M. Markushevich, *Brief Course of the Theory of Analytical Functions* (Nauka, Moscow, 1978).

Translation was provided by AIP

Journal of Experimental and Theoretical Physics, Vol. 91, No. 2, 2000, pp. 416–422.
Translated from Zhurnal Éksperimental'noĭ i Teoreticheskoĭ Fiziki, Vol. 118, No. 2, 2000, pp. 475–482.

SOLIDS
Electronic Properties

Cyclotron Resonance in Quasi-Two-Dimensional Conductors

A. V. Peschanskiĭ[1] and V. G. Peschanskiĭ[2, *]

[1]*Berkin Physicotechnical Institute of Low Temperatures, National Academy of Sciences of Ukraine, Kharkov, 61164 Ukraine*
[2]*Kharkov State National University, Kharkov, 61077 Ukraine*
**e-mail: vpeschansky@ilt.kharkov.ua*

Received March 10, 2000

Abstract—A theoretical analysis is made of the resonant absorption of RF electromagnetic wave energy in layered conductors having a quasi-two-dimensional electron energy spectrum. An analysis is made of the influence of possible drift of carriers into the conductor and their Fermi-liquid interaction on the position of the cyclotron resonance lines. A reason is given for the substantial difference between the cyclotron effective masses determined from the temperature dependence of the amplitude of the Shubnikov–de Haas oscillations and from measurements of the cyclotron resonance frequencies in [5–7]. It is shown that by means of an experimental investigation of cyclotron resonance in a magnetic field parallel to the layers, it is possible to find the carrier velocity distribution at the Fermi surface in layered organic conductors. *© 2000 MAIK "Nauka/Interperiodica".*

1. INTRODUCTION

The observation of Shubnikov–de Haas oscillations of the magnetoresistance of tetrathiofulvalene salts, layered conductors of organic origin having a quasi-two-dimensional electron energy spectrum [1–3], suggests that these possess a metallic type of conductivity and that the carrier dispersion law in these salts can be conveniently determined using methods fairly well substantiated in the theory of metals [4]. In these methods the electron energy spectrum is reconstructed by means of an experimental investigation of the physical properties of these conductors in a strong magnetic field. In addition to intensive studies of quantum oscillation effects and galvanomagnetic phenomena in charge transfer complexes based on tetrathiofulvalene, various experimental studies of RF phenomena in these conductors in the millimeter wavelength range have recently been reported.

In layered conductors the electrical conductivity parallel to the layers is considerably higher than that along the normal **n** to the layers. This is most probably attributable to the abrupt anisotropy of the conduction electron velocities at the Fermi surface $\varepsilon(\mathbf{p}) = \varepsilon_F$ so that their energy

$$\varepsilon(\mathbf{p}) = \sum_{n=0}^{\infty} \varepsilon_n(p_x, p_y)\cos\{anp_z/\hbar + \alpha_n(p_x, p_y)\}, \quad (1)$$

depends weakly on the projection of the momentum $p_z = \mathbf{pn}$ on the normal to the layers. The Hermitian nature of the single-particle Hamiltonian is ensured by the relations

$$\begin{aligned}\varepsilon_n(p_x, p_y) &= \varepsilon_n(-p_x, -p_y),\\ \alpha_n(p_x, p_y) &= -\alpha_n(-p_x, -p_y).\end{aligned} \quad (2)$$

The coefficients of the cosines in formula (1) generally decrease rapidly with increasing number n, and the maximum value of the function $\varepsilon_1(p_x, p_y)$ at the Fermi surface is $\eta\varepsilon_F \ll \varepsilon_F$, where η is the quasi-two-dimensionality parameter of the electron energy spectrum, a is the distance between the layers, and $\hbar$ is Planck's constant.

Resonant interaction between carriers and an electromagnetic wave propagating normal to the layers has been observed in various organic conductors [5–7] in a fairly strong magnetic field **H** when the reversal frequency of the conduction electrons $\Omega = eH/m^*c$ is higher than their collision frequency $1/\tau$ and comparable to the electromagnetic wave frequency ω. The cyclotron effective mass m^* of the carriers determined in a magnetic field parallel to the normal **n** to the layers in a $(BEDO\text{-}TTF)_2KHg(SCN)_4$ conductor was approximately three times heavier than the free electron mass m_0 [5, 6] whereas in $(BEDO\text{-}TTF)_2ReO_4(H_2O)$ it was almost the same as m_0 [7].

The carrier effective masses determined in [5–7] differed appreciably from the effective cyclotron masses determined using the temperature dependence of the amplitude of the Shubnikov–de Haas oscillations of the magnetoresistance [in the $(BEDO\text{-}TTF)_2ReO_4(H_2O)$ charge transfer complex the values of the cyclotron effective masses differed by a factor of 2.5–3 whereas in $(BEDO\text{-}TTF)_2KHg(SCN)_4$ they differed by a factor of approximately 1.5]. Even more surprising was the substantial difference, by a factor of 27, between the carrier free drift time in a static field and in an RF field in the millimeter range [7].

This factor provided us with the stimulus to analyze the reason for such an abrupt difference between the cyclotron effective masses and the free drift times of the conduction electrons, which casts doubt on one of the

spectroscopic methods of studying the electron energy spectrum in organic conductors noted above.

Cyclotron resonance in metals in a magnetic field parallel to the surface of the sample [8] has proved to be a highly sensitive method of studying the carrier dispersion law in metals. However, the authors of [5–7] preferred to study resonant absorption in cases where the Poynting vector and the magnetic field are orthogonal to the surface of a quasi-two-dimensional conductor. Under these conditions the resonant frequencies are shifted as a result of carrier drift into the sample [9] and the error in the determination of the cyclotron effective masses from the position of the resonant line increases. Although the carrier drift velocity along the normal to the layers $\bar{v}_z$ is low (of the order of $v\eta$, where v is the characteristic Fermi velocity of the conduction electrons along the layers), at such high electromagnetic wave frequencies $\omega \simeq 10^{11}$ s^{-1} the skin layer depth δ may be lower than or comparable to $l\eta = v\tau\eta$, which is the displacement of the carriers across the layers over the free drift time τ. In this case, it is very important to allow for the influence of the Doppler effect on the profile of the cyclotron resonance line.

We shall consider the resonant absorption of the energy of electromagnetic waves propagating along the normal to the layers (z-axis) in a layered conductor taking into account Fermi liquid effects.

The conduction electrons responsible for the electronic properties of the conductors are a Fermi liquid [10, 11] and their energy spectrum depends on the carrier distribution function and the correlation function describing the component of the interelectron interaction not renormalized by the self-consistent field. As a result, the response of the electronic system in the conductors to an external influence depends strongly on the correlation function.

In static fields, allowance for Fermi-liquid effects generally leads to renormalization of the carrier energy in the gas approximation (see, for example, [4, 12]). However, in a variable field a Fermi-liquid analysis of electronic effects sometimes leads to very specific effects, unique cyclotron and spin waves in nonmagnetic conductors [13–15], "softening" of metals in a quantizing magnetic field [16].

If the quasi-two-dimensionality parameter of the conductor η is not too small, and specifically the distance between the quantized energy levels of the carriers is $\hbar\Omega \ll \eta\varepsilon_F$, a semiclassical description of the RF phenomena can be applied [15]. In this case, the quantum corrections to the conduction are small in terms of the smallness of the parameter $\hbar\Omega/\eta\varepsilon_F$ and in this approximation the carrier energy can be expressed in the following form:

$$\varepsilon(\mathbf{p}, \mathbf{r}, t) = \varepsilon(\mathbf{p}) + \Psi(\mathbf{p}, \mathbf{r}, t), \tag{3}$$

where $\varepsilon(\mathbf{p})$ is the energy of the conduction electrons in the gas approximation (1), and the function

$$\Psi(\mathbf{p}, \mathbf{r}, t) = \int \Phi(\mathbf{p}, \mathbf{p}')\delta f(\mathbf{p}', \mathbf{r}, t)\frac{2d^3p'}{(2p\hbar)^3} \tag{4}$$

allows for correlation effects associated with the interelectron interaction, $\Phi(\mathbf{p}, \mathbf{p}')$ is the Landau correlation function, and $\delta f(\mathbf{p}, \mathbf{r}, t) = f - f_0\{\varepsilon(\mathbf{p})\}$ is a nonequilibrium correction to the Fermi carrier distribution function $f_0\{\varepsilon(\mathbf{p})\}$ which should be determined by solving the transport equation

$$\frac{\partial f}{\partial t} + \frac{d\mathbf{r}}{dt}\frac{\partial f}{\partial \mathbf{r}} + \frac{d\mathbf{p}}{dt}\frac{\partial f}{\partial \mathbf{p}} = W_{col}\{f\}. \tag{5}$$

The equation of motion for the carriers then has the form

$$\frac{d\mathrm{p}}{dt} = e\mathbf{E} + \frac{e}{c}\left[\frac{\partial \varepsilon}{\partial \mathbf{p}} \times \mathbf{H}\right] - \frac{\partial \varepsilon}{\partial \mathbf{r}}, \tag{6}$$

and the collision integral $W_{col}\{f\}$ is made to vanish by the equilibrium Fermi function $f_0(\varepsilon)$ which depends on the energy ε of the elementary excitations allowing for correlation effects.

The complete system of equations for the problem consists of the Maxwell equations

$$\mathrm{rot}\mathbf{H} = -i\omega\mathbf{E} + 4\pi\mathbf{j}/c, \tag{7}$$

$$\mathrm{rot}\mathbf{E} = i\omega\mathbf{B}, \quad \mathbf{B} = \mathbf{H} + 4\pi\mathbf{M} \tag{8}$$

and the transport equation (5) which can be used to find the relationship between the current density

$$\begin{aligned}\mathbf{j}(\mathbf{r}, t) &= \int e\frac{\partial \varepsilon}{\partial \mathbf{p}} f(\mathbf{p}, \mathbf{r}, t)\frac{2d^3p}{(2\pi\hbar)^3} \\ &= -\int e\mathbf{v}\psi(\mathbf{p}, \mathbf{r}, t)\frac{\partial f_0\{\varepsilon(\mathbf{p})\}}{\partial \varepsilon}\frac{2d^3p}{(2\pi\hbar)^3} = \langle e\mathbf{v}\psi\rangle\end{aligned} \tag{9}$$

and the electric field of the wave $\mathbf{E}(\mathbf{r}, t)$.

In conductors possessing no magnetic ordering, the magnetization $\mathbf{M}$ and the magnetic susceptibility $\chi_{ij} = \partial M_i/\partial B_j$ are generally small and there is no need to distinguish between the magnetic field $\mathbf{H}$ and the magnetic induction $\mathbf{B}$. We shall assume that the perturbation of the carrier system by the electromagnetic wave is fairly weak and in expression (9) for the electric current density we confine ourselves to a linear approximation for the weak electric field. We shall take the collision integral in the τ approximation, i.e., when

$$W_{col}\{f\} = \frac{f_0(\varepsilon) - f}{\tau} = \frac{\psi}{\tau}\frac{\partial f_0(\varepsilon)}{\partial \varepsilon}. \tag{10}$$

Solving the Maxwell equations in the eigenfunction basis of the integral collision operator can only refine numerical factors which are of the order of one and in order to determine the magnetic field dependence of the surface impedance and the damping length of the elec-

tromagnetic waves it is quite sufficient to use the τ approximation for the collision integral.

In this approximation the transport equation (5) has the following form:

$$\left\{\frac{\partial\Psi}{\partial t} + e\mathbf{E}\mathbf{v} - \frac{\partial\psi}{\partial t} - \mathbf{v}\frac{\partial\psi}{\partial\mathbf{r}} - \frac{\partial\psi}{\partial t_H}\right\} \times \frac{\partial f_0\{\varepsilon(\mathbf{p})\}}{\partial\varepsilon} = \frac{\psi}{\tau}\frac{\partial f_0\{\varepsilon(\mathbf{p})\}}{\partial\varepsilon} \tag{11}$$

or

$$\frac{\partial\psi}{\partial t} + \mathbf{v}\frac{\partial\psi}{\partial\mathbf{r}} + \frac{\partial\psi}{\partial t_H} + \frac{\psi}{\tau} = \frac{\partial\Psi}{\partial t} + e\mathbf{E}\mathbf{v}, \tag{12}$$

where

$$\mathbf{v} = \frac{\partial\varepsilon(\mathbf{p})}{\partial\mathbf{p}}, \quad \frac{\partial\psi}{\partial t_H} = \frac{e}{c}[\mathbf{v}\times\mathbf{H}]\frac{\partial\psi}{\partial\mathbf{p}}.$$

The Maxwell equations then become linear and the electromagnetic wave can e considered to be monochromatic having the frequency ω. This assumption in no way affects the general nature of the problem since its solution for an arbitrary time dependence of the field is a superposition of the solutions of the Maxwell equations with different harmonics. Thus, in the Maxwell equations (7) and (8) differentiation of the electromagnetic waves with respect to time is replaced by multiplying them by $-i\omega$. Subsequently, t will denote the time of charge motion in the magnetic field as given by

$$d\mathbf{p}/dt = \frac{\mathbf{e}}{c}\mathbf{v}\times\mathbf{H}. \tag{13}$$

Following Reuter and Sondheimer [18], we continue the electric field to the region of negative z as an even function and use a Fourier transformation. If the surface of the sample ($z = 0$) on which the wave is incident is a crystal symmetry plane and reflects the carriers specularly, in the magnetic field orthogonal to the layers, the relationship between the Fourier transforms of the current density $j_\alpha(k)$ and the electric field $E_\beta(k)$ is local:

$$j_\alpha(k) = \sigma_{\alpha\beta}(k)E_\beta(k), \quad (\alpha,\beta) = (x,y). \tag{14}$$

In this case, using simple transformations we can easily find $E_\alpha(k)$ and then using the inverse Fourier transformation:

$$E_\alpha(z) = \frac{1}{\pi}\int_0^\infty dk E_\alpha(k)\cos(kz), \tag{15}$$

we can find the distribution of the electric field of the wave in the conductor.

The Landau correlation function $\Phi(\mathbf{p}, \mathbf{p}')$ may be expressed as an expansion in terms of a complete set of orthonormalized functions $\phi_n(\mathbf{p})$:

$$\Phi(\mathbf{p},\mathbf{p}') = \sum_{n=0}^{\infty}\Phi_n\phi_n(\mathbf{p})\phi_n(\mathbf{p}'), \tag{16}$$

$$-\int\phi_n(\mathbf{p})\phi_m(\mathbf{p})\frac{\partial f_0(\varepsilon_0)}{\partial\varepsilon_0}\frac{2d^3p}{(2\pi\hbar)^3} = \langle\phi_n(\mathbf{p})\phi_m(\mathbf{p})\rangle = \delta_{nm}, \tag{17}$$

and the function $\Psi(\mathbf{p}, z, t)$ can be sought in the form

$$\Psi(\mathbf{p},z,t) = \int dk\exp\{ikz - i\omega t\} \times \sum_{n=0}^{\infty} eE_j(k)\Psi_{nj}(k)\phi_n(\mathbf{p}). \tag{18}$$

Then, the integral equation

$$\Psi(\mathbf{p},z,t) = \int\Phi(\mathbf{p},\mathbf{p}')\{\Psi(\mathbf{p}',z,t) - \psi(\mathbf{p}',z,t)\} \times\frac{\partial f_0(\varepsilon')}{\partial\varepsilon'}\frac{2d^3p'}{(2\pi\hbar)^3} \tag{19}$$

for the function $\Psi(\mathbf{p}, z, t)$ reduces to a system of algebraic equations for the Fourier components $\Psi_{nj}(k)$, i.e.,

$$(1+\Phi_n^{-1})\Psi_{nj}(k) + i\omega\sum_{m=0}^{\infty}\langle\phi_n\hat{R}_k\phi_m\rangle\Psi_{mj}(k) = \langle\phi_n\hat{R}_k v_j\rangle, \tag{20}$$

where

$$\hat{R}_k g(t) = \int_{-\infty}^{t} dt' g(t') \times\exp\{\nu(t'-t) + ik[z(t') - z(t)]\}, \tag{21}$$

and $\nu = 1/\tau - i\omega$.

The solution of the transport equation (12) allowing for (20) can be used to find the Fourier transform of the components of the RF electrical conductivity tensor

$$\sigma_{ij}(k) = e^2\langle v_i\hat{R}_k v_j\rangle - i\omega e^2\sum_{n=0}^{\infty}\langle v_i\hat{R}_k\phi_n\rangle\Psi_{nj}(k). \tag{22}$$

The depth of penetration of the electromagnetic field in the conductor, determined by the roots $k = k_1 + ik_2$ of the dispersion equation

$$\det\left\{\left(k^2 - \frac{\omega^2}{c^2}\right)\delta_{\alpha\beta} - \frac{4\pi i\omega}{c^2}\sigma_{\alpha\beta}(k)\right\} = 0, \tag{23}$$

naturally depends on the interelectron interaction, although for $kl\eta \ll 1$ allowance for interelectron Fermi-

liquid interaction has little influence on the position of the resonant lines since the k dependence of the resonant denominator of the resolvent $\hat{R}_k$,

$$\hat{R}_k g(t) = \frac{\int_{t-T}^{t} dt' g(t') \exp\{\nu(t'-t) + ik[z(t') - z(t)]\}}{1 - \exp\{(1/\tau - i\omega + ikv_z)T\}}, \quad (24)$$

is negligible. In this case, the width of the resonant line is mainly determined by the ratio T/τ, where $T = 2\pi/\Omega = 2\pi m^* c/eH$ is the period of the charge motion in the magnetic field.

Under conditions of the anomalous skin effect when $kl\eta \geq 1$, the resonant denominator in formula (24) depends strongly on the velocity of the carrier drift into the sample. Since the roots of the dispersion equation (23) are complex, a shift of the resonant frequency is accompanied by broadening of the resonant line [19, 20].

The authors of [7] evidently determined the carrier free drift time from the width of the resonant line, which was strongly broadened. In order to understand the size of the error in the determination of the cyclotron effective masses in [7], we shall analyze the resonant behavior of the surface impedance for the case when the constant $\varepsilon_1(p_x, p_y)$ is equal to $\eta\varepsilon_F$ and all the other functions $\varepsilon_n(p_x, p_y)$, where $n \geq 2$ are zero. In addition, $\alpha_n(p_x, p_y) = 0$ for any n. In the case, the velocity of the carrier motion along the normal to the layers

$$v_z = -\eta\varepsilon_F \frac{a}{\hbar} \sin\frac{ap_z}{\hbar},$$

does not depend on t and the velocity of the electron motion parallel to the layers in the principal approximation with respect to the parameter η does not depend on p_z. The resolvent of the kinetic equation then has the fairly simple form:

$$\hat{R}_k g(t) = \sum_{-\infty}^{\infty} g_n \frac{1}{1/\tau - i\omega + in\Omega} \exp\{in\Omega t\}. \quad (25)$$

Assuming that the function $\varepsilon_0(p_x, p_y)$ is isotropic, i.e., only depends on $p_\perp = (p_x^2 + p_y^2)^{1/2}$, in order to calculate the RF electrical conductivity we only need to know the first harmonic with $n = \pm 1$ of the periodic function $\phi_m(t, p_z, \varepsilon)$:

$$\phi_m(t, p_z, \varepsilon) = \sum_{-\infty}^{\infty} \phi_m^n(p_z, \varepsilon) \exp\{in\Omega t\}. \quad (26)$$

In the gas approximation for a Fermi system of carriers, the dispersion equations have the form

$$k_\pm^2 c^2 \{(k_\pm v\eta)^2 + (1/\tau - i\omega \pm i\Omega)^2\}^{1/2} = i\omega\omega_p^2, \quad (27)$$

where ω_p is the frequency of the plasma oscillations of the electron gas.

Resonant absorption of millimeter wave energy by electrons can only occur when $kr\eta \ll l$, where $r = v/\Omega$ is the radius of curvature of the trajectory of a conduction electron in the magnetic field. The resonant line width

$$\Delta H/H \simeq \{(kr\eta)^2 + (r/l)^2\}^{1/2} \quad (28)$$

in the collisionless limit is then determined by the skin layer depth $\delta \simeq 1/k$ and the resonant impedance

$$Z_\alpha = -\frac{8i\omega}{c^2} \int_0^\infty dk \frac{c^2}{k^2 c^2 - 4\pi i\omega\sigma_\alpha(k)} \quad (29)$$

where

$$H = H_{res} = \frac{m^* c}{e}\{\omega - 2k_1 k_2 vl\eta^2\} \quad (30)$$

has the form

$$Z_{res} = Z(H_{res}) \simeq Z(0)\{kr\eta\}^{1/2}. \quad (31)$$

Here $\sigma_\alpha(k)$ are the diagonal components of the tensor $\sigma_{\alpha\beta}(k)$.

It is easy to see that the resonant value of the magnetic field depends not only on the effective cyclotron mass $m^* = p_\perp \partial p_\perp/\partial\varepsilon(p_\perp)$ to within small corrections proportional to η which is the same for all cross sections of the Fermi surface with the plane $p_z = \text{const}$ but also depends on the free drift time of the carriers and the skin layer depth. The real k_1 and imaginary k_2 parts of the roots of the dispersion equation (27) have the same order of magnitude and thus in formula (31) and all subsequent formulas k denotes their modulus.

For $kr\eta \geq 1$, i.e., $\delta \leq r\eta$, an electron barely has time to undergo a complete orbit of the magnetic field during its motion in the skin layer and no cyclotron resonance occurs.

The depth of penetration of the electromagnetic waves for $kr\eta \geq 1$

$$\delta \simeq \{vc^2\eta/\omega\omega_p^2\}^{1/3}, \quad (32)$$

in the millimeter range of electromagnetic waves is of the order of 10^{-5} cm. The skin layer depth is of the same order of magnitude in resonance when

$$r/l \ll kr\eta \ll 1.$$

The ratio 1:3:1000 between the values of the electrical conductivity along the crystallographic axes in $(BEDO\text{-}TTF)_2ReO_4(H_2O)$ at room temperature [7] suggests that the quasi-two-dimensionality parameter of the electron energy spectrum η is approximately 1/30. Since long mean-free paths, of the order of 10^{-3} cm, are needed to observe resonance, it is readily understood that the case of an anomalous skin effect ($\delta \leq l\eta$) was achieved in the experiment reported in [7].

The shift of the resonant frequency as a result of carrier drift into the sample

$$\frac{\Omega_{res} - \omega}{\omega} \simeq (kl\eta)(kr\eta), \tag{33}$$

under the experimental conditions in [7] was very substantial so that the results of this study are qualitative. In order to explain the difference between these results and the known values of the effective carrier masses in these compounds there is no need to use Fermi liquid effects although allowance for these under conditions of the anomalous skin effect strongly influences the cyclotron wave spectrum studied in detail by Silin [13–15] and later workers (see, for example, [21, 22]) and the literature cited there).

The results of [13–15] can easily be generalized to the case of an abruptly anisotropic electron energy spectrum. In layered conductors the interaction of conduction electrons from various layers is appreciably suppressed and it is quite appropriate to assume that the correlation function depends weakly on the projections of the momentum on the normal to the layers.

For the case of an isotropic dependence of the carrier energy on their quasimomentum in the plane of the layers the Landau correlation function can be conveniently expressed as an expansion in terms of Legendre polynomials:

$$\Phi(\mathbf{p}, \mathbf{p}') = \sum_{n=0}^{\infty} L_n P_n(\cos(\theta - \theta')), \tag{34}$$

where $\cos\theta = p_x/p_\perp$ and $\cos\theta' = p'_x/p_\perp$.

In order to determine the Fourier components of the electrical conductivity tensor we only need to know the coefficient of the first Legendre polynomial. Simple calculations can give the following expressions for the components $\tilde{\sigma}_{\alpha\beta}(k)$ allowing for the Fermi-liquid correlations of the conduction electrons:

$$\tilde{\sigma}_{xx}(k) = \tilde{\sigma}_{yy}(k) = \left\{\sigma_{xx}(k) + \frac{4\pi i\omega\Phi}{\omega_p^2(1+\Phi)}[\sigma_{xx}^2(k) + \sigma_{xy}^2(k)]\right\}D(\omega), \tag{35}$$

$$\tilde{\sigma}_{xy}(k) = -\tilde{\sigma}_{yx}(k) = \sigma_{xy}(k)D(\omega), \tag{36}$$

where $\sigma_{\alpha\beta}(k)$ are the Fourier transforms of the components of the electrical conductivity tensor in the gas approximation, and

$$D(\omega) = \left\{1 + \frac{8\pi i\omega\Phi}{\omega_p^2(1+\Phi)}\sigma_{xx}(k) + \left\{\frac{4\pi i\omega\Phi}{\omega_p^2(1+\Phi)}\right\}^2[\sigma_{xx}^2(k) + \sigma_{yy}^2(k)]\right\}^{-1}. \tag{37}$$

In cases of weak interelectron interaction when the Fermi-liquid interaction constant $\Phi = L_1 m^*/2\pi\hbar^2 a$ is small, the dispersion equation (23) neglecting quadratic and higher-order small terms with respect to the parameter $\Phi \ll 1$ has the form

$$k_\pm^2 c^2\left\{(k_\pm v\eta)^2 + \left(\frac{1}{\tau} - i\omega \pm i\Omega\right)^2\right\}^{1/2} = \omega\omega_p^2\left\{i + \frac{\omega\omega_p^2 L_1}{4\pi e^2 v^2}\left[(k_\pm v\eta)^2 + \left(\frac{1}{\tau} - i\omega \pm i\Omega\right)^2\right]^{-1/2}\right\}. \tag{38}$$

For $\Phi \simeq 1$ the roots of the dispersion equation (23) taking into account (35)–(37) depend strongly on the Fermi-liquid interaction although they are of the same order of magnitude as those neglecting interelectron interaction, so that the shift of the resonant frequencies determined by formula (33) acquires an insignificant numerical factor of the order of one as a result of correlation effects. Consequently, the cyclotron effective masses can only be reliably determined from the position of the cyclotron resonance line in the experimental geometry achieved in [5–7] when $\delta \gg \eta(rl)^{1/2}$.

In cases where the dependence of the carrier energy on the projections of their momentum in the layer plane is significantly anisotropic, in the expansion $\Phi(\mathbf{p}, \mathbf{p}')$ it is more convenient to use basis functions proportional to the Fourier components of the conduction electron velocity. This choice of basis appreciably simplifies the system of equations (20). Apart from numerical factors of the order of one which depend on the specific type of carrier dispersion law, the position and width of the resonant line are the same as those for an isotropic function $\varepsilon_0(\mathbf{p}_\perp)$, i.e., the criterion for the reliability of determining the cyclotron effective mass is the same as before.

In a magnetic field $\mathbf{H} = (0, H\sin\vartheta, H\cos\vartheta)$ deflected from the normal to the layers by the angle ϑ, the relationship between the Fourier transforms of the current density and the RF field is nonlocal:

$$j_i(k) = \sigma_{ij}(k)E_j(k) + \int dk' Q_{ij}(k, k')E_j(k'). \tag{39}$$

The kernel of the integral operator $Q_{ij}(k, k')$ depends strongly on the surface state of the sample, i.e., on the probability of specular reflection of carriers. Conduction electrons gliding along the smooth surface of the sample make a fairly large contribution to the RF current when $\vartheta \simeq 1$ and this is taken into account by the nonlocal term in formula (39).

In order to determine the skin layer depth we need to correctly solve the problem allowing for a boundary condition for the Boltzmann transport equation [23–25]. However, the resonant behavior of the impedance is merely associated with singularities of the tensor $\sigma_{\alpha\beta}(k)$.

As ϑ increases, the drift velocity of the conduction electrons along the normal to the layers decreases $\bar{v}_z = \eta v_F \cos\vartheta$ and the Doppler effect has a weaker influence on the cyclotron resonance frequency. As a result not only the shift of the resonant frequency but also the resonant line width decrease. For ϑ close to $\pi/2$ the carrier orbits ε = const, $p_H = \mathbf{pH}/H$ = const are highly elongated and the condition $\Omega\tau \gg 1$ can only be satisfied in regions of very strong magnetic fields which are realistically unattainable for $(\pi/2 - \vartheta) \ll 1$.

For $\vartheta = \pi/2$ carriers of energy ε_F move over open periodic orbits in momentum space having the comparatively small period

$$T(p_H) = \frac{c}{eH}\int_0^{2\pi\hbar/a}\frac{dp_z}{v_x} \tag{40}$$

and almost constant velocity v_x. In this case, the periodicity of the carrier motion may reappear many times over the free drift time τ and the carriers can only drift in the layer plane, moving only along the z-axis by a value of the order of ηr_0 where $r_0 = c\hbar/eHa$.

The velocity of the carriers in the layer plane $\mathbf{v}_\perp = (v_x, v_y, 0)$ for $\vartheta = \pi/2$ varies slowly with time since p_y = const and

$$p_x(t) = p_x(0) - \int_0^t dt\frac{eHv_z(t)}{c}, \tag{41}$$

and for the model carrier dispersion law used earlier

$$\varepsilon(\mathbf{p}) = \varepsilon_0(p_\perp) + \eta\varepsilon_F\cos\frac{ap_z}{h}, \tag{42}$$

far from the self-intersecting cross section of the Fermi surface $p_H = p_c$ to within small corrections in terms of the parameter η, $v_z(t)$ is a harmonic function:

$$v_z(t) = -\eta\varepsilon_F\frac{h}{a}\sin\Omega t, \quad \Omega = \frac{eHv_x(0)}{c}. \tag{43}$$

Using relation (43) we obtain the following asymptotic expression for $\sigma_{\alpha\beta}(k)$ for $\eta \ll 1$:

$$\sigma_{\alpha b}(k) = e^2\int\frac{2dp_y v_\alpha v_\beta}{(2\pi\hbar)^3 v_x} \times \int_{-\infty}^{0} dt J_0\left\{2kr\eta\sin\left(\frac{\Omega t}{2}\right)\right\}\exp\{\nu t\}, \tag{44}$$

where $J_0(u)$ is a Bessel function.

Cyclotron resonance is completely observable for $kr\eta \geq 1$ when the skin layer depth is smaller than or comparable to the largest displacement of the carriers into the sample whereas for $kr\eta \ll 1$ the resonant dependence of $\sigma_{\alpha\beta}(k)$ on the magnetic field is only observed in small corrections proportional to η^2.

For $kr\eta \gg 1$ the main contribution to the integral over t in formula (44) is made by small vicinities near the steady-state phase points on the open electron trajectory so that, in addition to cyclotron resonance, when

$$\omega T_{extr} = 2\pi n, \quad n = 1, 2, 3, \ldots \tag{45}$$

electron transport of the electromagnetic field into the sample takes place over the distance $r\eta$ in the form of narrow bursts as predicted by Azbel' [26].

The width of the cyclotron resonance lines in a magnetic field parallel to the layers for any relationship between l and δ/η is determined only by the free drift time of the carriers involved in forming the resonance. The resonant denominator in formula (24) does not depend on the roots of the dispersion equation and consequently, the Fermi-liquid description of the resonant effects does not change the position of the resonant lines compared with the gas approximation.

The period of the carrier motion over the open trajectory has a minimum at the central cross section of the Fermi surface $p_H = 0$ and from the cyclotron resonance condition $\omega T(0) = 2\pi n$ we can determine the velocity v_x at the central cross section of the Fermi surface with fairly good accuracy.

An increase in $T(p_H)$ with increasing p_H is accomplished on the self-intersecting orbit $p_H = p_c$ where the period T goes to infinity. For a fairly complex carrier energy spectrum additional extreme values of $T(p_H)$, and consequently, additional resonant frequencies, may appear on the path between $p_H = 0$ and $p_H = p_c$. However, cyclotron resonance at frequencies satisfying the condition $\omega T(0) = 2\pi n$ will always occur for any type of electron energy spectrum.

By studying experimentally cyclotron resonance for various orientations of the magnetic field in the layer plane, we can determine the mean carrier velocities $\bar{v} = 2\pi r_0/T(0)$ in the plane xy and ultimately, to within ηv, find the velocity distribution over the Fermi surface.

In a magnetic field deflected from the surface of the sample the resonant frequencies depend strongly on the Fermi liquid interaction of the carriers. The most reliable information on correlation effects in layered organic conductors in a magnetic field may be obtained by comparing the results of an experimental study of resonant absorption of the energy of electromagnetic waves propagating parallel and perpendicular to the layers by these conductors.

ACKNOWLEDGMENTS

The authors are grateful to V.P. Silin for discussion of the results which was very useful to us.

REFERENCES

1. M. V. Kartsovnik, V. N. Laukhin, V. N. Nizhankovskiĭ, and A. A. Ignat'ev, Pis'ma Zh. Éksp. Teor. Fiz. **47**, 302 (1988) [JETP Lett. **47**, 363 (1988)].

2. M. V. Kartsovnik, P. A. Kononovich, V. N. Laukhin, and I. F. Shchegolev, Pis'ma Zh. Éksp. Teor. Fiz. **48**, 498 (1988) [JETP Lett. **48**, 541 (1988)].
3. I. D. Parker, D. D. Pigram, R. H. Friend, *et al.*, Synth. Met. **27**, A387 (1988).
4. I. M. Lifshits, M. Ya. Azbel', and M. I. Kaganov, *Electron Theory of Metals* (Nauka, Moscow, 1971; Consultants Bureau, New York, 1973).
5. S. V. Demishev, N. E. Sluchanko, A. V. Semeno, and N. A. Samarin, Pis'ma Zh. Éksp. Teor. Fiz. **61**, 299 (1995) [JETP Lett. **61**, 313 (1995)].
6. S. V. Demishev, A. V. Semeno, N. E. Sluchanko, *et al.*, Phys. Rev. B **53**, 12794 (1996).
7. S. V. Demishev, A. V. Semeno, N. E. Sluchanko, *et al.*, Zh. Éksp. Teor. Fiz. **111**, 979 (1997) [JETP **84**, 540 (1997)].
8. M. Ya. Azbel' and É. A. Kaner, Zh. Éksp. Teor. Fiz. **32**, 896 (1957) [Sov. Phys. JETP **5**, 730 (1957)].
9. M. Ya. Azbel' and V. G. Peschanskiĭ, Pis'ma Zh. Éksp. Teor. Fiz. **5**, 26 (1967) [JETP Lett. **5**, 19 (1967)].
10. L. D. Landau, Zh. Éksp. Teor. Fiz. **30**, 1058 (1956) [Sov. Phys. JETP **3**, 920 (1956)].
11. V. P. Silin, Zh. Éksp. Teor. Fiz. **33**, 495 (1957) [Sov. Phys. JETP **6**, 387 (1958)].
12. A. A. Abrikosov, *Fundamentals of the Theory of Metals* (Nauka, Moscow, 1987; North-Holland, Amsterdam, 1988).
13. V. P. Silin, Zh. Éksp. Teor. Fiz. **35**, 1243 (1958) [Sov. Phys. JETP **8**, 870 (1958)].
14. V. P. Silin, Usp. Fiz. Nauk **93**, 185 (1967).
15. V. P. Silin, Fiz. Met. Metalloved. **29**, 681 (1970).
16. V. N. Bagaev, V. I. Okulov, and E. A. Pamyatnykh, Pis'ma Zh. Éksp. Teor. Fiz. **27**, 156 (1978) [JETP Lett. **27**, 144 (1978)].
17. V. G. Peschanskiĭ, Zh. Éksp. Teor. Fiz. **114**, 676 (1998) [JETP **87**, 369 (1998)].
18. E. H. T. Reuter and E. H. Sondheimer, Proc. R. Soc. London **195**, 336 (1948).
19. M. Ya. Azbel' and V. G. Peschanskiĭ, Zh. Éksp. Teor. Fiz. **54**, 477 (1968) [Sov. Phys. JETP **27**, 260 (1968)].
20. V. G. Peschanskiĭ, O. Yung, and K. Yasemides, Fiz. Nizk. Temp. **6**, 479 (1980) [Sov. J. Low Temp. Phys. **6**, 294 (1980)].
21. D. Pines and P. Nozieres, *Theory of Quantum Liquids* (Benjamin, New York, 1966; Mir, Moscow, 1967).
22. A. S. Kondrat'ev and A. E. Kuchma, *Electron Liquid of Normal Metals* (Leningrad. Gos. Univ., Leningrad, 1980).
23. L. A. Falkovsky, Adv. Phys. **32**, 753 (1983).
24. V. I. Okulov and V. V. Ustinov, Fiz. Nizk. Temp. **5**, 213 (1979) [Sov. J. Low Temp. Phys. **5**, 101 (1979)].
25. V. G. Peschansky, Sov. Sci. Rev., Sect. A **16**, 1 (1992).
26. M. Ya. Azbel', Zh. Éksp. Teor. Fiz. **39**, 400 (1960) [Sov. Phys. JETP **12**, 283 (1960)].

Translation was provided by AIP

Journal of Experimental and Theoretical Physics, Vol. 91, No. 2, 2000, pp. 423–432.
Translated from Zhurnal Éksperimental'noĭ i Teoreticheskoĭ Fiziki, Vol. 118, No. 2, 2000, pp. 483–494.

NONLINEAR PHYSICS

Transport of a Passive Scalar and Lagrangian Chaos in a Hamiltonian Hydrodynamic System

S. D. Danilov, V. A. Dovzhenko, and I. G. Yakushkin*

Oboukhov Institute of Atmospheric Physics, Russian Academy of Sciences, Moscow, 109017 Russia
**e-mail: yakushk@omega.ifaran.ru*

Received January 20, 2000

Abstract—An experimental and numerical study is made of the chaotic behavior of Lagrangian trajectories and transport of a passive tracer in a quasi-two-dimensional four-vortex flow with a periodic time dependence of the Euler velocity field. Quantitative measurements are made of tracer transport between isolated vortices in physical space and in "action" variable space. The theory of adiabatic chaos is used to interpret the measurements. The simplest phenomenological models of liquid particle random walks are proposed to describe the anomalous transport in terms of the action. *© 2000 MAIK "Nauka/Interperiodica".*

1. INTRODUCTION

The understanding and description of processes of transport of a passive scalar by nonsteady-state two-dimensional flows of an incompressible fluid is currently one of the most topical problems in hydrodynamics, having numerous applications. A remarkable property of these flows is that the stream function which completely determines their properties is an analog of energy so that the motion of liquid particles can be described in terms of the Hamiltonian mechanics of systems with 3/2 degrees of freedom [1, 2]. As we know, dynamic chaos occurs in such a system even in cases where the stream function has a periodic time dependence. In terms of hydrodynamics we should talk about Lagrangian chaos in a regular Eulerian velocity field. Similar situations occur when vibrational hydrodynamic regimes are established, during wave propagation along streams, and so on.

The Hamiltonian nature of the equations of motion of Lagrangian particles means that many well-known results based on perturbation theory, symbolic dynamics, and so on, can be applied. A laboratory study of liquid flows then opens up additional possibilities for studying general problems relating to the description of dynamic chaos. Of course, we should not forget that hydrodynamic systems correspond to a certain particular class of Hamiltonians whose general properties are far from clear.

The complexity of the behavior of Lagrangian particles in inhomogeneous flows prevents us from obtaining a simplified kinetic description suitable over a wide range of scales. A common problem for dynamic systems with a time-dependent Hamiltonian (stream function) is the relationship between regularity and randomness in the dynamics of the particle flows and also between the dynamic and statistical approaches to their description [3, 4]. The description of processes with medium and small scales is the most complex. For Hamiltonian systems it is usually effective to use "action" and "phase" variables. The time dependence of the Hamiltonian leads to rapid phase mixing and slow action mixing. A statistical (kinetic) approach can be successfully developed to describe action mixing [3]. In the simplest cases this leads to the Fokker–Planck equation. However, the space–time inhomogeneity of flows may result in anomalous diffusion, i.e., laws for spreading of particle ensembles which differ substantially from Fick's law. Superdiffusion determined by the extension of the flow lines appears in the direction of the main system of flow lines. Subdiffusion may occur perpendicular to the flow lines because in certain sections the flow lines exhibit a hyperbolic character [5–10]. In these cases, it is quite natural to attempt to obtain nonlocal diffusion equations based on various mathematical models of random walks assuming jumps over random distances and across random time intervals, i.e., assuming "traps" and "flights" [6]. These equations take the form of a Montroll–Weiss equation [10], a fractal generalization of the Fokker–Planck equation [7, 8], and so on. The integral kernels appearing in these equations are either calculated using a dynamic description of processes within the cell or are considered as generalizations of phenomenological coefficients.

Qualitatively each specific stream function may be characterized by certain relationships between the parameters of the steady-state and nonsteady-state flow components. Depending on these parameters, various chaos and transport regimes are established which require different approaches for their description. The main dimensionless parameter is the ratio of the amplitudes of the nonsteady-state and steady-state components of the stream functions, which characterizes the degree of perturbation of the base flow. Another important parameter which is naturally called the adiabaticity

1063-7761/00/9102-0423$20.00

parameter is the ratio of the characteristic time of motion in the base flow to the time of variation of the stream function.

Most of the results obtained for hydrodynamic and for other Hamiltonian systems refer to cases of small or fast perturbations when the base flow defines the main coordinate system [11–13]. If the base flow describes a closed system, for example a system of vortices separated by separatrices, in the absence of any perturbation the motion in the system will take place along closed flow lines within each vortex. The presence of a time-periodic perturbation in a Hamiltonian system describing the trajectories of Lagrangian particles in the flow being studied leads to randomization of the trajectories inside the vortices and their random walk between vortices, and consequently to intersection of the steady-state separatrices. If the nonsteady-state field component is small, it follows from the Kolmogorov–Arnold–Moser theory that stable invariant tori are conserved near the center of the vortex. Particles located in the central regions do not go outside these, although the motion may become randomized near resonant trajectories for which the period of rotation about the center is a multiple of the perturbation period. Results obtained using a Poincaré mapping or by calculating the Melnikov function indicate that a near-separatrix layer also appears where the motion is chaotic. As the amplitude of the perturbation increases, the resonant layers expand and join with the separatrix layer, causing its thickness to increase. Phase instability leads to particle transport along the separatrix and intervortex exchange. If the perturbation becomes sufficiently large, it should be expected that the motion will be chaotic at all points in the system being analyzed.

Of considerable interest is the case when the stream functions of the main and perturbing flows are comparable but the time rearrangement of the motion takes place fairly slowly. This situation has been considered for several dynamic systems and has been called adiabatic chaos [14–19]. As the adiabaticity parameter tends to infinity, the particle trajectories are determined by the conservation of the adiabatic invariant (action) everywhere except for a certain vicinity of the point of intersection of the trajectory with the separatrix whose position depends parametrically on time. The region of randomization is determined by the region of existence of instantaneous separatrices.

The present paper is devoted to studying the validity of existing theoretical concepts for fairly large perturbations and not very large adiabaticity parameters. The values of these parameters are typical of most real hydrodynamic systems. We present and analyze results of a laboratory study of the transport of a passive tracer by a four-vortex quasi-two-dimensional flow in which the velocity field is the sum of steady-state and harmonically time-dependent components [20]. The qualitative character of the intervortex random walk which indicates a regime close to adiabatic chaos was described in [21]. In the present study, on the basis of laboratory experiments and numerical integration performed using the measured velocity field, we attempt to give a quantitative description of the transport of a passive scalar in action space. In Section 2 we consider the properties of the hydrodynamic velocity field in the Eulerian description. In Section 3 we describe the main results of the laboratory experiment and in Section 4 we give an interpretation of the results of the laboratory and numerical experiments from the point of view of adiabatic chaos theory. In Section 5 we examine the simplest analytic models suitable for describing the general properties of Lagrangian trajectories and diffusion of a passive scalar in action space in the system under study. The main results are discussed in the Conclusions.

2. PROPERTIES OF THE VELOCITY FIELD IN A FOUR-VORTEX SYSTEM

The four-vortex quasi-two-dimensional flow studied using a laboratory experiment is excited magnetohydrodynamically in a cell having horizontal dimensions $L_x = 24$ cm, $L_y = 12$ cm filled with a thin layer of electrolyte and placed in a magnetic field having a specially selected configuration. The amplitude of the velocity field in the vortices is determined by the magnitude of the dc electric current passed between the electrodes positioned on the large sides of the cell. At a critical current $J_{cr} \approx 215$ mA the four-vortex flow becomes unstable and self-oscillations are excited in the system, these being conserved as far as extremely high supercriticality values. The supercriticality is defined as $s = J/J_{cr} - 1$ where J is the instantaneous value of the current strength. The oscillations are expressed in the periodic reclosure of the vortices along each of the flow diagonals. The velocity field was measured experimentally using track photographs (the measurements were made by V.A. Dovzhenko and V.A. Krymov) taken every 5 s (flow period 47.5 s) at a current $J = 450$ mA. At this current the flow is in a supercritical regime with a supercriticality value of 1.1. The flow properties and procedure for reconstruction of the velocity field were described in detail in [20,21]. An analysis of the measurements revealed that the two-dimensional velocity field can be considered to be nondivergent and consequently it is determined by the stream function $\psi(x, y, t)$ which is related to the velocity field by the expressions

$$v_x = \frac{\partial \psi}{\partial y}, \quad v_y = -\frac{\partial \psi}{\partial x}. \tag{1}$$

The number of tracks is such that the field of the stream function was reliably reconstructed using a 64×32 point mesh. We subsequently used an expansion of the experimental stream function in terms of spatial harmonics

$$f_{mn} = \sin(m\pi x/L_x)\sin(n\pi y/L_y),$$

which satisfy the boundary condition that the stream function goes to zero at the cell walls. The steady-state component of the stream function is given by a combination of even harmonics whereas the oscillating component includes only odd harmonics whose amplitudes obey a harmonic time dependence. In order to make a numerical simulation of Lagrangian trajectories and passive tracer transport, we confined ourselves to allowance for a few leading harmonics having the maximum amplitudes so that the liquid flow was determined by the stream function

$$\psi = \psi_0(x, y) + \psi_1(x, y, t), \tag{2}$$

where

$$\psi_0 = A_{22}\sin\left(\frac{2\pi x}{L_x}\right)\sin\left(\frac{2\pi y}{L_y}\right) + A_{42}\sin\left(\frac{4\pi x}{L_x}\right)\sin\left(\frac{2\pi y}{L_y}\right),$$

$$\psi_1 = A_{11}\sin\left(\frac{\pi x}{L_x}\right)\sin\left(\frac{\pi y}{L_y}\right)\sin(\Omega t) - A_{31}\sin\left(\frac{3\pi x}{L_x}\right)\sin\left(\frac{\pi y}{L_y}\right)\cos(\Omega t) - A_{13}\sin\left(\frac{\pi x}{L_x}\right)\sin\left(\frac{3\pi x}{L_y}\right)\sin(\Omega t).$$

Here A_{ij} are the amplitudes of the harmonics whose experimental estimates are: A_{22} = 3.1 cm^2/s, A_{42} = 1.1 cm^2/s, A_{11} = 4.1 cm^2/s, A_{31} = 2.8 cm^2/s, and A_{13} = 1.2 cm^2/s. Refinement of the description used for the numerical calculations does not improve the agreement with the experimental results but increases the computation time many times. In addition to the stream function, the flow is also characterized by the vorticity $\omega(x, y, t) = \Delta\psi$ and by an analog of the Gaussian curvature of the relief K which indicates the local divergence of the trajectories,

$$K = \frac{\partial^2\psi}{\partial x^2}\frac{\partial^2\psi}{\partial y^2} - \left(\frac{\partial^2\psi}{\partial x\partial y}\right)^2. \tag{3}$$

The most important parameter can be considered to be the ratio of the amplitudes of the fundamental harmonics of the nonsteady-state and steady-state components, $\alpha = A_{11}/A_{22}$, in our case 1.3, and the adiabaticity parameter β which we arbitrarily define as the ratio of the maximum vorticity calculated for the fundamental harmonic to the angular frequency of the time variation. In our case β = 8.2.

For a slowly varying stream function the behavior of the system is in many respects determined by the rearrangement of the flow lines which takes place over the period of the oscillations. Figure 1 shows that this rearrangement takes place for the flow established at supercriticality 1.1. The time during which four separate deformed vortices can be distinguished is the same as the time when the bridge between vortices having the same vorticity sign disappears (Fig. 1a). At this time the entire system is divided into four vortex regions separated by separatrices of which two rotate clockwise and two rotate counterclockwise. Subsequently the separatrix separates into three unconnected branches (two outer and one inner) and the system is divided into five regions (Fig. 1b). In addition to the isolated vortices rotating about elliptic points, there is a region of drift motion about two elliptic and one hyperbolic points. The areas of these regions vary with time and at a certain time the elliptic points merge with the hyperbolic point and the inner separatrix collapses into a point (Fig. 1c). This series of events is then repeated for another pair of vortices. In the model velocity field the central hyperbolic point does not convert to an elliptic one although the ensuing difference only affects a small part of the phase space.

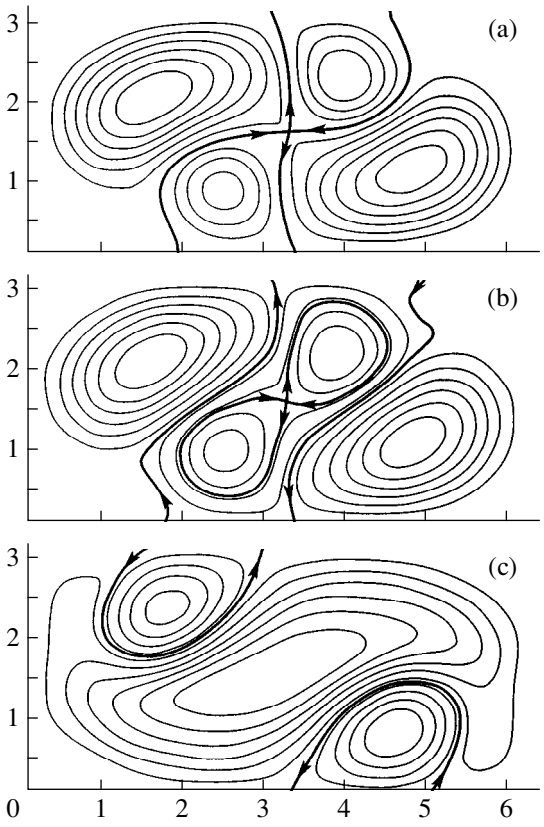

Fig. 1. Rearrangement of instantaneous stream function lines during an oscillation period for a flow having the supercriticality 1.1: (a) four separate deformed vortices at the instant when the bridge between vortices having the same vorticity sign disappears; (b) formation of a new bridge; (c) disappearance of the hyperbolic point at the center followed by a similar chain of events for another pair of vortices. The stream function is calculated using the experimentally measured velocity field. Arbitrary units of length are plotted on the axes.

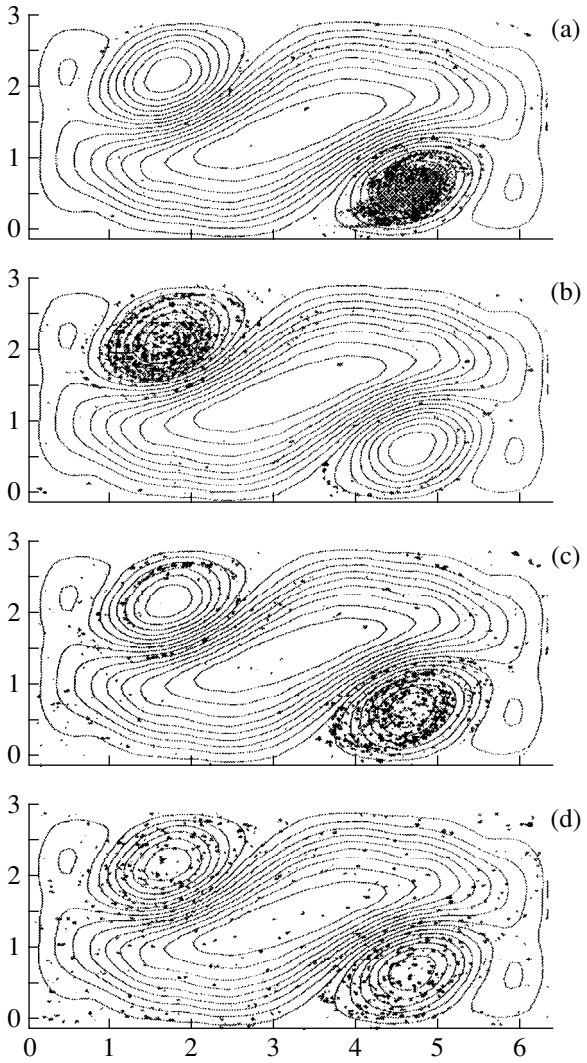

Fig. 2. Behavior of a tracer initially positioned in a single vortex (laboratory experiment): (a) distribution at time taken as the initial time; (b) after T; (c) after $2T$; (d) after $12T$. Arbitrary units of length are plotted on the axes.

3. EXPERIMENTAL RESULTS

The dynamics of a Lagrangian particle in an incompressible two-dimensional velocity field are described by a system of Hamilton equations

$$\frac{dx}{dt} = \frac{\partial \psi}{\partial y}, \quad \frac{dy}{dt} = -\frac{\partial \psi}{\partial x}. \tag{4}$$

Bronze powder was used to study these dynamics in a laboratory experiment. As a result of surface tension the powder particles are not deposited on the bottom of the cell but form clusters at the liquid surface, having typical dimensions between fractions of a millimeter and a millimeter. These clusters move as liquid particles because of their small sizes and mass. We used a system for digital analysis of video images to obtain information on the spatial distribution of the tracer particles: the frames of the video images of the tracer field were converted into intensity distributions. These distributions were filtered to remove the background associated with irregularities of the reflection coefficient of the bottom, weak reflections from surrounding objects, and too-small particles. This experimental technique has the disadvantage that the concentration field of the passive tracer is only arbitrarily identified with the intensity field of the image of particles of different sizes and there is a known degree of uncertainty. As a result of their finite dimensions, as they move the clusters may decay into smaller ones and combine although the relative contribution of this type of event is small. In order to reduce the influence of the variable number of particles, the distributions were constructed for a relative number of particles. In previous experiments [21] we used different impurities which were not suitable for a quantitative analysis.

We initially placed the tracer particles in one of the vortices and then measured the intensity distributions in a specific phase of the period over a long time interval (10–15 periods). We then systematically recorded five frames for this phase. By superposing these we obtained track images of the velocity field and by comparing these with the existing experimental measurements we were able to obtain the field of the stream function for the selected phase of the period. The juxtaposition operation is elementary since the centers of the vortices are displaced during an oscillation period and we only need to match these centers.

Figure 2 shows the evolution of the spatial distribution of an tracer placed initially in one of the vortices over twelve periods (we give the distribution at the time taken as zero, and after one, two, and twelve periods). Lines giving the instantaneous stream functions are plotted on each distribution. As we can see, in this particular phase the flow is divided into two separate and two combined vortices distributed over the diagonals. The observations showed that the vortices distributed along one diagonal (having the same direction of rotation) exchange particles to a large extent per period. Over several periods we observe mixing between vortices of the same sign whereas relatively few particles penetrate into the other circulation. As a result of the mixing we observe the formation of elongated (phase-extended structures) which exist for several periods. With each period an increasing number of particles leave the vortices, forming a chaotic cloud covering the near-separatrix layer and penetrating into the other circulation. Figure 3, constructed using the experimental data, shows the relative numbers of particles n in two counterclockwise-rotating vortices as a function of time. The upper curve shows the total number of particles in the vortices. It can be seen that long-lived periodic oscillations of the number of particles occur in each vortex. Mixing between vortices of the same sign may be estimated as over a time interval of five or six periods. Over this time exchange with other regions is relatively weak and the total number of particles does not decrease too rapidly. The overall behavior of the

particle trajectories indicates features such as randomness and regularity.

4. ADIABATIC CHAOS IN A FOUR-VORTEX SYSTEM

For $1/\beta \ll 1$, which is satisfied in our case, the theory of adiabatic chaos can be applied to understand how the mixing occurs [14–19]. In a system with slowly varying flow parameters, the motion of liquid particles outside the vicinity of the separatrices is determined by the constant value of the adiabatic invariant (the action I) which can be constructed by a standard method for each subregion of the phase space bounded by the separatrices [18]. The action at a fixed time is equal, to within $1/2\pi$, to the area bounded by a curve with a constant value of the stream function if this value is positive. If the region inside the curve is doubly connected, we define the action in terms of the total area of the two subregions. For negative values of the stream function we define the action as the area outside the closed curve. By this definition, the action is continuous as it passes across the separatrices.

Figure 4 gives the time-dependent positions of the inner and outer separatrices on the action–time plane (using a model representation of the stream function and expressing the action in arbitrary units). The solid curve corresponds to the main (outer) separatrix separating the different circulations and the dashed curve gives the inner separatrix. The separatrices isolate three regions in the range of action values. The relationship between the areas of the different regions is a fundamental characteristic of the system which in our case depends primarily on the coefficient α associated with the supercriticality of the system. In the adiabatic limit the action is invariant. Trajectories whose initial action is located in region 1 do not intersect the separatrices and remain near the initial value of the action, not leaving the vicinity of one of the elliptic points, i.e., the central nucleus of one of the vortices. These trajectories are absent if no hyperbolic point exists between the vortices (which is characteristic of experimental flow and may be achieved for model flow by slightly increasing the parameter α). Trajectories in regions 2 and 3 intersect the separatrices as a result of which the action undergoes random jumps proportional to α/β [16–19]. These trajectories undergo action mixing. If a particle is situated in region 2, it intersects the inner separatrix and is entrained into the diagonal circulation but remains within a region having the same direction of rotation. This corresponds to mixing between vortices. Finally, particles in region 3 intersect both inner and outer separatrices. This is a transition region where the motion is less adiabatic and where particles initially belonging to different circulations are mixed. The relative width of the region of nonadiabaticity near the separatrix depends on the parameter $1/\beta$.

Figure 5a shows particle trajectories with different initial values of the action obtained by numerical modeling. For a particle whose trajectory does not intersect the separatrix (region 1) the changes in action are small. The action undergoes oscillations corresponding to particle motion along orbits and estimated analytically in [16, 18]. The number of these oscillations over an oscillation period also gives an estimate of the adiabaticity parameter. For a particle which only intersects inner separatrices (region 2) action jumps can be seen at the intersections but these are small. A particle moving in region 3 exhibits appreciable oscillations of the action and large jumps as it intersects the separatrix.

When a trajectory intersects a separatrix, the action at it changes depending on the phase. As a result of the

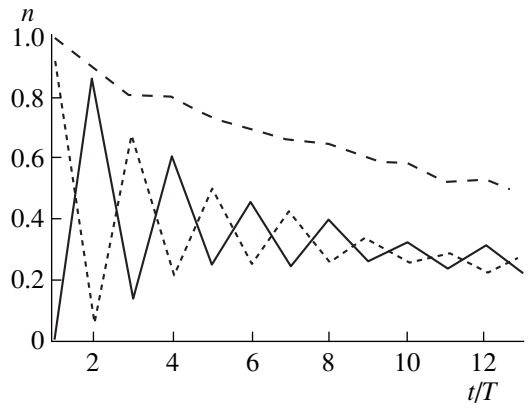

Fig. 3. Relative numbers of particles in two counterclockwise-rotating vortices. The dashed curve gives the total number of particles in two vortices. Normalized to the number of particles initially in the vortex.

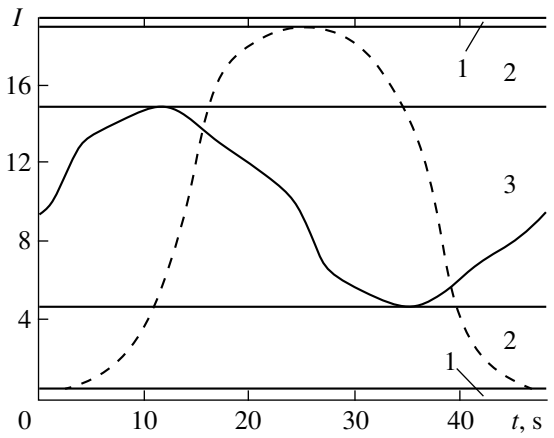

Fig. 4. Action at the separatrices of a model velocity field during an oscillation period. The solid curve corresponds to the global separatrix while the dashed curve corresponds to the inner separatrix. The action is given in arbitrary units. The intersection of the separatrices corresponds to the situation in Fig. 1a, a transition from diagonal circulation in one direction to diagonal circulation in the other. The situation in Fig. 1c is not achieved for the model field. The horizontal lines divide the entire range of variation of the action into regions (1, 2, 3) with different mixing characteristics.

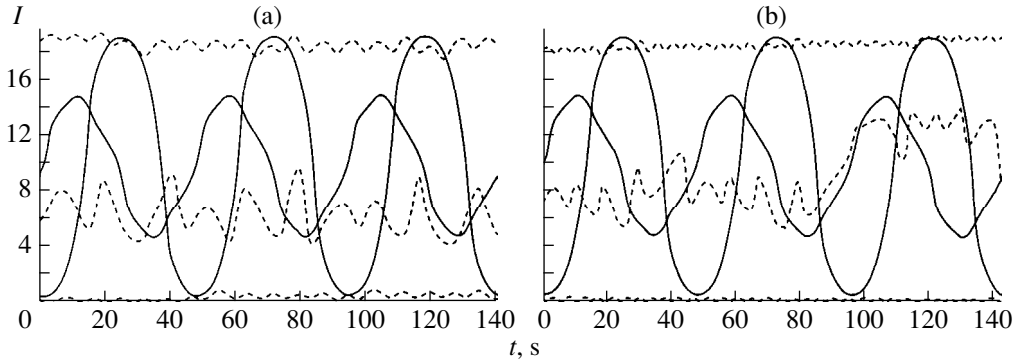

Fig. 5. Action for three particles in regions 1, 2, and 3 for (a) the model velocity field and (b) the doubled velocity field.

evolution of phase instability, the change in the action may be considered to be a random quantity whose spread amplitude depends on the parameter α/β. In an numerical experiment we can increase the adiabaticity parameter by increasing the amplitudes of all the harmonics in the expansion of the stream function. In Figs. 5b and 5c the particle velocities and consequently the adiabaticity parameter are doubled. The figure shows that the variations in the action decrease as the adiabaticity parameter increases although the action jumps for particles whose trajectories are confined near the separatrix may be appreciable.

The theory of adiabatic chaos can provide a fairly good interpretation of the experimental results. The entire flow is clearly divided into separate regions with different mixing rates within these regions. Region 1 is not observed for the experimental flow because of the influence of higher harmonics neglected in the numerical simulation (in model flow this occupies a small part of the phase space). Mixing between regions 2 and 3 only takes place as a result of particles whose action is situated near the boundaries of the regions. Consequently this mixing is a slower process. Figure 6a shows histograms constructed using the results of the laboratory experiment described above, which give the evolution of the particle distribution in terms of the action plotted in arbitrary units for the entire flow. The entire action range is divided into 20 intervals where the regions of high and low values (four intervals each) correspond to the interior of the isolated and combined vortices (region 2). The central part corresponds to the near-separatrix layer (region 3). The thin solid line shows the initial particle distribution over the action while the heavy solid line shows the distribution after 12 oscillation periods. Each region is characterized by a more or less uniform concentration distribution whereas equalization of the action concentrations between the regions is a slow process. This is demonstrated in Fig. 6b which gives the time evolution of the relative numbers of particles inside the isolated vortices (counterclockwise rotating), the combined vortices (clockwise rotating), and in the separatrix layer. We note that although phase mixing takes place considerably faster, it also does not immediately lead to a uniform distribution which suggests that additional "islands" of stability may exist in phase space. Attention was drawn to this effect in [21] although it requires further study.

Figures 6c–6f refer to a similar experiment but the particles were situated in the separatrix layer not inside a vortex. Figures 6c and 6e were plotted for oscillation phases shifted by half a period. The heavy lines correspond to observation times of 16 and 18 periods. In Fig. 6c the region of isolated vortices corresponds to higher values of the action. The dip near the 15th interval corresponds to the position of the outer separatrix for this phase. Here the wall regions of the cell where the tracer particles penetrate to a lesser extent also make a contribution. After half a period the outer separatrix corresponds to the fifth interval and we observe a dip there. Figures 6d and 6f show that from $t = 15T$ (T is the oscillation period of the system) the numbers of particles in each region are almost constant but the difference between the two type 2 regions is already appreciable. We made special measurements for two phases of the period in order to show that these are not associated with the choice of phase. Quite clearly the difference disappears at an even longer time. Some difference between the similar dependences in Figs. 6d and 6f may be attributed to the fact that the action boundary between the vortices and the separatrix layer is not exact because the action step is too coarse.

5. ANALYTIC MODELS OF TRANSPORT IN ACTION SPACE

Experiments have shown that the behavior of the Lagrangian trajectories of liquid particles transporting a passive scalar combines regular and stochastic traits. By isolating a compact particle cloud at a certain time, we can see that up to a specific moment it moves over certain orbits with barely varying action, its phase becoming extended as would occur in a steady-state spatially inhomogeneous flow. The isolated particles or particle clusters gradually begin to drift to other orbits. Thus, we obtain a process similar to random walk in

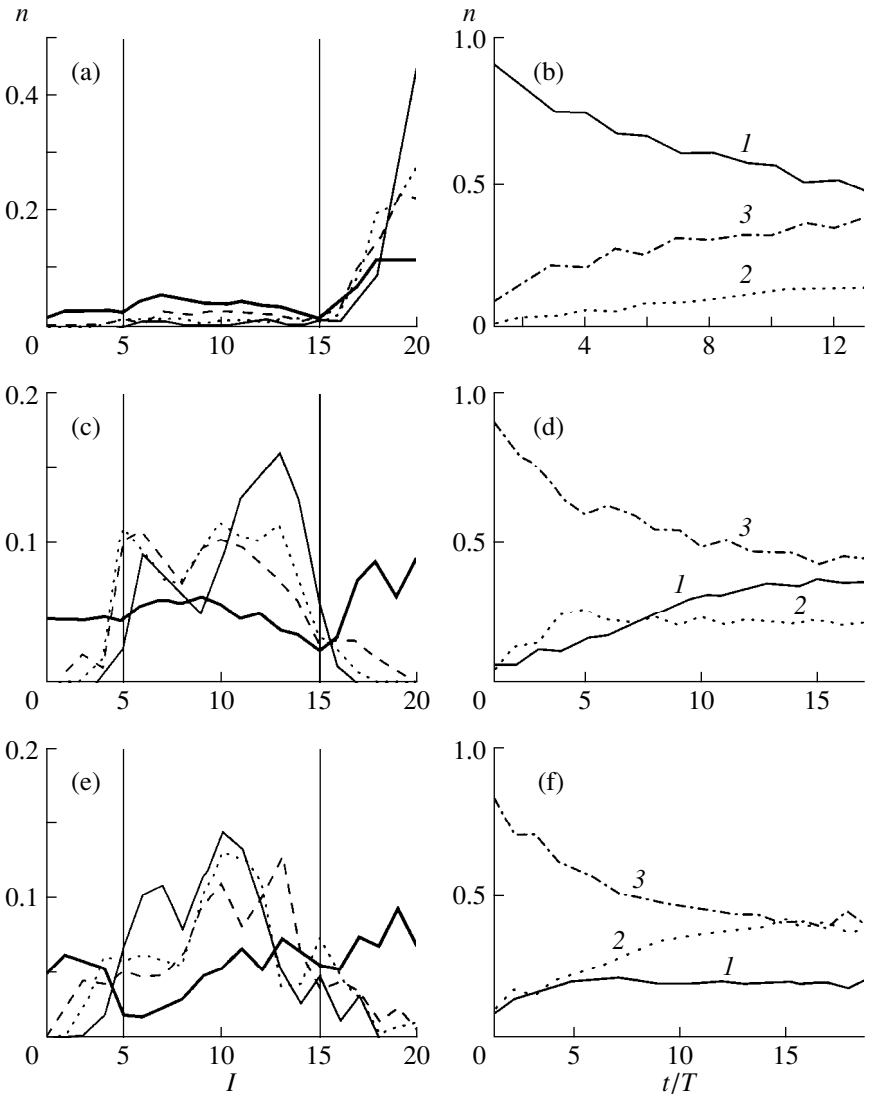

Fig. 6. (a), (c), and (e): distributions of the relative particle concentration over the action; (b), (d), and (f): and relative numbers of particles in the vortices (curves *1*), combined vortices (curves 2), and the separatrix layer (curves *3*). (a), (c), and (b): the thin solid line gives the initial distribution, the heavy solid line gives the final distribution after (a) 12, (c) 16, and (e) 18 periods; the dotted curve gives the distribution after one period and the dashed curve gives that after two periods. The particles are located in, (a) and (b), the vortex or, (c)–(e) the separatrix layer. Observations are made at times, (c) and (d), $t_0 + nT$ and, (e) and (f), $t_0 + (n + 1/2)T$.

action space. Through each point on the action–time plane there passes an infinite number of trajectories which can be considered as belonging to a random ensemble on the basis of the assumption that the successive action jumps across the separatrices are independent [16–19]. The characteristics of the process are the particle lifetime in a particular orbit and the jump in action space. Similar models were considered in [9] for example for the simplest flows.

We shall describe the trajectories $I(t)$ using a Poincaré mapping [3] at times $t_n = t_0 + nT$. The description of the process can also be simplified by roughly approximating the range of action values. We shall consider two models in which the random sequence $I(n)$ is a Markov process. The first model assumes random jumps in action space at times t_n which are described by the transition probabilities $W(I_i, I_j)$. The second model considers particle random walks on the plane (I, t) which are described by the transition probability $W(I_i, t_l, I_j, t_m)$.

In order to select the model for the description we consider the dependences of $I(t_0 + T)$ on the initial action $I(t_0)$ plotted in Fig. 7 which were obtained by numerical simulation for various values of the adiabaticity coefficient, Constructing these dependences involves following a large number of particles which is technically difficult in a laboratory experiment. The distributions plotted in Fig. 7 were obtained by integrating 5000 trajectories where the initial particle coor-

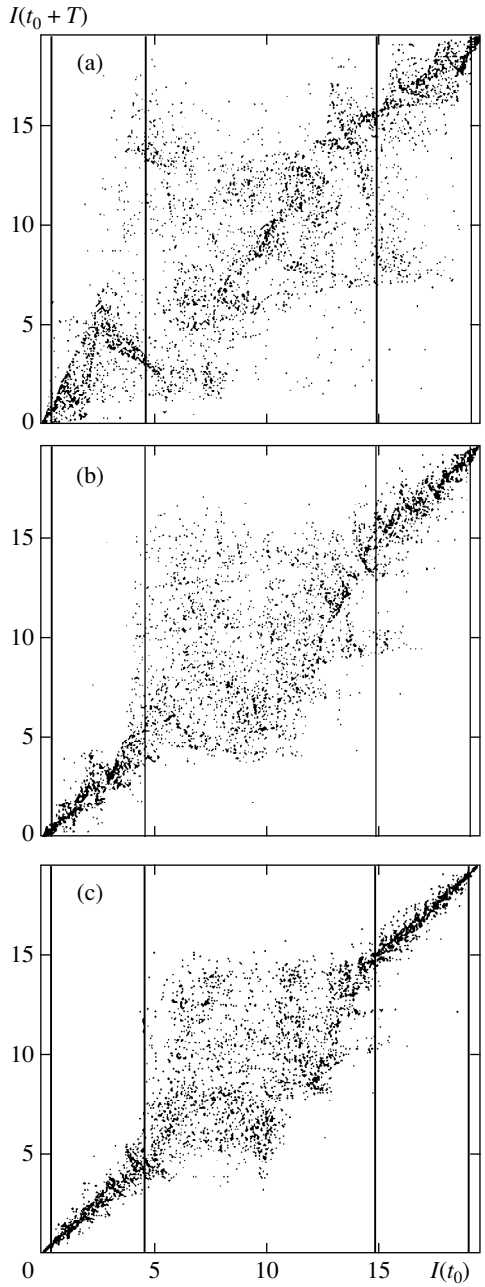

Fig. 7. Dependence of $I(t_0 + T)$ on $I(t_0)$ plotted for 5000 particles with random coordinates uniformly distributed over the phase plane of the flow: (a) model velocity field; (b) doubled field; (c) quadrupled velocity field.

dinates are distributed uniformly over phase space. The initial time was taken as the time when the outer separatrix divides the phase space into parts of equal action. As we have already noted, two regions 2 and 3 participating in the mixing can be identified in action space (separated by the vertical straight lines). In the separatrix region 3 mixing takes place fairly rapidly. In region 2, however, the particles are delayed around the initial action value. In Fig. 7a these differences are not yet very defined. However, in Figs. 7b and 7c where the velocities and adiabaticity coefficient are doubled and quadrupled, the two mixing processes can be identified quite clearly. If the mixing is characterized in terms of the mean square displacement of the action per period, it decreases with increasing adiabaticity. At the same time equalization takes place considerably faster inside region 3. For a doubled velocity field the concentration is almost equalized within two or three periods. The pattern observed in the laboratory experiment corresponds to slower mixing than that shown in Fig. 7. The reason for the greater "regularity" of the Lagrangian particle trajectories in the laboratory experiment can be found in the details of the velocity field which are not reproduced by the model field. Unfortunately, even the complete experimental field contains defects near the hyperbolic points which have low absolute values but are important for obtaining the more regular behavior observed in the laboratory experiment [21].

We shall consider mixing in the near-separatrix region using the first random walk model. Then, in order to describe the evolution of the particle number concentration we can use the Chapman–Kolmogorov equation for the particle number probability density for a given action:

$$f(I_i, n) = \int f(I_j, n-1) W(I_j, I_i) dI_j. \qquad (5)$$

For small perturbations of the steady-state velocity field (for small α) we can convert from this equation to the Fokker–Planck equation or its generalizations. In our case, however, the entire near-separatrix region begins to fill even after one period, as shown in Fig. 7. Thus, assuming that this filling takes place more or less uniformly, we express the transition probability in the form

$$W(I_1, I_2) = C\delta(I_2 - I_1) + (1 - C)/(D_3,) \qquad (6)$$

where D_3 is selected from the normalization conditions.

The solution of the equation describing the time-exponential equalization of the concentration within region 3 has the form

$$\begin{aligned} f(I, n) &= f(I, 0)\exp(n\ln C) \\ &+ \langle f\rangle(1 - \exp(n\ln C)), \end{aligned} \qquad (7)$$

where $\langle f\rangle$ is the concentration averaged over the layer. The coefficient C can be roughly estimated from the numerical or laboratory experiment using the mean-square displacement of the action per period. For the case of a doubled velocity field this value gives an estimate of the mixing time of around one period. It should be noted that the dependences in Fig. 7 still demonstrate some nonuniformity in the mixing of the action per period which suggests that the selected model is approximate. In addition, the equalization in region 3 is masked by mixing with the regions 2. The agreement between the model (7) and the experiment is improved by increasing the adiabaticity coefficient.

Particle exchange between regions 2 and 3 is more conveniently described using a different model in which the particle state in the region will be characterized by the lifetime in this region $\tau_2(m)$ and $\tau_3(m)$, respectively where m is the number of intersections of the boundary. For both regions we introduce the lifetime probability density $\varphi_{2,3}(\tau_{2,3})$. We shall assume that the lifetime in the region after the transition does not depend on the preceding lifetime. The probability density functions of the particle lifetimes in regions 2 and 3 determined using the numerical experiment are plotted in Fig. 8. The probability density function is plotted using the results of integrating the trajectories of 764 particles over 500 periods. As we can see, the function decreases with time almost according to a power law, which is consistent with existing theoretical concepts on the distribution of particle residence times in "traps" [5–10]. In the main time interval the exponent is close to –2. The "tail" of the function at long times has a "noise" character, indicating that the accumulated statistics is inadequate. Using the Montroll–Weiss approach [6, 8, 10], we write the expression for the particle concentrations in the layers in the form

$$n_i(t) = n_i(0)$$

$$- n_i(0)\sum_{m=1}^{\infty}\langle(\theta[t-t_i(2m-1)]-\theta[t-t_i(2m)])\rangle$$

$$+ n_j(0)\sum_{m=1}^{\infty}\langle(\theta[t-t_j(2m-1)]-\theta[t-t_j(2m)])\rangle,$$

where for the moments of the transition we have the expressions

$$t_i(2m-1) = t_i(1) + \sum_{k=1}^{m-1}(\tau_j(k)-\tau_i(k)),$$

$$t_i(2m) = t_i(1) + \tau_j(1) + \sum_{k=1}^{m-1}(\tau_i(k)+\tau_j(k)).$$

In this description we have gone over to a continuous time normalized per period since the particle transport over a single period can be considered to be small. We also note that the particle selected inside the region is characterized by two lifetimes. "forward" and "backward" (from the time of arrival until the time of observation and from the time of observation until the time of leaving the region) so that we need to define the distributions t_i (1). For simplicity we shall subsequently assume that the particles are at the interface between the layers, i.e., $n_i(0) = 0$, $t_{i,j}(1) = 0$. Then, using the properties of a θ-function and the independence of the successive particle residence times in the layers, we find

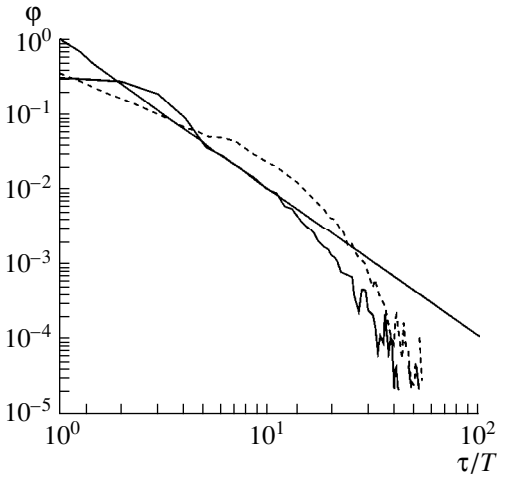

Fig. 8. Probability density of particle lifetimes in regions 2 (solid curve) and 3 (dashed curve) for transport in a model velocity field. The straight line gives the power law closest to the observed distribution.

$$n_i(t) = \frac{n_j(0)}{2\pi}\int\frac{dp}{p}\exp(pt)Q(p), \tag{8}$$

where the integral is taken over the complex plane and

$$Q(p) = \frac{S_j(p)[1-S_i(p)]}{1-S_i(p)S_j(p)},$$

$$S_i(p) = \langle\exp(-p\tau_i)\rangle = \int\exp(-p\tau)\psi_i(\tau)d\tau.$$

For $t \gg 1$ when the main contribution to the integral is made by the values of the function in the integrand for small p we have

$$n_i(t) = n_j(0)\left[\frac{1}{4}+\frac{1}{4}\int_0^t\psi(\tau)d\tau\right]. \tag{9}$$

In accordance with the numerical experiment we take

$$\psi(\tau) = \frac{2t_0}{\pi(\tau^2+t_0^2)}. \tag{10}$$

We then have

$$n_i(t) = n_j(0)\left(\frac{1}{2}-\frac{1}{2\pi}\frac{t_0}{t}\right). \tag{11}$$

This result indicates that the diffusion is anomalous, i.e., that the equalization of the concentrations is slower than exponential, which agrees qualitatively with the experimental results plotted in Figs. 6b, 6d, and 6f.

6. CONCLUSIONS

Laboratory, numerical, and analytic studies have been made of passive tracer transport in a nonsteady-state vortex hydrodynamic system. The fairly slow change in the velocity field in the system means that the experiment can be interpreted from the point of view of adiabatic chaos theory. The Lagrangian trajectories of liquid particles combine features of regularity and randomness, and the diffusion in action space is anomalous: they are accelerated in the near-separatrix layer and slowed in regions adjacent to the centers of the vortices. An approximate quantitative description of the diffusion process in action space can be obtained using generalized models of particle random walks. In this description phenomenological transition probabilities determined experimentally are introduced in the theoretical model. The theoretical models can be applied for fairly high values of the adiabaticity coefficient. It should also be noted that in order to achieve correspondence between the numerical and laboratory experiments the velocity field must be reconstructed very carefully, particularly near the singular points of the system. The phase mixing is also not completely uniform but this process requires further study. Of particular interest is a study of transport in hydrodynamic systems under conditions of two-dimensional turbulence [22].

ACKNOWLEDGMENTS

The authors are grateful to O.I. Karpilova for taking part in the experiments. This work was supported by the Russian Foundation for Basic Research (project nos. 98-05-64479, 99-05-64350, and 99-05-64351).

REFERENCES

1. V. I. Apnol'd, Usp. Mat. Nauk **24**, 225 (1969).
2. H. J. Aref, Fluid Mech. **143**, 1 (1984).
3. A. J. Lichtenberg and M. A. Lieberman, *Regular and Stochastic Motion* (Springer-Verlag, New York, 1982; Mir, Moscow, 1984).
4. G. M. Zaslavskiĭ, R. Z. Sagdeev, D. K. Chaĭkovskiĭ, *et al.*, Zh. Éksp. Teor. Fiz. **95**, 1723 (1989) [Sov. Phys. JETP **68**, 995 (1989)].
5. M. B. Isichenko, Rev. Mod. Phys. **64**, 961 (1992).
6. J.-P. Bouchaud and A. Georges, Phys. Rep. **195**, 127 (1990).
7. G. M. Zaslavsky, Physica D (Amsterdam) **76**, 110 (1994).
8. K. V. Chukbap, Zh. Éksp. Teor. Fiz. **108**, 1875 (1995) [JETP **81**, 1025 (1995)].
9. W. R. Young and S. Jones, Phys. Fluids A **3**, 1087 (1991).
10. S. Jones, Phys. Fluids **7**, 898 (1995).
11. V. Rom-Kedar, A. Leonard, and S. Wiggins, J. Fluid Mech. **214**, 347 (1990).
12. W. Hackborn, M. Ulucakly, and T. Yuster, J. Fluid Mech. **346**, 23 (1997).
13. E. Boss and L. Thompson, J. Phys. Oceanogr. **29**, 288 (1999).
14. I. M. Lifshits, A. A. Slutskin, and V. M. Nabutovskiĭ, Zh. Éksp. Teor. Fiz. **41**, 939 (1961) [Sov. Phys. JETP **14**, 669 (1962)].
15. A. V. Timofeev, Zh. Éksp. Teor. Fiz. **75**, 1303 (1978) [Sov. Phys. JETP **48**, 656 (1978)].
16. A. I. Neĭshtadt, Fiz. Plazmy **12**, 992 (1986) [Sov. J. Plasma Phys. **12**, 568 (1986)].
17. J. R. Cary, D. F. Escandy, and J. L. Tennyson, Phys. Rev. A **34**, 4256 (1986).
18. A. I. Neĭshtadt, D. K. Chaĭkovskiĭ, and A. A. Chepnikov, Zh. Éksp. Teor. Fiz. **99**, 763 (1991) [Sov. Phys. JETP **72**, 423 (1991)].
19. D. L. Vainshtein, A. A. Vasiliev, and A. I. Neishtadt, Chaos **6**, 514 (1996).
20. S. D. Danilov, F. V. Dolzhanskii, V. A. Dovzhenko, *et al.*, Chaos **6**, 297 (1996).
21. S. D. Danilov, V. A. Dovzhenko, O. I. Kappilova, *et al.*, Izv. Akad. Nauk, Fiz. Atmos. Okeana **35**, 810 (1999).
22. O. Cardoso, B. Gluckmann, O. Parcollet, and P. Tabeling, Phys. Fluids **8**, 209 (1996).

Translation was provided by AIP